HIGH PRECISION RADIAL-VELOCITY MEASUREMENTS OF LATE-TYPE EVOLVED STARS

A THESIS
SUBMITTED IN PARTIAL FULFILMENT
OF THE REQUIREMENTS FOR THE DEGREE
OF
DOCTOR OF PHILOSOPHY IN ASTRONOMY
IN THE
UNIVERSITY OF CANTERBURY
by

I. N. Cummings

University of Canterbury
1998

PHYSICAL
SCIENCES
LIBRARY
THESIS
copy 2

Abstract

Late-type evolved stars include the variable red giants, like Mira and semi-regular variables, and the pulsating supergiant RV Tauri stars. Despite this, K-type giants in the past were generally believed to be constant in photometry and radial velocity, but in the last decade it has been discovered that this is not necessarily the case. This was the motivation for spectroscopic observations of 44 late-type evolved stars to be carried out over three years, in the hope of helping to determine how common K giants variable in radial velocity are and whether the variations are related to those seen for other late-type evolved stars.

The observations were obtained at Mount John University Observatory and used with digital cross-correlation to achieve relative radial velocities of 50 m/s precision. At this precision all but eight of the observed stars were found to be variable in radial velocity. Thirteen stars also had broad-band photometry taken, because any one of orbital motion, rotation with starspots, pulsation and the motion of large convective cells could cause apparent radial-velocity variations. Knowledge of the relationship between light and radial-velocity variations can help distinguish between these different mechanisms.

The timescales for these different mechanisms were also estimated to help determine which was responsible for the variations observed. Generally the observed K-giant radial-velocity timescales were of the order of a few hundred days, which indicates they are due to one of binary motion, rotational modulation or non-acoustic non-radial pulsation. However, for M giants and supergiants the situation was very different with both short-term and long-term radial-velocity timescales being found in most stars. In most cases the short-term timescale is due to acoustic pulsation, while the long-term timescale could be due to any one of binary motion, surface features (including the motion of large convective cells) or non-acoustic non-radial pulsation.

Contents

List of Tables

Chapter 1

An introduction to red giants and supergiants

Red giants and supergiants are stars in an advanced state of stellar evolution. At the very least they have almost finished burning their stellar core of hydrogen and have contracted off the main sequence towards the right of the HR diagram (see Figure 1.1). As their core contracts the shell

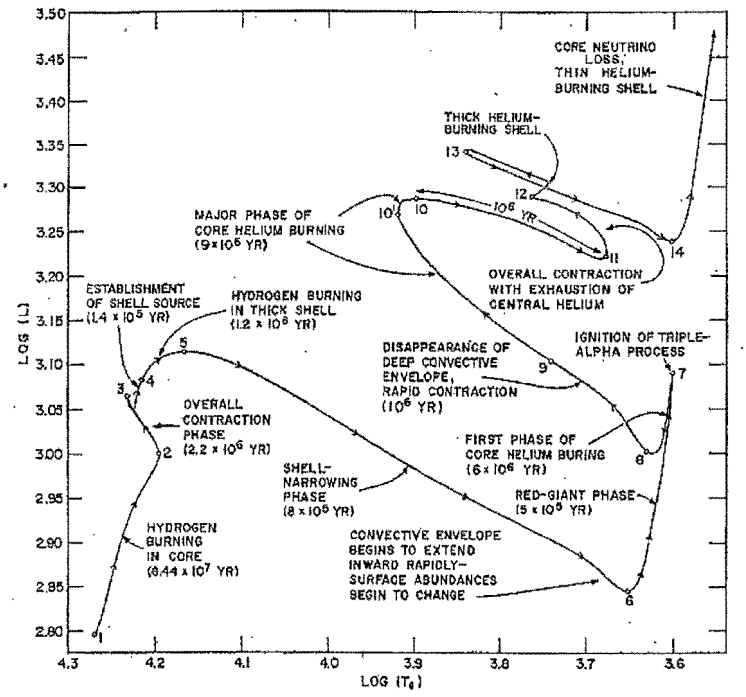

Figure 1.1: The evolutionary path of a metal-rich 5 $M_\odot$ star on the HR Diagram (from Iben [98] Figure 1). The red-giant tip is labelled (6), the instability strip is around (10'), the star is in its first giant branch from (6) to (7) and its second after (14). It should be noted that more massive stars are initially more luminous and therefore only the more massive stars ever become supergiants.

of hydrogen surrounding the core begins to burn (which slowly adds to the mass of the core), the radius of the star increases[1] and as a direct result the surface envelope cools causing the star to get

[1] Core contraction rises the temperature. A higher temperature in the core means a steeper temperature gradient in the star, which would imply more energy is being taken out. Usually this exceeds the energy production, so the star expands to lessen the temperature gradient.

redder. The drop in temperature also causes the envelope to become convective and this continues until the core contraction allows burning of the heaver elements left from hydrogen and the stars radius decreases again. When the heavier elements are exhausted the star may contract onto the giant region again in a similar manner (see Clayton §6-7 [36] and Iben [98] for more details). The second contraction into the red-giant region occurs as the star burns its helium shell and this is called the asymptotic giant branch (AGB). It is here that most of the stars observed for this thesis lie (some K giants will be in the first giant branch). AGB stars are very near their Hayashi line[2], which is the locus of fully convective stars in hydrostatic equilibrium (for further details see Hansen & Kawaler [69] §7.3.3 and Kippenhahn & Weigert [107] Chapter 24). As stars enter and leave the red-giant phase of their evolution they pass through the region of the HR diagram traditionally regarded as the "instability strip".

The instability strip lies to the left of the late-type stars on the HR diagram (see Figure 1.2). It is so called because of the large number of pulsating variable stars that lie in this region. Bound-

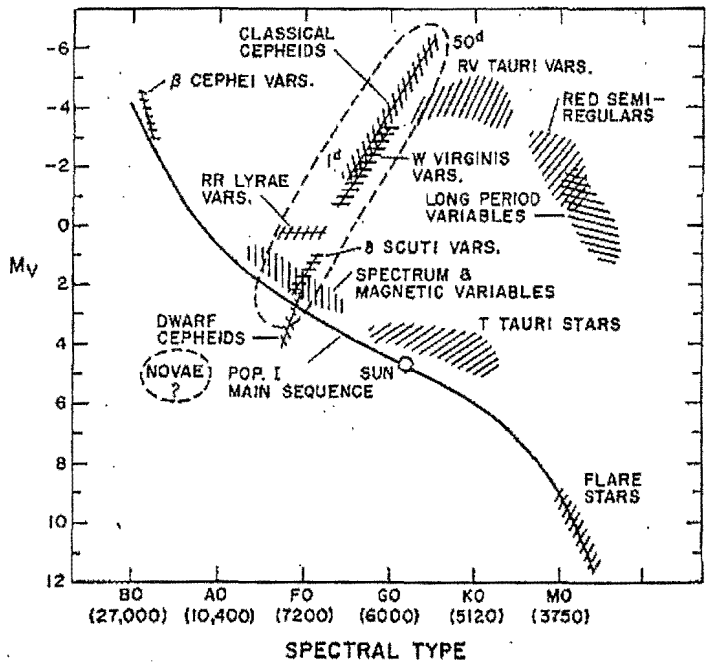

Figure 1.2: The location of various types of intrinsic variables on the HR diagram (from Cox [40] Figure 3.1). The instability strip is the nearly vertical oval shown by dashed lines.

ing the region containing the late-type giants and supergiants are the red variables, made up of the Mira/Long Period Variables (LPV) and the not as well understood semi-regular and irregular variables, and the the late-type supergiants RV Tauri stars. However, for a long time it was believed that the centre of the late-type giants' and supergiants' location on the HR diagram was an oasis of stability.

But as the precision of the radial-velocity measurements improved, spurred on by the hunt for Jupiter size planets and the desire to find the brown dwarfs which might explain the missing mass

[2]This line bounds the "forbidden" zone to the far right of the HR diagram. It is considered forbidden because it is not possible to build, using mixing-length theory, a fully convective model of a star in hydrostatic equilibrium if the temperature falls beneath a certain level. Hence only stars with time dependent convection and/or not in hydrostatic equilibrium will be found to the right of this line. Interestingly pulsating stars are not in hydrostatic equilibrium (see Clayton [36] page 130–134).

of the Galaxy, it became clear that this was not the case. One of the first stars to disturb this picture was the K giant Arcturus (α Boo). Observations of more K giants soon revealed it was not alone in its low-amplitude variability and that the radial-velocity variations being found were complex and not easily explained. They are multi-periodic, span up to two orders of magnitude in period and no one explanation seems consistent with all the variations seen in one star. Despite being sandwiched between the instability strip and the red variables, it is not clear if the variability is related to Cepheids or Miras, or if K giants are a new class of variable stars. The K giants known to show radial-velocity variations have been studied intensively, but there are not a large number of these. It is known that some K giants show no radial-velocity variability at the 10 m/s level and this leads to the question of how common these variations are. Observations of more of these stars are needed to see how common this phenomenon is, to help determine the cause of the variations and establish their relationship to other known variable stars.

It was with this in mind that research for this thesis was begun in 1993 with a wide variety of K and M giants and supergiants being surveyed for radial-velocity variations. Their spectral types were chosen to range across the less well understood region of the HR diagram, from K giants to red-irregular variables and hopefully to shed light on the causes of the small-amplitude radial-velocity variations found there, particularly those being found in the K giants, which previously were thought to be constant. It also was hoped the data obtained from this survey could help answer the question of the variable K giants relationship to the previously known variables, and whether there was any region of the HR diagram from Cepheids to red variables that could be regarded as being constant in radial velocity.

A brief history of the discovery of radial-velocity variability in K giants and how stellar variability is catalogued, along with a table with the designations given to the stars surveyed, follows.

1.1 The history of radial-velocity variation in K giants

In 1982 a number of people reported on the radial-velocity variation of α Boo. Campbell et al. [32] (see P.H. Smith et al. [157]) reported orally that the star had varied by about 100 m/s over two days and M.A. Smith [154] found a small spread of radial velocity over three days, which the author attributed to night-to-night errors. M.A. Smith was interested in finding oscillation analogous to the five-minute oscillations that had recently been found in the Sun and in 1983 (M.A. Smith [155]) he published a paper suggesting that his radial-velocity measurements in 1980 (with errors of 7 m/s) showed the detection of variations in α Tau and α Boo on the timescale of a few hours and with semi-amplitudes of under 10 m/s. He offered no explanation for these variations, but did note that they were far shorter than those expected for an analogue of the Sun's oscillations.

It was not until 1987 that the variability of α Boo was again reported. P.H. Smith et al. [157] published a paper reporting evidence of a periodic variation of about 1.8 days and 160 m/s during the end of 1985, which was compatible with the earlier oral presentation of Campbell et al. [32], but at odds with the timescale found by M.A. Smith [155]. The causes of this variation were unknown, but possibilities included radial pulsation in the second overtone and convective cells. Soon after this variability was confirmed by the independent research of Cochran [37] who (with radial-velocity measurements with $\sigma \approx 15-20$ m/s) found a period of about 2 days and a change in radial velocity of more than 200 m/s. The incompatibility with M.A. Smith's 1980 radial-velocity observations was noted and Cochran speculated that α Boo may have changed the timescale and amplitude of its radial-velocity variation in the time between the observations. He also discussed the possible explanations for these radial-velocity variations. Orbital motion was quickly discounted, as such a small period would mean a low mass companion would have to have an orbit within the red-giant

envelope. The period predictions of radial pulsation in the fundamental mode were too long, but he noted that there is no reason for only one mode to be present and multiple modes, such as are common for non-radial pulsation, could easily explain the data seen so far.

With the radial-velocity variation of α Boo now established beyond doubt, interest in its and other K giants' behaviour grew. In 1989 Irwin et al. [99] published newly reduced radial-velocity measurements for 1981–1985 of α Boo with a precision of 13 m/s. Short-timescale variations were certainly present and they thought the short-period components seen by other people might be the result of multi-periodicity resulting from global non-radial acoustic oscillations, like those of the Sun. However, the paper was mainly interested in the presence of a long-term period of up to 640 days. This is significantly longer than the expected radial-pulsation periods, so the main plausible explanations were:

- The presence of large and long-lived convective cells.
- Rotational modulation through starspots. In favour of this explanation $P_{\rm rot}(\max) \approx P_{\rm obs}$ and there were significant periodicities found in the variation of line widths in many lines (although the variations were only a few per cent).
- Orbital motion with a low-mass companion.
- Long-period beating of close short periods — this was not favoured as it does not produce as good a fit to the data.

That α Boo was not alone in its variations became apparent with the publication of Walker et al.'s [170] 1989 paper entitled "*Yellow giants: A new class of radial-velocity variable?*". Five K giants and one K supergiant had been observed from 1980 to 1986 and all[3] were found to be variable in radial velocity with amplitudes of 30 to 300 m/s. In every case the stars showed a significant variation on a long timescale, which was larger than their variations on shorter timescales. Also three of the stars showed significant variation on timescales less than a day and according to Hoffleit [92] all stars vary in light. Interestingly, while some like α Boo show a periodic variation which might be associated with rotation, some also have a highly variable chromospheric He I 10830 Å[4]. Furthermore, there is a nice correlation between the stars' radial-velocity scatter about the long-term mean and both the chromospheric K-line intensity and the amount of He I 10830 Å variability. However there is no correlation between the presence or absence of short-term radial-velocity variations and the K-line emission and the K-line intensities have long-term variations. This seemed to indicate there might be a link between long-term variations and chromospheric activity and they speculated about the presence of a long-period non-radial g-mode[5] pulsation which transports mechanical energy into the chromosphere. Nevertheless, they finish this important paper by saying that without more extensive data they cannot say whether these stars represent an extension of the Mira variables or Cepheids/RR Lyrae stars, or are in fact in a class all of their own!

As it was now apparent that radial-velocity variation may be a common intrinsic, yet unexplained phenomenon amongst the previously believed to be constant K giants, the behaviour of these stars began to be reassessed — for example Walker et al. [171] published a paper casting doubt on γ Cep being a good candidate for a Jupiter mass companion when it became clear in 1992 that it was a K giant. Case studies of examples of these stars also began to published. One of these papers was the 1993 paper of Hatzes & Cochran [73] on the previously observed stars α Boo, α Tau and β Gem

[3]The six stars were α Ari, α Tau, β Gem, α Hya, α Boo and ϵ Peg

[4]Temperatures of over 20000 K are needed for this line to form and densities of over 10^{12} electrons per cm^3 are needed for the line to be in emission rather than absorption (see Querci [136] page 138)

[5]For more details on non-radial pulsation, particularly p and g modes, see §2.3.5

which investigates the long periods previously noticed in these stars (more on β Gem, especially on chromospheric emission, was published at about the same time by Larson et al. [112]). The periods for data acquired over 1988–1991 (with a precision of about 20 m/s) are between 233 and 643 days with amplitudes of 100 to 500 m/s. Signs of short-term variations are also present in α Boo and α Tau. Although the time-span covered by these observations is not concurrent with any previously published work, α Boo's 233-day period is in agreement with the previous data sets and indicates the radial-velocity variation seems to have been present for at least the last 10 years with the same amplitude and phase! Similarly, α Tau's 643-day period indicates its long-period radial-velocity variation is long lived and coherent. There is less data for β Gem, but what there is, including the period found by Larson et al., does not seem to indicate this star is any different. So an explanation is needed for coherent long periods that persist for a decade. In addition, as other authors' work indicates the chromospheric He I 10830 Å line of α Boo has a period of 233 days, this explanation may also need to explain variations in He I 10830 Å (although β Gem is known to have a constant He I 10830 Å, according to Larson et al. it does have changes in chromospheric emission with a period of 589 days). The arguments for and against the main known causes of radial-velocity variation being responsible for these long periods are:

- If it was caused by low-mass companion the companion would have to be of Jupiter mass for all 3 stars. This is unlikely.
- As far as radial pulsation is concerned, Cepheid $P = P(R, M)$ relations give periods too short by a factor of 100 and the change in radius of the stars predicted by the radial-velocity curve is about 10%, which should produce large-photometric variations, but no such brightness variations[6] have been found.
- Non-radial pulsations are plausible. For M supergiants and K giants the ratio of radial to tangential mass-element displacements, particularly for g-modes, is very small so photometric variations would, as is seen, be small. On the other hand stochastic shocks produced by acoustic waves could provide a mechanism for forming the He I 10830 Å line but in order to do so the waves would have to have periods as short as the shortest seen in these stars. However α Boo's He I 10830 Å line needs to vary with a long period and its hard to see how this could arise from such short-period acoustic waves.
- Rotational modulation by surface features is plausible, as the maximum $P_{\rm rot}$ is not too small (it is too small for β Gem unless a recently derived value for $v_{\rm equ}\sin(i)$ is wrong — Larson et al.) and changes in He I 10830 Å may be further evidence in favour of this explanation[7]. However, variations lasting 10 years, coherent yet not causing photometric variations or large changes in line width, seem to discount star spots or plages.

While the longer period radial-velocity variations were a continuing mystery, the shortest periods seen in these stars seem to be explicable by pulsation. The first star to have a convincing explanation of it variations by pulsation was α Boo. In 1990 the idea of acoustic oscillations in this star began to become very popular — Balmforth et al. [7] investigated whether such pulsations might be excited in α Boo and concluded that it was indeed possible[8] and Belmonte et al. [17] presented a paper interpreting the simultaneous photometric and spectroscopic observations of α Boo over 10 days in 1988 as a combination of radial pulsation and many non-radial acoustic oscillations. This mixed pulsational mode explanation of the shorter periods of α Boo was taken up again in

[6] Hoffleit [92] does list these stars as variable, but a search of the literature did not reveal any such photometric variations being published (private communication)

[7] If He I 10830 Å formed on the star's surface in an active region then its variation might reflect the rotational period of the star

[8] They considered the growth rates of radial modes

1994 and compared with other possibilities by Hatzes & Cochran [75]. They presented results of intensive observations taken over 8 nights in 1992, which show periods of 2.46, 4.03 and perhaps even 8.5 days. The 1.84-day period seen by observers around 1985 was not present and as it is unlikely that either period is in error, they feel the only logical conclusion is that the star has switched modes. Although there is some uncertainty regarding the mass of this star, the most likely scenario is that α Boo was originally radially pulsating with a 1.84-day period then switched to a lower mode pulsation of period 2.46 days where this latter period could be fundamental or first over-tone depending on the mass. In favour of this radial-pulsation explanation, if the Cepheid's velocity-amplitude relationship is used photometry should have a variation of a few milli-magnitudes, which is what was found by Belmonte et al. with a period of about 2.5 days. However, non-radial pulsations can not be discounted. If the 8.5-day period is present in the data and if it was to be the fundamental radial mode of the star, then the two shorter periods are not well explained by first and second over-tone modes, which could mean they are non-radial pulsations. Regardless of the fine details, they conclude that α Boo's short-period variations are certainly caused by some kind of pulsation.

In 1994 Hatzes & Cochran [75] noted that not all K giants exhibit short-term variations. For one of the stars they observed they predicted a radial fundamental mode which should have been easily detectable, yet no significant radial-velocity variations were seen at all. They therefore urged others to undertake more observations to see if radial pulsations are indeed present in other K giants. By the end of the year they published another paper, on the K giant β Oph, yielding further light on the short-term variations seen in these stars (Hatzes & Cochran [74]). Their observations on β Oph in 1989 and 1992 give periods of 0.8 or 0.5 days and 0.3 days respectively. These short periods can only result from pulsation, as a low mass binary would have its semi-major axis within the stellar radius and the period of rotation expected for a giant star is the order of a hundred days. If the 1989 and 1992 periods are indeed different then this star, like α Boo, must be mode switching. The two possibilities for pulsation are radial or non-radial. The former could explain the 0.3-day period with a second over-tone pulsation if the current best value of $\log g$ is too low. If $\log g$ is correct, then high-order radial modes are needed to account for such a short period. Non-radial acoustic pulsations could easily explain these periods, however, as oscillations with $l = 1, 2$ yield periods of 2–16 hours for late-type stars.

Further evidence for the presence of non-radial pulsations comes from a later paper in 1996 on β Oph. In it Hatzes & Cochran [76] report the existence of another period in this star of 13 days. This period is too long for radial pulsation, yields a binary orbit very close to the star and is far too short to be rotational modulation, as the rotational velocity implied by a 13-day period would be a significant fraction of the break-up velocity of the star (a 142-day period is present, however, that could be explained by rotation). Hence this period is best explained by non-radial pulsation, in this case in a g-mode. This means that β Oph is like α Boo, in that it is multi-periodic with periods present that span two orders of magnitude. These two stars may represent a new class of radially and non-radially pulsating stars.

1.2 Types of variable stars

Stellar variability types are for the most part assigned from considerations of the variability of stellar photometry. The following designations of stellar types are important for late-type evolved stars and the meaning of the letter abbreviations are generally standard, although a small amount of variation

[9]This star is not present in the Michigan 2-D survey of spectral types so this value is taken from the SC2000

[10]This star is present in The Sky Catalogue 2000.0 V2 [91] as a spectroscopic binary (no other stars have this distinction)

Star Name	Hipparcos I. D.	Spectral Type	GCVS+NSV Variability Type	Hipparcos Variability	Hipparcos Variability Type
3 Cet	355	K3Ib[9]	var?	M	
η Scl	2210	M2/M3III	LB	U 2	L
γ Phe[10]	6867	K4/K5 III	LB:	P 1	SR Δ
ψ Phe	8837	M4III	SR	U 2	SR
τ^4 Eri	15474	M3/M4III	LB	U 2	L
γ Hyi	17678	M1III		U 2	SR $\star$
γ Ret	18744	M4III	SR	U 2	I Δ
η^2 Pic	23649	K5III	var?		
ϵ Col	25859	K1II/III			
β Col	27628	K1.5III†			
η^2 Dor	29353	M2III	var?	U 2	I Δ
o^1 CMa	33152	K3Iab	LC	U 2	LC
σ CMa	33856	K4III	LC	U 2	L
L^2 Pup	34922	M5e	SRB	P 1	SRB
π Pup	35264	K3Ib†	var?	U 2	SR Δ
HR 3017	37819	K4III	var?	U 2	
NS Pup	40091	K4III	LC	U 2	L
ϵ Car	41037	K3:III+B2:V†	E:	U 2	E:
β Vol	41312	K1III	var?		
λ Vel	44816	K4III	LC	U 2	L
κ Pyx	44824	K4/K5III	var?	U 2	
N Vel	46701	K4/K5III	CST:	M	
V337 Car	50371	K3II	LC	M	
GZ Vel	50555	K3II	LC	U 2	LC
γ Cha	51839	K5III	var?	M	
HR 4177	52102	K4/K5III:		D	
ϵ Mus	59929	M5III	SRB:	U 2	SR
ϵ Cru	60260	K3/K4III	var?		
γ Cru	61084	M4III†	var?	U 2	I Δ
2 Cen	67457	M5III	SRB	U 2	SR
σ Lib	73714	M3/M4III	SRB		
ϵ TrA	76440	K1/K2III		C	
δ^1 Aps	80047	M4III	LB:	U 2	LB:
α Sco	80763	M1.5Iab†	LC	U 2	L Δ
HR 6166	81304	K5III		U 2	
α TrA	82273	K2II		M	
ϵ Sco	82396	K2IIIb†	var?		
β Ara	85258	K0/K1Ib		M	
η Sgr	89642	M2III	LB:	U 2	L
62 Sgr	98688	M4III	LB	U 2	L
ω Cap	102978	K4III	var?	M	
24 Cap	104234	K5/M0III		U 2	$\star$
δ^2 Gru	111043	M3III	LB:	U 2	LB:
β Gru	112122	M5III(W)†	LC:	U 2	LC:

Table 1.1: **Variability types for the stars surveyed for this thesis.** GCVS is the 1985 General Catalogue of Variable Stars [105] and NSV is the New Suspected Variable Catalogue [104]. (var?) designations under variability type are stars which were in the NSV, but were not given a variability type. More details on the Hipparcos variability designations are available in Table 1.2. The spectral types have been taken from the Michigan Catalogues of Two-Dimensional Spectral Types [96, 94, 95, 97] whenever possible († means the spectral type given in the catalogue was actually taken from another source). In all cases (:) means the identification, be it of variability or spectral type, is uncertain.

Flag	Origin	Description
C	Main Cat.	Star not detected as variable
D	Main Cat.	Duplicity variable (may be due to multiple system)
M	Main Cat.	Possibly micro-variable
P	Main Cat.	Periodic Variable (supersedes D)
U	Main Cat.	Highly likely micro-variable and 'unsolved' (incl. irregular & semi-regular)
□	Main Cat.	Could not be identified as variable or constant
1	Main Cat.	Variability less than 0.06 mags
2	Main Cat	Variability 0.06 to 0.6 mags
3	Main Cat	Variability more than 0.6 mags
$\star$	Var. Annex	Newly-classified variable
Δ	Var. Annex	Newly-assigned variability type

Table 1.2: **Descriptions of "Hipparcos variability" for Table 1.1.** These originate from the Hipparcos catalogue §2.1 and §2.4 where "Main Cat" is the type of variability as given by the main Hipparcos catalogue and "Var. Annex" is for variability given in the variability annex. The Variability Annex uses variability types from the GCVS and NSV catalogues, where available, and updates and defines types as appropriate.

within the literature exists (see Table 1.1 for the designations given to the 44 K and M giants and supergiants surveyed by this thesis). The General Catalogue of Variable Stars [105] (GCVS) and Sky Catalogue 2000.0 [91] (SC2000) are the main references used to obtain the following descriptions of variable star types. The interchangeability of the designation (I) and (L) should be noted, as should the seemingly arbitrary way with which these irregular and often under-observed stars have their variations equated to an eruptive or pulsating nature. As a general rule, it is safest simply to take (I) to mean irregular and (L) to mean slow irregular.

(E) Eclipsing binary system. In order for this to be seen the inclination of the binary orbit must be so near 90 degrees that one star passes in front of the other along the observer's line of sight[11]. Hence periodic changes of the apparent combined brightness of the system are seen.

(I) The exact meaning of this designation varies depending on the literature. In all cases it refers to irregularly varying stars, as does L. GCVS uses I to indicate eruptive variable stars which have been poorly studied (as does the Hipparcos Catalogue). By contrast SC2000 uses I for pulsating stars.

(L) SC2000 uses L to mean slow irregular variables which show very poor, if any, periodicity. Stars may be attributed to this type if insufficiently studied. GCVS uses the same definition of this variable type, but associates the variations with pulsating variables.

(Lb) Slow irregular variable giants of spectral type K, M, C and S. This may also refer simply to a slow red variable if the star's spectral type and luminosity are unknown.

(Lc) Slow irregular variables which are late-type supergiants.

(M) Mira Ceti-type variables. These stars are pulsating giants with M, C or S-type spectra showing emission lines. The light curves show long-period variations with light amplitudes from 2.5 to 11 magnitudes in V. These stars have periods longer than 80 days and are sometimes also called long-period variables.

(RV) RV Tauri-type variables. These stars are radially pulsating supergiants with a spectral type that varies between F–G at maximum light and K–M at minimum light. The light curves show alternating deep and shallow minima with amplitudes of up to 4 magnitudes in V. The

[11] The chance of this happening is not very high unless the stars are in a close binary orbit (see §2.1 for the definition of a close binary orbit, as it is being used here)

minima can vary in depth and cause the primary and secondary minima to "switch". The time between successive primary minima is typically 30–150 days. This class is also sometimes split into two subclasses, RVa and RVb, where the latter also exhibits a longer-term variation in radial velocity and light of 600–2500 days (for more details see Pollard [133] page 260).

(SB) Spectroscopic binary system. This will not be apparent from photometric observations, but this designation is included here because radial-velocity measurements can detect these systems and hence this is a possible explanation of radial-velocity variations seen in the stars surveyed.

(SR) Semi-regular variables. These stars are giants or supergiants of intermediate to late type whose variability is mainly caused by pulsation (this type may also include variation due to rotational modulation). The light curves are quite periodic, but show occasional irregularities. The periods range between 20 and 1000 days or more and the amplitudes are diverse, but generally less than those of Mira Ceti-type variables.

(SRa) Semi-regular giants of spectral type M, C or S with a persistent period. For many of these stars their only difference from Mira variables is the the difference in amplitude of their light curves.

(SRb) Semi-regular giants of spectral type M, C or S with a poorly defined periodicity. This designation is also given to stars whose regular periodicity is alternated with slow irregular changes.

(SRc) Semi-regular supergiants of spectral type M, C or S.

(SRd) Semi-regular giants and supergiants of F, G or K spectral type. Some stars have emission lines in their spectra.

For more details on variable star types also see Hoffmeister [93], Strohmeier [160], Chapter 11 of Allen [4] and in particular for light curves see Chapter 3 of Sterken & Jaschek [159].

Chapter 2

Causes of radial-velocity variations

Radial-velocity variations can be caused by a diverse range of phenomena, from real variations due to binary orbits and pulsations to apparent variations caused by surface phenomena. Often light variations are associated with the mechanism and its relationship to the radial-velocity variations can be invaluable in determining the cause of the observed variations. The causes of radial-velocity variations and the resulting changes in velocity and luminosity will now be discussed in more detail.

2.1 Binary orbits

Two bodies will exert a gravitational force on each other, and if they are in a uniform gravitational field and do not have enough kinetic energy to escape their mutual gravitational pull, then it can be shown (for a derivation see Kibble [106] Chapters 4 and 7) that their orbit about their centre-of-mass will be an ellipse. This motion will have a period whose square is proportional to the cube of the semi-major axis, divided by the total mass of the system. When two stars are in such a closed orbit it is called a binary system.

Binary systems can be classified according to their method of observation. The disadvantage of this is each classification is not unique and to a large degree will be determined by the distance the system is away from the Earth. Nonetheless the techniques used to observe these different classes of binaries are quite distinct, so this classification system will now be described. The most important type for this thesis is spectroscopic binaries. These are binaries which are discovered spectroscopically from variations in their radial velocities as they orbit about their centre-of-mass. Other types of binaries include: visual binaries, which can be resolved as two separate stars using a telescope; astrometric binaries, which are discovered by the measurements of the positions of one component against a background of field stars; spectrum binaries, which have a composite spectrum, but changes in radial velocity too small to detect; eclipsing binaries, which have their orbital plane at $i \approx 90\,\mathrm{deg}$, so that they eclipse each other as they orbit their centre-of-mass, hence causing periodic variations in light and ellipsoidal variables, which also cause a periodic variation in light due to distortion in their mutual gravitation field. For more details on classification systems see Batten [14] Chapter 1.

The last of these is an example of a close binary system, where here "close" means the stars orbit so near to each other that they undergo tidal interaction, as opposed to meaning one component affects the evolution of the other (Batten [14] page 6). Close binary systems typically must have periods of only a few days, or less, and come in three flavours: detached, semi-detached and contact. These systems show a variety of complex effects in their photometry and radial velocities includ-

ing: apsidal motion[1]; reflection of one component's light by the other; distortion of the light curve (ellipsoidal variables) due to the non-spherical components presenting faces of different area to the observer; mass transfer between components and its resulting circumstellar matter, which can cause abrupt changes of period, light-curve distortion and radial-velocity curve distortion (see Batten [14] Chapter 4 and 8). For more details on close binary systems see Batten [14], Strohmeier [160] Chapter 7 and Hoffmeister [93] Chapter 4.

As at least[2] 30% of late-type giants are in spectroscopic binary systems (see Jascheck & Gonez [100]), it is quite plausible that a significant number of the late-type giants and supergiants observed for this thesis have radial-velocity variations that are due to their being in a binary orbit. For wide binary orbits (systems which are not close) stars will have a radial-velocity curve that, unless the eccentricity is significantly greater than zero, looks sinusoidal. It will be very regular and repeat exactly[3]. If the eccentricity of the system is large the radial-velocity curve will still repeat exactly, but will be distorted from a sine curve (see Figure 2.1).

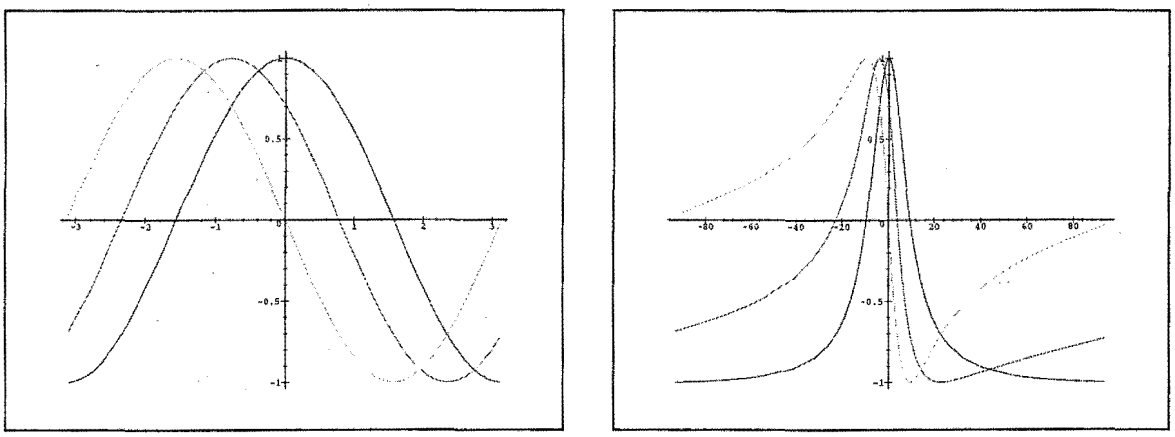

Figure 2.1: These two figures give, within a constant value, the observed radial velocities for binary systems between times of $-P/2$ and $P/2$, where P is the period of the orbit. The three curves in each figure (from the top left) have longitudes of periastron of 90, 45 and 0 degrees respectively. The figure to the left is the radial velocities for a circular orbit while that to the right is those for a highly eccentric ($e = 0.9$) orbit. As can be seen, the latter is highly distorted from a sine curve and changes significantly depending on the orbit's orientation with respect to the observer.

No photometric variations will be visible in a wide binary system unless it is an eclipsing binary. In this case the photometric variations consist of two minima in the light every period, corresponding to the eclipse of one star by the other. The light will be constant between these two dips. The two minima will be of unequal depth unless the two stars are of the same surface brightness and will

[1]The direction of the major axis of a system is called the line of apsides. If the two bodies can be considered mass points, the gravitational field they are in is uniform and they move in accordance with Newton's laws, then this line should be constant. For close binaries the first of these conditions is invalid and the line of apsides rotates (see Batten [14] Chapter 6).

[2]This 1970 figure is based on observations comparing radial-velocity dispersion in constant radial velocity stars with dispersion for non-intrinsic variables. This gives the percentage of stars variable in radial velocity. The limiting precision of the time means the radial-velocity variability of intrinsic K-giant variables is in the noise level and hence the 30% figure found for them is valid as the percentage of large amplitude spectroscopic binaries. The total percentage of late-type giants in binary systems is most likely larger than this, due to the limiting precision of the observations (see Batten [14] Chapter 2 for a discussion of this selection effect), but any higher precision studies will need to be careful to remove small-amplitude intrinsic variables from their sample.

[3]Unless the star is in a close binary or it is not a binary but a multiple star system

only be equally spaced if the orbit is circular, or if the longitude of periastron[4] is 90 or 270 degrees (see Figure 2.2).

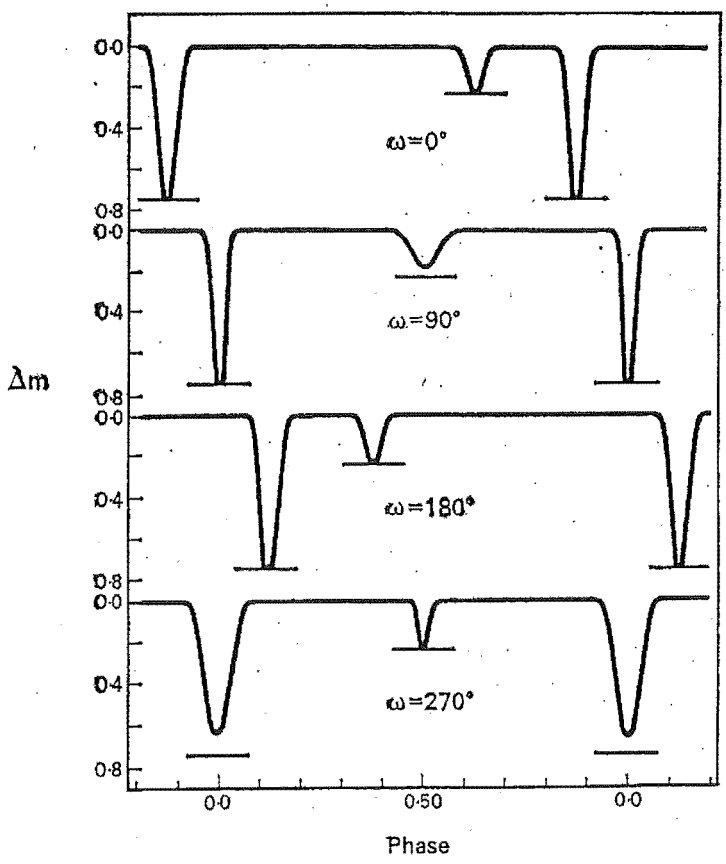

Figure 2.2: This figure illustrates the effects of eccentricity on epochs, widths and depths of minima for an eclipsing binary system, at different values of the longitude of periastron (ω). This binary has an eccentricity of 0.4 and, as can be seen, the two minima are equally spaced only when ω is 90 or 270 degrees. This is Strohmeier's [160] Figure 54.

2.2 Surface features

Both rotation and macroturbulence cause line broadening. In the case of the convective cell component of macroturbulence the line broadening is asymmetric. This would lead to an error in the determination of the absolute radial velocity of the star, as the true position of the line is hard to determine. But, as this thesis determines radial velocities by the cross-correlation of two spectra, as long as the two spectra have the same profiles the cross-correlation will be symmetric and therefore the relative radial velocity obtained will be free of such error. However if the asymmetry were to change with time, a relative radial-velocity variation would be found. Such a change could arise if the convective cell distribution were to fluctuate far from its mean or if the star were rotating and had some kind of surface feature like a starspot. Even for solar-type stars it is thought convective cell distributions and starspots might cause radial-velocity variations of tens of metres per second (see Dravins & Nordlund [47] §7).

[4]The longitude of periastron is the angle between the line of apsides and the line formed where the plane of the orbit intersects the plane of the sky

2.2.1 Convective cells

Energy generated in the centre of a star can be carried out in a variety of ways. This is mainly done via the mechanism of heat transfer[5] and in the diffusive-heat transfer cases of radiative transfer and conduction, the heat transported is proportional to the temperature gradient. However in the simple case of the standard-model polytrope[6], the heat flux is directly proportional to the temperature gradient times the inverse of the stellar opacity — so a very high opacity, or large flux, would require the temperature gradient to increase accordingly. There is a certain limit to this and when this is reached convection occurs (all stars later than about F5, depending on luminosity class, have at least partially convective envelopes). Convection is not a radiative process, instead actual cells of gas rise and fall, transporting heat as they do so. To see how this is possible consider a mass element which is displaced to a larger radius. It will expand to enable its pressure to remain the same as its surroundings, but in general its temperature and density will not be equal to its surroundings. Now if the mass element is denser than it surroundings, it will sink back to its original position and any energy transportation must be by another means. But if the surroundings are denser than the mass element it will continue to rise and energy is transported out of the star as heat from the hot mass element leaks into the cooler surroundings. This places a condition on when energy transport by convective cells occurs. If the cells expand adiabatically, the requirement that the cell be less dense than its surroundings becomes a requirement that the magnitude of the change in temperature (with radius) of the star be greater than the magnitude of the change in temperature (with radius) of the cell. Hence the convection instability condition[7] for a star is that its temperature gradient be greater than the adiabatic temperature gradient. Of course to preserve mass cells must also, in a similar manner, sink down into the star. There are no fully satisfactory models for this complex behaviour, but a common one is the mixing-length model. In this each convective cell rises or falls adiabatically for a distance, l, called the mixing length. After travelling this distance the cell thermalizes with the local environment (for more details see Clayton [36] §3-5).

The Sun uses convection to transport energy to around the bottom of its photosphere. There the convective cells give rise to a mottled appearance and are known as granulation (see Figure 2.3). There are also much larger convective cells seen on the Sun and these are simply called supergranulation[8]. With stars, however, it is not possible to see the individual convective cells — just the integrated stellar light. This typically results in a broadening[9] of stellar lines due to the velocities of the cells as they rise and descend. Such broadening of stellar lines is called macroturbulence[10], although this parameter can include contributions from not just granulation and supergranulation, but even things like very small amplitude, short period oscillations. See Gray [56] Chapter 18, Gray [60] or Gray [59] for more details.

However, over the last few decades it has been proposed that in red giants and supergiants convective cells may not simply result in line broadening. In 1975 Schwarzschild [149] published a paper which concluded for red giants and supergiants the minimum size of the convective cells dominating the brightness fluctuations is so large that at most a few hundred of them could occupy the total

[5]Heat is energy possessed by a substance in the form of kinetic energy — e.g. atomic translation and rotation vibration. Another significant source of energy transfer is neutrino emission and this emits energy directly from the interior into space, without interacting with the stellar matter.

[6]A polytrope is a gaseous sphere in hydrostatic equilibrium (the pressure and gravity forces on each volume element in the sphere sum to zero), in which pressure, P, and density, ρ, are related by $P = \alpha\rho^{(n+1)/n}$, where n is called the polytropic index and α is any constant. A polytrope with a polytropic index of 3 is called the standard model.

[7]As cells do not necessarily expand adiabatically, satisfying this condition does not guarantee convection

[8]This weak convective pattern arises beneath granulation and gas flowing from the centre of the supergranules to their edge concentrates magnetic fields at their boundaries. The enhanced magnetic fields at their borders become visible in formations in the chromosphere.

[9]Importantly, as the descending cells are less luminous than the ascending ones, the broadening will be asymmetric!

[10]This can be distinguished from micro-turbulence and rotational broadening by the "shape" of the broadening

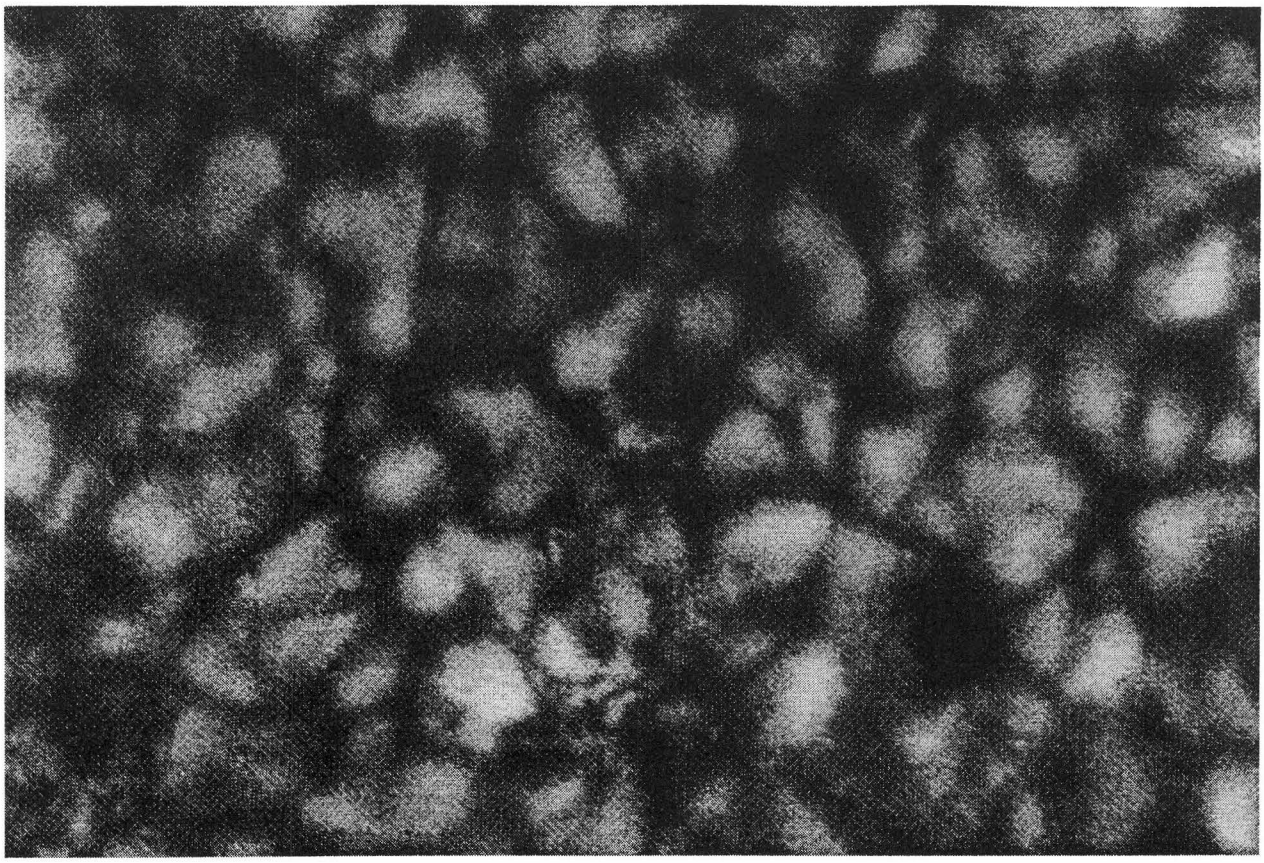

Figure 2.3: This photograph is part of Gray's [59] Figure 4-2. It shows granulation on the surface of the Sun. The typical diameter of these cells is 2000 km (Schwarzschild [149]) and their typical velocity is of the order of 1 km/s (Gray [56] page 442).

stellar surface at any one time. He indicated it was plausible that there are actually only tens of cells present and hence these few cells could cause brightness variations of a factor of two, on a timescale of a couple of hundred days — hence explaining some irregular variables. Strangely this interesting proposal remained unexplored until 1984 when Antia et al. [6], amongst other things, tested Schwarzschild's hypothesis. They calculated convective modes, where their models used mixing-length theory with the effects of turbulent pressure included and in some cases a nonlocal[11] formalism. They concluded that the convective cells that dominate the brightness variations will not only be small in number but, as Schwarzschild hypothesized, they can account for luminosity variations in the integrated starlight of a factor of two (on the timescale of 40 days for a low-mass model giant). Hence this could explain the observed phenomenon of irregular variation that occurs in all late-type stars having extensive convection zones (possibly superimposed on regular variations due to pulsation).

This, of course, has implications for the apparent radial velocity of any such stars. With such a small number of large convective cells rising and falling, instead of seeing line broadening either line shifts or variable asymmetry of lines will be seen and hence radial-velocity variations will be found. These velocity variations would presumably be on similar timescales and of a similar irregular nature, to the photometric variations. In addition, if the integrated starlight were brighter

[11] Nonlocal means it is necessary to know information for a range of radii before a statement about a given point can be made. In this case the standard expression for convective velocity is replaced by a differential equation which includes the effect of the aerodynamic drag experienced by the cells.

it would imply more cells rising than falling[12], hence the radial velocity would be negative (with respect to the centre of mass of the star) — similarly if the integrated starlight were fainter the radial velocity would be recessional. As the mean convective cell velocities of Antia et al.'s models are about 5 km/s at the stellar surface (Schwarzschild also assumed the mean convective velocities would be 5 km/s, as this is about the speed of sound), these radial-velocity variations will have amplitudes of about $3.5/\sqrt{N}$ km/s, if N is the number of cells present.

That convective cells have radial-velocity variations with amplitudes of about the mean convective cell velocity, $\overline{v}$, divided by the square-root of the number of cells present will now be shown. Cells will be considered to either be rising at velocity $\overline{v}$, or descending at velocity $\overline{v}$, and it will be assumed that each cell has an equal probability of doing either. This is then a binomial distribution *and this means the population has a mean number of cells rising of $0.5N$, where N is the number of cells on the visible face of the star, and the standard deviation of the population will be $0.5\sqrt{N}$. Then, in a given set of observations of the star, there is a reasonable chance of seeing $(0.5N + 0.5\sqrt{N})$ cells rising (and therefore $(N - 0.5N - 0.5\sqrt{N}) = 0.5(N - \sqrt{N})$ cells descending). Assuming that the average radial velocity of these cells will be the radial velocity observed from the integrated starlight (probably not the case, as the falling cells are darker then the rising cells) means there is a reasonable chance of observing a radial velocity of*

$$\frac{\overline{v} \times 0.5(N + \sqrt{N}) - \overline{v} \times 0.5(N - \sqrt{N})}{N} = \frac{\overline{v}}{\sqrt{N}}.$$

For more details on the Binomial distribution see Bevington & Robinson [21] Chapter 2. However, limb darkening and projection effects will mean the maximum radial velocity observed will be somewhat less than this. If $\overline{v}$=5 km/s, then taking limb darkening/projection factor of $\frac{17}{24}$ the expected amplitude becomes $3.5/\sqrt{N}$.

2.2.2 Rotational modulation

A number of surface features are capable of causing line asymmetries, which in a rotating star would result in an apparent radial-velocity variation on the timescale of the rotational period of the star[13]. Long lasting convective cells, starspots and starpatches are all possibilities for this rotational modulation. These possibilities will now be discussed (for this extensive use has been made of Gray [60] and Gray [59], Lecture 7).

Starspots

The most famous star known to have starspots is the Sun. These spots on the Sun are called sunspots and they form the prototype of the starspot. Sunspots are much cooler than the effective temperature of the Sun, as are starspots, and both have variable H and K emission lines (which, in the Sun's case, vary in phase with sunspot numbers). However, there are a number of features of sunspots which are not necessarily present for starspots including the fact that sunspots do not have granulation occurring in their umbra[14] (they are velocity quiet by comparison to the photosphere) and sunspots are associated with magnetic fields. That these things will be true for starspots is not a foregone conclusion because the starspots found in stars, so far, do differ from sunspots in some important (if observationally biased) ways. These differences include that starspots can cover up to 20–40% of the apparent disc of the star and they can last for hundreds of days. If magnetic fields are associated with starspots as well as sunspots it is interesting, because it leads to the speculation that rotation impels starspots by activating a magnetic dynamo. But if this was the case, then strongly spotted stars must either be young or in a binary system where orbital synchronism has

[12] Unless a region of convective overshooting is being observed

[13] Unless during the period of observation the surface features are evenly spaced about the star's latitude and at the same longitude, in which case the observed timescale will be the rotational period divided by the number of features present

[14] The dark central region of a sunspot

prevented "spin down"[15].

It is obvious that the presence of a "dark" spot on a rotating star will cause photometric variations as the star rotates and the spot's projected area (to the observer) changes. However, such a spot will also cause changes in line asymmetry which will be seen as apparent radial-velocity variations[16]. This can be seen by considering a star which has its rotational axis perpendicular to the line of sight and a large dark spot about its equator (see Figure 2.4). As the spot appears on

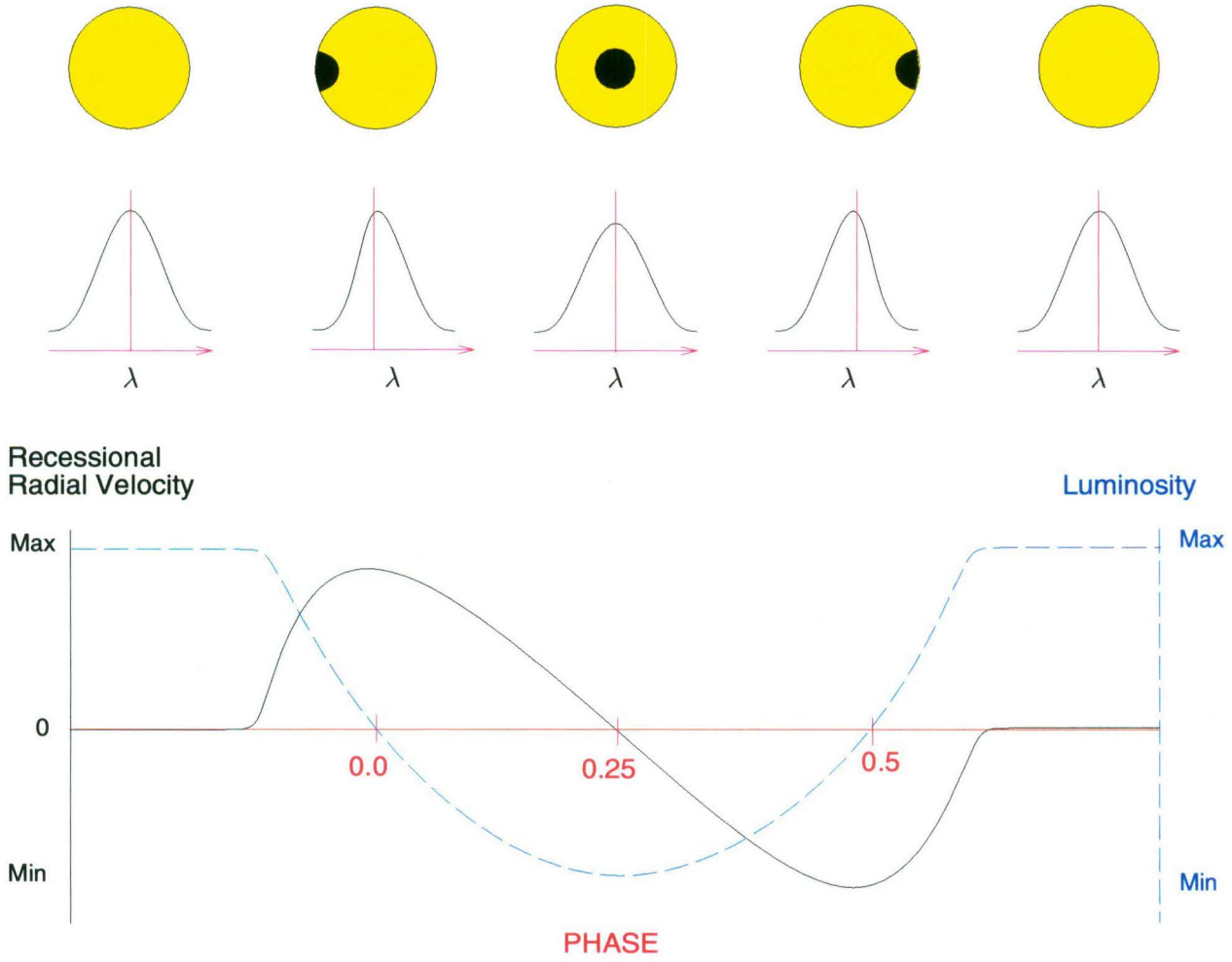

Figure 2.4: The effect of a starspot on a rotating star's photometry (dashed line), line profiles and apparent radial velocity (solid line). As the spot first appears from behind the star the line profile has flux removed from shorter wavelengths, so the recessional radial velocity becomes positive as the star becomes fainter. When the spot is face on to the observer the star is at its faintest, but as the line profile is symmetric the measured recessional radial velocity is zero.

[15]Giants of a later spectral type than G5 undergo a fivefold decrease in rotation from 20–30 km/s to about 5 km/s (see Gray [57]). Subgiants behave similarly except the sudden decrease occurs slightly earlier at about G0 (see Gray & Nagar [62]). The main sequence also undergoes a sudden, if slower, decrease of from over 100 km/s for F0 stars to about 5 km/s for K0 stars (see Fukuda [52]).

[16]If the broadening due to rotation, of a line, is sufficiently greater than other forms of broadening then, as the spot rotates across the surface of the star, it will appear as an emission like "bump" in the absorption profiles (rather then just an asymmetry). This bump will move across the line profile as the starspot is rotated and the resulting variation in line profile can be used to create a model of the starspot — this is called Doppler imaging. For how this profile modelling is done see, for example, Vogt & Penrod [169] and Vogt et al. [168].

the apparent disc of the star (from behind the star) it is coming towards the observer. This will mean that the shorter wavelength wing of a rotationally broadened line will have less light due to the darkness of the spot. Hence the line is asymmetric and any symmetric fit would find it to have a recessional velocity (with respect to the star's centre of mass). Similarly when the spot has rotated to the other side of the star's visible face and is receding from the observer, there is less light in the longer wavelength wing of the line and hence the line will yield a negative recessional velocity.

Hence a rotating star with starspots may result in both photometric and radial-velocity variations. Any such variations will be regular and be on the timescale of the rotational period[17] but will not be coherent, since the spots will decay and new ones will be formed. The magnitude of the photometric variations depends on the size and temperature of the spot, as do the velocity variations, but the amplitude of the apparent velocity variations must always be less than $v_{\rm equ}\sin(i)$[18]. When a star is at maximum brightness lines will be symmetric and the radial velocity will be "zero". As the star becomes fainter the radial velocity of the star will become recessional and continue to be so until the star has reached minimum brightness. Then as the star slowly brightens, its recessional radial velocity will become negative. The star will reach minimum brightness 0.25 in phase before it will reach minimum recessional velocity.

Starpatches

Unlike a starspot a starpatch has no analogy in the Sun. It is an area on the surface of a star with a very different granulation velocity dispersion. This means the area causes different line broadening and if such a patch is on a rotating star this will cause the line asymmetry to vary. Starpatches and starspots may be part of the same phenomenon, although starpatches and sunspots are certainly not (one has granulation in it, while the other does not and sunspots only occur with magnetic fields, while starpatches are believed not to have them). Starspots and starpatches do have some things in common. Both can take up large fractions of the visible disc, have lifetimes of several years and are not restricted to low latitudes (although all but the last may be a selection effect, as larger and more persistent features are easier to observe).

This surface feature came to light in 1988 with the publication of a paper on the G8V star ξ Boo (Toner & Gray [166]). As this is the prototype starpatch the results of its modelling will now be described, even though the star is of a different type to the red giants and supergiants surveyed in this thesis. This star was primarily analysed using line bisectors[19] and an indication of the relative radial velocity determined in the form of a "velocity span"[20]. The span velocities had a period of 6.4 days and an amplitude of 64 m/s. A (phase-shifted) variation of the same period was found in the ratio of the equivalent widths of the VI and Fe II lines. Although not detailed in this paper photometric variations for this star, with the same period and an amplitude of 0.01–0.02 magnitudes, are found to lag behind the span velocities by 0.25 of a period (see Gray [59] Figure 7-16). This 6.4-day period stayed phase coherent over the four observing seasons. These variations were successfully modelled using a single starpatch which was 3.7% cooler than the rest of the star, took up $10 \pm 5\%$ of the visible disc and had a granulation velocity dispersion in the patch that was 1.5 to 2 times larger than that of the surrounding photosphere.

The line asymmetries which have been mentioned are caused by the changing average radial velocity

[17] See footnote 13 this chapter

[18] This is the projected radial velocity of the stellar limb

[19] A bisector is a curve which bisects a line profile — i.e at many levels of flux the line profile is split exactly in half (from wing to wing) and this forms a point on the bisector. This is a useful way of determining the asymmetry of a line.

[20] The velocity span is the difference in velocity between a point near the top of the bisector and a point near the bottom

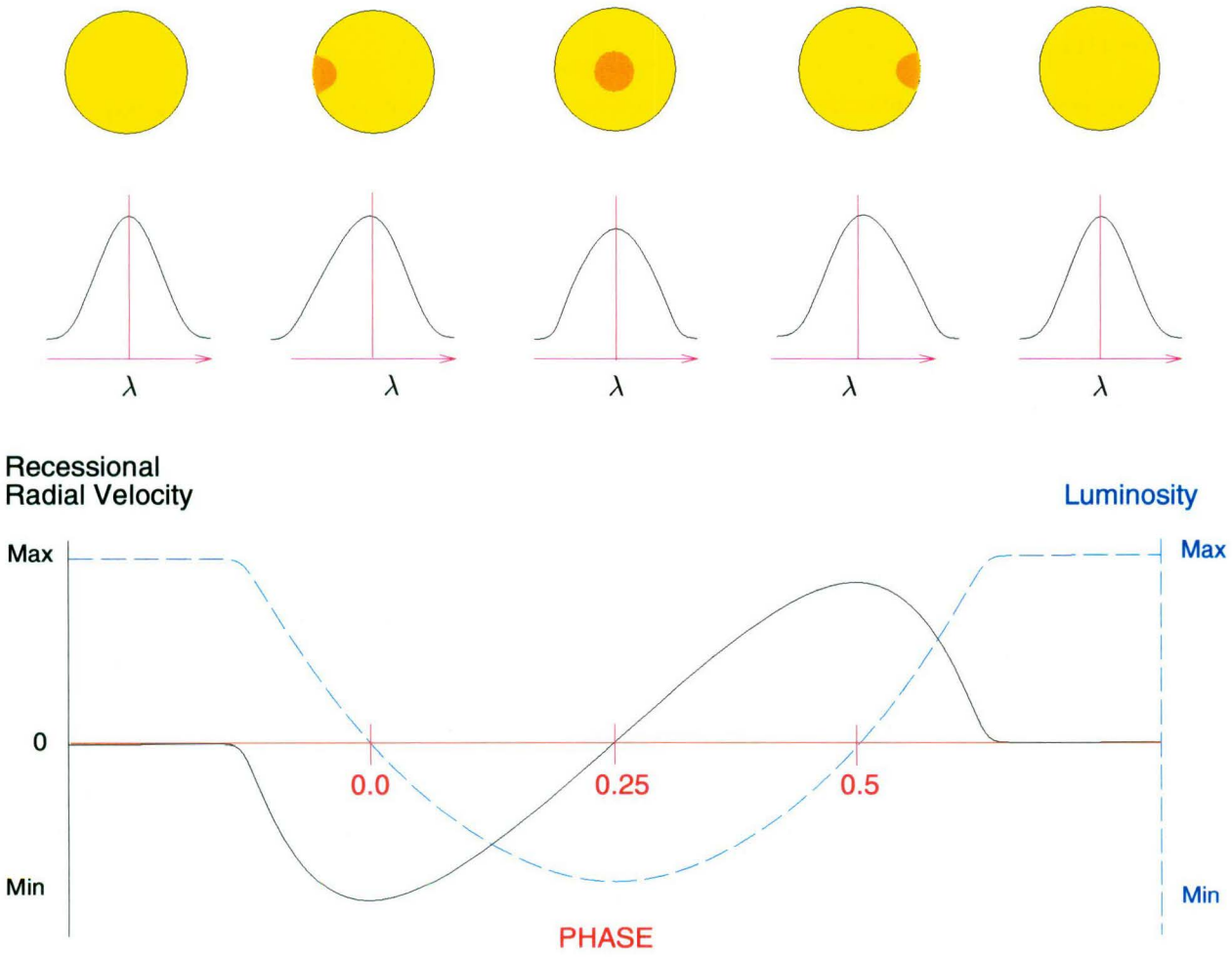

Figure 2.5: The effect of a starpatch on a rotating star's photometry (dashed line), line profiles and apparent radial velocity (solid line). As the spot first appears from behind the star the line profile is broadened at shorter wavelengths, so the recessional radial velocity becomes negative as the star becomes fainter. When the spot is face on to the observer the star is at its faintest, but as the line profile is symmetric the measured recessional radial velocity is zero.

of the starpatch (any effects due to the slightly darker nature of the patch will be neglected here). It causes extra broadening centred on its average velocity, which means that as the starpatch comes towards the observer the line will be more broadened to shorter wavelengths and hence the line will be seen to be Doppler shifted to a negative recessional velocity (see Figure 2.5). In the same way, as a starpatch recedes from the observer the line profile is broadened at longer wavelengths, so the line is seen to be receding. As photometrically a starpatch appears similar to a starspot (only the magnitude of the variations will be less), unlike starspots a starpatch will have its apparent radial-velocity variations 0.25 in phase ahead of its photometric variations. Such a starpatch would be expected to result in regular variations in radial velocity and also, if detectable, in photometry. Like starspots the period should be that of the star's rotational period[21] and the amplitude of the radial-velocity variation must be less than $v_{\rm equ}\sin(i)$. It is unknown if the period will be coherent — ξ Boo's starpatch certainly persisted for a period longer than the length of time observations were obtained for this thesis.

[21] See footnote 13 this chapter

Convective cells

Any long-lasting large convective cells would have a very similar effect on apparent radial velocities and photometry as starspots, only the timescale of the variations of the convective cells would be present along with the period of rotation of the star.

2.3 Pulsation

A star is said to be pulsating if it is undergoing, often periodic, expansions and contractions. These expansions and contractions result in variations in light and radial velocity. Not only that, but large oscillations can cause shock waves (see §2.3.4), mass loss and dust clouds — the Mira variables are an example of pulsating stars that are believed to suffer from all these effects (see, for example, Bowen [25]).

The theory of stellar pulsation and approaches to modelling the pulsations can be split up into the study of linear adiabatic radial, linear non-adiabatic radial, nonlinear radial and non-radial pulsations. In reality all stellar pulsations are almost certainly one of the last two; however, for some stars, the first two form a good approximation to the reality and, due to their relative simplicity, much of the earlier work on pulsation focused on linear adiabatic and linear approximately non-adiabatic pulsations. In more recent times the advent of fast computers has allowed the study of the more complex completely non-adiabatic, nonlinear and non-radial pulsations. The behaviour of a star undergoing these various subsets of pulsation will now be discussed (Cox's 1974 review paper [39] and 1980 text [40] have been used extensively for the following, with the addition of Unno et al. [167] for non-radial pulsations).

2.3.1 Linear adiabatic radial pulsation

Assuming a radial linear adiabatic pulsation means assuming a small-amplitude spherically symmetric pulsation which takes place without energy leaving the system. This is clearly not going to be the case in a star, but results from the study of this simple case give useful insights into the pulsational behaviour of a wide range of stars.

To study linear adiabatic radial pulsations the mass, momentum and energy conservation equations are linearized and combined together where they form a second-order partial-differential equation (PDE). If an oscillatory separable solution is then sought[22] the PDE assumes the form of a second-order ordinary-differential equation (ODE) and is called the linear wave equation. In the adiabatic case this is a real, homogeneous and linear ODE and with the addition of two boundary conditions it is the well known Sturm-Liouville boundary value problem (for more details on this problem see, for example, Myint-U [126] §7.1–7.2). The solution to this problem is unique, has an arbitrary amplitude[23] and discrete frequencies of oscillation (often called eigenvalues). These frequencies are real and are called in order of their increasing size the fundamental, first overtone, second overtone and so on. Solutions to a Sturm-Liouville system (often called eigenfunctions) which is self-adjoint[24] have nodes, the number of which increases with the size of the eigenvalue — the fundamental has no nodes, the first overtone one, the second overtone two and so on. Hence the solution is a standing wave for which the frequency of the oscillation increases with the number of nodes. But a standing wave solution is equivalent to requiring the wave coming up from the stellar interior undergoes perfect reflection when it comes to the atmosphere. While such perfect reflection is a

[22] That is, a solution of the form $\delta r = \xi(r_0)\exp(i\omega t)$, where δr is the variation from the static radius, r_0, is sought. This is not the general solution for a partial differential equation of this form — even in the adiabatic case.

[23] As the ODE is homogeneous and linear, the multiplication of any solution by a constant value must also be a solution

[24] The boundary conditions for a pulsating star usually are such that this is the case

good approximation for the lower modes of many stars, as Bowen [25] points out, such a reflection is out of the question for LPV and presumably other late-type giants and supergiants. Even for stars for which perfect reflection at the atmosphere is a good approximation, the study of linear adiabatic radial pulsations has the limitation that nothing can learnt about the amplitude of the pulsation or the growth of the pulsation (as the frequency is real it has no decay component).

However, knowing that a unique solution exists does not make its obtention any easier — in fact generally analytical solutions do not exist for the radial component of the linear adiabatic wave equation (LAWE). Instead solutions have to be found by the use of finite-difference or fitting methods. The latter method involves starting from, say, the outer boundary condition, guessing the frequency of pulsation, then integrating inwards with the goal of matching the inner boundary condition. Usually the correct solution is best obtained by "matching" inside-out and outside-in integrations. For the finite-difference method of solution the aid of computers is essential. A solution by finite differences requires dividing the region into a mesh. In this case the region is the star, or some outer envelope of the star, and it is divided into zones of set mass. Mass conservation is thereby preserved and for each zone there is an energy and momentum conservation equation. For every equation the derivatives in the conservation equations are replaced by finite differences[25] hence the finer the mesh the more accurate the solutions obtained. This can be written in matrix form and hence the problem becomes one of solving a matrix for its eigenvalues (the frequencies) and eigenfunctions. This can be achieved via iterative methods, usually a secant method. There are several nice things about this method of solving linear equations. One is that it usually converges to a solution rapidly — one of the most time consuming things about this is actually forming the initial equilibrium model! Another is that it is not significantly more difficult to use this to solve the linear non-adiabatic case. For more details on using finite-difference methods to create linear radial models see Cox [38] Chapter V, Castor [35] and Cox [40] §8.12b.

The pulsation constant

The pulsation constant is given by a relationship between the mean density of a star and its pulsation period and this relationship follows from the LAWE (see, for example, Cox [40] §8.6 or Cox [39] §5.4). When the LAWE is applied to a homologous[26] group of stars, it is found that (with a few assumptions) for each star in the group, the angular frequency of the pulsation squared is proportional to the star's average density, ρ_m (the proportionality constant depends on the oscillation mode). This means, for a given mode and a homologous group of stars, $Q = P\sqrt{\rho_m}$, where P is the period of the pulsation and Q is the pulsation constant. Although real stars are not homologous to one another, for most pulsating stars the pulsation constant turns out to be a slowly varying function of stellar parameters.

2.3.2 Linear non-adiabatic radial pulsation

Assuming a radial linear non-adiabatic pulsation means assuming a small-amplitude spherically symmetric pulsation which, unlike linear adiabatic pulsation, can have energy leaving the system. This is essential because acoustic transmission of energy into the atmosphere (see Bowen [25]) should occur for many pulsating star types and hence the adiabatic models will not be sufficient.

Similarly to the adiabatic case, there are two approaches to the study of linear non-adiabatic radial pulsations. One is the study of the linear non-adiabatic wave equation (LNAWE) which is

[25] I.E. for the ith zone, if the mass shell is DM_i in size, replace $\frac{dy}{dm}$ by $\frac{y_{i+1}-y_i}{DM_i}$ where y_k is the value of variable y on the kth interface between zones

[26] Let there be two stars with mass M_1, M_2 and radius R_1, R_2. Let $r_1 = \frac{R_1}{R_2}r$ and $m_1(r)$ be the mass of the first star contained within radius r. Then if $m_1(r_1) = \frac{M_1}{M_2}m_2(r)$ the first star is homologous to the second star.

a complex, linear, non-homogeneous and second-order ODE with two boundary conditions, but unlike the LAWE it does not form a well known problem and hence is often studied by assuming a quasi-adiabatic approximation[27], which is not valid for many stars (see, for example, Ledoux [115] and Cox [41] page 1081). Alternatively the three conservation equations and the energy transport equation can be used directly, while still assuming the variables are separable and oscillatory. If this approach is taken then four first-order, linear, complex and homogeneous ODEs result, which will hence yield four arbitrary constants (as well as the arbitrary frequency of oscillation). For each equation a boundary condition is imposed and hence only one arbitrary constant remains. For physical reasons this is taken to be the amplitude of the oscillations and hence the linear calculation will yield no information about the amplitude of the variations of stars. This also means that only for discrete values of frequency will the boundary conditions be satisfied.

As mentioned in the previous section, finite-difference methods can be used to find solutions (fitting techniques, like for the adiabatic case, can be used but the solutions diverge unless required to approach the adiabatic case when doing an outside-in fit). The resulting solutions differ from the adiabatic ones in a number of important ways. As mentioned they still have an arbitrary amplitude, but the eigenvalue is not real so it can have a complex component which would correspond to decay or excitation — hence pulsational stability can be studied! The real part of the eigenvalue still corresponds to oscillations and the period of the oscillations is not expected to be that different from the adiabatic case[28], as the non-adiabatic effects are often small and usually only in the outer layers of the star (see Figure 2.6 for an illustration). As the oscillations are non-adiabatic, particularly in the outer layers, it is not possible to have standing waves in stars and hence there must be components of running waves. This means there will not be nodes of zero amplitude variations in the star and in finite-difference methods some of the zones go though their oscillations with a phase lag with respect to others. For Cepheid-type stars using radiative energy transfer (Cox [40] §9.2c), the non-adiabatic periods are only a few percent less than the adiabatic and the pulsations are nearly standing waves, but the phase of the luminosity and density are appreciably different — particularly at the stellar exterior (more on this below).

In 1986, based on finite-difference methods, Ostlie & Cox [128] published a linear non-adiabatic survey of the region of the HR diagram in which the stars considered in this thesis are mainly located. Appropriately for such cool stars convective zones were included, although the convection was not time-dependent. The resulting fundamental and first overtone model periods were fit as a function of mass and radius yielding a simple formula for period prediction in terms of the stars fundamental parameters[29]. For the stars surveyed for this thesis this means the stars should be, typically, pulsating with periods of between 10 and 100 days (in the fundamental mode — see §4.9 for more details).

Time-dependent convection[30]

Convection is the principle mechanism for transporting energy throughout much of the envelope of AGB stars and if the timescale of pulsation is of the same order of magnitude as the timescale of convection (how long it takes for a cell to travel one mixing length) it is likely that pulsation and

[27] In the quasi-adiabatic approximation it is assumed that variables can be considered to be small perturbations about their adiabatic solution values

[28] However strange modes, which have no counterpart in adiabatic predictions, are sometimes found

[29] Although it should be noted that, in June of 1997 in a private discussion, A.N. Cox noted that lack of time-dependent convection and inaccurate opacities meant the predicted fundamental periods could be out by a factor of two

[30] Time-dependent convection can be important for both linear and nonlinear pulsation calculations. However, it is especially important for nonlinear pulsations as dissipation effects strongly influence the resulting amplitudes and growth rates (Ostlie [127] page 95).

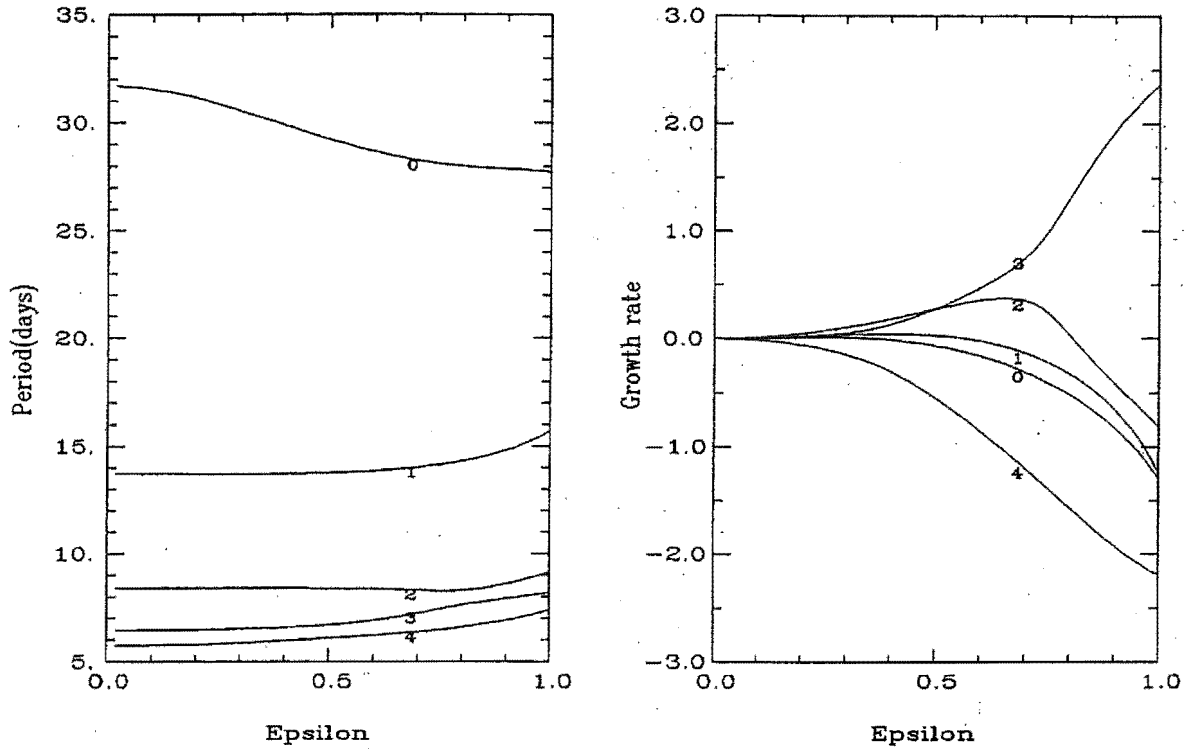

Figure 2.6: To the right are the growth rates and to the left are the periods for a linear radial pulsation model of luminosity 3559 $L_{\odot}$. Epsilon takes the model from fully adiabatic, 0.0, to fully non-adiabatic, 1.0 (the fundamental mode is the curve labelled (0), the first overtone (1) and so forth). This is Figure 1 of Aikawa [3].

convection will strongly influence each other. Hence the inclusion of time-dependent convection in stellar modelling may be essential for an accurate picture of what is taking place in the star.

When primitive time-dependent convection is included in the modelling of RR Lyrae stars (Ostlie [127]) some general features become clear. One is that in the presence of the coupling of pulsation and convection, the growth rates of pulsation modes can change markedly. Another is in the nonlinear case, convergence to a limit cycle is very difficult (for more on limit cycles, including their definition, see §2.3.3). But determining limit cycles is essential to determining the pulsational behaviour of a star!

Pulsation instability

A star may have many regions of damping and driving in its layers, so for pulsation to exist the total effect of all the driving regions has to be greater than the damping regions. In order for driving to occur work needs to be done by the star as it expands and contracts — this work can then go into the kinetic energy of the pulsation. Hence nuclear sources, as they add heat preferentially at maximum compression, always cause driving (this is called the ϵ-mechanism). However for most stars, stellar pulsation is mostly an envelope phenomenon, so the nuclear driving is negligible. Work, and therefore driving, will also be done on a mass element if energy is preferentially removed at maximum expansion and it is therefore this which is the important thing for most stars. Hence if the stellar luminosity increases with expansion driving will be done. But luminosity variations are mainly a result of opacity variations (hence the opacities used by models are very important) and normally opacity decreases with compression — which would mean that the stellar luminosity

will increase with compression and the situation will be one of damping instead of driving. This is called radiative damping[31] and is present in all stars, at least in their inner envelope. Coupled with the fact that the stellar temperature usually increases with compression (and luminosity is proportional to the fourth power of temperature for radiative transfer) it would be expected that stars should be very stable!

However, it is certainly true that some stars are pulsating. Exactly what mechanisms could cause such an instability has only been realized in the latter half of this century. In order to see whether damping or driving predominates the LNAWE can be integrated over the entire (relevant) radius of the star (see, for example, Ledoux [115] or Cox [39] §5.5). When this is done, it becomes apparent that the main thing (if there are no nuclear sources) determining whether or not a star is driven or damped, is how the change in luminosity (from the static case) varies with mass. For radiative transfer, the relative luminosity perturbations undergo a marked dip in ionization zones. This dip occurs for two reasons. One is because there are smaller temperature variations, as the energy instead goes into ionizing atoms, there are smaller luminosity variations. The other is that opacity is (in most cases) inversely proportional to some power of temperature and directly proportional to some power of density, so small temperature variations can mean opacity increases with compression and therefore luminosity decreases. This results in driving and is called the κ-mechanism. However for thin ionization zones where the variations in the incident luminosity are approximately adiabatic, the luminosity leaving the zone should be equal to that incident and hence the marked dip in luminosity variations on entering the ionization zone must become a similar rise before the ionization zone is left. This means the outer half of ionization zone results in damping and hence the two components cancel. However if the ionization zone is sufficiently far out in the star, the inner of the ionization zone can be adiabatic and the outer non-adiabatic. At this transition region stars typically have constant relative luminosity variations and hence the second half of the ionization zone does not contribute any damping! For the stars in the instability strip this transition region corresponds to the location of the helium ionization zone.

The cause of instability described above is, however, valid only for radiative stars. The stars surveyed for this thesis are all cool, with the dominant form of energy transport in their envelopes being due to convection, not radiation. Moreover, it is the onset of convection which is believed to terminate the instability strip on its cooler edge (see Cox [40] §19.3). However, while the hydrogen ionization zone is in a region of convective instability the outer parts of the hydrogen ionization zone are convectively inefficient, so instead energy is transported by radiative transfer (see Keeley [102]). But the envelope is highly non-adiabatic in the outer half of the hydrogen ionization zone (Wood [180]) and in LPVs, at least, so extended that it occupies a significant fraction of the envelope (Cox [39] §9.5.1)). Hence while the luminosity undergoes a marked dip in the hydrogen ionization zone, it is not necessary for it to undergo a corresponding rise, so strong driving results.

The phase lag

On the basis of adiabatic theory, maximum luminosity would be expected to occur at minimum radius. However, observations of the regular light and radial-velocity curves of Cepheid variables clearly show that maximum luminosity occurs about quarter of a period after minimum radius. In addition, while the initial linear non-adiabatic calculations did yield a phase lag, it did not give the correct relationship — causing many researchers to believe the phase lag was a nonlinear effect.

In fact the phase lag is entirely a linear effect, although it is significantly affected by nonlinear effects. But it was not until 1968, four years after the first nonlinear models gave the correct phase lag, that it was finally physically explained using linear theory (Castor [34]). The missing piece of

[31] Although any energy transport mechanism will do

the puzzle is that, despite the helium ionization zone being responsible for driving the pulsation in Cepheids, it is the hydrogen ionization zone which is responsible for the phase lag.

It is, in fact, very simple. Ionization zones occur at some constant temperature, so when the temperature of the star changes as it oscillates, it causes the hydrogen ionization zone to move backwards and forwards though the star's mass zones. Now, as is expected on the basis of adiabatic theory, at minimum radius the largest luminosity is impinging on the deepest ionization zone, i.e the hydrogen ionization zone. This is when the hydrogen ionization zone is moving out through the star the fastest. Hence for a sinusoidal pulsation the zone is the closest to the stellar surface quarter of a period after minimum radius. Since for radiative transfer the luminosity emerging from the star is largest when the mass above the hydrogen zone is smallest (see Cox [39] §7), the maximum luminosity will occur at the maximum velocity of expansion. Hence for a radiative pulsating star, the radial velocity and luminosity of the star are expected to be in anti-phase, as is shown in Figure 2.7.

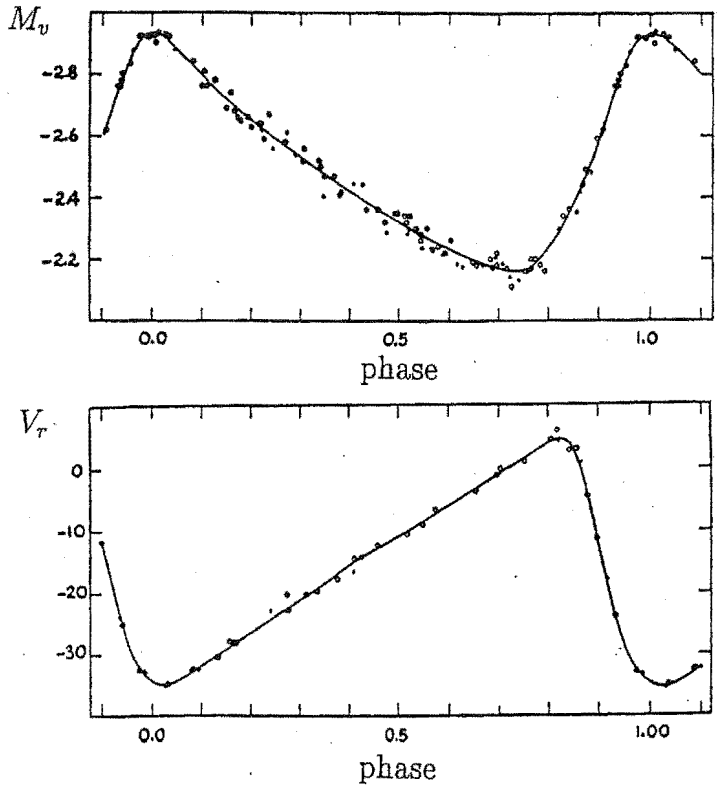

Figure 2.7: The top curve is the visual magnitude and the bottom recessional radial velocity (in km/s) for δ Cep. Maximum luminosity occurs at the maximum velocity of expansion for the star — a phase lag of quarter of a period from the simplest pulsation theory. This is an adaptation of Figure 3.2 from Cox [40].

Of course the stars surveyed for this thesis have mainly convective, not radiative, envelopes. However, both models of late-type giant stars (Keeley [102]) and observations of the relatively regular Mira variables (see Hinkle et al. [90] Figure 2) indicate that late-type giants simply undergoing linear radial pulsations will have a phase lag between visual luminosity and the photospheric radial velocity similar to that of Cepheids.

2.3.3 Nonlinear radial pulsation

When the surface amplitude of the radius variations is calculated for pulsating stars from observations, it is generally found to be too large to be considered a linear effect. Not only that, but the simple sinusoidal pulsation found using linear models does not correspond to the non-sinusoidal radial-velocity and light curves observed (see, for example, Figure 2.7). Hence nonlinear effects in stellar pulsation can not be neglected.

The solution of the three general radial conservation equations and the energy transport equation is not trivial. There are only two known models for which analytic solutions exist and they are both adiabatic. Hence numerical models are essential and these tend to involve finite-difference techniques. Typically models are calculated by zoning the star into mass shells, then stepping forward in time from the initial state. This allows the study of pulsational growth, decay and, unlike the linear case, the way the amplitude and modes of the oscillation vary with time.

For a given zone let the model's parameters, evolving with time, be called the system solution. The set of all parameters approached by the solution as time approaches infinity is called a limit set, and if the set forms a closed curve in parameter space it is called a limit cycle. The limit cycle is clearly periodic in time and it may either attract or repel solutions — in that a solution slightly to either side of the limit cycle may either tend towards or away from the limit cycle as time increases. Hence only an attracting limit cycle gives a stable solution. As time is stepped forward for a model limit cycles will be approached and the period of the limit cycle is found, as might be expected, to be "close" to some linear period[32] (Aikawa [3] §3).

When radiative nonlinear calculations are made, it is found that if the effective temperature is lowered the pulsation goes from regular and periodic to chaotic variations (see, for example, Kovàcs & Buchler [111]). Depending on the ratio of luminosity to mass this "route to chaos" follows one of two well known paths. For medium ratio population II Cepheids this path is via "period doubling bifurcations" (also known as a Feigenbaum route), which transverses a path from regular periods, to periods of apparently double the length (due to every second minimum being of a different size), to irregular variations. In fact the authors believe that RV Tauri stars variations are a consequence of their being the lower temperature relations of the periodic W Vir stars and hence have period doubling bifurcations.

The other route to chaos is undergone by stars with a higher luminosity to mass ratio and is that of "tangent bifurcation" (also known as a Pomeau-Manneville route). This chaotic route results in pulsations which show long stretches of periodic pulsation interrupted intermittently by chaotic bursts (see Aikawa [2]). Both types of chaotic behaviour can be caused by the strong dissipation of energy when the system solution is around its limit cycle (Taleuti [162] §4.2). What type of chaotic motion results will depend on what return path is taken to the limit cycle.

While such models are generally only radiative, possibly due to the difficulty in finding limit cycles for time-dependent convection (see the §2.3.2), it is very tempting to speculate that the smooth observational transition (with decreasing temperature) from W Vir to RV Tau and then semi-regular variables, can be explained in terms of nonlinear radial pulsations and a route to deterministic chaos[33]. However such a link has yet to be proven. Nonetheless if this was the cause of the irregular variations in the late-type evolved stars studied for this thesis, it would be expected that these

[32] Although there has been a suggestion that this may not be the case for LPVs cooler than about 2700 K, see Yàari & Yuchman [183]. Their final "fundamental" period is generally shorter than the linear fundamental period (the star's slow, with respect to the pulsational period, change in internal energy structure, caused by the nonlinear pulsation itself, causes this). Fortunately all 44 stars surveyed for this thesis are hotter than this.

[33] So called because the chaotic oscillations occur in a deterministic system

chaotic visual magnitudes and radial velocities should have timescales approximately equal to the period predictions of linear theory, unless the star is a RV Tauri star in which case variations of apparently two (or four, or eight, ...) times the length of the linear non-adiabatic limit cycle will be observed. However, the phase relationship between the two observables would no longer be as simple (see Figure 2.8).

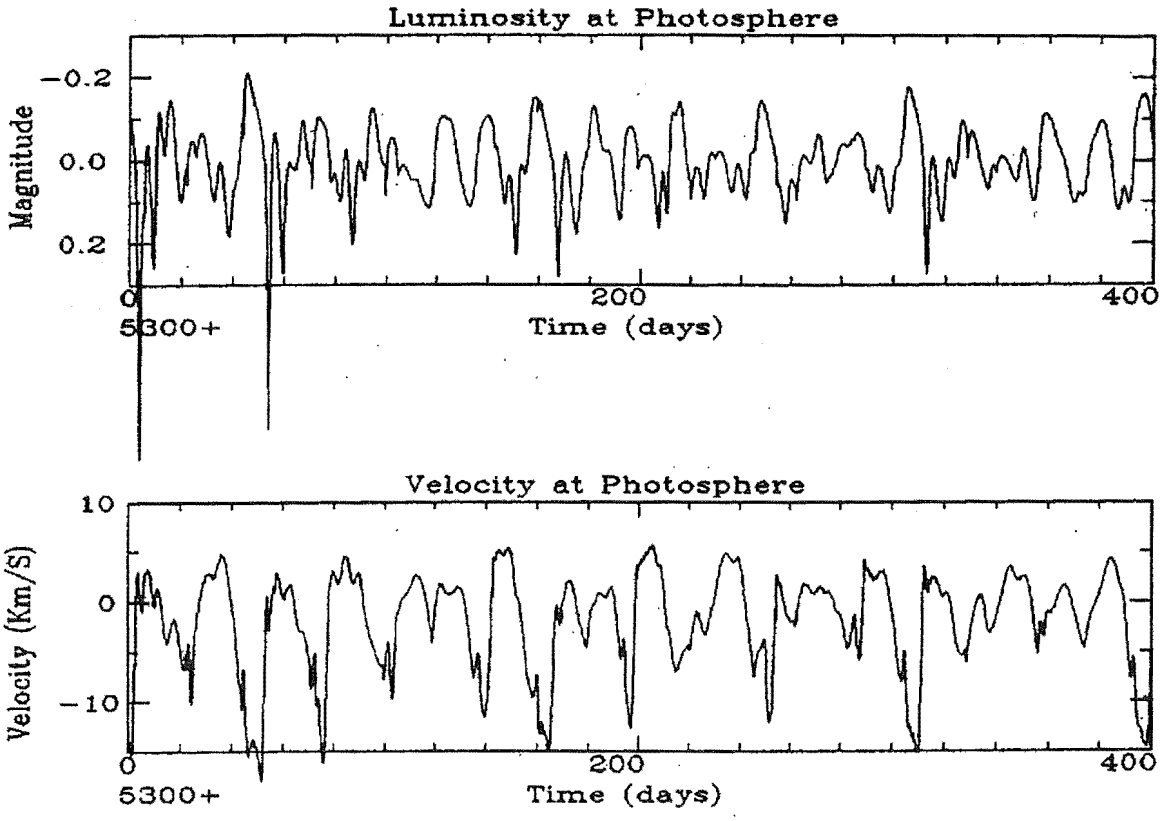

Figure 2.8: Bolometric magnitude and velocity[35] (km/s), where contraction is taken as positive, at the photosphere of a 4600 $L_\odot$ model (here luminosity, instead of effective temperature, has been taken as the free parameter for the "route to chaos"). This star is in the chaotic regime and, as can be seen, both the radial velocity and luminosity are irregular. While as a whole it is true that maximum luminosity occurs at minimum recessional velocity, as is predicted by non-adiabatic linear theory, there are many short regions where this is no longer the case. The phase relation found would depend on how many periods the object was observed for. This is Figure 3c from Aikawa [3].

2.3.4 Shock waves

As a gas is compressed a compression wave propagates out from the compression boundary at the local speed of sound. When the gas is compressed this local speed of sound increases, meaning the signals sent by the compression travel faster than the earlier signal and hence "try to catch up" and overtake the gas from earlier in the compression. This is prevented by viscous forces, thermal

[35]The differs from observed recessional radial velocity as obtained from the measurements of a photospheric line. Typically the radial velocity will be approximately 17/24 of the actual velocity of the photosphere due to foreshortening (the projection of the star's surface radial movement onto the line of sight means the radial velocity observed is smaller than the real surface velocity, except at the centre of the visible disc) and limb darkening (the visible disc of the star is fainter to the edges). For more details see Cox [40] §3.4.

conduction and other microscopic processes. The region where this occurs is the order of the mean free path for the gas in thickness and this region propagates through the gas with the pressure and density behind and in front of it being quite constant, yet very different. This discontinuity is called a shock wave and its temperature is very hot, resulting in the post-shock material being of a higher temperature then the pre-shock material. In the case of an isothermal shock wave there is a region of cooling behind the shock wave, so the temperature of the two regions is equal. This results in the gas behind the shock wave moving at the same speed as the shock and lots of internal energy being radiated in the discontinuous shock-cooling region (for further details see Dyson & Williams [49] pages 116–138 and Rosseland [139] pages 131–138).

In pulsating stars shock waves form when gas is moved by the pulsational driving. One simple model is to take the base of the photosphere, or slightly below it, as a sinusoidally moving piston and see the effect of this pulsation on the atmosphere. When this is done, an outwardly moving shock can form as the infalling photospheric gas from the previous pulsation meets with the outwardly moving photosphere. Population II Cepheids, RV Tauri and Mira/LPV stars[36] all show evidence of radial-velocity changes consistent with such a picture (see Figure 2.9, and Hinkle et al. [90]). However Mira/LPV stars do not show such a radial-velocity variation in the visual-

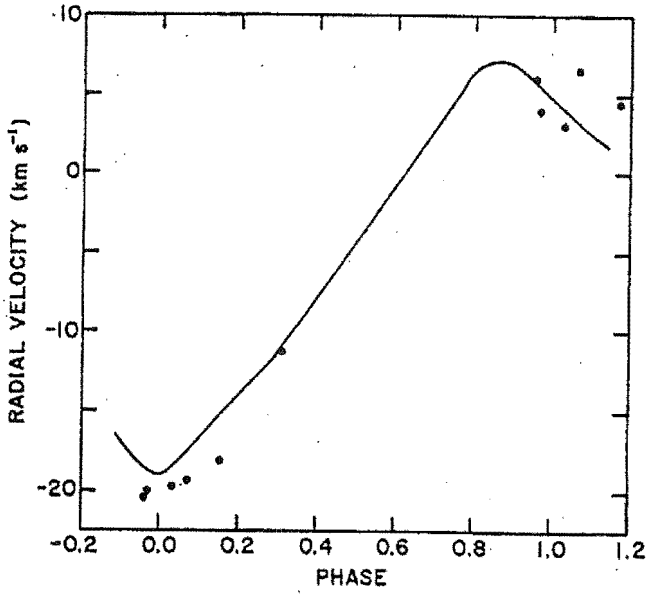

Figure 2.9: Photospheric radial velocities when a shock wave periodically passes though the photosphere. Line doubling occurs due to the presence of both infalling photospheric gas and the outwardly moving photosphere. This is taken from Hinkle et al. [90] Figure 16. The star is χ Cygni and the atomic lines used to obtain the velocities are in the 8000 Å region.

blue region of the spectrum (the blue end of the visual being chosen for observation because of its relative lack of blending). This failure of visual absorption line velocities to behave as expected, especially with Mira stars which have dramatic regular changes of brightness, was a cause for much puzzlement in understanding the physical nature of the variability. Infrared spectroscopy showing that indeed a shock wave and pulsation were present only solved part of the problem — why did the visual not show this? In 1986 there were two plausible explanations for this (refer to Querci [136]

[36]Querci [136] (page 125) notes that data is scarce, and the case is not as clear as for Mira-stars, but that the existence of some "S" shaped velocity curves for **semi-regular stars** suggests they may be pulsating by some Mira like mechanism

pages 121–125) which will now be briefly described.

In 1979 Hill and Willson [85] used the simple model of pulsational driving at the photosphere base to present a new interpretation of the absorption and emission line velocities of LPV stars in terms of two shocks simultaneously present in the atmosphere. The second shock wave is the tail end of the previous shock, which persists for about one period. Observations at 1 μm reflect the region of the star near the lowest (emerging) shock wave, but visual absorption lines (and molecular TiO bands) must form just ahead of the upper shock or well after it, where the gas has had time to cool to less than 3000 K. They show that if the "free fall period" of the gas (how long it would take for the shocked gas to get back to its initial position, under the influence of gravity alone) becomes more than half the pulsational period of the photosphere, then the velocities of the gas will become aperiodic with erratic variations from cycle-to-cycle. As this is far more likely to occur at the upper shock, this can explain regular IR and visual-magnitude observations (the visual continuum originates in the lower shock also) at the same time as irregular visual-velocity behaviour. From a histogram of visual spectra over 4000–7000 Å and IR molecular lines Willson et al. [179] concludes the two-shock model is the best physical interpretation of the spectral variations seen. However, Querci [136] does not support this conclusion and instead favours the following alternative explanation.

Hinkle et al.'s [90] IR spectroscopic observations of the Mira variable χ Cygni form the basis of another explanation, which avoids the need to have a shock wave persisting for a period. They hypothesise that not only are the blue-visual lines are formed above the nicely behaved IR lines, but they are formed in the infalling gas from an 800 K stationary shell which is the order of 10 stellar radii away from the photosphere. This shell is thought to be gas ejected from the star by a particularly violent oscillation and supported by the dissipation of shock energy. They also note that the opacity that is preventing the blue-visual from seeing deeper into the atmosphere must be highly wavelength dependent[37] , because observations of atomic lines in the 8000 Å region show a nice "S" curve (see Figure 2.9).

Either way, the existence of shock waves will result in visual radial velocities that are at best regular but discontinuous, like Figure 2.9, or at worse featuring "gross cycle-to-cycle variations". The latter case occurs when the atomic lines in question are formed at such distance above the base photospheric pulsation that they no longer follow the photospheric continuum's regular magnitude variations. As Willson [177] emphasised at a conference in 1978, talking about the Hill and Willson [85] paper, lines whose variations make physical sense and/or have consistent phasing in relation to the light curve are formed near the lower shock, as they are following the photospheric changes. Of course, consistent phasing indicates lines following the photospheric changes regardless of the number of shocks present. This is interesting, because according to Pilachowski et al. [132] and Willson [178] L^2 Pup's behaviour implies the presence of shock waves, yet the visual radial velocities observed for this thesis agree well with the light variations when simultaneous data were collected (see §4.6). This would imply L^2 Pup's observed lines vary in the same manner as the photosphere, which might not be expected for a star with a semi-regular, or perhaps even Mira (Willson [178]), classification.

For more information on shock waves, particularly with respect to Mira/LPV stars, see Bowen [24, 25], Hinkle et al. [87, 88, 89], Pilachowski et al. [132], Willson [177, 178] and Wood [181].

[37] If the continuum opacity decreases from 3000 Å to 8000 Å, as is the case if the principal source of opacity is Rayleigh scattering, then lines seen in the blue region of the spectrum will be formed at a higher layer then lines seen in the red region. This dependence of LPV stars radial velocities on wavelength is discussed in Pilachowski et al. [132].

2.3.5 Non-radial pulsations

All pulsations can be considered to be non-radial with radial pulsations taken to be a special case of these. However, the general non-radial pulsation equations are significantly more complex than the radial case. A linear non-adiabatic non-radial pulsation, which is assumed to oscillate in time and have angular variations in the form of a spherical harmonic, forms a complex differential equation system of the sixth order — even in the adiabatic case it is a fourth-order system in real variables, which is significantly more difficult to solve than the radial adiabatic second-order real system.

Despite this, the more general non-radial pulsation does have some things in common with its special case. Adiabatic non-radial oscillations in time can only be either completely oscillatory or completely decaying, so it is necessary to consider non-adiabatic non-radial pulsations in order to study the growth or decay of pulsations. Similarly, in order to predict the amplitudes of non-radial pulsations it is necessary to study non-linear non-radial pulsations. Despite this, due to its relative simplicity linear adiabatic non-radial pulsations are often studied to give insight into the behaviour of non-radial pulsations. Usually spatial variations are assumed to be spheroidal, that is it is assumed that the angular variations can be represented by a spherical harmonic (see Figure 2.10). Along with toroidal modes[38] (where the star undergoes a "kind of slow twisting"

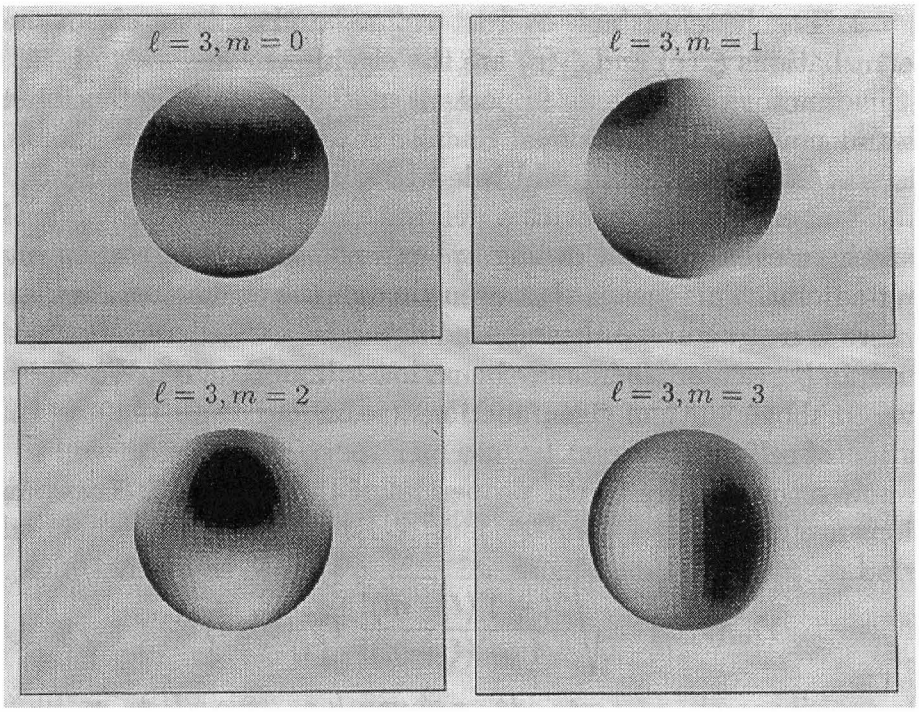

Figure 2.10: These figures show the change in the spherical harmonic, Y_m^l, with its order l and its azimuthal order, m. Light regions represent a positive value for the real part of Y_m^l and dark regions a negative value. The order of the spherical harmonic gives the total number of nodal lines (zero Y_m^l) on the surface of the sphere, while m gives the number of nodal lines that pass through the axis. This is Figure 10.2 from Hansen [69].

motion), spheroidal modes form a complete set of motions in that all non-radial movements can be represented as a sum of these modes (see Cox [40] §17.3 for more details).

Unfortunately the resulting LAWE does not form a Sturm-Liouville problem, so while discrete

[38] These are sometimes called r-modes and are unimportant in non-rotating stars

time frequencies are necessary to satisfy the boundary conditions a unique ordering of the frequencies is not possible. In fact the angular frequency is related to the spheroidal mode, the order of the harmonic, as well as the order of the frequency, in a manner illustrated by Figure 2.11. As

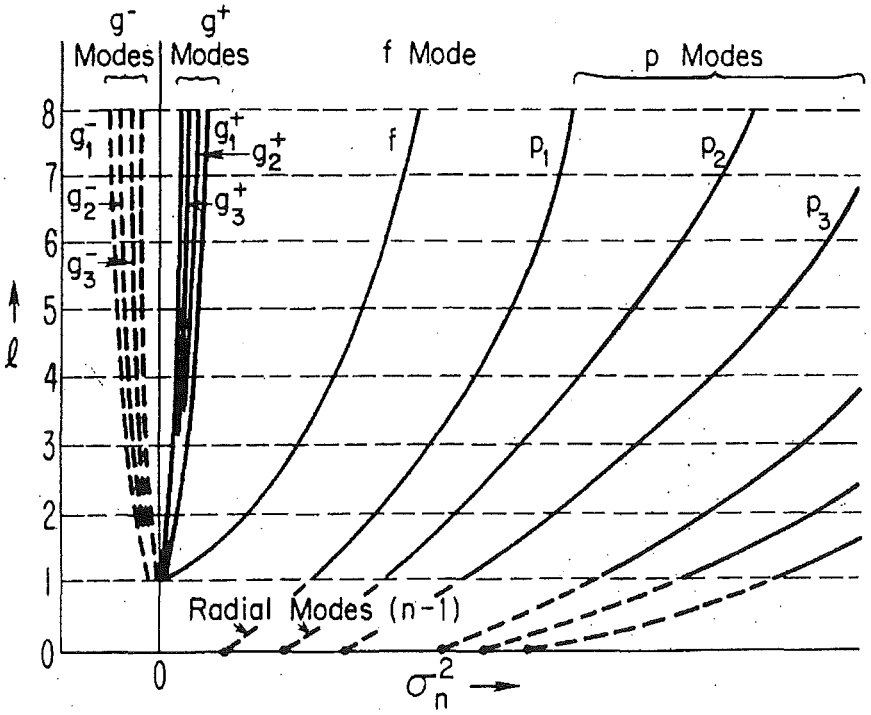

Figure 2.11: The relationship between frequency, σ_n, order of spherical harmonic, l, and the type of oscillation for a linear adiabatic non-radial pulsation (radial modes are given by $l = 0$). Non-adiabatic effects will not change this situation significantly. This is Figure 17.2 from Cox [40].

can be seen, the frequency does not form a unique set and in fact can be split into three cases which are commonly called p, g and f-modes (see Cox [40] §17.7, 17.8, 17.12 and 17.13). In the case of very small or very large oscillation frequencies, if the Cowling approximation is valid[39] a Sturm-Liouville system can be formed with the correct choice of eigenfunction (in the g-mode case the inverse square of the frequency of oscillation is the eigenvalue, in the p-mode its square is). Hence in these special cases, a standing wave is formed with the number of nodes equal to the order of the mode (just like in the radial case, see §2.3.1).

p-modes are predominantly radial (in that high order p-modes undergo much larger radial movements than in the plane tangential to the radius vector) and are characterized by large changes in density and pressure during oscillations. Their changes in amplitude become relatively large near the stellar surface and their frequency of oscillation is predominantly determined by the outer stellar layers. For p-modes the frequency of oscillations increases with mode number and when the spherical harmonic describing the angular variations is at its lowest order this mode is equivalent to a radial oscillation. As can be seen from Figure 2.11, p-modes always have shorter periods than the radial mode (except, of course, when in the lowest order spherical harmonic). These are also sometimes called acoustic oscillations, because for high orders their frequency is similar to what would be expected for the propagation of a sound wave (see Cox [40] page 264).

g-modes, on the other hand, are sometimes called gravity modes because the "buoyancy of the

[39] In the Cowling approximation the Euclidean perturbations in the gravitational potential are ignored

gravitational field is the restoring force" (Hansen [69] page 393). They are predominantly transverse (higher order g-modes undergo a much larger tangential movement than radial movement) and have small changes in density and pressure. They do, however, have relatively large interior movements and their frequency is predominantly determined by the deep inner stellar layers. For g-modes the frequency of oscillation goes to zero as their mode number increases and this mode of oscillation has no radial counterpart. As can be see by Figure 2.11, g-modes are always longer in period than radial modes and can be split into two cases called g^+ and g^- modes. In the adiabatic pulsation case, these have variations which are either completely oscillatory in time or completely decaying. The latter is strongly associated with convection and higher order g^- modes even have the same time of decay as the characteristic convection time. In fact g^- modes can not exist in a star that is completely stable against convection and in order for oscillatory g-modes (g^+ modes) to exist in a star it can not be fully convective. See Sorouti [158] for an investigation of the relationship between g-modes and convection.

There is only a single frequency for the f-mode and this is determined more or less evenly by the entire star. In the case of a homogeneous compressible star this mode is characterized by having divergence-free adiabatic displacements hence this is often called a Kelvin mode, after the first person to investigate such a mode (Cox [40] page 237). Like g-modes the f-mode has no radial counterpart.

More on the behaviour of mass movements caused by p and g-modes can be obtained by considering non-adiabatic linear oscillations. For very high order (in time) p-modes, it is then possible to show (if waves propagating radially are assumed, see Cox [40] §17.12) that variations in density lag behind radial displacements by approximately 90 degrees, which is the same relationship as for purely radial pulsations. Not only that, but tangential lag radial displacements by the same amount. Similarly, for very high order g-modes it is possible to show that variations in tangential displacements lead radial displacements by approximately 90 degrees and density and radial displacements are in anti-phase (this latter is only true if the motions are adiabatic).

When very simple stellar models are considered, it is found that stars are propagating entirely in either an acoustic or gravity mode (with some evanescent regions[40]). However, for more complicated stellar models that have, for example, alternating convective and radiative zones or are inhomogeneous chemically, being in one frequency of pulsation means the star may have mixed modes — in that in one region the oscillations may be gravity waves and in another they may be acoustic waves (see Cox [40] §17.10). As evolved stars, such as those observed for this thesis, may have both convective and radiative zones and certainly are not homogeneous chemically, any pulsations they have may not be of a single mode type throughout the star.

Indeed for large spherical-harmonic orders the red-giant model of Shibahashi & Osaki [150] shows non-radial oscillations which consist of gravity modes (effectively trapped within the nuclear-burning shell), acoustic waves in the envelope and an evanescent zone in between. They conclude that red-giant models are vibrationally stable against the non-radial gravity modes, but make no comment on the stability of the acoustic envelope modes.

However in the same volume, Ando [5] published a paper considering, amongst other things, the stability of acoustic waves in the envelope. In this useful paper, linear acoustic non-adiabatic non-radial pulsations in late-type stars were calculated and growth rates and pulsation periods for giants and supergiants with spherical-harmonic orders of 10 to 1000 found. For those periods excited, the

[40] When the radial displacements of non-radial pulsation form standing waves, the mode associated with the oscillation is said to be trapped. By contrast if the radial displacements are not oscillating in space at all then the modes are said to be evanescent.

coolest of these model giants had pulsation periods of a few hours and supergiants a dozen days or less (as the harmonic order lowers periods equal to the radial pulsation predictions should be found). However as Hatzes [72] points out, current radial-velocity techniques are incapable of detecting pulsation modes of either g or p type with a harmonic order of greater than six.

In this interesting paper published in 1996, Hatzes investigates the radial-velocity variations that will be found when a cross-correlation technique is used to reduce observations of a cool-giant star, which is slowly rotating and pulsating non-radially in a prograde sectoral mode[41] (considered because it should produce the largest radial-velocity variations). Both g and p-modes are considered and the radial-velocity variations produced are nearly sinusoidal, as is illustrated in Figure 2.12 (for an idea of what is happening to the spectrum throughout all this and to see how different spherical harmonics affect things, see Schrijvers [148]). Unsurprisingly, the observed amplitude of the radial-velocity variations decreases as the angular order of the harmonic increases (see Figure 2.12). It should be noted that while at all times the size of the g-mode's observed radial-velocity

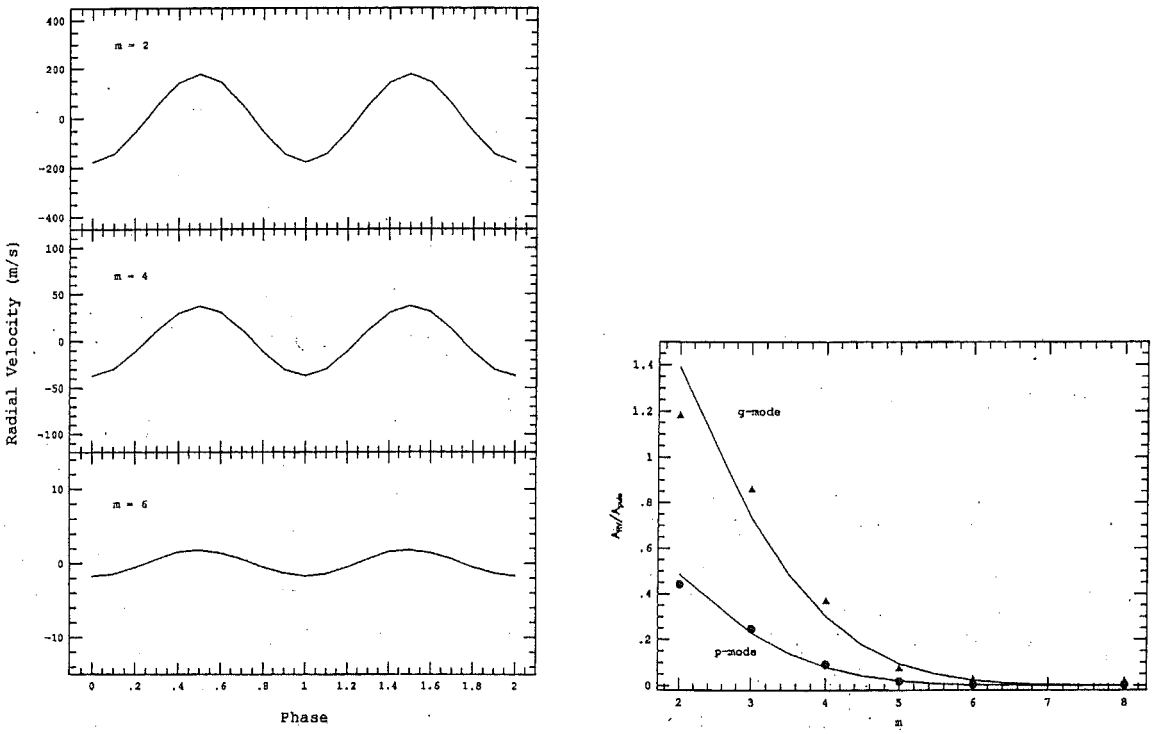

Figure 2.12: The left-hand figure seen here is the radial-velocity variations of a cool, slowly rotating, giant which is undergoing a sectoral p-mode pulsation with a pulsational amplitude of 400 m/s. The expected reduction in pulsational amplitude, with increasing order of spherical harmonic, is illustrated in more detail in the right-hand figure. Both these figures originate from Hatzes [72].

variations to oscillation amplitude is larger than that of the p-modes, the pulsational amplitude of g-modes is expected, generally, to be much smaller than that of p-modes and hence p-modes more easily detectable. This implies that for radial velocities of the precision obtained for this thesis (i.e. 50 m/s), acoustic pulsations of harmonic order two and amplitudes of greater than about 100 m/s should be detectable (or 500 m/s for a harmonic order of four and so on). So while these simulations are simplistic, they do indicate that it is possible to observe some low (harmonic) order acoustic oscillations with low amplitudes.

[41] In prograde sectoral modes the spherical harmonic, $Y_m^l(\theta, \phi)$, has $l = -m$ (where l is the order of angular variation). In a rotating star the oscillation in time depends on m as well as l, as rotation splits the non-radial oscillations frequencies (see Cox [40] §19.1 and the next section).

This leaves the obvious question of what the non-radial pulsational amplitudes will be for the stars observed for this thesis. Unfortunately as has been mentioned, prediction of the actual amplitude of non-radial pulsations requires non-linear non-radial theory, which is prohibitively complex. However, at least in the case of solar-like oscillations another approach can be taken. Solar-like oscillations are acoustic oscillations which are excited by turbulent convection in the outer part of the star (as opposed to those excited by the κ-mechanism, which are expected to be much larger in amplitude). Hence stars which have convective outer regions, such as those observed for this thesis, might be expected to have such solar-like oscillations. The approach taken by Kjeldsen & Bedding [108], to predict the integrated starlight radial-velocity amplitude for such oscillations, is by a form of scaling up from the Sun's amplitude. When this is done it predicts that a K giant, such as Arcturus, should have oscillation amplitudes for solar-like pulsations of 62 m/s and variations in luminosity of 0.2%. Also, if the Sun is any indication, many p-modes will be excited and the dominant one will have a period of a few days.

Non-radial pulsations in a rotating star

Most of the non-radial pulsation theory discussed so far is developed assuming a non-rotating star. However, in the presence of rotation a number of things change. One is that the degeneracy in the spherical-harmonics azimuthal order, m, is removed. This is called rotational splitting and means that the star's oscillation frequency becomes slightly longer or shorter, depending on m. Late-type evolved stars rotate very slowly (see §4.10), so this effect can be disregarded.

More importantly, rotation means that the observed period of the "pattern" on the surface of the star (see Figure 2.10) differs from the oscillation period. If $P_{\rm rot}$ is the rotation period, the variation due to the pulsation itself could be ignored and if the rotation axis is though the spherical-harmonic axis then the pattern will repeat every $P_{\rm rot}/m$ days. Alternatively in the absence of rotation, if the period of oscillation is $P_{\rm puls}$ the pattern will appear to rotate in the azimuthal direction, ϕ, with an angular velocity of ϕ/m (taking on the appearance of an azimuthal running wave) and will repeat every $P_{\rm puls}$ days. Hence, the presence of both together means the observed period will be

$$P_{\rm obs} = \frac{P_{\rm puls}}{1 - mP_{\rm puls}/P_{\rm rot}}.$$

For the stars observed for this thesis, acoustic pulsations predictions are typically no more than 10% of the shortest possible rotational period (see Table 4.25 and 4.28). This means that the observed period for a non-radial acoustic pulsation may vary by about 30% from the real period if $m \leq 3$, which might make it as long as the predicted fundamental radial pulsation, but not much longer. A non-radial g-mode pulsation, however, has a period of the order of the rotation for these stars and as a result may be observed to be much longer or shorter than the actual oscillation period.

In addition, when non-vanishing rotations are present toroidal non-radial pulsation become a possibility. For a non-differentially rotating star, to first order in rotation frequency the expected pulsation period is

$$\frac{P_{\rm puls}}{P_{\rm rot}} = \frac{l(l+1)}{m(2-l(l+1))}$$

(see Papaloizou & Pringle [129]). This means for a low spherical-harmonic order r-mode pulsation ($l, m \leq 3$), pulsation periods are expected to be between one fourth and one and a half times the rotation period (although if $l = 1$ then higher order terms in rotational frequency become important and a much longer pulsation period is possible). Allowing for the modulation of these periods by the rotation of the star means that the observed period due to r-mode pulsation may be as short as two tenths of the rotation period. It should also be noted that r-modes have no radial

displacements, so there is not expected to be any light variation associated with them (Kambe & Osaki [101]).

Chapter 3

Spectroscopic instrumentation and reduction

3.1 Introduction

In the early 1840 s Doppler correctly predicted a change in frequency of light when the source and the observer were moving with respect to each other. Within a decade (although it was published much later) Fizeaus predicted, at a lecture, that this Doppler shift would mean the velocity of stars along the line-of-sight could be measured from the change in wavelength of spectral lines. However, it was not until 1871 that the first indisputable observation of the optical Doppler effect was made, when the spectra from the receding and approaching limbs of the Sun were displayed simultaneously and the corresponding shift in lines seen, by Vogel. Initial attempts at radial-velocity measurement were done by detecting the spectra visually and the error in such observations usually as large as the radial-velocity shift itself. By the 1890 s Keeler was obtaining Doppler shifts with a probable error[1] of only 1.8 km/s using a visual spectrograph, but by this stage radial velocities using a photographic detector were underway and made the visual technique obsolete.

The first reliable radial-velocity measurements, with an average probable error of 2.6 km/s, were made by Vogel in the late 1880 s, using a spectrograph and photographic detector. Using Vogel's techniques large-scale radial-velocity surveys were undertaken, of all stars brighter than 5.51 magnitudes at Lick Observatory (directed by W. Campbell, published as the Lick Radial-Velocity Catalogue in 1928) and of stars with large proper motions or parallaxes at Mt Wilson (Adams, Kohlshutter and Joy, published in 1923 with additional radial velocities published in 1950). For more details on these early radial-velocity measurements and projects see Hearnshaw [80, 81, 79, 82].

However, radial velocities with a precision of better than about 1 km/s were not obtained until 1967, by Griffin [65] using a physical mask to cross-correlate with the stellar spectrum and recording the resulting cross-correlation function photo-electrically. This idea was able to achieve a precision of under 500 m/s (for example CORAVEL). In 1974 the idea of a digital cross-correlation was suggested (Simkin [151]), where a detector records the spectrum and it is cross-correlated later using a computer. Application of this method with a reference spectrum[2] of a known radial velocity yielded a radial-velocity precision of approximately 250 m/s (see Hill [84] and Latham [113]). The main obstacles to getting better radial-velocity precision, with or without the use of some form of cross-correlation, are:

[1] The probable error is defined such that half of the observations of an experiment are expected to fall within the mean plus or minimum the probable error. See Bevington & Robinson [21] page 31, for example.

[2] In the following a reference spectrum refers to some stellar exposure which is compared to the current stellar exposure, usually with respect to cross-correlation. Whereas, a comparison spectrum will refer to the lamp spectrum used to determine the rest wavelengths incident on the detector.

(a) Flexure of the spectroscope when mounted on the telescope. This causes equipment to move and can cause the comparison lamp spectra taken before and after the stellar spectra to be inappropriate.

(b) Thermal effects, for a similar reason. For the Mt John system a change in temperature of 0.01 degrees equates to a change in radial velocity of 20 m/s (see Murdoch [124] §5.1.4). It is thought that the worst of this is due to the aluminium échelle grating mount which supports the échelle grating and the steel micrometer which adjusts the grating, as the expansion coefficient is quite different for these materials.

(c) Guiding errors. If the slit width is not uniformly illuminated asymmetric lines and therefore erroneous measurements of the lines, will result. Even if the guiding is consistent, unless the light is perfectly centred on the slit a systematic error in the measured radial velocity will occur.

Most instrumental errors, such as these, can be put down to a large extent to the rays from comparison lamp and star light following different paths inside the spectrograph (this means that instrumental problems affect them differently, see Griffin & Griffin [67]). In addition improvement in the following areas is also important:

(d) Improved laboratory measurements of the wavelengths of lines present in the stellar spectra and comparison lamp.

(e) The careful choice of the lines in the comparison spectrum and stellar spectrum so as to avoid line blending which causes spurious wavelength shifts.

The problems (a) and (c) can be avoided to a large extent by the use of a fibre feed, although whenever the slit-fibre feed arrangement is altered a systematic error in radial velocity will be introduced. Observations of a known constant star can be taken and these used to correct for this systematic error — these will be called run corrections. A fibre feed also restricts (b) as the spectrograph can be kept in a thermally controlled cabinet.

The stellar component of (d) and (e) can be avoided to a certain extent by cross-correlating the stellar spectrum with another similar spectrum. This spectrum could be of a star of similar spectral type and constant radial velocity, a synthetic spectrum, or some reference spectrum of the same star. The last of these is the method used to reduce observations for this thesis and while in many respects it is by far the simplest, it does mean that only relative radial velocities will be obtained[3].

The reduction in errors from a few hundred metres a second to only a few tens of metres a second has largely been accomplished by superimposing the reference spectrum over the stellar spectrum, thereby ensuring that the light path for the two is identical. The basic method is to place an absorbing media ahead of the slit, so that the star light passes through this during the exposure. The method of reduction uses an observation of the stellar spectra without the absorbing media being present and the knowledge of the "transmission function" of the absorbing media itself to disentangle the stellar-media spectrum obtained for each observation. There are three main types of absorbing media which have been used, O_2, HF and I_2, of which only the latter two have had an automated reduction procedure. The reduction procedure for the last two differs significantly, as HF was chosen as the absorption media because it avoids blends with stellar lines — however it requires a metre long absorption cell and is a dangerous gas (see Campbell et al. [33] for more details on this). Its use has been superseded by I_2, which only requires a 10 cm length cell. However it blends with all stellar lines, due to its plentiful spectra and as a result a complicated and careful reduction system is needed (which includes deconvolutions, see Marcy & Butler [120] for

[3]This means the systematic errors in reference lamp wavelengths of (d) are not important

more details on this). The payoff for this extra effort is high, however, as in 1996 radial velocities with a precision of 3 m/s were reported (see Butler et al. [31]).

However, over November 1988 to September 1991 Murdoch [124] was able to achieve a typical precision of 55 m/s without doing this, but by the careful reduction of the magnitude of the instrumental shifts using a fibre-fed échelle and digital cross-correlation. While the precision obtained by this approach is an order of magnitude less than the best produced by superposition of spectra, the equipment and reductions are easily undertaken. The intrinsic limiting precision of the method may be much higher, the ELODIE fibre-fed échelle spectrograph is believed to give an accuracy better than 15 m/s for stars brighter than 9th magnitude (see Baranne et al. [8] for more details on this).

3.2 Equipment

In November 1993 spectroscopic observations began for this thesis. It was hoped by even more reduction in the magnitude of instrumental error and the replacement of the previous Reticon linear-diode-array (LDA) detector with a CCD chip that even more precise radial velocities would be obtainable (differences in instrumentation from that used by Murdoch [124] are designated "**new**"). The general physical layout of the system is shown in Figure 3.1.

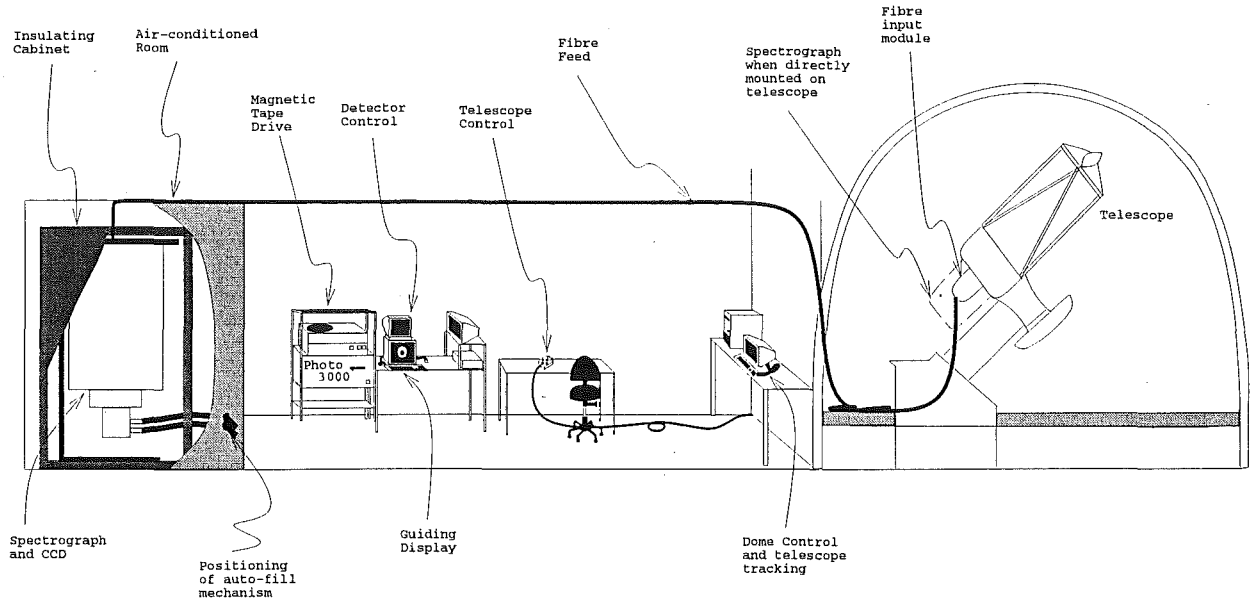

Figure 3.1: Schematic illustration of the layout for equipment used to obtain observations for this thesis.

The telescope used for the observations is the one-metre McLellan reflector telescope, at the f/8 Cassegrain focus. There are two viewing mechanisms available in the fibre-feed module for observing stars. The first provides a wider field which is used to find the star initially. In the second narrower field of view the light falls directly onto the fibre end and an aluminized wedge reflects the light which does not fall down the fibre for use in telescope guiding. A system of rotating mirrors allows light from either the star, the comparison lamp, or a quartz-halogen white lamp to pass down the fibre, ensuring that for the most part the comparison and stellar light follow the same paths. For the comparison lamp a thorium-argon hollow-cathode emission lamp was used.

The fibre feed is a 25 metre Spectran step-index ultraviolet-transmitting, 105 μm core diameter,

optical fibre. The fibre input corresponds to 2.5 arc seconds of sky. The ends of the fibre are cleaved to achieve clean terminations then interfaced to optically polished glass windows by refractive index matching glycerine drops. At the input end the window is a glass wedge with an aluminized back, which lies in the focal plane of the telescope. A 120 μm pin hole in the aluminization allows most of the starlight to pass into the fibre. At the output end the beam emerges at a focal ratio of approximately f/5.2 and this is converted back to f/8, in order to match the focal ratio of the spectrograph collimator, by passage through an f/1.8 camera lens — this almost doubles the fibre core to 180 μm. Before it reaches the collimator the light is passed through an 85 μm slit giving a resolution of 178 mÅ at order 44 (for the resolution at other orders see Table 3.1). For more details on the fibre-feed and spectrograph see Kershaw & Hearnshaw [103] and Hearnshaw [78].

Order	λ Range (Å)	λ_C (Å)	$\delta\lambda_C$ (mÅ)	P (Å/mm)
41	5618–5643	5630	191	2.09
42	5484–5509	5499	186	2.04
43	5357–5381	5369	182	2.00
44	5235–5259	5249	178	1.95
45	5119–5142	5132	174	1.91
46	5008–5030	5020	170	1.87

Table 3.1: **Resolution & dispersion over the six CCD orders.** This table gives some of the vital statistics for the CCD over the wavelength range observed for this thesis where: λ Range is the range of wavelengths incident over the entire order, from edge-of-CCD to edge-of-CCD; λ_C is the wavelength in the centre of the used part of the order, i.e. between the first and last thorium line positions; $\delta\lambda_C$ is the resolution at λ_C; P is the plate-factor, also known as the dispersion.

At this point it should be noted that this is a "velocity resolution" of 10.2 km/s at order 44. This, in addition to line-blending problems and low-pixel resolution, were the reasons that line-profile variations (either line bisectors or even equivalent widths) were not investigated for the data. As radial-velocity variations were typically less than 1 km/s (see §4.2), it was not believed likely that any variations in line shape due to the cause of the radial-velocity variation would be visible. The biggest observed $(R-I)_C$ colour variation was 0.065 magnitudes (see §4.7) and if Bohlender et al. [22] is any indication (although these values are for changes in lines at about 8000 Å) this will result in an equivalent width variation of less than 20 mÅ, which is about one tenth of the resolution.

The échelle spectrograph is mounted vertically on a trolley in a temperature-controlled, polystyrene-insulated cabinet — typically kept to 25.0 ± 0.1^0 C. This cabinet is in turn located in an air-conditioned room which is sealed at the start of each observing run — typically kept to 18^0 C (**new**)[4]. The detector is cooled automatically, without opening the cabinet, by a system of pipes from the adjacent corridor which run the coolant from a store, through the room, through the cabinet, and into the CCD dewar. The vapour resulting from this is similarly passed into the corridor by a system of pipes. As well as minimizing the temperature disturbing effects of cold vapour entering the cabinet, this also allows an automatic cut off when the dewar is full. In order to decrease the chance of dramatic temperature related radial-velocity shifts during exposures the cooling was done at the end of each night of observation and as early before the beginning of each night as the dewar's vacuum would allow.

[4]The temperature control for the room is nowhere near as fine as for the cabinet and was seen to fluctuate around the set temperature by up to a degree. For the temperature inside the cabinet to be stable it was found to be necessary to have the cabinet set to a temperature which was at least 4^0 C above the highest temperature the room reached.

The spectrograph's échelle grating has 79 grooves/mm and a blaze angle of $\theta_B = \arctan(2) = 63^0 26'$. At diffraction order 44 it has a dispersion of 1.95 Å/mm (for the dispersion at other orders see Table 3.1). To separate the different orders a cross grating is placed after the échelle. The cross grating has 150 grooves/mm, a blaze angle of $\theta_B^C = 2.2^0$ and is used in its first order, which equates to a wavelength of about 5000 Å near the Lithrow condition. The échelle and cross gratings are tilted until orders 41–46 are present on the CCD (see Figures 3.2 and 3.3 for typical CCD spectra and Table 3.1 for the wavelength range of the orders).

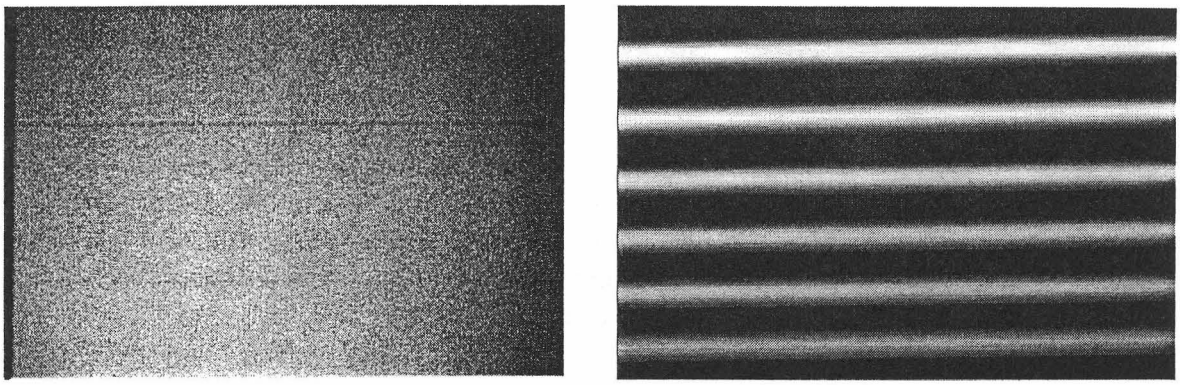

Figure 3.2: These plots are of raw CCD images. The image to the left is the median of three DARK images. To the right is a dark-subtracted flat-field image, where the orientation is with the 41st order at the top, the 46th order at the bottom and wavelength increasing from left to right.

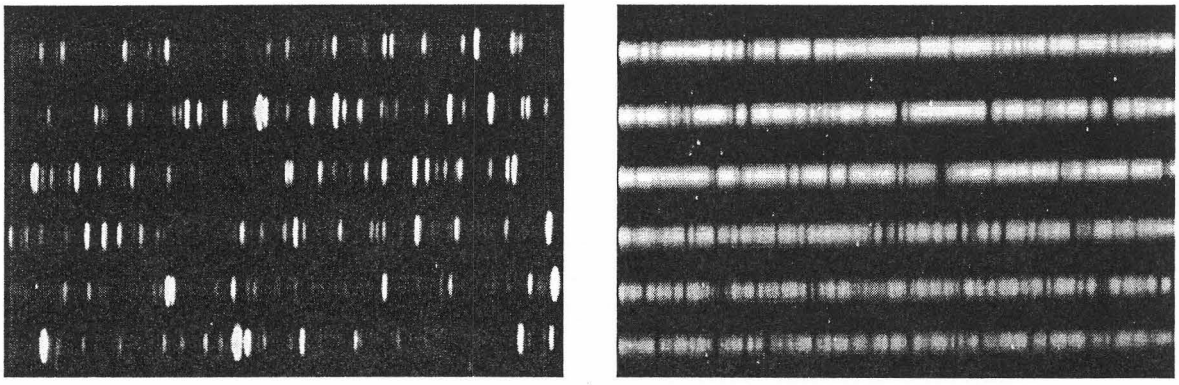

Figure 3.3: These plots are of raw CCD images. The image to the left is the dark-subtracted comparison spectrum of thorium-argon. To the right is a typical dark-subtracted K-type stellar spectrum, in this case of ω Cap. For both images the orientation is with the 41st order at the top, the 46th order at the bottom and wavelength increasing from left to right.

The detector is based around the Photometrics 3000 CCD camera system (**new**). The system consists of a CH210 camera head (CCD, mechanical shutter, dewar and flash ring), which is connected by a cable to a CE200 camera electronics unit, which is located in the spectrograph's temperature-controlled room, which in turn is connected to the Photometrics PM3000 computer which resides in the data room.

The CCD is a liquid-nitrogen-cooled Thomson TH7882 CDA CCD chip overcoated with Metachrome II, for enhanced ultraviolet and blue response. The chip is 576×384 pixels in size, each pixel is 23 μm square and the chip is cooled to -110 ^{0} C to give low dark current. At the beginning of an

exposure a flash ring between the mechanical shutter and the quartz window in front of the chip is illuminated for 70 ms, depositing about 300 electrons on each pixel to minimize the occurrence of reduced charge transfer efficiency that is associated with very low signal levels, before the mechanical shutter to the chip is opened (for further details see Pollard [133] §6.2–6.4).

The CE200 is the detector's electronics unit. As well as providing power and CCD timing signals it amplifies the analogue image signal, noise filters it, then digitizes it to 14 bits with a 50 kHz analogue-to-digital converter. The Photometrics PM3000 computer allows control of the camera using the Forth base-level software. The exposures are taken with a gain of 100, which equates to 4.31 electrons per ADU. According to tests performed by Pollard [133] §6.4.5, the linearity of the CCD chip is excellent over the range of 30–13200 analogue-to-digital-units (ADUs).

3.3 Observations and reductions

The sequence of spectroscopic observations each night was that of three flash-ring only images (called dark images, see Figure 3.2), one white-light exposure (called a flat-field, see Figure 3.2) and then after setting the telescope on the desired star, a comparison spectrum (called a thorium for short, see Figure 3.3), the stellar spectrum (see Figure 3.3 for a typical K-type stellar spectrum), then immediately after another comparison spectrum. The darks had their median taken and were saved as one image on magnetic tape. This is necessary because the flash ring does not evenly illuminate the CCD, therefore its subtraction from all other observations is necessary. This subtraction was generally done to all other spectroscopic images before they were written to magnetic tape.

The flat-field is necessary because not only does the échelle and cross grating throw more light out in different orders and different wavelengths, but different pixels do not have exactly the same sensitivity to a given wavelength of light. A flat-field is taken to help remove this undesirable effect and this correction is known as flat-fielding.

Observations are taken with a thorium spectrum on each side of the stellar spectra in order to minimize errors due to thermal or atmospheric-pressure changes. In addition to the expansion and contraction of the instrumentation due to thermal changes, both of these changes result in a variation in the refractive index of the air which also causes a shift of spectral line positions on the detector. The effect of a temperature change of 0.1^0 at 24^0 on the refractive index of the air equates to a change in velocity of a few tens of meters a second, at the wavelength observed. Unlike the temperature the atmospheric-pressure is not controlled in anyway and the effect of a change in pressure of 1 millibar gives an apparent radial-velocity shift of 80 m/s (see Murdoch [124] §5.1.4). Averaging the dispersion solutions obtained just before and just after the stellar exposures will be accurate as long as the temperature and pressure changes are linear during the exposure and as long as the signal was received evenly during the exposure (both erratic guiding and cloud can effect this).

These observations were all written to magnetic tape and taken back to the University of Canterbury for reduction. The Fortran program **ccd_to_vax**, written by W. Tobin in 1989, is used for reading off the 9-track 1600 bpi magnetic tape written by the Photometrics PM3000 CCD system. By default the files are output in FITS format (extension .MT). Once the images have successfully been read off the magnetic tapes they are reduced down to six one-dimensional orders by the use of the image-reduction program **Figaro**[5].

Figaro has its own image format, so it is initially necessary to convert the images from FITS to the **Figaro** format. Once this is done, conversion to the one-dimensional form used for cross-

[5]This image reduction package was originally written in Caltech and continues to be developed by AAO

correlation is undertaken as follows (for a step-by-step guide see Appendix F):

1. The CCD images are rotated and cleaned of cosmic rays.
2. The CCD orders are straightened to remove S-distortion.
3. Then the CCD orders are collapsed into one dimension.
4. At this stage both the thorium and stellar spectra are flat-fielded. Why this is done after the CCD orders are collapsed, and why the thorium spectra is also flat-fielded are discussed in §3.4.
5. Then the collapsed spectra are output to ASCII files, with the order number on the first line in the file.

The resulting files are then ready for cross-correlating by adaptations of the Turbo Pascal programs written by Murdoch [124] for this purpose. These adaptations are mainly to allow the reduction of six different orders[6] by the same program and to allow for the different length of the CCD from the LDA. The first step in the process of obtaining the relative radial velocity of a stellar spectrum is to find the dispersion solution for each of the two thorium spectra corresponding to the stellar spectrum. The program to do this is called **ccddisp** (previously called **dispfit**) and it does so by fitting a gaussian to a predefined set of lines in each thorium spectrum and fitting a quadratic to the pixel location as a function of wavelength. The average of this for the two thoriums is taken to be the dispersion solution suitable for the stellar exposure (for further details see Appendix F.5 and Murdoch [124] Appendix B).

The velocity shift between the stellar spectrum and some reference spectrum can now be found. For this thesis another spectrum of the star is nominated to be the reference spectrum for all observations, although this does not have to be the case. This was done by first rebinning the pixels of the stellar spectrum and its reference into bins of equal shifts in logarithmic wavelength. The rebinning is done by assuming that the light had a constant distribution across the pixel. In actual fact this is not the case, but this is not found to make a large difference to the relative radial velocities obtained (this is discussed in §3.5.4). When this is done only bins which are in between the wavelength of the first and last lines used to find the dispersion solution are kept to form the cross-correlation function, as extrapolation of the dispersion solution may add unwanted error. In addition, only bins which are estimated to have spectra of the same rest wavelength are kept, as the cross-correlation of two non-identical spectra will result in an asymmetric cross-correlation function which will result in an error in the relative radial-velocity determination (for a discussion of possible causes of cross-correlation function asymmetry see §3.5.2).

Once the stellar spectrum and its reference are rebinned, the cross-correlation function of the two spectra was formed by taking the Fast-Fourier Transform of the two spectra. The program which does this is called **ccdxrun** (previously called **cross**). While still in the frequency domain an optimum filter is applied to the cross-correlation's Fourier transform (see §3.5.2), then the cross-correlation is transformed back. The resulting cross-correlation function has data points at intervals of 2.4 km/s and it is then fitted by the sum of three gaussians to obtain the best estimation of the position of the cross-correlation function peak and therefore the radial-velocity shift (why a single gaussian is not sufficient is discussed in §3.5 and §3.5.4). Once the peak is found, its position is corrected for the difference in motion of the Earth about the barycentre of the solar system for the two exposures and the resulting radial velocities written to a file (for further details see Appendix F.6 and Murdoch [124] Appendix B).

[6] Although for the most part the six orders are reduced independently

This file thus contains the relative radial velocities for six different orders. An average of the six orders is taken and this written to another file. The error in this average is taken to be the internal standard deviation of the relative radial velocity given by the six orders. The Turbo Pascal program which takes the average of the six orders is called **ccdskyrc** and where radial velocities from the Sun are available[7] the program uses these to apply a run-correction to the average radial velocity of the stellar exposure (for further details on this see Appendix F.7.1).

Two reduction steps for which the correct approach was found to be crucial for the resulting radial-velocity precision were flat-fielding and cross-correlation function fitting. These will now be discussed in more detail.

3.4 Flat-fielding

Flat-fielding is carried out to achieve two things. The first is to remove the pixel-to-pixel signal sensitivity variations and the second is to remove the variation along the spectral orders which has been caused by the blaze function of the échelle[8]. The former is more important to a cross-correlation data reduction as it contributes a high frequency signal to the data and may result in asymmetry in the cross-correlation function. However noise has a similar effect, so a close eye must also be kept on what is happening with it. To achieve these goals stellar images should be divided by an image where all wavelengths of light enter the spectrograph with equal intensities[9] — a source of light equal in all wavelengths is white light (i.e. a flat-field). The presence of this variation along the orders, due to the blaze function of the échelle and especially due to pixel-to-pixel variations, can cause the centre of lines to be uncertain by making them appear asymmetric. However, while variations due to pixel non-uniformity should be removed, from a signal-to-noise point of view it is desirable to retain the variation of light perpendicular to the orders (for the equipment used for this thesis this is mainly due to the fibre-feed and slit[10] and the general reduction of CCD sensitivity at longer wavelengths), as the outer edges of the orders have a lower signal-to-noise and hence give a "less certain" indication of line position. Hence, when collapsing the orders down to one-dimension (adding up the rows), the pixels being collapsed should contribute to the result according to the signal present. For this reason, collapsing the stellar and flat-field spectra before flat-fielding is the preferred method of applying the flat-field. Precisely how this differs from the more commonly used two-dimensional flat-field division then collapse method will now be explored.

3.4.1 Removing instrumental effects that may cause apparent line position shifts

The signal in the pixel located at row and column (i, j) in the CCD, after its orders have been straightened, will be denoted by $R_{i,j}$, where the incident flux is F_{incident}. Then ignoring readout noise $R_{i,j} = p_{i,j}(\lambda) \times F_{\text{incident}}$, where $p_{i,j}$ is the sensitivity of the pixel at (i, j) to the wavelength λ. For a given order if no photon noise was present F_{incident} would equal (ignoring the smearing effect of the slit) $F_{\text{incident}} = l(\lambda) \times c(h) \times f(\lambda)$, where $l(\lambda)$ is due to the blaze function of the échelle, $c(h)$ is mainly due to the fibre-feed, slit and CCD sensitivity, and $f(\lambda)$ is the true distribution of light emitted from the star (see Figure 3.4 for explanation of the relationship between variables

[7]Equipment changes were meant to eliminate the need for run corrections; however, it soon became apparent that this was not the case and in August 1994 exposures of the Sun began to be taken to use for run-correction determination

[8]It is also believed that some of the variations in signal over the surface of the CCD are due to the presence of dust on mirrors and glass inside the spectrograph

[9]By dividing out the effect for a source of equal intensities for all wavelengths the orders are effectively normalized

[10]The profiles of the orders are gaussian-like, rather than box-like with tapering edges, as the collimator has a sigmatism designed to spread the light perpendicular to the orders (from the days of photographic plate detectors). The effect of the cross-grating is minimal as observations take place in the centre of its first order.

$[j, i, \lambda, h]$). However the presence of noise in the signal can not be ignored.

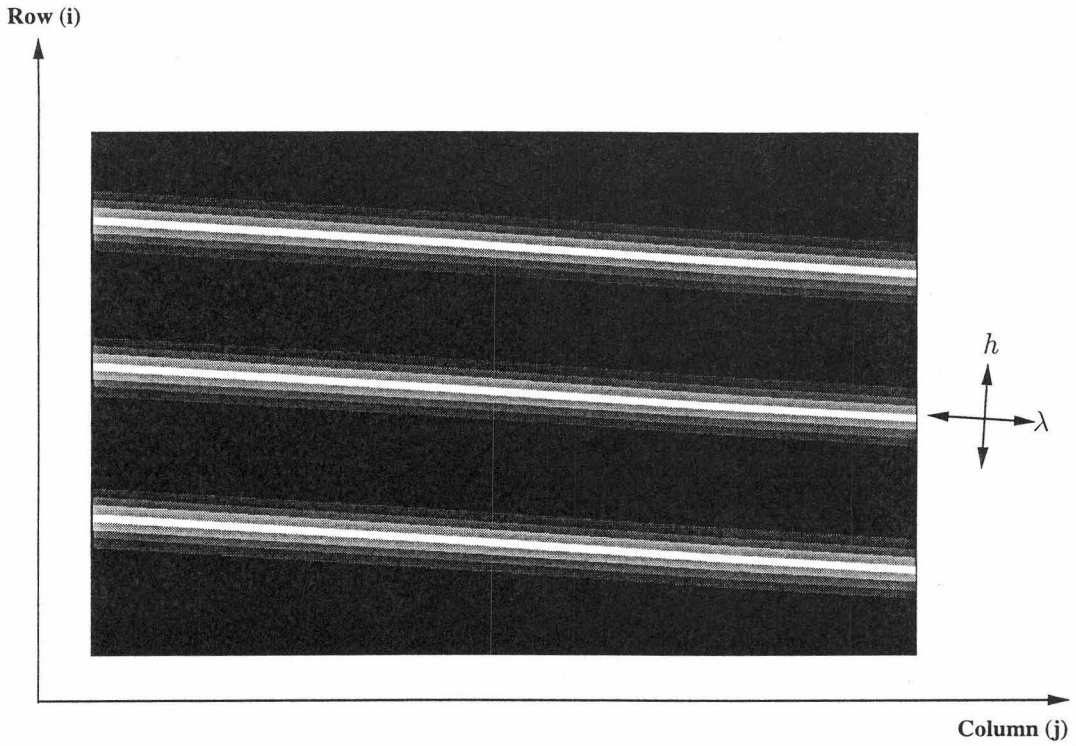

Figure 3.4: These are the unstraightened CCD orders. It can be seen that when the CCD orders have been straightened h is simply related to i and λ to j.

Ideally to remove the effect of pixel-to-pixel variations $p_{i,j}(\lambda)$ should divided out[11]. Also it would be desirable to divide out $l(\lambda)$, as it varies with wavelength and hence is a potential problem. However, $c(h)$ does not vary with wavelength and to divide it out would be equivalent to scaling across the orders so every row contributed to the collapsed order equally — resulting in noisy data. So the ideal final one-dimensional spectrum would be[12]

$$\mathcal{F}_j = \frac{1}{l(\lambda)} \frac{1}{\sum c(h)} \sum_i^M \frac{R_{i,j}}{p_{i,j}(\lambda)},$$

where i ranges over the M rows in a given order. There are two easy techniques for removing such variations from data — they are both forms of flat-fielding and how they pertain to the ideal case will now be discussed. In all cases the images in question have had their orders straightened.

Dividing the entire CCD chip by a flat-field image

In this approach the two-dimensional CCD image is divided through by the flat-field image, then the result has its orders collapsed to produce the required one-dimensional orders. The result of

[11] Variations in $p_{i,j}$ across (i) will affect the average signal seen at a given (j). But this effect is not constant across (i), so failure to remove the variation of $p_{i,j}$ across (i) could result in an apparent wavelength shift of lines when the spectrum is collapsed. As will be shown, when the two flat-fielding techniques are compared to the ideal, dividing collapsed signal by the average $p_{i,j}$ (collapse then flat-field) will only remove this harmful variation if $p_{i,j} \approx \overline{p_j}$.

[12] Where division by $\sum c(h)$ is for the sake of normalization

this is pixels with their signal in the form of[13]

$$\mathcal{F}_j^1 = \frac{1}{M}\sum_i^M \frac{F_{i,j}}{S_{i,j}},$$

where $S_{i,j}$ is the flat-field reading in pixel (i,j) and $F_{i,j}$ is the signal readout of the same pixel for the stellar spectrum. This has the effect of dividing out not only the intensity variation along the order and from pixel-to-pixel, but the "gaussian" cross-profile of the orders (due to $c(h)$), so every row of pixels ends up contributing equally after flat-field division.

Using standard error propagation (see, for example, Bevington & Robinson [21] Chapter 3) the noise in row i and column j of the flat-fielded spectrum is

$$\sigma^2_{\frac{F_{i,j}}{S_{i,j}}} = \left(\frac{F_{i,j}}{S_{i,j}}\right)^2 \times \left(\frac{\sigma^2_{F_{i,j}}}{F^2_{i,j}} + \frac{\sigma^2_{S_{i,j}}}{S^2_{i,j}}\right).$$

When the orders are collapsed, by adding up the pixel rows in each order, column j has an error of

$$\sigma^2_{\mathcal{F}_j^1} = \frac{1}{M^2}\sum_i^M \left(\frac{F_{i,j}}{S_{i,j}}\right)^2 \times \left(\frac{\sigma^2_{F_{i,j}}}{F^2_{i,j}} + \frac{\sigma^2_{S_{i,j}}}{S^2_{i,j}}\right).$$

Because $F_{i,j}/S_{i,j}$ should be approximately constant with respect to i, as both F and S only differ along the columns (as $l(\lambda)$ and $c(h)$ are the same for both of them), for column j the following result is obtained:

$$\left(\frac{\sigma_{\mathcal{F}_j^1}}{\mathcal{F}_j^1}\right)^2 \approx \frac{1}{M^2}\sum_i^M \left(\frac{\sigma^2_{F_{i,j}}}{F^2_{i,j}} + \frac{\sigma^2_{S_{i,j}}}{S^2_{i,j}}\right).$$

For the CCD exposure, $R_{i,j}$, the noise is of the form[14] $\sigma^2_{R_{i,j}} = R_{i,j} + N^2_{\mathrm{RO}}$, where the first term is due to photon noise and the second to readout noise. Substituting these into the above it can be seen that

$$\left(\frac{\sigma_{\mathcal{F}_j^1}}{\mathcal{F}_j^1}\right)^2 \approx \frac{1}{M^2}\sum_i^M \left(\frac{1}{F_{i,j}} + \frac{1}{S_{i,j}}\right) + \frac{N^2_{\mathrm{RO}}}{M^2}\sum_i^M \left(\frac{1}{F^2_{i,j}} + \frac{1}{S^2_{i,j}}\right).$$

Dividing the collapsed stellar image by the collapsed flat-field

Here the flat-field and the stellar images are both collapsed (using the same pixels), then the one-dimensional spectrum is divided by the one-dimensional flat-field. At the end of all this the pixel signal has the form

$$\mathcal{F}_j^2 = \frac{\sum_i^M F_{i,j}}{\sum_k^M S_{k,j}} = \frac{F_{\mathrm{T},j}}{S_{\mathrm{T},j}}.$$

The effect of this is to treat the pixels along the columns in the order as though they are just one long pixel. If variations in pixel sensitivity along the height of the order could be neglected, this technique could also be thought of as dividing each row by the flat-field spectrum (as is typically done), then when collapsing the columns weighting each row to give the order breadth back its natural "gaussian" form. The $c(h)$ variation is left intact and correspondingly it will be shown that this has a better signal-to-noise than the other method.

[13] Where division by M is for the sake of normalization

[14] Where the units are photons, not ADUs and assuming that as far as the photon errors are concerned the incident flux can be taken to equal the readout flux

Using standard error propagation the noise in column j of the collapsed stellar spectrum and flat-field are

$$\sigma^2_{F_{\mathrm{T},j}} = \sum_i^M \sigma^2_{F_{i,j}} \text{ and } \sigma^2_{S_{\mathrm{T},j}} = \sum_i^M \sigma^2_{S_{i,j}}$$

respectively. Hence the error in the flat-fielded spectrum is

$$\sigma^2_{\frac{F_{\mathrm{T},j}}{S_{\mathrm{T},j}}} = \left(\frac{F_{\mathrm{T},j}}{S_{\mathrm{T},j}}\right)^2 \times \left(\frac{\sigma^2_{F_{\mathrm{T},j}}}{F^2_{\mathrm{T},j}} + \frac{\sigma^2_{S_{\mathrm{T},j}}}{S^2_{\mathrm{T},j}}\right).$$

When the appropriate form for the noise is used, the collapsed pixel's noise (relative to the signal) becomes

$$\left(\frac{\sigma_{\mathcal{F}_j^2}}{\mathcal{F}_j^2}\right)^2 = \frac{1}{\sum_i^M F_{i,j}} + \frac{1}{\sum_i^M S_{i,j}} + \frac{MN^2_{\mathrm{RO}}}{(\sum_i^M F_{i,j})^2} + \frac{MN^2_{\mathrm{RO}}}{(\sum_i^M S_{i,j})^2}.$$

Disregarding the readout noise, both for simplicity and because it should be very small in comparison to the photon noise, comparison of the signal-to-noise ratio for the two flat-fielding methods reveals that this second method has a better signal-to-noise. This is because it can be shown by induction that

$$\frac{1}{M^2}\sum_i^M \frac{1}{a_i} \geq \frac{1}{\sum_i^M a_i},$$

if $a_i > 0$ (the equality sign holds when a_i is constant for all i)[15].

How do the two flat-fielding techniques compare to the ideal?

Ignoring the noise present in any flat-fielded spectrum (the flat-field is taken as near the maximum signal-to-noise as the CCD linearity will allow, see §3.2) the act of flat-fielding then collapsing a spectrum produces, in terms of the pixel variations and grating effects,

$$\mathcal{F}_j^1 = \frac{1}{M \times l(\lambda)} \sum_i^M \frac{R_{i,j}}{p_{i,j}(\lambda)c(h)}.$$

The alternative of collapsing the spectrum and collapsing the flat-field then dividing one by the other gives

$$\mathcal{F}_j^2 = \frac{1}{l(\lambda)} \frac{\sum_i^M R_{i,j}}{\sum_i^M p_{i,j}(\lambda)c(h)}.$$

Comparing these with the ideal case a number of things can be noted. If no photon or readout noise was present in the spectrum itself (at times a very bad assumption) both of these methods would give the same result as the ideal. If $p_{i,j}(\lambda)$ was the same for all rows of a set j, $\mathcal{F}_j^2 = \mathcal{F}_j$ would be true (for a good CCD this assumption is approximately correct). Alternatively if $c(h)$ was the same for every row in an order, $\mathcal{F}_j^1 = \mathcal{F}_j$ (a very bad assumption indeed, unless only a very small bit of the order breadth is used).

So collapsing then flat-fielding, in addition to giving a better signal-to-noise, is nearer to the desired spectrum. However to check this, data from collapsing the images then flat-fielding and flat-fielding and then collapsing the images were compared (along with data which had not been

[15]This can be shown by first assuming it is true for some M, defining $A = \sum_i^M a_i$ and $\alpha = A\sum_i^M 1/a_i \geq M^2$, so that the $M+1$ case can be written as LHS$= \alpha/A + 1/a_{M+1}$ and RHS$= (M+1)^2/(A + a_{M+1})$. Multiplying these so they have the same denominator and subtracting off the resulting RHS, LHS$\geq (A - Ma_{M+1})^2$ and RHS$= 0$ can be obtained. This clearly satisfies LHS$\geq$RHS. The $M = 2$ case is simple and can be easily shown to be the case and hence this is proved by induction for all $M \geq 2$.

flat-fielded at all). This is presented in §3.4.2 and some interesting complications are explored.

Closer inspection reveals a third flat-fielding option which, while more complicated, potentially could combine the better signal-to-noise of the second method (which was used during the data-reduction for this thesis) and the better pixel sensitivity variation removal of the first method. It has been noted, in consideration of the preferred method, that ignoring the pixel-to-pixel variations it is very similar to flat-fielding by the two-dimensional method, then weighting each row back to its natural "gaussian" form. Importantly, if this is done the better signal-to-noise ratio is kept, but the individual pixel-to-pixel variations are properly removed, resulting in a spectrum very near the ideal. This would require weighing each column in the two-dimensionally flat-fielded spectrum by the average in that column for the flat-field, before collapsing. This is not easily achieved using the **Figaro** *image reduction package, but could be worth investigation by future researchers. Another approach is to change the equipment so that a flat-field spectrum can be created where the orders are artificially broadened, to give the flat-field a box-like shape over the width of the stellar exposure. This is what is done for the ELODIE project (see Baranne et al. [8]).*

3.4.2 Testing the flat-fielding options

The issue of flat-fielding turns out to be even more complex than the above arguments might suggest. The dispersion solution actually varies within the breadth of the order, due to the orientation of the lines (see Figure 3.5), so the dispersion solution obtained by simply straightening the orders then collapsing then into one dimension is actually a weighted average (the outer edges of the orders contribute less as they have less signal) of the dispersion solutions within the order. For spectra

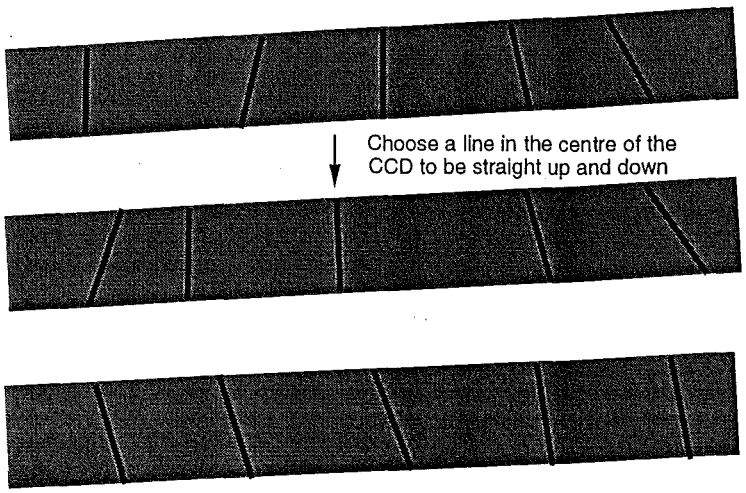

Figure 3.5: This schematic thorium spectrum illustrates how the lines across the CCD vary in their orientation to the rows.

that have not been flat-fielded this effect more or less cancels out, as the dispersion solution above the order centre "cancels" with that below. However the smooth-field is not perfectly aligned with the stellar spectrum on the CCD (see Figure 3.6), which is surprising as it too passes down the fibre feed like the stellar spectra, but probably reflects the different paths taken by the flat-field and the stellar image to become incident on the fibre entrance. So if a stellar spectrum is flat-fielded then collapsed (so that the line positions at the edges contribute "equally" with that in the centre), the same cancellation doesn't occur as one edge of the order generally ends up giving a greater contribution than the other[16].

[16]One other result of this is the line profiles change shape slightly (in an asymmetric way). This is also one reason why stellar spectra, not flat-field spectra, are used to straighten the orders.

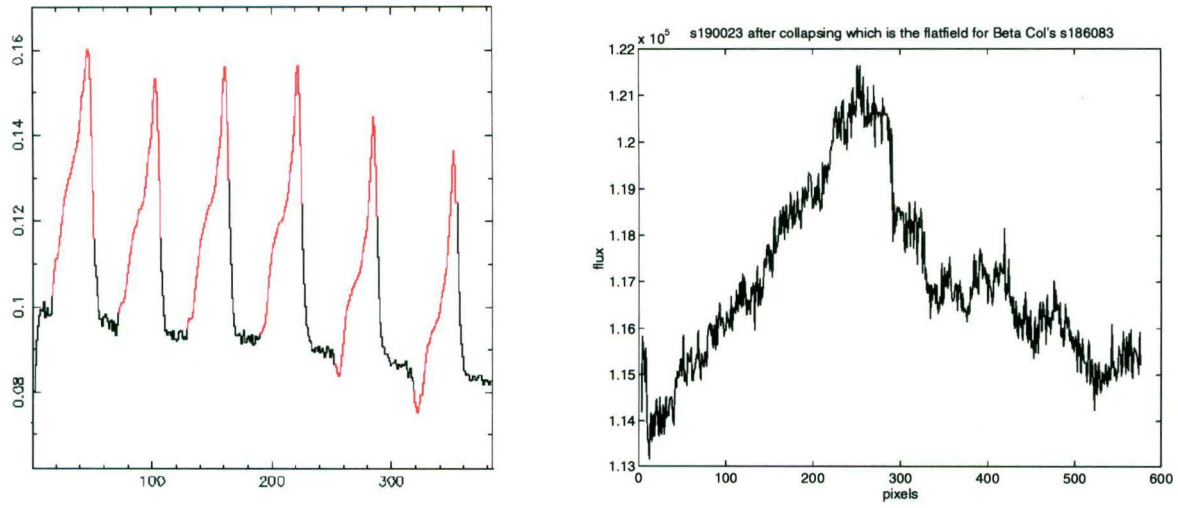

Figure 3.6: The left-hand figure shows the average ADU count in columns for the straightened then flat-fielded (not collapsed) image of β Col (stellar image s186-08 and flat-field image s190-02). The x-axis is the column number, the y-axis the "normalized" ADU count and the location of the stellar orders before flat-fielding is shown in **red**. As can be seen, this is far from the box-like order profiles expected if the flat-field and stellar image were properly aligned. The right-hand figure shows the collapsed flat-field. Its jagged nature clearly shows that a badly placed thorium line could suffer a small apparent shift in position.

This resulted in (using the same dispersion solutions for all three cases) an apparent velocity shift of two to four hundred metres a second between the flat-fielded then collapsed spectrum of the typical K type star β Col and the spectrum which had not been flat-fielded. In the case of flat-fielding then collapsing the spectrum, the flat-fielding effectively shifts the lines along the CCD. The direction of shift, for a given line, is determined by the position of the line at the edge of the order that contributes most! When the spectra are collapsed then flat-fielded the radial velocities are very similar to those where the spectra are not flat-fielded.

This result stresses the fact that to avoid inconsistencies it is necessary to do the same flat-fielding procedure to the thorium spectra as to the stellar spectra. While the averaging problem that arises if a stellar spectrum is flat-fielded then collapsed doesn't arise if a spectrum is collapsed then flat-fielded (hence the differences between the not flat-fielded spectra and the collapsed then flat-fielded spectra for β Col were slight), the thoriums still need to be flat-fielded (having been collapsed) as the pixel-to-pixel variations could cause an apparent shift in a thorium line position and therefore degrade the quality of the dispersion solution obtained (see Figure 3.6).

It should be noted that any non-alignment between the thorium spectra and the stellar spectrum may, however, result in the collapsed dispersion solution being correspondingly inappropriate for the collapsed stellar spectra. This is unavoidable, regardless of the flat-fielding option chosen. Fortunately, while the thorium spectra, like the flat-field spectra, may not be perfectly aligned with the stellar spectra, visual inspection implies any difference is far smaller. This is slightly surprising, as the most obvious difference between the three spectra is that the stellar fibre input will have a "shadow" in it due to the secondary mirror, which will correspond to the central cone of angles being missing. If this was the cause of the misalignment between flat-field and stellar spectra, the thorium and flat-field alignment might be expected to agree well.

3.5 The cross-correlation function

The concept central to the determination of relative radial velocities in this thesis is the cross-correlation. Hence some relevant definitions and characteristics will be explored, before some complications are investigated. The continuous cross-correlation function is defined as

$$c(x) = g(x) \otimes h(x) = \int_{-\infty}^{\infty} g(x+y)h(y)dy,$$

where x is called the lag of the cross-correlation function. The Fourier transform of the cross-correlation function is $G(f)H^*(f)$, where $G(f)$ is the Fourier transform of g and $H(f)$ is the Fourier transform of h. The discrete cross-correlation is defined to give a function which is as close as possible to the cross-correlation for the continuous data. This is done by defining the discrete cross-correlation function to be

$$c(l\Delta x) = \sum_{i=0}^{N-1} g((l+i)\Delta x)h(i\Delta x),$$

where $c_j \equiv c(j\Delta x)$, $g_j \equiv g(j\Delta x)$ and $h_j \equiv h(j\Delta x)$ are functions with a period of $N\Delta x$. l is called the lag of the discrete cross-correlation function and the discrete Fourier transform of c_l is $G_k H_k^* \equiv G(\frac{k}{N\Delta x})H^*(\frac{k}{N\Delta x})$.

The question is: what form will the cross-correlation function resulting from the cross-correlation of two stellar spectra take? Initially, for simplicity, continuous cross-correlations will be considered. The continuous cross-correlation of two real functions where one is just the other shifted by some amount, say δx, is a symmetric function with its peak at the shift, i.e.[17]

$$\begin{aligned} h(x) \otimes h(x+\delta x) &= \int \exp(2\pi i f(\delta x - x)) \mid H(f) \mid^2 df, \\ &= \int \cos(2\pi f(\delta x - x)) \mid H(f) \mid^2 df, \end{aligned}$$

if $h(x)$ is real. However, it is the cross-correlation of two stellar spectra that is of interest and it will be assumed that the stellar lines are gaussian in shape[18] and are, over the wavelength observed, of equal width — not to mention that all lines are shifted by the same amount in radial velocity. But the Fourier transform of a gaussian with a peak at zero is another gaussian with its peak at zero[19]. That is

$$\mathrm{FT}(\exp(-(\frac{x}{d})^2)) = \frac{\pi^{1/2}}{d} \times \exp(-(fd\pi)^2),$$

and from this it can be deduced that the cross-correlation of two gaussians, g_1 and g_2, is another gaussian as

$$\begin{aligned} \mathrm{FT}(g_1 \otimes g_2) &= \mathrm{FT}(\exp(-(\frac{x-b}{d})^2))\mathrm{FT}^*(\exp(-(\frac{x-\beta}{\delta})^2)), \\ &\propto \exp(-(fd\pi)^2 - 2i\pi fb) \times \exp(-(f\delta\pi)^2 + 2i\pi f\beta), \\ &= \exp(-(d^2+\delta^2)(f\pi)^2) \times \exp(-2i\pi f(b-\beta)), \\ &\propto \mathrm{FT}(\exp(-(\frac{x-(b-\beta)}{\sqrt{d^2+\delta^2}})^2)), \end{aligned}$$

[17] This can be seen by taking a Fourier transform of both functions, multiplying them together and transforming the result back

[18] This is not really true, due to the effect of micro-turbulence, macro-turbulence and rotational broadening (see §4.10 for more details on these broadening mechanisms). In addition, the observed lines will have additional broadening due to the instrumental profile, which is unlikely to be gaussian. The effect of this on the radial velocities obtained will be similar to that of line blending (discussed later in this section), though less severe.

[19] See, for example, Brigham [28] Figure 2-11

where the translation theorem for Fourier transforms has been used. Clearly when the Fourier transform is reversed it will result in a gaussian with a peak at $(b-\beta)$ and a half-width[20] of $\sqrt{d^2+\delta^2}$.

Of course stellar spectra do not consist of just one line, but many. To investigate this, the spectra will be considered to be the summation of gaussians and for simplicity the continuum will be neglected and an emission spectrum used. Therefore the spectrum, $\mathcal{S}$, is of the form $\mathcal{S}=\sum_l \mathcal{S}_l$, where $\mathcal{S}_l$ is the gaussian appropriate for line l. Then it can be seen that the continuous cross-correlation of the two spectra, $\mathcal{S}$ and $\mathcal{T}$, leads to $\mathcal{S}\otimes\mathcal{T}=\sum_{i,j}\mathcal{T}_i\otimes\mathcal{S}_j$, which is a sum of gaussians. The case of two different exposures of the same star (ignoring noise and assuming that the spectra are normalized) will now be considered. Therefore all $\mathcal{T}_i$ and $\mathcal{S}_j$ have half-width, W, and $\mathcal{S}(x)=\mathcal{T}(x-x_0)$, where x_0 is the shift of the spectrum between the two exposures. So if $A_{i,j}=a_i\times a_j$ (where a_l is the normalized amplitude of line l), then

$$\mathcal{S}\otimes\mathcal{T}=\sum_l A_{l,l}\exp(-(\frac{x-x_0}{\sqrt{2}W})^2)+\sum_{\substack{i,j\\ i\neq j}} A_{i,j}\exp(-(\frac{x-(x_i-x_j)-x_0}{\sqrt{2}W})^2).$$

The first sum will be the largest at $x=x_0$ and is itself a gaussian, as it is a sum of gaussians with the same peak location and half-width. When the lines in the spectrum are sufficiently far away from each other, the peaks of the other summations (occurring at $x=x_0+(x_i-x_j)$) will not contribute significantly to the main cross-correlation function peak. In other words, if $|x_i-x_j|\gg\sqrt{2}W$ for all lines the peak of the cross-correlation function can be considered to be gaussian. Unfortunately the wavelength region where the stars for this thesis were observed is heavily blended[21], so this is not the case and the cross-correlation functions obtained are often obviously non-gaussian in form (see Figure 3.7, this is actually one of the more gaussian of the cross-correlation functions). A better

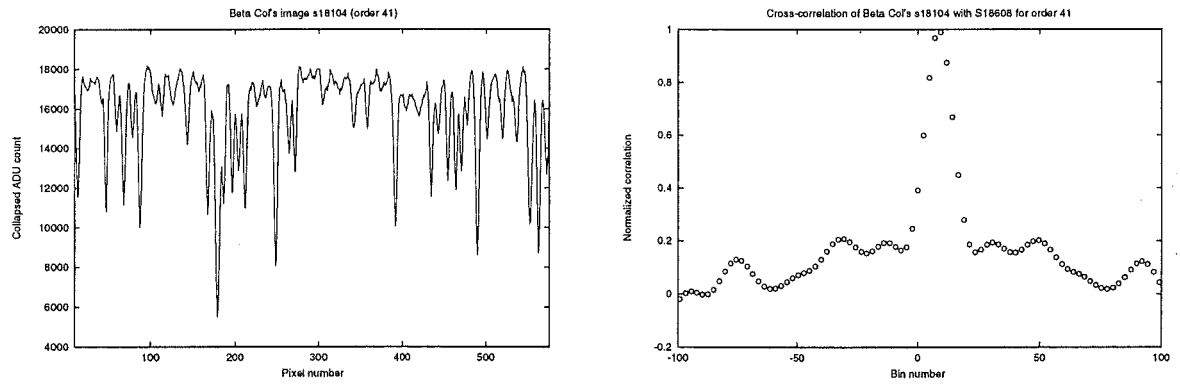

Figure 3.7: The left-hand diagram is the 41st order of a typical K-type star, β Col. The right-hand diagram is the cross-correlation function that results from two such spectra. So that only the more gaussian data are fitted, the fit is set to be to 11 bins in total.

fit would use the sum of one main gaussian and many small additional gaussians, which (assuming the exposures are identical, but shifted) would be symmetrically distributed in position about the main gaussian and of the same half-width. This is effectively changing the number parameters for the fit from 3 to $(3+2n)$, where n is the number of small gaussians being added to one side of the main gaussian. It might be thought that as long as this sum of gaussians is symmetric about

[20]For this thesis, the value of $|x-x_0|$ (where x_0 is the peak location) at which the gaussian equals e^{-1} of its maximum height will be called the half-width

[21]This wavelength region was chosen to avoid telluric lines (see §3.5.2 for why this is important) and to be at the CCD chip's best quantum efficiency, which is less than 8500 Å (see Figure 6.2 Pollard [133] for the variation of the chip's quantum efficiency with wavelength)

the main peak, a simple gaussian fit should find the correct peak regardless — and indeed it would in the continuous non-windowed case. But as the data are discrete and windowed it is not that simple.

3.5.1 The effect of discrete data on cross-correlation function fitting

The data being cross-correlated are discrete, not continuous, which raises the question of the effect of discrete data on cross-correlation function fitting. The fit to the cross-correlation function being used is of the least-squares form. It is found that if the points are evenly distributed about the true peak (i.e. each is at the same height as another on the opposite side of the peak) the gaussian will fit the peak well. Unfortunately, this is not normally the case and, depending on the number of points used for the fit, the two bottom points to be fitted may be of dramatically different height. This "drags" the fit to the side with the more points, in order to minimize the squares, and hence the resulting peak fit is correspondingly off the true peak[22] (see Figure 3.8 and Figure 3.9). This will be called the odd-even effect and its causes will be discussed in §3.5.2 and §3.5.4, although the basic reason is that the the curve being fitted to the cross-correlation function does not agree with the data points' distribution.

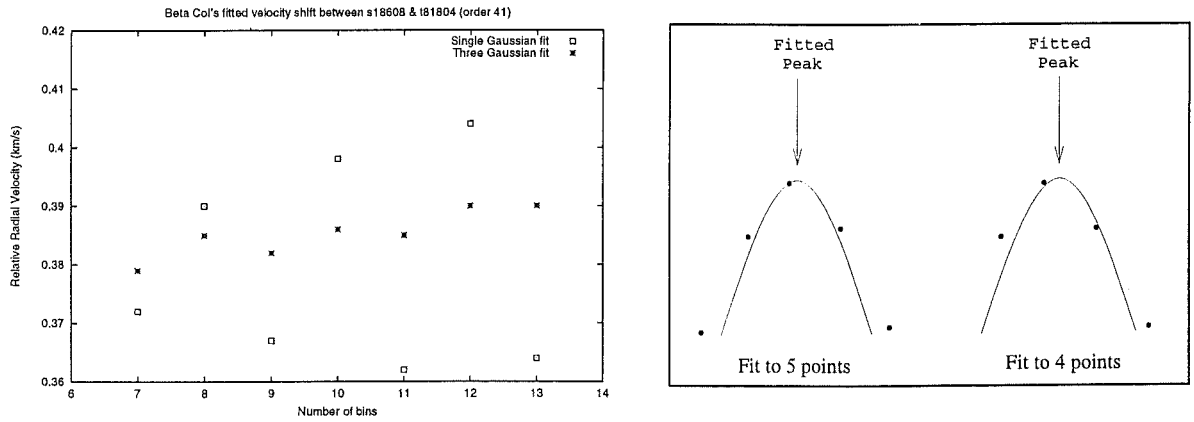

Figure 3.8: The left-hand diagram shows an example of the resulting radial velocities when a different number of points are fitted for the real cross-correlation function pictured in Figure 3.7, both using a single gaussian as the fitting function[23] and using a three-gaussian fit. Clearly the undesirable odd-even effect is reduced, if not entirely eliminated, by a three-gaussian fit (see also Figure 3.9, which shows how poorly a single gaussian fits the clearly non-gaussian cross-correlation function of order 45). The right-hand side shows a schematic diagram illustrating what happens during the odd-even effect. In this case an odd number of points has two bottom points of almost the same height and the fit to the peak is good. However when an even number of points is used, the difference in height of the two bottom points is large and a shift in fitted peak position occurs.

Using an extra set of gaussians in the fit reduces the problem. While more than $n = 1$ extra gaussians may be significantly involved in the main peak, just extending the cross-correlation fit from 3 to 5 parameters means such an uneven set of fitting points will result in a modulation of the positions and heights of the secondary gaussians, rather than a change in the position of the

[22] This is noticeable due to the poor pixel resolution of the spectra — the cross-correlation function is typically only about 11 bins wide, see Figure 3.7

[23] Although the number of points being fitted to increases, the cross-correlation function is less gaussian in its wings so instead of the odd-even affect disappearing it gets worse

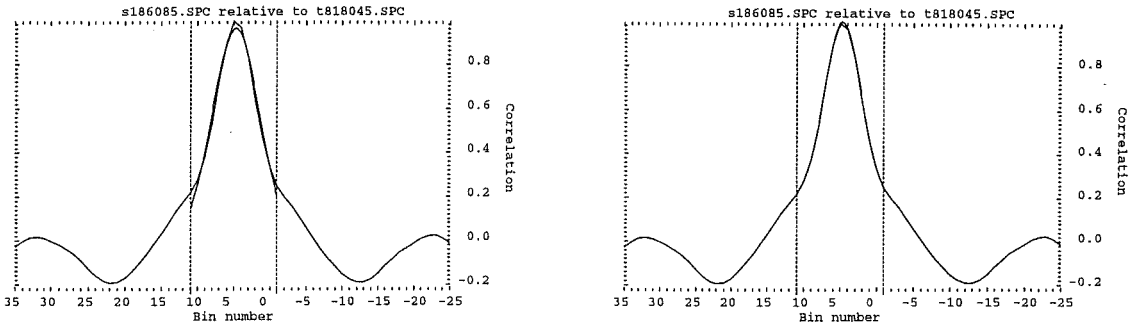

Figure 3.9: Order 45 produces one of the least gaussian cross-correlation functions for a K giant. The resulting single-gaussian fit is shown on the left and the sum of three gaussians fit on the right. The fit was made to 13 data points, rather than the usual 11, to emphasise the single-gaussian fit's inadequacy.

primary (and important) peak[24]. This problem was also discussed by David & Verschueren [45] who take the different approach to minimizing the error of combining the nearest odd and even fit.

3.5.2 Asymmetry and cross-correlation function fitting

Asymmetry of the cross-correlation function causes an apparent shift in central peak position when a symmetric function is fitted to the data (this also happens in the continuous case). One of the symptoms of this is a cross-correlation function which shows different peak positions depending on the number of points fitted to it, i.e. a manifestation of the odd-even effect. Asymmetry will occur if the two spectra to be cross-correlated are not identical. This could be caused by:

- Cross-correlation of two spectra of different spectral types. This problem is avoided in this thesis by cross-correlating stellar spectra by a reference spectrum of the same star (therefore obtaining relative radial velocities).
- Noise in the two spectra. Noise in the spectra causes the points in the cross-correlation function to be less accurately determined. So either the error in the points should be passed to the fitting procedure (determined according to the spectral flux), or there will be an extra error arising in the peak position due to signal-to-noise considerations. In the former case, possible noise asymmetry is taken into account by the error returned by the fitting procedure (this is done by the reduction software, see Appendix F.6.2).
- The differing response of the CCD's pixels with wavelength (see Figure 3.6) will mean that spectra taken on different runs are unlikely to be identical — flat-fielding can minimize this effect.
- Filtering of the cross-correlation function is undertaken to remove such high frequency signals[25]. The question is, could this cause asymmetry problems itself? Filtering is done by applying $\mathrm{FT}(c) \times O$, where O is the filter. This means that the filtered cross-correlation function is

$$\widetilde{c} = c * o,$$

[24]There are not enough bins to fit to, for more than a five parameter fit

[25]This should mean that the error in the fit returned by the fitting procedure should be on the high side

where $*$ represents a convolution and o is the inverse Fourier transform of O. If c is symmetric and o is symmetric then $\widetilde{c}$ will be symmetric also. But for o to be symmetric it is necessary that O be symmetric about zero (for more details on the filtering procedure see below).

- Telluric lines in the spectra. These come from the Earth's atmosphere and will be at the same wavelength for each exposure; however, the spectrum is expected to shift greatly due to intrinsic radial-velocity shifts and the movement of the Earth's orbit. There should be none of these at the wavelengths being observed — the wavelengths have been chosen to avoid such lines (see Moore et al. [123] page 348, for regions of Atmospheric O_2 and H_2O).

- Limb darkening effects. The observed radial velocity of a star is composed of an average over the visible disc of the star. In the case of stars varying due to pulsation or apparently varying due to some surface feature, the average is dependent on projection and limb darkening effects. However limb darkening varies with spectral region (see Cox [40] §3.4), so this means that the observed radial-velocity shift is wavelength dependent. Although over the small wavelength range observed for this thesis this is bound to be a small effect, it could cause an asymmetry in the cross-correlation function of the spectra of such stars and a difference in radial velocity from order-to-order.

The non-continuous nature of the data, i.e that the spectra are in a finite window and discrete, can also contribute to an asymmetry arising, the main reasons being:

- There needs to be an equal number of points of zero value added to the spectrum in order to prevent window leakage (see below for a definition and discussion of leakage). This means that the cross-correlation function at zero lag has more non-zero summations added to it than other lags and therefore, unless the cross-correlation function peak is at zero lag, the function will be asymmetric. A way of avoiding this (to a certain extent) is to divide the cross-correlation function by $(N - l)$, where N is the number of non-zero bins and l is the lag. Surprisingly, this makes little systematic difference and might even be considered to be marginally worse than just using a data set with a zero mean. This is discussed below in "the finite window problem".

- Another, not entirely disconnected, reason is that the finite data-window size and radial-velocity shifts (and barycentric shift) mean the two spectra to be cross-correlated are of slightly different spectra and so an asymmetry in the cross-correlation function arises (see Figure 3.10). This actually makes a huge difference and may well be the main contributing feature to cross-correlation function asymmetry for the data used in this thesis. To minimize this effect a reference spectrum with a barycentric velocity of zero is desirable[26] and because of this non-identical spectra have been set to zero during the reduction (the procedure **Samespectra** is responsible for this[27], see Appendix F.6.2).

- Not only are the data discrete and in a finite window, the pixels that integrate the data are of a finite width, so the pixel readings are not exactly equivalent to the continuous spectrum reading at a point. Discrete theory is designed to give a discrete cross-correlation function as near to the continuous as possible, but the pixel readings are not truly discrete. This is not believed to make a large difference to the precision of the relative radial velocities obtained, as is discussed in §3.5.4.

[26] This has not been done for the reductions made for this thesis and as a result slightly more of some spectra have been thrown away than is necessary

[27] This is done according to the difference in barycentric correction between the two spectra. While this is valid for the stars observed for this thesis, as their intrinsic variations account for less than a bin's movement, for other projects it would be preferable to do a second iteration, setting the non-identical spectra to zero based on the initial estimated radial-velocity shift. As the data are discrete even if the exact shift in bins was known, unless it is an integral number of bins, the different spectrum can only be removed to within a bin. Hence the two spectra must sample slightly different ranges of the continuous spectrum.

Filtering the cross-correlation function

The signal read out of the CCD pixels is a combination of the Doppler shifted flux, readout noise and pixel sensitively. The flux itself also contains photon noise. Noise and instrumental effects are undesirable in spectra, as they may lead to an asymmetry in the cross-correlation function. Wiener optimal filtering (see Press et al. [134] §12.6) finds the noise, $N(f)$, in the Fourier transform of the data, $C(f)$, by fitting a function at higher frequencies than the data is expected to have. This noise function is then removed by multiplying the data by the optimal filter, which is

$$O(f) = \frac{|S(f)|^2}{|S(f)|^2 + |N(f)|^2},$$

where $|S(f)|^2 = |C(f)|^2 - |N(f)|^2$. This filter is optimum in the sense that integrated over all f it minimizes $|O(f)C(f) - D(f)|^2$, where $D(f)$ is the data without any noise (or pixel sensitivity effects). For the Fourier transform of the cross-correlation function $|N(f)|^2$ is determined by fitting a constant (by least squares) to the power of the data (above a certain frequency) and a straight line to the power at low frequencies, where noise is assumed to be a slight fraction of the power, to give $|S(f)|^2$. The result of applying such a filter to the Fourier transform of the cross-correlation function is shown in Figure 3.11.

The technical details will now be briefly discussed. Dealing with non-periodic, non-continuous, data a number of problems can occur with the Fourier transform of the data (see, for example, Brigham [28] and Brault & White [27]). These include:

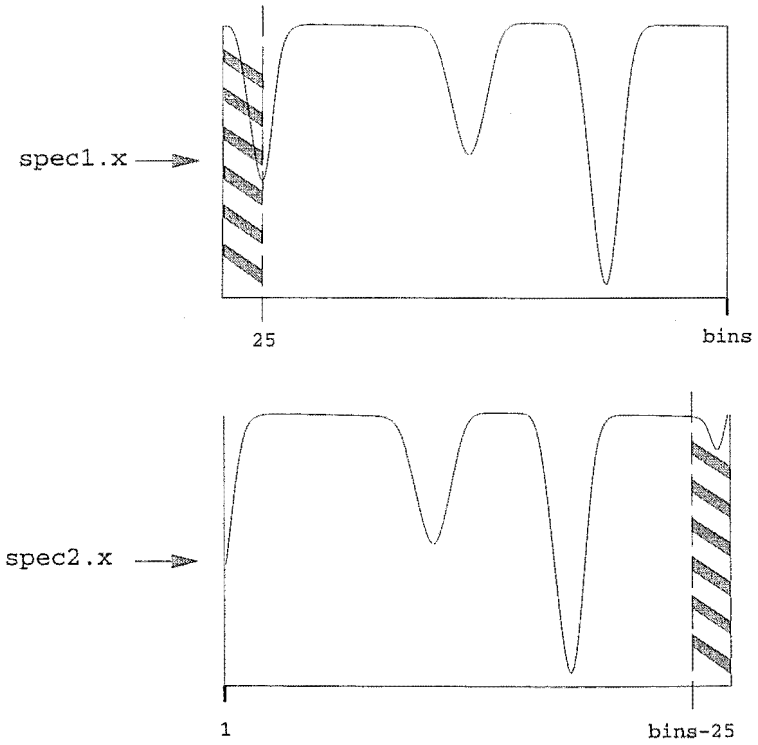

Figure 3.10: Due the the radial-velocity shift between these two spectra, they have different rest-wavelengths incident on the data window. The shift shown here equates to 25 bins, so in order for these samples to be the same the shaded areas should be set to zero.

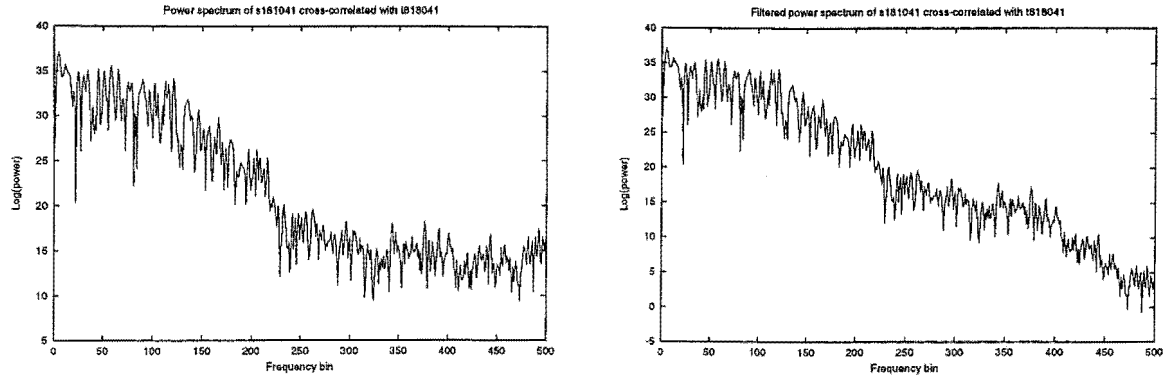

Figure 3.11: These diagrams illustrate the effect of applying an optimum filter to the Fourier transform of the cross-correlation function (for the 41st order of a K giant). To the left is the cross-correlation function before filtering and to the right is the cross-correlation function after a Wiener optimum filter has been applied. The original spectra had had their means subtracted, cosine bells applied and their array padded with zeros.

- Aliasing: distortion of the discrete Fourier transform, away from the continuous Fourier transform, due to under-sampling of data in the measurement domain (see Figure 3.12). This causes the overlap of repetitions (present due to the finite sampling) and is dependent on the width of the Fourier transform of the sampled function. To guarantee that no aliasing occurs, it is best to choose the sampling interval to be half that of the reciprocal of the frequency component which is highest in the Fourier transform of the underlying continuous function[28].

- Leakage: this is caused by dealing with a finite data window. It can happen in the measurement domain if a convolution or cross-correlation is performed (which is also known as wraparound or overlap — see Figure 3.13) and this is related to the fact that Fourier transforms assume periodic data. It can also happen in the frequency domain (see Figure 3.14).

Obviously corruption of the cross-correlation function will hinder determination of its peak and corruption of the data in the frequency domain will make determination of the optimum filter difficult. Little can be done about aliasing, as the measurement spacing is set by the CCD. However something can be done about both forms of leakage. Leakage in the measurement domain can be removed entirely by the extension of the data sequence (padded with zeros) to double the data-array length. Leakage in the frequency domain can be reduced by replacing the "box" function of the finite data window with one that has a less smearing Fourier transform — applying a cosine bell to the outer edges of the "box" function is one way of doing this. This is known as end-region masking and this should only be applied to data with a zero mean[29].

Hence the method for successful optimum filter determination is to subtract the mean from both sets of data, then apply a cosine bell to the data edges and finally (for an uncorrupted cross-correlation function) pad the array out to at least two times the length of the data with zeros (at least two times is necessary because to use a Fast Fourier transform the data arrays need to be 2^n bins in length).

[28]This is the Nyquist frequency. It should be noted that pure sine waves have delta-functions as their Fourier transforms and hence can not cause aliasing in this sense.

[29]Otherwise the "smoothing" effect of the end-region masking is much larger than is necessary, smoothing the data to its mean value is really what is desired (see Brault & White [27]). As will be explained below, data with a zero mean is also desirable for cross-correlation function fitting.

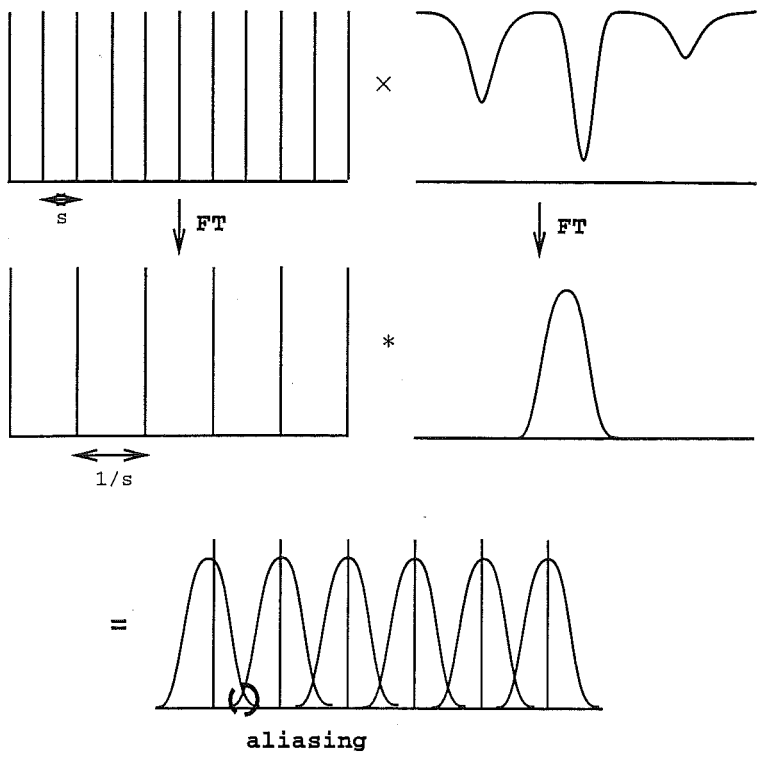

Figure 3.12: The effect of aliasing in the frequency domain is to cause overlap between the repetitions, due to the finite sampling.

The finite window problem

Pure experimentation quickly reveals it is necessary to divide the non-mean subtracted spectra's cross-correlation functions by $(N - \text{lag})$ in order to accurately find the peak[30]. This will be called regularization. However, mean-subtracted spectra not only do not need this to be done, but even give slightly better peak predictions than do the non-mean subtracted and regularized cross-correlation functions. That this is to be expected will now be shown.

If $\bar{\mathcal{T}}$ and $\bar{\mathcal{S}}$ are the means of the two spectra, and $\delta\mathcal{T}_i$ and $\delta\mathcal{S}_{i+l}$ are the deviations from the mean of their respective ith and $(i+l)$th bins, then the lth coefficient for the mean-subtracted cross-correlation function is

$$\mathcal{K}_l = \sum_{i=0}^{N-l} (\mathcal{T}_i - \bar{\mathcal{T}})(\mathcal{S}_{i+l} - \bar{\mathcal{S}}) = \sum_{i=0}^{N-l} \delta\mathcal{T}_i \delta\mathcal{S}_{i+l},$$

as the mean subtracted bins greater than $(i+l) = N$ are set to zero. By comparison, the lth coefficient for the non-mean subtracted and non-regularized cross-correlation function is

$$\mathcal{C}_l = \bar{\mathcal{T}}\bar{\mathcal{S}}(N-l) + \bar{\mathcal{T}} \sum_{i=0}^{N-l} \delta\mathcal{S}_{i+l} + \bar{\mathcal{S}} \sum_{i=0}^{N-l} \delta\mathcal{T}_i + \mathcal{K}_l.$$

The important thing is what happens near $l = k$, where k is the value at which $\mathcal{S}$ and $\mathcal{T}$ coincide. Then

$$\bar{\mathcal{T}} \sum_{i=0}^{N-l} \delta\mathcal{S}_{i+l} \approx \bar{\mathcal{S}} \sum_{i=0}^{N-l} \delta\mathcal{T}_i,$$

[30]This is unnecessary if all non-identical spectra (to within a bin) are set to zero. This could also be avoided by padding the data array, not with zeros, but with the mean value of the data.

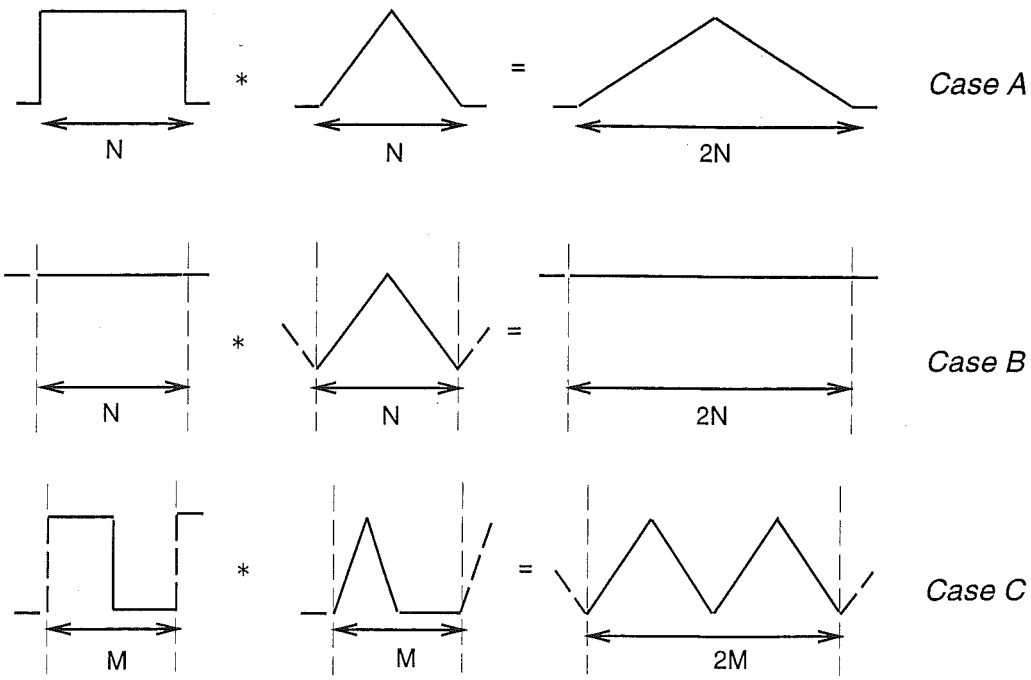

Figure 3.13: The effects of leakage in the measurement domain, caused by the assumption of periodic data and the finite window size. Case *A* illustrates the resulting cross-correlation from two functions of infinite length. Case *B* shows the effect if those same two functions are only defined over their non-zero length N. Finally case *C* demonstrates the effect of padding an array out to two times the length of the data with zeros — this fixes the corrupting effect of wraparound.

but they still are approximately equal to zero (for $l \ll N$). The same is not true of $\mathcal{K}_l$, as at $l \approx k$

$$\mathcal{K}_l \approx \sum_{i=0}^{N-l} (\delta\mathcal{T}_i)^2,$$

and therefore $\mathcal{K}_l$ becomes a significant contribution to $\mathcal{C}_l$. However $(\delta\mathcal{T}_i)^2$ is highly dependent on i, so $\mathcal{K}_l$ is not simply proportional to $(N-l)$. Hence while $\mathcal{C}_l$ needs to be regularized due to its major contributor being proportional to $(N-l)$, this also results in an undesirable $\mathcal{K}_l/(N-l)$ term which corrupts the cross-correlation function. The non-regularized and mean-subtracted cross-correlation function is found to give far better results.

The mean-subtracted and normalized cross-correlation function is defined as

$$\tilde{\mathcal{K}}_l = \frac{\mathcal{K}_l}{\sum_{i=0}^{N-1} \delta\mathcal{T}_i^2 \sum_{j=0}^{N-1} \delta\mathcal{S}_j^2}.$$

It has an error in each point (for $l \ll N$), due to the spectra's signal-to-noise, of[31]

$$\sigma^2 \approx \frac{\sigma_{\overline{\mathcal{T}}}^2}{\sum \delta\mathcal{T}_i^2} + \frac{\sigma_{\overline{\mathcal{S}}}^2}{\sum \delta\mathcal{S}_i^2}.$$

Similarly to thorium lines (see §3.5.3), $\sigma_{\overline{\mathcal{T}}}$ can be obtained from

$$\sigma_{\overline{\mathcal{T}}}^2 = \overline{\mathcal{T}} + MN_{\mathrm{RO}}^2 + \overline{\mathcal{T}}^2/\overline{\mathcal{S}} + M(\overline{\mathcal{T}}N_{\mathrm{RO}}/\overline{\mathcal{S}})^2,$$

where $\overline{\mathcal{S}}$ is the mean value of the spectrum's flat-field, N_{RO} is the readout noise of the CCD and M is the breadth of the order collapsed to form the one-dimensional spectrum.

[31] To see this consider Murdoch et al. [125] Equ. 2.4

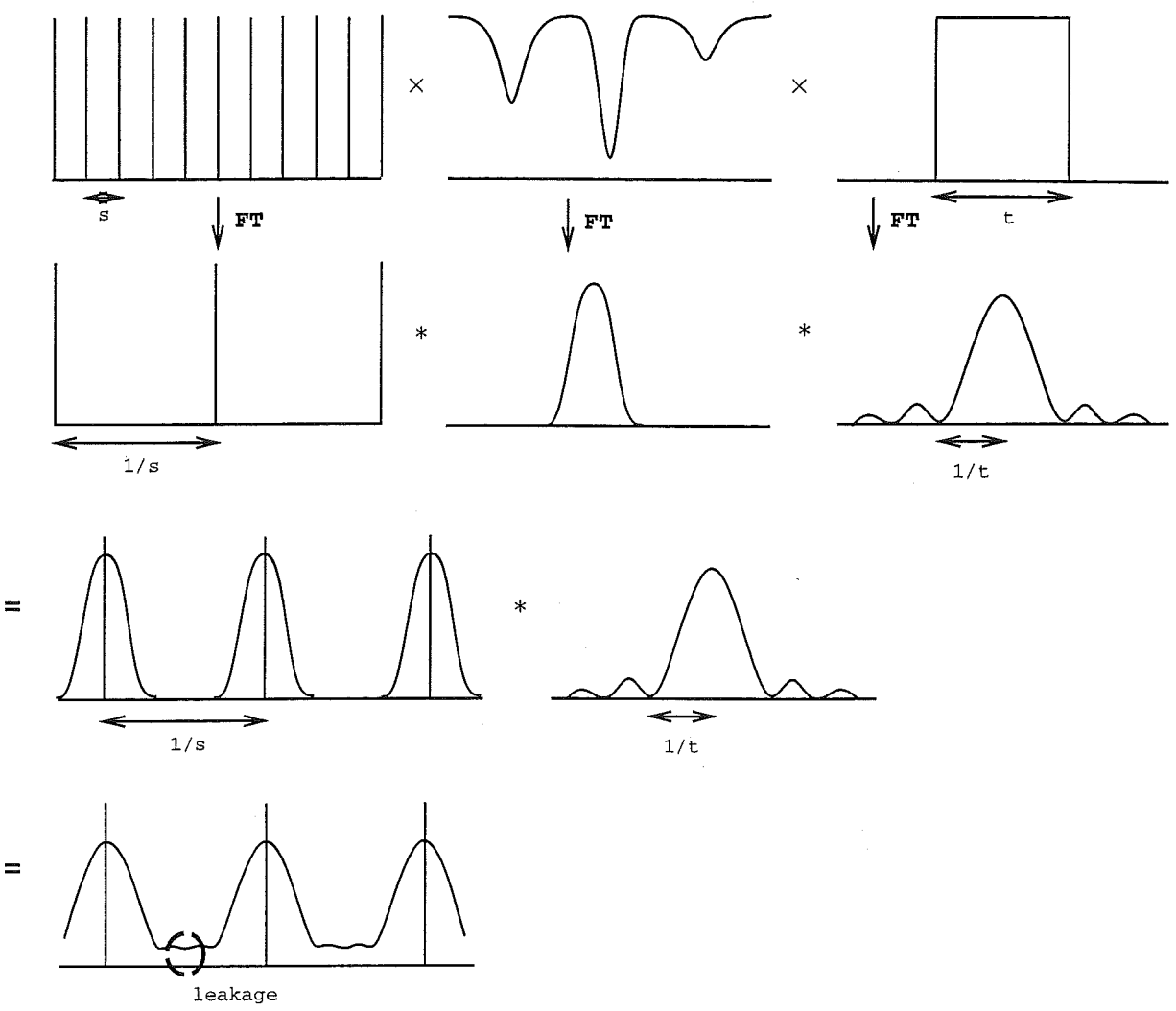

Figure 3.14: The effects of leakage in the frequency domain. Despite no aliasing being present, the smearing effect of the box transform can cause corruption between frequencies.

3.5.3 The predicted error in the position of the cross-correlation function

The cross-correlation of two spectra, such as those in Figure 3.15, will now be considered. The wavelength of the first non-zero bin[32] for each spectrum will be denoted λ_a and λ_b, respectively. The bin numbers in the rebinned spectra are related to wavelength by $b_\lambda = (\ln\lambda - \ln\lambda_i)/\delta\ln\lambda + 1$, where λ_i is the wavelength of the first non-zero bin and $\delta\ln\lambda$ is defined by taking λ to be the wavelength of the last thorium line used for the dispersion solution and b to be its default pixel number. If the two spectra have been rebinned to have the same $\delta\ln\lambda$ cross-correlating the two, as functions of bin number, would lead to a function with a peak at bin $\beta + (b_{\lambda_a} - b_{\lambda_b})$. The error in the position of this cross-correlation function is therefore

$$\sigma_\beta^2 + (\sigma_{b_{\lambda_a}}^2 + \sigma_{b_{\lambda_b}}^2).$$

The error in the cross-correlation function peak position, σ_β, from gaussian fitting, is affected by the signal-to-noise of the two spectra. The errors $\sigma_{b_{\lambda_a}}$ and $\sigma_{b_{\lambda_b}}$ are a result of the errors in the dispersion solution and can be obtained from the three dispersion coefficients and their errors. Rebinning the two spectra to have the same $\delta\ln\lambda$ is done by defining the windows so that both λ_a

[32]Ignoring the effect of **Samespectra** for simplicity

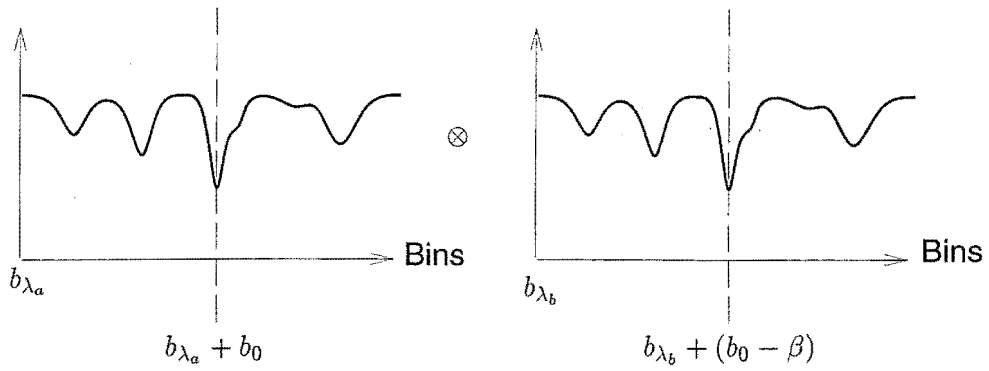

Figure 3.15: The first spectrum has its first non-zero bin at wavelength λ_a and the second has it at λ_b. The second spectrum is shifted by $(b_{\lambda_a} - b_{\lambda_b} + \beta)$ bins to a shorter wavelength, where bins are in $\delta \ln \lambda$ increments.

and λ_b equal the wavelength of the first thorium line.

The errors returned by the least-squares fitting routines are in bins, in both the peak-position and dispersion-solution case. These need to be translated into km/s and how this is done will now be described. As bin position is related to wavelength, the error in wavelength is found from

$$\lambda = \exp(\ln \lambda_i + (b-1)\delta \ln \lambda) \quad \text{to be} \quad \sigma_\beta = \frac{\sigma_\lambda}{\lambda \delta \ln \lambda}.$$

Consideration of the non-relativistic Doppler formula reveals that

$$\sigma_v = c\frac{\sigma_\lambda}{\lambda_0} \approx c\frac{\sigma_\lambda}{\lambda} = c\sigma_\beta \delta \ln \lambda,$$

so the error due to cross-correlation function fitting, in km/s, can be obtained directly from this. As far as the error from the dispersion solutions is concerned, for each spectrum a dispersion solution of the form

$$n = a_1 + a_2(\lambda - \lambda_c) + a_3(\lambda - \lambda_c)^2$$

has been found, where n is pixel number (see Appendix F.5) and λ_c is the average of the first and last thorium lines' wavelength. As $(\lambda - \lambda_c)$, a_2 and a_3 are all small, the error in the position of a pixel is $\sigma_n \approx \sigma_{a_1}$. Now assuming the dispersion relation holds with the given a_1, a_2 and a_3, the errors in the pixel positions are related to those in the wavelength by

$$\sigma_\lambda = \frac{\sigma_n}{a_2 + 2a_3(\lambda - \lambda_c)} \approx \frac{\sigma_n}{a_2}$$

to first order, as a_3 is much smaller than a_2. In light of this, the error in spectrum position, arising from a single dispersion solution, is

$$\sigma_v \approx c\frac{\sigma_{a_1}}{a_2 \lambda_c}.$$

So the total error in the cross-correlation function peak position is

$$\sigma_{\text{pred}} = c((\delta \ln \lambda \sigma_\beta)^2 + \left(\frac{\sigma_{a_1}}{a_2\lambda_c}\right)^2_{\text{d}_1} + \left(\frac{\sigma_{a_1}}{a_2\lambda_c}\right)^2_{\text{d}_2})^{\frac{1}{2}}.$$

The error in the dispersion solution

The uncertainty in fitting a quadratic polynomial to thorium-line positions as a function of wavelength is related to the uncertainty in fitting a gaussian to each of the thorium lines, which in turn is related to the signal-to-noise of the thorium lines. How this last is determined will now be described.

Following §3.4 and letting the collapsed then flat-fielded, but now also scaled by some constant α, thorium spectrum be called $T_j = \alpha F_{\mathrm{T},j}/S_{\mathrm{T},j}$, the noise in pixel j of a line is

$$N_j = T_j \times \left(\left(\frac{1}{T_j}\right)\left(\frac{\alpha}{S_{\mathrm{T},j}}\right) + \frac{1}{S_{\mathrm{T},j}} + M\left(\frac{N_{RO}}{T_j}\right)^2\left(\frac{\alpha}{S_{\mathrm{T},j}}\right)^2 + M\left(\frac{N_{RO}}{S_{\mathrm{T},j}}\right)^2\right)^{\frac{1}{2}},$$

where M is the number of rows collapsed to make the one-dimensional order. The smooth-field is reasonably flat (see Figure 3.6), i.e. $S_{\mathrm{T},j} \simeq \overline{S_{\mathrm{T}}}$, so substituting the $\overline{S_{\mathrm{T}}}$ into the above equation (with the average being abbreviated to $\overline{S}$) and taking $\alpha = \overline{S}$ as the scaling factor to be applied after the flat-field division, the noise in pixel j of a thorium line can be closely approximated by

$$N_j = T_j \times \left(\frac{1}{T_j} + \frac{1}{\overline{S}} + M\left(\frac{N_{RO}}{T_j}\right)^2 + M\left(\frac{N_{RO}}{\overline{S}}\right)^2\right)^{\frac{1}{2}}.$$

Making the further approximation that for a particular order the flat-field mean is constant from exposure-to-exposure, the Turbo Pascal procedure **linenoise** looks at T_j and determines the noise that should be associated with it (the procedure contains the mean flat-field flux for each order, see Appendix F.5.2). It is necessary to work this out anew for each thorium exposure, as they vary greatly in flux due to the exact alignment of the equipment from run-to-run (how the thorium light falls on the fibre input and how the fibre output is incident on the slit) and perhaps also due to the deterioration of the glycerine drop. By finding out the noise for each point of the line that is to be fitted and passing it to the gaussian fitting procedure, a better fit is enabled.

Testing the predicted errors

When the predicted errors are compared to the observed scatter for the radial-velocity variations of the sky, it quickly became apparent that they do not account for the variations. Specifically, the order-to-order variations are greater than that predicted and so are the exposure-to-exposure errors (see Table 3.2 for the standard deviation of the sky's radial velocities within one run). If the predicted error is exact, there is generally much less than a 0.1% chance that the observed standard deviation has the correct fitting function, i.e. that the data is constant. As the Sun is constant within the precision of this thesis, it must be concluded that there is less than a 0.1% chance that the predicted error is exact (see §4.2 for full details on the application of the F-test).

In addition, it seems that the scatter between different exposures is greater than that between the orders, although this difference is not great (this is also apparent in §4.2, where all the sky exposures have their exposure-to-exposure scatter compared to their order-to-order scatter, after run-corrections have been performed). Hence there must be some extra (not accounted for by the error predictions) error present which varies from order-to-order and perhaps also an additional exposure-to-exposure error (i.e. the same for all orders — hence not observed when the scatter between the orders are considered). What could cause these?

Some factors that will cause errors in radial velocity that generally do not vary from order-to-order, but do vary from exposure-to-exposure are:

- That the barycentric/heliocentric correction is only approximate. There is a small error due to some planetary effects; for example, the correction doesn't take into consideration the

Order Number	N	σ_{N-1} (km/s)	$\sqrt{\langle\sigma^2_{\rm pred}\rangle}$ (km/s)	$\sqrt{F}$ $[N{-}1,\infty]$
41	19	0.083	0.017	4.87
42	19	0.071	0.006	12.66
43	19	0.057	0.010	5.67
44	19	0.056	0.008	6.94
45	19	0.061	0.010	5.97
46	19	0.069	0.010	6.87
HJD (days)	N	σ_{N-1} (km/s)	$\sqrt{\langle\sigma^2_{\rm pred}\rangle}$ (km/s)	$\sqrt{F}$ $[N{-}1,\infty]$
0178.622	6	0.053	0.011	5.04
0178.626	6	0.043	0.011	4.07
0178.629	6	0.047	0.011	4.39
0178.631	6	0.043	0.011	3.90
0179.627	6	0.075	0.011	6.84
0179.631	6	0.063	0.011	5.90
0180.627	6	0.046	0.011	4.27
0180.630	6	0.050	0.011	4.76
0180.632	6	0.068	0.011	6.14
0180.635	6	0.027	0.011	2.45
0180.637	6	0.054	0.011	5.08
0182.607	6	0.063	0.011	5.93
0182.610	6	0.050	0.011	4.60
0182.613	6	0.035	0.011	3.20
0182.616	6	0.059	0.011	5.51
0182.620	6	0.054	0.011	5.12
0183.636	6	0.033	0.011	2.99
0183.639	6	0.033	0.011	3.04
0183.643	6	0.089	0.011	8.37

Table 3.2: **The F-test: sky exposures in April 1996.** This table gives the standard deviation, σ_{N-1}, of the N relative radial velocities found for sky exposures during one run in 1996; the average error in the relative radial velocities, $\sqrt{\langle\sigma^2_{\rm pred}\rangle}$, predicted by the error in the dispersion solution and the fit to the cross-correlation function; and the F-test values that arise from these. The first set gives the scatter between different exposures taken during the run, for each of the six orders. The average standard deviation for this is 66 m/s and the average predicted error is 10 m/s, which gives an F-test value of $\sqrt{F} = 6.6$. The second set gives the scatter between the relative radial velocities given by the six orders, for each of the 19 exposures taken during the run (where the HJD is given in days after 2450000). The average standard deviation for this is 52 m/s and the average predicted error is 11 m/s, which gives an F-test value of $\sqrt{F} = 4.7$.

effect of Jupiter on the Earth, although the effect of Jupiter on the solar system barycentre is taken into account. This is believed to amount to less than 6 m/s and in the short exposure time case of the Sun probably less than 4 m/s (see Murdoch [124] §5.1.5).

- Scattering of sky light off turbulent air cells. This will affect sky exposures only and will be random from exposure-to-exposure.

- That the average dispersion solution is not appropriate. This is caused by a number of things — the most frequent is the blocking of starlight during the exposure by cloud. Also,

for long exposures there is a chance that the temperature/air pressure will rise during the exposure then fall again — so the average dispersion is not well predicted by simply taking a thorium before and after the stellar exposure. This will be random from exposure-to-exposure. However as sky exposures are so short, this effect is not expected to be significant for them. The effect of this may also differ from order-to-order.

Factors that cause errors in radial velocity that will be different from order-to-order, but are not already taken into account:

- The effect of CCD pixel size and the sampling interval. A single line generally does not fall symmetrically into pixels and as this will vary from exposure-to-exposure, at the very least this will cause small asymmetries in the cross-correlation function. For a constant star this would be expected to cause an error from order-to-order, which would be systematic within a run, but change randomly from run-to-run. In addition, the larger the pixel the worse the "smearing" effect of non-finite pixel size would be expected to be. The rebinning procedure considers this finite pixel size when rebinning pixel flux into bin flux, but it can not do a perfect job as there is no way of knowing exactly the distribution of the flux that falls across each pixel. It does a very rough job by assuming that the flux was constant across the face of the pixel. The size of the error resulting from this is expected to depend on the width of the lines in pixels (only about six in the thorium case and 10 in the stellar case) and probably on the number of lines in the spectra, as this effect may be evened out as line number increases.

In order to try to duplicate the order-to-order variations observed in the sky spectra, a synthetic spectrum was generated and this will now be discussed.

3.5.4 Testing the effect of CCD resolution

In order to test if the finite pixel width, assumed constant flux distribution across the pixel face, or simply the small CCD resolution could be causing the bigger than expected velocity errors, synthetically generated spectra were used. The synthetic spectrum was assumed to be

$$F(\lambda) = \sum_{i=1}^{N} \alpha_i \exp(-(\frac{\lambda - \lambda_i}{W})^2)$$

at the surface of the star and therefore

$$\tilde{F}(\lambda) = \sum_{i=1}^{N} \alpha_i \exp(-(\frac{\tilde{\lambda}(v,\lambda) - \lambda_i}{W})^2)$$

at the Earth, where[33] $\tilde{\lambda}(v,\lambda) = \lambda(\frac{1-v/c}{1+v/c})^{\frac{1}{2}}$. The échelle is assumed, for simplicity, to distribute the light as $n = a_1 + a_2(\lambda - \lambda_c)$ (i.e. a linear, rather than quadratic, dispersion). By integrating $\tilde{F}(\lambda)$ over each pixel face[34] the flux "readout" for each pixel was obtained. As well as this the actual flux at the logarithmic bins was generated. By using such a synthetic spectrum, the radial velocities obtained from current rebinning and cross-correlation function fitting could be compared to the true radial velocities, as well as the radial velocities obtained using a more sophisticated rebin procedure and from the cross-correlation of the actual flux incident at discrete intervals of $\delta \ln \lambda$.

[33] To see this a line at the stellar surface which is centred at λ_0 and has a half-width of W, will be considered. The convention for positive recessional velocity is that $v/c = (1-(\lambda_0/\lambda)^2)/(1+(\lambda_0/\lambda)^2)$ and this can be inverted to give $\lambda/\lambda_0 = ((c+v)/(c-v))^{\frac{1}{2}}$, which indicates that at the Earth the line will be centred at $\lambda_0((c+v)/(c-v))^{\frac{1}{2}}$ and have a half-width of $W((c+v)/(c-v))^{\frac{1}{2}}$. This is a gaussian with the same form as given.

[34] Using Simpson's rule, $\int_{x_i}^{x_f} \tilde{F}(x)dx \cong (\tilde{F}_i + 4\tilde{F}_{\text{centre}} + \tilde{F}_f)/3$, to approximate $\int \exp(-x^2)dx$ (see, for example, Hildebrand [83] page 116)

The alternative rebin did not assume that the flux fell constantly across the pixel face, but instead assumed the flux distribution across the pixel face and its nearest neighbours was quadratic. A quadratic distribution across the face of the pixels would mean that the integrated flux read out of pixels n_{i-1}, n_i and n_{i+1} would be

$$n_{i-1} = [d_0 x + d_1 x^2/2 + d_2 x^3/3]^{\text{End } p_{i-1}}_{\text{Start } p_{i-1}},$$

$$n_i = [d_0 x + d_1 x^2/2 + d_2 x^3/3]^{\text{End } p_i}_{\text{Start } p_i},$$

$$n_{i+1} = [d_0 x + d_1 x^2/2 + d_2 x^3/3]^{\text{End } p_{i+1}}_{\text{Start } p_{i+1}},$$

for a distribution of flux of $(d_0 + d_1 x + d_2 x^2)$. But these three equations can be solved to give d_0, d_1 and d_3 in terms of the observed fluxes n_{i-1}, n_i and n_{i+1}. The quadratic solution is then used to find the flux that is to go into the logarithmic bins.

The synthetic spectrum was generated based[35] on the wavelength range of the CCD order 46. Varying the spectra used, the number of pixels along the spectrum and the method for obtaining the cross-correlation function the following was found:

- As would be expected, setting dissimilar spectra to zero improved the radial velocities obtained greatly for large radial-velocity shifts (as discussed in §3.5.2, a change in radial velocity between two spectra means different rest-wavelengths will be incident on the CCD). Hence this was always done for the synthetic spectrum tests.

- Assuming a quadratic flux distribution across the pixel face produced radial velocities little, if any, better than assuming a constant distribution, but it takes much longer in CPU time. Using the exact flux at the logarithmic bins gave similar radial velocities to the finite pixel width cases. Hence the order-to-order variation can not be blamed on the effect of rebinning, or even on the smearing effect of finite pixel width.

- For a set spectrum, number of data points fitted to and so on, the error in the fitted radial velocity varied periodically, depending on the true radial-velocity shift (see Figure 3.16). The amplitude of this periodic variation varied, depending on the synthetic spectrum used. The amplitude was typically less than 30 m/s for spectra which, like the sky, are not badly blended. Surprisingly, this was true even for a single gaussian line fitted by a single-gaussian fit, although in this case the amplitude was only about 7 m/s (when a similar number of pixels to the CCD chip were used).

- Varying the CCD resolution (the number of pixels over a wavelength interval) made a large difference to the amplitude of this periodic variation, in the single-gaussian case at least. However, increasing the number of lines present did not have any systematic effect.

- Fitting the gaussian down to a level of small slope also decreased the amplitude of this periodic variation in the single-gaussian case (see Figure 3.17). This contrasts with the worsening effect shown in Figure 3.8.

- Because the synthetic spectra have no noise the "error" in the points to be fitted was set to (almost) zero. The result of this was that no matter how good, or bad, the fit to the cross-correlation function was to the eye, the error in peak position returned was zero! Clearly the σ_β values returned by the cross-correlation function fitting procedure are not a good approximation to the departure of the fit from the data points. This helps explain the difference between the observed scatter and that predicted.

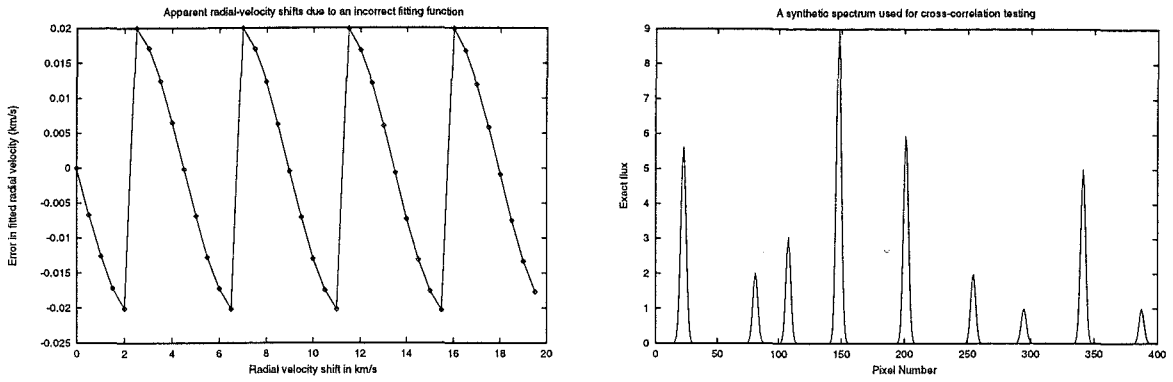

Figure 3.16: The figure on the left shows the error in radial velocity when two Doppler-shifted synthetic spectra, evaluated at exactly $\delta \ln \lambda$ wavelength increments, are cross-correlated. These errors arise when a three-gaussian fit to nine data points was used — fitting the cross-correlation using a single-gaussian fit resulted in similar error, but of double the amplitude. The "discontinuity", visible at shifts of half bins, is where the cross-correlation function has its top nine data points with the lowest point first on one side of the peak, then on the other (see Figure 3.8). The figure on the right is the synthetic spectrum that was cross-correlated.

The odd-even effect (see §3.5.1) was also seen in the synthetic spectra when the number of points being fitted to was varied and the cause of this is believed to be the same as that which causes the effect seen in Figure 3.16. The error in this figure repeats itself with a period of shifted velocity of 4.49 km/s. This corresponds to the spectra being shifted exactly one bin and therefore (as non-identical spectra were removed, as prescribed by §3.5.2) the spectra are identical again. In all other instances, there is an error in the fitted peak which is due to two non-identically sampled spectra being cross-correlated to produce a set of cross-correlation function points which are not symmetrically spread around the function's maximum. This would be fine if the cross-correlation function underwent the correct fit — but it only undergoes the approximation of a three gaussian fit. The fitting procedure thinks that it is fitting the cross-correlation function correctly, as it is expecting to be fitting to a function which is exactly the sum of three gaussians and returns its error accordingly.

Fitting the cross-correlation of a spectrum consisting of a single gaussian reveals a subtle twist to this, reflecting that even with non-blended lines and when exactly the same spectra are within the data windows the cross-correlation function will not be exactly a gaussian, and a significant error in fitted radial velocity will result. This is believed to be caused by several things, one of which being that the discrete cross-correlation function is only an approximation to discretely sampling the cross-correlation of two continuous functions and hence the cross-correlation of two discretely sampled gaussians is not exactly a discretely sampled gaussian, unless the shift between the two is an integer number of bins[36]. Another is that while the lines are gaussian functions of wavelength, they are not gaussian functions of bin number. These problems will usually be present in addition to the fact that **Samespectra** (see Appendix F.6.2) can only set the two sampled spectra to be identical within one bin and the resulting error can be quite large. In fact for about the first 10 km/s of shifts, illustrated in Figure 3.16, these are the only causes of fitted radial-velocity error, because the edges of the spectrum being shifted are basically zero. Fortunately the amplitude of this effect is reduced by improved CCD resolution; however, this does mean that, even in the absence of line blending, the limiting precision when cross-correlating two spectra with the CCD

[35] Actually the wavelength range used is 5000–5030 Å, rather than the 5008–5030 Å of order 46

[36] The proof, in §3.5, that the continuous cross-correlation of two gaussians is also a gaussian uses the time-shifting theorem of Fourier transforms. This time-shifting theorem also exists in the discrete case, but it only holds for integer shifts (see, for example, Brigham [28] §8-3).

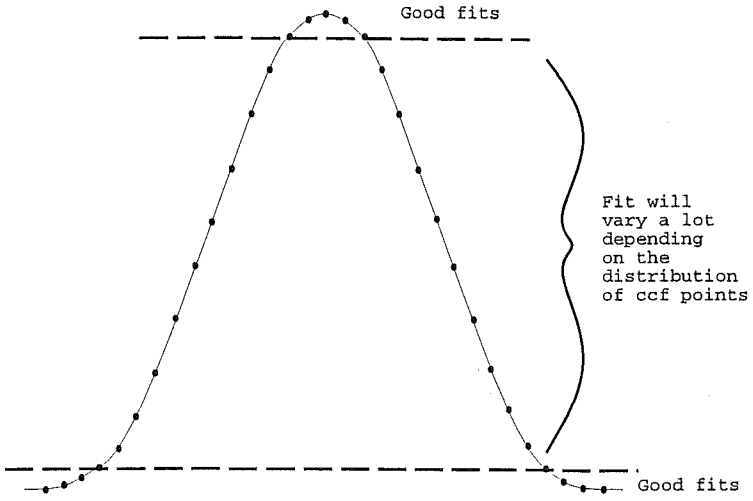

Figure 3.17: The amplitude of the periodic error, shown in Figure 3.16, is reduced by fitting the cross-correlation function down to a level of small slope. This is because the position of the bottom data point exerts less "drag" on the fit. However, this contrasts with the worsening effect shown in Figure 3.8. This is because there will be less drag only if the cross-correlation function data points' distribution is no less "fitting-function like" in these regions. Hence fitting further down on the cross-correlation functions obtained from the Mt John spectroscopic observations will result in worse, rather than better, radial velocities.

chip and the wavelength region used for this thesis is of the order of tens of metres a second (the precise value being dependent on the exact spectra involved).

That the amplitude of the errors depends on the spectrum being cross-correlated means is it is unjustified to do run-corrections on an order-by-order basis, because the run-correction determined for one of the Sun's orders will not be any more appropriate for that same order in another star than the mean run-correction. Another important thing to note is that as far as the error returned by the fitting function is concerned, a similar thing happens with dispersion solutions. A strong signal-to-noise, but poorly fitted thorium line (due to, say, line blending) is reported to have a small error and so contributes too much to the dispersion solution.

The question naturally arises as to how systematic this spectrum-dependent error is. For example, will it remain the same from differential radial velocity to differential radial velocity? To consider this question consider the synthetic spectra and échelle above and use the rough approximation that the radial velocity error for order o can be written as

$$E_o = a_o \sin(\omega v_t + s),$$

where v_t is the real velocity shift between spectra, ω is related to pixel width, a_o is the amplitude of the variation (which is spectrum dependent) and s reflects the rest-wavelengths shifts on the CCD (which will be most significant from run-to-run). When the lines in a stellar spectrum are shifted by an integral number of bins relative to the reference spectrum, as a result of the combination of systematic shifts caused by the échelle and the star's change in radial velocity, then $E_o = 0$. So within a run the error is very systematic, but from run-to-run it is not.

3.5.5 Averaging the radial velocities from the six orders

It was initially intended to use σ_{pred} to obtain a weighted mean of the six orders. However as σ_{pred} is not the total error of the relative radial velocity for a specific order, and perhaps also exposure, this was not feasible. Of course, the alternative of assuming the error is the same for all exposures

and orders is also unjustified, but there is little choice. So the average radial velocity for exposure i from the six orders is

$$\overline{v}[i] = \frac{\sum_{o=1}^{6} v[o,i]}{6},$$

where $v[o,i]$ is the relative radial velocity obtained for order o. The error in this mean is then

$$\sigma_{\overline{v}}[i] = (\frac{\sum_{o=1}^{6}(v[o,i] - \overline{v}[i])^2}{30})^{\frac{1}{2}}.$$

A similar approach is taken to find run-corrections from the Sun's exposures, for further details see Appendix F.7.1.

3.6 Star selection

When this research was proposed a list of 44 late-type evolved stars had already been drawn up for observation (see Table 1.1 for the list of these 44 stars). This list had known spectroscopic binaries and Mira variables excluded, and preference was given to stars of known small-amplitude light variability. To facilitate fast and frequent observations, only stars brighter than fifth magnitude had been considered (with the equipment described in §3.2 and good, but not exceptional weather conditions, a fifth magnitude star observed for twenty minutes can give a signal-to-noise of about 150 in the continuum of the collapsed spectrum). Far southern declinations ($\delta < -30^0$), in addition to a wide spread of right ascensions, were also preferred.

After slightly over a year of spectroscopic observations had been obtained it was decided to discontinue observing some stars, in order to observe the remaining ones more intensively. It was initially intended to discard about half of the stars, but the desire to continue observing several potentially constant stars and the lack of an even distribution in right ascension of the preferred stars, led to about two thirds of the stars being retained. The choice of the stars for which observations should be continued was made as follows:

- Stars were placed in groups according to the nature of the radial-velocity variation, i.e. regular or erratic, short-term, long-term, or both short and long-term variations. Typical examples of these types were kept with a preference for larger changes in radial velocity.
- There were exceptions to this based on reports in the literature of the stars' radial-velocity variability. Although known spectroscopic binaries were deliberately excluded from the initial observing list, γ Phe had been missed and hence this star, along with α Sco which was being observed for a similar project by another group of researchers, had their observations discontinued.
- 3 Cet, at a declination of $\delta = -10^0$, was seasonal, so despite quite large radial-velocity variations it was also discontinued.
- Four of the least variable in radial velocity stars were kept, chosen over a range of right ascension, in order to help establish an upper limit to the precision of the radial-velocity measurements. These four stars were all K giants.

Table 4.4 contains radial-velocity information on all 44 stars, split into two groups corresponding to stars for which observations were continued and stars which were not. The desired frequency of observations for the remaining 31 stars was also determined at this stage, again based upon the nature of the radial-velocity variations.

Soon after the subset of stars were discontinued, broad-band photometry at Mt John University Observatory began to be taken for 13 of the remaining 31 stars (due to high demand for such

service observing, it was not feasible for observations of more stars to be undertaken). The 13 stars were chosen with a preference for those with radial-velocity variations of 400 m/s or more, as usually larger radial-velocity variations will mean any brightness variations are larger (see Cummings et al. [43] for the magnitude of the observed radial-velocity variations, at the time which this decision was made). Using the groupings from determining which stars to discontinue observing spectroscopically, it was initially decided to keep four stars from each category of: (A) stars showing only long-term, relatively regular, variations; (B) stars showing both short-term and long-term variations; (C) stars with short-term variations, but no long-term trends. What was considered to be the most typical examples of these types were chosen, the only complication being that only three type (C) stars had radial-velocity variations bigger than 400 m/s and it was necessary to include a star with a slightly smaller amplitude. However, comparison of the stars' spectral types revealed that these stars were made up of:

(A) three stars of spectral type K, one of M

(B) one star of spectral type K, three of M

(C) four stars of spectral type M.

This distribution is somewhat spectral type M dominated, especially with respect to short-term variations. In order to try and redress this situation, it was decided to add another K-type star to this observing list, making a total of 13 stars to be monitored photometrically. No type (C) stars were suitable, so it was decided to use a type (B) star. The two possibilities for this were π Pup and λ Vel, the former being preferred for the simple reason that it is fainter and hence better for the photometric equipment being used.

Chapter 4

Data analysis and results

4.1 Finding periods in the radial velocities and photometry

Finding the periods[1] present in an unevenly sampled data set is not a trivial task. However, there are a number of different approaches available some, not necessarily unrelated, ones are:

Interpolation: By laying a grid of evenly spaced times on the data it is possible to interpolate evenly spaced data points from the values observed — then treat by a Fast Fourier transform method. The success of this method for non-periodic or only sparsely sampled data is doubtful as determination of the value at grid point values is fraught with difficulty.

CLEAN: This name actually refers to a particular program, but there are other similar methods. The discrete Fourier transform of the data set is obtained and from it the unwanted effects of the spectral-window function[2] are removed leaving behind the periodicities of the data set. This nonlinear deconvolution in the frequency domain is apparently equivalent to least-squares interpolation in the time domain. For further details see Roberts et al. [138].

Lomb-Scargle normalized periodogram[3]: This is a Fourier transform method which defines a normalized periodogram. It has the desirable features of having statistical behaviour essentially identical in the even and unevenly spaced data cases, its analysis is exactly equivalent to the least-squares fitting of a sine function[4], $C(\omega)\sin(\omega t + \theta(\omega))$, to the data in the time domain, and time-translation invariance is retained. For more details see Scargle [142] and Press & Teukolsky [135].

Phase dispersion method: A range of potential periods is considered and the data phased to each. The phased curve which has the minimum dispersion (or scatter) corresponds to the period which best fits the data. The important thing here is the method of deciding what constitutes the "least scatter". One simple and frequently used method is the Jurkevich periodogram method (for more details see DuPuy & Hoffman [48]). It is not coincidental that this is referred to as a periodogram method — it has been shown to be equivalent, in most cases, to

[1] In this section the terms periodicity and period are used in recognition of the fact that the examples assume a periodic data set, as often do the methods of finding these periods.

[2] The discrete data can be considered to be a continuous function which has been multiplied by a finite, unevenly spaced, array of delta functions (with a delta function at each observation point). The Fourier transform of this array of delta functions is called the spectral-window function and, as the data are unevenly spaced, this will not simply be another array of delta functions convolved with a sinc function (the Fourier transform of a box).

[3] A periodogram is spectral power (the Fourier transform times its complex conjugate) as a function of angular frequency. For its conventional definition see, for example, Scargle [142]. The conventional definition makes no assumption about the shape of the data other than it should be periodic.

[4] Usually expressed as $A(\omega)\sin(\omega t) + B(\omega)\cos(\omega t)$, where $C(\omega)$ equals $\sqrt{A^2(\omega) + B^2(\omega)}$ and $\theta(\omega)$ equals invtan$(B(\omega)/A(\omega))$. A linear least-squares fit is performed at every period by adjusting the parameters A and B.

the conventional Fourier analysis (Swingler [161]). It requires no assumptions on the shape of the data curve.

Selfcorrelation: This method was first suggested by Percy & Lin [130] in 1991. It is based on considering the difference in the value of the data at two different times. If the data are periodic with a period of $\mathcal{P}$ and if the two different times are $\mathcal{P}$ apart then the difference should be zero. The formulation of the method allows its application to non-evenly spaced data and it also requires no assumptions on the shape of the data curve.

It was decided to use one Fourier transform method, the Lomb-Scargle periodogram, to find the periodicities present in the data sets and to initially check its results using selfcorrelation. The problems associated with finding periods using Fourier transforms and details on the period finding methods used will now be described.

4.1.1 The effect of discrete (evenly spaced) data on a Fourier transform

The Fourier transform of a periodic continuous function will have its peak power at the frequency pertaining to that period. If the function is a pure sinusoid of period $\mathcal{P}$ then the Fourier transform is two delta functions symmetrically distributed about zero frequency at $\pm 1/\mathcal{P}$. Things become complicated, however, when the initial data set is discretely sampled. To see this, the simple case of evenly spaced discrete data in a finite data window will now be considered.

Consider a signal of the form $\cos(2\pi t/\mathcal{P})$ which has been sampled at intervals of S, over a time range of h (see Figure 4.1). It is desired to find the period of this by consideration of the Fourier transform of its discretely observed data points. But if the entire range of frequencies was considered periods would be found not just at $1/\mathcal{P}$, but also at $(1/S \pm 1/\mathcal{P})$ and so on. So to find the period of the signal, by considering the Fourier transform of the observed data, frequencies greater than $1/2S$ should not be considered (this is equal to the Nyquist frequency[5]) — to avoid the higher frequency repetitions due to the discrete observation times.

So there is an upper limit to the frequencies that should be searched for peaks. Is there a lower limit? This question will be answered by the considering the three cases:

1. $1/h < 1/\mathcal{P} \Rightarrow h > \mathcal{P}$
2. $1/h \geq 2/\mathcal{P} \Rightarrow 2h \leq \mathcal{P}$
3. $2/\mathcal{P} > 1/h > 1/\mathcal{P} \Rightarrow \mathcal{P} < 2h < 2\mathcal{P}$.

In the first case there is no problem and the Fourier transform can safely be considered right down to $f = 0$ and the peak of the power spectrum can still be found.

In the second case, however, it is impossible to find the period from the Fourier transform at all as leakage (see Figure 4.2 and §3.5.2 for the definition of leakage, as it is used here) from the finite data window is such that the maximum power spectrum is at $f = 0$ and the period signature is completely swamped.

[5]The Nyquist frequency is the critical sampling of a sine wave. At this frequency it is not possible to distinguish waves of shorter periods from those already present in $f \in [0, f_{\text{nyq.}}]$. At this point the exact location of the false peaks, due to evenly spaced discrete data spacing, will be considered explicitly for the case where the data sampling has been such that $Sn = \mathcal{P}$, where n is some whole number. Then the false peaks due to the sampling of the data will be located at $(n \pm 1)/\mathcal{P}$. So the lowest frequency false peak will be smaller than the true frequency, $1/\mathcal{P}$, unless $n > 2$. If $n = 3$ have the familiar situation that the false frequency is located at double the frequency of $1/\mathcal{P}$, in other words at half the period.

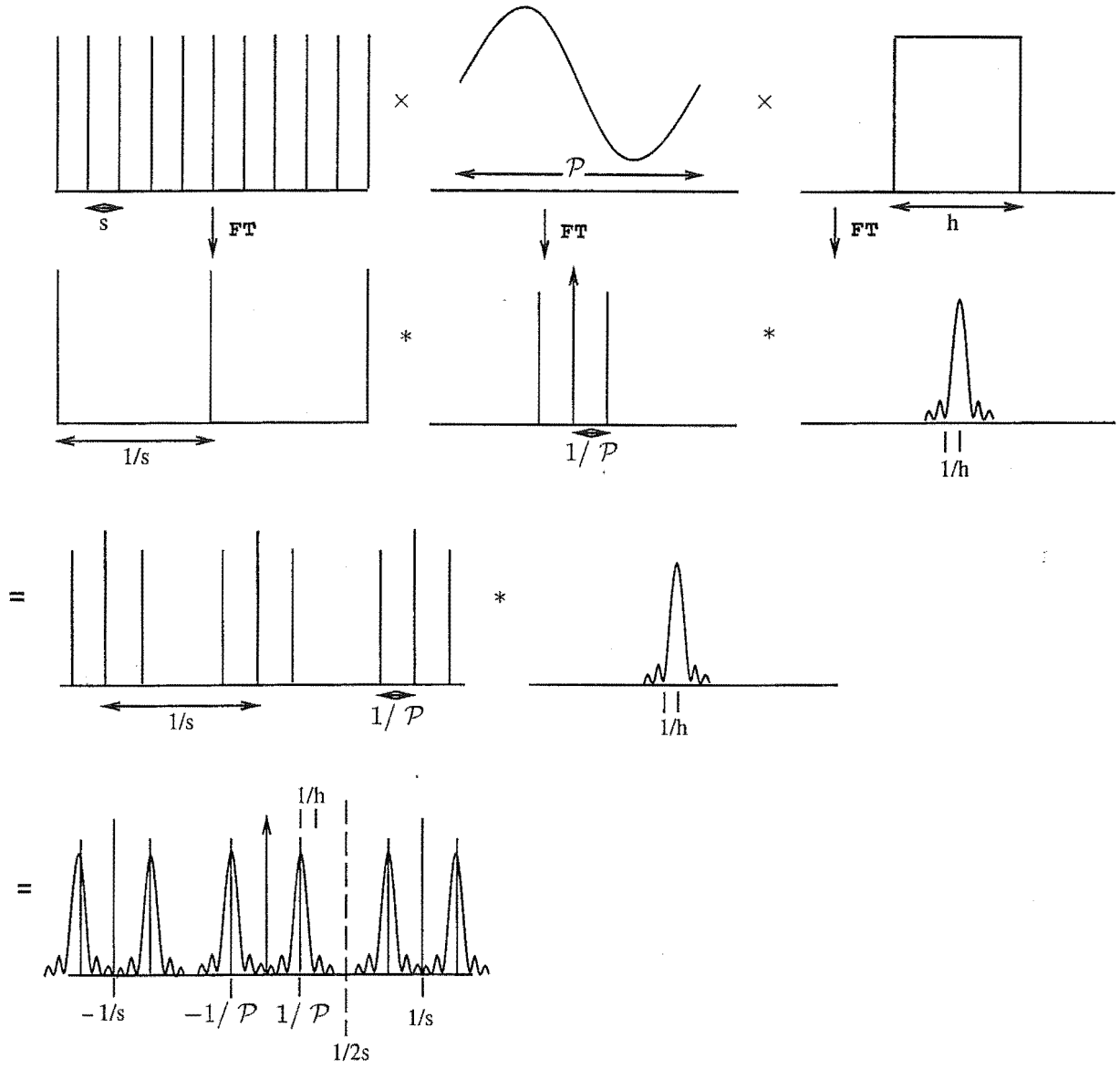

Figure 4.1: The Fourier transform of a discretely sampled evenly spaced sine wave in a finite data window. The higher frequency repetitions of the sine wave, at $(1/S \pm 1/\mathcal{P})$ and higher, due to the discrete sampling should be noted. As should the secondary peaks around $1/\mathcal{P}$, at $(1/\mathcal{P} \pm 1/h)$, due to the finite data window.

In the third case while leakage still causes a maximum at $f = 0$, the signature of the period is present and a careful choice of lower frequency limits is necessary to allow a simple search for the maximum power spectrum to correctly identify the period. As can be seen (see Figure 4.3), in this case the local minimum is located at m which is less than $1/2h$. So as long as the search for maxima in the power spectra starts above $f_{\min} = 1/2h$, the peak corresponding to the period can be found.

Even with this careful choice of frequency limits between which to search the peak may be slightly shifted from the actual period, due to the contribution from the side lobes of the finite data window's Fourier transform (see Kovács [110] for more on frequency shifts in Fourier analysis). Also

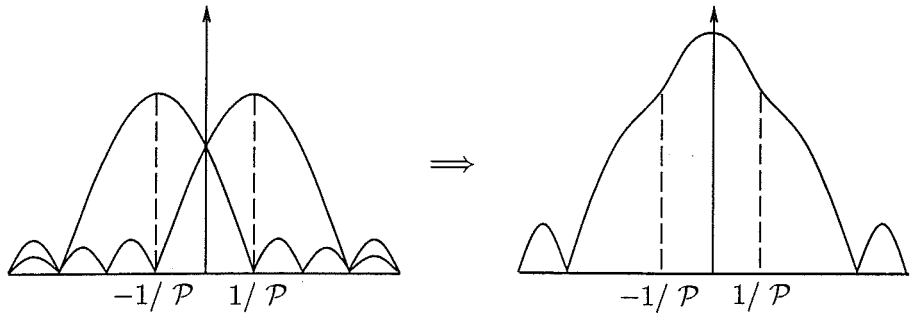

Figure 4.2: The Fourier transform of a periodic function whose period is greater than two times the data window (in the case shown here $\mathcal{P}= 2h$). The period signature is swamped by leakage from the finite data window.

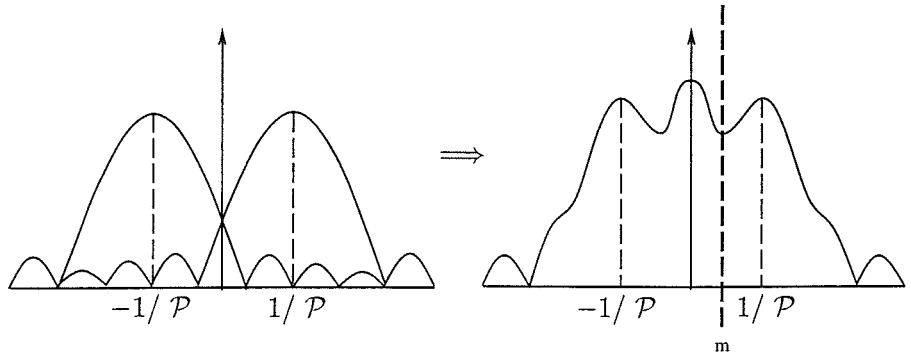

Figure 4.3: The Fourier transform of a periodic function whose period is greater than the size of the data window, but less than double the size. The maximum power spectrum peak for frequencies greater than m is at $1/\mathcal{P}$.

power in the peak will not entirely be due to the amplitude of the periodicity, for the same reason. This is true in all cases, but due to the closeness of the period and the observation length case three is especially bad. Similarly aliasing still may interfere with the peaks (even when only below the Nyquist frequency is considered), although it should be remembered that aliasing depends on the width of the transform of the periodic function (see §3.5.2 for the definition of aliasing, as it is being used here), so in the case of a pure sinusoid, as in Figure 4.1, aliasing can never occur.

For more details on Fourier transforms, particularly with respect to discrete evenly spaced data in a finite data window, see Brigham [28], Bracewell [26] and Brault & White [27].

4.1.2 Fourier transforms of unevenly spaced data

Unlike evenly spaced observations, periods can be distinguished safely at higher frequencies than the Nyquist frequency for unevenly spaced data. However, there is still a danger that the uneven data set is introducing several higher frequency repetitions of the true periodicity present, due to the spectral-window function. The spectral-window function will also contain leakage, due to the finite time over which observations were collected, so the lowest frequency restriction should always be observed[6]. These things particularly become a problem when searching for secondary periods. There are two options to get around the problem of extra peaks due to the data spacing and false

[6]Unless it is desired to remove this period component and it is obvious that the period is longer than double the size of the data window

secondary peaks (because of the finite data window these will be located at $(1/\mathcal{P} \pm 1/h)$) around a true periodicity.

One is to guess at an initial period from the Fourier transform then create a synthetic data function by sampling the sine wave at the same positions and truncating it so it has the same data window. This synthetic function can then be Fourier transformed, compared to the actual data's Fourier transform and hence any false bumps due to the initial period made apparent. It is a variation of this method that CLEAN employs.

The other option is to do something which is often referred to as prewhitening. For this technique the dominant peak in the Fourier transform is identified; then, the amplitude and phase of the periodicity found and subtracted from the data (for this to work the form of the periodicity must be known — for example it would not be successful if an elliptical binary orbit was removed using a sine wave). The residuals left behind are minus that periodicity and hence false peaks, due to the spectral-window function, can not be present. This method does have problems however. It is essential that the period, amplitude, phase and function of each periodicity are exactly identified or the residuals may contain false periodicities. This is not as easy as it sounds and the problems the Fortran program **T6** has doing this will be discussed in §4.1.3. There is also another subtler problem that means even if aliasing and leakage are not adding to the power of the main peak, it is still not entirely due to the amplitude of the periodicity at that frequency alone. This is because the set of Fourier transforms given by the unevenly spaced data will not be independent (see Scargle [142] §IIIb). The best that can be done is an uncorrelated set, in which case the powers can form a set of approximately independent variables. But this is entirely dependent on the shape of the spectral-window function, hence prewhitening, even in oversampled data sets of known shape, will typically not remove the periodicity completely[7].

4.1.3 Using T6 to find periods

Periods were found by the use of **T6**, a Fortran program originally written in 1991 by Warrick Lawson, which uses the 1988 code[8] of Press et al. [135] to find periods using the Lomb-Scargle normalized periodogram. These periods were then removed by **T6** by scanning through phase space to find the best-fit phase for the maximum frequency peak and subtracting off the cosine function with the appropriate phase for this fit (this means that it is difficult to remove periods significantly longer than the period of observations). The basic assumption of this is that the unevenly spaced data can be considered as the sum of sinusoidal functions.

T6 also provides the user with an indication of the reality of the periods found, called the Lomb-Scargle probability (LSP). The LSP gives the probability that the peak found will occur in a spectrum of pure noise (for details on how the LSP is obtained and a discussion on its interpretation see Press & Teukolsky [135] and the Appendix in Lawson [114]). The number of frequencies searched[9], M, is basically proportional to the highest frequency which means that the LSP increases as the highest frequency considered increases (as the more frequencies searched, the more likely it is to find a surplus peak, the LSP increases with M). Hence to prevent falsely low LSP creeping in, at no stage was a high frequency less than the average Nyquist frequency used. However, to ensure that short periods were not missed two times the average Nyquist frequency was initially used on all full sets

[7] That is, if another periodicity is present this may alter the periodogram amplitude at the frequency corresponding to the dominant period, as the amplitude at a given frequency depends on not only on that frequency, but the amplitudes at other independent frequencies too

[8] This code does not use weighted data points

[9] These are called by **T6** the number of independent frequencies. As it is important to remember that the powers that pertain to these frequencies are not independent, this terminology is avoided here

of radial-velocity data[10]. This was not done with the photometry obtained by the Mt John service observers, because the photometry was obtained at regular intervals, unlike the radial velocities which were constrained by available telescope time, and hence the average Nyquist frequency is not as bad an indication of the frequencies which can be distinguished[11].

The following things pertaining to **T6** are inherent in this thesis:

- Generally the highest frequency considered for all data was the mean Nyquist frequency.
- The frequency space was searched in intervals of 0.0001 d^{-1}. This means periods are not searched in even increments, as frequencies of $(0.001, 0.0011, ..., 0.1, 0.1001)$ actually equate to periods of $(1000, 909, ..., 10, 9.99)$ days.
- A LSP of less than 0.01 (less than a 1% probability of arising from a spectrum of pure noise) is taken to mean a significant periodicity.
- The dominant period is the period found by **T6** to have the largest spectral power and the secondary is the first prewhitened period found (and so on).
- **T6** iteratively finds the frequency with the largest power and removes it. It does not comment on the coherence of the harmonic found or necessarily imply that the signal is periodic. Hence the frequencies found by **T6** in data sets are only referred to as timescales.

Prewhitening and other complications

Unfortunately the prewhitening requirement of exact period, amplitude, phase and function is not well obeyed by the **T6** method. For a start the exact period will not quite be obtained, due to interference from other periodicities and higher frequencies' sinc (higher frequencies are due to the data spacing — sinc functions are the Fourier transforms of the finite data window) functions. Both these can cause the maximum peak to be slightly off from the actual peak. The exact amplitude will be a problem for the same reason, as well as the Fourier transforms' lack of orthogonality. The function could be a problem as **T6**, in both its method of periodogram calculation and for its prewhitening, assumes the data can be represented by a sum of sinusoids.

For a strictly periodic variation the situation is not too bad. All functions will period $\mathcal{P}$ can be represented by the sum of sines and cosines in the form of

$$\sum_{n=0}^{\infty}(a_n \sin(n2\pi t/\mathcal{P}) + b_n \cos(n2\pi t/curly P)) = \sum_{n=0}^{\infty} c_n \sin(n2\pi t/\mathcal{P} + \theta_n).$$

This means that a periodic non-sinusoidal function, continuously sampled, will have a power spectrum with delta functions at not only $1/\mathcal{P}$, but at $(n/\mathcal{P})$ also[12] (for binary-like curves the frequency of maximum power will be at $1/\mathcal{P}$, see the right-hand side of Figure B.7 for such a power spectrum). So if **T6** finds the correct amplitude for the dominant frequency all the frequency components of the periodic variation can be removed iteratively through prewhitening. However as the data is discretely sampled and in a finite data window, the spectral-window function may mean the different frequency components, and other periodicities, interfere and therefore hamper this.

The situation is, however, far worse when periodicities change with time, for example mode switching and mode amplitude changing. In the mode switching case, a regular period will be replaced

[10] With the exception of the radial-velocity "constant" stars: the sky, V337 Car, α TrA, β Col and β Vol

[11] The average Nyquist frequency for the photometry was also much higher for the photometry than the radial velocity for the same reason

[12] These higher frequency components of the periodic variation will be called higher harmonics

over a short period of time with another regular, but different, periodicity. To see the effect of this on the Fourier transform, this will be considered as the addition of two simple, discretely sampled, periods where the finite data window of one starts where the finite data window of the other ends. Therefore the Fourier transform will be the addition of two cases similar to those shown in Figure 4.1. For simplicity say that the two periods were observed for the same length of time. This means the Fourier transform created by the addition of the two individual transforms will be smeared by twice as much as it would have been if only one period was present[13] over the entire range of time. This is not disastrous, but the following is. If prewhitening is now undertaken it would cause havoc, as the dominant periodicity will only be present in one segment of the data set and hence trying to remove it from the data set as a whole would cause it to be introduced into the other part, where it would interfere with the existing periodicity. Changing the function used for prewhitening will not help.

Another time varying periodicity which is common in variable stars is the amplitude of their periodicity varying with time. Take the simple case of $y(t) = a(t)\sin(\omega t)$. When Fourier transformed the result will be two delta functions smeared through by the Fourier transform of $a(t)$. So an amplitude varying with time will cause a smearing effect which is dependent on how the amplitude varies. For example if the amplitude is effectively constant over the length of time observed, then the smearing effect is nil. But if the amplitude were to increase linearly then decrease, at the same rate, back down to its initial value, then the smearing effect would be that of a convolution with a sinc^2 function. Again the problem is prewhitening will not be able to remove this, no matter what function is used. What is left behind will be $(\alpha - a(t)\sin(\omega t))$, where α is the amplitude of the power spectrum found at ω. This will only be equal to $a(t)$ if the amplitude variation with time is negligible during the observations.

The above relatively regular cases should give a good idea of the kind of problems associated with finding periods in semi-regular and irregular variables. Basically the periodicity may be picked up by considering a subset of the data where it is more regular and/or stronger. Alternatively, if strong enough, the periodicity may be picked up by considering the whole data set; however, its removal by prewhitening in this latter case will not be successful. Hence if a periodicity is suspected of being at all irregular then care must be taken when interpreting the periodicities left by prewhitening, even if the function used for the prewhitening is a good approximation of the variations present.

4.1.4 Using "selfcorrelation" to find periods

Percy & Sen [130] suggested in 1991 a method of considering the correlation of a data set with itself that does not require an evenly spaced data yet, they proposed, would be very useful for analysing the periods, amplitudes and irregularities in data sets. They termed their correlation method autocorrelation, although it does not correspond to autocorrelation as defined in texts such as Press et al. [134] so I shall refer to it as selfcorrelation. The method they prescribe is as follows: decide on the periodicities to be considered, $[0, \mathcal{P}\ (\max)]$; divide this interval into N bins of time; for all pairs of observations, $([t_i, m_i], [t_j, m_j])$, for which $(t_i - t_j)$ falls into a given bin, b_k, average $|m_i - m_j|$; plot the average against b_k. When the data, m, are periodic with period $\mathcal{P}$, the curves show minima at bins of $0, \mathcal{P}, 2\ \mathcal{P}$, etc and a maxima of about $(\sigma + 1.2A)$ at bins of $0.5\ \mathcal{P}, 1.5\ \mathcal{P}, 2.5\ \mathcal{P}$ etc (where σ is the observational scatter and A is the amplitude of the variation). A Turbo Pascal program called **percysen** has been written to carry out this correlation.

This behaviour of the selfcorrelation at every period and half period will now be demonstrated. If

[13] If only one period were present and the data were so divided up interference due to the different phases of the two added segments (which would be at the same frequency as its the same period) would cancel out the broadening effect. This is unlikely to happen in the case of two independent periods.

Δt be the size of the bins and $\mathcal{T}_0$ is the minimum periodicity it is wished to consider, then

$$<m>(b_k) = \frac{1}{n}\sum_{(i,j)}^{n} |m_i - m_j|,$$

where the summation only runs over the $n(k)$ sets of observations, (i,j), for which $(t_i - t_j) > \mathcal{T}_0$ (where $i \geq j$ and $k = (t_i - t_j)\mathrm{div}\Delta t$). For simplicity $\mathcal{T}_0 = 0$ and an evenly spaced data set for which $(t_{j+1} - t_j) = \Delta t$ will be considered. This means that $k = (i - j)$ and hence at $k = 0$ the selfcorrelation function reaches a minimum and, if periodic, at every lag corresponding to a whole multiple of $\mathcal{P}$ thereafter. Furthermore, the data sampled will be considered to come from a simple sine function $A \sin \omega t$. This means the summation is simply

$$<m>(i - j) = A<|\sin \omega t_i - \sin \omega t_j|>,$$

which at $(t_i - t_j) = 0.5\ \mathcal{P}$ becomes

$$<m>(0.5\ \mathcal{P}) = A<|\sin \omega t_i - \sin \omega (t_i - 0.5\ \mathcal{P})|> = 2A<|\sin \omega t_i|>.$$

The limit of $<\sin \omega t_i>$ over half a period is

$$\frac{\int_0^\pi \sin(\omega t) dt}{\pi} = \frac{-1}{\pi}[\cos(\omega t)]_0^\pi = 0.6$$

which implies that at $(t_i - t_j) = 0.5\ \mathcal{P}, 1.5\ \mathcal{P}, 2.5\ \mathcal{P}$ the selfcorrelation function should reach a value of $1.2 \times A$.

Clearly an important part of getting the useful behaviour illustrated above, is that a reasonable number of "points" are present in each bin. However, no periods of the size of the bins will be able to be detected. So there is a need to balance these two effects when choosing the bin size — in other words the average number of $(t_i - t_j)$ that will fall in the bins needs to be known. If the number of bins over the observed data window is N (and the number of data points is D), the total number of unique observation pairs divided by N will be the average number of observation pairs in a bin. Now the first point in the data set has D points in its selfcorrelation set it can match to, the second point has $(D - 1)$ points and so on (as (t_a, t_b) should be included but not the negative time lag (t_b, t_a)). This forms a series for which the summation is $\frac{D(D+1)}{2}$ (for even D). So the average number of points which will fall into a bin will be[14] $\frac{D(D+1)}{2N}$.

Comparison to periodograms

This method was applied to both Mt John photometric and spectroscopic data and the results compared to those found by use of the Lomb-Scargle periodogram (see Tables 4.1 and 4.2). It should be noted that, as this is a test of the two methods, only the more variable stars with plenty of points, have been used (see §4.3 and §4.2).

For the most part the periodicities found by both methods agree, although some periods are not as obviously represented by the selfcorrelation method, particularly if other periods are present. Things can become confusing with the selfcorrelation method as periods are not removed as found. This is illustrated by the radial velocities of ω Cap (Figure 4.4) and the visual photometry of δ^1 Aps (Figure 4.5). The selfcorrelation for ω Cap is clearly exhibiting the effects of strong period of about

[14] If all possible lags are used. If only some lags are used, due to restrictions on the periodicities considered, then this will be different. In the case of a periodicity restriction to some maximum, $\mathcal{P}$ (max), the average will be larger than this!

Star	Lomb-Scargle Sig. $\mathcal{P}$	selfcorrelation $\mathcal{P}$
2 Cen	556	500,1000
62 Sgr	588,164,96	650
β Gru	833,59,15	800,110,24,55,80
δ^1 Aps	1000,455,29,48	450,910
δ^2 Gru	$\geq$1429,23	2*800
ϵ Car	833	850
ϵ Col	$\geq$1250	2*900
ϵ Mus	63,625,88	35,65
η^2 Dor	667,101	650
η Scl	None	None?
γ Cru	556,13,17	500-600,25,115
γ Ret	909,345	>1000
GZ Vel	>2500,267	$\gg$1000,250,600
HR 4177	435	400,900
HR 6166	476	500
κ Pyx	526	400-500
L^2 Pup	140,435	140-160,850
λ Vel	1429,1429,714,1429	$\gg$1000
NS Pup	$\geq$1380	$\gg$1000
N Vel	625	450,650
o^1 CMa	179,769,167,23,44	180,380,700
ω Cap	476,250,500,213	480
π Pup	1250,37,47	>1200,30,115
ψ Phe	588,189	600
σ CMa	$\geq$1250,667	500,1200
σ Lib	556,120	600
τ^4 Eri	588,33	550,1150,70

Table 4.1: **T6 versus percysen: radial velocities.** This table compares the periods obtained from radial velocities using **T6** and **percysen**. For the selfcorrelation method the lags considered were over 0–1350 days (based roughly on the length of times observations were obtained) and on average there are 10 points per bin (any bins with less than 5 data points have were removed). Dips in the selfcorrelation are somewhat subjective, so only obvious and large dips are listed and those underlined may be the same periodicities found using **T6**.

480 days and this agrees well with the periodogram[15]. However δ^1 Aps's periodogram has two similar significant short periodicities present and these are not distinct in the selfcorrelation.

4.2 Radial velocities for the 44 surveyed stars

In November 1993 spectroscopic observations of 44 K and M giants and supergiants began to be taken on the McLellan 1-metre telescope at the Mt John University Observatory. All 44 stars were observed up to and including March 1995. Then a subset of 13 of these stars was discontinued, leaving behind stars showing a range of relative radial-velocity behaviour for more intensive investigation (for more details on how these stars were chosen see §3.6). The remaining 31 stars were observed up to and including February 1997, giving a span of observations which covers slightly

[15]This star also illustrates the main "problem" with prewhitening. The dominant period is clearly not a sine and as a result it reappears as the "tertiary" period!

Star	Lomb-Scargle Sig. $\mathcal{P}$	selfcorrelation $\mathcal{P}$
β Gru	57	55,100,350,400
δ^1 Aps	48,60	50,100,140,190,250,280,350,400
δ^2 Gru	24	25,47,75,95
ϵ Mus	44,33,1111,29,63	25,35,125,275,380
η Scl	34	None
γ Cru	1111	20,225,500,700
L^2 Pup	141,1111,244	140
o^1 CMa	179,238,64,108	140,190,380,520
τ^4 Eri	294,88	320,600

Table 4.2: **T6 versus percysen: V_J.** This table compares the periods obtained from Mt John V_J photometry using **T6** and **percysen**. For the selfcorrelation method the lags considered were over 0–800 days (based roughly on the length of times observations were obtained) and on average there are 10 points per bin (any bins with less than 5 data points have were removed). Dips in the selfcorrelation are somewhat subjective, so only obvious and large dips are listed and those underlined may be the same periodicities found using **T6**.

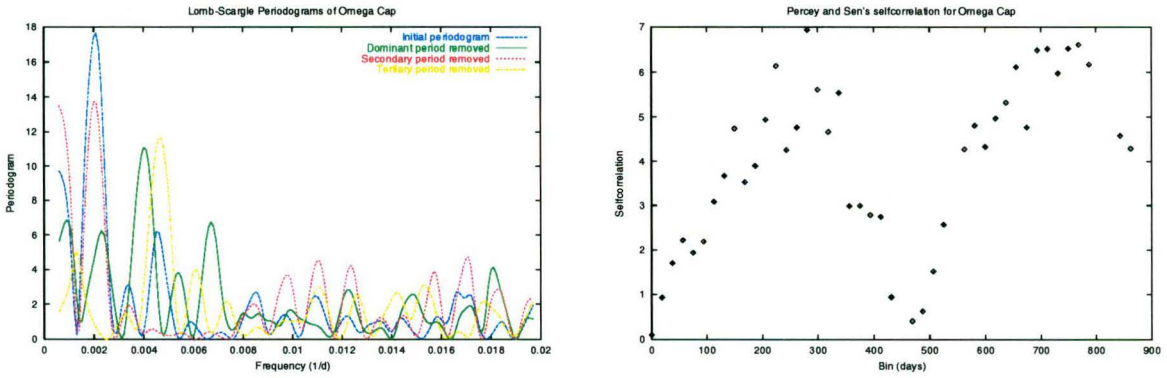

Figure 4.4: The left-hand plot shows the Lomb-Scargle normalized periodograms for ω Cap's radial-velocity data. All periodograms for all prewhitened data are included up to but excluding those for which a significant peak was not present (in the LSP sense). The right-hand plot shows the selfcorrelation for the same data set.

over three years in most cases. For details on how these observations were reduced to give relative radial velocities see §3.3 and for plots of the relative radial velocities see Appendix A.

The probability of the relative radial velocities obtained for a star having the observed scatter, yet coming from a star constant in relative radial velocity, can be estimated by the use of the F-test[16]. An F-test (from Bevington & Robinson [21] §11.4) is undertaken by evaluating

$$F[\nu_1, \nu_2] = \frac{\chi^2_{\nu_1}}{\chi^2_{\nu_2}} = \frac{s_1^2/\sigma_1^2}{s_2^2/\sigma_2^2},$$

[16] An F-test with one of the degrees of freedom equal to infinity is equivalent to a chi-squared test. Hence for a chi-squared test, it is essential to know the errors in the data exactly and this is not the case here.

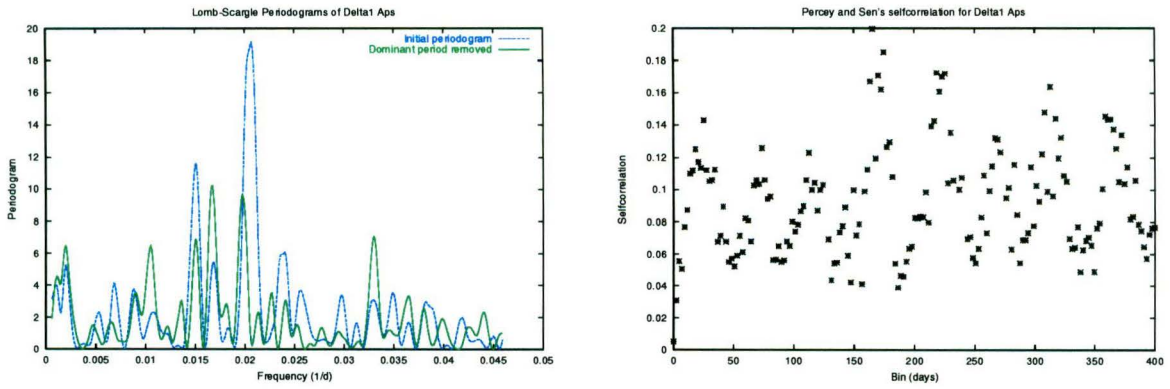

Figure 4.5: The left-hand plot shows the Lomb-Scargle normalized periodograms for δ^1 Aps's V_J data. All periodograms for all prewhitened data are included up to, but excluding, those for which a significant peak was not present (in the LSP sense). The right-hand plot shows the selfcorrelation for the same data set.

where in both cases σ^2 is the true standard deviation of the parent population[17], s is an estimation of the standard deviation, χ^2_ν is the reduced chi-squared for the data and its fitting function[18] and ν is the number of degrees of freedom[19]. When this is compared to a standard F-distribution table, the probability that such a large F would be obtained from random sets of data if the fitting functions are correct can be found. If in both cases the parent population is the same then $\sigma_1 = \sigma_2$ and obtaining an F-value becomes a case of obtaining two estimates of the standard deviation of the parent population, so that

$$F[\nu_1, \nu_2] = \frac{s_1^2}{s_2^2}$$

can be evaluated. One estimation is given by the variance of experimental data points (sampling the parent population) about the fitting function. Let these data points be called x_i and then if the fitting function is a constant value the variance is given by

$$s_1^2 = \sigma^2_{N-1} = \frac{\sum_{i=1}^{N}(x_i - \langle x \rangle)^2}{N-1},$$

where $\langle x \rangle$ is the average of x_i and is assumed to be the fitting function. As this fitting function is a constant the number of degrees of freedom for this is $\nu_1 = N - 1$. However, to determine F another estimate of the standard deviation of the population, s_2, is also needed.

Hence the probability that the relative radial velocities obtained for a star come from a star constant in relative radial velocity can be found by evaluating σ^2_{N-1}/s_2^2, where σ^2_{N-1} is the variance o the N relative radial velocities, v_i, about their average, $\langle v \rangle$, and s_2 is another estimation of th standard deviation of the population. Each v_i is determined by the average of the relative radia velocities of six orders, with the addition of a "run correction" value (for more details on this se Appendix F.7.1). As each of the six orders is expected to be sampling the same value of relativ radial velocity an estimation of the standard error, σ_v^i, of v_i is given by the standard deviation o the six orders' relative radial velocities (with an additional value representing the error in the ru

[17] A parent population is the infinite set of data points which the experimental data points are assumed to sampl The parent distribution is the probability distribution of the parent population.

[18] Estimating the variance of a parent population's data requires an estimation of how the parent population i believed to vary. This is called the fitting function.

[19] If the fitting function is determined from n data points using m parameters then the number of degrees of freedo is $\nu = n - m$

correction). Therefore $\langle v \rangle$ has an error of

$$\sigma^2_{\langle v \rangle} = \sum_i (\sigma^i_v)^2 (\frac{\partial \langle v \rangle}{\partial v^i})^2 = \sum_i (\sigma^i_v)^2 (\frac{1}{N})^2 = \frac{\langle \sigma^2_v \rangle}{N}.$$

If each standard error estimation, σ^i_v, is smaller than the real error by some constant amount then the real error in the average will be

$$\sigma^2_{\langle v \rangle} = \sum_i ((\sigma^i_v)^2 + \kappa))(\frac{1}{N})^2 = \frac{\langle \sigma^2_v \rangle + \kappa}{N},$$

where κ is that constant amount. However, the error in the mean relative radial velocity $\langle v \rangle$ is equal to $\sigma/\sqrt{N}$, where σ is the true standard deviation of the parent population. Therefore $\sigma^2_{\langle v \rangle} N$ provides an estimation[20] of the variance of the parent population which can be used for s^2_2 and, as each σ^i_v is obtained from the variance of the relative radial velocity of six orders about their average value, the number degrees of freedom of this estimation is $\nu_2 = 5$. Then the F-test value is

$$F[N\text{-}1, 5] = \frac{\sigma^2_{N-1}}{\sigma^2_{\rm est}},$$

where $\sigma^2_{\rm est} = \langle \sigma^2_v \rangle + \kappa$. Hence at a 1% significance level saying a star is variable in relative radial velocity is equivalent to saying that $\sigma_{N-1} \geq 3.0 \times \sigma_{\rm est}$ (except in the case of the 13 stars which were discontinued — for these see any F-distribution table such as Bevington & Robinson [21] C.7).

The standard error estimation, σ^i_v, can be smaller than the real error by some constant amount because it suffers from the disadvantage that it can not pick up errors which vary randomly from exposure-to-exposure, but are the same for all orders in an observation (for a discussion on the possible causes of such an error see §3.5.3). It would give a better idea of the reality of the observed radial-velocity variations if this error, κ, could be estimated in some way and hence included as detailed above. However, errors due to line blending and so on, which are spectral type related, might be expected to be contained in σ^i_v as these effects do vary from order-to-order (for more on these kind of problems and minimizing them see §3.5.1 and §3.5.4). Hence it does not seem unreasonable to expect that this additional error will not, at least to first order, be a function of spectral type and hence that κ can be obtained from the Sun and used for all stars. The Sun was observed in order both to provide a calibration from run-to-run and to provide another indication of the accuracy[21] being obtained within a run. Having removed the effects of the movements of planets such as Jupiter the Sun's relative radial velocity is expected to give a constant value, so κ has been estimated by choosing it to give the Sun an F-test value of unity. The value necessary to do this is $\kappa = 9.05 \times 10^{-4}$. Hence the F-test was carried out not just using the error estimated by consideration of the scatter from order-to-order for each point, $\sqrt{\langle \sigma^2_v \rangle}$, but also from assuming the error in the relative radial-velocity determinations is actually

$$\sigma_{\rm est} = \sqrt{\langle \sigma^2_v \rangle + 9.05 \times 10^{-4}}.$$

The resulting variances and F-test values are presented in Table 4.3. The average error in the relative radial-velocity measurements (plus the additional constant) implies the relative radial velocities have a typical precision[22] of about 50 m/s, although this can be worse for cooler stars. An

[20] This estimation does not assume the relative radial velocities are constant for every observation (just for the six orders), so for a star which is intrinsically variable $\sigma^2_{N-1} > \sigma^2_{\langle v \rangle} N$

[21] As the Sun is constant in relative radial velocity its radial-velocity measurements give an indication of how close the relative radial velocities being obtained come to the true values

[22] It should be noted that the average error in a radial-velocity measurement, $\langle \sigma_v \rangle$, will actually be less than $\sqrt{\langle \sigma^2_v \rangle}$

Star	N	σ_{N-1} (km/s)	$\sqrt{\langle\sigma_v^2\rangle}$ (km/s)	$\sigma_{\rm est}$ (km/s)	$\sqrt{F}_{\langle\sigma_v^2\rangle}$ $[N-1,5]$	$\sqrt{F}_{\rm est}$ $[N-1,5]$
24 Cap	14	0.162	0.044	0.053	3.72	3.06
3 Cet	16	0.716	0.039	0.049	18.57	14.64
α Sco	28	0.760	0.054	0.062	14.14	12.34
β Ara	24	0.165	0.029	0.042	5.60	3.91
ϵ Cru	20	0.189	0.036	0.047	5.24	4.03
ϵ Sco	24	0.089	0.030	0.042	2.96	2.09
ϵ TrA	15	0.095	0.033	0.045	2.87	2.13
η^2 Pic	26	0.130	0.034	0.045	3.84	2.87
η Sgr	17	0.168	0.040	0.050	4.17	3.34
γ Cha	16	0.217	0.024	0.039	8.94	5.62
γ Hyi	24	0.229	0.036	0.047	6.35	4.88
γ Phe	18	11.536	0.061	0.068	187.72	168.60
HR 3017	22	0.180	0.043	0.052	4.22	3.45
2 Cen	61	0.459	0.058	0.065	7.97	7.07
62 Sgr	50	0.846	0.052	0.060	16.22	14.05
α TrA	76	0.109	0.031	0.043	3.57	2.55
β Col	46	0.089	0.025	0.039	3.55	2.28
β Gru	91	0.844	0.056	0.064	14.98	13.22
β Vol	43	0.101	0.029	0.041	3.53	2.43
δ^1 Aps	70	1.080	0.087	0.092	12.37	11.70
δ^2 Gru	72	0.387	0.051	0.059	7.61	6.55
ϵ Car	60	0.582	0.038	0.048	15.40	12.05
ϵ Col	54	2.847	0.027	0.041	103.67	69.90
ϵ Mus	76	0.628	0.063	0.070	9.96	8.99
η^2 Dor	68	0.333	0.041	0.051	8.13	6.55
η Scl	50	0.582	0.050	0.059	11.58	9.94
γ Cru	106	0.326	0.041	0.051	8.00	6.44
γ Ret	61	0.803	0.055	0.062	14.70	12.88
GZ Vel	41	0.551	0.029	0.042	18.99	13.18
HR 4177	34	0.375	0.034	0.046	10.96	8.23
HR 6166	45	0.184	0.030	0.042	6.19	4.35
κ Pyx	44	0.245	0.035	0.046	7.07	5.34
L^2 Pup	50	2.282	0.331	0.333	6.89	6.86
λ Vel	70	0.787	0.030	0.042	26.26	18.53
N Vel	41	0.269	0.035	0.046	7.70	5.83
NS Pup	34	0.496	0.040	0.050	12.44	9.93
o^1 CMa	80	1.251	0.082	0.088	15.18	14.26
ω Cap	38	3.143	0.032	0.044	97.91	71.44
π Pup	88	0.368	0.035	0.046	10.65	8.03
ψ Phe	60	0.631	0.068	0.074	9.31	8.51
σ CMa	55	0.858	0.035	0.046	24.23	18.47
σ Lib	50	0.674	0.040	0.050	16.93	13.51
sky	266	0.040	0.027	0.040	1.51	1.00
τ^4 Eri	83	0.409	0.049	0.057	8.39	7.14
V337 Car	38	0.104	0.049	0.058	2.12	1.81

Table 4.3: **The F-test: radial velocities.** This table gives the standard deviation, σ_{N-1}, of the N relative radial velocities; the error in the relative radial velocities, $\sqrt{\langle\sigma_v^2\rangle}$, predicted by the scatter between the relative radial velocities of the six orders; the predicted error in the relative radial velocities plus a constant value to combat any errors which affect all six orders evenly; and the two F-test values that arise from these. It should be noted that the first set of stars had their observations discontinued after about one year.

alternative method of determining the precision of the relative radial velocities is to consider the standard deviation of the radial velocities of a constant star. However, the scatter will be spectral type dependent and it is necessary to be certain that the star is constant. For the purposes of this thesis the only star guaranteed to be constant is the Sun and accordingly a lower bound on the precision of the relative radial velocities is 40 m/s. In addition to the Sun, four of the stars were chosen for further observations because of the comparative constancy of their relative radial velocities. If they really are constant then the precision of the relative radial velocities is no better than 100 m/s. However, there is no guarantee that these four stars are indeed constant. As can be seen, to a 1% significance level, the F-test indicates that all stars observed for the duration are variable except for the Sun and those four stars observed for their constancy, α TrA, β Col, β Vol and V337 Car (taking the estimation of error that sets the Sun's F-test value equal to one). The stars for which observations were discontinued also all appear to be significantly varying at the 1% level, except for 24 Cap, η^2 Pic, ϵ Sco and ϵ TrA.

The relative radial velocities were searched for timescales using the Fortran program **T6** (for more on period finding using **T6** and relevant terminology see §4.1, for the radial-velocity periodograms themselves see Appendix B[23]). The results are displayed in Table 4.4, where the last timescale displayed is not significant. As can be seen most of the 31 stars observed for the full 3 years have significant timescales (in the Lomb-Scargle sense), with the exception of η Scl and most of the stars observed for their constancy in relative radial velocity. Interestingly, the relative radial velocity standard star α TrA has a significant timescale of 57 days. Of the stars for which observations were discontinued early on, only the spectroscopic binary γ Phe has a period for which sufficient observations have been taken for it to be considered significant.

4.3 Mt John $V_J, (B-V)_J, (V-R)_C$ and $(V-I)_C$ photometry

4.3.1 Introduction

Photometry obtained by service observers at Mt John University Observatory was reduced closely following the method described by Hardie [70]. Some time consuming elements of the reduction procedure have not, however, been followed by the service observers if experience has showed it to make little difference to precision of the resulting photometry. For completeness a short description of the observing method will nonetheless be given here (this also owes much to Gilmore [55] and Tobin [165]).

Instrumental, or natural, magnitudes are determined as follows. First all integrations from the photomultiplier are turned into counts per second. This is then corrected for the dead time[25] (this is a set value of 200–300 nanoseconds which is not changed for different seasons, but is telescope dependent). The sky counts are then subtracted and the natural magnitudes hence determined for V, $B-V$, $V-R$ etc. For clarity, from now on these natural magnitudes will be referred to as v, $(b-v)$ and $(v-r)$ respectively.

Having determined the natural magnitudes, the next step to is deal with atmospheric extinction.

[24]Even after all LSP significant timescales are removed this is often much larger then the precision of the relative radial velocities. This may be due to the remaining radial-velocity variations being too erratic to form a significant periodogram peak, or it may be a sign of the failure of **T6** to completely remove the existing timescales. For more on problems associated with prewhitening see §4.1.3.

[23]The radial-velocity data have also been phased to the dominant timescale, when it is only a fraction of the observation window (taken to be a timescale of less than 900 days). The plots of the phased data are given in Appendix C.

[25]After detecting a pulse the amplifier/counter has to wait a time before it can detect another pulse. This is the dead time and must be corrected for. It is very important for high count rates.

Star	N	$\mathcal{P}$ (days)	(LSP, σ_{N-1})
24 Cap	14	93	(3.5E-01,0.162)
3 Cet	16	526	(6.9E-02,0.716)
α Sco	28	139	(1.4E-02,0.760)
β Ara	24	112	(5.0E-01,0.165)
ϵ Cru	20	270	(8.4E-02,0.189)
ϵ Sco	24	52	(2.9E-01,0.089)
ϵ TrA	15	135	(4.1E-01,0.095)
η Sgr	17	345	(7.6E-01,0.168)
η^2 Pic	26	909	(4.8E-02,0.130)
γ Cha	16	435	(6.2E-02,0.217)
γ Hyi	24	244	(1.6E-01,0.229)
γ Phe	18	192, 172	(4.3E-03,11.53),(2.0E-02,0.732)
HR 3017	22	556	(2.5E-01,0.180)
2 Cen	61	556, 37	(1.1E-05,0.459),(1.6E-02,0.320)
62 Sgr	50	588, 164, 96, 119	(8.7E-05,0.846),(5.3E-04,0.558),(1.7E-03,0.400),(7.9E-02,0.304)
α TrA	76	57, 46	(4.1E-04,0.109),(3.5E-01,0.090)
β Col	46	159	(3.4E-02,0.089)
β Gru*	91	833, 59, 15, 19	(2.4E-09,0.844),(8.0E-09,0.580),(6.7E-06,0.376),(6.6E-02,0.296)
β Vol	43	476	(4.5E-01,0.101)
δ^1 Aps*	70	1000, 455, 29, 48, 175	(2.7E-09,1.080),(2.5E-05,0.595),(2.1E-04,0.415),(1.8E-03,0.322),(2.9E-01,0.263)
δ^2 Gru*	72	1429, 23, 20	(1.7E-04,0.387),(1.5E-03,0.303),(4.3E-02,0.249)
ϵ Car	60	833, 104	(5.2E-09,0.582),(1.8E-02,0.270)
ϵ Col	54	1250, 294	(4.4E-04,2.847),(2.0E-02,2.118)
ϵ Mus	76	63, 625, 88, 69	(2.0E-05,0.628),(2.1E-06,0.484),(3.7E-04,0.368),(4.6E-02,0.301)
η^2 Dor	68	667, 100, 62	(6.6E-06,0.333),(6.1E-04,0.237),(2.2E-01,0.198)
η Scl	50	49	(2.5E-02,0.582)
γ Cru*	106	556, 13, 16, 40	(1.7E-09,0.326),(1.7E-04,0.237),(2.5E-05,0.203),(3.1E-01,0.169)
γ Ret	61	909, 345, 41	(7.1E-03,0.803),(7.8E-03,0.625),(1.9E-02,0.524)
GZ Vel	41	2000, 270,1667	(5.9E-06,0.551),(1.8E-03,0.281),(5.4E-02,0.197)
HR 4177	34	435, 208	(4.9E-05,0.375),(7.3E-02,0.163)
HR 6166	45	476, 667	(2.2E-05,0.184),(4.7E-01,0.107)
κ Pyx	44	526, 196	(7.5E-03,0.245),(3.2E-01,0.193)
L^2 Pup	50	141, 435, 123	(2.9E-06,2.282),(1.7E-04,1.304),(1.7E-02,0.898)
λ Vel	70	1429, 714,1429, 556	(4.6E-12,0.787),(7.1E-06,0.277),(2.2E-05,0.211),(5.1E-02,0.159)
N Vel	41	625, 112	(2.7E-05,0.269),(4.3E-01,0.144)
NS Pup	33	1429,1429	(1.4E-05,0.495),(1.4E-02,0.197)
o^1 CMa*	80	179, 769, 167, 23, 44, 118	(8.9E-05,1.251),(2.5E-05,0.980),(2.5E-04,0.766),(6.8E-04,0.613),(8.6E-03,0.504),(1.9E-02,0.437)
ω Cap	38	476, 250, 500, 213,1250	(7.9E-07,3.143),(5.6E-04,0.751),(3.9E-05,0.468),(3.2E-04,0.240),(2.5E-02,0.149)
π Pup	88	1250, 37, 47, 31	(1.3E-10,0.368),(2.4E-03,0.226),(6.8E-03,0.195),(1.4E-01,0.172)
ψ Phe	60	588, 189, 77	(8.0E-05,0.631),(1.9E-03,0.460),(3.4E-02,0.372)
σ CMa	55	1250, 667, 49	(3.9E-09,0.858),(1.5E-04,0.307),(9.2E-02,0.216)
σ Lib	50	556, 120, 95	(5.9E-07,0.674),(7.1E-03,0.341),(8.7E-02,0.275)
sky	266	10	(7.7E-01,0.040)
τ^4 Eri	83	588, 33, 135	(2.0E-08,0.409),(3.9E-03,0.278),(2.4E-01,0.242)
V337 Car	38	286	(1.0E-01,0.104)

Table 4.4: **Period search of radial velocities.** The result of running **T6** on the Mt John relative radial velocities, where N is the number of data points for each star, LSP is the Lomb-Scargle probability of the timescale and σ_{N-1} is the $N-1$ standard deviation of the data[24] (before that timescale's removal by prewhitening). Generally these results are with **T6** ran over the default range of frequencies, but stars labelled with a ($\star$) had timescales so short it was necessary to search to two times the Nyquist frequency (see §4.1.3, this was done for the radial velocities of most stars initially). It should be noted that the first set of stars had their observations discontinued after about one year and the last timescale tabulated here does not have a significant Lomb-Scargle probability.

The coordinates of the star are precessed to the observation date and the air mass, X, hence calculated for the time of the reading. This is done separately for each star in the set of comparison, check and variable. The natural magnitudes, corrected for atmospheric extinction, are then

$$m^o_{\rm nat}=m_{\rm nat} - k_m X = m_{\rm nat} - (k^1_m + k^2_m(b-v))X.$$

It should be noted that the Mt John service observers use mean extinction values k and do not bother about secondary extinction in R and I (and they hardly ever measure k^2 — just k^1). In addition, despite the fact that the atmosphere may well not be uniform it is assumed that not only is k independent of time, but it is also independent of the position in the sky. In other words it is assumed that $k = k(\lambda) \neq k(\alpha, \delta, t)$, even though strictly speaking the latter is more realistic. k can be determined by the observation of any non-variable stars.

Transformations from the natural system to the standard Johnson-Cousins system also needs to be performed. According to Hardie (his equation 20) any two colour-index measurements of the same black body on different natural systems are related by

$$C_2 = \eta C_1 + \zeta_C,$$

where η and ζ are constants for the transformation between these two systems. For magnitudes this is

$$m_2 = m_1 + \epsilon C_1 + \zeta_m,$$

where ϵ and η are known as "scale factors" and ζ as "zero-point" constants. It is important to note, however, that different constants are found for different luminosity classes of stars — while the Mt John service observers have not been meticulous about this point, the redder standards they use are giants. The colour the Mt John service observers use for magnitudes is[26] $(b-v)$.

Following Hardie (his equation 28a) for differential photometry

$$\Delta V = \Delta v - k_V \Delta X + \epsilon \Delta (b-v)$$

and so on is calculated, where here Δ means the difference in values between the comparison and the variable star. A pseudo-non-differential magnitude is obtained from this by adding the value $V^{\rm tbl}_{\rm cmp}$ onto the differential (from the comparison star) values of magnitude (and similarly colour) obtained for each of the variable, check and "star 5"[27]. It should be noted that as the variable stars are so bright all stars, including the comparison, are observed with a neutral density filter. As the comparison is also observed with a neutral density filter, this drop of 2.5–3.0 magnitudes is automatically accounted for in the differential photometry.

Precisely how atmospheric extinction corrections and transformation to the Johnson-Cousins system, from the natural system, are performed is illustrated below for the visual magnitude.

First the secondary extinction, k^2, is determined by observing one pair of stars of very different colours at different air masses. For each observation, (i), $x(i) = \Delta(C(i)X(i))$ and $y(i) = \Delta v(i)$ are calculated, where here Δ means the difference between the two stars. As the natural visual magnitude corrected for extinction is

$$v_0 = v - (k^1_V + k^2_V C)X$$

[26] The Mt John service observers say it is difficult to reproduce a standard response in the filter-photomultiplier system for filters other than $(B-V)$

[27] Due to the redness of the check and comparison stars another "constant" star was always observed, in case either of the former turned out to actually be varying. This star was usually called "star 5".

and k^1 and k^2 are constants, for each airmass the difference between the two corrected natural magnitudes is

$$\Delta v_0(i) = \Delta v(i) - k_V^1 \Delta X(i) - k_V^2 \Delta(C(i)X(i)).$$

If the pair of stars are very close together it can be said that $\Delta X = 0$ and this equation becomes

$$y(i) = \Delta v_0(i) + k_V^2 x(i).$$

Hence a least-squares straight-line fit to a x-y graph of observations of the star pair will give the secondary extinction as the slope of the graph.

The Mt John service observers then calculate the primary extinction to first order. By recalling that the natural atmospheric extinction corrected magnitude is

$$v_0 = v - k_V X$$

and the standard system magnitude is

$$V = v_0 + \epsilon(b - v) + \zeta_V,$$

it can be seen that the difference in visual magnitude between this same star at very different air masses is

$$0 = \Delta v - k_V \Delta X + \epsilon \Delta(b - v).$$

To first order this means that

$$k_V^1 = \frac{\Delta v}{\Delta X},$$

where the second-order extinction coefficient is ignored on this first pass and $\epsilon\Delta(b - v)$ is considered to be a second-order term, as the Johnson-Cousins and Mt John systems are so similar that $\epsilon \approx 0$. This is calculated for a number of different stars and averaged.

Now it is possible to calculate the "zero point", ζ_V, for the transformations to the standard system. For standard stars the value of

$$(V - v_0) = V - v + k_V X$$

is calculated, where v is measured, k_V is known to first order and V is the tabulated value of the star in the standard system. As

$$(V - v_0) = \epsilon(b - v) + \zeta_V$$

a plot of $(b - v)$ against the calculated values should yield a straight line of slope ϵ and y intercept ζ_V. Any points which are too far from the line of best fit are discarded at this stage and the best fit line recalculated.

As ϵ is now known it is now possible to determine a better value for the primary extinction coefficient with second-order terms being included (and everything being re-calculated accordingly). It should be noted that while continued iterations would probably improve the solution still further, these are not performed by the Mt John service observers.

4.3.2 Results for stars observed photometrically

After about 500 days of spectroscopic observations, broad-band photometry of 13 stars began in conjunction with the radial-velocity observations at Mt John University Observatory. The photometry was initially obtained on both the Optical Craftsmen (OC) and the Boller & Chivens (B&C) telescopes (later mainly on the OC) with the use of neutral-density filters because of the brightness of the stars. Photometric observations were continued for a short time after the spectroscopic observation stopped — an observing range generally between August 1995[28] and September 1997[29].

[28] ϵ Mus, γ Cru, δ^1 Aps and L^2 Pup began to be observed in March 1995, with other stars being added in as they became visible from July 1995

[29] π Pup, τ^4 Eri and γ Cru were observed until during November 1997

β Gru, γ Cru and π Pup are so bright that the addition of a cardboard mask to act as an aperture stop to reduce the light was also necessary. Hence corrections needed to be applied to these three stars, in order to merge their data together (due to the different nature of the two telescopes they required different masks). For plots of the obtained V_J, $(B-V)_J$ and $(R-I)_C$ photometry for these 13 stars see Appendix D.

A number of complications became apparent during the observations of these stars, beginning with one arising from the use of the masks. γ Cru's check star was observed without a mask ("star 4") and occasionally with a mask ("star 6") to facilitate examination of the mask corrections (generally only the variable was observed using the mask). It was initially assumed that the mask corrections would be different for different telescopes, but the same within a telescope. Examination of γ Cru's "star 6" revealed that this was definitely not the case! Observations taken on the OC seemed to be consistent for all colours from run-to-run but observations taken on the B&C varied by up to 0.2 magnitudes in the worst case of $(V-I)_C$ (see left-hand Figure 4.6). The worst

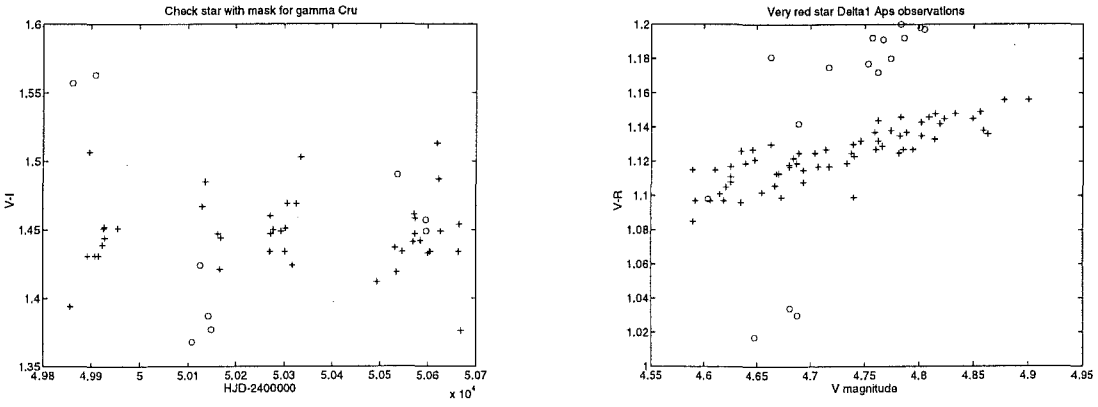

Figure 4.6: To the left is the masked check star for γ Cru where (+,o) are symbols for the OC and B&C telescopes respectively. It seems that the effect of the mask on the star's magnitude varies with time for the B&C telescope — possibly due to problems with that telescope's photomultiplier. To the right is the red star δ^1 Aps (it has $(V-R)_C = 1.14$). For the most part the points about 0.05 redder than main line and those about 0.08 bluer are both from the B&C telescope, (o), while the rest are from the OC, (+). The separation occurs because the redness of δ^1 Aps means its standard transformation is not well known. The variation between B&C data is probably also due to the photomultiplier problems.

of this difference occurred during an unobserved interval of several months, so the exact date of the dramatic change can not be pin-pointed and therefore its cause can only be guessed at. The only known contender for this unfortunate change is the photomultiplier tube in the B&C. It began to behave undesirably and was replaced during the Mt John observations of these stars. Hence it was decided to use only OC colour data for these three stars.

Another complication arises due to the extreme redness of many of the observed stars. That all was not well again was noticed after comparison of observations from the two telescopes. A plot of $(V-R)_C$ against V for many stars revealed an interesting phenomenon wherein a series of points would be 0.04 magnitudes redder than the main bulk of points (and a few a lot bluer — see right-hand Figure 4.6). This was not seen in the check stars or any other colour and was initially most puzzling. However, the explanation is indeed an "instrumental" one. As few stars with $(V-R)_C > 0.7$ are non-variable, the transformation coefficients to the Cousins system are not well determined for these redder stars and hence this shows up in different values of reduced $(V-R)_C$ for different telescopes (with their different transformations). As check stars are bluer (generally)

the problem usually is not seen for them. The points a lot bluer are the B&C observations after the replacement of the photomultiplier tube, meaning a different set of transformation coefficients, yet again, even though on the same telescope! In explanation of the fact that this separation only seems to appear in $(V-R)_C$, the Mt John service observers note that the $(V-R)$ coefficients are the most difficult to determine with any accuracy. To minimize this problem for $(V-R)_C$ colours it has been decided to only consider OC values, for stars which have the misfortune to have $(V-R)_C \geq 0.97$ as it is these stars which have the obvious separation of observed colour between telescopes.

In Tables 4.5 to 4.7 the variances in V_J, $(B-V)_J$ and $(R-I)_C$ photometry (the latter derived from $(V-R)_C$ and $(V-I)_C$ reductions) are considered, as are their timescales and the relationship between the V_J magnitude changes and changes in colour. This relationship has been determined in terms of the Linear Correlation Co-efficient (Bevington & Robinson [21] §11.2),

$$r = \frac{N\sum x_i y_i - \sum x_i \sum y_i}{[N\sum x_i^2 - (\sum x_i)^2]^{\frac{1}{2}}[N\sum y_i^2 - (\sum y_i)^2]^{\frac{1}{2}}},$$

where x_i and y_i are the variables for which the correlation is sought. The LCC, r, has been calculated for the relationship between colour and V_J for all stars and the results are given in Tables 4.6 to 4.7. If $r = 0$ then there is no correlation between x and y, while $r = \pm 1$ would indicate complete correlation (positive or negative, depending on the slope of the line).

The $(V-R)_C$ and $(V-I)_C$ photometry is considered as $(R-I)_C$ only. The expense is losing a colour, but the advantage is it allows for consideration of a colour wholly independent of V_J. This is important because then the LCC is not subjected to false correlations due to the obvious relation between $(V-m)_C$ and V_J. In the case of constant stars with a smaller variance in m_C than V_J (this occurs frequently, as instrumental constraints often mean there is more light in the V_J filter and photon noise is proportional to the square root of this) this correlation leads to a very "significant[30]" LCC between V_J and $(V-m)_C$, which is entirely due to the random variations in V_J and should had a slope of one. $(R-I)_C$ versus V_J does not have this problem and hence even correlated variations of small magnitudes can be taken seriously. This effect is perfectly illustrated by the check stars in Table 4.6 and 4.7 where in the $(B-V)_J$ case the LCC is significant[31] for many check stars and for the variable ϵ Col (even though its check star has a bigger variance than it does!). When the independent colour $(R-I)_C$ is considered the situation changes dramatically with no check stars showing a significant trend. It is from this that it is concluded that for the most part the large LCC of $(V-m)_C$ and V_J in constant stars is due to random errors in V_J and $(V-m)_C$ not being independent, rather than some systematic observational problem such as errors in extinction coefficients or transformation constants. Hence, only if a star has a significant LCC($(V-m)_C$) value and is significantly varying, by the F-test, in both V_J and $(V-m)_C$[32] can it be concluded that there is a real correlation between colour and magnitude. However, if the star has a significant LCC($m_1 - m_2$) value where the colour is independent of V_J, then it can always be concluded that there is a real correlation between colour and magnitude.

When viewing Tables 4.5 to 4.8, it should be borne in mind that to a 1% significance level, saying a star is variable in colour or light is equivalent to saying that[33] $\sigma_{star} \geq 1.45 \times \sigma_{chk}$. A Linear

[30] But of small magnitude. What values of LCC are "significant" is discussed below.

[31] Although the slope of best fit is not ± 1, it is still thought that the effect is due to the correlation between V_J and $(V-m)_C$. This is because the error in the slope determinations is quite high. To see this, consider the check star of β Gru and δ^2 Gru. These two stars share the same comparison and check stars, but despite the check star having mostly the same data points the addition of a mere 8 to the latter changed its slope by 0.1.

[32] A star intrinsically varying in visual magnitude, but constant in colour may show a "false" correlation between V_J and $(V-m)_C$ as the latter will still reflect the random errors in V_J

[33] Using the F-test with the estimated error in colours and magnitude taken to be the observed variance in the check

Star	N	F_{MJ} $[N\text{–}1, N\text{–}1]$	$\mathcal{P}$ (days)	(LSP, σ_{N-1})
β Gru	68	70.22	57, 39	(2.0E-04,0.067),(3.3E-02,0.052)
check	68		250	(3.5E-02,0.008)
δ^1 Aps	82	124.16	48, 60, 526	(3.9E-07,0.078),(2.9E-03,0.056),(5.6E-02,0.048)
check	82		27	(3.9E-01,0.007)
δ^2 Gru	66	25.00	24, 526	(3.3E-06,0.040),(3.7E-01,0.027)
check	68		250	(3.5E-02,0.008)
ϵ Col	63	0.45	26	(2.1E-01,0.006)
check	63		54	(8.2E-01,0.009)
ϵ Mus	112	81.00	44, 32,1111, 29, 63, 49	(1.3E-05,0.063),(2.2E-07,0.053),(1.9E-03,0.042),(4.5E-03,0.038),(6.2E-05,0.034),(1.2E-02,0.029)
check	113		37	(1.9E-01,0.007)
η Scl	53	16.00	34, 182	(3.9E-03,0.036),(2.0E-01,0.029)
Star 5	53		357	(4.4E-01,0.009)
γ Cru	110	19.18	1111, 89	(3.1E-07,0.035),(1.0E-01,0.028)
check	101		1111, 103	(2.7E-06,0.008),(6.6E-01,0.006)
κ Pyx	52	2.79	88	(1.1E-01,0.010)
check	52		34	(8.7E-01,0.006)
L^2 Pup	84	837.52	141,1111, 244, 32	(5.6E-10,0.463),(1.9E-10,0.283),(1.0E-03,0.164),(4.6E-02,0.140)
check	83		417, 63	(7.6E-04,0.016),(5.0E-02,0.014)
o^1 CMa	68	31.70	175, 238, 64, 108, 89	(1.7E-07,0.045),(1.8E-04,0.028),(8.2E-04,0.022),(3.2E-03,0.018),(3.5E-02,0.015)
check	68		24	(4.6E-02,0.008)
ω Cap	42	1.39	1250, 132	(3.6E-04,0.013),(6.4E-02,0.008)
check	42		196	(2.9E-01,0.011)
π Pup	88	5.95	625, 109, 34, 18	(7.0E-04,0.022),(2.1E-04,0.019),(4.6E-03,0.016),(2.0E-01,0.014)
check	88		345	(2.2E-02,0.009)
τ^4 Eri	79	11.29	294, 88, 159	(9.5E-04,0.047),(4.4E-03,0.040),(2.4E-02,0.034)
check	80		118	(2.4E-02,0.014)

Table 4.5: **Period search and F-test values for Mt John's V_J.** This table shows the results of using **T6** to search for periods in Mt John V_J photometry. N is the number of data points and the F-test value is obtained by assuming the true error of the data is the $N-1$ standard deviation of the check (or in η Scl case "Star 5", as the check star is varying). The last timescale tabulated here does not have a significant Lomb-Scargle probability.

Star	N	LCC	slope	$F_{\rm MJ}$ $[N\text{–}1, N\text{–}1]$	$\mathcal{P}$ (days)	(LSP, σ_{N-1})
β Gru	60	-0.1498	-0.0275	2.92	182	(2.0E-01,0.013)
check	60	-0.4306	-0.3929		1111	(7.1E-01,0.008)
δ^1 Aps	82	-0.1403	-0.0325	5.06	250, 127, 313	(3.3E-06,0.018),(1.1E-03,0.014),(3.2E-02,0.012)
check	82	-0.2476	-0.2765		588	(1.4E-01,0.008)
δ^2 Gru	66	0.0419	0.0096	1.14	45	(3.3E-01,0.009)
check	68	-0.4876	-0.4999		435	(2.7E-01,0.008)
ϵ Col	63	-0.4833	-0.5824	0.32	263	(9.8E-01,0.008)
check	63	-0.0240	-0.0372		68	(5.8E-01,0.014)
ϵ Mus	112	-0.0068	-0.0017	2.69	625, 345	(6.9E-06,0.016),(7.5E-02,0.013)
check	113	-0.4695	-0.6824		286	(3.0E-02,0.009)
η Scl	53	-0.2865	-0.0885	1.00	714	(8.5E-02,0.011)
star 5	53	-0.2567	-0.3200		185	(2.1E-01,0.011)
γ Cru	93	0.2673	0.1294	4.00	1667, 323, 167, 125	(1.1E-03,0.016),(9.9E-03,0.014),(4.0E-03,0.012),(5.2E-02,0.011)
check	84	0.0383	0.0385		417, 32	(7.2E-03,0.008),(3.1E-01,0.007)
κ Pyx	52	-0.1085	-0.1392	1.46	400	(1.4E-02,0.013)
check	52	-0.4539	-0.7633		90	(9.8E-01,0.011)
L^2 Pup	84	0.7497	0.1758	29.48	145, 909, 400, 51	(2.8E-10,0.109),(1.1E-03,0.064),(3.0E-03,0.054),(3.3E-02,0.047)
check	83	-0.0154	-0.0191		23	(6.2E-01,0.020)
o^1 CMa	68	0.4066	0.1704	2.56	476, 204, 23	(2.3E-06,0.019),(3.4E-03,0.013),(5.5E-01,0.011)
check	68	-0.5949	-0.8921		52	(3.7E-02,0.012)
ω Cap	42	-0.3272	-0.2259	1.00	313	(2.2E-01,0.009)
check	42	-0.5448	-0.4551		667	(2.1E-01,0.009)
π Pup	70	0.0947	0.0889	1.39	370, 769	(3.0E-04,0.020),(7.8E-01,0.016)
check	70	-0.5943	-1.0872		400	(8.8E-02,0.017)
τ^4 Eri	79	0.3902	0.1393	1.12	1111, 200	(2.2E-04,0.017),(4.4E-02,0.014)
check	80	-0.1516	-0.1822		417, 189	(7.7E-04,0.016),(1.8E-01,0.014)

Table 4.6: **Period search, F-test values and correlation with $V_{\rm J}$ for Mt John's $(B-V)_{\rm J}$.** This table shows the results of using **T6** to search for periods in Mt John $(B-V)_{\rm J}$ photometry. N is the number of data points and the F-**test** value is obtained by assuming the true error of the data is the $N-1$ standard deviation of the check (or in η Scl case "Star 5", as the check star is varying). The slope is the slope of a line of best fit though the $(B-V)_{\rm J}$-$V_{\rm J}$ diagram, with equally weighted data points. A slope of the order of -1 may imply any correlation between $(B-V)_{\rm J}$ and $V_{\rm J}$ is due to the variation in $V_{\rm J}$. The last timescale tabulated here does not have a significant Lomb-Scargle probability.

Star	N	LCC	slope	F_{MJ} $[N\text{–}1, N\text{–}1]$	$\mathcal{P}$ (days)	(LSP, σ_{N-1})
β Gru	60	0.8216	0.4027	19.10	56, 112	(6.1E-04,0.034),(1.5E-01,0.027)
check	60	0.0861	0.0813		86	(6.6E-01,0.008)
δ^1 Aps	66	0.8604	0.3779	16.00	49, 500, 50, 93, 42	(6.5E-05,0.036),(5.1E-05,0.028),(2.2E-03,0.021),(7.9E-03,0.017),(4.1E-01,0.015)
check	66	0.0572	0.0749		50	(4.3E-01,0.009)
δ^2 Gru	58	0.7127	0.3704	11.70	120	(2.4E-02,0.021)
check	60	0.0861	0.0813		86	(6.6E-01,0.008)
ϵ Col	63	0.0259	0.0283	0.46	161	(5.3E-01,0.007)
check	63	-0.0883	-0.1033		45	(4.2E-01,0.010)
ϵ Mus	94	0.8127	0.4010	7.78	44	(2.3E-02,0.030)
check	95	-0.2799	-0.4527		38	(3.2E-01,0.011)
η Scl	42	0.9045	0.5098	9.00	1000	(1.9E-01,0.021)
Star 5	42	0.0848	0.0676		59	(8.8E-01,0.007)
γ Cru	93	0.4344	0.3721	12.25	370, 169, 227	(2.7E-07,0.028),(7.3E-04,0.021),(1.4E-02,0.018)
check	84	0.0048	0.0048		101	(4.6E-02,0.008)
κ Pyx	52	0.3565	0.5174	2.31	435	(1.9E-02,0.014)
check	52	0.2367	0.3594		44	(7.3E-01,0.010)
L^2 Pup	66	-0.0740	-0.0104	19.98	156, 625, 88, 233	(3.7E-04,0.065),(8.8E-03,0.051),(8.8E-03,0.044),(3.6E-02,0.037)
check	65	0.1642	0.1364		370	(1.1E-01,0.014)
o^1 CMa	68	0.8187	0.3278	2.56	179, 108	(1.9E-06,0.018),(2.1E-02,0.012)
check	68	0.2097	0.2992		49	(1.4E-01,0.011)
ω Cap	42	0.3698	0.2790	0.83	61	(8.5E-01,0.010)
check	42	0.1303	0.1315		48	(8.3E-01,0.011)
π Pup	70	0.1013	0.1380	3.28	370, 38	(8.8E-05,0.029),(2.8E-01,0.023)
check	70	0.0502	0.0849		385	(6.1E-02,0.016)
τ^4 Eri	63	0.7094	0.3853	2.69	1000	(1.9E-02,0.023)
check	64	0.0605	0.0582		42	(2.8E-01,0.014)

Table 4.7: **Period search, F-test values and correlation with V_J for Mt John's $(R-I)_C$.** This table shows the results of using **T6** to search for periods in Mt John $(R-I)_C$ photometry. N is the number of data points and the F-**test** value is obtained by assuming the true error of the data is the $N-1$ standard deviation of the check (or in η Scl case "Star 5", as the check star is varying). The slope is the slope of a line of best fit though the $(R-I)_C$-V_J diagram, with equally weighted data points. As $(R-I)_C$ is independent of V_J this is just added for completeness (compare Table 4.6). The last timescale tabulated here does not have a significant Lomb-Scargle probability.

Star	F_V [N–1, N–1]	N	$\mathcal{P}_V$ (days)	F_{B-V} [N–1, N–1]	N	$\mathcal{P}_{B-V}$ (days)	F_{R-I} [N–1, N–1]	N	$\mathcal{P}_{R-I}$ (days)
β Gru	70.22	68	57, 39	2.92	60	182	19.10	60	56, 112
check		68	250		60	1111		60	86
δ^1 Aps	124.16	82	48, 60, 526	5.06	82	250, 127, 313	16.00	66	49, 500, 50, 93, 42
check		82	27		82	588		66	50
δ^2 Gru	25.00	66	24, 526	1.14	66	45	11.70	58	120
check		68	250		68	435		60	86
ϵ Col	0.45	63	26	0.32	63	263	0.46	63	161
check		63	54		63	68		63	45
ϵ Mus	81.00	112	44, 32,1111, 29, 63, 49	2.69	112	625, 345	7.78	94	44
check		113	37		113	286		95	38
η Scl	16.00	53	34, 182	1.00	53	714	9.00	42	1000
Star 5		53	357		53	185		42	59
γ Cru	19.18	110	1111, 89	4.00	93	1667,323,167,125	12.25	93	370, 169, 227
check		101	1111, 103		84	417, 32		84	101
κ Pyx	2.79	52	88	1.46	52	400	2.31	52	435
check		52	34		52	90		52	44
L^2 pup	837.52	84	141,1111, 244, 32	29.48	84	145,909,400,51	19.98	66	156, 625, 88, 233
check		83	417, 63		83	23		65	370
o^1 CMa	31.70	68	175, 238, 64, 108, 89	2.56	68	476, 204, 23	2.56	68	179, 108
check		68	24		68	52		68	49
ω cap	1.39	42	1250, 132	1.00	42	313	0.83	42	61
check		42	196		42	667		42	48
π pup	5.95	88	625, 109, 34, 18	1.39	70	370, 769	3.28	70	370, 38
check		88	345		70	400		70	385
τ^4 Eri	11.29	79	294, 88, 159	1.12	79	1111, 200	2.69	63	1000
check		80	118		80	417, 189		64	42

Table 4.8: **Summary of Mt John's timescales and F-test values** . This table summarises the data given in Tables 4.5 to 4.7. The last timescale tabulated here does not have a significant Lomb-Scargle probability.

Correlation Coefficient of more than $(0.403, 0.361, 0.306)$ for $(40, 50, 70)$ points has only a 1% probability of arising from an uncorrelated population. This will be called a significant LCC. It should also be noted that: γ Cru's check star has had 9 data points removed, as for these data points its comparison and check stars were those of ϵ Mus; δ^2 Gru shares the same check star as β Gru, but for its $(B-V)_J$ colour both OC and B&C values will be considered. So what can be gleaned from all this, with respect to the 13 stars observed?

- β Gru has statistically significant variations present at the 1% level in all of V_J, $(B-V)_J$ and $(R-I)_C$. V_J and $(R-I)_C$ have dominant significant timescales of 57 days and perhaps not surprising, in light of this, there is a significant relationship between the magnitude of the star and its $(R-I)_C$ colour. In addition the LCC coefficient is positive, reflecting the relationship of reddest colour at minimum visual luminosity, which can clearly be seen in Figure 4.7.

- δ^1 Aps has statistically significant variations present at the 1% level in all of V_J, $(B-V)_J$ and $(R-I)_C$. V_J and $(R-I)_C$ have dominant significant timescales of 50 days and again there is a significant relationship between the magnitude of the star and its $(R-I)_C$ colour. In addition the LCC coefficient is positive, reflecting the relationship of reddest colour at minimum visual luminosity, which can clearly be seen in Figure 4.8.

- δ^2 Gru has statistically significant variations are present in V_J and $(R-I)_C$ only, although only the former has a significant timescale (25 days — not even the dominant timescale in colour!). According to the LCC there is, however, still a significant relationship between this colour and the magnitude (see Figure 4.7).

- ϵ Col has no statistically significant variations present. Nor does it have any significant timescales, nor does the LCC imply any relation between V_J and $(R-I)_C$.

- ϵ Mus has statistically significant variations present at the 1% level in all of V_J, $(B-V)_J$ and $(R-I)_C$. $(R-I)_C$ has no significant timescales while V_J has many, although the dominant timescale in both cases is 44 days. In addition, the LCC shows a significant relationship between these two magnitudes and as for all of the stars with such a relationship (and statistically significant variations), the LCC is positive. Inspection of Figure 4.8 indicates it is likely that this star also has its reddest colour at minimum visual luminosity.

- η Scl has statistically significant variations present in V_J and $(R-I)_C$, although only the former has a significant timescale (and this is not the same as $(R-I)_C$'s dominant timescale). Despite this, the LCC between V_J and $(R-I)_C$ is the largest of all the stars in this colour (see Figure 4.9).

- γ Cru has statistically significant variations present at the 1% level in all of V_J, $(B-V)_J$ and $(R-I)_C$. In addition, the LCC shows a significant relation between brightness in V_J and $(R-I)_C$, although the same timescales are not found by **T6** in these data sets (see Figure 4.9).

- κ Pyx has statistically significant variations present in V_J and $(R-I)_C$ only, although neither has a significant timescale (and even their dominant timescale is not the same). Despite this, the LCC between V_J and $(R-I)_C$ is significant (just, see Figure 4.10 – this correlation does not appear convincing by eye!).

---

stars means the degrees of freedom for the two variances are both equal to $N-1$, i.e. $F_{MJ}[N\text{-}1, N\text{-}1] = (\sigma_{star} \div \sigma_{chk})^2$. As both degrees of freedom vary with N, the exact value is highly N dependent and hence an appropriate table, such as Bevington & Robinson [21] C.7, should be consulted. See §4.2 for more details on using the F-test.

- L^2 Pup has statistically significant variations present at the 1% level in all of V_J, $(B-V)_J$ and $(R-I)_C$. The dominant and tertiary significant timescales for both V_J and $(B-V)_J$ are 143 days and ≈1000 days and the LCC shows a strong correlation between these two observables. The LCC coefficient is positive, reflecting the relationship of reddest colour at minimum visual luminosity, which can clearly be seen in Figure 4.10. Unusually, the LCC between V_J and $(R-I)_C$ is not significant.

- o^1 CMa has statistically significant variations present at the 1% level in all of V_J, $(B-V)_J$ and $(R-I)_C$. The dominant significant timescale of 177 days seen in V_J is also dominant significant in $(R-I)_C$ and the LCC implies a correlation between the two. The secondary timescale in $(B-V)_J$ is very similar to this, so perhaps not surprisingly the LCC also implies a correlation between $(B-V)_J$ and V_J. In both cases the LCC coefficient is positive, although only in the former is a relationship of reddest colour at minimum visual luminosity obvious (see Figure 4.11) because for $(B-V)_J$ the dominant variation is of double the V_J period.

- ω Cap has no statistically significant variations present, although its V_J magnitude does have a significant timescale of 1250 days. This can indicate the star is not varying in an random way and this could be due to either a intrinsic variation of small amplitude, or the errors in photometry being systematic. Which of these things is the case may be determined by considering the the variations of the check star. If the timescale is present in the check then the variation is probably be due to systematic errors. In this case the dominant timescale is only present in the variable which may indicate that it is intrinsic.

- π Pup has statistically significant variations present in V_J and $(R-I)_C$ only. However these data sets do not share any timescales.

- τ^4 Eri has statistically significant variations present in V_J and $(R-I)_C$. In addition, the LCC shows a strong correlation between brightness in V_J and $(R-I)_C$, although the same timescales are not found by **T6** in these data sets (see Figure 4.12).

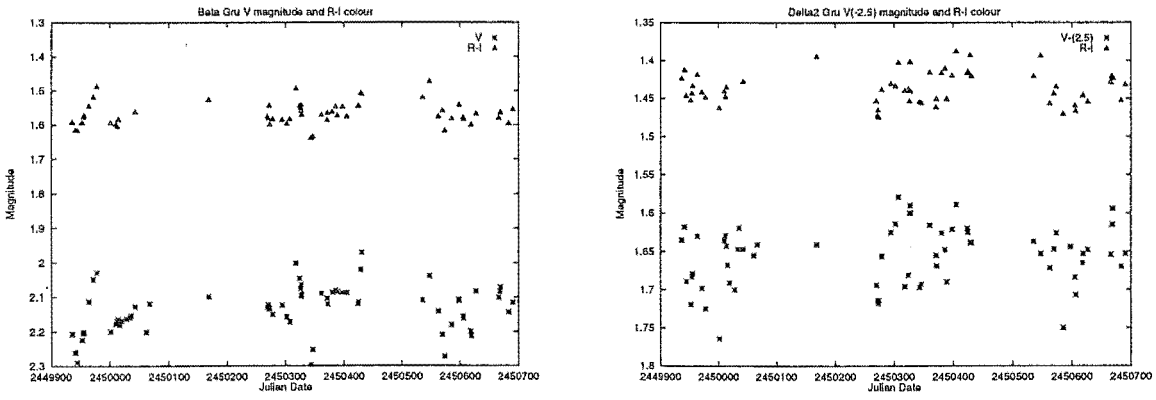

Figure 4.7: The left-hand figure is that of β Gru's V_J magnitude and $(R-I)_C$, illustrating the relation between brightness and colour. The right-hand figure is a similar diagram for δ^2 Gru.

4.4 Hipparcos and Tycho photometry

The Hipparcos catalogue [50] has proved to be essential for the analysis for this thesis. Not only have the trigonometric parallaxes been used to help find radii and masses for all the original 44 stars (see §4.5), but the visual photometry (obtained over 1989.85 to 1993.21) has enabled the comparison of radial-velocity and photometric timescales for stars that could not be observed photometrically at

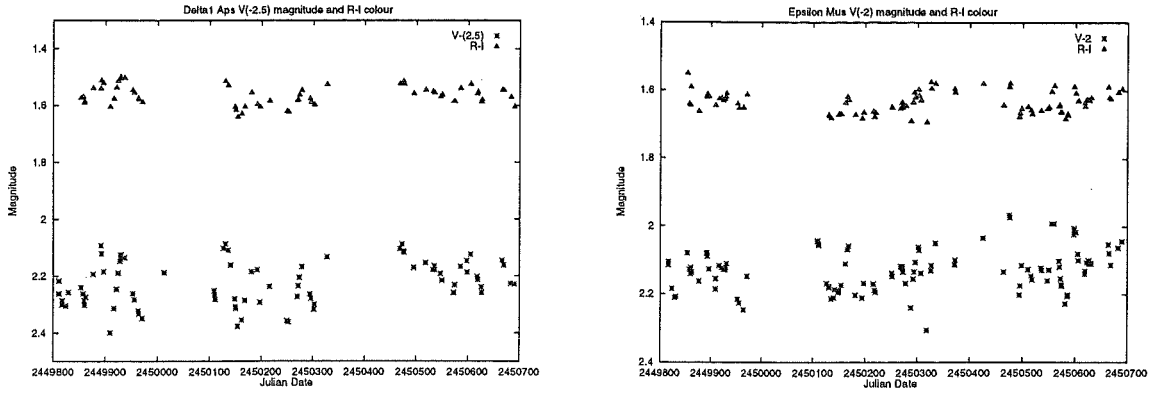

Figure 4.8: The left-hand figure is that of δ^1 Aps' V_J magnitude and $(R-I)_C$, illustrating the relation between brightness and colour. The right-hand figure is a similar diagram for ϵ Mus.

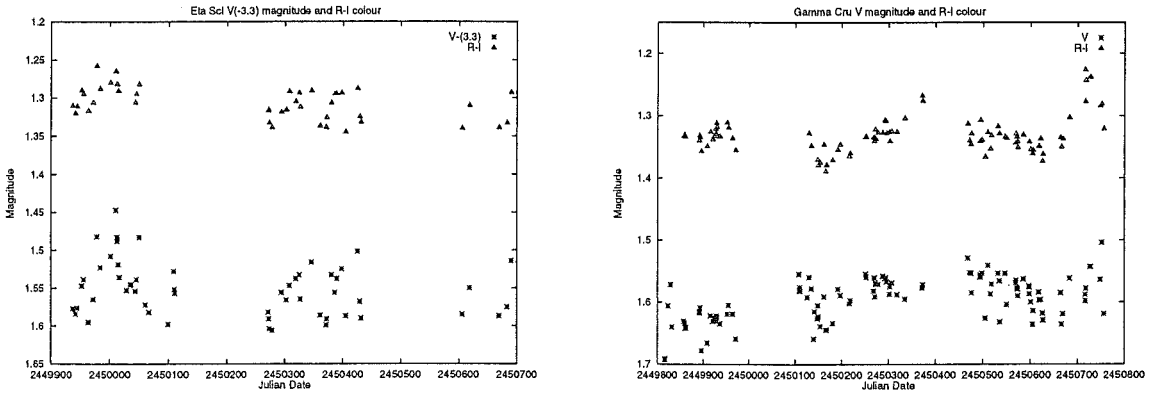

Figure 4.9: The left-hand figure is that of η Scl's V_J magnitude and $(R-I)_C$, illustrating the relation between brightness and colour. The right-hand figure is a similar diagram for γ Cru.

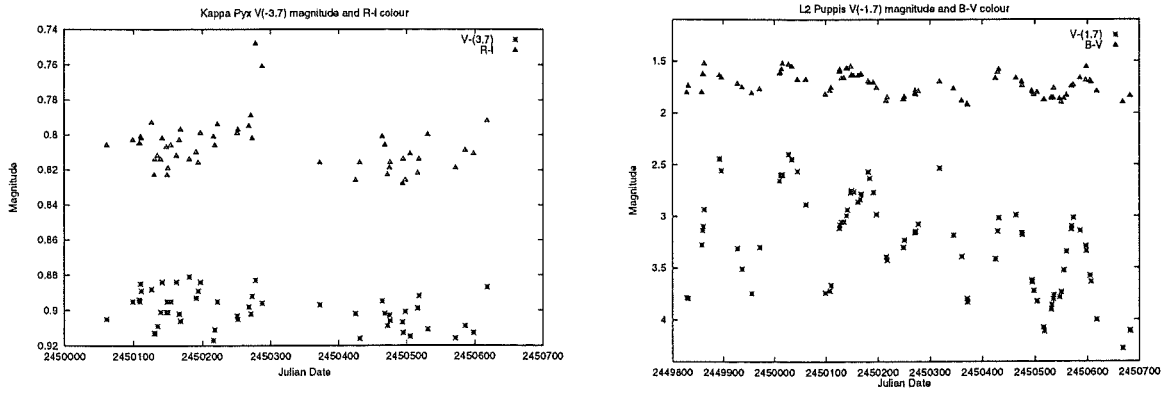

Figure 4.10: The left-hand figure is that of κ Pyx's V_J magnitude and $(R-I)_C$, illustrating the relation between brightness and colour. The right-hand figure is that of L^2 Pup's V_J magnitude and $(B-V)_J$, illustrating the relation between brightness and colour. This shows the largest variation in $(B-V)_J$.

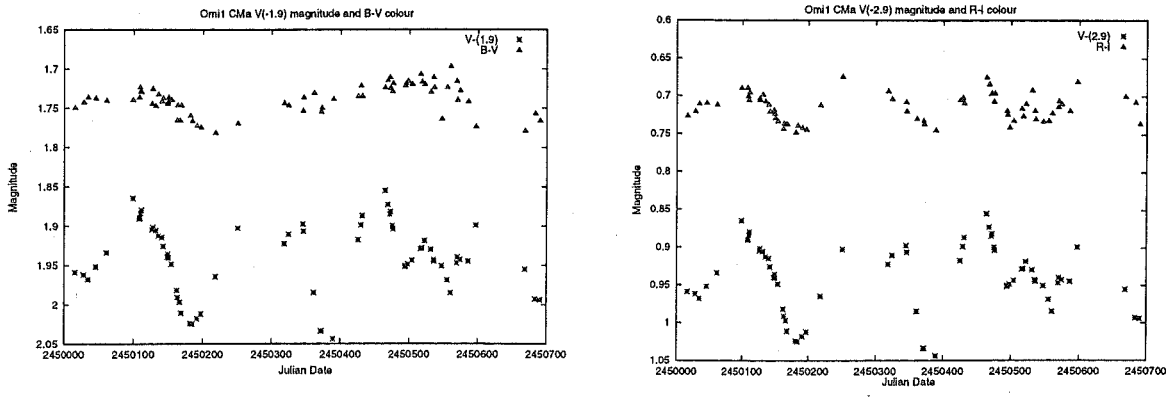

Figure 4.11: The left-hand figure is that of o^1 CMa's V_J magnitude and $(B-V)_J$, illustrating the relation between brightness and colour. The right-hand figure is a similar diagram for o^1 CMa with V_J and $(R-I)_C$. This is the only star to show significant correlation between V_J magnitude and both colours.

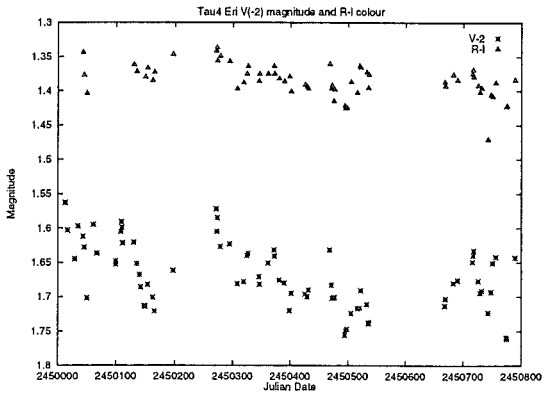

Figure 4.12: This figure is that of τ^4 Eri's V_J magnitude and $(R-I)_C$, illustrating the relation between brightness and colour.

Mt John. The results of using a Lomb-Scargle periodogram to find the timescales in the Hipparcos photometry are shown in Table 4.9. For a graphical display of the Hipparcos photometry for all 44 stars see Appendix E. The Tycho photometry has similarly been searched for timescales (see Table 4.10 and 4.11) and transformations[34] to Johnson colours used to merge together the three photometry data sets, so that this in turn could be considered for timescales (see Table 4.12 for all three visual magnitudes merged together and 4.13 for the Mt John and Tycho $(B-V)$ colours merged together). It is important to consider the Hipparcos, Tycho and Mt John photometry separately for several reasons. The most striking is that the Hipparcos photometry has by far the the best accuracy of all the data sets and hence its sole consideration could reveal low amplitude timescales that might otherwise be missed (the errors are $\sigma_{MJ(V)} \approx 0.01$, $\sigma_{T(V)} = 0.012$ and $\sigma_{H(V)} = 0.0015$ magnitudes respectively). The other reason for considering the data sets separately is that the Mt John photometry has been obtained in conjunction with radial velocities and for non-coherent periods the important thing is magnitudes and radial velocities taken over the same period of time. However, there are some reasons why considering the merged data as well as the individual data sets might be advantageous. With the addition of the Mt John data, the merged data will span a longer time so longer periods will be more apparent. Merging the Hipparcos and Tycho data together will mean more closely spaced observations and therefore a better chance of

[34]These are only applied when the data sets are merged together, as the transformations are not exact and it is felt better to look for timescales in the actual observables where possible

picking up shorter periods.

4.4.1 Transformations

In order to merge the three data sets together the Hipparcos and Tycho data has been transformed to the Johnson filter system. Transformations from the Hipparcos magnitude, H_P, to the Johnson visual magnitude, V_J, were achieved by simple linear interpolation using the Hipparcos catalogue's Table 1.3.5[35]. In this table $(H_P - V_J)$ is given as a function of $(V-I)_C$, where the $(V-I)_C$ used is that given in the main Hipparcos catalogue (field H40). It was felt best to retain this $(V-I)_C$ in all cases, rather than using the Mt John values for the 13 stars observed photometrically, for a number of reasons. One is that $(V-I)_C^{HIP}$ has already been used in the processing of the Hipparcos photometric data, so it was felt best to remain consistent with this. Another is that the Mt John data cover a smaller period of time and for a star variable in $(V-I)_C$ there is a risk that $(V-I)_C^{MJ}$ may not be an appropriate average for the period of time the Hipparcos photometry covers. Transformations for the Tycho system were more difficult; however, even though the Tycho filters are very similar to those of Johnson. How to transform $(B-V)_T$ to $(B-V)_J$ and V_T to V_J are described in §1.3 Appendix 4 of the Hipparcos printed volume 1. The problem, in both cases, is that for M stars the TiO band becomes important and the corrections differ dramatically depending on its presence (see Figure 4.13). This is especially true in the V_T case where the correction can no longer be found in terms of $(B-V)_T$. The incorrect use of an equation to determine the correction in the V_T case can easily lead to an error of up to 0.06 magnitudes and the range of spectral types where the two corrections agree is extremely small.

The only mitigating feature is one of the defining characteristics of a star being considered M0 or later is that TiO bands are present. For lack of anything better, this technique of considering the spectral type and assuming it is a good indication of the presence or not of TiO has been used[37] (where for consistency the designation of spectral type used is that given in the Hipparcos Main Catalogue). At all times "average" corrections have been used and this will introduce errors in stars very variable. This is necessary for all V transformations, as $(V-I)_C$ may be used and this colour was not observed — rather a single average value is tabulated in the main Hipparcos catalogue. For the $(B-V)$ corrections the "average" $(B-V)_T$ given in the Hipparcos catalogue has also been used for consistency. It should be noted, however, that as parasite[38] data points have been left in the Tycho data, but were not used to determine the average given in the catalogue, the average used to determine the correction may not correspond exactly with the average of the Tycho data points used in the following analysis.

[35] A more accurate transformation of Hipparcos H_P into Johnson V is described by Harmanec [71]

[36] In fact the stars would have to have
$(B-V)_T = 0.7864 \pm 0.0407\sqrt{-10073 + 7062(V-I)_C - 2431(V-I)_C^2 + 825(V-I)_C^3}$
for the two different transformation equations to agree. None of the 42 (only 42 of the 44 stars surveyed for this thesis were observed by the Tycho experiment) stars that have been observed have this, not even those considered to be K5/M0 in spectral type!

[37] This is not an ideal situation. One alternative is to find the mean corrected V_T and $(B-V)_T$ using the different equations and compare them to the mean corrected Hipparcos H_P and (when available) the mean Johnson colour and magnitude from the Mt John data. One difficulty with this is stars variable in colour and magnitude may well not yield the same average when different data sets are compared anyway! While they should have the same average for Hipparcos and Tycho data sets, as they are taken at similar times, if these two disagree it would be hard to pinpoint exactly which transformation is at fault — the Hipparcos transformation could be incorrect in which case comparing it to the two different V_T averages will not be of a great deal of use.

[38] A transit are flagged as disturbed by a parasite if a fairly bright star was close in transit time to that of the star considered. For further details on this and rejection criteria for transits see the Hipparcos printed volume 1 §2.2.

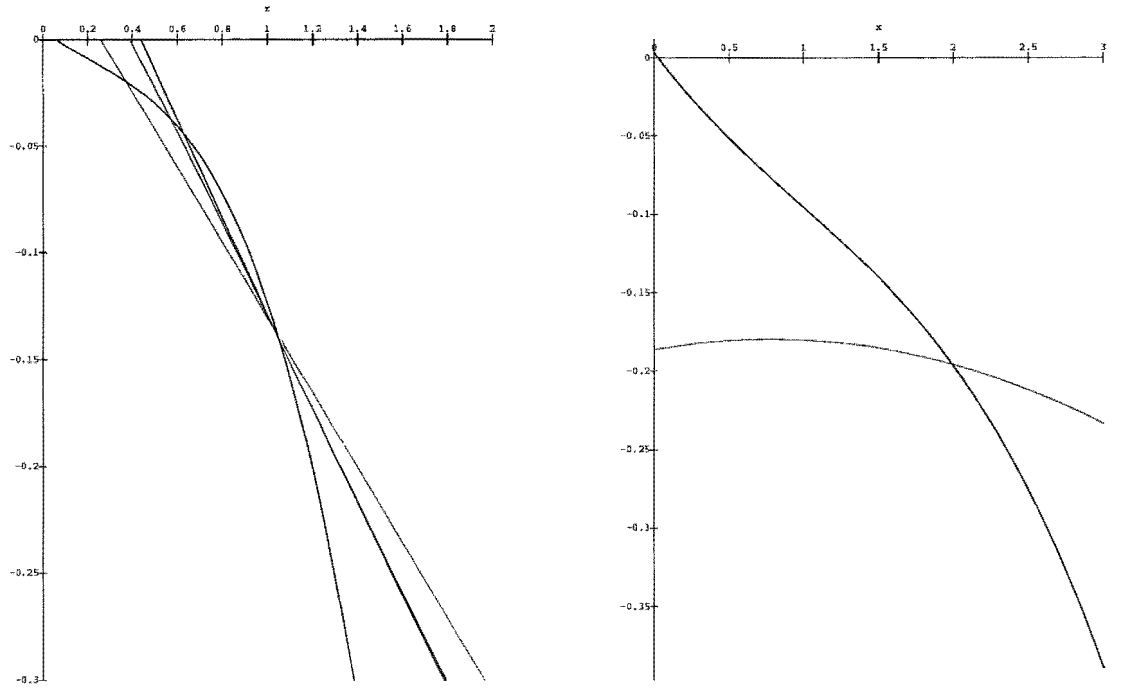

Figure 4.13: In the left-hand figure corrections for $(B-V)_T$ are given for different giants and supergiants (the x-axis is $(B-V)_T$ and the y-axis is the correction, i.e. $(B-V)_J-(B-V)_T$).
Black is appropriate for giants with $(B-V)_T < 0.65$,
yellow for giants with $0.65 < (B-V)_T < 1.10$,
green for giants with $1.10 < (B-V)_T < 1.7$,
red for bright/supergiants with $1.0 < (B-V)_T < 2.2$ and
blue is appropriate for all M giants affected by TiO bands.
In all but the last case the corrections are very similar in the adjoining $(B-V)_T$ ranges. But the difference between the correction obtained from considering the redder giants and supergiants (green and red) and M giants (blue) is $0.01 \rightarrow 0.04$, so it is essential that the presence or absence of TiO bands is known to make a successful correction.

Similarly in the right-hand figure corrections for V_T for giant stars of spectral type G–K are shown in **black**, where the x-axis is $(B-V)_T$. For M giants the absorption by TiO means the correction becomes unrelated to $(B-V)_T$ so the correction is obtained using $(V-I)_C$, which is the x-axis for the **red** plot. The range of spectral types where these two corrections agree is small[36] and the difference between the two corrections can easily be $0.03 \rightarrow 0.06$, so it is essential to know which of the two corrections is the correct one to apply, even for stars whose spectral type indicates that the TiO bands are only just developing.

4.4.2 Comparison of photometric timescales

As the Hipparcos, Tycho and Mt John photometry data are independent, if the same periods appear in at least two data sets they are almost certainly real with the following proviso concerning the use of the period finding program **T6**. The problem arises if a period to be removed by prewhitening is not, in fact, sinusoidal. As discussed in §4.1.3, in such a case the period will not be removed properly and may interfere with the obtainment of other periodicities. Hence the same problem will occur in all data sets when **T6** is applied to remove a non-sinusoidal period and modified, but similar, periods may be found in the residuals of all data sets. In this way the presence of a period in more than one data set does <u>not</u> guarantee that the period is in fact "real".

Star	N	$\mathcal{P}$ (days)	(LSP, σ_{N-1})
3 Cet	137	156, 24, 20	(9.9E-06,0.008),(2.2E-03,0.007),(9.4E-02,0.007)
η Scl	76	48, 32, 109, 41, 333, 44	(8.9E-07,0.036),(2.1E-04,0.026),(8.9E-03,0.021),(9.4E-04,0.018),(4.9E-03,0.015),(2.3E-02,0.013)
γ Phe	156	97, 98, 83, 19, 37, 19	(3.6E-25,0.034),(3.7E-14,0.018),(1.2E-06,0.013),(5.4E-06,0.012),(9.1E-03,0.010),(1.3E-02,0.009)
ψ Phe	118	23, 22, 39, 25, 35, 30, 20, 139	(3.2E-10,0.040),(2.7E-05,0.030),(1.9E-05,0.025),(9.9E-06,0.021),(7.2E-05,0.019),(1.9E-04,0.016),(3.2E-04,0.014),(1.2E-02,0.013)
τ^4 Eri	111	256, 27, 38	(3.1E-08,0.020),(2.0E-03,0.015),(8.1E-02,0.014)
γ Hyi	112	500, 22, 35, 435	(1.7E-07,0.017),(8.9E-05,0.013),(6.2E-04,0.012),(1.4E-02,0.010)
γ Ret	88	833, 270, 51, 68, 87	(3.2E-06,0.052),(3.3E-03,0.041),(8.0E-04,0.035),(2.1E-04,0.030),(5.0E-02,0.025)
η^2 Pic	97	26	(1.3E-02,0.008)
ϵ Col	134	192	(7.6E-02,0.005)
β Col	116	43	(6.1E-01,0.004)
η^2 Dor	94	88, 29, 32	(7.6E-07,0.023),(4.7E-05,0.018),(1.4E-02,0.015)
o^1 CMa	235	1250, 81, 39, 27, 37, 14, 217, 17, 46, 11, 63, 23, 24, 54, 18	(8.2E-30,0.071),(3.2E-15,0.045),(2.2E-15,0.037),(5.1E-14,0.031),(1.4E-11,0.025),(9.8E-10,0.022),(7.5E-10,0.019),(5.2E-07,0.017),(5.7E-06,0.015),(2.3E-04,0.014),(1.2E-05,0.013),(1.0E-07,0.012),(4.9E-06,0.011),(7.8E-03,0.010),(1.2E-02,0.010)
σ CMa	138	1250, 169, 500, 909, 35, 43, 137, 99, 19, 133	(2.5E-13,0.030),(4.8E-10,0.021),(3.6E-09,0.016),(8.4E-06,0.013),(1.4E-04,0.011),(2.2E-04,0.010),(2.5E-03,0.009),(2.3E-03,0.009),(7.9E-03,0.008),(9.1E-02,0.007)
L^2 Pup	106	139, 24, 46,1111, 25, 99, 74, 167, 42	(1.3E-15,0.257),(7.2E-07,0.132),(3.1E-05,0.104),(4.8E-04,0.088),(8.2E-04,0.077),(1.7E-03,0.068),(1.1E-03,0.061),(2.3E-03,0.054),(1.6E-02,0.048)
π Pup	111	1429, 111, 27, 63, 24, 21, 72	(1.0E-07,0.018),(5.8E-05,0.014),(1.1E-03,0.012),(5.5E-05,0.011),(8.5E-05,0.009),(1.3E-03,0.008),(3.2E-02,0.007)
HR 3017	93	74, 32, 38	(3.8E-04,0.009),(2.3E-05,0.008),(1.4E-02,0.006)
NS Pup	135	1429, 80, 53	(1.7E-14,0.011),(3.2E-08,0.007),(1.5E-02,0.006)
ϵ Car	79	435, 41, 31, 38, 27, 47, 60	(1.1E-04,0.022),(3.3E-03,0.018),(1.2E-03,0.016),(7.6E-04,0.013),(5.8E-04,0.011),(1.5E-04,0.009),(5.1E-02,0.007)
β Vol	111	23	(1.2E-01,0.006)
λ Vel	112	909, 204, 23, 58, 233, 30	(3.6E-16,0.024),(6.2E-05,0.013),(2.5E-06,0.011),(9.6E-05,0.009),(1.6E-03,0.008),(1.1E-02,0.007)
κ Pyx	189	19, 50, 81, 12	(1.1E-09,0.009),(1.1E-04,0.008),(1.0E-04,0.007),(1.1E-02,0.007)
N Vel	116	82, 28, 526, 37, 22	(2.0E-05,0.008),(1.2E-05,0.007),(3.2E-04,0.006),(9.3E-04,0.005),(4.2E-01,0.005)
V337 Car	111	40, 22, 72, 35	(1.4E-04,0.008),(1.1E-04,0.007),(1.2E-03,0.006),(6.3E-02,0.005)
GZ Vel	141	19, 400, 23, 42, 25, 17	(4.1E-07,0.010),(8.3E-04,0.009),(4.1E-04,0.008),(2.8E-03,0.007),(9.9E-04,0.007),(7.1E-02,0.006)
γ Cha	105	32, 23	(9.2E-04,0.009),(5.6E-02,0.008)
HR 4177	109	58	(1.1E-02,0.015)
ϵ Mus	133	20, 64, 105, 19, 32, 54, 92, 43, 33, 30	(5.1E-09,0.058),(2.4E-09,0.046),(2.5E-06,0.037),(3.9E-03,0.031),(9.8E-04,0.029),(3.1E-04,0.026),(2.8E-03,0.024),(6.1E-03,0.022),(5.1E-03,0.020),(1.8E-02,0.018)
ϵ Cru	145	36	(1.2E-01,0.007)
γ Cru	150	22, 18, 15, 17, 16, 98, 49	(2.7E-12,0.026),(1.4E-09,0.020),(1.1E-07,0.016),(9.0E-03,0.013),(8.3E-04,0.012),(9.2E-03,0.011),(1.8E-02,0.011)
2 Cen	91	83, 74, 500, 52, 169, 39	(3.0E-07,0.047),(3.1E-06,0.036),(1.5E-04,0.029),(2.0E-04,0.024),(1.3E-05,0.020),(2.5E-01,0.017)
σ Lib	38	86, 54, 106	(4.9E-05,0.048),(1.3E-04,0.030),(1.9E-02,0.017)
ϵ TrA	229	14	(2.0E-02,0.005)
δ^1 Aps	131	48, 19, 278, 64, 75, 23, 37, 18, 49, 35, 29	(1.4E-08,0.067),(1.7E-06,0.055),(6.2E-06,0.046),(2.4E-07,0.039),(6.9E-07,0.033),(3.8E-06,0.027),(9.3E-06,0.023),(4.4E-03,0.020),(3.8E-03,0.019),(2.5E-03,0.017),(2.2E-02,0.015)
α Sco	71	1111, 33, 217, 39, 30	(1.4E-10,0.044),(1.2E-04,0.027),(5.0E-08,0.021),(4.8E-04,0.013),(4.2E-02,0.010)
HR 6166	57	45, 56	(4.8E-05,0.010),(1.4E-02,0.007)
α TrA	129	23, 15	(4.0E-05,0.006),(3.5E-01,0.005)
ϵ Sco	47	123	(3.3E-01,0.005)
β Ara	84	1250, 50	(6.8E-04,0.008),(7.2E-02,0.007)
η Sgr	55	139	(2.7E-01,0.012)
62 Sgr	82	625, 31, 47, 36, 27	(9.9E-08,0.044),(1.2E-07,0.032),(7.2E-08,0.022),(4.7E-05,0.016),(4.2E-02,0.012)
ω Cap	99	37, 143, 99, 143	(7.7E-10,0.008),(2.3E-06,0.005),(1.7E-04,0.004),(8.9E-01,0.004)
24 Cap	54	43	(1.7E-02,0.016)
δ^2 Gru	89	50, 32, 30	(3.3E-09,0.030),(2.5E-04,0.020),(1.4E-02,0.017)
β Gru	73	63, 50, 55, 72, 35, 74, 42	(1.5E-05,0.068),(8.8E-08,0.052),(3.8E-05,0.034),(2.4E-04,0.027),(1.1E-04,0.022),(7.3E-04,0.017),(2.3E-02,0.014)

Table 4.9: **Period search of Hipparcos' H_P.** This tables shows the result of running **T6** over default range on Hipparcos H_P photometry, where N is the number of data points. The last timescale tabulated here does not have a significant Lomb-Scargle probability.

Star	N	$\mathcal{P}$ (days)	(LSP, σ_{N-1})
3 Cet	151	30	(4.0E-02,0.031)
η Scl	90	48, 26, 27	(4.9E-05,0.046),(4.3E-03,0.038),(1.5E-01,0.034)
γ Phe	244	97, 100, 42, 10	(3.5E-30,0.044),(2.6E-10,0.030),(8.2E-03,0.027),(2.2E-01,0.025)
ψ Phe	143	23, 22, 18, 21, 123	(8.5E-13,0.050),(3.4E-05,0.037),(1.5E-03,0.033),(7.9E-03,0.030),(3.4E-02,0.028)
τ^4 Eri	131	244, 25	(6.7E-06,0.031),(9.6E-02,0.027)
γ Ret	120	833, 85, 270, 27, 21, 64	(1.6E-09,0.066),(4.3E-04,0.050),(2.2E-04,0.044),(1.7E-03,0.039),(6.6E-03,0.035),(8.6E-02,0.032)
η^2 Dor	116	89, 28	(6.8E-06,0.039),(2.0E-01,0.032)
o^1 CMa	260	1429, 37, 323, 39, 44, 172, 10, 217, 91, 11	(6.5E-33,0.083),(5.9E-16,0.052),(1.0E-12,0.044),(6.9E-10,0.038),(1.2E-09,0.034),(3.6E-05,0.031),(2.8E-04,0.029),(6.2E-03,0.027),(1.5E-03,0.026),(1.7E-02,0.025)
σ CMa	182	13, 14, 278	(1.7E-12,0.040),(2.6E-03,0.032),(3.8E-02,0.030)
L^2 Pup	126	139, 24, 22,1111, 123, 26, 75, 34, 27, 25	(1.6E-18,0.314),(1.4E-08,0.161),(7.5E-06,0.128),(5.8E-05,0.112),(1.2E-05,0.098),(1.6E-06,0.084),(1.7E-03,0.071),(3.8E-04,0.064),(7.0E-03,0.057),(3.1E-02,0.052)
π Pup	133	20, 256, 56, 88	(2.2E-07,0.030),(4.0E-05,0.025),(1.7E-03,0.022),(4.7E-01,0.020)
HR 3017	127	32, 179	(9.8E-03,0.030),(4.4E-01,0.028)
NS Pup	154	16, 33	(2.6E-04,0.031),(8.1E-01,0.028)
β Vol	123	28	(6.9E-01,0.019)
λ Vel	120	1000, 244	(3.6E-08,0.032),(5.5E-02,0.025)
N Vel	138	1000	(8.1E-02,0.023)
V337 Car	146	26	(3.6E-01,0.028)
GZ Vel	143	23	(1.5E-01,0.030)
γ Cha	113	25	(1.1E-01,0.027)
ϵ Cru	166	13	(5.5E-01,0.017)
γ Cru	201	22, 24	(1.7E-08,0.046),(1.0E-02,0.040)
2 Cen	96	83, 74, 526, 52, 24	(1.7E-07,0.062),(7.7E-06,0.048),(1.6E-04,0.040),(4.4E-04,0.034),(2.2E-02,0.029)
σ Lib	48	54, 263	(9.0E-06,0.053),(3.7E-02,0.031)
δ^1 Aps	169	48, 15, 23, 60, 77	(2.4E-09,0.084),(2.5E-12,0.071),(3.9E-06,0.056),(8.5E-06,0.050),(7.1E-02,0.044)
α Sco	82	1111, 95, 39	(1.1E-03,0.070),(1.6E-03,0.060),(1.8E-01,0.051)
η Sgr	76	227	(5.6E-01,0.028)
62 Sgr	87	31, 625, 47	(4.3E-06,0.049),(2.8E-04,0.039),(3.5E-02,0.034)
δ^2 Gru	104	51, 156, 30	(2.3E-08,0.039),(6.7E-04,0.030),(1.3E-02,0.026)
β Gru	111	63, 21, 93, 55, 112, 49, 51, 39	(4.1E-11,0.087),(4.0E-10,0.059),(5.8E-06,0.042),(6.6E-06,0.035),(1.3E-04,0.029),(3.5E-03,0.025),(2.5E-03,0.023),(6.6E-01,0.020)

Table 4.10: **Period search of Tycho's V_T.** This table shows the result of running **T6** over default range on Tycho V_T photometry, where only points with both B_T and V_T photometry present have been used and N is the number of data points. The last timescale tabulated here does not have a significant Lomb-Scargle probability.

THE LIBRARY
UNIVERSITY OF CANTERBURY
CHRISTCHURCH, N.Z.

Star	N	$\mathcal{P}$ (days)	(LSP, σ_{N-1})
3 Cet	151	45	(1.0E+00,0.063)
η Scl	90	29	(3.1E-01,0.055)
γ Phe	244	102	(9.5E-02,0.037)
ψ Phe	143	29	(1.0E-01,0.050)
τ^4 Eri	131	29	(5.8E-01,0.038)
γ Ret	120	909	(1.1E-01,0.054)
η^2 Dor	116	29	(2.6E-02,0.064)
o^1 CMa	260	1429, 28	(8.6E-08,0.048),(8.5E-01,0.044)
σ CMa	182	1111, 105	(1.2E-08,0.061),(8.9E-01,0.052)
L^2 Pup	126	38, 208, 55, 133	(4.0E-05,0.085),(4.0E-03,0.075),(2.2E-04,0.068),(4.4E-02,0.060)
π Pup	133	28	(3.8E-02,0.034)
HR 3017	127	37	(3.3E-01,0.051)
NS Pup	154	37	(4.9E-01,0.058)
β Vol	123	24	(1.0E+00,0.027)
λ Vel	120	1111, 333	(4.5E-09,0.042),(6.8E-02,0.032)
N Vel	138	17	(2.9E-01,0.032)
V337 Car	146	14	(6.8E-02,0.038)
GZ Vel	143	32	(9.9E-01,0.050)
γ Cha	113	53	(4.7E-01,0.045)
ϵ Cru	166	24	(8.7E-01,0.030)
γ Cru	201	20	(1.0E+00,0.043)
2 Cen	96	52	(6.0E-02,0.044)
σ Lib	48	89	(2.3E-01,0.040)
δ^1 Aps	171	42	(1.1E-01,0.061)
α Sco	82	526	(9.3E-01,0.098)
η Sgr	76	56	(1.0E+00,0.034)
62 Sgr	87	233	(1.4E-01,0.047)
δ^2 Gru	104	27	(5.1E-01,0.044)
β Gru	111	63, 55	(3.6E-04,0.036),(2.5E-02,0.032)

Table 4.11: **Period search of Tycho's $(B-V)_T$.** This table shows the result of running **T6** over default range on Tycho $(B-V)_T$ photometry, where only points with both B_T and V_T photometry present have been used and N is the number of data points. The last timescale tabulated here does not have a significant Lomb-Scargle probability.

Star	N	$\mathcal{P}$ (days)	(LSP, σ_{N-1})
3 Cet	286	149	(3.4E−01, 0.033)
η Scl	219	48, 56, 39, 34, 625, 28	(1.6E−12, 0.041), (2.9E−05, 0.034), (2.1E−04, 0.032), (4.0E−03, 0.030), (2.3E−03, 0.028), (1.9E−02, 0.027)
γ Phe	400	97, 98, 18, 6, 14	(2.1E−54, 0.040), (2.1E−20, 0.026), (7.8E−07, 0.023), (3.1E−05, 0.022), (1.3E−02, 0.021)
ψ Phe	261	23, 22, 18, 21, 11, 17, 122, 10	(8.5E−24, 0.046), (6.6E−11, 0.034), (2.1E−09, 0.030), (8.4E−08, 0.027), (1.4E−07, 0.025), (1.4E−05, 0.022), (7.7E−03, 0.021), (1.1E−01, 0.020)
τ^4 Eri	321	244, 2500, 23, 85, 30	(7.9E−10, 0.036), (1.2E−09, 0.033), (2.4E−07, 0.030), (3.9E−04, 0.028), (1.3E−02, 0.027)
γ Hyi	112	500, 22, 35, 435	(1.5E−07, 0.017), (8.0E−05, 0.013), (6.6E−04, 0.012), (1.5E−02, 0.010)
γ Ret	208	833, 12, 20, 53, 23, 24, 16, 12, 14	(1.4E−16, 0.060), (7.9E−09, 0.047), (1.1E−07, 0.041), (2.7E−08, 0.037), (1.4E−04, 0.033), (1.3E−03, 0.031), (2.2E−03, 0.029), (9.9E−04, 0.027), (1.6E−02, 0.025)
η^2 Pic	97	26	(1.2E−02, 0.008)
ϵ Col	197	3333, 1250, 32	(1.9E−15, 0.007), (7.6E−06, 0.006), (7.7E−01, 0.006)
β Col	116	31	(5.8E−01, 0.004)
η^2 Dor	206	89, 11, 147	(7.4E−12, 0.033), (3.9E−06, 0.027), (7.1E−02, 0.025)
o^1 CMa	563	1250, 37, 92, 27, 38, 196, 46, 10	(1.2E−58, 0.080), (2.0E−20, 0.056), (2.8E−17, 0.051), (1.1E−13, 0.047), (4.7E−08, 0.044), (1.2E−04, 0.042), (1.9E−07, 0.041), (2.7E−02, 0.039)
σ CMa	320	14, 13, 11, 6, 94	(3.5E−21, 0.038), (2.2E−09, 0.031), (4.6E−05, 0.028), (4.5E−03, 0.027), (2.7E−02, 0.026)
L^2 Pup	317	139, 5000, 909,1250, 24, 22,3333, 294, 34, 65, 42, 74	(1.9E−28, 0.403), (2.7E−31, 0.301), (7.0E−13, 0.220), (2.4E−23, 0.195), (4.2E−10, 0.155), (3.8E−06, 0.141), (6.2E−04, 0.133), (1.1E−04, 0.128), (4.1E−04, 0.121), (5.1E−03, 0.116), (1.8E−03, 0.112), (1.2E−02, 0.108)
π Pup	332	5000, 164, 112, 57, 455, 71, 27	(1.9E−37, 0.032), (4.6E−09, 0.021), (3.5E−07, 0.020), (7.7E−05, 0.018), (2.1E−04, 0.018), (3.4E−03, 0.017), (1.2E−02, 0.016)
HR 3017	220	32, 14, 24	(9.4E−05, 0.024), (3.1E−03, 0.022), (8.9E−02, 0.021)
NS Pup	289	11, 20	(3.0E−07, 0.026), (6.7E−02, 0.024)
ϵ Car	79	435, 41, 31, 38, 27, 47, 60	(1.1E−04, 0.022), (3.3E−03, 0.018), (1.1E−03, 0.016), (7.8E−04, 0.013), (5.5E−04, 0.011), (1.8E−04, 0.009), (5.7E−02, 0.007)
β Vol	234	28	(8.6E−01, 0.015)
λ Vel	232	1000, 238, 23, 204	(1.2E−22, 0.029), (4.8E−04, 0.021), (3.1E−03, 0.020), (3.8E−01, 0.019)
κ Pyx	241	3333, 83, 46, 37, 909	(2.5E−13, 0.012), (1.4E−08, 0.010), (5.7E−06, 0.009), (1.1E−04, 0.008), (1.3E−02, 0.008)
N Vel	254	12, 11	(7.2E−04, 0.018), (4.3E−02, 0.017)
V337 Car	257	26	(9.6E−02, 0.023)
GZ Vel	284	26	(5.2E−02, 0.026)
γ Cha	218	61	(1.8E−02, 0.021)
HR 4177	109	58	(1.2E−02, 0.015)
ϵ Mus	245	63, 45, 32, 2500, 41, 27, 30, 39, 112, 36, 75, 34, 25, 45, 26, 143, 51, 333	(1.3E−08, 0.061), (2.0E−06, 0.055), (1.4E−07, 0.051), (1.2E−09, 0.046), (1.2E−04, 0.041), (1.2E−03, 0.038), (1.5E−04, 0.036), (8.1E−06, 0.034), (1.7E−04, 0.032), (1.5E−03, 0.030), (1.6E−03, 0.028), (3.0E−03, 0.027), (5.9E−03, 0.025), (4.6E−03, 0.024), (6.5E−03, 0.023), (7.5E−03, 0.022), (7.6E−03, 0.021), (2.1E−02, 0.020)
ϵ Cru	311	9	(1.7E−01, 0.013)
γ Cru	461	22, 1429, 18, 16, 15	(8.2E−17, 0.041), (3.6E−08, 0.037), (1.9E−04, 0.035), (8.8E−03, 0.034), (1.4E−01, 0.033)
2 Cen	187	83, 74, 526, 14, 47, 27, 39	(2.6E−15, 0.055), (2.4E−12, 0.043), (2.1E−08, 0.035), (9.6E−08, 0.030), (3.8E−04, 0.027), (2.7E−03, 0.025), (2.8E−01, 0.023)
σ Lib	86	54, 250, 28, 32	(6.1E−11, 0.051), (1.9E−04, 0.030), (1.1E−03, 0.024), (1.0E + 00, 0.020)
ϵ TrA	229	14	(1.5E−02, 0.005)
δ^1 Aps	384	48, 15, 27, 66, 61, 17, 133, 16, 476, 156, 15, 15, 36, 769	(3.7E−26, 0.079), (1.0E−18, 0.065), (7.9E−11, 0.056), (3.7E−10, 0.052), (9.9E−09, 0.048), (9.1E−07, 0.045), (8.1E−05, 0.042), (1.0E−03, 0.041), (6.0E−05, 0.039), (1.1E−03, 0.037), (4.6E−04, 0.036), (2.7E−03, 0.035), (2.2E−03, 0.034), (1.9E−01, 0.033)
α Sco	153	1000, 95, 12, 17	(8.1E−10, 0.059), (4.5E−06, 0.049), (3.5E−04, 0.043), (2.8E−01, 0.039)
HR 6166	57	45, 56	(5.2E−05, 0.010), (2.2E−02, 0.007)
α TrA	129	23, 22	(3.5E−05, 0.006), (3.1E−01, 0.005)
ϵ Sco	47	123	(3.1E−01, 0.005)
β Ara	84	1250, 50	(8.2E−04, 0.009), (6.8E−02, 0.007)
η Sgr	131	17, 21	(8.3E−03, 0.024), (2.7E−01, 0.023)
62 Sgr	169	31, 15, 36, 556	(6.2E−12, 0.050), (1.6E−10, 0.040), (9.1E−07, 0.033), (6.5E−02, 0.029)
ω Cap	141	833, 98, 185, 65	(3.0E−10, 0.010), (2.5E−05, 0.007), (2.4E−03, 0.006), (9.9E−02, 0.006)
24 Cap	55	43	(2.8E−02, 0.018)
δ^2 Gru	259	24, 2500, 49, 80, 125, 303, 26	(5.3E−13, 0.039), (9.5E−16, 0.034), (2.0E−07, 0.028), (9.4E−06, 0.025), (3.1E−03, 0.024), (1.4E−03, 0.022), (4.7E−01, 0.021)
β Gru	252	63, 55, 50, 34, 3333, 83, 61, 141, 47	(5.3E−14, 0.079), (6.5E−12, 0.067), (2.8E−08, 0.058), (1.6E−07, 0.052), (8.9E−07, 0.047), (6.5E−04, 0.043), (1.2E−03, 0.041), (8.3E−03, 0.039), (2.3E−02, 0.037)

Table 4.12: **Period search of merged visual photometry**. This table shows the results of running **T6** on the visual photometry from Hipparcos, Tycho and Mt John merged, where N is the number of data points. The last timescale tabulated here does not have a significant Lomb-Scargle probability.

Star	N	$\mathcal{P}$ (days)	(LSP, σ_{N-1})
η Scl	143	66	(8.3E–01, 0.044)
τ^4 Eri	210	5000, 1250, 29	(4.2E–13, 0.039), (1.6E–04, 0.034), (8.5E–01, 0.031)
o^1 CMa	328	1429, 28	(6.6E–09, 0.044), (8.0E–01, 0.041)
L^2 Pup	210	3333, 2500, 139, 357,1429, 156, 227, 294	(8.8E–34, 0.215), (5.2E–13, 0.119), (1.3E–09, 0.097), (7.4E–06, 0.084), (3.5E–05, 0.077), (3.5E–07, 0.071), (6.1E–03, 0.063), (1.1E–02, 0.060)
π Pup	203	370	(1.1E–01, 0.030)
γ Cru	294	5000, 20	(6.4E–13, 0.042), (1.0E+00, 0.037)
δ^1 Aps	253	5000, 65	(1.7E–21, 0.067), (2.1E–01, 0.052)
δ^2 Gru	170	5000, 169	(1.4E–05, 0.039), (1.4E–01, 0.035)
β Gru	171	5000, 54, 263, 55	(3.1E–16, 0.042), (2.0E–04, 0.031), (5.4E–03, 0.029), (2.2E–02, 0.027)

Table 4.13: **Period search of merged $(B-V)$ photometry.** This table shows the results of running **T6** on the $(B-V)$ photometry from Tycho and Mt John merged, where N is the number of data points. Not all the 13 stars observed photometrically at Mt John are present here because
a) data from the Tycho photometry annex B was not available at the end of 1997 so ϵ Col, κ Pyx and ω Cap could not be included
b) ϵ Mus was not observed by the Tycho experiment.
The last timescale tabulated here does not have a significant Lomb-Scargle probability.

The transformation of data sets to the Johnson system is not exact and in fact a systematic shift of over 0.01 magnitudes is seen between the Mt John data and the transformed Hipparcos/Tycho photometric values. Hence when the entire data window is searched for timescales often ones longer than 2000 days are found, which were not in the individual data sets. This is a spurious effect and these timescales should be ignored. However, any systematic effect between Tycho and Hipparcos data sets will be much more subtle and the risk of this producing superfluous and spurious timescales can not be ignored. Caution should therefore be paramount in the consideration of the merged data sets' timescales and at most these should be used to confirm the presence of a timescale already existing in at least one of the three data sets.

The Mt John data has had its F-test value (variance of the variable divided by the assumed error) calculated by assuming the variability of the check star is the error. Neither the Tycho nor Hipparcos photometry have such a thing as check stars, so the average standard error of the data points is taken as the assumed error (in the same manner as for the radial velocities, see §4.2). However unlike the radial velocities, the standard error given for each data point is determined from photon statistics, rather than an estimation based on the scatter in radial velocity from order-to-order. Hence it must be assumed that this error is not an estimation, but rather the exact standard deviation of the population (i.e. degrees of freedom equal to infinity). As this is probably not precisely the case, for the Hipparcos and Tycho data significantly varying will be taken to mean that the probability of getting such a large F-value, from a constant population with errors exactly as given by photon statistics, is less than or equal to 0.1%. Then, for the number of points observed for these stars, a 0.1% significance level of variability is certainly reached if $\sqrt{F}[N{-}1, \infty] \geq 1.25$, where $\sqrt{F}$ is the square root of the F-test value for the photometry data set. Comparison of the timescales significant in the three visual magnitude data sets (see Table 4.14) reveals the following information, where the Tycho photometry annex B has not been included in this analysis. As far as significantly varying data is concerned, all stars except β Col and ϵ TrA are significantly varying in H_P and all except 3 Cet, HR 3017, NS Pup, N Vel, GZ Vel, γ Cha and ϵ Cru are significantly vary in V_T (annex A). By comparison, in the Mt John data ϵ Col and ω Cap were not considered to be significantly varying in their visual photometry. In addition:

- η Scl has a dominant 48-day timescale in both Hipparcos and Tycho data. A timescale of $\approx$30 days is also present in all three data sets. Unsurprisingly, the dominant timescale for all the merged data is 48 days with a 34-day timescale also present.
- γ Phe has a dominant 97-day timescale in both Hipparcos and Tycho data. Hence, as might be expected, the dominant timescale is 97 days in the merged data sets.
- ψ Phe has timescales in the range of 18–23 days present in the Hipparcos and Tycho data. A 23-day timescale is dominant and a 22-day timescale secondary in both cases. The merged data set shows exactly the same phenomena, having a dominant timescale of 23 days and a secondary of 22 days.
- τ^4 Eri has a dominant timescale of $\approx$250 days in both Hipparcos, Tycho and perhaps even in the Mt John data. The merged data set reflect this by having the same dominant timescale.
- γ Ret has a dominant timescale of 833 days in both Hipparcos and Tycho data. Also present in both is a timescale of 270 days. Unsurprisingly, the dominant timescale of the merged data set is 833 days.
- η^2 Dor has a dominant timescale of 89 days in both Hipparcos and Tycho data. Again, the dominant timescale of the merged data, 89 days, reflects this.
- o^1 CMa has dominant timescale of $\approx$1350 days in both Hipparcos and Tycho data. Timescales of $\approx$38, 46, 11 and 217 days are also present in both data sets, although with so much

prewhitening it is hard to tell what is a real timescale and what is an artifact of the simplistic prewhitening procedure. The dominant Mt John timescale of ≈175 days is present in the Tycho data while a timescale of ≈64 days is present in both Mt John and Hipparcos data. The merged data for this star also has many timescales, the dominant of which is 1250 days. While timescales of 37 and 196 days also are present, the latter is found after so much prewhitening it may well be unreal.

- L^2 Pup has a dominant timescale of ≈140 days in all three data sets! A 1111-day timescale is also present in all three data sets. The secondary timescale in both Hipparcos and Tycho data is 24 days. It should hence come as no surprise that the dominant timescale in the merged data is 139 days. Timescales of the order of 1111 days and 24 days are also present, although the latter's presence is confused by the vast number of timescales which appear to be present in the merged data and the doubtful nature of prewhitening.

- π Pup has timescales of ≈25 and ≈60 days present in both Hipparcos and Tycho data. A 111-day timescale is also present for Hipparcos and Mt John data. When the data sets are merged the primary and secondary timescales are unrelated. The 60-day timescale may be present, but with so much prewhitening it is hard to say whether or not this is real.

- HR 3017 has a 32-day timescale present in both the Hipparcos data and Tycho data, although only the Hipparcos is variable at the 0.1% level. As might be foreseen, the dominant significant timescale for the merged data is also 32 days.

- λ Vel has a dominant timescale in both Hipparcos and Tycho data of ≈950 days. When these data sets are merged again it seems that the same dominant timescale, at 1000 days, is present.

- ϵ Mus was not observed by the Tycho satellite, so only Hipparcos and Mt John data can be compared. Timescales of 44, 33, ≈63 and ≈22 days are present in both the Hipparcos and the Mt John photometry, but with so much prewhitening it is hard to tell what is a real timescale and what is an artifact of the simplistic prewhitening procedure. When the Hipparcos and Mt John data are merged the dominant resulting timescale is 63 days, with a secondary of 45 days and a tertiary of 32 days.

- γ Cru's dominant timescale for both Hipparcos and Tycho data is 22 days. Mt John's only significant timescale is not present in either of the other two data sets. As is common, when the data sets are merged the dominant timescale is also 22 days.

- 2 Cen has timescales of 83, 74, ≈510 and 52 days present in both the Hipparcos and Tycho data, in that order! As might be anticipated, when these two data sets are merged most of these timescales persist. The "first three" are 83, 74 and 526 days and a 47-day timescale is also present, which may correspond to the 52-day timescale seen in the individual data sets.

- σ Lib's timescale of 54 days is present in both Hipparcos and Tycho data. When these data sets are merged the 54-day timescale is still the dominant one found.

- δ^1 Aps' timescale of 49 days is dominant in all three data sets. A ≈62-day timescale is also present for all. In addition, Hipparcos and Tycho share timescales in the 15–23 day range. In the merged data the dominant timescale is 48 days and timescales of 15–66 days are also present, but the last are found after many prewhitening applications which as always casts doubt upon their reality.

- α Sco's dominant timescale for Hipparcos and Tycho data is 1111 days. Similarly the merged data has a dominant timescale of 1000 days.

Star	$\sqrt{F_H}$ $[N-1,\infty]$	N	Hipparcos $\mathcal{P}$ (days)	$\sqrt{F_T}$ $[N-1,\infty]$	N	Tycho $\mathcal{P}$ (days)	$\sqrt{F_M}$ $[N-1,N-1]$	N	Mt John $\mathcal{P}$ (days)
3 Cet	1.62	137	156, 24, 20	0.97	151	30			
η Scl	5.83	76	48, 32, 109, 41, 333, 44	1.53	90	48, 26, 27	4.00	54	34, 182
γ Phe	8.22	156	97, 98, 83, 19, 37, 19	2.02	244	97, 100, 42, 10			
ψ Phe	6.75	118	23, 22, 39, 25, 35, 30, 20, 139	2.01	143	23, 22, 18, 21, 123			
τ^4 Eri	3.49	111	256, 27, 38	1.36	131	244, 25	3.36	79	294, 88, 159
γ Hyi	3.63	112	500, 22, 35, 435						
γ Ret	8.51	88	833, 270, 51, 68, 87	2.56	120	833, 85, 270, 27, 21, 64			
η^2 Pic	1.63	97	26						
ϵ Col	1.21	134	192				0.67	63	26
β Col	1.15	116	43						
η^2 Dor	3.83	94	88, 29, 32	1.29	116	89, 28			
o^1 CMa	14.59	235	1250, 81, 39, 27, 37, 14, 217, 17, 46, 11, 63, 23, 24, 54, 18	3.63	260	1429, 37, 323, 39, 44, 172, 10, 217, 91, 11	5.63	68	175, 238, 64, 108, 89
σ CMa	6.21	138	1250, 169, 500, 909, 35, 43, 137, 99, 19, 133	1.47	182	13, 14, 278			
L^2 Pup	28.58	106	139, 24, 46,1111, 25, 99, 74, 167, 42	14.51	126	139, 24, 22,1111, 123, 26, 75, 34, 27, 25	28.94	84	141, 1111, 244, 32
π Pup	4.68	111	1429, 111, 27, 63, 24, 21, 72	1.94	133	20, 256, 56, 88	2.44	88	625, 109, 34, 18
HR 3017	2.01	93	74, 32, 38	1.19	127	32, 179			
NS Pup	2.24	135	1429, 80, 53	1.17	154	16, 33			
ϵ Car	6.99	79	435, 41, 31, 38, 27, 47, 60						
β Vol	1.50	111	23	1.29	123	28			
λ Vel	6.29	112	909, 204, 23, 58, 233, 30	1.89	120	1000, 244			
κ Pyx	1.94	189	19, 50, 81, 12				1.67	52	88
N Vel	2.20	116	82, 28, 526, 37, 22	1.15	138	1000			
V337 Car	2.06	111	40, 22, 72, 35	1.32	146	26			
GZ Vel	2.04	141	19, 400, 23, 42, 25, 17	1.09	143	23			
γ Cha	2.08	105	32, 23	1.08	113	25			
HR 4177	2.30	109	58						
ϵ Mus	8.28	133	20, 64, 105, 19, 32, 54, 92, 43, 33, 30				9.00	112	44, 32, 1111, 29, 63, 49
ϵ Cru	1.53	145	36	1.12	166	13			
γ Cru	5.02	150	22, 18, 15, 17, 16, 98, 49	2.45	201	22, 24	4.38	110	1111, 89
2 Cen	6.52	91	83, 74, 500, 52, 169, 39	3.14	96	83, 74, 526, 52, 24			
σ Lib	8.72	38	86, 54, 106	2.26	48	54, 263			
ϵ TrA	1.09	229	14						
δ^1 Aps	9.83	131	48, 19, 278, 64, 75, 23, 37, 18, 49, 35, 29	2.99	169	48, 15, 23, 60, 77	11.14	83	48, 60, 526
α Sco	7.92	71	1111, 33, 217, 39, 30	3.26	82	1111, 95, 39			
HR 6166	2.15	57	45, 56						
α TrA	1.46	129	23, 15						
ϵ Sco	1.44	47	123						
β Ara	2.28	84	1250, 50						
η Sgr	2.20	55	139	1.40	76	227			
62 Sgr	7.47	82	625, 31, 47, 36, 27	1.93	87	31, 625, 47			
ω Cap	1.81	99	37, 143, 99, 143				1.18	43	1250, 132
24 Cap	3.00	55	43						
δ^2 Gru	4.71	89	50, 32, 30	1.64	104	51, 156, 30	5.00	66	24, 526
β Gru	10.69	73	63, 50, 55, 72, 35, 74, 42	6.24	111	63, 21, 93, 55, 112, 49, 51, 39	8.38	68	57, 39

Table 4.14: **Summary of visual photometry timescales and F-test values.** This table summaries the timescales present in the visual photometry and gives the F-test values for the three data sets, where N is the number of data points. The last timescale in the data set is not significant.

- 62 Sgr has timescales of 625 and 31 days present in both Hipparcos and Tycho data. When these data are merged together the dominant timescale is 31 days, but the 625-day timescale is not present as a significant timescale at all.
- δ^2 Gru's dominant Hipparcos and Tycho timescale is 51 days. A timescale of $\approx$30 days is also present in these two data sets, although it is not significant in the LSP sense in either. Notably, Mt John's dominant timescale of 25 days is not present in these sets, but when the data sets are merged together it is found that the dominant timescale is 24 days!
- β Gru's dominant timescale for the Hipparcos and Tycho data is 63 days. This may or may not equate to Mt John dominant timescale of 57 days – timescales of 50 and 55 days are also present in the Hipparcos and Tycho data. The Mt John data also has a secondary timescale of 39 days, which may or may not be related to that of 35 days in the Hipparcos data. When these three data sets are merged together the dominant timescale is 63 days, the secondary is 55 days.

As far the relationship between $(B-V)_{\rm T}$ and $V_{\rm T}$ is concerned, the only stars variable at the 0.1% level in $(B-V)_{\rm T}$ are σ CMa (just), L^2 Pup, λ Vel, γ Cru, α Sco and β Gru. For these stars (as $(B-V)$ and V are not in fact uncorrelated, as has been discussed in §4.3) Table 4.15 reveals that:

- Despite the same timescales being present in both $(B-V)_{\rm T}$ and $V_{\rm T}$ for L^2 Pup and λ Vel their LCC is not significant at the 1% level.
- γ Cru has the same dominant timescale present in both data sets, although it is not significant in the LSP sense $(B-V)$'s case. As might be expected the LCC for these observables is significant (see Figure 4.14).
- α Sco does not have the same timescales present in the two observables, but despite this the LCC is significant (see Figure 4.14).
- β Gru has the same dominant significant timescale present in both data sets and as might be expected the LCC for these observables is significant (see Figure 4.15).

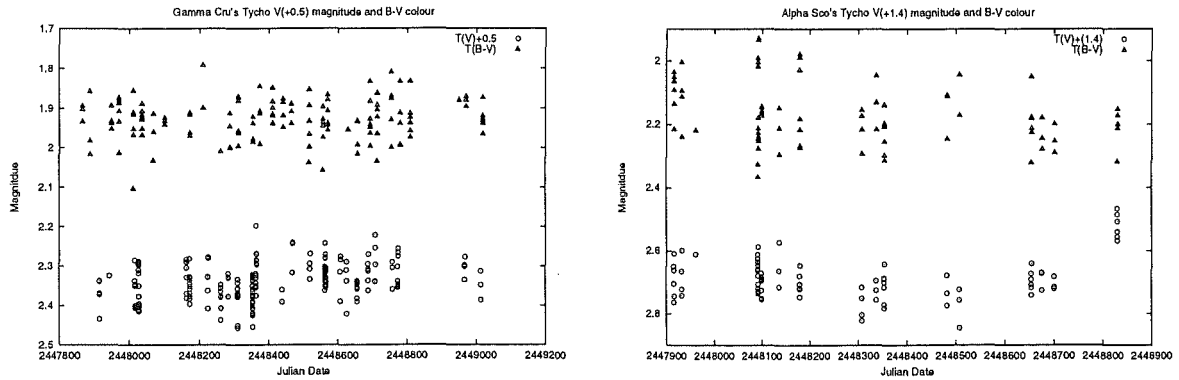

Figure 4.14: The left-hand figure is that of γ Cru's $V_{\rm T}$ magnitude and $(B-V)_{\rm T}$, illustrating the relation between brightness and colour. The right-hand figure is a similar diagram for α Sco.

However, caution in interpreting the magnitude and colour as being correlated for γ Cru, α Sco and β Gru is still needed, because the slope determined by a straight-line fit is a large fraction of negative one and the data plots do not reveal a convincing relationship between the two. Even more condemning, the negative value of LCC would indicate the star was bluest at minimum visual luminosity, which contrasts with all the relationships found from the uncorrelated Mt John colour (see §4.3), including that for β Gru!

Star	LCC	Slope	$\sqrt{F_{(V,B-V)}}$ $[N-1,\infty]$	N
3 Cet	-0.280⋆	-0.6856	(0.97,0.94)	151
η Scl	-0.267	-0.2918	(1.53,0.86)	90
γ Phe	0.031	0.0021	(2.02,0.91)	244
ψ Phe	-0.319⋆	-0.2932	(2.01,0.99)	143
τ^4 Eri	-0.399⋆	-0.5039	(1.36,0.87)	131
γ Ret	-0.434⋆	-0.3460	(2.56,1.02)	120
η^2 Dor	-0.051	-0.0761	(1.29,0.99)	116
o^1 CMa	0.286⋆	0.1773	(3.63,1.01)	260
σ CMa	0.040	0.1008	(1.47,1.17)	182
L^2 Pup	0.070	0.0089	(14.51,1.94)	126
π Pup	-0.089	-0.0831	(1.94,1.15)	133
HR 3017	-0.150	-0.1725	(1.19,1.03)	127
NS Pup	-0.249⋆	-0.4403	(1.17,1.05)	154
β Vol	-0.273⋆	-0.3335	(1.29,0.98)	123
λ Vel	0.135	0.1986	(1.89,1.31)	120
N Vel	-0.211	-0.2941	(1.15,0.85)	138
V337 Car	-0.338⋆	-0.4288	(1.32,0.94)	146
GZ Vel	-0.296⋆	-0.5006	(1.09,0.89)	143
γ Cha	-0.323⋆	-0.5340	(1.08,0.91)	113
ϵ Cru	-0.281⋆	-0.4453	(1.12,0.99)	166
γ Cru	-0.559⋆	-0.5274	(2.45,1.32)	201
2 Cen	-0.363⋆	-0.2382	(3.14,1.10)	96
σ Lib	0.158	0.0560	(2.26,0.90)	48
δ^1 Aps	-0.213⋆	-0.1464	(2.99,1.04)	171
α Sco	-0.329⋆	-0.5137	(3.26,2.61)	82
η Sgr	-0.488⋆	-0.5976	(1.40,0.90)	76
62 Sgr	-0.335⋆	-0.3227	(1.93,0.89)	87
δ^2 Gru	-0.346⋆	-0.4369	(1.64,0.93)	104
β Gru	-0.661⋆	-0.2738	(6.24,1.42)	111

Table 4.15: **Correlation between Tycho's $(B-V)_T$ and V_T.** This table investigates the correlation between Tycho $(B-V)_T$ and V_T using the LCC. A $\star$ means the chances of a linear correlation coefficient this high arising from a random population is less than 1%, when N points are sampled. The slope was determined by a straight-line fit where the deviations have been taken to be the standard error for each data point. A slope of the order of -1 may mean the changes in $(B-V)$ are due to its lack of independence from V.

4.5 Fundamental stellar parameters

Given the colour and luminosity class of a star it is possible to estimate its effective temperature and if the star's bolometric luminosity is also known, from this obtain its radius and mass. Finding the bolometric luminosity of a star is difficult, but given its apparent magnitude, parallax and colour it can be estimated. However, this method of estimating the fundamental parameters of a star suffers from a number of complications. One of these is that any star in a binary system may give a misleading parallax value[39], which will lead to an incorrect estimation of bolometric luminosity and hence mass and radius. Another is that interstellar reddening can affect colours

[39]The parallax for a star is determined by measuring the star's displacement against the background, as the earth moves about the Sun. If the star actually moves itself this will lead to an erroneous measurement.

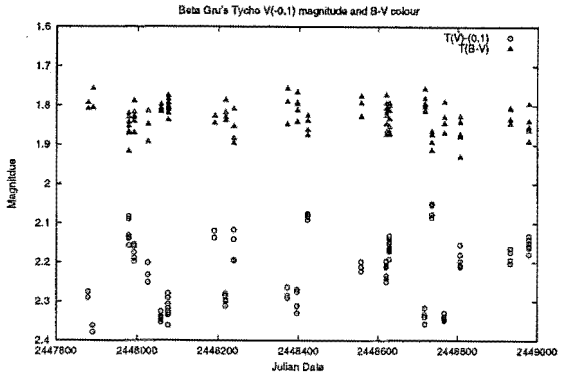

Figure 4.15: This figure is that of β Gru's $V_{\rm T}$ magnitude and $(B-V)_{\rm T}$, illustrating the relation between brightness and colour.

and therefore may lead to poor estimates of all the calculated parameters.

A Turbo Pascal program, **hr_diag**, has been written to calculate effective temperature, radius and mass for normal giants using $(V-R)_{\rm C}$ and $(V-I)_{\rm C}$ colours (such as were obtained for 13 stars at Mt John University Observatory) and bolometric luminosity. If the star is present in the Hipparcos main catalogue [50] then **hr_diag** can use the values of $(V-I)_{\rm C}$, $V_{\rm J}$ and parallax tabulated there to calculate all parameters (the results from using the Hipparcos catalogue for the calculation of mass and radius are given in Table 4.16). The details of **hr_diag**'s exact method for calculation of these fundamental parameters will now be given.

4.5.1 Calculating mass, radius and effective temperature using hr_diag

hr_diag has several different variations for the calculation of a star's fundamental parameters, depending on how the user would like their bolometric luminosity obtained. These actions are split into two main cases, one only using Hipparcos catalogue data[40] and the other which does not. In the latter, the user inputs $(V-R)_{\rm C}$ and $(V-I)_{\rm C}$ for the star and **hr_diag** uses them and Table 3 of Bessell [18] to estimate the effective temperature of the star (this assumes the star is a normal giant) by taking the average effective temperature estimated from $(V-I)_C$ and $(R-I)_C$ to be $T_{\rm eff}$. In the former case, the Hipparcos main catalogue data can be used to determine $T_{\rm eff}$. However, as it only contains $(V-I)_{\rm C}$ this is not as accurate as using the average of two independently determined temperatures.

To consider the effect of determining the effective temperature from only one colour, **hr_diag** has been ran using the same bolometric luminosity as used for Table 4.16, but inputting two independent colours (given by the Mt John photometry) for use in calculating the effective temperature. The 15 stars[41] for which Mt John photometry is available have their resulting parameters given in Table 4.17. If the average $T_{\rm eff}$, determined from the two independent colours, gives the true effective temperature then this indicates that using only $(V-I)_{\rm C}$ to determine $T_{\rm eff}$ will introduce an error of only a few percent (the estimated error in Table 4.17). It is important to note that the different prediction of temperature from the two colour indices can arise from a number of sources. This can occur if the colours determined are inaccurate due to problems with the photometry reduction procedure (this is true of $(V-R)_{\rm C}$ and is discussed further in §4.3). This could also occur

[40] Of course, with variable stars the Hipparcos data (and therefore the estimated effective temperature, radius and mass) may not be appropriate for the period of time over which observations for this thesis were obtained

[41] Two stars which were observed initially were soon discontinued, so actually 15 stars with two colour indices available, not just 13!

if the calibration of effective temperature and colour is wrong. This may occur for supergiants, as the temperature calibration was made for normal giants. Interestingly, in the case of supergiants π Pup and o^1 CMa the temperature determined by the two independent colours agree well. This might indicate that the temperature calibration, while strictly only for normal giants, in fact gives reasonable results for supergiants also. In support of this idea o^1 CMa's effective temperature, which has been given by Lutz & Pagel [118] as $T_{\rm eff} = 4165$ K, is in agreement with the average value predicted by **hr_diag** within 3%.

In the case of two colours being available, previous to the calculation of $T_{\rm eff}$ an attempt is made to determine the interstellar reddening from the colours. However, the reddening corrected values of the colours are only poorly estimated, so these are not used for the $T_{\rm eff}$ calculation. Despite this, the method employed will now be outlined. An adaptation of the method detailed in Landolt-Börnstein [143], §4.1.1.6, is used. Following this a reddening-free co-efficient, $\mathcal{Q}$, is defined as

$$\mathcal{Q} = \frac{E_{V-R}}{E_{R-I}}(R-I)_{\rm true} - (V-R)_{\rm true} = \frac{E_{V-R}}{E_{R-I}}(R-I)_{\rm obs} - (V-R)_{\rm obs},$$

where E_{V-R} is the colour excess of $(V-R)$, i.e. $(V-R)_{\rm obs} = (V-R)_{\rm true} + E_{V-R}$. To determine the ratio $\frac{E_{V-R}}{E_{R-I}}$ as a function of the unreddened Cousins colour $(V-R)_{\rm true}$, Taylor's [164] Table 3 is used[42]. The appropriate ratio for the star is estimated by taking the average of ratio values obtained from $(V-R)_{\rm C}$ and $(R-I)_{\rm C}$ colours, where it is assumed that $\frac{E_{V-R}}{E_{R-I}} = F(C_{\rm true}) \approx F(C_{\rm obs})$. Then $\mathcal{Q}$ is determined using this approximate ratio. At this point Landolt-Börnstein takes one colour to be a linear function of the other, assumes the ratio of reddening is approximately constant, then determines first one intrinsic colour from this $\mathcal{Q}$ value then the other. But as $(R-I)_{\rm C}$ is not a nicely linear function of $(V-R)_{\rm C}$ and this reddening ratio is far from constant, a more sophisticated approach is necessary to find the intrinsic colours from the known $\mathcal{Q}$. First $\mathcal{Q}$ is calculated for all $(V-R)_{\rm true}$ points in Taylor's table. Then, as $\mathcal{Q}$ can be considered as a function of $(V-R)_{\rm true}$ the estimated value of $\mathcal{Q}$ is used to find the $(V-R)_{\rm true}$ value appropriate to it. Unfortunately, $\mathcal{Q}$ is not monotonic for $(V-R)_{\rm true} < 0.8$ (see Figure 4.16). Hence only reddenings with $(V-R)_{\rm true} \geq 0.8$ are considered, which is somewhat limiting. This, along with only the approximate reddening ratio for the star being calculated, means $\mathcal{Q}$ is very approximate (the reddening ratio is far from constant with $(V-R)_{\rm C}$) and the reddening corrections calculated are rather untrustworthy[43].

After $T_{\rm eff}$ has been calculated **hr_diag** needs to know the bolometric luminosity, $L_{\rm bol}$, in order to go any further. This can be inputted by the user or estimated from Landolt-Börnstein [143] §4.4.1, Table 3b. Alternatively, if the program has been directed to use the Hipparcos main catalogue it will calculate $L_{\rm bol}$ itself. This is done by using the Hipparcos apparent magnitude and parallax to give the absolute magnitude of the star. This gives $L_{\rm bol}$ if the bolometric correction, BC, is known and this in turn can be estimated, for a late-type star, from $(V-I)_{\rm C}$ using Bessell & Wood's [20] relation[44]

$$BC = 0.3 - 0.62(V-I)_{\rm C} - 0.14(V-I)_{\rm C}^2.$$

This luminosity is then used to calculate the stellar radius from the simple and exact formula

$$\frac{L_{\rm bol}}{L_\odot} = \left(\frac{R}{R_\odot}\right)^2 \left(\frac{T_{\rm eff}}{T_\odot}\right)^4,$$

[42] Actually Table 3 gives $E_{V-R} = a_{V-R}E_{B-V} + b_{V-R}E_{B-V}^2$ and a similar relation for $(R-I)$ where $b \ll a$. E_{B-V} is unknown and the second term means E_{B-V} does not cancel out of the ratio. So the second term is taken as the "error" in E_{V-R}'s determination and discarded, which allows E_{B-V} to cancel out of $\frac{E_{V-R}}{E_{R-I}}$.

[43] In fact, according to this method of determining "reddening" the observed stars are often bluer then they should be, which is not a good sign!

[44] This is valid for all late-type stars and hence can be used for both giants and supergiants

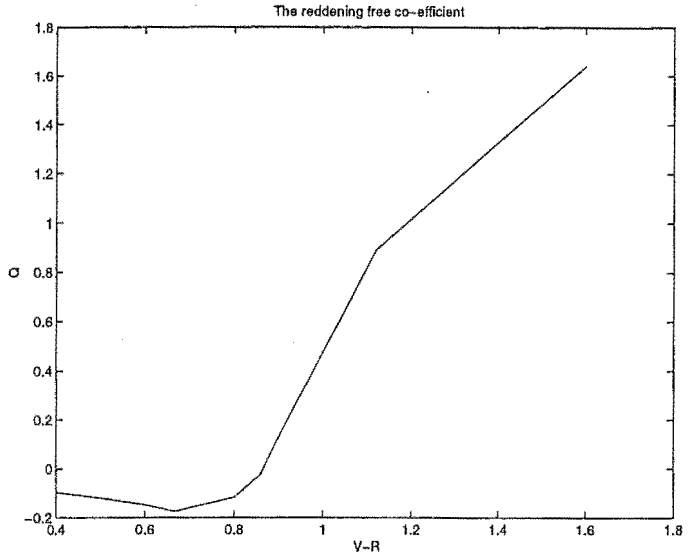

Figure 4.16: The reddening-free co-efficient, $\mathcal{Q}$, as a function of Cousins $(V-R)_C$. Unfortunately, this is not a monotonic function so determining unique values of $(V-R)_C$ from a given $\mathcal{Q}$ is not always possible (the plotted function was determined from Taylor's [164] Table 3).

where $T_\odot = 5760$ K is the effective temperature of the Sun.

The final step of **hr_diag** is to estimate the star's mass and this is found by the use of the previously calculated $T_{\rm eff}$ and $L_{\rm bol}$. Both Bessell [19] (Table 8a & b) and Schaller et al. [145] give grids[45] of effective temperature and luminosity (assuming solar abundance) for mass. Bessell is the preferred grid for all but the hottest of the stars and the left-hand plot in Figure 4.17 shows this grid. Close consideration of the Bessell's grid values reveals the approximate relationship between $T_{\rm eff}$, the bolometric luminosity in solar units, $\mathcal{L}_{\rm bol}$, and mass in solar units, $\mathcal{M}$, to be of the form $\mathcal{L}_{\rm bol} = B(\mathcal{M})T^\alpha$. The function $B(\mathcal{M})$ is generally complicated, but over the mass range 1–15 solar masses it can be approximated by $B(\mathcal{M}) \approx C\ \mathcal{M}^{1.65}$ (see the right-hand side of Figure 4.17). Hence the relatively simple relation $\mathcal{L}_{\rm bol} \approx K\ \mathcal{M}^{1.65}\ T^\alpha$ is obtained. In the case of stars being cool enough for Bessell's grid, this simple formula[46] is employed to estimate the uncertainty in the mass calculation (for more details see below). It should be noted that these mass-luminosity-temperature grids assume a certain rate of mass loss. If the star suffers unexpected mass loss these grids will no longer be valid and hence any mass obtained from them incorrect.

[45] Valid for both giants and supergiants!

[46] All tables have values interpolated linearly between grid points, as cubic splines can not seem to handle things like the fact that for Schaller's models luminosity is not always a monotonically increasing function of temperature (for a given initial mass). This relation does; however, mean that a linear interpolation between logarithmic values of $\mathcal{L}_{\rm bol}$, $\mathcal{M}$ and T (in Bessell's case) is well justified.

[47] See, for example, Schatzman & Praderie [146] §3.4.5

[48] The program **hr_diag** finds effective temperature assuming the star is a normal giant. As mass and radius are found using effective temperature, they will reflect any error in its estimation. Hence caution should be used when considering the fundamental parameters of supergiants like 3 Cet, o^1 CMa, π Pup, α Sco and β Ara (see Table 1.1 for spectral types). Fortunately, if o^1 CMa is any indication the error in effective temperature (and therefore mass and radius) will be small.

[49] See footnote 48, Chapter 4

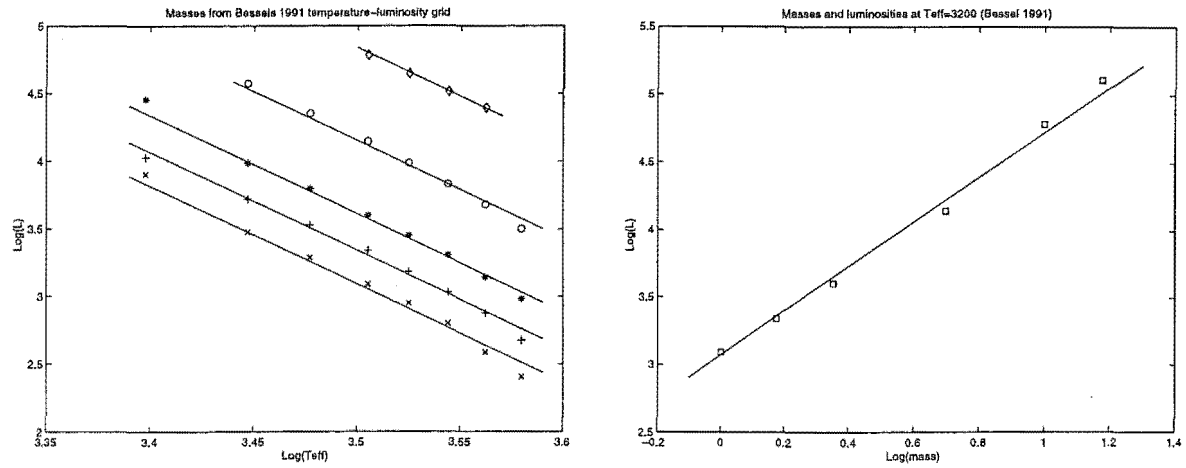

Figure 4.17: The left-hand graph is plotted from Bessell's [19] Table 8a & b and gives mass as a function of bolometric luminosity and effective temperature for a star of solar abundance type. The masses are (from the bottom up) 1, 1.5, 2.25, 5 and 10 solar masses, respectively. By plotting Bessell's luminosity (in solar units) and effective temperature grid as logarithms it can be seen that, for a given mass, $\log(\mathcal{L}_{\rm bol})$ is very nearly a linear function of $\log(T_{\rm eff})$. In fact, similar to the relation for white dwarfs[47], each mass curve is not only a straight line but each straight line has approximately the same slope so that $\log(\mathcal{L}_{\rm bol}) \simeq -7.24\log(T_{\rm eff}) + b(\mathcal{M})$, where -7.24 is the straight lines' slope. The figure to the right shows the relation between $\log(\mathcal{L}_{\rm bol})$ and $\log(\mathcal{M})$ at the cross-section in temperature of $T_{\rm eff} = 3200$ K. This is approximately a straight line of slope 1.65 and hence to first order $b(\mathcal{M}) \simeq 1.65\log(\mathcal{M}) + C$. This leads to the nice result that $\mathcal{L}_{\rm bol} \simeq 3.0012 \times 10^{28}\ \mathcal{M}^{1.65}\ T_{\rm eff}^{-7.24}$.

Calculation of errors

When **hr_diag** is directed to use the Hipparcos catalogue it assumes the parallax errors are the dominant error and calculates the error in the mass and radius accordingly. How this is done will now be described. Bolometric luminosity, parallax and apparent magnitude are related via

$$M_v = m_{\rm V} + 5 - 5\log(\pi) = M_{\rm bol} - BC$$

and

$$\log(\mathcal{L}_{\rm bol}) = 1.89 - 0.4M_{\rm bol},$$

where π is the parallax, $M_{\rm V}$ is the absolute visual magnitude and $m_{\rm V}$ is the apparent magnitude. These lead to

$$\mathcal{L}_{\rm bol} = \frac{10^{(-0.11-0.4(m_{\rm V}+BC))}}{\pi^2}$$

so that if apparent magnitude and bolometric correction are known exactly then

$$\frac{\delta\,\mathcal{L}_{\rm bol}}{\mathcal{L}_{\rm bol}} = 2\frac{\delta\pi}{\pi},$$

where error propagation for standard errors (see, for example, Bevington & Robinson [21] §3.2) has been used. Similarly as

$$\frac{d\log_a(u)}{dx} = \frac{\log_a(e)}{u} \times \frac{du}{dx},$$

the error in the absolute visual magnitude is

$$\delta M_{\rm V} = 2.1715\frac{\delta\pi}{\pi}.$$

Star	Spectral Type	$T_{\rm eff}$ (K)	D (pc)	M_v	$\mathcal{L}_{\rm bol}$	$\mathcal{R}$	$\mathcal{M}$	$\mathcal{G}$
2 Cen	M5III	3442	54	0.51±0.09	650± 50	72±3	0.93±0.05	$\mathcal{B}$
24 Cap	K5/M0III	3841	160	-1.5±0.3	1000±300	70±10	2.3±0.4	$\mathcal{S}$
3 Cet	K3Ibvar	3938	493	-3±1	5000±5000	160±70	5±4	$\mathcal{S}$
62 Sgr	M4III	3582	137	-1.3±0.2	1800±400	110±10	2.4±0.3	$\mathcal{B}$
α Sco	M1Ib+B2.5V	3466	185	-5.3±0.7	120000±70000	1000±300	17±6	$\mathcal{B}$
α TrA	K2IIb-IIIa	4080	127	-3.6±0.2	4900±800	140±10	7.4±0.6	$\mathcal{S}$
β Ara	K3Ib-II	4030	185	-3.5±0.3	5000±1000	140±20	7.0±0.8	$\mathcal{S}$
β Col	K1.5III	4523	26	1.02±0.03	51± 2	11.6±0.2	1.52±0.02	$\mathcal{S}$
β Gru	M5III	3551	52	-1.52±0.08	2500±200	133±5	2.8±0.1	$\mathcal{B}$
β Vol	K2IIIvar	4523	33	1.17±0.03	44± 1	10.8±0.2	1.42±0.02	$\mathcal{S}$
δ^1 Aps	M5III	3528	235	-2.2±0.3	5000±1000	190±30	4.3±0.7	$\mathcal{B}$
δ^2 Gru	M4.5IIIa	3585	100	-0.9±0.2	1200±300	90±10	1.9±0.3	$\mathcal{B}$
ϵ Car	K3III+B2V	4426	194	-4.6±0.2	9000±2000	160±20	8.1±0.3	$\mathcal{S}$
ϵ Col	K1II/III	4545	85	-0.79±0.09	260± 20	26±1	3.12±0.09	$\mathcal{S}$
ϵ Cru	K3/K4III	4140	70	-0.63±0.09	300± 20	34±1	1.91±0.06	$\mathcal{S}$
ϵ Mus	M5III	3486	93	-0.8±0.1	1700±100	113±5	2.0±0.1	$\mathcal{B}$
ϵ Sco	K2IIIb	4523	20	0.78±0.04	63± 2	13.0±0.2	1.64±0.02	$\mathcal{S}$
ϵ TrA	K0III	4485	66	0.00±0.09	130± 10	19.0±0.8	2.09±0.09	$\mathcal{S}$
η^2 Dor	M2.5III	3699	206	-1.6±0.2	1500±300	94±9	2.6±0.3	$\mathcal{B}$
η^2 Pic	M2IIIvar	3966	145	-0.8±0.2	410± 60	43±3	1.7±0.1	$\mathcal{S}$
η Scl	M2/M3III	3639	168	-1.3±0.3	1400±300	100±10	2.3±0.3	$\mathcal{B}$
η Sgr	M2III	3665	46	-0.20±0.09	490± 40	55±2	1.18±0.06	$\mathcal{B}$
γ Cha	M0III	3898	127	-1.4±0.1	800±100	63±4	2.2±0.2	$\mathcal{S}$
γ Cru	M4III	3623	27	-0.56±0.04	790± 30	72±1	1.49±0.03	$\mathcal{B}$
γ Hyi	M2III	3767	66	-0.83±0.08	620± 40	59±2	1.66±0.07	$\mathcal{B}$
γ Phe	K5II-III	3886	72	-0.9±0.1	520± 50	50±2	1.69±0.08	$\mathcal{S}$
γ Ret	M4III	3608	150	-1.4±0.2	1800±300	110±8	2.5±0.2	$\mathcal{B}$
GZ Vel	K3II	4030	457	-3.7±0.5	6000±2000	150±30	7±1	$\mathcal{S}$
HR 3017	K4III	3835	426	-4.5±0.5	16000±8000	290±70	10±2	$\mathcal{S}$
HR 4177	K4/K5III:	3943	568	-4.1±0.9	9000±7000	200±80	7±3	$\mathcal{S}$
HR 6166	K5III	3892	104	-0.9±0.2	530± 90	51±4	1.7±0.1	$\mathcal{S}$
κ Pyx	K4/K5III	3926	149	-1.3±0.2	700±100	57±6	2.1±0.3	$\mathcal{S}$
L^2 Pup	M5e	3332	61	0.5±0.2	1300±200	107±8	1.3±0.1	$\mathcal{B}$
λ Vel	K4Ib-II	3909	176	-4.0±0.2	9000±2000	210±20	8.1±0.5	$\mathcal{S}$
N Vel	K5III	3966	73	-1.15±0.08	590± 40	51±2	2.05±0.09	$\mathcal{S}$
NS Pup	K4III	3949	575	-4.4±0.7	12000±7000	230±70	9±2	$\mathcal{S}$
o^1 CMa	K3Iab	3972	606	-5.0±0.8	20000±20000	300±100	11±4	$\mathcal{S}$
ω Cap	K4III	3869	193	-2.3±0.4	2000±700	100±20	3.6±0.8	$\mathcal{S}$
π Pup	K3Ib	3932	336	-4.9±0.4	20000±7000	310±60	10±1	$\mathcal{S}$
ψ Phe	M4III SB	3585	99	-0.6±0.1	900±100	79±5	1.6±0.1	$\mathcal{B}$
σ CMa	K4III	3835	373	-4.4±0.5	14000±6000	270±60	9±2	$\mathcal{S}$
σ Lib	M3/M4III	3668	90	-1.5±0.2	1600±300	100±9	2.5±0.3	$\mathcal{B}$
τ^4 Eri	M3/M4III	3608	79	-0.8±0.2	1000±100	83±6	1.7±0.2	$\mathcal{B}$
V337 Car	K3II	4080	226	-3.4±0.2	4000±900	130±10	6.7±0.6	$\mathcal{S}$

Table 4.16: **Mass and radius estimates using the Hipparcos catalogue.** This table contains: mass in solar units, $\mathcal{M}$; radius in solar units, $\mathcal{R}$; bolometric luminosity in solar units, $\mathcal{L}_{\rm bol}$, and effective temperature estimates for all 44 stars surveyed for this thesis[48]. The spectral types are those given in the Hipparcos catalogue; D is the distance to the star in parsecs, as determined from the stars' parallax; the effective temperature, $T_{\rm eff}$, has been determined using the Hipparcos $(V-I)_{\rm C}$; the absolute magnitude, $M_{\rm V}$, has been determined using D and the Hipparcos apparent magnitude; $\mathcal{G}$ is which grid of luminosity-temperature-mass was used to determine the stars' mass, where $\mathcal{B}$ means that of Bessell [19] and $\mathcal{S}$ means that of Schaller et al. [145]. The estimated errors only take into consideration errors arising from the Hipparcos parallaxes.

Star	$(V-I)_C$	$(V-R)_C$	$\mathcal{L}_{\rm bol}$(HIP)	$T_{\rm eff}$	$\mathcal{R}$	$\mathcal{M}$
2 Cen	3.02†	1.20†	649.89	3438⋆	72	0.92
β Gru	2.68	1.11	2512.56	3513±13	136	2.65
δ^1 Aps	2.69	1.12	5018.33	3511±11	192	4.18
δ^2 Gru	2.48	1.05	1211.32	3576±12	91	1.83
ϵ Col	1.08	0.55	263.82	4506±62	27	3.06
ϵ Mus	2.77	1.14	1674.35	3498⋆	112	1.99
η^2 Dor	2.15†	0.86†	1496.35	3661±32	96	2.40
η Scl	2.31	1.01	1424.76	3633±9	96	2.23
γ Cru	2.31	0.98	790.30	3626±16	71	1.49
κ Pyx	1.66	0.85	687.29	3931±5	57	2.12
L^2 Pup	3.67	1.61	1252.07	3281⋆	110	1.15
ω Cap	1.76	0.91	2002.68	3885±16	99	3.71
o^1 CMa	1.53	0.82	20448.93	4023±23	295	11.83
π Pup	1.62	0.87	19917.16	3968±19	300	12.83
τ^4 Eri	2.37	0.99	1035.89	3605±18	83	1.73

Table 4.17: **Mass and radius estimates using Mt John photometry.** This table gives: the mass in solar units, $\mathcal{M}$; radius in solar units, $\mathcal{R}$, and effective temperature[49] as estimated from Mt John photometric colours and the Hipparcos catalogue's estimation of bolometric luminosity. Of particular interest is the effective temperature, $T_{\rm eff}$, as it is determined from the average value estimated by the colours $(V-I)_C$ and $(V-R)_C$ and its "error" is given by half the difference. For theses averages only OC data have been used for β Gru, γ Cru and π Pup. In addition, for $(V-R)_C$ only OC data has been used for δ^1 Aps, δ^2 Gru, ϵ Mus, η Scl, L^2 Pup and τ^4 Eri (for a discussion on why this is necessary see §4.3). The two stars with colours labelled with a † were only observed for a short period of time (and only OC data were used). The three stars with effective temperature labelled with a ⋆ had $(V-R)_C$ beyond that tabulated by Bessell's [18] Table 3 and hence only one colour was used for estimating the effective temperature.

Now as

$$\mathcal{L}_{\rm bol} = \left(\frac{T_{\rm eff}}{T_\odot}\right)^4 \mathcal{R}^2,$$

where $\mathcal{R} = R/R_\odot$, it similarly can be found that

$$\frac{\delta\,\mathcal{R}}{\mathcal{R}} = \frac{1}{2}\frac{\delta\,\mathcal{L}_{\rm bol}}{\mathcal{L}_{\rm bol}} = \frac{\delta\pi}{\pi}$$

if $T_{\rm eff}$ was known exactly. Not only that, but if Bessell's grid of luminosity-temperature-mass was used to determine the mass Figure 4.17 indicates that

$$\mathcal{L}_{\rm bol} \approx 3.0012 \times 10^{28}\, \mathcal{M}^{1.65}\, T_{\rm eff}^{-7.24},$$

which means that

$$\frac{\delta\,\mathcal{M}}{\mathcal{M}} = \frac{1}{1.65}\frac{\delta\,\mathcal{L}_{\rm bol}}{\mathcal{L}_{\rm bol}} = \frac{2}{1.65}\frac{\delta\pi}{\pi}.$$

However, when Schaller's grid is used the error predicted by this equation is on the high side and **hr_diag** instead uses "high and low" luminosity values to obtain the mass and its error.

4.6 Comparing the radial velocities and photometry

When comparing the radial-velocity and light-curve data sets, of particular interest is the existence of any timescales in both radial velocity and Mt John photometry. Much of this data was

obtained simultaneously and hence this can allow the comparison of how the radial velocity of a star changes with respect to brightness, which is important in determining the mechanism of the stellar variation. However, timescales in the Hipparcos or Tycho photometry may also be of interest for comparison with the radial velocities as the variation may be coherent or recurrent, although usually no phase information will be able to be determined. Timescales present in both the radial velocity and visual photometry of a star will be called the characteristic timescales of the star.

Comparing radial-velocity and visual-photometry data, particularly if the phase relation between the two is desired, is not a trivial task. The simplest approach is to compare the timescales found using **T6**. However this has a number of complications, one of the main ones being if the timescale is not the dominant one it will have been obtained using prewhitening, which unless the data consists of the sum of simple sinusoids is not ideal (see §4.1 for more details on prewhitening and its problems). One effect of the non-exact removal of periodicities is that the timescales in the residuals may be modified from their real values. Hence a star with variations of the same timescales in both radial velocity and photometry, but also with other dominant variations, may have different (although similar) apparent timescales found in the two data sets by **T6**. The ill effects of prewhitening are particularly of concern when the phase relationship between the two data sets is desired. Hence three approaches have been taken in the comparison of the Mt John photometry and radial velocities. The first is simply to use **T6** to find timescales and phase differences, the second is to view any concurrent data segments by eye and hence, at least for that segment of time, to determine the phase relationship. The third, appropriate for many pulsating stars, is to use the photometry to estimate the stellar angular diameter using the Barnes-Evans method and compare this with the concurrent radial velocities.

4.6.1 Comparing radial-velocity and light-curve periods

The results of running the period-finding program **T6** on the radial-velocity and photometry data for the 44 stars surveyed for this thesis are shown in Table 4.18. Of the 13 stars observed concurrently at Mt John seven (β Gru, δ^1 Aps, δ^2 Gru, ϵ Mus, L^2 Pup, o^1 CMa and π Pup) have the same timescales in their Mt John visual photometry and radial velocities. These stars have **T6**'s phases for their radial-velocity and light timescales compared below. The comparison of the phases of variations using **T6** suffers from the restriction that **T6** fits a simple sinusoid to the data to determine its phase at the first observed point. Hence the phase information is only appropriate for a completely sinusoidal data set. **T6** gives the phase, θ, of the fitted sine wave at time t and therefore for a sinusoid the shift in phase between the radial velocity and photometry is

$$\Delta\theta = 360 \times \frac{t_{\rm mag} - t_{\rm rv}}{\overline{P}} + (\theta_{\rm mag} - \theta_{\rm rv}),$$

where $\overline{P}$ is the average timescale found in the two data sets (as the same period is assumed to be present in both data sets). Obviously, even in the case of a sinusoidal variation, any error in the value of the period of the variation will be reflected as an error in the calculated change in phase. The difference in phase between the two data sets means the photometry reaches minimum brightness[50] $\Delta\theta$ before the radial velocity reaches maximum recession. In other words, maximum recessional velocity occurs $(180 - \Delta\theta)$ degrees[51] (which is equivalent to $(0.5\overline{P} - \frac{\Delta\theta}{360}\overline{P})$ days) before maximum visual luminosity.

This phase information provided by **T6** is compared to concurrent data plots of the stars, which are given for visual inspection of their phase relationship in Figures 4.18 to 4.24. The chosen regions

[50] As the largest magnitude is the minimum luminosity

[51] If this equal to 180 the data sets are said to be in anti-phase, equal to zero in phase and if it is less than 180 the visual luminosity is said to be lagging the radial velocity by $(180 - \Delta\theta)$

Star	Radial-velocity $\mathcal{P}$ (days)	Mt John $\mathcal{P}$ (days)	Hipparcos $\mathcal{P}$ (days)	Tycho $\mathcal{P}$ (days)
2 Cen	556, 37		83, 74, 500, 52, 169, 39	83, 74, 526, 52, 24
24 Cap	93		43	
3 Cet	526		156, 24, 20	30
62 Sgr	588, 164, 96, 119		625, 31, 47, 36, 27	31, 625, 47
α Sco	139		1111, 33, 217, 39, 30	1111, 95, 39
α TrA	57, 46		23, 15	
β Ara	112		1250, 50	
β Col	159		43	
β Gru	833, 59, 15, 19	57, 39	63, 50, 55, 72, 35, 74, 42	63, 21, 93, 55, 112, 49, 51, 39
β Vol	476		23	28
δ^1 Aps	1000, 455, 29, 48, 175	48, 60, 526	48, 19, 278, 64, 75, 23, 37, 18, 49, 35, 29	48, 15, 23, 60, 77
δ^2 Gru	1429, 23, 20	24, 526	50, 32, 30	51, 156, 30
ϵ Car	833, 104		435, 41, 31, 38, 27, 47, 60	
ϵ Col	1250, 294	26	192	
ϵ Cru	270		36	13
ϵ Mus	63, 625, 88, 69	44, 32, 1111, 29, 63, 49	20, 64, 105, 19, 32, 54, 92, 43, 33, 30	
ϵ Sco	52		123	
ϵ TrA	135		14	
η Scl	49	34, 182	48, 32, 109, 41, 333, 44	48, 26, 27
η Sgr	345		139	227
η^2 Dor	667, 100, 62		88, 29, 32	89, 28
η^2 Pic	909		26	
γ Cha	435		32, 23	25
γ Cru	556, 13, 16, 40	1111, 89	22, 18, 15, 17, 16, 98, 49	22, 24
γ Hyi	244		500, 22, 35, 435	
γ Phe	192, 172		97, 98, 83, 19, 37, 19	97, 100, 42, 10
γ Ret	909, 345, 41		833, 270, 51, 68, 87	833, 85, 270, 27, 21, 64
GZ Vel	2000, 270,1667		19, 400, 23, 42, 25, 17	23
HR 3017	556		74, 32, 38	32, 179
HR 4177	435, 208		58	
HR 6166	476, 667		45, 56	
κ Pyx	526, 196	88	19, 50, 81, 12	
L^2 Pup	141, 435, 123	141, 1111, 244, 32	139, 24, 46,1111, 25, 99, 74, 167, 42	139, 24, 22,1111, 123, 26, 75, 34, 27, 25
λ Vel	1429, 714,1429,556		909, 204, 23, 58, 233, 30	1000, 244
N Vel	625, 112		82, 28, 526, 37, 22	1000
NS Pup	1429,1429		1429, 80, 53	16, 33
o^1 CMa	179, 769, 167, 23, 44, 118	175, 238, 64, 108, 89	1250, 81, 39, 27, 37, 14, 217, 17, 46, 11, 63, 23, 24, 54, 18	1429, 37, 323, 39, 44, 172, 10, 217, 91, 11
ω Cap	476, 250, 500, 213,1250	1250, 132	37, 143, 99, 143	
π Pup	1250, 37, 47, 31	625, 109, 34, 18	1429, 111, 27, 63, 24, 21, 72	20, 256, 56, 88
ψ Phe	588, 189, 77		23, 22, 39, 25, 35, 30, 20, 139	23, 22, 18, 21, 123
σ CMa	1250, 667, 49		1250, 169, 500, 909, 35, 43, 137, 99, 19, 133	13, 14, 278
σ Lib	556, 120, 95		86, 54, 106	54, 263
τ^4 Eri	588, 33, 135	294, 88, 159	256, 27, 38	244, 25
V337 Car	286		40, 22, 72, 35	26

Table 4.18: **Summary of radial-velocity and visual-photometry timescales.** This table summarizes Tables 4.4, 4.5, 4.9 and 4.10 which give the timescales found by period search program **T6** in: the radial velocities obtained for this thesis; the V_J photometry obtained for this thesis; and the Hipparcos, H_P, and Tycho, V_T, visual magnitudes for the surveyed stars. The last timescale in the data set is not significant (in the LSP sense).

are those with the most simultaneous data. The results of a timescale search on these data subsets is given in Table 4.19 and discussed in the figure captions.

- β Gru has a significant timescale of about 58 days present in all data sets in Table 4.18, not to mention in Mt John $(R-I)_{\rm C}$ (and Tycho $(B-V)_{\rm T}$). Having removed the dominant 833-day timescale in radial velocity by prewhitening, the residual radial velocity (which has a 59-day period) and Mt John $V_{\rm J}$ photometry (which has a 57-day period) were compared. The data reaches maximum visual brightness, on average, 134 degrees (21 days) before maximum recessional velocity. This is not incompatible with the data taken over JD 2450260–2450400 days (see Figure 4.18). However, with so little simultaneous data it is hard to say any more for certain.

- δ^1 Aps has a significant timescale of about 48 days present in all data sets in Table 4.18, not to mention in Mt John $(R-I)_{\rm C}$. Having removed the 1000, 455 and 29-day timescales in radial velocity by prewhitening, the residual radial velocities (which have a 48-day period) were compared to the dominant Mt John $V_{\rm J}$ photometry (which has a 48-day period). The data reach maximum visual brightness, on average, 61 degrees (8 days) before maximum recessional velocity — approximately in phase. This is not verified by visual inspection of the data taken over JD 2449800–2450350 days (see Figure 4.19), where the two observables appear to be in anti-phase. This is probably due to interference of the 29-day timescale. In fact, when **T6** is ran on the right-hand figure the radial velocity has a dominant (although not significant in the LSP sense) timescale of 68, not 48, days.

  It is thought that the 68 and 29-day timescales in the radial velocity are related. The 68-day timescale being approximately double the length of the 29-day timescale could indicate that the 29-day timescale found by **T6** in the full data set might actually be a higher harmonic of an underlying non-sinusoidal 68-day timescale (see footnote 12, this chapter, for what is meant by a higher harmonic). This idea is supported by the fact that in the periodogram of the full data set the 68-day timescale is present as well as the 29-day timescale, and is <u>almost</u> the same size (see the left-hand side of Figure B.6)! In addition, there is a 60-day timescale present in the concurrent photometry and at least in the case of a classical pulsation radial-velocity variations of the amplitude of the 29-day timescale should be visible in photometry (see §4:9.1). Hence, on the strength of the independent verification of the timescale by the concurrent photometry, the ≈65-day timescale will be taken to be the real timescale of the star and the 29-day timescale to be false. In which case as the 48-day timescale is more prevalent in the photometry than the 60-day timescale, but visa-versa in the radial velocities, it should not be surprising that phase relationships determined by the simple method above are inaccurate. More concurrent data is be needed to clarify this. The most that can be said at the moment is that the star seems to have two characteristic timescales, 48 and ≈66 days, and over these timescales the observables are approximately in anti-phase.

- δ^2 Gru has a significant timescale of about 30 days present in all but the Tycho visual photometry. Having removed the dominant 1429-day timescale in radial velocity by prewhitening, the residual radial velocity (which has a 23-day period) and Mt John $V_{\rm J}$ photometry (which has a 24-day period) were compared. The data reaches maximum recessional velocity, on average, 43 degrees (8 days) before maximum visual brightness — approximately in phase. This is consistent with data subsets shown in Figure 4.18, which by visual inspection appear to be in phase.

- ϵ Mus has a significant timescale of 63 days present in all available data sets, although the dominant 44-day timescale in the Mt John $V_{\rm J}$ and $(R-I)_{\rm C}$ (and Hipparcos H_P) is not

present in the radial velocities[52]. Having removed the first four timescales in the Mt John V_J photometry, the residual photometry (which has a 63-day period) and radial velocity (which has a 63-day period) were compared. The data reach maximum recessional velocity, on average, 150 degrees (26 days) before maximum visual brightness — approximately in anti-phase. This seems to be in reasonable agreement with data taken over JD 2450100–2450350 days (see Figure 4.20), although the photometric variations seem to change from about 60 days to 30 days in length over this interval. A change in photometric timescale from about 60 days to about 30 could explain why a dominant photometric timescale of 44 days was found, although there is insufficient data to tell if a similar thing is occurring in the radial velocities.

- η Scl does not have the same timescales present in Mt John photometry and radial velocity and has too little simultaneous data to indicate the phase relationship, if any (see Figure 4.20).

- γ Cru does not have the same timescale present in the Mt John photometry and radial velocity when the entire data sets are considered, but when the data subsets shown in the right-hand side of Figure 4.21 were searched **T6** finds a characteristic $\approx$25-day timescale (although not significant in the LSP sense this is the dominant timescale in the Hipparcos and Tycho photometry). For all the data shown in Figure 4.21 to have compatible phase relationships, either the variations are very non-sinusoidal (which is quite possible), or the timescale of the variations is not 25 days but about 14 days (see the figure for a discussion of this). This is not unreasonable as both the Hipparcos photometry and the radial velocities have timescales of about 13 and 16 days present. Hence it is believed the variations plotted in Figure 4.21 are manifestations of these, with **T6** obtaining a slightly longer timescale due to the spectral-window function[53]. In which case, the radial velocity and visual photometry variations for these timescales are in anti-phase.

- L^2 Pup has an approximate 140-day timescale, dominant and significant in all data sets in Table 4.18, not to mention Mt John $(B-V)_J$. The data reach maximum recessional velocity, on average, 58 degrees (23 days) before maximum visual brightness — approximately in phase. However, the two data subsets shown in Figure 4.22 while approximately in phase, both have the radial velocity lagging the luminosity by 75 degrees (29 days). This discrepancy is puzzling and could indicate that the phase relationship between radial velocity and visual magnitude is changing with time. Despite the consistency of the phase relationship, when the individual data subsets are considered something is certainly changing — at about JD 2449440 days maximum luminosity corresponds to minimum radial velocity, but at about JD 2450260 days minimum radial velocity occurs about 50 days before maximum luminosity. Clearly the application of the Barnes-Evans method to determine the stellar diameter will be interesting in clarifying the relationship between radial velocity and visual magnitude for this star. Unfortunately, however, appropriate colours are not available for the earlier photometry.

  Interestingly, during an oral presentation at the RASNZ annual conference in 1998, Walker [174] indicated that he had continued to observe this star (for a discussion of earlier observations see Walker et al. [175]) and now found a secondary timescale of about 440 days, in addition to the dominant 139-day timescale. The secondary timescale in the radial velocities is of 435 days and while this was not observed in the concurrent Mt John visual photometry, a similar timescale is present (after significant prewhitening) in $(B-V)_J$.

[52]There is no sign of the tertiary 88-day radial-velocity timescale being present in the Mt John V_J, so it is doubtful that the 44-day timescale is a higher harmonic of the radial velocities' 88-day timescale

[53]There is no sign of the 25-day timescale in the periodogram for γ Cru's full radial velocities data set (see the right-hand side of Figure B.12), so it is doubtful that the 13-day timescale is a higher harmonic of a non-sinusoidal 25-day variation

It is possible that the ≈1000-day timescale found in the Mt John V_J and $(B-V)_J$ is related to this and the spectral-window function.

When the data subsets shown in Figure 4.22 are searched by **T6** for periods, another two characteristic timescales are found (although they are generally not significant in the LSP sense). These are of ≈55 and 67 days in length with a phase shift of 61 and -173 degrees respectively. These were obtained by prewhitening and are in addition to a strong dominant characteristic timescale, so it is difficult to verify the reality of these phase shifts. As none of these timescales are significant in the LSP sense (except for one data set's 62-day timescale, which could be a higher harmonic of the 141-day variation) or present in the full data sets, these timescales will be considered no further.

- o^1 CMa has a significant timescale of about 200 days present in all data sets in Table 4.18, not to mention in the Mt John $(R-I)_C$. The data reach maximum recessional velocity, on average, 108 degrees (52 days) before maximum visual brightness. This seems to be in reasonable agreement with data taken over JD 2450100–2450550 days, although the photometry has about twice the number of minima as the radial velocities (see Figure 4.23).

- π Pup has a significant timescale of about 36 days present in the radial velocities and photometry obtained at Mt John, but not in the Hipparcos and Tycho data. Having removed the dominant 1250-day timescale in radial velocity by prewhitening, the residual radial velocities (which have a 37-day period) were compared to the residual Mt John V_J photometry (which has a 34-day period) after its 625 and 109 day timescales had been removed. The data reach maximum visual brightness, on average, 38 degrees (4 days) before maximum recessional velocity. With so little simultaneous data it is difficult to say anything for certain, but over JD 2450130–2450160 days this phase relationship seems compatible with that observed (see Figure 4.24).

- τ^4 Eri does not have the same timescales present in Mt John photometry and radial velocity. However, the simultaneous photometry in Figure 4.24 does seem to indicate the radial velocity is in phase with the photometry.

For stars without concurrent photometric and radial-velocity data only a simple comparison of the timescales found using **T6** is possible, unless the time elapsed between the two data sets is much less than any characteristic timescale or the variations are very regular. When this is done the following additional stars (including two for which Mt John photometry was obtained but no similar timescales found) have timescales present in both radial velocity and visual photometry, where only dominant or significant (in the LSP sense) timescales are generally considered:

- 2 Cen has a dominant and significant radial-velocity timescale of ≈520 days. There is a similar tertiary significant timescale present in both its Hipparcos and Tycho visual photometry. The time between these two observation sets is 400 days, which is a large fraction of the characteristic timescale. In addition, the scatter in the Hipparcos data set (due to the other timescales) is too large to allow confirmation of the phase relationship of radial velocity leading luminosity by 67 degrees (94 days), proposed by **T6**, by visual inspection (see Figure 4.25). Hence the phase relationship for this star will be considered to be unknown.

[54] Previously published in Cummings et al. [44]
[55] Previously published in Cummings et al. [43]
[56] See footnote 54, Chapter 4
[57] See footnote 54, Chapter 4
[58] See footnote 54, Chapter 4
[59] As these data subsets have considerably more data points than the average, the default frequency range here generally is as long as two times the "average Nyquist frequency" for the entire data set

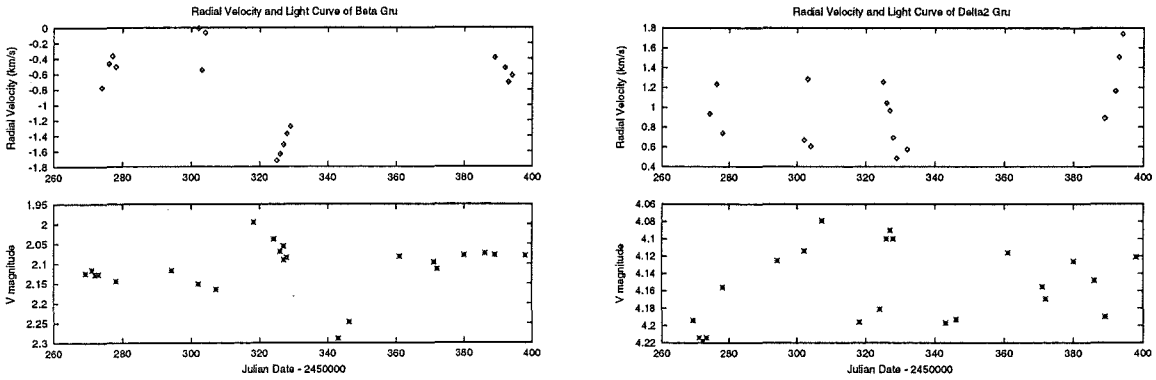

Figure 4.18: On the left-hand side concurrent radial-velocity and visual-photometry data for β Gru are given. At JD $\approx$2450320 days the visual magnitude increases as radial velocity decreases; however, there is too little simultaneous data to conclude anything else. **T6** finds dominant periods of $\approx$70 days, with the radial velocity lagging by 140 degrees (25 days) in these data subsets, although neither period is significant in the LSP sense. On the right-hand side are similar data for δ^2 Gru. There are too few points to know for sure, but the two data subsets may be in phase. **T6** finds a dominant period of 25 days in both data subsets (with radial velocity lagging photometry by only 1 day), but neither is significant (in the LSP sense).

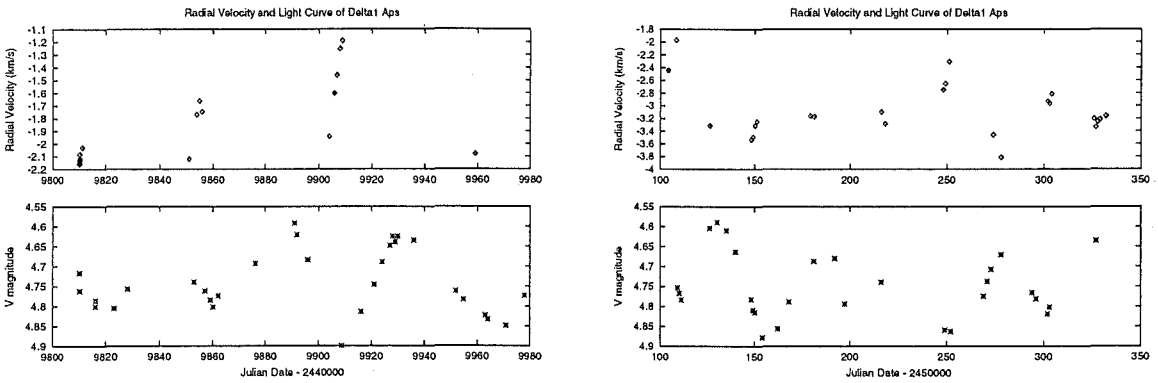

Figure 4.19: These two figures show concurrent radial-velocity and visual-photometric data for δ^1 Aps. On the left-hand side the two data subsets seem to be approximately in anti-phase with the radial velocity reaching a maximum slightly before the light reaches its minimum brightness. On the right-hand side it seems that both data subsets are also in anti-phase. Averaging the 68-day and 51-day dominant periods, **T6** finds to give one of $\approx$60 days in both data sets gives visual brightness lagging the radial velocity by 17 days (118 degrees), which supports the anti-phase relationship indicated by visual inspection (although only the photometric period is significant in the LSP sense).

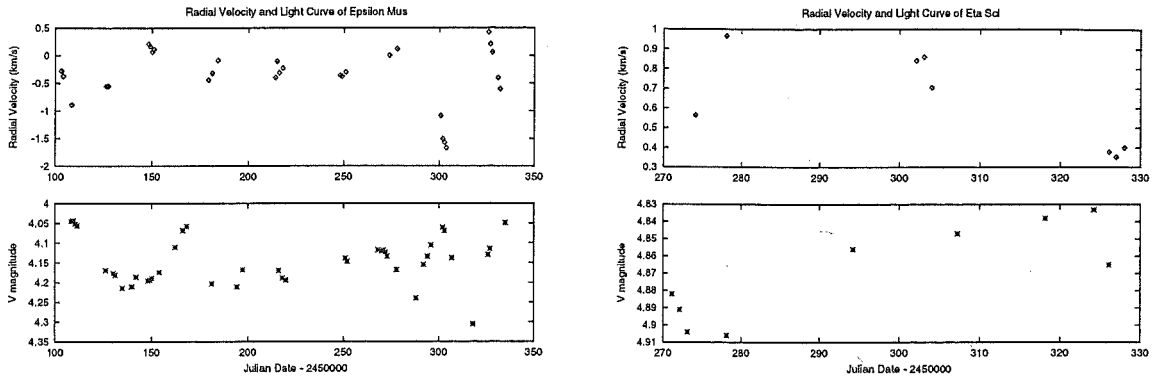

Figure 4.20: On the left-hand side are concurrent radial-velocity and visual-photometry data for ϵ Mus[54]. The two data subsets seem to be in anti-phase, although **T6** finds a dominant, significant, period of 16 days in the velocity and a dominant, but not quite significant period of 32 days in the light. On the right is a similar figure for η Scl which unfortunately has too little simultaneous data to indicate what the phase relationship between light and radial velocity is.

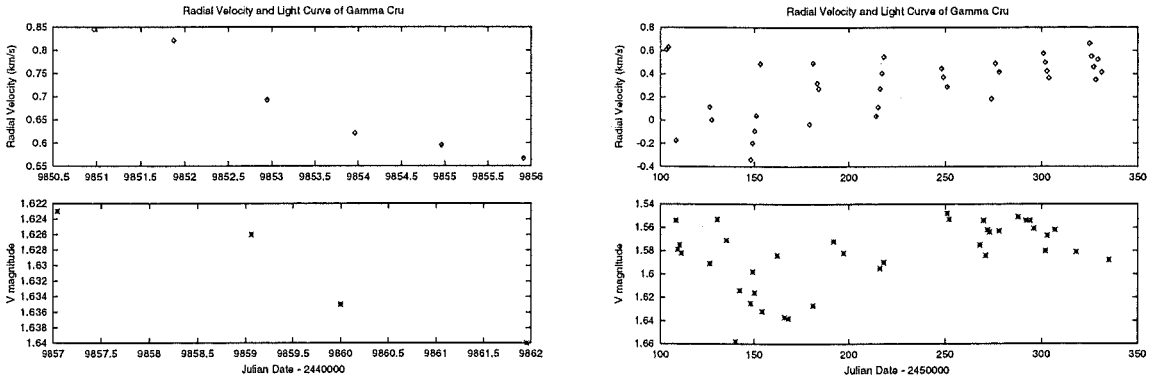

Figure 4.21: These figures show concurrent radial-velocity and visual-photometry data for γ Cru. On the right it is almost impossible to say what the phase relationship is by eye, as there are not enough simultaneous points. However, **T6** finds a dominant period of $\approx$25 days in radial velocity lagging the secondary period in photometry by 7 days/80 degrees (neither of which are significant in the LSP sense). Laying the two data curves in the left-hand figure end-to-end this does not agree with two sine curves with periods of 25 days, if radial velocity is lagging brightness by 7 days. To obtain a 7 day lag requires that either the two curves are very non-sinusoidal or the timescale is not 25 days, but $2 \times 7 = 14$ days.

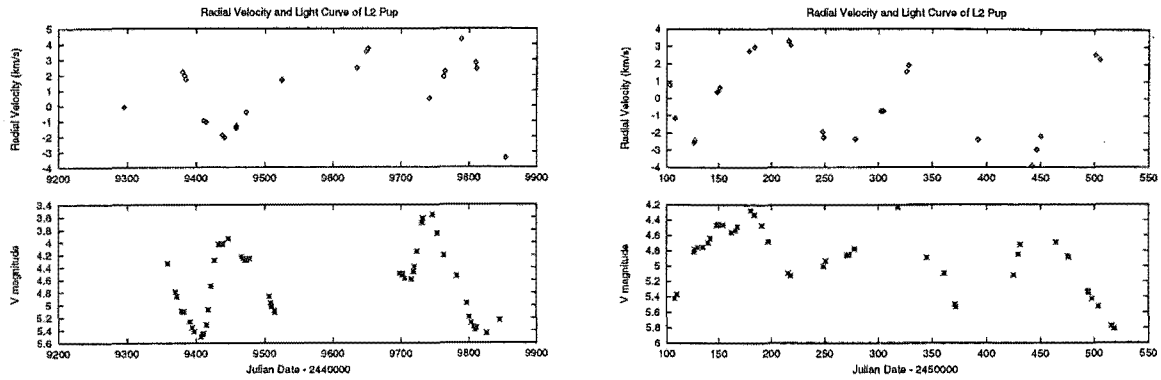

Figure 4.22: These figures show concurrent visual-photometry and radial-velocity data for L^2 Pup. The photometric data to the left were obtained by W.S.G Walker and H.O Williams[55] prior to the commencement of Mt John University Observatory photometry. To the right the observations of light and radial velocities were both obtained at Mt John Observatory[56]. **T6** reveals, as can be seen by eye (considering the minimum luminosity and radial velocity), that both these data subsets have radial velocity lagging visual brightness by about 29 days (75 degrees). This is not in agreement with the phase relationship indicated by the data sets as a whole, even though this is one of the most regularly varying stars observed for this thesis.

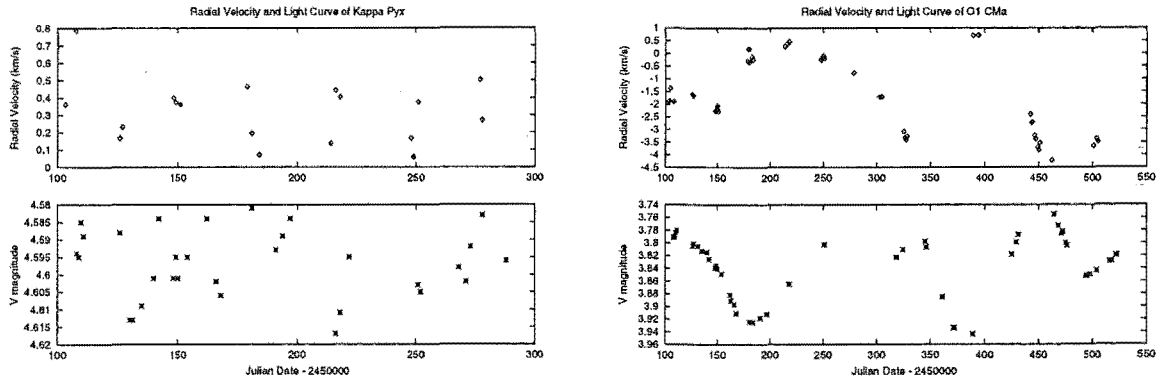

Figure 4.23: On the left-hand side concurrent radial-velocity and visual-photometry data for κ Pyx are given. Unfortunately, there are insufficient simultaneous data to come to any conclusion about the phase relationship between these two observables. To the right are similar data for o^1 CMa[57]. The radial-velocity curve appears to be non-sinusoidal and perhaps slightly non-periodic while the light curve seems to have double the number of minima as the radial-velocity curve. Despite this, visual inspection indicates the two observables are almost in anti-phase. This is confirmed by **T6** which indicates that radial-velocity leads maximum visual brightness by 55 days (108 degrees) for these data subsets.

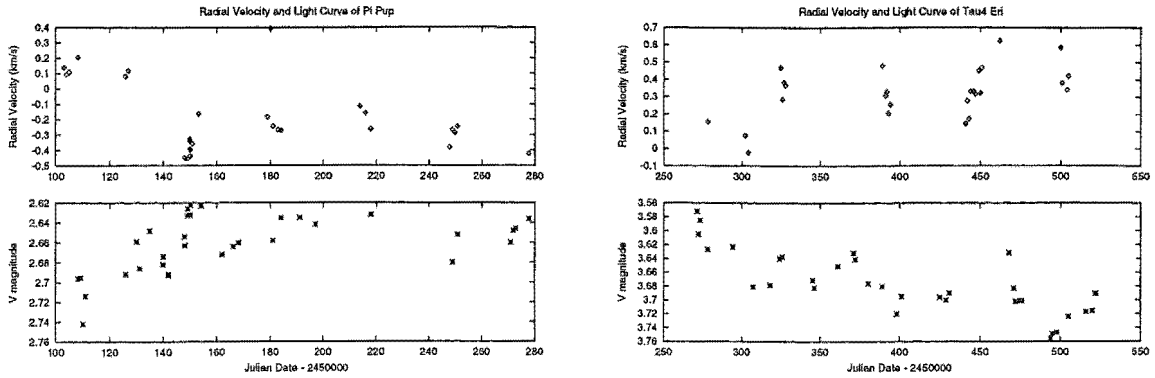

Figure 4.24: On the left-hand side concurrent radial-velocity and visual-photometry data for π Pup are given. The radial-velocity data really are too sparse to say anything for certain, but there does appear a timescale of a few tens of days with the radial velocity lagging the visual brightness slightly. To the right are similar data for τ^4 Eri[58]. For this star the radial velocity seems to be in phase with photometry.

- 62 Sgr has a $\approx$600-day timescale which is dominant and significant in both its radial velocity and Hipparcos visual photometry. There is also a similar secondary significant timescale in its Tycho visual photometry. The time between these two observation sets is 400 days, which is a large fraction of the characteristic timescale. Visual inspection of Figure 4.26 indicates the Hipparcos data is in phase with the radial velocities, which is in agreement with **T6** which finds the radial velocity to be leading the luminosity by 18 degrees (31 days). However, due to the large gap between observation times and not precisely defined minima and maxima, some doubt to the exact phase relationship between the two data sets must remain.

- η^2 Dor has a dominant and significant timescale of $\approx$90 days in all its available photometry. The radial velocity has a similar secondary significant timescale.

- η Scl has the same dominant timescale of 48 days in all its data sets, except for the Mt John photometry (in the radial-velocity case this is not significant in the LSP sense).

- γ Ret has the same dominant and significant timescale of $\approx$880 days in all its existing data sets. As can be seen in Figure 4.27, this is significantly longer than the 200 odd days gap in observations, although the variation is far from regular. **T6** finds the phase relationship between the radial velocity and Hipparcos photometry to be that of luminosity leading radial velocity by 29 degrees (66 days), but visual inspection indicates the minimum in luminosity occurs at about JD 2449000 days and JD 2449450 days in radial velocity, which would imply that these data sets are in anti-phase. This illustrates the problem with relying on the results of a sine fit to non-sinusoidal data!

- λ Vel has a long timescale of $\approx$1100 days, which is dominant and significant in all its data sets. The gap in time between these two data sets is only a fraction of this at about 300 days. **T6** finds the phase relationship between the radial velocity and Hipparcos photometry to be that of radial velocity leading luminosity by 45 degrees (114 days) — approximately in phase. This is not in agreement with the relationship indicated by visual inspection of Figure 4.28, which clearly shows the observables are approximately in anti-phase. In this case the estimation using **T6** is wrong because the period it found for the photometry was shorter than the radial velocity, due to the difference in observation window size. Just as for γ Ret, this illustrates how important it is to verify phase relationships by eye whenever possible.

Star	Obs. range	N	$\mathcal{P}$ (days)	(LSP, σ_{N-1})
β Gru(rv)	0274–0394	16	82	(1.7E-02,0.549)
β Gru(mag)	0269–0398	23	63	(1.0E-01,0.063)
δ^1 Aps(rv)	9810–9993	17	208	(6.0E-02,0.333)
δ^1 Aps(mag)	9810–9978	30	47, 67	(3.1E-03,0.079),(1.5E-02,0.045)
δ^1 Aps(rv)	0104–0332	24	68	(2.2E-02,0.418)
δ^1 Aps(mag)	0109–0327	28	51, 101, 43	(1.0E-03,0.082),(6.2E-03,0.038),(3.0E-02,0.024)
δ^2 Gru(rv)	0274–0394	16	25	(9.8E-02,0.358)
δ^2 Gru(mag)	0269–0398	22	24	(2.8E-02,0.045)
ϵ Mus(rv)	0103–0332	30	16, 114	(3.7E-03,0.529),(3.0E-01,0.312)
ϵ Mus(mag)	0108–0335	42	32	(1.1E-02,0.060)
η Scl(rv)	0274–0328	8	20	(2.2E-01,0.243)
η Scl(mag)	0271–0326	9	74	(2.5E-01,0.028)
γ Cru(rv)	9851–9856	6	9	(3.7E-01,0.118)
γ Cru(mag)	9857–9862	4	7	(5.3E-01,0.008)
γ Cru(rv)	0103–0331	35	21	(6.0E-02,0.260)
γ Cru(mag)	0108–0335	38	204, 31	(1.0E-03,0.029),(3.1E-01,0.019)
κ Pyx(rv)	0103–0278	18	62	(5.0E-01,0.179)
κ Pyx(mag)	0099–0288	32	17	(5.0E-02,0.010)
L^2 Pup(rv)	9295–9854	23	141, 76	(1.8E-03,2.155),(2.4E-01,0.829)
L^2 Pup(mag)	9358–9845	57	141, 62, 370	(1.1E-08,0.552),(1.3E-04,0.238),(2.0E-02,0.175)
L^2 Pup(rv)	0103–0505	24	156, 52	(4.9E-03,2.276),(2.1E-02,1.119)
L^2 Pup(mag)	0108–0518	44	141, 500, 58	(3.1E-06,0.402),(3.0E-04,0.196),(3.7E-02,0.129)
o^1 CMa(rv)	0103–0505	47	175, 526, 149, 96, 35	(4.6E-04,1.431),(3.0E-04,0.932),(3.0E-03,0.635),(2.0E-03,0.484),(1.4E-02,0.354)
o^1 CMa(mag)	0108–0522	48	182, 102, 61	(1.5E-06,0.050),(9.4E-05,0.026),(5.5E-02,0.017)
π Pup(rv)	0103–0278	28	60	(2.4E-02,0.230)
π Pup(mag)	0108–0278	33	17	(1.1E-02,0.029)
τ^4 Eri(rv)	0278–0505	26	122, 120	(3.3E-03,0.148),(1.5E-02,0.117)
τ^4 Eri(mag)	0271–0522	33	500, 47	(2.3E-03,0.045),(4.5E-02,0.029)

Table 4.19: **Period search on concurrent subsets of visual photometry and radial velocities.** This table gives the results of using **T6** to search for timescales in subsets of the Mt John V_J photometry (mag) and radial velocities (rv) when the default range of frequencies[59] were considered at intervals of 0.0001 days^{-1}. N is the number of data points, LSP is the Lomb-Scargle probability of the timescale and σ_{N-1} is the $N-1$ standard deviation of the data (before that timescale's removal by prewhitening). The last timescale in the data subset is not significant (in the LSP sense).

- N Vel has a dominant and significant timescale of ≈600 days in its radial velocity and a ≈600-day tertiary significant timescale which may be related in its Hipparcos visual photometry. The time between these two observation sets is 300 days, which is quite a large fraction of the characteristic timescale. In addition, the scatter in the Hipparcos data set (possibly due to the other timescales) is too large to allow confirmation of the phase relationship of luminosity leading radial velocity by 167 degrees (244 days), proposed by **T6**, by visual inspection (see Figure 4.29). Hence as for 2 Cen the phase relationship for this star will be considered to be unknown.

- NS Pup has the same dominant and significant timescale of 1429 days present in its radial velocity and Hipparcos visual photometry. The gap in time between these two data sets is only a small fraction of this at about 200 days. **T6** finds the phase relationship between the radial velocity and Hipparcos photometry to be that of radial velocity leading luminosity by 132 degrees (523 days) — approximately in anti-phase. Despite the large scatter in the Hipparcos data points this can be verified by consideration of Figure 4.30, the minimum in luminosity occurs at about 2448750 days which is 800 ahead of the minimum in radial velocity at JD 24495500 days.

- σ CMa has a dominant and significant timescale present in both its Hipparcos visual photometry and radial velocity, which is comparable to the the length of time for which observations were obtained. Hence this characteristic 1250-day timescale is much longer than the approximately 400 day gap in observations. **T6** finds the phase relationship between the radial velocity and Hipparcos photometry to be that of luminosity leading radial velocity by 153 degrees (530 days) — approximately in anti-phase. This can be verified by consideration of Figure 4.31, the maximum in luminosity clearly occurs at about 2448650 days which is 550 ahead of the maximum in radial velocity at JD 2449200 days.

- σ Lib has a dominant and significant Hipparcos timescale of ≈90 days and a similar tertiary, but not significant timescale in radial-velocity.

- τ^4 Eri has a secondary timescale of ≈29 days present in all its data sets, except for the Mt John photometry. This timescale is significant in all but the Tycho data.

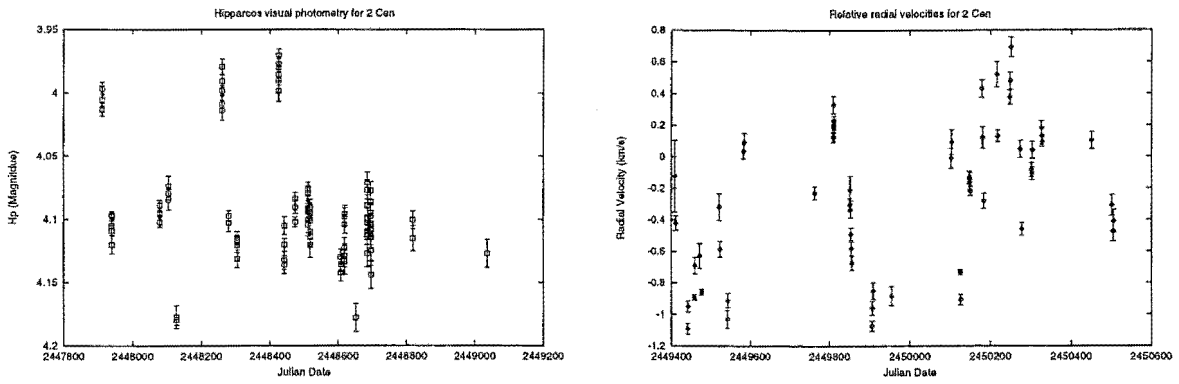

Figure 4.25: The Hipparcos photometry and radial velocities for 2 Cen. This star has a dominant and significant radial velocity timescale of ≈520 days and a similar tertiary significant timescale present its Hipparcos photometry. **T6** finds the phase relationship between the radial velocity and Hipparcos photometry to be that of radial velocity leading luminosity by 67 degrees (94 days). The other timescale in the Hipparcos data obscures the presence of this characteristic timescale, so no comment on the reality of this phase relation will be made.

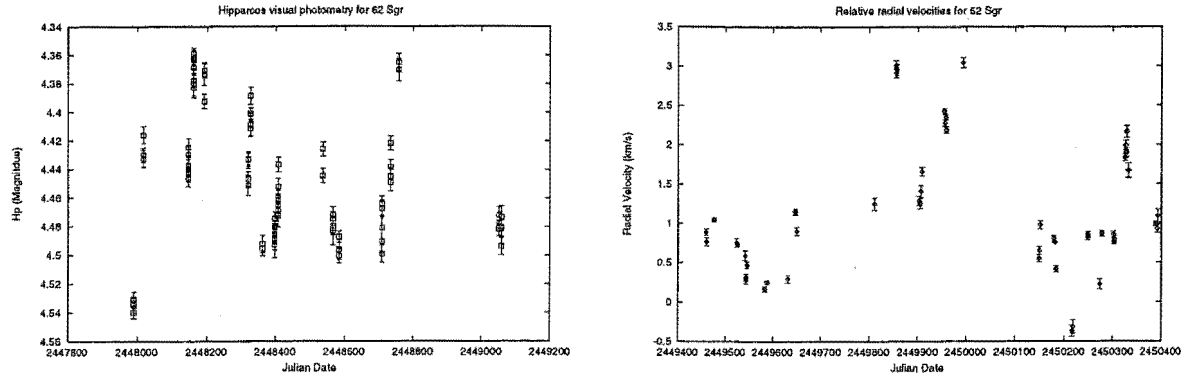

Figure 4.26: The Hipparcos photometry and radial velocities for 62 Sgr. This star has a ≈600-day timescale which is dominant and significant in both these data sets. **T6** finds the phase relationship between the radial velocity and Hipparcos photometry to be that of radial velocity leading luminosity by 18 degrees (31 days) — approximately in phase. By eye the maxima in luminosity seem to be at 2448175 and 2448775 days and minima in radial velocity at JD 2449625 and JD 2450225 days. This implies the next maximum luminosity will be at about JD 2449375 days, which is approximately in phase. However, due to the erratic nature of the two data sets there are questions on the exact location of the minima/maxima and therefore on the exact phase relationship between the two.

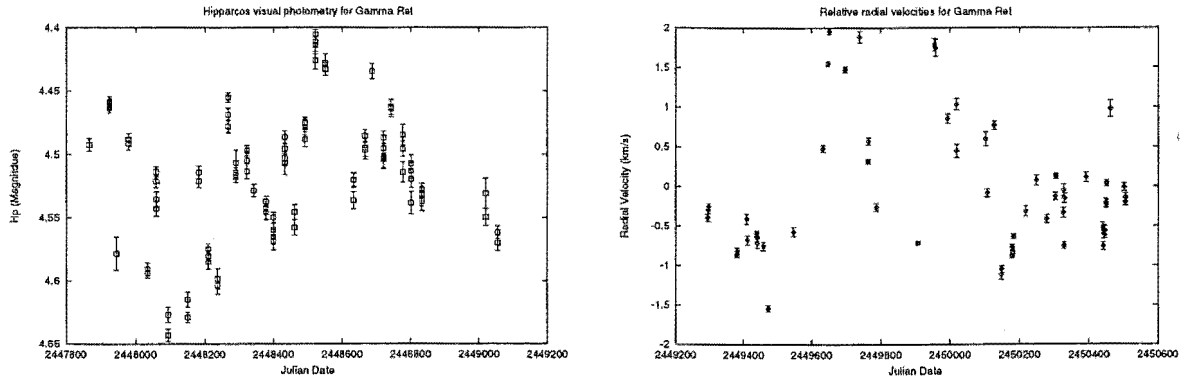

Figure 4.27: The Hipparcos photometry and radial velocities for γ Ret. This star has the same dominant and significant timescale of ≈880 days in both these data sets. **T6** finds the phase relationship between the radial velocity and Hipparcos photometry to be that of luminosity leading radial velocity by 29 degrees (66 days) — approximately in phase. However, by eye these data sets appear to be in anti-phase.

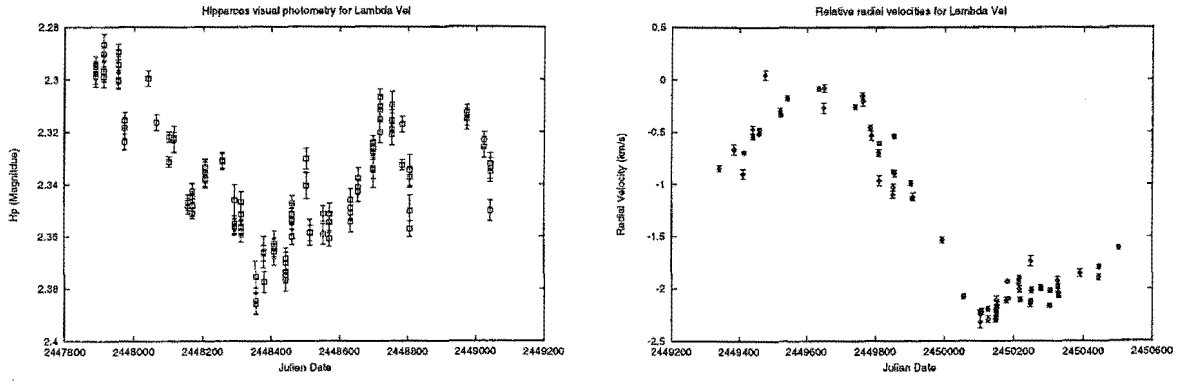

Figure 4.28: The Hipparcos photometry and radial velocities for λ Vel. This star has a long timescale of $\approx$1100 days which is dominant and significant in both these data sets. **T6** finds the phase relationship between the radial velocity and Hipparcos photometry to be that of radial velocity leading luminosity by 45 degrees (114 days) — approximately in phase. But by eye these data sets seem to be in anti-phase — a fact confirmed by the minimum luminosity being at 2448400 days and maximum radial velocity at JD 2449500 days.

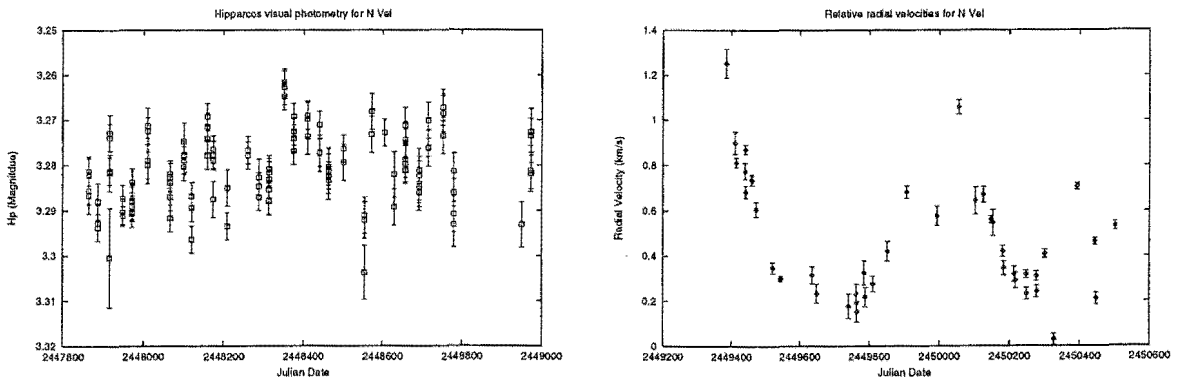

Figure 4.29: The Hipparcos photometry and radial velocities for N Vel. This star has a dominant and significant timescale of 625 days in its radial velocity and a tertiary significant timescale of 526 days which may be related in its Hipparcos visual photometry. **T6** finds the phase relationship between the radial velocity and Hipparcos photometry to be that of luminosity leading radial velocity by 167 degrees (244-days) — approximately in anti-phase. However, the presence this timescale is not clearly visible in the Hipparcos data so no comment on the reality of this phase relation will be made.

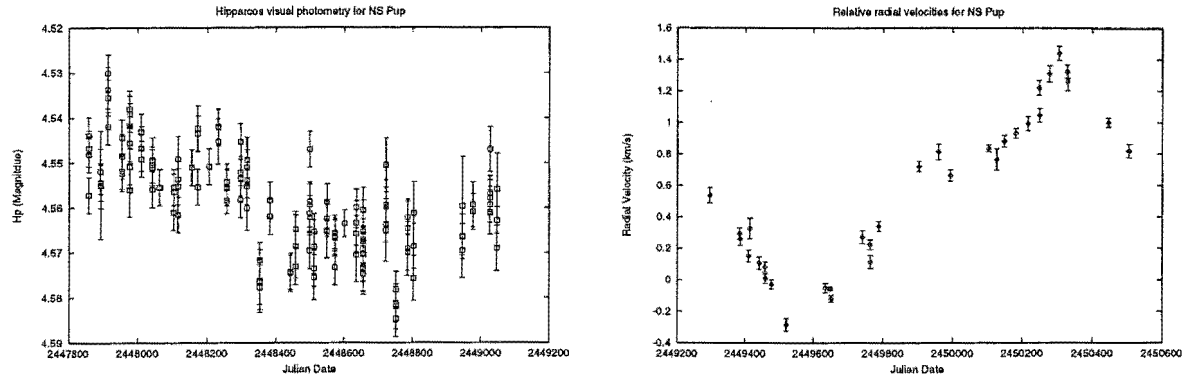

Figure 4.30: The Hipparcos photometry and radial velocities for NS Pup. This star has the same dominant and significant timescale of 1429 days present in both these data sets. **T6** finds the phase relationship between the radial velocity and Hipparcos photometry to be that of radial velocity leading luminosity by 132 degrees (523 days) — approximately in anti-phase. This agrees with these figures where the minimum luminosity occurs about 800 days ahead of minimum radial velocity.

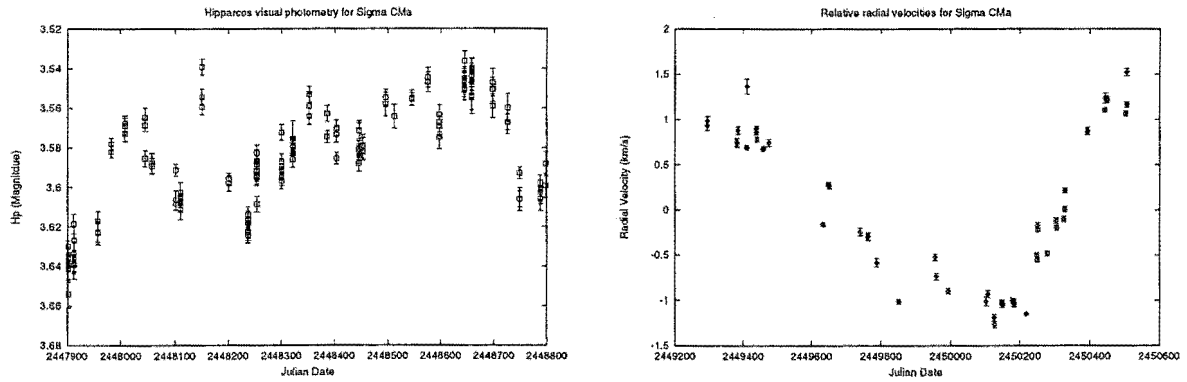

Figure 4.31: The Hipparcos photometry and radial velocities for σ CMa. This star has a dominant and significant timescale present in both in both these data sets which is comparable to the the length of time for which observations were obtained. **T6** finds the phase relationship between the radial velocity and Hipparcos photometry to be that of luminosity leading radial velocity by 153 degrees (530 days) — approximately in anti-phase. This agrees with these figures where the maximum luminosity occurs about 550 days ahead of maximum radial velocity.

4.6.2 Calculation of angular diameter from photometry

A well known method for determining the radius of stars is the Baade-Wesselink method. Following this if simultaneous photometric (magnitude and one colour) and radial-velocity measurements are available it is possible to obtain the radius of the star as a function of time. It is necessary to have enough photometric data that times of the same colour can be found (the same colour is assumed to mean the same surface flux[60]) and enough radial-velocity data that integration of the radial velocity between the two times is possible. Hence a very large amount of concurrent data is needed for stars which have variations which are not perfectly regular. Unfortunately, enough data is not available to do this for the 13 stars observed at Mt John. However, there is an important variation of this method known as the Barnes-Evans method which can be used to obtain angular diameters of stars, which can then be compared to the radial velocities obtained over the same range of time. This method and its assumptions will now be described in detail.

In 1969 Wesselink [176] used observations of 18 stars, of a variety of spectral and luminosity types, to determine a relation between the surface brightness of the star and the unreddened colour $(B-V)^0_{\rm J}$. Surface brightness was found from $s_V = V^0_{\rm J} + 5\log(\phi)$, where ϕ is the angular diameter, and plotted against $(B-V)^0_{\rm J}$. The resulting graph showed quite a good slowly varying correlation. In 1976 Barnes and Evans [11] followed this idea and determined a surface brightness related function, $F_V = 4.2207 - 0.1V^0_{\rm J} - 0.5\log(\phi)$, using the recently found angular diameters for cooler stars. They also determined F_V as a function of several different Johnson colours. As a result of this they determined that

- $(B-V)^0_{\rm J}$ ceases to be a significant index of energy distribution in very cool stars
- $(U-B)^0_{\rm J}$ is even worse
- $(R-I)^0_{\rm J}$ is much better and it is possible to do piecewise linear fits for stars cooler than the Sun using only two segments, but the scatter about the two lines can not wholly be attributed to observational error
- $(V-R)^0_{\rm J}$ is similarly a tight correlation that can be fitted with two straight lines. It is such a tight correlation, in fact, that the residuals can wholly be attributed to observational error!

After further investigation of this useful empirical relation (see Barnes & Evans [12, 13] and Barnes [9]) the redder colour relations were refined to

$$\begin{aligned} F_V &= 3.973 - 0.783(R-I)^0_{\rm J} && -0.32 \geq (R-I)^0_{\rm J} \leq 0.42 \\ &= 3.793 - 0.356(R-I)^0_{\rm J} && 0.42 \geq (R-I)^0_{\rm J} \geq 3.25 \\ &= 3.957 - 0.360(V-R)^0_{\rm J} && (V-R)^0_{\rm J} \leq 0.80 \\ &= 3.841 - 0.321(V-R)^0_{\rm J} && (V-R)^0_{\rm J} \geq 0.80. \end{aligned}$$

The $(V-R)^0_{\rm J}$ relations fit all luminosity classes equally well, but the goodness of fit for $(R-I)^0_{\rm J}$ depends on surface gravity. Hence Barnes & Evans concluded that $(V-R)^0_{\rm J}$ is the best indicator of surface brightness for all luminosity classes and their relations can be applied to a wide range of Spectral Types, O4–M8, S and C. They also noted that extinction effects should have little effect on the determination of angular diameters, as effects on colour and the visual magnitude tend to

[60] So the difference between the observed magnitude of the star must be entirely due to the difference in radius. It should be noted that if the bolometric correction can be taken to be the same at both times (the bolometric correction can be considered to be a function of colour alone, see §4.5) then the effective temperatures must be the same at both times as $(R_1/R_2)^2 = 10^{(-V_1/2.5)}/10^{(-V_2/2.5)} = L_{\rm bol_1}/L_{\rm bol_2}$ (because $M_V = -2.5\log(f_V R^2) + \text{const.}$) and $L_{\rm bol} = 2\pi\sigma R^2 T^4_{\rm eff}$.

cancel out. But the most interesting thing of all is the conjecture that "*variable stars during their cycles of variation continue to obey the* $(F_V, V-R)$ *relation*". This is based on the fact that the observed star set contains a variety of variable stars at random phases. Comparison of photometry and integrated velocity curves for the Cepheid star δ Cep in the second paper in their series and the paper Barnes et al. [10] seems to support this hypothesis.

However, this statement certainly is not true of general non-radial pulsation. This can be seen by considering (Unno et al. [167] §6.4) a non-radial pulsation of spherical harmonic order $l = 2$. It is possible for this to have the maximum expansion of the observed stellar disc at maximum compression along the line of sight. This means the recessional radial velocity is becoming negative (with respect to the centre-of-mass) as the stellar disc is becoming larger, just the opposite of what happens in the radial case. This leads to the radial velocity and diameter estimations being in disagreement. Hence this method only can be applied to radially pulsating stars. For examples of this failure for non-radially pulsating stars see Walker [173, 172].

So the angular diameters obtained should be consistent with the radial velocities unless the star is non-radially pulsating. However, there are some kinds of variable stars which are not intended to be included in the conjecture. For example, although it is possible for these mechanisms to cause variations in both colour and visual magnitude, it is unclear how starspots, starpatches and large-scale macro-turbulent variations would affect the angular diameters obtained and doubtful that any such variations in angular diameter would necessarily correspond to radial-velocity variations from spectroscopy obtained at the same time. For the sake of clarity the conjecture will now be restated: "*radially pulsating stars during their cycles of variation continue to obey the* $(F_V, V-R)$ *relation*".

In addition, there are some inherent assumptions in the Barnes-Evans method and if these assumptions are false these empirical relationships may well not hold. Just like the Baade-Wesselink method the Barnes-Evans method was developed with the following assumptions in mind:

(i) that visual surface brightness is a function solely of a specified colour index

(ii) if comparison to radial velocities is desired then the radial velocity curves must represent the pulsation of where the photospheric continuum is located.

Problems can arise with both these assumptions. It should be recalled, from §2.3.4, that in Mira variables the radial-velocity behaviour of the blue-visual spectra is not that of the photosphere. Such an effect would cause havoc with comparison of angular diameters predicted from photometry using the Barnes-Evans method and blue-visual Mira radial velocities. Even if shock waves are not involved, the separation of pulsating stars' reversing layer (where atomic lines are formed) and their photosphere may not remain constant, due to the effects of variable effective gravity and variable opacity (see Abt [1]). The assumption of a unique (F_V, colour) relation can also be violated. According to Abt [1] the following things can cause a colour variation not corresponding to its effective temperature variation:

(a) Too much colour in one filter. Shock waves can do this and cause the star RR Lyrae to have a systematic excess of ultraviolet radiation with phase of pulsation.

(b) Extreme sensitivity of continuous opacity to electron pressure or effective gravity.

(c) Unusual line blanketing[61].

[61] Line blanketing and line blocking are related to the distorting effect of absorption lines. In the case of line blocking, absorption lines remove flux from photometric filters and as a result the colours obtained for the star are distorted. Line blanketing is not unrelated and this term is often used to describe line-blocking effects. It can be

The last of these undesirable features is discussed in quite some detail by Schmidt [147]. If every effective temperature has a set line blanketing then this is not really a problem — a unique (F_V, colour) relation will still exist. However differential line-blocking (due to unusual turbulent velocity and gravity changes) can occur, which would mean that the same temperature may not have the same colour and therefore phases of equal colour are not necessarily phases of equal surface brightness[62]! One interesting thing to note at this stage is that the redder the spectrum the less line blanketing effects and therefore the less of a problem (c) will be (see pages 350 & 362 of Schmidt [147]). The significance of this will soon become apparent.

Angular diameters for the 13 Mt John stars

The Barnes-Evans technique for determining angular diameter from $(V-R)^0_J$ and $(R-I)^0_J$ were applied to the Mt John photometry, after using Taylor's [164] transformations to get from Cousins colours to quasi-Johnson colours. The quasi-Johnson system has the same scale and Balmer-jump properties of the Johnson system, but data has a higher precision than data native to the Johnson system. It is also missing the systematic variation with right ascension present in Johnson transformations, which is assumed to be due to a systematic error in the Johnson data (see Taylor [164] for more details). The transformation equations are

$$\begin{aligned}
(R-I)_{QJ} &= 1.313(R-I)_C - 0.099 && 0.079 \geq (R-I)_C \leq 0.531 \\
&= 1.070(R-I)_C + 0.030 && 0.531 \geq (R-I)_C \leq 1.40 \\
(V-R)_{QJ} &= 1.394(V-R)_C + 0.027 && -0.165 \geq (V-R)_C \leq 0.805 \\
&= 1.80(V-R)_C - 0.30 && 0.805 \geq (V-R)_C \leq 1.10.
\end{aligned}$$

Strictly speaking these should not be applied to red supergiants, because no such stars were used in the equations' determination. Also for some of the reddest stars the redder of the transformations have been applied even though the Cousins colour limits were exceeded[63]. No interstellar extinction corrections were attempted due to the proximity of the stars, the intrinsic difficulty of determining the correction amount and as extinction effects have little effect on angular diameter determinations anyway.

The resulting angular diameters were then compared to the radial velocities observed concurrently, with surprising results. For the star with the largest and most regular angular-diameter variations, L^2 Pup, the angular diameters obtained using the $(V-R)$ colours were not compatible with the radial velocities, while those obtained from the $(R-I)$ colours behave exactly as would be expected from the radial velocities (see Figure 4.32). It should be noted that for radial velocity and angular diameter to be "in agreement", maximum angular diameter should correspond to zero radial velocity (in the centre-of-mass frame of the star) with radial velocity about to become positive (in the centre-of-mass frame of the star). Similarly, minimum angular diameter should have radial velocity

---

used specifically to mean when the presence of absorption lines takes flux away from the continuum spectrum and causes the Planck curve (blackbody spectral-energy distribution) fitted to the flux, as a function of wavelength, to have its fitted peak shifted from the real value. Then the Planck temperature given by the peak of the fitted curve (by $\lambda_{max}T = 2.898 \times 10^{-3}$m.K), will not be the same as the Planck temperature of the underlying continuum, the real Planck temperature. As Abt uses line blanketing here to mean colour differences no real distinction between the two will be made in this thesis.

[62] From Wesselink [176] and Barnes & Evans first paper [11] $F_V = \log(T_{\rm eff}) + 0.1BC = \text{const.} - 0.1s_V$. Assuming BC to be constant if the colour is constant then if the temperature is different the surface flux must also be.

[63] In practice I have not found this to make a large difference to the shape of the angular-diameter curves but a bad transformation does alter the average angle diameter dramatically. It all depends on which is in error — the slope of the transformation or the zero point. The slope will effect more the variation shape and the zero point the magnitude of the angle. To see this let $C_J = \alpha C_C + \beta$ and $F_V = \delta C_J + \kappa$. Hence the angular diameter is $\phi = 10^{(2(4.2207-\kappa-\delta\beta))} \times 10^{(2(-\delta\alpha C_C - 0.1V_J))}$ and the important thing for determining the shape of the angular variation is the changes in $\delta\alpha C_C + 0.1V_J$!

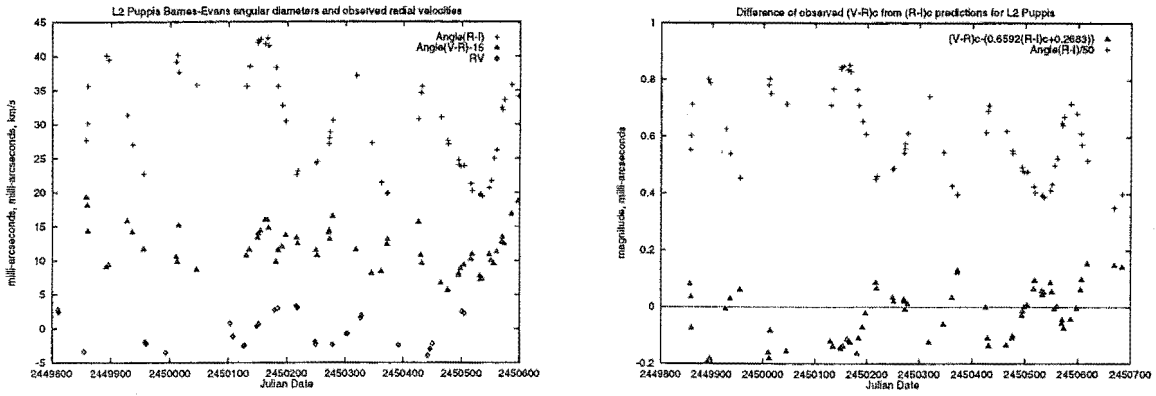

Figure 4.32: On the left are the angular-diameter variations from use of the Barnes-Evans method with $(V-R)$ and $(R-I)$. The resulting variations from the former clearly are not in agreement with radial velocities obtained over the same time range. On the right this situation is examined further by considering how $(V-R)_{\rm C}$ differs from the value predicted from $(R-I)_{\rm C}$ (using $F_V = 3.793 - 0.356(R-I)_{\rm J}$ and $F_V = 3.841 - 0.321(V-R)_{\rm J}$ to get $(V-R)$ in terms of $(R-I)$).

that is "zero" and about to become "negative".

The Barnes-Evans relations for these two colours imply there is a linear relationship between them, but clearly for L^2 Pup this is not the case. Assuming $(R-I)$ is giving the correct surface flux, as it gives angular diameters compatible with the radial velocities and comparing the value of $(V-R)$ predicted with that actually observed (see Figure 4.32), it immediately becomes obvious that the maximum deviation of $(V-R)$ from the surface flux relation occurs at maximum/minimum angular diameter. Such regular deviations from the Barnes-Evans linear $(F_V, V-R)$ relation are not unknown (see for example Hawley, Barnes & Moffett [77] and Burki & Meylan [30] for such an effect in RR Lyrae stars) and given the much better predictions of the $(F_V, R-I)$ relation, it is probable that the failure of the $(F_V, V-R)$ relation is due to some line-blanketing affect. Hence for the 13 Mt John stars the $(F_V, R-I)$ relation has been used to determine angular diameters rather than Barnes-Evans preferred choice of $(V-R)$.

The results determining angular diameter from $(R-I)$ are given in Table 4.20. A few things are immediately obvious. The redder stars seem to be up to a factor of two larger in average angular diameter than that predicted by using Hipparcos distances and the radii predicted from the positions of the stars in the HR Diagram[64] (the program **hr_diag** is used to determine this — for further details see §4.5.1). As this is only for the redder stars this has been put down to either the errors in the Mt John transformations to the standard colours (as discussed in §4.3), or the equations used to transform from Cousins to Johnson systems being inappropriate. Again the consistent behaviour of the very red star L^2 Pup is taken as a sign that only the magnitude of the angular diameters is being affected, not the shape of the variations.

Comparison of radial velocities and angular diameters found from photometry suffers from a lack of simultaneous data of sufficient frequency and despite clear variations in photometry, κ Pyx, o^1 CMa and τ^4 Eri did not have conclusive variations in angular diameter. However, the following things are apparent for these 13 stars where Table 4.4, Table 4.19 and Table 4.20 have been used to compare the timescales of the two data sets.

- β Gru has significant[65] variations in angular diameter with a dominant (but not significant

[64] This is true regardless of whether $(R-I)$ or $(V-R)$ is used to determine the angular diameters

[65] Variations are probably significant at the 1% level if $F_{\rm AD}[N-1, N-1] \geq 2.2$. However, as both degrees of freedom

Star	N	A_e (m arcsec.)	Mean (m arcsec.)	$F_{\rm AD}$ [N–1, N–1]	$\mathcal{P}$ (days)	(LSP, σ_{N-1})
β Gru	60	22.8±0.9	44.2±0.6	6.76	56	(1.2E-01,1.656)
check	60		1.67±0.02	1.00	88	(7.6E-01,0.023)
δ^1 Aps	66	7 ±1	13.3±0.2	5.02	476, 49	(1.6E-06,0.480),(1.7E-02,0.330)
check	66		2.65±0.04	1.01	50	(2.7E-01,0.043)
δ^2 Gru	58	8.1 ±0.9	13.8±0.2	3.61	286	(8.4E-02,0.378)
check	60		1.67±0.02	1.00	88	(7.6E-01,0.023)
ϵ Col	63	2.8 ±0.1	3.22±0.07	0.49	161	(7.2E-01,0.050)
check	63		0.98±0.02	1.21	45	(5.5E-01,0.019)
ϵ Mus	94	10.9±0.5	19.8±0.4	2.89	385, 44	(1.1E-06,0.671),(4.5E-02,0.520)
check	95		1.07±0.03	1.00	38	(3.2E-01,0.026)
η Scl	42	5.1 ±0.6	8.0±0.1	3.15	1429	(3.7E-02,0.184)
star 5	42		1.02±0.01	1.12	400	(7.2E-01,0.014)
γ Cru	93	23.7±0.4	37.4±0.5	9.00	385, 169, 86	(3.7E-09,1.643),(1.2E-05,1.120),(1.1E-01,0.901)
check	84		2.20±0.03	1.00	1000	(2.5E-02,0.031)
κ Pyx	52	3.4 ±0.4	3.73±0.07	1.69	417	(2.5E-02,0.087)
check	52		0.97±0.02	0.81	44	(8.1E-01,0.020)
L^2 Pup	66	16 ±1	29.9±0.8	90.25	141,1111, 86, 200, 73	(2.1E-09,7.254),(3.4E-07,3.536),(8.5E-04,2.315),(1.4E-03,1.872),(5.1E-02,1.528)
check	65		1.53±0.04	1.00	49	(5.4E-01,0.039)
o^1 CMa	68	5 ±2	4.51±0.09	1.00	185	(2.8E-02,0.085)
check	68		1.17±0.02	1.00	49	(1.0E-01,0.022)
ω Cap	42	4.6 ±0.8	5.1±0.1	0.61	60	(8.1E-01,0.079)
check	42		0.84±0.02	0.97	49	(6.6E-01,0.020)
π Pup	70	8 ±2	8.3±0.2	2.89	370, 156	(8.5E-05,0.408),(1.4E-01,0.324)
check	70		0.92±0.03	1.00	385	(1.4E-01,0.026)
τ^4 Eri	63	9.3 ±0.7	15.7±0.4	1.44	133	(2.6E-02,0.486)
check	64		0.91±0.03	1.00	42	(2.5E-01,0.028)

Table 4.20: **Period search and F-test values for Barnes-Evans' angular diameters.** This table gives angular diameters determined from Mt John $(R-I)_{\rm C}$ photometry and the Barnes-Evans method. The F-test (see §4.2) value is obtained by assuming the error in the photometry is the $N-1$ variance of the check star. Then $\sigma^2_{\rm AD} = {\rm AD}^2(4\delta^2\alpha^2\ln(10)^2\sigma^2_{\rm C_c} + 0.04\ln(10)\sigma^2_{\rm V_c})$ gives the error in the angular diameter, where δ is the slope of the Barnes-Evans relation between F_V and $(R-I)^0_{\rm J}$ colour and α is the slope of the quasi-Johnson transformation between Johnson $(R-I)$ and Cousins. A_e is the angular diameter found by using the Hipparcos parallax and the radii estimated by **hr_diag**, and "Mean" is the average angular diameter from Barnes-Evans. The last timescale tabulated here does not have a significant LSP and only OC telescope data has been used.

in the LSP sense) timescale of 58 days. This is the same as the secondary timescale present in the radial velocities and is the star's characteristic timescale. The variations in angular diameter may be in agreement with the radial velocities, but more concurrent data are needed to verify this (see Figure 4.33 for a comparison plot of radial velocities and angular diameters).

- δ^1 Aps has a significant variation in angular diameter at the 1% level, although only just. Its dominate timescale of $\approx$476 days is equal to the secondary timescale present in the radial-velocities. However, the relationship between radial velocity and angular diameters for this long-term trend is not compatible with that of a radial pulsation (see Figure 4.34). However, the much shorter-term variations may well be in agreement. Clearly more (and better quality photometric) concurrent data are needed to verify this.

- δ^2 Gru has a significant variation in angular diameter at the 1% level. However, the timescales of angular diameter and radial velocity do not seem to be connected. There are too little data for Figure 4.33 to shed any light on the situation.

- For both ϵ Col and ω Cap the timescales in radial velocity and angular diameter are unrelated. Nor does Figure 4.35 seem to reveal any obvious correlation between the two for these stars. As would be expected from stars without any significant variations in photometry, the angular diameter variations are not significant at the 1% level.

- ϵ Mus has a significant variation in angular diameter at the 1% level. The 44-day timescale is again present, although the comparison plot of angular diameter and radial velocity (Figure 4.34) does not show any obvious correlation.

- η Scl has a significant variation in angular diameter at the 1% level; however, the timescales of angular diameter and radial velocity do not seem to be connected. Again there are too little data for the comparison plot (Figure 4.36) to shed any light on the situation.

- γ Cru has significant variations in angular diameter, but none of its angular diameter timescales are present in the radial velocity. Figure 4.36 does seems to indicate, however, that the angular diameters and radial velocities are in agreement for the longer term trends.

- κ Pyx's dominant (but not significant in the LSP sense) timescale in the angular diameter variations is comparable with the dominant timescale in the radial-velocity variations, but Figure 4.37 does not seem to reveal any obvious correlation between these quantities. The timescales may well be coincidental, because this star does not have a significant variation in angular diameter at the 1% level.

- L^2 Pup's variations in angular diameter are significant and the dominant 141-day timescale is the same for both angular diameter and radial velocity (this timescale is the star's main characteristic timescale). The radial velocity tertiary timescale may be 4th significant timescale present in the angular diameter's. Comparison of the two curves (Figure 4.37) reveals a tight correlation that nicely illustrates the expected radial velocities for real angular-diameter variations. So despite the observed changes in phase relationship between radial velocity and visual magnitude, at all times for which Mt John OC photometry was obtained L^2 Pup's variations have been consistent with radial pulsation.

- o^1 CMa dominant (although not significant in the LSP sense) 185-day angular diameter timescale is the dominant timescale in the radial velocity and is the star's characteristic timescale. Figure 4.38 also reveals the data behave in a compatible manner. However, the

vary with N, the exact value is highly N dependent and hence an appropriate table, such as Bevington & Robinson [21] C.7, should be consulted (for further details on the F-test see §4.2, for further details on its application to photometry see §4.3).

star's angular-diameter variations are not significant and this means it is not conclusive that a real correlation is present.

- π Pup has significant variations in angular diameter. However, no angular-diameter timescales are present in the radial velocity, nor does Figure 4.38 reveal any related variations.

- τ^4 Eri dominant (but not significant in the LSP sense) angular-diameter timescale is also present as the tertiary (also not significant in the LSP sense) timescale in the star's radial velocities. There is insufficient concurrent data to clarify this (see Figure 4.39) and as this star does not have a significant variation in angular diameter at the 1% level, any similar timescales may well be coincidental.

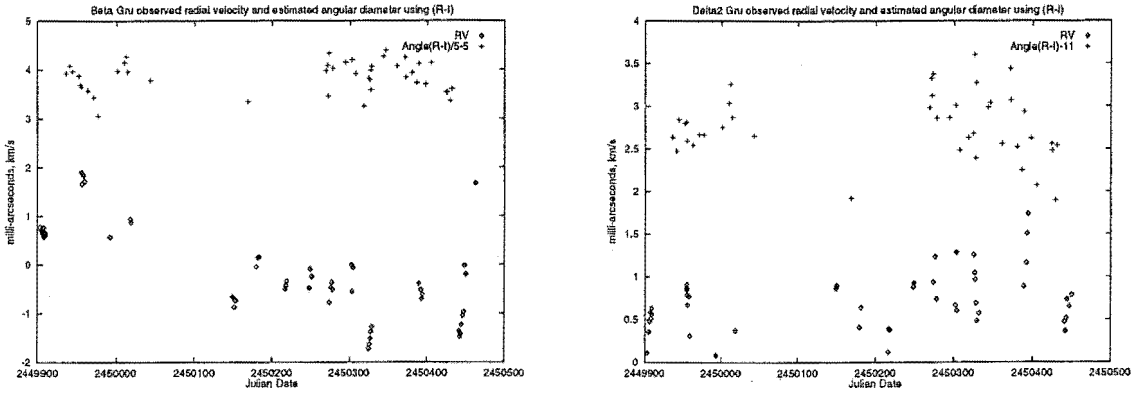

Figure 4.33: Angular-diameter variations using the Barnes-Evans method with $(R-I)_C$ are compared with radial velocities obtained from cross-correlations. The star to the left is β Gru and that to the right is δ^2 Gru.

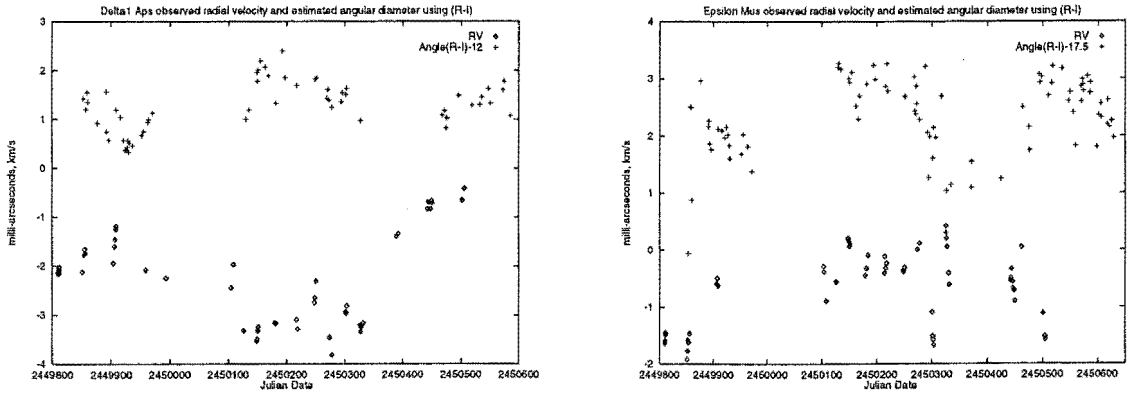

Figure 4.34: Angular-diameter variations using the Barnes-Evans method with $(R-I)_C$ are compared with radial velocities obtained from cross-correlations. The star to the left is δ^1 Aps and that to the right is ϵ Mus.

Hence, with the exception of L^2 Pup's characteristic 141-day timescale which strongly supports a radial-pulsation scenario and δ^1 Aps' 455-day radial-velocity timescale which is not consistent with radial pulsation, determination of the consistency of radial pulsation with the observed variations will either require many more concurrent observations with high quality photometry, or a different approach. One such different approach is to compare the predicted periods for radial pulsation with the observed timescales. This is done in §4.9.1.

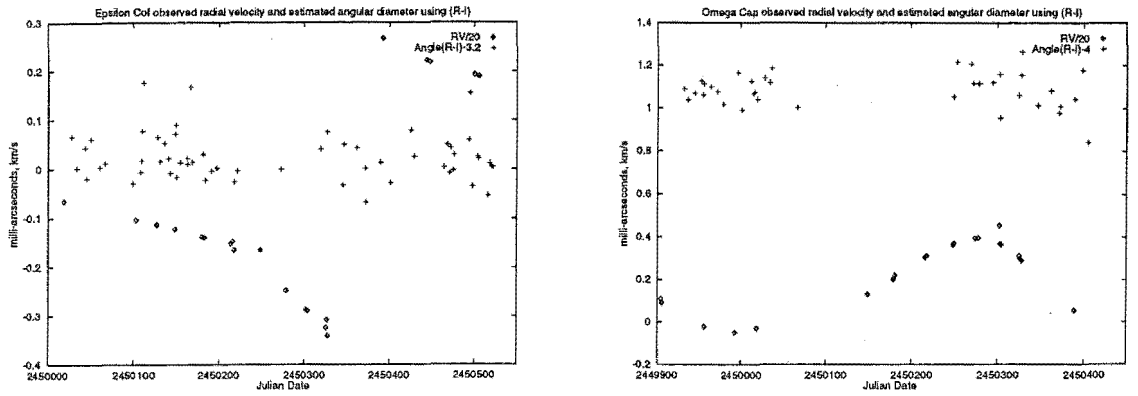

Figure 4.35: Angular-diameter variations using the Barnes-Evans method with $(R-I)_C$ are compared with radial velocities obtained from cross-correlations. The star to the left is δ^1 Aps and that to the right is ω Cap.

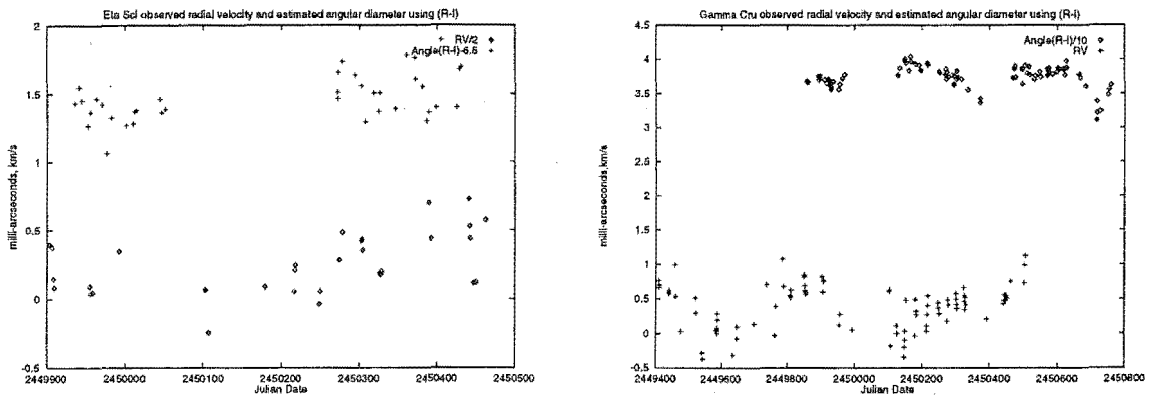

Figure 4.36: Angular-diameter variations using the Barnes-Evans method with $(R-I)_C$ are compared with radial velocities obtained from cross-correlations. The star to the left is η Scl and that to the right is γ Cru.

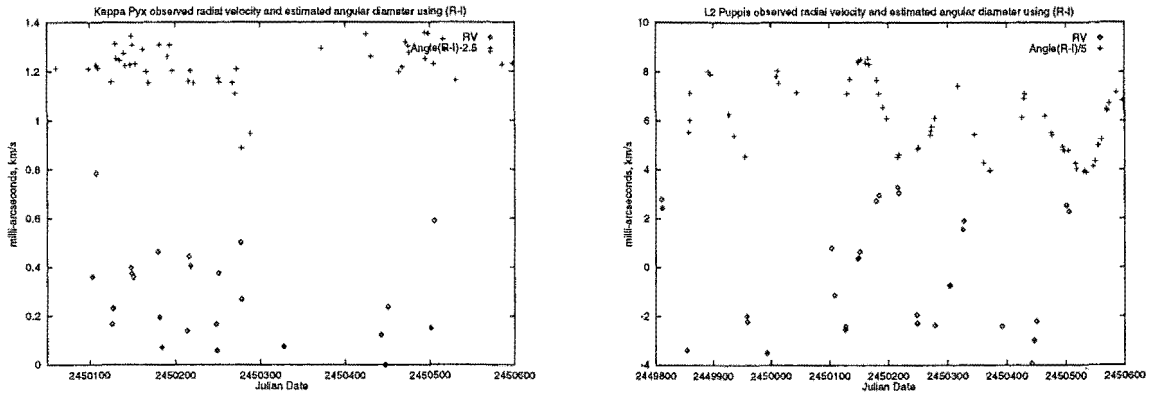

Figure 4.37: Angular-diameter variations using the Barnes-Evans method with $(R-I)_C$ are compared with radial velocities obtained from cross-correlations. The star to the left is κ Pyx and the right is L^2 Pup.

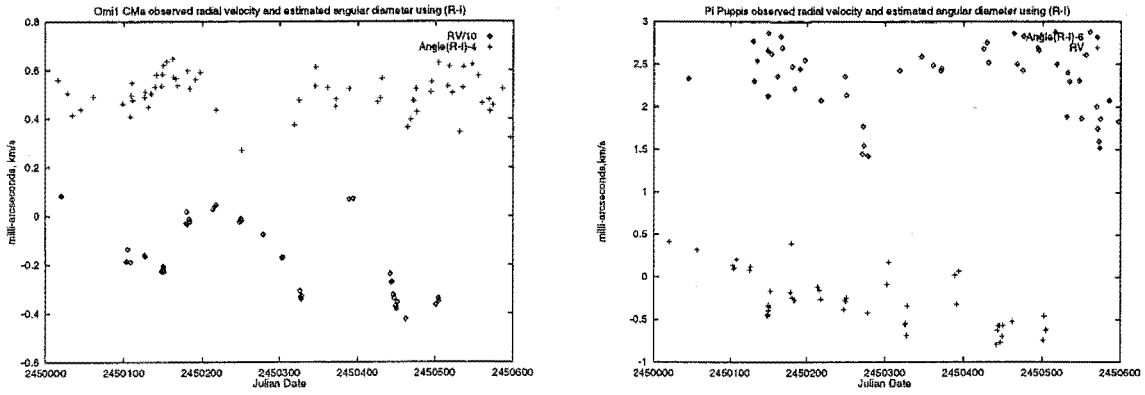

Figure 4.38: Angular-diameter variations using the Barnes-Evans method with $(R-I)_C$ are compared with radial velocities obtained from cross-correlations. The star to the left is o^1 CMa and the right is π Pup.

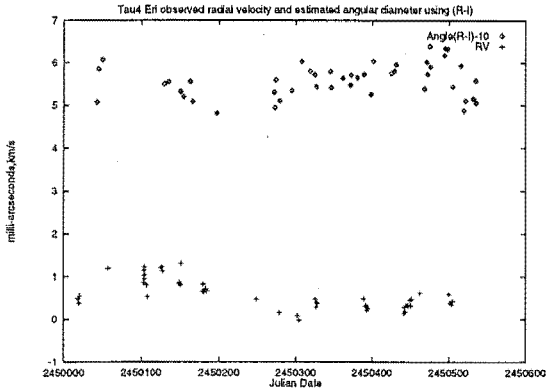

Figure 4.39: Angular-diameter variations using the Barnes-Evans method with $(R-I)_C$ are compared with radial velocities obtained from cross-correlations for τ^4 Eri.

4.7 Potential binary systems

If a star is a member of a binary system no variations in light are expected unless the star is a close or eclipsing binary (for the definition of these and more details on binary systems see §2.1). In the former case the period observed in the radial velocity is expected to be only a few days in length. As none of the observed radial-velocity timescales are of such a short length, none can be attributed to orbital motion in a close binary system. Hence for any characteristic timescales found in this thesis to be attributable to a binary mechanism, the light variation would have to be due to the two components eclipsing each other in a wide binary system. Wide binary systems are rare, as they require that the inclination of the orbital plane be approximately 90 degrees, but not impossible and two well known cases are ζ Aur[66] and ϵ Aur[67]. Wide eclipsing binaries have two light minima every period and are constant in between, but no such light variations have been observed in the Hipparcos or Mt John visual photometry, which leads to the conclusion that any characteristic timescales are either present in the photometry and radial velocity coincidentally, i.e. arising from different mechanisms, or the characteristic timescales are not due to a binary orbit.

[66] A late-type supergiant with a smaller B dwarf secondary and a orbital period of $2\frac{1}{3}$ years, this star is in the prototype ζ Aur system. Its eclipse is atmospheric and such systems allow deductions of the atmosphere of the primary. See Batten [14] pages 162–165 and Sahade & Wood [140] pages 120–142 for more details.

[67] This star has the exceptionally long period for an eclipsing binary of 21.7 years. For more details see Sahade & Wood [140] pages 152–157.

Orbits in wide binary systems lead to strictly repeating radial-velocity variations and unless the eccentricity of the orbit is significantly greater than zero the variations will look sinusoidal. However, if another cause of velocity variation is present its superposition on the binary variations may cause the radial-velocity variation to appear erratic (this will also occur if the star is a member of a multiple star system rather than a binary). Hence all stars have had the Fortran program **orbsol** (also known as **BX**) used on their radial velocities. This program was written to determine the elements of a spectroscopic binary from its radial-velocity values[68] and underwent its last major rewrite in 1988 by T. Mazeh[69].

When a single-line spectroscopic binary is observed, however, only a limited number of orbital parameters may be obtained. If the observed star is denoted by the number one, see Figure 4.40

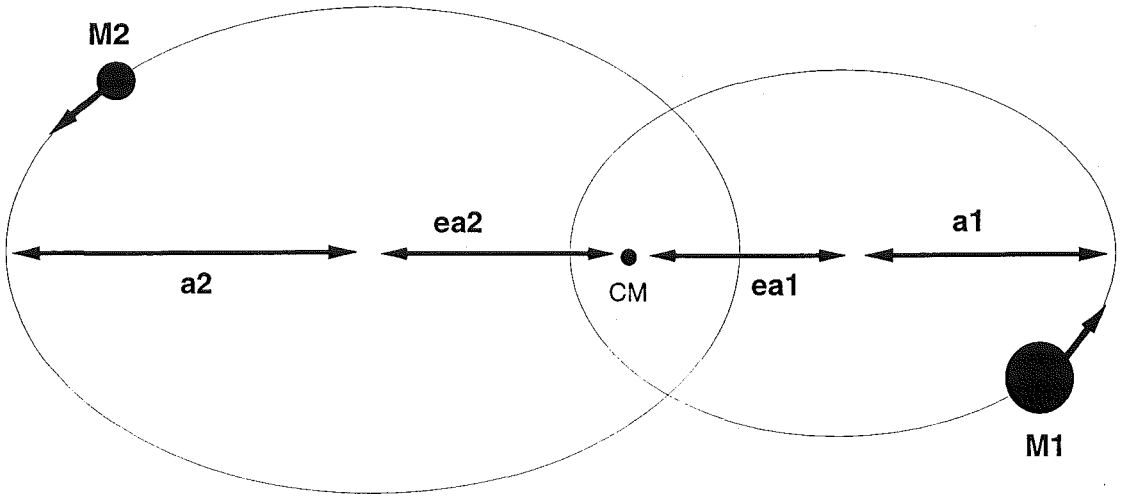

Figure 4.40: The elliptical orbits of two stars of masses M_1 and M_2 about their centre-of-mass, CM. Their movement with respect to each other also forms an ellipse of the same period and eccentricity.

(not necessarily more massive than the secondary star, but certainly more luminous[70]), then the parameters that may be determined are:

- $a_1 \sin(i)$, where a_1 is the semi-major axis of the primary star and i is the inclination of the orbital plane to the tangent plane of the celestial sphere at the star. It should be noted that $\frac{M_1}{M_2} = \frac{a_2}{a_1}$.
- P_{bin}, the period of the orbit.

[68]For a detailed, if somewhat out-dated in places, discussion of obtaining spectroscopic elements for a spectroscopic binary from its radial velocities see Petrie [131]

[69]Its main routine was written in 1973 and has been modified by P.K. Barker and M.J. Rensing. It has also undergone a few minor changes by the author of this thesis.

[70]If the primary star is more than a magnitude brighter than the secondary then the lines of the secondary star will not be detectable and in fact no double-lined or composite spectra have been detected amongst the 44 stars observed for this thesis, with the exception of ϵ Car which has the composite spectrum K3III+B2:V (see Table 1.1). However, this does not guarantee that the secondary is much fainter, because a star of similar spectral type in a small-amplitude binary will not be resolvable — instead a changing asymmetry in the stellar lines may be observed. Regardless, the presence of merged spectra from a visually close binary will modify the observed radial velocities away from that of the primary star's true radial velocity (as a cross-correlation is being performed rather then individual line velocities being measured), although the observed velocities will still be regular and strictly periodic. The orbital parameters fitted by **orbsol** will have a smaller amplitude and perhaps some modification of other orbital parameters. How much the radial velocities differ will depend on the relative brightness of the secondary (see Hill [84] for examples of the effect different luminosity ratios have on radial velocities obtained using cross-correlation).

- e, the eccentricity of the orbit.
- ω, the angle between the direction to the ascending node and that to the point of closest approach (called the periastron) of the two stars, often called the longitude (or argument) of periastron.
- T_0, the time at which the two stars pass through periastron.
- $f_M = \frac{M_2^3 \sin^3(i)}{(M_1+M_2)^2}$, the mass function.

Even knowing the mass of the primary star will not solve the system, because of the unknown $\sin(i)$ factor. However, knowing the mass and the radius of the primary star does enable the determination of the minimum possible mass of the secondary star, in the following two ways. One method is based on the knowledge of M_1 and the variation of $\sin(i)$. As the mass function is a cubic in M_2 it can be solved in terms of the known parameters f_M, M_1 and the unknown $\sin(i)$ (where $\sin(i) \in [0,1]$). The solutions to the cubic are found to have only one real root for M_2. This root approaches infinity as $\sin(i) \to 0$ and approaches[71]

$$\mathcal{M}_{\sin(i)} = \frac{f_M}{3} + \frac{f_M^{1/3}(2f_M^2 + 18 f_M M_1 + 27 M_1^2 + 3\sqrt{3} M_1^{3/2}\sqrt{4 f_M + 27 M_1})^{1/3}}{32^{1/3}} + \frac{f_M^{2/3}(f_M + 6M_1)}{3(f_M^2 + 9 f_M M_1 + \frac{3}{2}(9M_1^2 + \sqrt{3} M_1^{3/2}\sqrt{4 f_M + 27 M_1}))^{1/3}}$$

as $\sin(i) \to 1$, and this latter gives the minimum[72] value of M_2 when $\sin(i)$ is varied between zero and unity.

Another method for finding the minimum mass of the secondary star is based on the requirement that the distance between the primary and secondary star must be greater than the radius of the primary at all times. If α is defined as the ratio of the two masses then $M_2 = \alpha M_1$ and $a_1 = \alpha a_2$. The mass function can then be written as

$$f_M = M_1 \sin^3(i) \left(\frac{\alpha^3}{(1+\alpha)^2}\right).$$

As the minimum distance between the two stars for a binary system must be greater than the radius, R_1, of the primary, $(1-e)(a_1 + a_2) > R_1$ must be true. Rewriting this as $(1-e)a_1(\alpha+1)/\alpha > R_1$ and using the mass function relation, it can be shown that

$$a_1 \sin(i)(1-e)\left(\frac{M_1}{f_M}\right)^{\frac{1}{3}} \frac{(\alpha+1)}{\alpha}\left(\frac{\alpha^3}{(1+\alpha)^2}\right)^{\frac{1}{3}} > R_1.$$

The factor

$$\tilde{R} = a_1 \sin(i)(1-e)\left(\frac{2M_1}{f_M}\right)^{\frac{1}{3}}$$

can be found from the orbital parameters and mass estimations. Simplifying the equation in terms of this reduces it to

$$\tilde{R} \times \left(\frac{1+\alpha}{2}\right)^{\frac{1}{3}} > R_1.$$

[71] The mathematical package Mathematica was used to solve the cubic

[72] To see that no extremum occur between $\sin(i) = 1$ and $\sin(i) = 0$ consider the original cubic. Defining $s = \sin^3(i)$, considering f_M and M_1 to be constants and M_2 a function of s, the derivative of the cubic yields $dM_2/ds = -M_2^3/(3sM_2^2 + 2f_M M_2 + f_M M_1)$. For an extrema to occur this must equal zero. However, this could only occur if $M_2 = 0$ or the denominator became infinity and both are impossible.

Hence for the minimum distance between the two stars to be greater than the primary star's radius, it follows that

$$\alpha > 2\left(\frac{R_1}{\tilde{R}}\right)^3 - 1.$$

Hence another independent minimum mass is obtained where if $\tilde{R}/R_1 < 1$ then the binary pair must have $M_2 > M_1$. The larger the ratio, $\tilde{R}/R_1$, the more "likely" it is that the binary is real, in that when $\tilde{R}/R_1 > 1.26$ all combinations of masses result in the two stars at minimum separation being further apart than the radius of the primary star. However, if $\tilde{R} \ll R_1$ then only systems where the secondary is significantly more massive than the primary can satisfy the condition. The minimum secondary mass implied by this will be referred to as

$$\mathcal{M}_{R_1} = M_1\left(2\left(\frac{R_1}{\tilde{R}}\right)^3 - 1\right).$$

The results of using **orbsol** to fit a binary orbit to radial-velocity curves and the minimum masses for the secondary star (using the mass and radius tabulated in Table 4.16) are shown in Table 4.21. Having removed the potential binary orbit using **orbsol**, the residual radial velocities were searched for remaining timescales using **T6**. If a binary's period is found in the residuals by **T6** then it has not been removed properly by **orbsol** and this is a good indication that the variation is not consistent with a binary orbit (see Table 4.22 for the results of searching the residuals for timescales). It may be noticed that the binary period found by **orbsol** often does not correspond to that dominant timescale found by **T6** in the same data set and sometimes does not correspond to a significant (in the LSP sense) **T6** timescale at all (see Table 4.23 for a comparison of the period found by **orbsol** with the nearest timescale found by **T6**). This is because **orbsol** finds the best initial orbital period by doing a preliminary[73] full parameter orbital fit to the data, which is then used as the starting period for a more refined orbital fit. So the period it finds is that most appropriate to a binary orbit, not necessarily that with the greatest periodogram power (see §4.1.3 for details on how **T6** finds its timescales).

It should be noted that the best binary fit found by **orbsol** of 249 days for α Sco and 870 days for HR 4177 are approximately double the length of those found by **T6**, leading to the speculation that in both cases the dominant timescale found by **T6** might actually be a higher harmonic of the longer period (see footnote 12, this chapter, for what is meant by a higher harmonic). This possibility is strengthened for α Sco by the consideration of its radial-velocity periodogram (see the left-hand side of Figure B.3) which show that the shorter frequency peak found by **orbsol** is present and only slightly smaller in amplitude than the dominant frequency. The same is not true of HR 4177, however, which may only have had the longer period found because of a gap in observations of almost 400 days.

When $\tilde{R}/R_1$ is considered[75] it becomes apparent that for a number of stars such a binary orbit could only arise if the secondary mass was significantly bigger than that of the primary, despite its lower luminosity. This is true of 24 Cap, α Sco, α TrA, β Ara, HR 3017 and V337 Car. In some cases, 24 Cap, β Ara, ϵ Sco, γ Hyi, HR 3017, η^2 Pic and V337 Car, the errors in the determined f_M are extremely large, meaning the minimum masses and $\tilde{R}$ have errors of 100% or more and this minimum mass can not be relied on. It should be noted that an f_M value with a large error does not necessarily mean the binary fit is not real — for example another intrinsic variation may lead to large errors in the derived orbital parameters of a real binary system.

[73]This will be called the default period. This is found by using **orbsol**'s period search option over 40 days to about the length of the observation range.

[74]See, for example, Petrie [131] or Batten [14] Chapter 1

[75]In no case is the secondary mass implied by $\mathcal{M}_{\sin(i)}$ bigger than the primary star's mass

Star	$P_{\rm bin}$ (days)	K (km/s)	e	ω (degrees)	T_0	f_M ($M_\odot$)	$a\sin(i)$ ($R_\odot$)	$\sigma_{\rm bin}$ (km/s)	$\mathcal{M}_{\sin(i)}$ ($M_\odot$)	$\mathcal{M}_{R_1}$ ($M_\odot$)	$\tilde{R}/R_1$	F_K [N–1, N–6]	N
2 Cen	480 ± 10	0.49 ± 0.06	0.4 ± 0.1	100± 10	9380 ± 30	(5 ± 2)E-06	4.4 ± 0.6	0.32	0.02	-0.85	2.80	1.2±0.3	61
24 Cap	94 ± 2	0.4 ± 0.3	0.5 ± 0.2	110 ± 30	9304 ± 9	(4 ± 9)E-07	0.7 ± 0.4	0.09	0.02	4.12	0.90	10 ±10	14
3 Cet	800	1.1 ± 0.1	0	N/A	8778.8±0.1	1.1E-04	17.4	0.32	0.17	-5.11	5.08	6 ±1	16
62 Sgr	650 ± 20	0.9 ± 0.1	0.3 ± 0.1	180 ± 20	9570 ± 30	(5 ± 2)E-05	11 ± 1	0.54	0.08	-2.21	3.20	1.5±0.4	50
α Sco	249 ± 6	1.4 ± 0.3	0.7 ± 0.1	80 ± 10	9542 ± 3	(3 ± 2)E-05	5 ± 1	0.36	0.23	5758	0.18	7 ±3	28
α TrA	57.3 ± 0.2	0.11 ± 0.03	0.4 ± 0.1	60 ± 20	9404 ± 4	(6 ± 5)E-09	0.12± 0.03	0.09	0.01	44.66	0.66	0.8±0.4	76
β Ara	110 ± 4	0.4 ± 0.3	0.6 ± 0.3	40 ± 20	9470 ± 3	(4 ± 9)E-07	0.7 ± 0.5	0.12	0.03	50.73	0.62	7 ±9	24
β Col	156 ± 1	0.08 ± 0.02	0.5 ± 0.2	60 ± 20	9140 ± 10	(6 ± 4)E-09	0.2 ± 0.1	0.07	0.00	-1.51	8.31	0.6±0.3	46
β Gru	1187	0.79 ± 0.09	0	N/A	8675.8±0.1	6.1E-05	18.5	0.62	0.09	-2.80	6.31	0.8±0.2	91
β Gru	1187	1.1 ± 0.2	0.66 ± 0.08	33 ± 7	9990 ± 10	6.1E-05	19 ± 4	0.55	0.09	-2.23	2.13	1.8±0.6	91
β Vol	483	0.06 ± 0.02	0	N/A	9420.8±0.4	1.1E-08	0.6	0.10	0.00	-1.42	33.88	0.2±0.1	43
δ^1 Aps	940 ± 10	1.38 ± 0.07	0.45 ± 0.05	278 ± 4	9450 ± 10	(18± 3)E-05	23 ± 1	0.39	0.18	-3.68	2.40	6.3±0.6	70
δ^2 Gru	3000	0.5 ± 0.1	0	N/A	8027.2±0.3	3.3E-05	28.1	0.33	0.06	-1.85	14.95	1.0±0.5	72
ϵ Car	860 ± 20	0.82 ± 0.06	0.11 ± 0.06	330 ± 20	9190 ± 90	(5 ± 1)E-05	14 ± 1	0.25	0.18	-8.03	5.26	5.4±0.8	60
ϵ Col	1430 ± 30	6.1 ± 0.2	0.847 ± 0.009	260 ± 2	8920 ± 30	(50± 5)E-04	91 ± 4	0.19	0.47	-3.09	5.72	510 ±30	54
ϵ Cru	242	0.16 ± 0.05	0	N/A	9407.2±0.3	1.1E-07	0.8	0.15	0.01	-1.90	7.56	0.6±0.4	20
ϵ Cru	242	0.2 ± 0.1	0.5 ± 0.4	310 ± 30	9400 ± 10	1.4E-07	0.9 ± 0.5	0.13	0.01	-1.82	3.51	1 ±1	20
ϵ Mus	807	0.48 ± 0.09	0	N/A	9452.9±0.2	9.3E-06	7.7	0.53	0.04	-1.92	5.10	0.4±0.2	76
ϵ Sco	52 ± 1	0.11 ± 0.04	0.5 ± 0.3	70 ± 30	9364 ± 3	(5 ± 6)E-09	0.10± 0.04	0.07	0.00	-1.54	3.16	1 ±1	24
ϵ TrA	143	0.09 ± 0.03	0	N/A	9414.6±0.4	1.0E-08	0.2	0.09	0.00	-2.09	9.75	0.5±0.3	15
η^2 Dor	660 ± 20	0.39 ± 0.07	0.6 ± 0.1	129 ± 10	9750 ± 20	(2 ± 1)E-06	4.1 ± 0.8	0.23	0.03	-2.17	2.36	1.5±0.5	68
η^2 Pic	290 ± 10	0.18 ± 0.05	0.5 ± 0.3	160 ± 20	9200 ± 30	(1 ± 1)E-07	0.9 ± 0.3	0.10	0.01	-1.62	3.32	1.7±0.9	26
η Scl	322	0.4 ± 0.1	0	N/A	9102.9±0.2	2.9E-06	2.8	0.53	0.03	-2.14	3.42	0.4±0.2	50
η Sgr	137	0.15 ± 0.06	0	N/A	9364.2±0.4	4.8E-08	0.4	0.17	0.00	-1.06	2.71	0.4±0.3	17
γ Cha	390 ± 20	0.37 ± 0.08	0.3 ± 0.1	60 ± 20	8970 ± 50	(2 ± 1)E-06	2.7 ± 0.6	0.11	0.02	-2.18	4.11	6 ±3	16
γ Cru	584 ± 8	0.41 ± 0.05	0.66 ± 0.06	139 ± 8	9539 ± 9	(18± 7)E-07	3.6 ± 0.5	0.23	0.02	-1.12	2.00	1.6±0.4	106
γ Hyi	139 ± 5	0.3 ± 0.2	0.4 ± 0.3	330 ± 30	9240 ± 20	(3 ± 5)E-07	0.7 ± 0.4	0.18	0.01	-0.87	1.62	1 ±2	24
γ Phe	194.2±0.3	15.97± 0.07	0.015 ± 0.005	30 ± 20	9230 ± 20	(82± 1)E-03	61.3 ± 0.3	0.20	0.92	-1.64	4.14	3190 ±30	18
γ Ret	930 ± 50	0.9 ± 0.2	0.4 ± 0.1	290 ± 20	9600 ± 50	(6 ± 3)E-05	16 ± 3	0.61	0.09	-2.40	3.59	1.2±0.4	61
GZ Vel	3000	1.0 ± 0.1	0	N/A	8834.7±0.1	3.4E-04	61.0	0.22	0.32	-7.42	13.91	11 ±3	41
HR 3017	41 ± 1	0.3 ± 0.2	0.8 ± 0.2	110 ± 20	9268 ± 5	(3 ± 5)E-08	0.1 ± 0.1	0.13	0.02	14073	0.11	2 ±3	22
HR 4177	870 ± 20	0.63 ± 0.07	0.16 ± 0.08	120 ± 20	9390 ± 60	(22± 7)E-06	11 ± 1	0.13	0.12	-6.56	3.75	12 ±3	34
HR 6166	510 ± 10	0.23 ± 0.02	0.28 ± 0.09	180 ± 20	9030 ± 40	(6 ± 2)E-07	2.3 ± 0.2	0.10	0.01	-1.70	5.81	2.7±0.6	45
κ Pyx	531 ± 7	0.38 ± 0.07	0.4 ± 0.1	320 ± 10	9470 ± 20	(2 ± 1)E-06	3.5 ± 0.7	0.17	0.03	-2.07	4.33	2 ±1	44
L^2 Pup	140 ± 1	3.0 ± 0.3	0.21 ± 0.08	30 ± 20	9373 ± 9	(4 ± 1)E-04	8.2 ± 0.8	1.25	0.10	0.45	1.14	2.9±0.6	50
λ Vel	1410 ± 90	1.02 ± 0.03	0.21 ± 0.06	73 ± 7	8440 ± 80	(14± 2)E-05	28 ± 1	0.15	0.26	-7.99	5.13	23 ±2	70
N Vel	660 ± 10	0.38 ± 0.04	0.41 ± 0.08	19 ± 9	9400 ± 20	(28± 9)E-07	4.5 ± 0.5	0.13	0.03	-2.03	5.91	4.2±0.9	41
NS Pup	1250 ± 40	0.65 ± 0.03	0.20 ± 0.06	100 ± 10	9350 ± 50	(33± 5)E-06	15.6 ± 0.8	0.13	0.16	-8.41	4.35	12 ±1	33
o^1 CMa	5000	3.8 ± 1.3	0	N/A	9673.3±0.2	2.9E-02	377.0	1.15	1.94	-10.84	11.32	6 ±4	80
ω Cap	472 ± 2	4.19 ± 0.05	0.22 ± 0.01	41 ± 2	9367 ± 6	(34± 1)E-04	38.2 ± 0.4	0.20	0.44	-3.44	3.85	220 ±5	38
π Pup	1300 ±100	0.46 ± 0.04	0.23 ± 0.09	230 ± 20	9510 ± 90	(12± 3)E-06	12 ± 1	0.22	0.13	-9.82	3.46	2.2±0.4	88
ψ Phe	580 ± 20	1.0 ± 0.2	0.55 ± 0.09	362 ± 7	9660 ± 20	(3 ± 2)E-05	9 ± 2	0.40	0.05	-1.33	2.42	3 ±1	60
σ CMa	1300 ±100	1.19 ± 0.08	0.29 ± 0.03	274 ± 9	9000 ± 100	(20± 4)E-05	30 ± 2	0.19	0.31	-8.76	3.49	20 ±3	55
σ Lib	590 ± 20	0.96 ± 0.09	0.17 ± 0.09	20 ± 20	9240 ± 50	(5 ± 2)E-05	11 ± 1	0.33	0.08	-2.47	4.23	4.3±0.8	50
τ^4 Eri	590 ± 10	0.43 ± 0.05	0.1 ± 0.1	240 ± 70	9900 ± 200	(5 ± 2)E-06	4.9 ± 0.5	0.29	0.03	-1.70	5.04	1.1±0.2	83
V337 Car	283 ± 9	0.21 ± 0.06	0.84 ± 0.05	330 ± 10	9300 ± 30	(4 ± 4)E-08	0.6 ± 0.2	0.07	0.01	76.27	0.54	4 ±3	38

Table 4.21: **Orbital solutions**. This table gives the orbital solutions found by the Fortran program **orbsol**. As **orbsol** is written to find the best binary fit to the data, the period found by the "period search" option was used as the starting point for all other fits (with the occasional exception). Initial period searches took place over 40–2000 days for all stars, except those which were culled in which case period searches took place over 40–500 days. However, δ^2 Gru, GZ Vel, o^1 CMa and 3 Cet have periods present which are much longer than the observation window — hence they are too long to be picked up by **orbsol** and a forced fit to an orbit of long period was used. In addition **orbsol** was not able successfully to obtain a non-circular orbital solution (for the initial period) for β Vol, ϵ Mus, ϵ TrA, η Scl and η Sgr. In the case of β Gru and ϵ Cru a non-circular orbital solution for the initial period was only possible if the period was not allowed to vary. T_0 is the epoch time minus 2440000 (periastron for a non-circular orbit), $\sigma_{\rm bin}$ is the standard deviation of the data about the orbital fit, $\mathcal{M}_{\sin(i)}$ and $\mathcal{M}_{R_1}$ are the minimum mass from different methods, $\tilde{R}/R_1$ is a ratio such that $\tilde{R}/R_1 < 1$ means $M_2 > M_1$, $F_K[N\text{–}1, N\text{–}6]$ is the F-test value comparing constant data with the binary model, N is the number of radial-velocity points used for the fit and all other parameters have their usual meanings[74]. The values of $\mathcal{M}_{\sin(i)}$, $\mathcal{M}_{R_1}$ and $\tilde{R}/R_1$ given in this table were determined from the radius and mass estimations given in Table 4.16.

Star	Type	N	$\mathcal{P}$ (days)	(LSP, σ_{N-1})
2 Cen	$\mathcal{G}$	61	75	(1.9E-02,0.302)
24 Cap	$\mathcal{G}$	14	55	(8.9E-01,0.074)
3 Cet	$\mathcal{C}$	16	71	(2.2E-01,0.264)
62 Sgr	$\mathcal{G}$	50	81, 118	(2.2E-03,0.511),(1.2E-02,0.394)
α Sco	$\mathcal{G}$	28	500	(3.0E-02,0.326)
α TrA	$\mathcal{G}$	76	31	(4.3E-01,0.087)
β Ara	$\mathcal{G}$	24	37	(9.7E-01,0.108)
β Col	$\mathcal{G}$	46	84	(2.7E-02,0.070)
β Gru*	$\mathcal{C}$	91	56, 30, 370, 16	(3.4E-05,0.601),(2.3E-06,0.481),(4.5E-03,0.352),(1.0E-02,0.305)
β Gru*	$\mathcal{G}$	91	30, 56, 15, 24	(5.3E-05,0.531),(1.8E-06,0.427),(2.6E-04,0.323),(7.3E-02,0.270)
β Vol	$\mathcal{C}$	43	63	(4.8E-01,0.090)
δ^1 Aps*	$\mathcal{G}$	70	29, 43, 23	(1.5E-04,0.379),(1.1E-03,0.294),(2.1E-01,0.197)
δ^2 Gru*	$\mathcal{C}$	72	23, 20	(3.3E-04,0.317),(1.1E-02,0.252)
ϵ Car	$\mathcal{G}$	60	104, 70	(7.0E-05,0.244),(4.1E-02,0.179)
ϵ Col	$\mathcal{G}$	54	137	(2.3E-01,0.180)
ϵ Cru	$\mathcal{C}$	20	44	(9.2E-01,0.129)
ϵ Cru	$\mathcal{G}$	20	44	(1.0E+00,0.111)
ϵ Mus	$\mathcal{C}$	76	63, 88	(8.4E-06,0.509),(1.3E-02,0.385)
ϵ Sco	$\mathcal{G}$	24	33	(1.0E+00,0.064)
ϵ TrA	$\mathcal{C}$	15	65	(5.2E-01,0.070)
η^2 Dor	$\mathcal{G}$	68	101, 476	(3.2E-03,0.219),(1.4E-01,0.188)
η^2 Pic	$\mathcal{G}$	26	667	(4.4E-02,0.092)
η Scl	$\mathcal{C}$	50	72	(5.2E-02,0.500)
η Sgr	$\mathcal{C}$	17	222	(8.8E-01,0.143)
γ Cha	$\mathcal{G}$	16	87	(9.2E-01,0.090)
γ Cru*	$\mathcal{G}$	106	13, 16, 37	(6.9E-03,0.223),(4.1E-03,0.200),(1.3E-01,0.177)
γ Hyi	$\mathcal{G}$	24	85	(7.8E-01,0.160)
γ Phe	$\mathcal{G}$	18	56	(7.1E-01,0.168)
γ Ret	$\mathcal{G}$	61	370	(2.3E-02,0.581)
GZ Vel	$\mathcal{C}$	41	263	(2.9E-02,0.205)
HR 3017	$\mathcal{G}$	22	222	(1.6E-01,0.113)
HR 4177	$\mathcal{G}$	34	99	(6.7E-01,0.118)
HR 6166	$\mathcal{G}$	45	182	(9.1E-01,0.061)
κ Pyx	$\mathcal{G}$	44	192	(5.1E-01,0.164)
L^2 Pup	$\mathcal{G}$	50	435, 122	(3.0E-04,1.183),(2.5E-02,0.832)
λ Vel	$\mathcal{G}$	70	250	(8.0E-02,0.145)
N Vel	$\mathcal{G}$	41	114	(1.3E-01,0.123)
NS Pup	$\mathcal{G}$	33	476	(7.2E-02,0.119)
o^1 CMa*	$\mathcal{C}$	80	175, 42, 909, 18	(2.5E-05,1.113),(1.7E-04,0.831),(6.1E-04,0.668),(1.7E-02,0.529)
ω Cap	$\mathcal{G}$	38	1250, 109	(4.3E-03,0.187),(7.6E-01,0.140)
π Pup	$\mathcal{G}$	88	58, 103	(4.6E-04,0.211),(2.0E-02,0.181)
ψ Phe	$\mathcal{G}$	60	233, 196	(4.9E-04,0.385),(3.1E-01,0.298)
σ CMa	$\mathcal{G}$	55	49	(2.0E-01,0.185)
σ Lib	$\mathcal{G}$	50	119, 65	(1.5E-03,0.308),(3.7E-02,0.234)
τ^4 Eri	$\mathcal{G}$	83	33, 263	(6.5E-03,0.277),(3.1E-01,0.243)
V337 Car	$\mathcal{G}$	38	65	(7.9E-01,0.067)

Table 4.22: **Period search of binary residuals.** This table gives the results of running **T6** on the residual values left after the binary fit of Table 4.21 has been removed. Generally **T6** used the default range of frequencies, but stars labelled with a ($\star$) were searched to two times the Nyquist frequency in the original data set and hence for consistency (see Table 4.4) the residuals have been searched to two times the Nyquist frequency also. Here: type $\mathcal{G}$ means the removed orbital fit was a general one, whereas $\mathcal{C}$ means it was circular; N is the number of data points for each star; LSP is the Lomb-Scargle probability of the timescale and σ_{N-1} is the $N-1$ standard deviation of the data (before that timescale's removal by prewhitening). The last timescale tabulated here does not have a significant Lomb-Scargle probability.

Star	$\mathcal{P}_{\mathbf{T6}}$ (days)	$\sigma_{\mathbf{T6}}$ (km/s)	$P_{\rm bin}$ (days)	$\sigma_{\rm bin}$ (km/s)	$F_{\mathbf{T6}}$ [N–4, N–6]	N
2 Cen	556	0.33	479	0.32	1.05	61
24 Cap	93	0.12	94	0.09	1.75	14
3 Cet (C)	526	0.42	800	0.32	1.70	16
62 Sgr	588	0.58	645	0.54	1.14	50
α Sco	139	0.53	249	0.36	2.18	28
α TrA	57	0.09	57	0.09	1.04	76
β Ara	112	0.15	110	0.12	1.60	24
β Col	159	0.08	156	0.07	1.21	46
β Gru (C)	833	0.59	1187	0.62	0.91	91
β Gru	833	0.59	1187	0.55	1.15	91
β Vol (C)	476	0.09	483	0.10	0.86	43
δ^1 Aps	1000	0.61	940	0.39	2.43	70
δ^2 Gru	1429	0.31	3000	0.33	0.88	72
ϵ Car	833	0.28	858	0.25	1.23	60
ϵ Col	1250	2.18	1429	0.19	131.77	54
ϵ Cru (C)	270	0.14	242	0.15	0.86	20
ϵ Cru	270	0.14	242	0.13	1.14	20
ϵ Mus (C)	625	0.51	807	0.53	0.91	76
ϵ Sco	52	0.08	52	0.07	1.18	24
ϵ TrA (C)	135	0.08	143	0.09	0.75	15
η^2 Dor	667	0.24	660	0.23	1.12	68
η^2 Pic	909	0.10	290	0.10	0.98	26
η Scl (C)	49	0.50	322	0.53	0.90	50
η Sgr (C)	345	0.14	137	0.17	0.68	17
γ Cha	435	0.11	391	0.11	1.06	16
γ Cru	556	0.24	584	0.23	1.10	106
γ Hyi	244	0.19	139	0.18	1.08	24
γ Phe	192	0.81	194	0.20	16.20	18
γ Ret	909	0.64	934	0.61	1.10	61
GZ Vel (C)	2000	0.29	3000	0.22	1.76	41
HR 3017	556	0.15	41	0.13	1.31	22
HR 4177	435	0.17	870	0.13	1.71	34
HR 6166	476	0.11	513	0.10	1.23	45
κ Pyx	526	0.20	531	0.17	1.38	44
L^2 Pup	141	1.35	140	1.25	1.16	50
λ Vel	1429	0.28	1413	0.15	3.58	70
N Vel	625	0.15	662	0.13	1.31	41
NS Pup	1429	0.21	1245	0.13	2.54	33
o^1 CMa (C)	769	1.12	5000	1.15	0.95	80
ω Cap	476	0.78	472	0.20	15.33	38
π Pup	1250	0.23	1304	0.22	1.09	88
ψ Phe	588	0.47	578	0.40	1.39	60
σ CMa	1250	0.32	1328	0.19	2.77	55
σ Lib	556	0.35	586	0.33	1.13	50
τ^4 Eri	588	0.28	587	0.29	0.95	83
V337 Car	286	0.09	283	0.07	1.62	38

Table 4.23: **Comparison of T6 and orbsol.** This table compares the period and scatter of the best binary fit found by **orbsol**, $P_{\rm bin}$, (see Table 4.21) with those of the nearest sinusoidal period found by **T6**, $\mathcal{P}_{\mathbf{T6}}$ (see Table 4.4). Those binary fits for which general orbital fits were not possible are indicated by a C, $\sigma_{\rm bin}$ is the standard deviation of the data about the binary fit, $\sigma_{\mathbf{T6}}$ is the standard deviation of the data about the fit found by **T6**, $F_{\mathbf{T6}}[N\text{–}4, N\text{–}6]$ is the F-test value comparing a sinusoidal fit with the binary model and N is the number of data points.

As far as orbital periods remaining in the residuals after the removal of the fitted orbits, the only star to suffer such a fate is L^2 Pup. This star has a best binary fit with a period of 140 days, but has a timescale of 122 days still present in the residuals which is probably due to the spectral-window function and a failure of **orbsol** to removed the 140-day timescale entirely. However, as this period is the star's characteristic period it is unlikely to be due to a binary orbit anyway (unless it is a coincidence). Interestingly in the case of 62 Sgr, δ^1 Aps, λ Vel, ω Cap and σ CMa not only did the binary fit remove the dominant timescale well, but even though these fits are for almost circular orbits it also removed the secondary timescale. Hence to determine which of the binary fits performed by **orbsol** are significantly better than the sine fits performed by **T6** the F-test was used (see §4.2 for more details on the F-test). Assuming the underlying radial-velocity population is consistent with a sine, the scatter of the data about **T6**'s sine fit, $\sigma_{\mathbf{T6}}$, provides an estimate of the standard deviation of the real population (of degrees of freedom $N-4$). Another estimation of the standard deviation of the real population is provided by the scatter of the data points about the fitted binary orbit, σ_{bin}, (of degrees of freedom[76] $N-6$). These both provide estimates of the standard deviation of the real population, but may have different fitting functions (the real population being sampled is considered to be either varying as the sine fitted by **T6**, or varying as the binary orbit fitted by **orbsol**). As the data come from the same population, the true standard deviations (of which $\sigma_{\mathbf{T6}}$ and σ_{bin} are estimates) are equal and hence if the F-test value, $F_{\mathbf{T6}}[N\text{–}4, N\text{–}6] = (\sigma_{\mathbf{T6}} \div \sigma_{\text{bin}})^2$, is significantly different from one then one of the estimations of standard deviation must be assuming the wrong fitting function. Hence if[77] $F_{\mathbf{T6}}[N\text{–}1, N\text{–}6] \gtrsim 2.2$ (for $N > 40$) then there is less than a 1% chance that F could have arisen from a population that is fitted by **T6**'s sine, rather than the alternative binary orbit. So from Table 4.23 it can be seen that this means that δ^1 Aps, ϵ Col, γ Phe, λ Vel, ω Cap and σ CMa (NS Pup is borderline) are fitted significantly better (at the 1% level) by a binary orbit, which explains the removal of the secondary timescale (in all but the 62 Sgr case) as prewhitening failure on the part of **T6**.

Although a binary orbit removed the periods of 2 Cen, 62 Sgr, γ Ret, λ Vel, N Vel, NS Pup and σ CMa reasonably well, there is doubt that radial-velocity variations of these timescales are due to a binary system, as these are the stars' characteristic timescales. In addition, the following stars have the same timescale present in photometry as that of their fitted binary orbits (which are not the stars' characteristic timescale as **T6** did not find them to be present in the radial velocities). This may cast doubt on a binary explanation for these stars' main radial-velocity variations: α Sco's binary period of 249 days is similar to the $\approx$220-day timescale present in the Hipparcos photometry; ϵ Mus' binary period of 807 days may be related to the $\approx$1000-day timescale present in the Mt John photometry; η Scl's binary period of 322 days is also present in the Hipparcos photometry, but it is after so much prewhitening that this may not be real; η Sgr's 137-day binary period is the dominant (although not significant in the LSP sense) timescale in the Hipparcos photometry; HR 3017's 41-day binary period may be related to the secondary Hipparcos and dominant Tycho photometry timescales of 32 days; o^1 CMa's long-term binary period may be related to the dominant Hipparcos and Tycho photometric timescale of $\approx$1300 days.

As the potential superposition of other intrinsic variations means it is difficult to determine the reality of a binary orbit from the errors in the **orbsol** fit, the following method has been employed to determine which orbital solutions are a reasonable fit to the radial-velocity variations. This involves the use of the F-test again, this time to determine when the amplitude of the binary orbit is significantly greater than the scatter of the data about the orbital fit. The scatter found from sampling a sine curve is $K/\sqrt{2}$, where K is the amplitude of the sine (for how to find the scatter

[76] See, for example, Petrie [131] Equ.(5)

[77] As both degrees of freedom vary with N the exact value is highly N dependent and hence an appropriate table, such as Bevington & Robinson [21] C.7, should be consulted

from a continuous function see footnote 87, this chapter). Hence if the real population is one of constant radial velocity, the amplitude of a binary orbit fitted to the data provides an estimate of the standard deviation of the real population[78]. Another estimation of the standard deviation of the real population is provided by the scatter of the data points about the binary fit, $\sigma_{\rm bin}$. Hence $K/\sqrt{2}$ and $\sigma_{\rm bin}$ both provide estimates of the standard deviation of the real population, but have different fitting functions (where this time the real population being sampled is considered to be either constant in radial velocity, or varying in a way consistent with the fitted binary orbit). As the data come from the same population, the true standard deviations (of which $K/\sqrt{2}$ and $\sigma_{\rm bin}$ are estimates) are equal and hence the F-test value is $F_K[N\text{-}1, N\text{-}6] = (K/\sqrt{2} \div \sigma_{\rm bin})^2$, where one of the estimations of standard deviation must be assuming the wrong fitting function. Hence there is less than 1% chance that F could arise from the constant fitting function if[79] $F_K[N\text{-}1, N\text{-}6] \gtrsim 2.2$ (for $N > 40$). In which case, at the 1% significance level it can be said that the data are consistent with the fitted binary orbit. Alternatively, if $F_K[N\text{-}6, N\text{-}1] = (\sigma_{\rm bin} \div K/\sqrt{2})^2 \gtrsim 2.2$ then there is less than 1% chance that this could arise from the binary fitting function. Hence at the 1% level it can be said that the data are inconsistent with the fitted binary orbit. The results of applying this to the 44 stars fitted for binary curves is also given in Table 4.21.

The amplitude of the binary orbit is not always well known, which leads to an error being associated with the determined F-value. Taking the minimum amplitude for the fit (the tabulated F-value minus its error) α Sco, δ^1 Aps, ϵ Car, ϵ Col, γ Phe, GZ Vel, HR 4177, L^2 Pup, λ Vel, N Vel, NS Pup, ω Cap, π Pup, ψ Phe, σ CMa and σ Lib have $F_K[N\text{-}1, N\text{-}6]$ values which at the 1% level indicate data consistent with the binary fit. 3 Cet, HR 6166 and o^1 CMa all have values which are just under the significance level. This is not to say the part of the variations in the other stars can not be due to their presence in a binary system, just that if that is the case the amplitude of the binary orbit is not significantly above the other variations. Stars with a consistent binary fit will now be discussed in more detail. Despite not being significant, δ^2 Gru has been included because its fit is of an arbitrary fixed period and hence it may be in a similar binary orbit, which would have a much smaller $\sigma_{\rm bin}$. L^2 Pup will be excluded from the discussion, because **orbsol** failed to remove the period properly.

- 3 Cet's orbital period was fixed arbitrarily[80] at 800 days, as it seemed to have a very long period present and a circular orbital fit was attempted. This seems to fit the observed radial velocities reasonably well (see Figure 4.41). It can not quite be considered to fit the data well at the 1% level; however, this may be due to a bad choice of arbitrary period or to the real orbit being non-circular.

- α Sco's best orbital fit[81] has a period of 249 days and an eccentricity of 0.7. This seems to fit the observed radial velocities reasonably well (see Figure 4.41). However, the binary-orbit fit requires that the secondary mass be significantly larger than the primary star's mass. Even more of concern is that there are some indications that this timescale may be present in the Hipparcos photometry and if this is the case a binary orbit explanation is put in doubt.

- δ^1 Aps' best orbital fit has a period of 940 days and an eccentricity of 0.45. This seems to fit the observed radial velocities reasonably well and its removal leaves behind its characteristic

[78] This has the advantage, over simply considering the scatter about a constant value, of not reflecting the other intrinsic variations present and not being misleadingly small if only a few data points define the maxima/minima of the binary fit

[79] See footnote 77, this section

[80] There is an upper limit to how long the arbitrary period can be set to if the star is in a circular binary orbit. This is because for a circular orbit $f_M = 8.597 \times 10^{-9} K^3 P_{\rm bin}$ and as the set period increases so does the fitted amplitude. Hence the longer the arbitrary period the larger the implied minimum mass of the secondary star.

[81] α Sco is in a visual binary orbit with a period of 878 years, which is far too long to be noticeable over the time stars were observed for this thesis (see Worley & Heintz [182] for more details on this orbit, this star is the only one of the 44 stars observed for this thesis to be present in this catalogue of visual binaries)

≈67 and 48-day timescales[82], which are clearly present in addition to the long term one in Figure 4.42.

- δ^2 Gru's orbital period was fixed arbitrarily[83] at 3000 days, as it seemed to have a very long period present and a circular orbital fit was attempted. This seems to be a tolerably good fit to the observed radial velocities (see Figure 4.42), although a definite short-term variation is visible about it. This short-term variation is found in the residual to be the 24-day characteristic timescale. The binary fit can not be considered to fit the data well at the 1% level, but has been included for consideration here as it will be affected by a bad choice of arbitrary period or the real orbit being non-circular.

- ϵ Car's best orbital fit has a period of 860 days and an eccentricity of 0.11. This seems to fit the observed radial velocities reasonably well with the observed scatter probably being due to the 104-day timescale remaining in the residuals (see Figure 4.43, this timescale was found by **T6** in the original data set after prewhitening, but it was not significant in the LSP sense).

  Interestingly a similar period has been seen in the photometry for this star by Gaposchkin [54], who suggested that this was due to the star's presence in an eclipsing binary system. **T6** did not find this timescale in the Hipparcos data, but it does assume a sinusoidal fit. Hence the Hipparcos visual photometry was phased to 860 days (see Figure 4.44) to see if a period of such a length was present. This phased plot is not incompatible with an eclipsing-binary-like curve, with scatter of about 0.02 mag obscuring the expected region of constant luminosity. However this would make the binary system of ϵ Car a wide eclipsing binary system, which would mean that $\sin(i) \approx 1$ and therefore the secondary's mass would be only 0.18 ± 0.01 solar masses, which is unlikely if the secondary is to be the B-type main-sequence star seen in ϵ Car's composite spectrum. In addition, the phase relationship between radial velocity and luminosity seen in Figure 4.44 is incompatible with surface features, so it seems likely that the light variation seen by Gaposchkin is coincidental.

- ϵ Col's best orbital fit has a period of 1430 days and an eccentricity of 0.847. Despite the period being longer than the observation window, this is in excellent agreement with the stars radial velocities, as is shown in Figure 4.43. In fact, this orbit bears a remarkable similarity to one of the sample curves in Figure 2.1.

- γ Phe's best orbital fit has a period of 194.2 days and an eccentricity of 0.015 (see Figure 4.45). This gives an excellent fit to the observed radial velocities and in fact this star is a known binary with orbital elements that agree well with those found here (see Luyten [119]). This is the only star[84] of the 44 observed for this thesis that is present in the "*Eighth catalogue of the orbital elements of spectroscopic binary systems*" Batten [15].

- GZ Vel's orbital period was fixed arbitrarily[85] at 3000 days, as it seemed to have a very long period present and a circular orbital fit was attempted. This seems to fit the observed radial velocities reasonably well (see Figure 4.45).

- HR 4177's best orbital fit has a period of 870 days and an eccentricity of 0.16. This seems to fit the observed radial velocities reasonably well (see Figure 4.46).

[82] See §4.6.1 for a discussion of why the 29-day timescale is actually believed to be a higher harmonic of a 65-day timescale

[83] See footnote 80, this section

[84] Known spectroscopic binaries were deliberately excluded from the list of stars initially chosen for observation. This star's binary designation was clearly missed!

[85] See footnote 80, this section

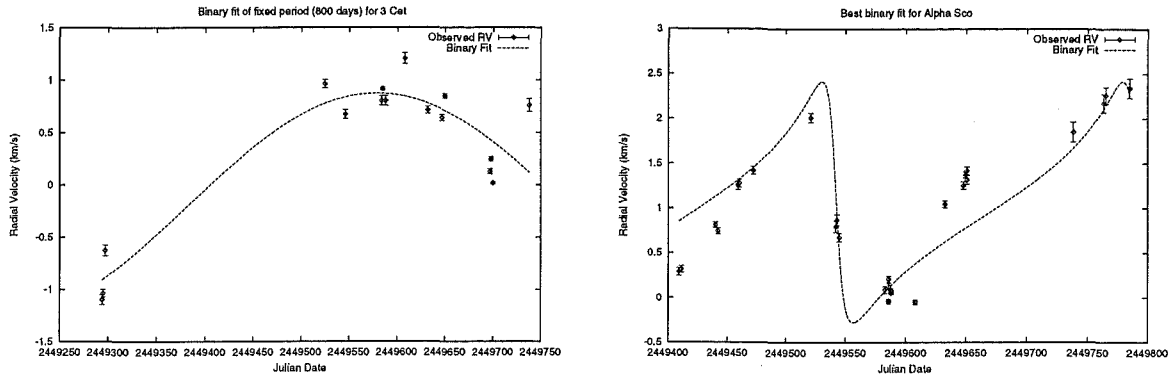

Figure 4.41: On the left are the radial-velocity data for 3 Cet and the orbital fit resulting from an assumed 800-day circular orbit. On the right side is a similar plot for α Sco and the best orbital fit, which has a period of 249 days and eccentricity of 0.7.

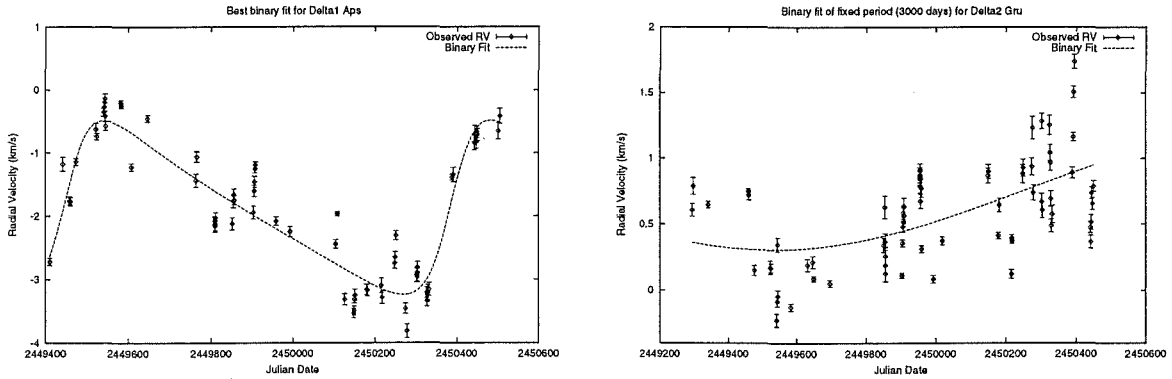

Figure 4.42: On the left are the radial-velocity data for δ^1 Aps and the best orbital fit, which has a period of 940 days and eccentricity of 0.45. On the right is a similar plot for δ^2 Gru and the fit resulting from an assumed 3000-day circular orbit.

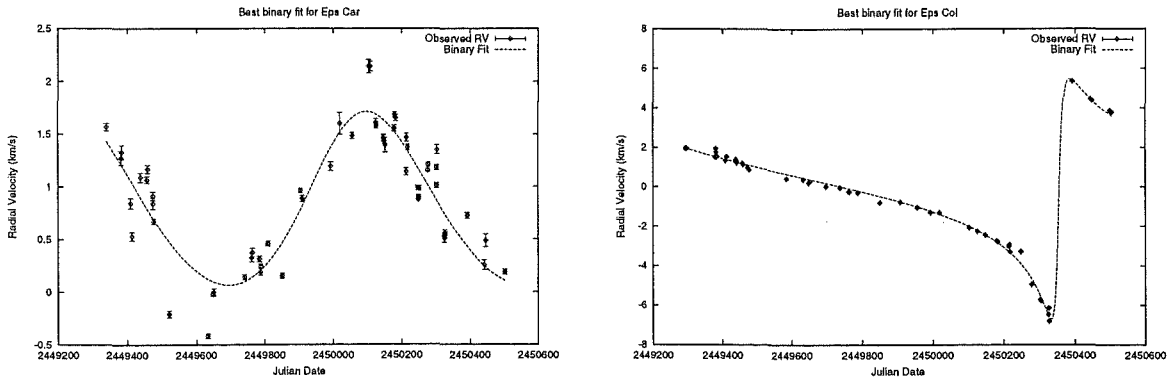

Figure 4.43: On the left are the radial-velocity data for ϵ Car and the best orbital fit, which has a period of 860 days and eccentricity of 0.11. On the right is a similar plot for ϵ Col which has a highly eccentric orbit and a period of 1430 days.

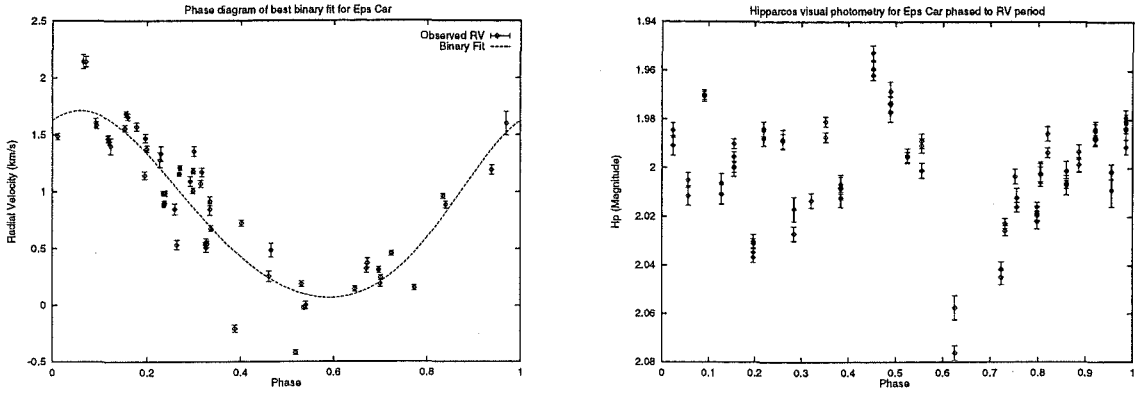

Figure 4.44: The radial-velocity data for ϵ Car is to the left, phased to the best binary period. To the right is the Hipparcos visual photometry for this star, phased to the same period and using the same epoch.

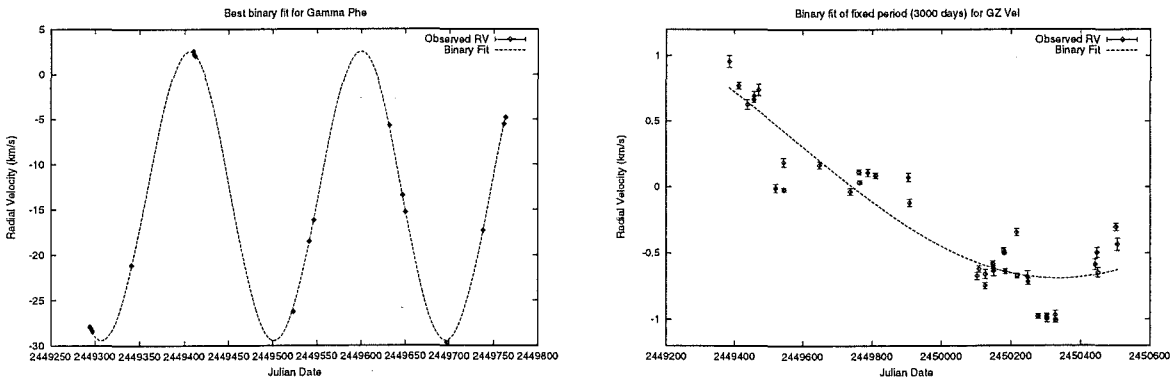

Figure 4.45: On the left are the radial-velocity data for γ Phe and its almost circular orbit of best fit, which has a period of 194.2 days. On the right is a similar plot for GZ Vel and the fit resulting from an assumed 3000-day circular orbit.

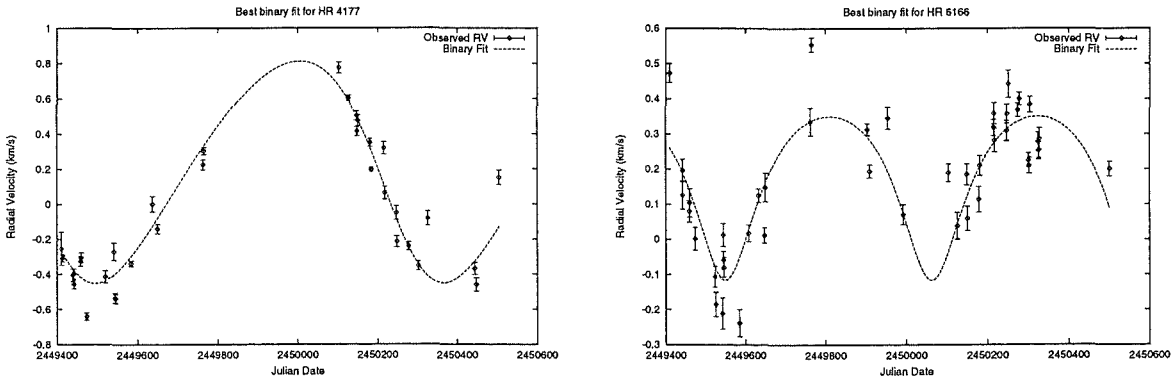

Figure 4.46: On the left are the radial-velocity data for HR 4177 and the best orbital fit, which has a period of 870 days and eccentricity of 0.16. On the right is a similar plot for HR 6166 and the best orbital fit, which has a period of 510 days and eccentricity of 0.28.

- HR 6166's best orbit fit has a period of 510 days and an eccentricity of 0.28. The fit to the radial velocities seems poor and indeed it is not quite a good fit at a 1% level (see Figure 4.46). In addition, the orbital fit being non-sinusoidal means the fit is less significant than the circular orbit assumed (for details see the more extreme case ψ Phe). Given the erratic variation of the data yet lack of any other significant (in the LSP sense) timescale, along with the marginal significance of the fit, it does not seem convincing that this variation is due to the star's presence in a binary system.

- λ Vel's best orbital fit has a period of 1410 days and an eccentricity of 0.21 (see Figure 4.47). Despite being comparable in length to the observation window, this is a highly significant fit and agrees well with the observed radial velocities. However, this is a characteristic timescale which means either this radial-velocity variation is not due to a binary system, or the similar timescale in the photometry is coincidental. At first sight it seems possibly coincidental, as **T6** finds the timescale in the Hipparcos photometry to be only 909 days. However, consideration of these variations (see §4.6.1 and Figure 4.28) reveals that the radial-velocity and Hipparcos visual-photometry variations do seem to be related. Therefore a binary orbit explanation of this radial-velocity variation is cast in doubt.

- N Vel's best orbital fit has a period of 660 days and an eccentricity of 0.41 (see Figure 4.47). The fit to the radial velocities is tolerable, but this is the star's characteristic timescale which means either this radial velocity is not due to a binary system, or the similar timescale in the photometry is coincidental. It is possible that the presence of these two similar timescales is coincidental as the relationship illustrated Figure 4.29 is far from compelling, but given the sometimes erratic variation of the data (yet lack of any other significant timescale, in the LSP sense) it still does not seem convincing that this variation is due to the star's presence in a binary system.

- NS Pup's best orbital fit has a period of 1250 days and an eccentricity of 0.20 (see Figure 4.48). Despite being comparable in length to the observation window, this agrees well with the observed radial velocities. However, this is the star's characteristic timescale (see §4.6.1 and Figure 4.30) and while the variations in Hipparcos photometry are not large they are very similar to the radial-velocity variations. Hence it is doubtful that this radial-velocity variation is due to the star's presence in the fitted binary orbit.

- o^1 CMa's orbital period was fixed arbitrarily[86] at 5000 days, as it seemed to have a very long period present and a circular orbital fit was attempted. This seems to fit the observed radial velocities reasonably well despite its fixed period (although the fit is not quite significant at the 1% level) and its removal leaves behind the star's characteristic 175-day timescale, which is clearly present in addition to the long-term one in Figure 4.48. However, there are some indications that this timescale may be present in the Hipparcos photometry, which either means that the presence of the timescales in both observables is coincidental, or that the radial-velocity variations are not due to a binary system. At first sight it seems possibly coincidental, as **T6** finds the timescale in the Hipparcos photometry to be only 1250 days. However, consideration of the variation (see Figure E.19) reveals it could be significantly longer than this, as the observation window is of this order. Therefore, just as in the case for both λ Vel and NS Pup, a binary orbit explanation of this radial-velocity variation is cast in doubt.

  This long-term Hipparcos photometry variation and the 175-day characteristic timescale mean the photometric variations for this star closely resemble that of an RVb-type RV Tauri star (see Figures D.11 and E.19). Interestingly, it has been suggested that in these stars the

[86] See footnote 80, this section

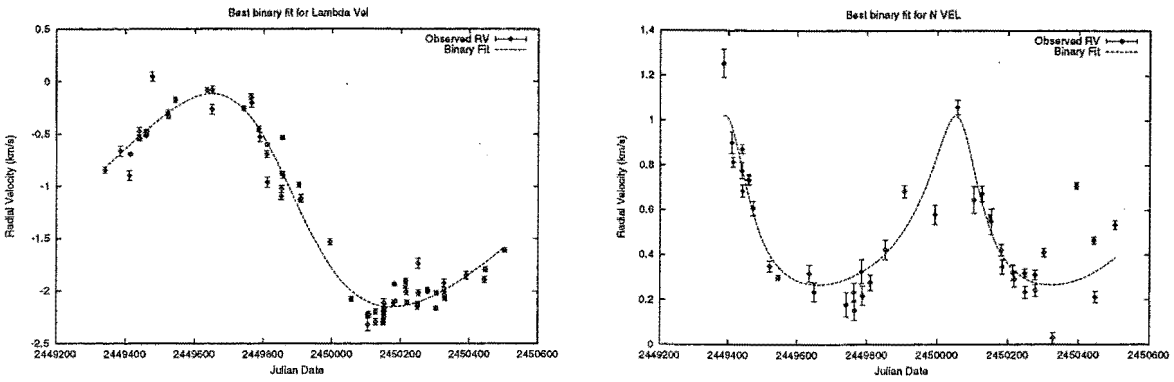

Figure 4.47: On the left are the radial-velocity data for λ Vel and the best orbital fit, which has a period of 1410 days and eccentricity of 0.21. On the right is a similar plot for N Vel and the best orbital fit, which has a period of 660 days and eccentricity of 0.41.

long-term variation is actually due to some form of binary dust eclipse or binary interaction (see Pollard [133] §9.1.2 for more details); however, these possibilities have not been investigated for the stars surveyed for this thesis as such things are usually reserved for close binary systems.

- ω Cap's best orbital fit has a period of 472 days and an eccentricity of 0.22. This is in excellent agreement with the star's radial velocities, as is shown in Figure 4.49.
- π Pup's best orbital fit has a period of about 1300 days and an eccentricity of 0.23. Despite being comparable in length to the observation window, this seems to tolerably fit the observed radial velocities. Its removal leaves behind a 58-day timescale, which is clearly present in addition to the long-term one in Figure 4.49 and is probably related to the 37 and 47-day timescales found in the original data set by **T6**.
- ψ Phe's best orbital fit has a period of 580 days and an eccentricity of 0.55. While the fit to the radial velocities is tolerable, there is insufficient data at periastron to make it convincing (see Figure 4.50). This is because the fit's very non-sinusoidal nature[87] means the scatter of such an orbit is quite a bit less than that for a sine of the same amplitude, so in fact this can not be considered to be a good fit at the 1% level.
- σ CMa's best orbital fit has a period of 1300 days and an eccentricity of 0.29. Despite being comparable in length to the observation window, this is a highly significant fit and agrees well with the observed radial velocities (see Figure 4.50). However, this is the star's characteristic timescale (see §4.6.1 and Figure 4.31). The Hipparcos photometry and radial-velocity variations are both large and are found to have timescales of exactly the same length by **T6**. Hence it is doubtful that this radial-velocity variation is due to the stars presence in the fitted binary orbit.
- σ Lib's best orbital fit has a period of 590 days and an eccentricity of 0.17 (see Figure 4.51). The fit to the radial velocities is reasonable and the scatter about the orbital fit may be due to the presence of the 119-day timescale which remains in the residuals (this is the secondary timescale found by **T6** in the original data).

The fit of the following two stars are inconsistent at the 1% level with the fitted binary orbit

[87] From Bevington & Robinson [21], page 13, the scatter of a function $g(x)$ is $\frac{1}{x_0}(\int_0^{x_0} g(x)^2 dx - \int_0^{x_0} g(x)dx)$. Hence the smaller the area of $g(x)$ about the average $\int_0^{x_0} g(x)dx/x_0$, the smaller the scatter.

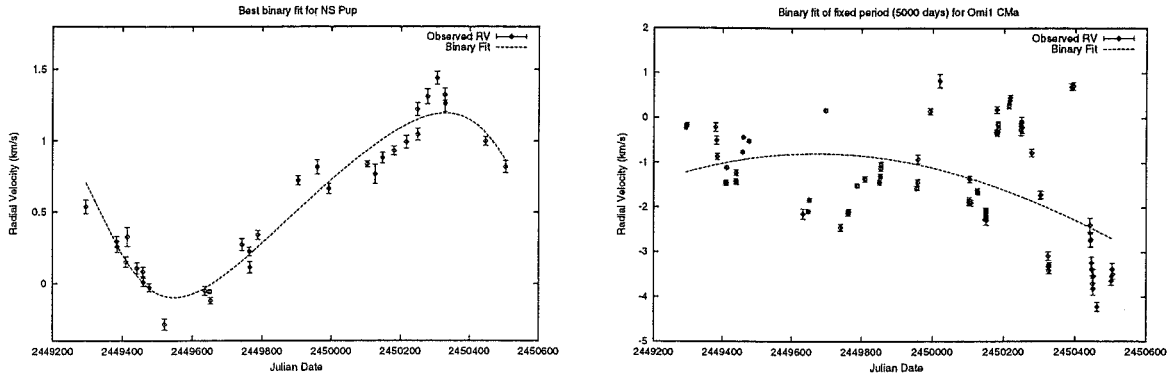

Figure 4.48: On the left are the radial-velocity data for NS Pup and the best orbital fit, which has a period of 1250 days and eccentricity of 0.20. On the right is a similar plot for o^1 CMa and the fit resulting from an assumed 5000-day circular orbit.

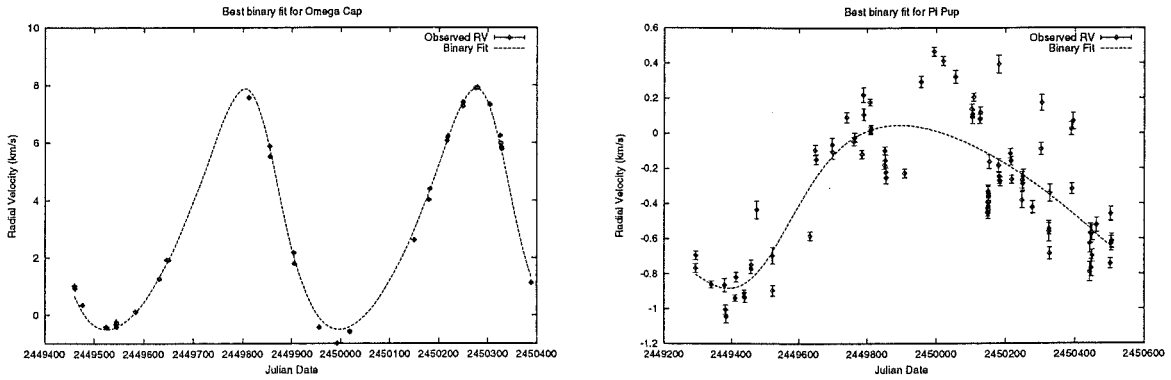

Figure 4.49: On the left are the radial-velocity data for ω Cap and the best orbital fit, which has a period of 472 days and eccentricity of 0.22. On the right is a similar plot for π Pup and the best orbital fit, which has a period of 1300 days and eccentricity of 0.23.

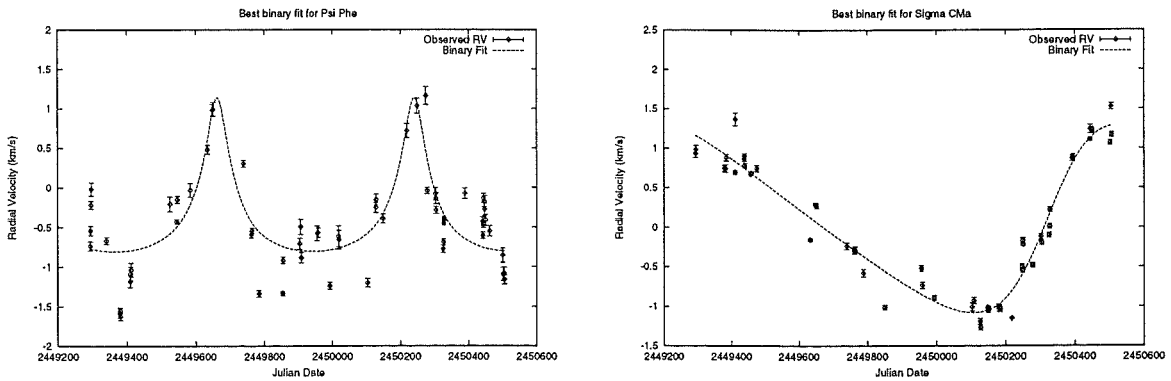

Figure 4.50: On the left are the radial-velocity data for ψ Phe and the best orbital fit, which has a period of 580 days and eccentricity of 0.55. On the right is a similar plot for σ CMa and the best orbital fit, which has a period of 1300 days and eccentricity of 0.29.

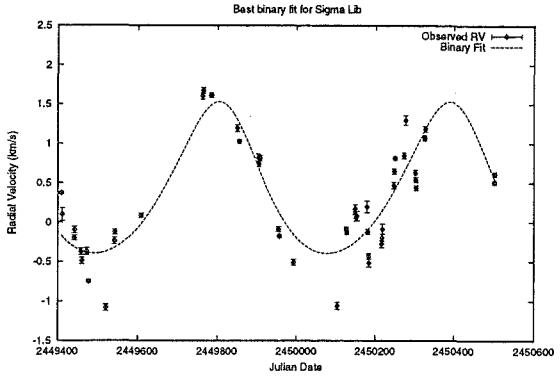

Figure 4.51: This figure shows σ Lib's radial-velocity data and its best orbital fit which has a period of 590 days and eccentricity of 0.17.

(the tabulated F-value plus its error, inverted): β Vol and ϵ Mus. In addition, η Scl is very nearly inconsistent by this same measure. While generally other stars may still owe part of their radial-velocity variations to their presence in a binary system and to other intrinsic variations, the following stars have orbital fits so poor that their variations can not be ascribed to a binary orbit: α TrA, β Col, ϵ Sco, ϵ TrA, η Sgr and HR 3017. Of these only η Sgr and HR 3017 have significant variations in radial-velocity and for these two stars the period of the binary orbit is similar to timescales present in the photometry, which would cast doubt on a binary interpretation of the radial-velocity variations anyway.

4.8 Reality of radial-velocity timescales

As was discussed in §4.1.3 many things, including non-regular, incoherent or multi-periodic variations, may result in **T6** finding a timescale which is not a good indication of the actual variations present. Hence to help prevent the consideration of false timescales, the following things should be taken into account before stars' timescales are considered further:

1. Stars should be significantly varying in radial velocity (at the 1% level, see §4.2 for how this was determined).

2. All timescales found by **T6** should be LSP significant (at the 1% level, see §4.1 for more details on **T6**).

3. When **orbsol** produces a significantly better fit to the data then **T6** (at the 1% level, see §4.7) the relevant timescale should be removed using the binary model.

4. No more than two prewhitenings, including the removal of binary-like variations by **orbsol**, should be performed before the timescale was found.

5. If a radial-velocity timescale found by **T6** is half[88] the frequency of another timescale found by **T6**, then the possibility that these represent manifestations of a single non-sinusoidal variation should be seriously considered. Similarly if the second largest peak in the periodogram is LSP significant (at the 1% level) and at half the frequency of the largest peak, then the possibility that the highest peak is a higher harmonic of the real non-sinusoidal timescale should also be considered (see Appendix B for the radial-velocity periodograms and footnote 12, this chapter, for what is meant by a higher harmonic).

[88] Or one third or one fourth etc, but this becomes hard to determine

6. An exception to items (1), (2) and (4) may be made if the timescale is independently verified — for example if it is a characteristic timescale (determined in §4.6) or has been reported in the literature by other researchers.

In view of these criteria the list of revised radial-velocity timescales is presented in Table 4.24. The following stars need further explanation:

- **orbsol** found α Sco's best binary fit to be 249 days and inspection of this star's periodogram (see Figure B.3) revealed that the variations are consistent with non-sinusoidal changes with the 139-day timescale found by **T6** being a higher harmonic of the smaller frequency. In addition, Smith et al. [156] observed radial-velocity variations of 260 ± 20 days (superimposed on a longer timescale of five or more years). So the 249-day periodic radial-velocity variation of α Sco is made up of at least two sine functions, one of which is of half the period of the other. When two such sine functions are added together the amplitude of the resulting periodic function is between about $(0.7A_0 + 0.85A_1)$ and $(0.7A_0 + A_1)$ (if these are greater than A_0), depending on the exact phase relationship between them, where A_0 is the amplitude of the longer period sine and A_1 is the amplitude of the higher harmonic. Using the amplitude of the peaks for α Sco found by **T6** as A_0 and A_1, $(0.7A_0 + A_1)$ is in agreement with the amplitude fitted by **orbsol**, so this has been taken as the amplitude of the radial-velocity variation.

- After removal of the dominant and secondary periods, β Gru has three significant periodogram peaks, with that having the highest peak corresponding to a timescale of 15 days (see Figure B.5). The other two peaks are approximately equal in height and one corresponds to 29 days, which is half the frequency of the 15-day peak. While this could indicate the 15-day timescale found by **T6** is a higher harmonic of an underlying 29-day timescale, both timescales are also present (along with the 59-day timescale) after the dominant period's removal. Hence it may be that they represent higher harmonics of a 59-day non-sinusoidal period, so these lower frequency timescales will not be discussed in the following sections.

- δ^1 Aps is believed to have a radial-velocity variation of $\approx$65 days, not the 29 days found by **T6** (see §4.6.1 for a discussion of why). Like α Sco the shorter period is believed to be a higher harmonic. The amplitude of the 29-day timescale was found to be 0.357 km/s and as the $\approx$65-day timescale is of almost the same amplitude, the approximate amplitude of the radial-velocity variation was estimated to be $(0.7 + 0.9) \times 0.357 = 0.571$ km/s.

- o^1 CMa has a very long-term radial-velocity variation present, which seems likely to be related to a similar long-term trend in the Hipparcos photometry (see §4.7). The variation is significantly longer than the data window and the 769-day radial-velocity timescale found by **T6** may be related to it and the spectral-window function.

4.9 Pulsations

A star undergoing pulsation is expected to have its radial velocity and photometry to behave in certain ways. If the pulsation is radial, it is expected that the timescales of pulsation will be similar to those predicted by linear non-adiabatic theory (although in the case of LPVs cooler than about 2700 K it can be significantly shorter). However, the photometric and radial-velocity curves are not necessarily expected to be regular. If shock waves are present the visual brightness might be expected to vary regularly while, depending on their formation level in the atmosphere, radial velocities obtained from atomic lines might vary irregularly (see §2.3.4). Not only that, but numerical models of nonlinear radial pulsation show that as the effective temperature of stellar models is lowered, the star's photometry and radial velocity begin to behave chaotically (see §2.3.3 for more details). Also, if radial velocity or photometry shows erratic behaviour due to shocks or chaotic

Star	$\mathcal{P}$ (days)	$A_{\rm rv}$ (km/s)	$\mathcal{P}_C$ (days)
24 Cap	✗		
3 Cet	None		
α Sco	$\approx$249	$\approx$1.4	$\approx$250
β Ara	None		
ϵ Cru	None		
ϵ Sco	✗		
ϵ TrA	✗		
η Sgr	None		
η^2 Pic	✗		
γ Cha	None		
γ Hyi	None		
γ Phe	194.2	15.97	
HR 3017	None		
2 Cen	556	0.444	$\approx$520
62 Sgr	588, 164, 96	0.944, 0.556, 0.388	$\approx$600
α TrA	✗		
β Col	✗		
β Gru	833, 59	1.043, 0.625	58
β Vol	✗		
δ^1 Aps	940, $\approx$65, 43	1.38,$\approx$0.6, 0.241	48, $\approx$65
δ^2 Gru	1429, 23	0.363, 0.238	24
ϵ Car	833	0.693	
ϵ Col	1430	6.1	
ϵ Mus	63, 625, 88	0.563, 0.538, 0.305	63(+30?)
η^2 Dor	667, 100	0.363, 0.231	$\approx$95
η Scl	49	0.411	48
γ Cru	556, 13, 16	0.353, 0.160, 0.159	13,16
γ Ret	909, 345	0.638, 0.512	$\approx$880
GZ Vel	2000, 270	0.796, 0.287	
HR 4177	435	0.483	
HR 6166	476	0.219	
κ Pyx	526	0.190	
L^2 Pup	141, 435	2.532, 1.275	140, $\approx$440
λ Vel	1410	1.02	$\approx$1100
N Vel	625	0.324	
NS Pup	1250	0.65	$\approx$1350
o^1 CMa	179, 769?	1.064, 0.963?	177,$\gtrsim$ 1250
ω Cap	472, 1250	4.19, 0.154	
π Pup	1250, 37, 47	0.400, 0.159, 0.129	35
ψ Phe	588, 189	0.638, 0.420	
σ CMa	1300	1.19	$\geq$ 1250
σ Lib	556, 120	0.785, 0.323	$\approx$100
sky	✗		
τ^4 Eri	588, 33	0.429, 0.183	$\approx$29
V337 Car	✗		

Table 4.24: **Revised radial-velocity timescales.** $\mathcal{P}$ are the timescales believed to be present in the stars' radial velocities, $A_{\rm rv}$ are the amplitudes of the timescales and $\mathcal{P}_C$ are the characteristic timescales (see §4.6 for what is meant by a characteristic timescale, an approximation sign is used if the timescale is not known to within a day or so). Generally the timescales and amplitudes are those determined by **T6**, unless a binary fit was found to fit the data significantly better at the 1% level. The exceptions to this are discussed in the text. A ✗ indicates the relative radial velocities are not significantly varying at the 1% level.

pulsation, the phase relationship may not be that expected from simple linear pulsation — i.e. recessional velocity and visual brightness in anti-phase. In the case of chaotic behaviour the stellar

radius and radial-velocity changes should still be consistent, but if the radial velocity comes from material above the base photosphere pulsation and is interfered with by a shock even this may not be the case.

If the pulsation is non-radial, the periods are expected to be shorter than the fundamental-mode radial-pulsation prediction in the case of acoustic modes, probably longer in the case of gravity modes and between two tenths and one and a half times the rotation period in the case of toroidal modes. As the last two can be of a similar length to the period of rotation they are particularly dependent on the exact details, such as the relative period and orientation, of the rotation and pulsation. In addition, r-modes are not expected to give rise to variations in light. For late-type stars, non-radial modes of a high spherical harmonic order are expected to be acoustic modes in the envelope, but high spherical harmonic order pulsations are not important for the 44 stars observed for this thesis, as their radial-velocity precision will probably only enable the detection of harmonic orders less than four. As is the case for radial pulsations, in order to determine pulsation amplitudes, nonlinear calculations need to be undertaken for the stars in question. In lieu of these, the amplitudes for solar-like oscillations (which are believed to be smaller than those expected from κ-type mechanisms) can be calculated by scaling up from the Sun. See §2.3.5 for further details.

4.9.1 Using mass and radius to determine radial pulsation modes

In order to determine pulsation modes for the 44 stars which have been observed for this thesis the period predictions of Ostlie & Cox [128] have been used. Ostlie & Cox used linear non-adiabatic pulsation modelling of stars (for which convection is important) to derive period-mass-radius relations for the fundamental-mode and first-overtone pulsation. They did so by creating models which cover the region of the HR diagram where the giant stars observed for this thesis reside, although primarily their interest was in the behaviour of Mira variables. These relations are

$$P_0 = (1.202 \times 10^{-2}) \frac{\mathcal{R}^{1.86}}{\mathcal{M}^{0.73}} \text{ days}$$

for the fundamental mode and

$$P_1 = (2.512 \times 10^{-2}) \frac{\mathcal{R}^{1.59}}{\mathcal{M}^{0.51}} \text{ days}$$

for the first overtone, where $\mathcal{M}$ and $\mathcal{R}$ are the stars' mass and radius in solar units[89].

Given that the periods are determined from

$$P = a \frac{\mathcal{R}^b}{\mathcal{M}^c}$$

error propagation (see, for example, Bevington & Robinson [21] §3.2) leads to

$$\frac{\delta P}{P} = b \frac{\delta \mathcal{R}}{\mathcal{R}} - c \frac{\delta \mathcal{M}}{\mathcal{M}},$$

where the covariant terms can not be neglected as the errors in $\mathcal{R}$ and $\mathcal{M}$ are related. It should be noted that if Bessell's mass-luminosity-temperature grid was used to obtain stellar mass and the Hipparcos catalogue to find luminosity (see §4.5) this can be simplified to

$$\frac{\delta P}{P} = \left(\frac{b}{2} - \frac{c}{1.65} \right) \frac{\delta \mathcal{L}_{\text{bol}}}{\mathcal{L}_{\text{bol}}},$$

[89] It should be noted that these obey a similar relation to the pulsation constant (see §2.3.1), but calculated for Mira-type variables

where it has been assumed that the main source of errors is the determination of the stellar parallax. See Table 4.25 for the resulting periods[90] for all 44 stars where the mass and radius tabulated in Table 4.16 have been used. In this table o^1 CMa is given twice, as its mass and radius are known more accurately from Sasselov [141] and Lutz & Pagel [118] (the errors in its parallax are large[91]).

For the five stars considered to be supergiants in the Michigan catalogue (see Table 1.1), the fundamental period has also been calculated using the relation for fundamental-mode radial pulsation in supergiants from Schaller [144]. The relation appropriate for such cool stars is

$$\log P_0 = -0.339 M_{\rm bol} - 2.951 \log T_{\rm eff} + 10.407,$$

where the assumptions on stellar evolution pertaining to mass are included within this formula. The results, generally still using the estimated fundamental parameters from Table 1.1, are as follows:

- 3 Cet's fundamental period is estimated to be 20 ± 20 days. The prediction of a 20-day fundamental period for a supergiant pulsation contrasts with the Ostlie and Cox prediction of approximately 40 days for a giant pulsation — this difference is due to the different stellar models used.
- α Sco's fundamental period is estimated to be 500 ± 200 days. This is not significantly different from the giant model prediction of approximately 500 days. Interesting, this prediction is more in agreement with the Ostlie and Cox predictions than those for 3 Cet, perhaps indicating some overlap in the two sets of models.
- β Ara's fundamental period is estimated to be 19 ± 5 days. The prediction of a 19-day timescale contrasts with the giant model prediction of approximately 30 days.
- o^1 CMa's fundamental period is estimated to be 47 days using Lutz & Pagel's apparent magnitude and effective temperature, and 70 ± 40 days using the Hipparcos and **hr_diag**'s predictions.
- π Pup's fundamental period is estimated to be 70 ± 20 days. The prediction of a 70-day timescale contrasts with the giant model prediction of approximately 90 days.

While the fundamental periods are of the same order of magnitude for both predictions, the formula pertaining to supergiants generally results in periods about 25% smaller. However, in both the supergiant and giant cases if the star has lost far more mass than was allowed for when predicting mass from luminosity and effective temperature, the periods can be a great deal longer than those predicted[95]. For supergiants, observed periods can be 1.5–4 times longer than that predicted for what is believed to be this very reason (see Lovy et al. [116] and Schaller [144]). If $M_{\rm true}$ is the true mass, $M_{\rm pred}$ is the predicted mass and E_M is the fraction of mass remaining then $M_{\rm true} = E_M M_{\rm pred}$. If the predicted period is of the form $P_{\rm pred} = aR^b/M^c$, for it to equal the observed period, $P_{\rm obs}$, the fraction of mass left must be $E_M = (P_{\rm pred}/P_{\rm obs})^{1/c}$. This means a period four times longer than that observed (using Ostlie and Cox's relation) equates to a mass loss of 85%, over and above any mass loss allowed for in the evolution calculations!

[90] The 13 stars observed photometrically at Mt John have already had these predictions compared to their timescales at a conference on stellar pulsation at Los Alamos in June of 1997, see Cummings et al. [44]

[91] Also **hr_diag** assumes stars are normal giants (which is not the case for this star) to obtain effective temperature and any errors in effective temperature will be reflected in the resulting estimation of mass and radius. Fortunately the errors introduced into effective temperature by this assumption are not expected to be large (see §4.5.1).

[92] Determined by eye, from Figure 4.19

[93] Determined from the short-term "25-day" timescale (see §4.6.1 for more details)

[94] In L^2 Pup's case the phase given for the 140-day timescale is that for the two data subsets not the "average"

[95] Also the lack of time-dependent convection and inaccurate opacities can result in period predictions significantly in error, see the subsection on pulsational instability in §2.3.2 and also footnote 29 in Chapter 2

Star	P_0	P_1	$v_{osc}/\delta M_V$	$\mathcal{P}_C$	A_{rv}/A_V	Phase (deg.)
2 Cen	36 ± 1	23.4 ± 0.9	16.3	≈520	21.1?	
24 Cap	19 ± 3	15 ± 2	20.3			
3 Cet	40 ± 20	30 ± 10	21.3			
62 Sgr	40 ± 4	28 ± 3	17.6	≈600	18.3?	in phase
α Sco	500 ±200	300 ±100	16.5	≈250	61.7?	
α TrA	28 ± 3	24 ± 2	22.9			
β Ara	29 ± 5	24 ± 4	22.3			
β Col	0.85± 0.01	1.00± 0.02	28.1			
β Gru	50 ± 2	35 ± 1	17.3	58	10.5	-134
β Vol	0.78± 0.01	0.93± 0.02	28.1			
δ^1 Aps	72 ± 9	50 ± 7	17.1	48, ≈65	$\approx 7^{92}$	anti-phase
δ^2 Gru	33 ± 4	24 ± 3	17.7	24	5.6	43
ϵ Car	34 ± 5	29 ± 4	26.9			
ϵ Col	2.3 ± 0.1	2.5 ± 0.1	28.4			
ϵ Cru	5.2 ± 0.3	4.9 ± 0.2	23.5			
ϵ Mus	48 ± 2	33 ± 1	16.7	63(+~30?)	21.9	150
ϵ Sco	0.98± 0.02	1.15± 0.02	28.1			
ϵ TrA	1.68± 0.08	1.86± 0.08	27.6			
η^2 Dor	29 ± 3	22 ± 2	18.8	≈95	11.7?	
η^2 Pic	8.8 ± 0.7	7.5 ± 0.6	21.6			
η Scl	32 ± 4	23 ± 3	18.2	48	12.4?	
η Sgr	18.3 ± 0.8	13.5 ± 0.6	18.4			
γ Cha	15.0 ± 0.9	12.2 ± 0.7	20.9			
γ Cru	25.3 ± 0.5	18.2 ± 0.3	18.0	13, 16	17.4^{93}	anti-phase
γ Hyi	16.2 ± 0.6	12.6 ± 0.4	19.5			
γ Phe	12.0 ± 0.6	9.8 ± 0.5	20.7			
γ Ret	38 ± 3	28 ± 2	17.9	≈880	15.1?	anti-phase
GZ Vel	33 ± 9	27 ± 7	22.3			
HR 3017	90 ± 30	70 ± 20	20.2			
HR 4177	60 ± 20	40 ± 20	21.3			
HR 6166	12 ± 1	9.8 ± 0.9	20.8			
κ Pyx	13 ± 1	11 ± 1	21.2			
L^2 Pup[94]	60 ± 4	38 ± 3	15.2	140, ≈440	5.0	-75
λ Vel	52 ± 7	41 ± 5	21.0	≈1100	34.4?	anti-phase
N Vel	10.8 ± 0.4	9.2 ± 0.3	21.6			
NS Pup	60 ± 20	50 ± 20	21.4	≈ 1350	53.9?	132
o^1 CMa	90 ± 40	70 ± 30	21.7	177, $\gtrsim$ 1250	21.9, ?	108
o^1 CMa¶	51	41	23.8	"	"	"
ω Cap	25 ± 4	20 ± 4	20.6			
π Pup	90 ± 20	70 ± 20	21.2	35	14.6	-38
ψ Phe	30 ± 2	21 ± 1	17.7			
σ CMa	80 ± 20	60 ± 20	20.2	≥1250	37.7?	-153
σ Lib	32 ± 3	23 ± 2	18.5	≈100	7.1–14.1?	
τ^4 Eri	30 ± 2	21 ± 1	17.9	≈29	23.2?	in phase
V337 Car	24 ± 3	21 ± 3	22.9			

Table 4.25: **Period predictions for linear, non-adiabatic, radial pulsation.** This table shows the estimated periods for pulsations of Ostlie and Cox type, where P_0 is the fundamental and P_1 the first overtone period. $v_{osc}/\delta M_v$ is the estimated ratio of the amplitude of radial-velocity variations over visual-photometry variations for an acoustically pulsating star (in km/s per mag.). $\mathcal{P}_C$ is the characteristic timescale where the timescale and amplitude-ratio value tabulated is preferentially that of concurrent radial velocity and photometry (for more details see §4.6.1). When concurrent data has not been available, or does not have these timescales, the offending amplitude ratios have been marked with a ?, acknowledging that the amplitude of the pulsations may change over time. Phase is the number of degrees by which maximum recessional radial velocity leads maximum visual brightness (again, see §4.6.1 for more details) and if just in phase (or anti-phase) is tabulated the precise phase relationship is unknown. A_{rv}/A_V is the ratio of the amplitudes of the timescales, where A_V is appropriate for **T6** fitting a cosine to the visual-photometry data and A_{rv} is the revised radial-velocity amplitude (see §4.7). The masses and radii and temperatures used for these estimations are those given in Table 4.16 in every case except that of o^1 CMa¶, where Sasselov [141] has been used for the mass ($\mathcal{M}$= 9.5) and Lutz & Pagel [118] has been used for the radius and effective temperature ($\mathcal{R}$= 215 using gravity, mass and $g = \frac{GM}{R^2}$; $T_{\rm eff}$ = 4165K).

If the amplitude of the pulsating stars is not too large Kjeldsen & Bedding [108] show that

$$\frac{\delta\,\mathcal{L}_\lambda}{\mathcal{L}_\lambda} = \frac{v_{\rm osc}({\rm m/s})}{(\lambda/550{\rm nm})(T_{\rm eff}/5777K)^2} 2.01 \times 10^{-5}.$$

Here $v_{\rm osc}$ is the disc integrated radial-velocity oscillation amplitude and $(\delta\,\mathcal{L}_\lambda\ /\ \mathcal{L}_\lambda)$ is the resulting fractional variation in luminosity at wavelength λ. This is only appropriate for blackbodies and is calibrated for classical acoustic oscillations, but the predicted luminosity variations, when compared to those which are observed, are surprisingly good. For example, despite the exclusion of Mira variables in the calibration process Mira itself obeys the relation reasonably well, as do the solar-like oscillation in the Sun! If this is any indication, the deviation from this relation will be little over 30% for late-type evolved stars. This allows the prediction of the relationship between the observed radial-velocity amplitude and the observed visual-magnitude amplitude. Assuming the variation in luminosity is small and taking visual magnitude to mean $\lambda = 550$ nm, the equation $\log(\mathcal{L}_{550}) = 1.93 - 0.4M_{\rm V}$ can be used to obtain

$$\delta M_{\rm V} = \frac{\log(e)}{0.4}\frac{\delta\,\mathcal{L}_{550}}{\mathcal{L}_{550}},$$

which means that

$$\frac{v_{\rm osc}}{\delta M_{\rm V}} = \frac{0.4}{\log(e)}\left(\frac{T_{\rm eff}}{5777}\right)^2 \div (20.1 \times 10^{-3}) = 45.82\left(\frac{T_{\rm eff}}{5777}\right)^2,$$

in units of km/s per magnitude. This is the amplitude relation typically used for classical oscillators like Cepheids and the predictions for the 44 stars surveyed for this thesis are shown in Table 4.25.

All revised radial-velocity timescales and their amplitudes (in km/s) are given in Table 4.26. As has been mentioned, Table 4.25 contains the estimated periods for pulsations of Ostlie & Cox type and the estimated ratio of radial-velocity to visual-magnitude amplitude. In addition, this table contains a summary of the characteristic periods, their observed ratio of radial-velocity to visual-magnitude amplitude and the phase relationship between the two observables. Having predicted the radial-pulsation periods and amplitude ratio for the 44 observed stars the important question is whether any of these stars are pulsating in such a manner. This is easier to answer if concurrent photometry is available for the stars. In this case the question becomes "Should a variation present in radial velocity be observable in the concurrent photometry?" and if the photometric variations are compatible with a classical pulsation, "Is the timescale compatible with the linear radial period predictions?". In order to answer these questions the timescales' amplitudes have been considered (this will be called $A_{\rm rv}$, in the case of radial velocities and $A_{\rm V}$, in the case of visual photometry). As the precision of the Mt John photometry[96] is only slightly better than 0.01 magnitudes, in order for a timescale to be picked up in sufficiently sampled concurrent photometry, any radial-velocity variation would have to have a radial-velocity amplitude of significantly greater than $0.01 \times (v_{\rm osc}/\delta M_{\rm V})$. In addition, as the ratio for some characteristic timescales are significantly greater than that of predictions, the requirement for a radial-velocity timescale to be apparent in the concurrent visual photometry will be taken as $A_{\rm rv} \geq 0.02 \times (v_{\rm osc}/\delta M_{\rm V})$. The following may be deduced for the 13 stars for which concurrent Mt John photometry is available (only revised timescales, see §4.8 for details, are considered):

- The amplitude of β Gru's 833-day radial-velocity timescale should make it apparent in concurrent photometry; however, it is not characteristic so it is unlikely to be due to an acoustic pulsation. The revised radial-velocity timescale is 59 days, which is this star's characteristic

[96] If a timescale is not regular it need not necessarily be present in the higher accuracy Hipparcos photometry

timescale. β Gru's 58-day characteristic timescale is slightly larger than its predicted fundamental mode. Its radial velocity and visual photometry are in anti-phase[97], as would be expected of a "simple" pulsation (i.e. linear and without interference from shock waves) and the ratio of the radial-velocity variations to Mt John visual photometry variations is about $\frac{2}{3}$ of that predicted. The star's variation in both photometry and radial velocity are somewhat erratic, which may indicate that the star is undergoing nonlinear radial pulsation in its fundamental mode.

- The amplitude of δ^1 Aps' 940-day radial-velocity timescale should make it apparent in concurrent photometry; however, it is not so it is unlikely that it is due to an acoustic pulsation. In addition, the angular-diameter variations are not compatible with its variations in radial velocity, which is a sign that either shock waves are present or it is not a radial-pulsation (see §4.6.2, assuming that the 476-day timescale found for the angular diameters is a higher harmonic of a 940-day timescale). The other two revised radial-velocity timescales are believed to correspond to characteristic timescales of 48 and $\approx$65 days. δ^1 Aps' $\approx$65-day characteristic timescale is consistent with its predicted fundamental mode and only slightly longer than its predicted first overtone. The 48-day characteristic timescale is consistent with the predicted length of the star's first overtone pulsation. Its radial velocity and visual photometry are in anti-phase and the ratio of the radial-velocity variations to Mt John visual photometry variations are about $\frac{1}{2}$ of that predicted. The star's variation in photometry and radial velocity are comparatively regular and the entire picture seems consistent with linear radial multi-periodic pulsation in the star's fundamental and first overtone modes.

- The amplitude of δ^2 Gru's 1429-day radial-velocity timescale should make it apparent in concurrent photometry; however, it is not characteristic so it is unlikely to be due to an acoustic pulsation. δ^2 Gru's only other revised radial-velocity timescale is its 24-day characteristic timescale. This is consistent in length with a radial pulsation in its first overtone mode. Its phase relationship may be that of maximum luminosity at maximum radial velocity, which would not be expected for a simple pulsating star and could indicate shock waves or nonlinear pulsation, but there is too little concurrent data to know for sure. The ratio of the radial-velocity variations to Mt John visual-photometry variations is about $\frac{1}{3}$ of that predicted. This star's variations in both photometry and radial velocity are somewhat erratic and hence this 24-day timescale may be due to nonlinear pulsation in its first-overtone mode.

- ϵ Col's 1430-day radial-velocity timescale's amplitude should make it apparent in concurrent photometry; however, it is not characteristic so it is unlikely to be due to an acoustic pulsation.

- ϵ Mus' 625-day radial-velocity timescale's amplitude should make it apparent in concurrent photometry; however, it is not characteristic so it is unlikely to be due to an acoustic pulsation. Its 63-day timescale is its characteristic timescale and it also has an 88-day radial-velocity timescale, which need not be present in the photometry due to its small amplitude. This star's characteristic timescale is significantly longer than its predicted fundamental, although there are some indications that at times the timescale may half in size. Its radial velocity and visual photometry are in anti-phase and the ratio of the radial-velocity variations to Mt John visual photometry variations are about $1\frac{1}{4}$ times that predicted. So while the timescale is too long, everything else points towards radial pulsation being very plausible. This would be compatible if the star had lost 27% of its mass. As is common for these stars, its variations in both photometry and radial velocity are somewhat erratic so this 63-day timescale may be due to nonlinear pulsation in the star's fundamental mode. If the 63-day timescale is

[97] Of course **T6** finds the phase by fitting a sine wave to the data, so this means the two sine-wave fits are in anti-phase. If two sine waves are fitted to the radial-velocity and visual-photometry curves in Figure 2.7, which gives the relationship seen for both Cepheids and Mira variables, they would also be in anti-phase.

the fundamental period, the apparent ~30-day timescale may mean the star mode switches between the fundamental and a higher order mode. However, this would also mean that the 88-day timescale, if not some artifact of prewhitening failing to deal with mode switching, is either not a pulsation or is a non-acoustic non-radial mode (gravity or toroidal). While a mass loss of about 55% would equate to a fundamental period of a size compatible with the 88-day observed timescale, this would not be compatible with the 63-day timescale being a radial pulsation.

- η Scl's characteristic timescale is significantly longer than its predicted fundamental radial period; however, this is compatible with a radial pulsation if the star has lost 33% more of its mass than expected. While its phase relationship is unknown, the ratio of the radial-velocity variations to Hipparcos visual-photometry variations is about $\frac{2}{3}$ of that predicted. This star's variations in both photometry and radial velocity are somewhat erratic, so this 48-day timescale may be due to nonlinear pulsation in the star's fundamental mode. Unfortunately, this star was initially believed to be constant in visual photometry due to a varying check star, so insufficient concurrent Mt John photometric observations have been obtained for this timescale to be observed. Its velocity amplitude equates to a predicted visual amplitude of 0.02 magnitudes, so this should be visible with enough data.

- The amplitude of γ Cru's 550-day radial-velocity timescale means it need not be apparent in concurrent photometry. However, it is a factor of fifty longer than the radial prediction so if it is a pulsation it would have to be a non-acoustic non-radial mode. The only other revised radial-velocity timescales are the 13 and 16-day characteristic timescales. The latter is only slightly shorter than the predicted first overtone period of 18 days. The radial velocity and visual photometry seem to be in anti-phase, which is what is expected of a simply pulsating star, although there is too little concurrent data to be entirely sure of this. The ratio of the radial-velocity variations to Mt John visual-photometry variations is approximately equal to that predicted. This star's variations in both photometry and radial velocity are somewhat erratic, so the 16-day timescale may be due to nonlinear pulsation in the first overtone mode and the 13-day timescale due to some higher overtone or p-mode oscillation.

- κ Pyx's 526-day timescale has such a small radial-velocity amplitude that it need not be present in the concurrent photometry. However, it is far too long to be caused by an acoustic pulsation.

- L^2 Pup's characteristic ≈440-day timescale is too long to be due to an acoustic pulsation. The only other revised timescale in this star's full radial-velocity data set is its characteristic timescale of 140 days. This is double the length expected for radial linear pulsation. Also the ratio of the radial-velocity variations to Mt John visual-photometry variations is about $\frac{1}{3}$ of that predicted, which is surprisingly low. Its phase relationship is that of maximum luminosity almost quarter of a period before maximum radial velocity, which would not be expected for a simply pulsating star and could indicate shock waves or nonlinear pulsation. Indeed, in the literature this star has been indicated as potentially having shock waves (see §2.3.4 for more details), which can cause high mass loss and hence would modulate the period accordingly. Not only that, but as is expected of shock waves (as opposed to nonlinear pulsation) the radial-velocity variations are more irregular than the photometric variations. However, the calculation of the star's angular diameter in §4.6.2 reveals that the angular-diameter and radial-velocity variations are exactly what would be expected for a radial pulsation, which favours nonlinear pulsation rather than a shock-wave explanation. Regardless of the exact mechanism of irregularity, this star seems to be an ideal candidate for radial pulsation and an unexpectedly large mass loss, possibly helped by shock waves. This agrees with the literature, which has long described this star as a semi-regular variable.

- o^1 CMa's long-term/769-day radial-velocity timescale is over a factor of six times longer than the radial prediction, so if it is a pulsation it would have to be a non-acoustic non-radial mode. The only other revised timescale in the radial velocities is the star's 177-day characteristic timescale. As this star is a supergiant the appropriate period predictions to use are those derived using Schaller's relation. In which case, the predicted fundamental period of 47 days is over a factor of three times smaller than the observed 177-day timescale. However, the characteristic timescale's ratio of radial-velocity variations to Mt John visual-photometry variations is approximately equal to that predicted and the phase relation is that of being in anti-phase, which is what is expected for a simply pulsating star. In addition, Lutz & Pagel's absolute magnitude for o^1 CMa of $M_v = -4.7$ places this star on the HR diagram amongst the RV Tauri variables (see Figure 1.2) and the light curve of this star is exactly what would be expected of a RVb-type RV Tauri star (see Figures D.11 and E.19), so it is tempting to believe that this supergiant star is an RV Tauri star and therefore its 177-day timescale is from radial pulsation. But if this is the case the period prediction has failed, which could be due to the star having lost mass. This star would then be at the high end of extra mass loss in supergiants, having a mass thats only 18%[98] of that predicted by Sasselov.

  Interestingly, models based on W Vir stars indicate that the light curve of RV Tauri stars can be associated with double the number of minima as the radial surface velocity (see Buchler & Kovàcs [29] Figure 6), which is what is seen for o^1 CMa (see Figure 4.23). If this was the case then the linear fundamental period would actually be half[99] that observed, which agrees well with the predictions for this star, from the Hipparcos fundamental parameter predictions at least. This contrasts with the suggestion of Fokin [51] that the secondary minima in the light curve of RV Tauri stars is due to shock waves and alternations of the first overtone. o^1 CMa is not compatible with Fokin's suggestion, as first overtone variations should also be present in the radial velocities, but clearly are not[100] (again, see Figure 4.23)!

- The amplitude of ω Cap's 476-day radial-velocity timescale should make it apparent in concurrent photometry; however, it is not characteristic so it is unlikely to be due to acoustic pulsation. In addition, the 1250-day timescale is 50 times the length of its predicted fundamental mode, so if it is a pulsation it would have to be a non-acoustic non-radial mode.

- The amplitude of π Pup's 1250-day radial-velocity timescale is sufficiently small that it need not be apparent in concurrent photometry; however, it is almost 15 times the length of its predicted fundamental mode, so if it is a pulsation it would have to be a non-acoustic non-radial mode. Its 37-day timescale is a characteristic timescale and its 47-day radial-velocity timescale is of sufficiently small amplitude that it does not have to be present in the Mt John visual photometry. This star is a supergiant hence the fundamental period relation of Schaller is appropriate. Its characteristic period is significantly shorter than that of 70 ± 20 days predicted for its linear radial fundamental; however, it may be a higher order or a non-radial acoustic mode. Its phase relationship is almost in phase, which would not be expected for a simply pulsating star and may indicate chaotic pulsation or the presence of shock waves. The ratio of the radial-velocity variations to Hipparcos visual-photometry variations is about $\frac{2}{3}$ of that predicted. Pulsation in an acoustic mode can not be ruled out for this 35-day timescale, with the 47-day timescale perhaps being the star's fundamental radial mode.

[98] Using Ostlie and Cox's period relation to estimate mass loss

[99] Or one forth, or one eighth ...

[100] Radial velocities with a period equivalent to half the "formal" period have been observed in RV Tauri stars (see, for example, Pollard [133]). In the case of R Sct this is consistent with Fokin's model, in that the optical radial velocities repeat twice the star's "formal" period, while infrared radial velocities do not because the shocks are being produced above the infrared region. Two shocks are produced every formal period, with the second resulting from the first overtone (which is responsible for the second light minima). See Pollard [133] for more details on this star and §2.3.4 for more details on the effect shock waves have on the observed radial velocities.

- The amplitude of τ^4 Eri's 588-day radial-velocity timescale should make it apparent in concurrent photometry; however, it is not characteristic so it is unlikely to be due to an acoustic pulsation. Its only other revised timescale in radial velocity is the characteristic timescale of $\approx$29 days. This is the same size as the predicted fundamental radial period for this star. Its phase relationship may be that of maximum luminosity at maximum radial velocity, which would not be expected for a simple pulsating star and could indicate shock waves or nonlinear pulsation, but there is too little concurrent data to know for sure. The ratio of the radial-velocity variations to Hipparcos visual-photometry variations is about $\frac{2}{3}$ of that predicted. This timescale is not found by **T6** in the Mt John photometry, which is not surprising as its radial-velocity amplitude equates to an amplitude in magnitude variations of only 0.01, which is at the edge of Mt John's photometric precision. This star's variations in both photometry and radial velocity are somewhat erratic, so this $\approx$29-day timescale may be due to nonlinear pulsation in its fundamental mode.

Stars for which no photometry was obtained concurrently can not give as much information about the cause of the of radial-velocity variation unless the timescales are present long term. For some of these stars; however, the same characteristic timescale does seem to be present in both the radial velocity and the Hipparcos photometry. This may indicate a coherent or recurrent, if not necessarily regular, timescale. For stars without concurrent photometry the following things can be said[101]

- 62 Sgr's characteristic timescale of $\approx$600 days is over a factor 10 longer than that predicted for radial linear pulsation. However, it is also present in the Hipparcos photometry so unless this is a coincidence, the only form of pulsation this could be is a non-radial g-mode pulsation. The star also radial-velocity timescales of 164 and 96 days. The 164-day timescale is 3.7 times the maximum fundamental period predicted, so could only be due to acoustic pulsation if the star has suffered mass loss of 85% (in which case the 96-day timescale might be a higher acoustic pulsation mode). Even if the 164-day timescale is not caused by acoustic pulsation, the 96-day timescale can only be due to radial pulsation if the star has lost 67% of its mass.

- α Sco's characteristic timescale of $\approx$250 days is only slightly shorter than the Schaller predictions for the length of its fundamental pulsation, although its ratio of the radial-velocity variations to Hipparcos visual-photometry variations is unexpectedly large at about four times that predicted. In addition, Smith et al. [156] observed radial-velocity variations in this star of 260 ± 20 days and suggested this star, along with two others, might be undergoing non-linear radial pulsations.

- η^2 Dor's characteristic timescale of $\approx$95 days is approximately three times that predicted for radial linear pulsation. Its ratio of the radial-velocity variations to Hipparcos visual-photometry variations is about $\frac{2}{3}$ of that predicted. If this star is pulsating it either has suffered unexpected mass loss and is only one fourth of the mass predicted, or it is pulsating in a non-radial g-mode. In addition, the 667-day radial-velocity timescale for this star is over 20 times as long as the fundamental period predicted for radial linear pulsation. If this timescale is due to pulsation it would have to be a non-acoustic non-radial pulsation.

- σ Lib has timescales of approximately 100 days in its photometry and radial velocity. These are almost three times those expected for a linear radial pulsation and the ratio of the radial-velocity variations to Hipparcos visual-photometry variations is about $\frac{1}{3}$–$\frac{3}{4}$ of that predicted. If this star is pulsating it has either suffered unexpected mass loss and is only one fourth of

[101] As no concurrent photometry is available, timescales need not be present in both photometry and radial velocities. Hence the two things that are of interest are characteristic timescales, because they may represent a coherent or recurrent variation, and all timescales which are the same as those from the linear radial predictions. Only timescales given in Table 4.24 will be considered.

the mass predicted, or it is pulsating in non-radial g-mode. In addition, the 556-day radial-velocity timescale for this star is over 15 times as long as the fundamental period predicted for radial linear pulsation. If this timescale is due to pulsation it would have to be a non-acoustic non-radial pulsation.

The revised timescales in all other stars are too long to have been caused by any pulsation other than a non-acoustic non-radial mode. However, the largest amplitude revised timescales of 2 Cen, γ Ret, λ Vel, NS Pup and σ CMa are also present in the Hipparcos photometry so unless this is a coincidence, in these cases the only form of pulsation which could be responsible is a non-radial g-mode.

While predictions of the amplitude of radial pulsations are not generally available, the amplitude of the radius variations implied by the radial-velocity amplitude is and if this is too large a radial pulsation explanation of the variations can be ruled out. If the star is undergoing a sinusoidal pulsation so that $\delta R_\star = A_R \sin(2\pi \frac{t}{\mathcal{P}})$; then, the velocity of the stellar surface, $\frac{dR_\star}{dt}$, will be $2\pi A_R \cos(2\pi \frac{t}{\mathcal{P}})/\ \mathcal{P}$. This is related to the radial-velocity amplitude by factor involving limb darkening and projection effects, say (17/24), and hence the fractional amplitude of the variation in radius is

$$\frac{A_R}{R_\star} = \frac{A_{\rm rv}\,\mathcal{P}}{2\pi(17/24)R_\star}.$$

No real pulsations can have $A_R/R_\star$ too large a fraction of one. Hence this simple test was applied to all of the above timescales for which radial pulsation is believed to be possible. The the radius estimations given in Table 4.16 were used for this and they reveal that for these potential radial pulsation timescales $A_R < 0.1R_\star$.

4.9.2 Solar-like pulsation estimations

There are few predictions for non-radial pulsation in late-type stars, which are likely to be observable by radial-velocity observations of the precision obtainable for this thesis. One of the few which is available is the prediction of the non-radial solar-like oscillations, found by scaling up from the Sun following the method of Kjeldsen & Bedding [108]. These p-mode pulsations may be expected to be present in the late-type stars observed for this thesis, as they are believed to be excited by turbulent convection. This method has the advantage of also allowing the prediction of the amplitude of the oscillations. It is also believed that the amplitudes of acoustic pulsation driven by other methods will be larger than these.

This paper predicts for solar-like oscillations a power spectrum with a broad envelope of power centred at

$$\nu_{\rm max} = \frac{\mathcal{M}}{\mathcal{R}^2\,\sqrt{T_{\rm eff}/5777}} 263.52\ ({\rm d}^{-1}).$$

This frequency will equate to mode number

$$n_{\rm max} \approx 2.6\left(\frac{\mathcal{M}}{\mathcal{R}\,T_{\rm eff}/5777}\right)^{0.5} - 1.6.$$

The radial-velocity oscillation amplitude of the star will be

$$v_{\rm osc} = \frac{\mathcal{L}_{\rm bol}}{\mathcal{M}}(23.4 \pm 1.4) \times 10^{-5}\ ({\rm km/s})$$

and the many present oscillation modes should be separated by

$$\Delta\nu = \frac{\mathcal{M}^{0.5}}{\mathcal{R}^{1.5}} 11.66\ ({\rm d}^{-1}).$$

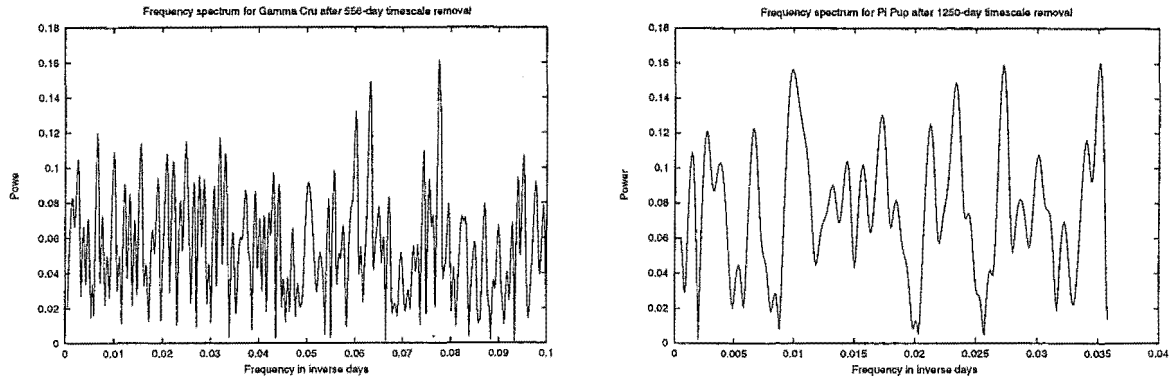

Figure 4.52: To the left is the frequency spectrum of radial velocities for γ Cru and to the right is a similar plot for π Pup (to aid comparison with Kjeldsen et al. these are not Lomb-Scargle periodograms[105]). Predictions for solar-like oscillations in these stars are for a broad envelope of power, centred around a maximum frequency with evenly separated frequencies. In γ Cru's case, the prediction is for a maximum at 0.097 d^{-1} and frequencies separated by 0.02 d^{-1}. This compares well to the power spectrum shown above, where the frequency of maximum power is 0.077 and when this is removed by prewhitening a frequency of (0.077-0.014) d^{-1} is found to be the maximum. In π Pup's case, the expectation is for a maximum at 0.036 d^{-1} and separations of 0.007 d^{-1}. Again this compares well to the power spectrum shown at the right, where the frequency of maximum power is 0.027 and when this is removed by prewhitening à frequency of (0.027-0.006) d^{-1} is found to be a maximum. However, in neither case is the expected "broad envelope of power" apparent.

Consideration of the radial-velocity oscillation timescales for the 44 stars observed for this thesis, as given in Table 4.26, reveals that the only stars with timescales compatible with those predicted for solar-like oscillations are[102] γ Cru and π Pup. Stars with timescales somewhat bigger, but not smaller, than the predicted frequency of maximum power have been included, because their larger maximum-power timescales can be explained by unexpected mass loss. The amplitude of these timescales are all consistent with that predicted, or slightly smaller as this can also occur if the star has lost unexpected mass[103]. However, this alone is not sufficient for a radial-velocity variation to be considered a candidate for solar-like oscillations. Such oscillations are associated with a broad spectrum of power with many similar periods separated by $\Delta\nu$. Fortunately γ Cru and π Pup all have two revised timescales present, which allows the comparison of their frequency separation with that predicted. The predictions and observed timescales are as follows:

- γ Cru's observed timescales are 13 and 16 days, which is a frequency separation of 1.4×10^{-2} d^{-1}. This compares favourably with the prediction of 2.4×10^{-2} d^{-1}.
- π Pup's observed timescales are 37 and 47 days, which is a frequency separation of 5.8×10^{-3} d^{-1}. This compares favourably with the prediction of 7.0×10^{-3} d^{-1}.

However, the two compatible stars γ Cru and π Pup certainly have not been observed frequently enough to say any more. See Figure 4.52 for the frequency spectrum of the data — there are insufficient observations for the tell-tale "comb-like pattern" (see Kjeldsen et al. [109]) typical of solar-like oscillations, to form.

[102] δ^1 Aps is not being included as it is believed that the real timescale is ≈65 days not 29 days (see §4.6.1)

[103] Using Bessell's approximate relationship for luminosity in terms of mass (see §4.5.1) means that approximately have $v_{osc} \propto \mathcal{M}^{0.65}$

[105] The Lomb-Scargle periodograms are the right-hand side of Figure B.12 and the left-hand side of B.20 respectively

Star	$P_{\rm max}$	$v_{\rm osc}$	$\mathcal{P}_{\rm rv}$	$A_{\rm rv}$
2 Cen	16.3±0.4	0.16±0.01	556	0.444
24 Cap	7.1±0.8	0.10±0.02	✗	
3 Cet	15±4	0.23±0.07	None	
62 Sgr	15±1	0.17±0.02	588, 164, 96	0.944, 0.556, 0.388
α Sco	160±40	1.6±0.5	$\approx$ 249	$\approx$ 1.4
α TrA	8.6±0.7	0.16±0.02	✗	
β Ara	9±1	0.15±0.03	None	
β Col	0.298±0.005	0.0078±0.0006	✗	
β Gru	18.6±0.6	0.21±0.02	833, 59	1.043, 0.625
β Vol	0.277±0.004	0.0072±0.0006	✗	
δ^1 Aps	24.9±2.6	0.27±0.05	940, $\approx$ 65, 43	1.38,$\approx$ 0.6, 0.241
δ^2 Gru	13±1	0.15±0.02	1429, 23	0.363, 0.238
ϵ Car	11±2	0.26±0.06	833	0.693
ϵ Col	0.75±0.04	0.020±0.002	1430	6.1
ϵ Cru	1.91±0.09	0.037±0.004	None	
ϵ Mus	19.2±0.6	0.20±0.02	63, 625, 88	0.563, 0.538, 0.305
ϵ Sco	0.344±0.007	0.0090±0.0007	✗	
ϵ TrA	0.58±0.02	0.015±0.001	✗	
η^2 Dor	10.6±0.8	0.14±0.02	667, 100	0.363, 0.231
η^2 Pic	3.4±0.3	0.056±0.008	✗	
η Scl	12±1	0.15±0.02	49	0.411
η Sgr	7.7±0.3	0.096±0.009	None	
γ Cha	5.6±0.2	0.087±0.009	None	
γ Cru	10.3±0.2	0.124±0.009	556, 13, 16	0.353, 0.160, 0.159
γ Hyi	6.4±0.2	0.087±0.008	None	
γ Phe	4.7±0.2	0.072±0.008	194.2	15.97
γ Ret	14.4±0.8	0.17±0.02	909, 345	0.638, 0.512
GZ Vel	10±3	0.18±0.06	2000, 270	0.796, 0.287
HR 3017	27±8	0.4±0.1	None	
HR 4177	19.2±6.8	0.3±0.1	435	0.483
HR 6166	4.7±0.4	0.072±0.01	476	0.219
κ Pyx	4.8±0.4	0.08±0.01	526	0.190
L^2 Pup	26±2	0.23±0.03	141, 435	2.532, 1.275
λ Vel	16±2	0.26±0.05	1410	1.02
N Vel	4.1±0.1	0.067±0.006	625	0.324
NS Pup	19±7	0.3±0.1	1250	0.65
o^1 CMa	27±10	0.4±0.2	179, 769?	1.064, 0.963?
o^1 CMa¶	16	0.353	"	"
ω Cap	7±1	0.13±0.03	472, 1250	4.19, 0.154
π Pup	28±7	0.5±0.2	1250, 37, 47	0.400, 0.159, 0.129
ψ Phe	12.0±0.6	0.14±0.02	588, 189	0.638, 0.420
σ CMa	25±7	0.4±0.1	1300	1.19
σ Lib	11.8±0.8	0.15±0.02	556, 120	0.785, 0.323
τ^4 Eri	11.8±0.6	0.14±0.02	588, 33	0.429, 0.183
V337 Car	8±1	0.14±0.03	✗	

Table 4.26: **Period predictions for solar-like acoustic oscillations.** This table contains predictions for solar-like pulsation amplitudes and periods for the 44 stars surveyed for this thesis. $P_{\rm max}$ is the period predicted to give a maximum in the radial-velocities power spectrum and $\mathcal{P}_{\rm rv}$ are the revised radial-velocity timescales taken from Table 4.24 (a ✗ means the relative radial velocities are not significantly varying at the 1% level). The masses and radii and temperatures used for these estimations are those given in Table 4.16 in every case except that of o^1 CMa¶, where Sasselov [141] has been used for the mass ($\mathcal{M}$= 9.5) and Lutz & Pagel [118] has been used for the radius, effective temperature and luminosity ($\mathcal{R}$= 215 using gravity, mass and $g = \frac{GM}{R^2}$; $T_{\rm eff}$ = 4165K; $\mathcal{L}_{\rm bol}$= 15205 using absolute magnitude, $M_{\rm V} = -4.7$, and the bolometric correction from Wood & Bessell's $BC = BC((V-I)_{\rm C})$ relation).

4.10 Surface features

Surface features can cause both radial-velocity and photometric variations (see §2.2 for more details). One of the most common causes of these is rotational modulation due to starspots, although

starpatches and long-lasting convective cells can cause similar effects. In all three cases, the observed timescales are expected to be that of the period of stellar rotation and radial-velocity variations are expected to be of an amplitude less than $v_{\rm equ}\sin(i)$. Known starspots and starpatches are long lasting, so the variations will be expected to be reasonably regular, but not coherent, as these features may last many rotational periods but are ultimately expected to decay. The amplitude of the radial-velocity and photometric variations, in all three cases, will depend on the exact size and relative temperature of the surface feature(s). Stars with starspots and long-lived convective cells should have their minimum luminosity occur 0.25 rotational periods before their minimum recessional radial velocity, while those with starpatches have their minimum recessional radial velocity occur 0.25 periods before minimum luminosity is reached[106].

In the absence of rotation, large convective cells can still cause radial-velocity and photometric variations if the number of convective cells is small. The amplitude of the resulting radial-velocity variations will be approximately equal to[107]

$$A_{\rm rv} = \frac{3.5}{\sqrt{N}}\ {\rm km/s},$$

where N is the number of convective cells on the visible stellar disc, and will have maximum recessional velocity approximately at minimum luminosity.

4.10.1 Estimating rotation from line widths

The line broadening visible in a stellar line is caused by a variety of different phenomena. For the determination of whether a stellar variation could be caused by rotational modulation, the important thing is the stellar rotation which, in theory, it is possible to find by consideration of the line broadening of the line. Unfortunately, it is impossible to use more advanced techniques of separating out rotational broadening from effects like macro-turbulent broadening, such as Fourier analysis of profiles (see Gray [59] Lecture 2), on the observed data. This is due to a combination of line blending meaning few lines are unblended enough to submit to profile analysis and poor pixel sampling resulting in lines which are often only 9 CCD pixels across, which gives only 9 data points to work with (which simply is not enough[108]). However, all is not lost — it is still possible to get an idea of the rotational broadening, as will now be shown. As individual line profiles are of little use, the line half-width will be calculated from the half-width of the cross-correlation function produced by the cross-correlation of two spectra. The resulting half-width of the cross-correlation function will be called $\mathcal{W}$ (km/s). It is caused by the following things:

- the micro-turbulent line broadening, w_ξ
- the radial-tangential macro-turbulent line broadening, ζ_{RT}
- the rotational line broadening, $v_{\rm equ}\sin(i)$
- the thermal broadening, w_T
- and the broadening effect of the instrumental profile, w_I.

[106] The motion of starspots, starpatches and cells could also cause variations in the observed colour of the star. As these surface features are cooler and darker than their surroundings, the relationship between colour and brightness might be expected to be that of minimum brightness when the star is reddest. For all stars for which a convincing timescale is present in radial velocity, visual magnitude and colour this is the relationship which is seen (see §4.3).

[107] Using the typical mean convective-cell surface velocity of Antia et al.'s [6] models (5 km/s) and a factor of $\frac{17}{24}$ to account for limb-darkening and projection effects

[108] As is discussed in Appendix G it is possible to add together unblended lines which will given more data points to deal with. Unfortunately this does not increase the Nyquist frequency of the Fourier transform as the fine detail in the profiles is still lost by the lack of pixel sampling (see footnote 2, Appendix G).

It will be assumed that the broadening profile of these act together as convolutions of their individual profiles (this is not completely true of the broadening effects of rotation and macroturbulence and basically requires assuming that macroturbulence is isotropic, see Gray [59] 1-28). It will also be assumed that these broadening profiles are gaussian which certainly is not true[109] of macroturbulence and rotational broadening (see Figure 4.53 for the real rotational and macroturbulence profiles). Hence the the star light incident on the fibre will be broadened with a half-width of

$$\mathcal{B}^2 = w_\xi^2 + w_\zeta^2 + w_{\rm rot}^2 + w_T^2,$$

where $w_{\rm rot}$ is the half-width of the gaussian which best fits the rotation profile and w_ζ is the half-width of the gaussian which best fits the macro-turbulent profile. In addition, it will also be assumed that $w_{\rm rot} = v_{\rm equ}\sin(i)$ and $w_\zeta = \zeta_{RT}$. Now if $\mathcal{W}$ is the half-width of the cross-correlation

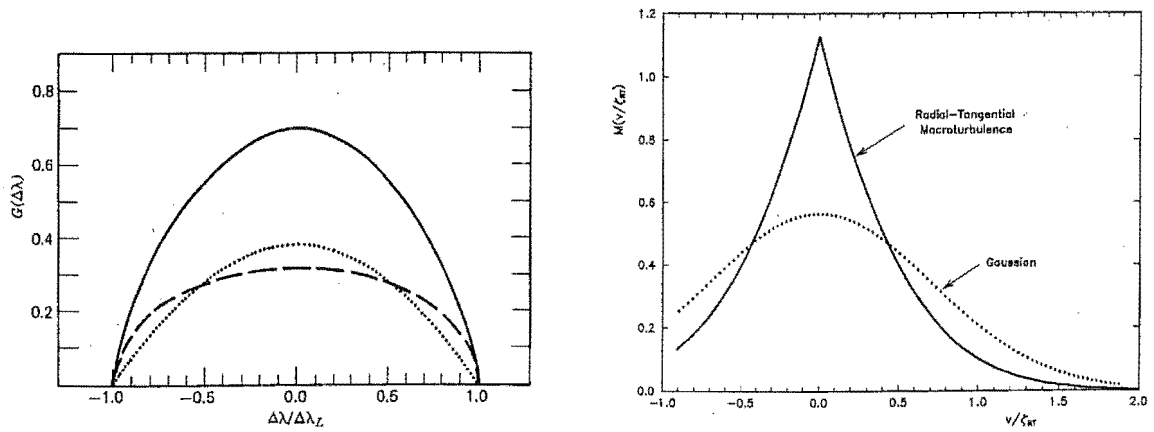

Figure 4.53: The left-hand figure shows the rotation profile, G, which broadens spectral lines in rotating stars (this is Figure 17.5 in Gray [61]). The solid line is the total profile, which is the addition of the dotted and dashed lines, and crosses the x-axis at what equates to $\pm v_{\rm equ}\sin(i)$ in velocity. The dotted line is zero in the case of no limb darkening. The right-hand figure shows the macro-turbulent profile, M, and compares it to the gaussian of half-width ζ_{RT} (this is Figure 18.4 in Gray [61]).

of two non-blended lines only then

$$\mathcal{W}^2 = 2(\mathcal{B}^2 + w_\mathcal{I}^2).$$

As has been mentioned, there is a large amount of line blending present in the stellar spectra obtained for this thesis, but the steps taken to combat this should also minimize the extra broadening effect on the half-width obtained from fitting the cross-correlation function profile (see §3.5 for more details). So in order to determine $v_{\rm equ}\sin(i)$, values of $\mathcal{W}, w_\xi, \zeta_{RT}, w_T$ and $w_\mathcal{I}$ need to be determined. The question is how to obtain these various line broadening parameters for a star. $\mathcal{W}$ is measured from the cross-correlation of two stellar spectra and similarly $w_\mathcal{I}$ can be measured from the cross-correlation of two thorium spectra, as the intrinsic broadening of the thorium lines is much less than the instrumental broadening and the thorium lines are unblended (thorium spectra taken at the same time as the two cross-correlated stellar spectra, are used). The thermal broadening is determined (in m/s) from

$$w_T = \left(\frac{2RT_{\rm eff}}{\mu_{\rm FE}}\right)^{\frac{1}{2}},$$

where $\mu_{\rm FE} = 56 \times 10^{-3}$kg/mole, $R = 8.3$J/mole and the value of $T_{\rm eff}$ given in Table 4.16 is used. w_ξ varies with luminosity, but little if at all with effective temperature, and can be estimated reasonably

[109] This is also not strictly true of the micro-turbulent profile, although it is common practice to assume this is the case (see Gray [61] page 405). This assumption holds well for weak lines, but stronger lines are a Voigt function.

reliably by the use the results of Luck & Bond [117] (average values are given by Gray [59] Table 3-1). ζ_{RT} can be a much larger effect and varies not only with luminosity, but also with effective temperature. Fortunately, it is a smooth and continuous function across the HR diagram (see Figure 4.54). As a function of $(B-V)_J$ this average macro-turbulence function can be described

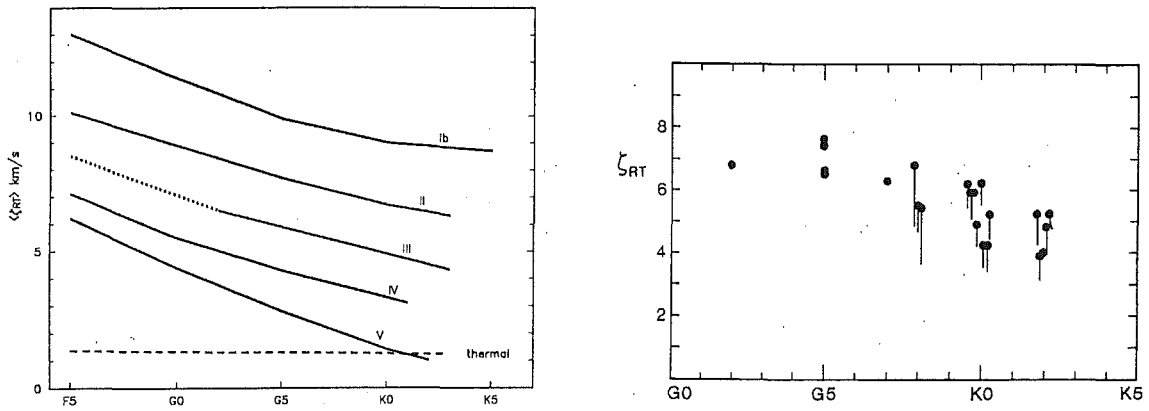

Figure 4.54: The left-hand plot shows the change in average macro-turbulence over the HR diagram (this is Figure 18.9 in Gray [61]). The average macroturbulence is a smooth and continuous function over the HR diagram and its relationship to $(B-V)_J$ and luminosity class is given on page 3-8 of Gray [59]. The scatter for late-type giants about this mean relation is illustrated in the right-hand plot (the macroturbulence is double-valued for weak and strong lines over G5 to K2 — the weak line values are the dots and the tails of the dots lie at the strong-line values), where ζ_{RT} is in km/s. The scatter about the mean value for a K2 giant is 61 m/s (this is Figure 12 in Gray [58]).

by (see Gray [59] page 3-8, — it is believed that these relations were calibrated using the results of Gray's Fourier analysis of profiles, which can disentangle the various broadening mechanisms like rotation and macroturbulence):

- $\langle\zeta_{RT}\rangle = 12.5 - 7.0(B-V)_J$ for giant stars
- $\langle\zeta_{RT}\rangle = 14.0 - 6.3(B-V)_J$ for bright giant stars
- $\langle\zeta_{RT}\rangle = 15.7 - 6.0(B-V)_J$ for supergiant stars

in units of km/s. Hence macroturbulence is estimated using the Mt John value of $(B-V)_J$, or if this is not available the Hipparcos values[110]. So the rotational broadening (in km/s) is obtained from

$$w_{\rm rot} = \left(\frac{\mathcal{W}^2}{2} - w_\xi^2 - \zeta_{RT}^2 - \frac{2RT}{\mu_{FE}} \times 10^{-6} - \frac{\mathcal{I}^2}{2} \right)^{\frac{1}{2}},$$

where $\mathcal{I}$ is the half-width of the cross-correlation function of two thorium spectra. The error in the estimated rotational broadening is

$$\sigma_{w_{\rm rot}} = \frac{1}{w_{\rm rot}} \left(\frac{\mathcal{W}^2\,\sigma_{\mathcal{W}}^2}{4} + \frac{\mathcal{I}^2\,\sigma_{\mathcal{I}}^2}{4} + w_\xi^2\,0.2^2 + \zeta_{RT}^2(0.061^2 + \sigma_{\langle\zeta_{RT}\rangle}^2) \right)^{\frac{1}{2}},$$

where $\sigma_{\langle\zeta_{RT}\rangle}^2$ is the error in the estimation of the mean macroturbulence due to the error in $(B-V)_J$, the scatter of stars' macroturbulence about the mean macroturbulence is taken to be[111] 0.061 km/s (see Figure 4.54) and $\sigma_{w_\xi} = 0.2$ km/s (Gray [59] page 3-17) is used. The results of this estimation are given in Table 4.27.

[110] The Hipparcos values are not used for all stars as L^2 Pup is highly variable in $(B-V)_J$ and some of the stars had a large error in the tabulated Hipparcos values

[111] Taking a larger value, like 0.5 km/s, typically makes no difference to the error to one significant figure, due to the larger errors in $\mathcal{W}$ and $\mathcal{I}$

Star	Spectral Type	$\mathcal{W}$ (km/s)	$\mathcal{I}$ (km/s)	w_T (km/s)	w_ξ (km/s)	$\langle\zeta_{RT}\rangle$ (km/s)	$v_{\rm equ}\sin(i)$ (km/s)
2 Cen	M5III	10.0 ± 0.9	6.4 ± 0.5	1.01	1.5	1.9 ± 0.6	5 ± 1
24 Cap	K5/M0III	10 ± 1	6.9 ± 0.4	1.07	1.5	1.27 ± 0.04	5 ± 1
3 Cet	K3Ib	14 ± 2	7.3 ± 0.5	1.08	2.5	5.99 ± 0.03	6 ± 2
62 Sgr	M4III	10.4 ± 0.9	6.5 ± 0.4	1.03	1.5	1.02 ± 0.06	5.5 ± 0.9
α Sco	M1.5Iab	18 ± 2	7.9 ± 0.4	1.01	2.5	4.51 ± 0.08	10 ± 2
α TrA	K2II	12 ± 1	6.6 ± 0.4	1.10	2.3	4.88 ± 0.01	5 ± 2
β Ara	K0/K1Ib	14 ± 1	7.7 ± 0.4	1.09	2.5	6.83 ± 0.02	5 ± 2
β Col	K1.5III	9 ± 1	7.2 ± 0.2	1.16	1.5	4.5 ± 0.4	0 ± 3.06
β Gru	M5III(W)	11 ± 1	6.7 ± 0.4	1.03	1.5	1.23 ± 0.09	6 ± 1
β Vol	K1III	9 ± 1	6.7 ± 0.5	1.16	1.5	4.58 ± 0.02	0 ± 1.81
δ^1 Aps	M4III	11 ± 1	6.5 ± 0.5	1.02	1.5	0.7 ± 0.1	6 ± 1
δ^2 Gru	M3III	9.9 ± 0.9	6.5 ± 0.4	1.03	1.5	1.38 ± 0.06	5.0 ± 0.9
ϵ Car	K3:III+B2:V	15 ± 2	6.7 ± 0.4	1.15	1.5	4.13 ± 0.02	8 ± 1
ϵ Col	K1II/III	9.4 ± 0.8	7.0 ± 0.3	1.16	1.9	4.44 ± 0.06	0 ± 2.67
ϵ Cru	K3/K4III	10 ± 1	6.8 ± 0.5	1.11	1.5	2.8 ± 0.4	4 ± 2
ϵ Mus	M5III	10.1 ± 0.9	6.5 ± 0.5	1.02	1.5	1.4 ± 0.1	5.2 ± 0.9
ϵ Sco	K2IIIb	10 ± 1	7.8 ± 0.4	1.16	1.5	4.5 ± 0.2	0 ± 2.68
ϵ TrA	K1/K2III	9.1 ± 0.9	6.8 ± 0.4	1.15	1.5	4.37 ± 0.02	0 ± 2.71
η^2 Dor	M2III	10.1 ± 0.8	6.2 ± 0.4	1.05	1.5	1.3 ± 0.3	5.4 ± 0.8
η^2 Pic	K5III	9 ± 1	6.3 ± 0.3	1.08	1.5	2.1 ± 0.4	4 ± 1
η Scl	M2/M3III	10.5 ± 0.9	7.1 ± 0.4	1.04	1.5	1.11 ± 0.08	5 ± 1
η Sgr	M2III	10 ± 1	6.7 ± 0.4	1.04	1.5	1.43 ± 0.03	5 ± 1
γ Cha	K5III	10 ± 1	7.1 ± 0.3	1.07	1.5	1 ± 2	5 ± 1
γ Cru	M4III	9.7 ± 0.8	6.7 ± 0.4	1.04	1.5	1.4 ± 0.1	4.7 ± 0.9
γ Hyi	M1III	10 ± 1	6.8 ± 0.4	1.06	1.5	1.4 ± 0.4	5 ± 1
γ Phe	K4/K5 III	18 ± 2	6.8 ± 0.4	1.07	1.5	1.7 ± 0.4	11 ± 2
γ Ret	M4III	10.7 ± 0.9	7.1 ± 0.5	1.03	1.5	2 ± 1	5 ± 1
GZ Vel	K3II	14 ± 1	7.2 ± 0.3	1.09	2.3	4 ± 1	7 ± 2
HR 3017	K4III	13 ± 2	6.4 ± 0.6	1.07	1.5	0.6 ± 0.5	8 ± 1
HR 4177	K4/K5III:	12 ± 1	7.2 ± 0.3	1.08	1.5	1.6 ± 0.1	7 ± 1
HR 6166	K5III	9.5 ± 0.9	6.4 ± 0.4	1.07	1.5	1.8 ± 0.5	5 ± 1
κ Pyx	K4/K5III	10.3 ± 0.8	6.6 ± 0.4	1.08	1.5	1.51 ± 0.09	5.3 ± 0.8
L^2 Pup	M5e	18 ± 2	7.1 ± 0.2	0.99	1.5	0.4 ± 0.8	11 ± 2
λ Vel	K4III	13 ± 1	6.7 ± 0.4	1.08	1.5	0.845± 0.09	8 ± 1
N Vel	K4/K5III	9 ± 1	6.4 ± 0.5	1.08	1.5	1.73 ± 0.02	5 ± 1
NS Pup	K4III	12 ± 1	7.2 ± 0.3	1.08	1.5	1.4 ± 0.6	7 ± 1
o^1 CMa	K3Iab	20 ± 2	6.7 ± 0.4	1.09	2.5	5.3 ± 0.1	13 ± 1
ω Cap	K4III	10.4 ± 0.9	6.4 ± 0.4	1.07	1.5	1.26 ± 0.06	5.6 ± 0.9
π Pup	K3Ib	14 ± 1	6.7 ± 0.5	1.08	2.5	6.2 ± 0.1	6 ± 2
ψ Phe	M4III	10.4 ± 0.8	7.1 ± 0.3	1.03	1.5	1.32 ± 0.04	5.1 ± 0.9
σ CMa	K4III	14 ± 1	6.7 ± 0.4	1.07	1.5	0.4 ± 0.1	8 ± 1
σ Lib	M3/M4III	10.4 ± 0.9	6.7 ± 0.4	1.04	1.5	0.8 ± 0.3	5.5 ± 0.9
τ^4 Eri	M3/M4III	11 ± 1	7.2 ± 0.3	1.03	1.5	1.1 ± 0.1	6 ± 1
V337 Car	K3II	12 ± 1	6.7 ± 0.4	1.10	2.3	4.29 ± 0.09	6 ± 1

Table 4.27: **Line broadening**. This table gives line broadening for the 44 stars observed for this thesis, leading to an estimation of rotational broadening from a cross-correlation function's gaussian half-width. The spectral type is that given in Table 1.1. The errors given for $\langle\zeta_{RT}\rangle$ are those resulting from the standard error in $(B-V)_{\rm J}$ (Hipparcos data) or the $N-1$ deviation about the mean value (for Mt John data[112]).

4.10.2 Surface-feature estimations

The rotational broadening is a very useful thing to know, as far as rotational modulation is concerned. Not only can no radial-velocity amplitude due to rotational modulation be greater than $v_{\rm equ}\sin(i)$, but the rotational period is

$$P_{\rm rot} = \frac{2\pi R}{v_{\rm equ}} = \sin(i)\frac{2\pi R}{v_{\rm equ}\sin(i)}$$

and hence an upper limit on the size of timescales that could be due to rotational modulation, $P_{\rm rot}/\sin(i)$, can be obtained. Using the radii for the 44 surveyed stars given in Table 4.16 this was found and is given in Table 4.28.

All the considerations so far have been carried out assuming any rotation will be uniform, specifically not differential[113]. However, for uniformly rotating stars the rotational velocity has an upper limit called the equatorial break-up velocity[114] (see Tassoul [163], page 12 and §12.2). When this is reached the effective gravity vanishes at the equator and this results in matter being shed from the equator in a continuous stream. For main sequence stars this has been calculated by Slettebak [153] (see Figure 4.55) and for late-type stars it is probably about 400 km/s. For all 44 stars observed for this thesis (except α Sco) this puts a lower limit on timescales which can be attributed to rotational modulation of a few days.

However for spectral types later than G5, giants' and supergiants' rotational broadening more than about 10 km/s is rare and usually indicates members of close binary systems (Bopp & Stencel [23]). This is a great deal less than the equatorial break-up velocity[115] (for $v_{\rm equ}\sin(i)$ for these stars see: Figure 4.55, for late-type giants; Gray's [63] Figure 2, for bright giants; and Gray's [64] Figure 2, for supergiants). and taking 20 km/s as the upper limit on the observed rotational velocity of late-type evolved stars has interesting implications for the timescales observed in stars' radial velocity and photometry. Even for a star of radius 50 $R_\odot$, an upper limit for the rotational velocity of 20 km/s means any timescale less than 120 days could not be due to rotational modulation! The minimum rotational periods possible due to rotational modulation, given an upper limit on $v_{\rm equ}$ of 20 km/s, are given in Table 4.28. Comfortingly, the values of $v_{\rm equ}\sin(i)$ obtained for the 44 stars observed for this thesis, from the widths of cross-correlations and estimations of micro-turbulence and macroturbulence, are all well below 20 km/s, as expected for stars of their luminosity and spectral class.

As has previously been mentioned, in the absence of rotation the presence of large convective cells can still cause radial-velocity variation. This surface mechanism may help explain erratic variations on timescales outside the limits placed on stars' rotational period. However, there are some limitations on the variations that can be caused by the ascent and decent of large convective cells. In addition to the number of cells that would be required to give rise to the amplitude of the observed variation, a convective cell can not travel further than the stellar radius before it thermalizes with its environment. The timescale that is expected to be observed is the mean life of a cell, so expect to have $t_{\rm cell} < \frac{R}{\overline{v}}$, where $\overline{v}$ is the mean convective velocity and is assumed to be 5 km/s at the stellar

[112] For stars variable in $(B-V)_{\rm J}$ this is larger than the actual precision of the data and is appropriate rather than the precision given by the check stars variance, as the half-width has only been calculated for one exposure and hence the value of $(B-V)_{\rm J}$ appropriate for this exposure will deviate from the mean colour value

[113] If a star was differentially rotating with the angular velocity decreasing towards the poles the broadening, $w_{\rm rot}$, would be smaller than the equatorial projected rotation, $v_{\rm equ}\sin(i)$, see Slettebak [153]

[114] When a star is differentially rotating this does not necessarily occur and instead the inner conditions of the model change dramatically, see Tassoul [163] page 315

[115] It is expected that stars with a range of inclinations will be observed and it is unreasonable to expect all stars observed to have had small values of $\sin(i)$

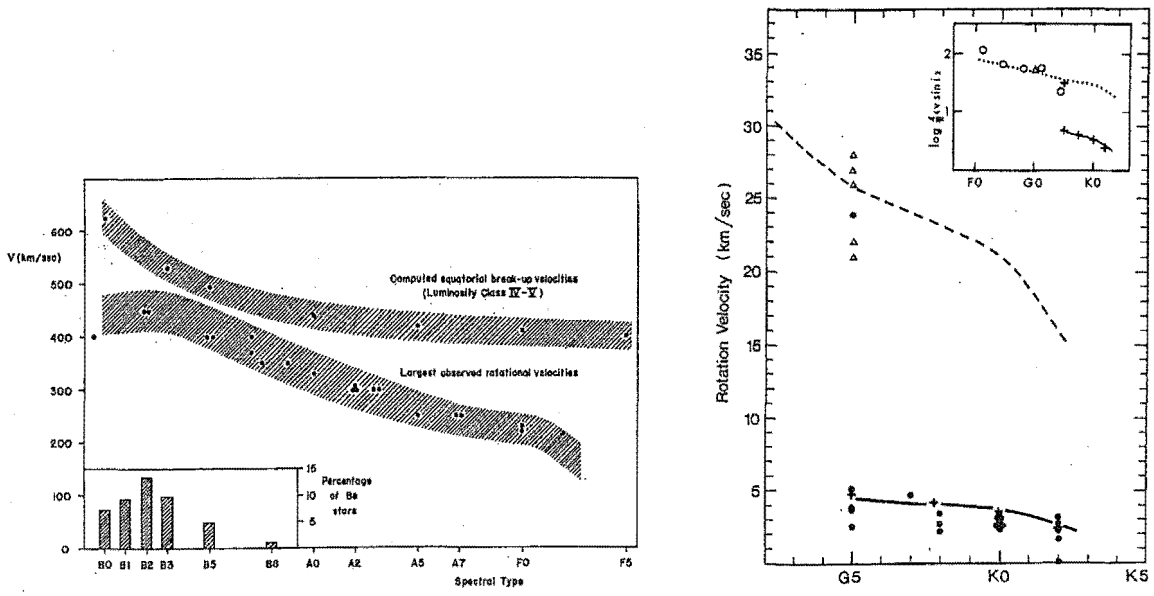

Figure 4.55: The left-hand figure shows the break-up velocities for main sequence uniform rotators as calculated by Slettebak [153] (this is his Figure 1). If this is any indication, a non-differentially rotating late-type star will have a break-up velocity of about 400 km/s. The right-hand figure shows the observed values of $v_{\rm rot}\sin(i)$ for giant stars. If this contains a range of rotational inclinations it would mean that giants of spectral type later than G5 have rotational velocities less than 20 km/s, which is a great deal less than the uniform body rotation break-up velocity (this is Figure 8 in Gray [58]).

surface and greater further into the star (Antia et al. [6]). For the stars observed for this thesis this is between 800 and 4000 days (except for α Sco). Hence this particular restriction rules out timescales longer than about 1000 days in giants. However, the assumption that the mixing length is equal to the dimension[116] of the convective cells (see Cox & Giuli [42] Chapter 14) and that the cells responsible for the observed radial-velocity variations take up the entire visible hemisphere of the star, allows an estimation of the expected mean life of the cells from the number of cells present. If the dimension of the cells, D, is equal to the mixing length then $t_{\rm cell} = \frac{D}{\overline{v}}$. Assuming that N cells are evenly distributed over the half sphere visible means that

$$\frac{2\pi R^2}{N} = A_{\rm cell} \approx \pi \left(\frac{D}{2}\right)^2,$$

where $A_{\rm cell}$ is the average surface area of a cell. Hence the mean life of these cells is

$$t_{\rm cell} = \frac{R}{\overline{v}} \left(\frac{8}{N}\right)^{\frac{1}{2}} = 3.99 \frac{R A_{\rm rv}}{\overline{v}^2}.$$

This equation highlights the dependence of the $t_{\rm cell}$ estimation on the amplitude of the variation.

If more than one type of cell is present things are not this simple. While the method of obtaining the number of cells required to give the observed timescale its amplitude is still valid, this simple method of estimating the mean life of the cells must be modified. Assuming that the cells may differ in size (in the Sun granules and super-granules are very different in size), but not significantly

[116]Here the dimension means the approximate linear size of the cell, from one edge to another. This is generally assumed to be the same in all directions, but the shape of the cells is not specified.

Star	P_{20} (days)	$P_{\rm rot}/\sin(i)$ (days)	$\mathcal{P}_{\rm rv}$ (days)	$A_{\rm rv}$ (km/s)	$N_{\rm dom}$	t_{100} (days)
2 Cen	182 ± 7	700 ± 100	556	0.444	58	89 ± 4
24 Cap	180 ± 20	700 ± 200	✗		24	90 ± 10
3 Cet	400 ± 200	1400± 800	None			190 ± 90
62 Sgr	280 ± 30	1000± 200	588, 164, 96	0.944, 0.556, 0.388	12	140 ± 10
α Sco	2400± 800	5000± 2000	≈249	≈1.4	5	1200± 400
α TrA	360 ± 30	1600± 600	✗			180 ± 10
β Ara	350 ± 50	1500± 500	None			170 ± 20
β Col	29.4± 0.4	∞	✗			14 ± 0
β Gru	340 ± 10	1200± 200	833, 59	1.043, 0.625	10	164 ± 6
β Vol	27.4± 0.4	∞	✗			13 ± 0
δ^1 Aps	480 ± 60	1500± 300	940, ≈65, 43	1.38, ≈0.6, 0.241	6	240 ± 30
δ^2 Gru	230 ± 30	900 ± 200	1429, 23	0.363, 0.238	87	110 ± 10
ϵ Car	410 ± 40	1000± 200	833	0.693	24	200 ± 20
ϵ Col	66 ± 3	∞	1430	6.1	0	32 ± 1
ϵ Cru	85 ± 3	500 ± 200	None			42 ± 2
ϵ Mus	280 ± 10	1100± 200	63, 625, 88	0.563, 0.538, 0.305	36	139 ± 6
ϵ Sco	32.8± 0.5	∞	✗			16 ± 0
ϵ TrA	48 ± 2	∞	✗			24 ± 1
η^2 Dor	240 ± 20	900 ± 200	667, 100	0.363, 0.231	87	120 ± 10
η^2 Pic	109 ± 8	500 ± 200	✗			53 ± 4
η Scl	240 ± 30	900 ± 200	49	0.411	68	120 ± 10
η Sgr	139 ± 6	600 ± 100	None			68 ± 3
γ Cha	160 ± 10	700 ± 200	None			78 ± 5
γ Cru	181 ± 3	800 ± 200	556, 13, 16	0.353, 0.160, 0.159	92	89 ± 2
γ Hyi	148 ± 5	600 ± 100	None			73 ± 3
γ Phe	127 ± 6	230 ± 30	194.2	15.97	0	62 ± 3
γ Ret	280 ± 20	1100± 200	909, 345	0.638, 0.512	28	140 ± 10
GZ Vel	390 ± 90	1100± 300	2000, 270	0.796, 0.287	18	190 ± 40
HR 3017	700 ± 200	1800± 500	None			360 ± 80
HR 4177	500 ± 200	1600± 700	435	0.483	49	300 ± 100
HR 6166	130 ± 10	600 ± 100	476	0.219	241	63 ± 5
κ Pyx	140 ± 20	500 ± 100	526	0.190	320	70 ± 7
L^2 Pup	270 ± 20	480 ± 80	141, 435	2.532, 1.275	1	130 ± 10
λ Vel	520 ± 50	1400± 200	1410	1.02	11	250 ± 20
N Vel	130 ± 5	600 ± 100	625	0.324	110	64 ± 2
NS Pup	600 ± 200	1700± 600	1250	0.65	27	290 ± 90
o^1 CMa	800 ± 300	1200± 500	179, 769?	1.064, 0.963?	10	400 ± 100
ω Cap	250 ± 50	900 ± 200	472, 1250	4.19, 0.154	0	120 ± 20
π Pup	800 ± 100	2700± 900	1250, 37, 47	0.400, 0.159, 0.129	72	380 ± 70
ψ Phe	200 ± 10	800 ± 100	588, 189	0.638, 0.420	28	98 ± 6
σ CMa	700 ± 200	1600± 400	1300	1.19	8	340 ± 70
σ Lib	250 ± 20	900 ± 200	556, 120	0.785, 0.323	18	120 ± 10
τ^4 Eri	210 ± 10	800 ± 200	588, 33	0.429, 0.183	62	102 ± 7
V337 Car	320 ± 40	1100± 300	✗			160 ± 20

Table 4.28: **Limits on surface-feature timescales.** This table gives the maximum and minimum allowable rotational periods for the 44 stars surveyed for this thesis, and for comparison also gives the timescales observed in the relative radial-velocity data. P_{20} is the rotational period that would be expected for the stars stars if they had a rotational velocity of 20 km/s, $\mathcal{P}_{\rm rv}$ is the revised radial-velocity timescales taken from Table 4.24 (a ✗ means the relative radial velocities are not significantly varying at the 1% level), $A_{\rm rv}$ is the revised amplitude, $N_{\rm dom}$ is the number of convective cells that would be required to give the amplitude of the first period tabulated and t_{100} is the estimated mean life of cells which give a radial-velocity amplitude of 100 m/s (if this number of convective cells were to completely cover the observable hemisphere of the star).

in mean velocity the observed timescales and estimated number of cells must obey

$$\left(\frac{8R^2}{\overline{v}^2}\right) = \sum_i N_i \, \mathcal{P}_i^2 \, .$$

If the cell sizes are not too different the expected timescales for such a situation should all be the order of

$$t_{\rm cell} \approx \frac{R}{\overline{v}} \left(\frac{8}{\sum_i N_i}\right)^{\frac{1}{2}} .$$

This illustrates that if there is more than one type of cell present, the observed lifetime should decrease according the total number of cells present. Hence the estimate for a single type of cell forms an upper limit on the expected timescales capable of producing the observed amplitude of variation. In addition, it should be noted that a smaller mean convective velocity will mean a larger expected timescale and if fewer cells than eight cells are present on the visible hemisphere, the mean lifetime estimated by this method will be longer than the time it would take for a cell to travel the length of the stellar radius.

Table 4.28 gives the number of cells required to give the largest amplitude observed timescale and the estimated mean lifetime of cells which would give rise to a radial-velocity amplitude of 100 m/s. To make allowance for the inaccuracy in the mean convective velocity, the amplitude ($A_{\rm rv}$) being slightly different from that assumed and the assumption that the mixing length equals the D, the upper limit on timescales that are good candidates to have been caused by the movement of large convective cells will be taken to be $2 \times t_{\rm cell}$. This factor will also be taken as the cut off for the lower limit of likely timescales. It should be noted that when more than one set of cells is suspected, requiring the estimated and observed timescales agree within a factor of two means the stellar radius estimated by calculation of $\sum_i N_i \, \mathcal{P}_i^2$ must also be correct within a factor of two.

Consideration of the radial-velocity timescales and amplitudes found for the 44 stars observed for this thesis leads to the following conclusions, where only revised timescales (see §4.8 for details) are discussed.

- The revised radial-velocity timescale for ϵ Car, HR 4177, λ Vel, N Vel, NS Pup and σ CMa are all too regular to have been caused by the ascent and descent of large convective cells and in the case of σ CMa the amplitude would imply fewer than 10 cells present on the visible surface of the stars.

- The characteristic timescales for η^2 Dor and η Scl are both too short to have been caused by a star rotating with a rotational velocity of less than 20 km/s. It is also unlikely that these timescales are due to the ascent and descent of convective cells, as the estimations are over a factor of two longer than these. However in η^2 Dor's case, the 667-day radial-velocity timescale is within the determined limits and hence could be caused by rotational modulation.

- The revised timescale for HR 6166 and κ Pyx are all two or more times larger than those estimated for the ascent and descent of large convective cells (see Table 4.55).

- 62 Sgr's 164 and 96-day timescales are also too short to have been caused by a star rotating with a rotational velocity of less than 20 km/s. These also are unlikely to be due to the ascent and descent of large convective cells, because even if both sets of cells were present the stellar radius implied by $(3.1 \sum_i N_i \, \mathcal{P}_i^2)^{0.5}$ is less than half of that estimated from Hipparcos data and visual photometry (see Table 4.16). However, the 588-day radial-velocity timescale is of the correct size to have been caused by rotational modulation.

- α Sco's characteristic $\approx$250-day timescale is too short to have been caused by a star rotating with a rotational velocity of less than 20 km/s. It is also unlikely that this variation is due to the ascent and descent of large convective cells on the visible hemisphere of the stars, as α Sco's radial-velocity variations are quite regular (see Figure A.3) and the amplitude would imply fewer than 10 cells present on the visible surface of the star.

- β Gru's characteristic 58-day is too short to have been caused by a star rotating with a rotational velocity of less than 20 km/s. It is also unlikely to be be due the ascent and descent of large convective cells, as the estimation is over a factor of two times longer than 58 days. However, this star's 833-day radial-velocity timescale is of the correct size to have been caused by rotational modulation, although it is over two times smaller than that estimated by the primitive convective cell estimations.

- δ^1 Aps' characteristic 48-day and $\approx$65-day timescales are too short to have been caused by a star rotating with a rotational velocity of less than 20 km/s. It is also unlikely that these variations are due to the ascent and descent of large convective cells, as the photometric variations are nice and regular (see Figure 4.19). However, this star's 940-day radial-velocity timescale is of the correct size to have been caused by rotational modulation. This timescale is not likely to have been caused by the ascent and descent of large convective cells, because it is less than half of the timescale estimated the amplitude would imply fewer than 10 cells present on the visible surface of the star.

- δ^2 Gru's 1429-day timescale is longer than the maximum rotational period possible for it, given its broadening. Nor could convective cells ascending and descending be responsible, because not only is the estimated timescale less than half of this, but the cells' long-lived nature would mean they should also cause rotational modulation. This casts doubt on this timescale being due to the presence of a surface feature. In addition, the star's characteristic 24-day timescale is too short to have been caused by a star rotating with a rotational velocity of less than 20 km/s. It is also unlikely that the 24-day timescale is due to the ascent and descent of convective cells, as the phase relationship between the Mt John photometry and radial velocity is that of maximum luminosity at maximum radial velocity for this timescale (see Table 4.25).

- ϵ Col's 1430-day timescale's amplitude is larger than $v_{\rm equ}\sin(i)$ for the star and hence can not be caused by any form of rotational modulation. It is also unlikely that convective cells are responsible, due to the great regularity of the radial-velocity variations (see Figure A.7) and as the amplitude of the variation is too large.

- ϵ Mus' characteristic 63-day timescale and its 88-day timescale are too short to have been caused by a star rotating with a rotational velocity of less than 20 km/s. The 63-day timescale is too regular to have been caused by the ascent and descent of large convective cells (see Figure 4.20) and such a picture is not compatible with the apparent photometric change in timescale. In addition, the 88-day timescale is less than half that estimated. However, this star's 625-day radial-velocity timescale is of the correct size to have been caused by rotational modulation.

- γ Cru's characteristic timescales of 13 and 16 days are too short to have been caused by a star rotating with a rotational velocity of less than 20 km/s. It is also unlikely that these timescales are due to the ascent and descent of convective cells, as the estimations are over a factor of two longer than these. However, this star's 556-day radial-velocity timescale is of the correct size to have been caused by rotational modulation.

- γ Phe's 194-day timescale's amplitude is larger than its $v_{\rm equ}\sin(i)$ and hence rotational modulation can not be the cause of this timescale. Convective cells also can not be responsible,

due to the great regularity of the radial-velocity variations (see Figure A.13) and the fact that the amplitude of the variation is simply too large!

- GZ Vel's 2000-day timescale is longer than the maximum rotational period possible, given its broadening. While large convective cells could be responsible for the observed radial-velocity amplitude, their long-lived nature would mean they should also cause rotational modulation. This casts doubt on this long timescale being due to the presence of a surface feature. The star's 270-day timescale is too short to have been caused by a star rotating with a rotational velocity of less than 20 km/s, but it could be caused by approximately 550 convective cells rising and falling.

- L^2 Pup's characteristic 141-day timescale is too short to have been caused by a star rotating with a rotational velocity of less than 20 km/s. It is also unlikely to be due to convective cell movement, as this would require the presence of only one convective cell! However, this star's characteristic timescale of $\approx$440 days is of the correct size to have been caused by rotational modulation, although it is over two times smaller than that predicted by the primitive convective cell estimations.

- o^1 CMa's characteristic 177-day timescale is too short to have been caused by a star rotating with a rotational velocity of less than 20 km/s. It is also unlikely that it is due to the ascent and descent of large convective cells on the visible hemisphere of the stars as the variation is too nice and regular (see Figure 4.23). However, this star's long-term/769-day radial-velocity timescale is of the correct size to have been caused by rotational modulation (if it is less than 1700 days), although it is over two times smaller than that predicted by the primitive convective cell estimations (unless its actually longer than about 2000 days, noting that as the length of the radial-velocity variation increases so does the amplitude, see §4.7).

- ω Cap's 476-day timescale is just within the viable radial-velocity amplitudes for rotational modulation. However, as the amplitude is 64% of the line half-width, the distortion of line profiles necessary to produce such a large amplitude should be easily visible when the spectra in question are viewed. To this end, two spectra have been plotted at maximum and minimum relative radial velocity (see Figure 4.56). No such dramatic line distortion is seen and hence it can be deduced that this 476-day timescale is not due to rotational modulation. Nor can this be due to convective cell movement, as the amplitude of the variation too large. However, the 1250-day radial-velocity timescale is only marginally longer than the longest expected from rotational modulation, although it is over a factor of two times larger than that predicted by the convective cell estimations.

- π Pup's characteristic timescale of 35 days and its 47-day timescale are both too short to have been caused by a star rotating with a rotational velocity of less than 20 km/s. In addition, it is unlikely that the 35-day timescale is due to the ascent and descent of convective cells, as the phase relationship between the Mt John photometry and radial velocity for this timescale is that of maximum luminosity at maximum radial velocity (see Table 4.25). It is also unlikely that the 47-day timescale is due to cell motion, as the estimated timescale is over a factor of two times longer than this. However, this star's 1250-day radial-velocity timescale is of the correct size to have been caused by rotational modulation, although it is unlikely to be due to the motion of convective cells, as it is too regular.

- ψ Phe's 189-day timescale is over a factor of two times shorter than that estimated for the ascent and descent of convective cells.

- σ Lib's characteristic timescale of $\approx$100 days is too short to have been caused by a star rotating with a rotational velocity of less than 20 km/s. In addition, it is unlikely to due to

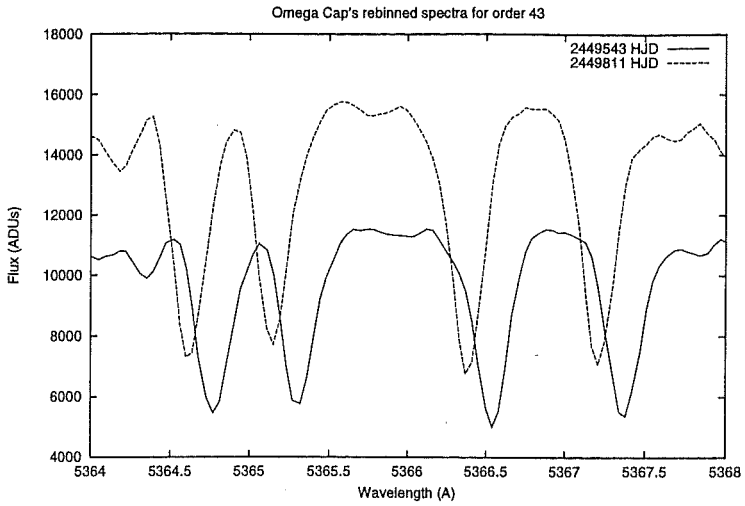

Figure 4.56: These observations of ω Cap are shifted in radial velocity by 8.0 km/s. This is approximately the maximum difference in radial velocity observed for this star and has a shift of approximately $2 \times 64\%$ of the half-width of the lines. Hence if this shift is due to an apparent radial-velocity shift such as rotational modulation, extreme line distortion should be visible (for examples of this line distortion see Figure 2.4 and 2.5). But upon visual inspection the two sets of lines do not appear to be different in shape and hence the observed radial-velocity shift can not be due to rotational modulation.

the ascent and descent of convective cells, as the estimated timescale is over a factor of two times longer than this. Nor is the star's 556-day radial-velocity timescale likely to be due to cells, as it is too regular. However, it is of the correct size to have been caused by rotational modulation.

- τ^2 Eri's characteristic $\approx$29-day timescale is too short to have been caused by a star rotating with a rotational velocity of less than 20 km/s. This is unlikely to be due to the ascent and descent of convective cells, as the phase relationship between the Mt John photometry and radial velocity is that of maximum luminosity at maximum radial velocity on this timescale (see Table 4.25). However, this star's 588-day radial-velocity timescale is of the correct size to have been caused by rotational modulation.

In all other stars the revised timescales can not be excluded from the hypothesis of their being caused by either of rotational modulation or the ascent and descent of large convective cells. Amongst these are the only stars whose characteristic timescales may be due to rotational modulation and for which a reliable phase relationship has been determined. These stars are σ CMa and NS Pup (see Table 4.25). In NS Pup's case, the phase relationship of radial velocity leading luminosity by 132 degrees is more consistent with the presence of a starpatch than a starspot, if indeed rotational modulation is the cause. The radial velocity is leading by more than the expected 90 degrees, but the two observables for this star are not concurrent so despite their long-term and regular nature the exact phase relationship may be slightly different. In σ CMa's case, the luminosity leads the radial velocity as for a starspot, although the amount it does so by is 157 degrees rather than the expect quarter of a period. As is the case for NS Pup the two observables are not concurrent, so their exact phase relationship may be slightly different and hence this is not incompatible with the picture of rotational modulation by a starspot.

Chapter 5

Conclusion

5.1 Discussion

Late-type evolved stars range across the HR diagram, bounded by the variable red giants like Mira and semi-regular variables and the pulsating supergiant RV Tauri stars. In the past decade it has been discovered that stars at the centre of the late-type evolved stars in the HR diagram are not necessarily, as previously thought, constant in photometry and radial velocity (for references to this see §1.1). Hence observations of 44 late-type evolved stars have been obtained for this thesis in the hope of helping to determine how common this phenomenon is, what is causing it, whether it is related to the variations seen for other known variable stars and whether there is any region in this part of the HR diagram that can be regarded as containing mainly constant stars.

In order to help answer these questions, more intensive radial-velocity observations have been undertaken for 31 of these stars (for a discussion of how these stars were chosen from the original 44 see §3.6). In addition, in order to help identify the mechanism of variation, 13 of the 31 stars were also observed photometrically (for a discussion of how these stars were chosen see §3.6). The radial-velocity and photometric data obtained from these stars have been Fourier analysed for timescales and these compared to predictions for acoustic pulsation, rotational modulation, large convective cell motion and binary orbits (see Chapter 4). The results of doing so are summarized in Table 5.1. Although non-acoustic, i.e. g-mode and r-mode, non-radial pulsation can not generally be ruled out, particularly for timescales which are not compatible with acoustic pulsation, little more can be said and hence these possible radial-velocity variation mechanisms will, for the most part, be neglected in the following discussion.

All but eight of the 44 stars surveyed for this thesis have a 1% or less chance of being constant in radial velocity (by the F-test, see §4.2). Hence it is tempting to hypothesize that there is no local region of the HR diagram which can be considered to contain mainly constant stars. However caution should be exercised when doing so, as the 44 stars were initially chosen for observation with a preference for those possibly varying in light (see §3.6), which introduces a major bias into the sample. Despite this bias, one thing about the variability of stars in this region of the HR diagram is clear and consistent with previous research (see §1.1). The initial sample of stars contains 16 variable M giants (and bright giants), 15 variable K giants (and bright giants), 4 variable K super-

[1]The long term timescale, assumed to be 5000 days when a binary orbital fit was attempted, in o^1 CMa could be due to rotational modulation if it is less than 1700 days in length (the fitted binary amplitude is consistent with this). Alternatively if the timescale is sufficiently longer than about 2000 days it could be due to the motion of large convective cells. As there is a similar long-term timescale in the Hipparcos photometry the view of variation due to a surface feature is favoured, although there is some question as to why this variation is not seen in the concurrent Mt John photometry.

[2]With the exception of N Vel for which the two timescales are believed to be coincidental

Star	Spectral Type	Best Binary fit Period	Potential Acoustic Pulsation	Potential Rot. Modulation	Potential Convective Cells
2 Cen	M5III	480 ± 10		**≈520**	**≈520**
62 Sgr	M4III	650 ± 20	164, 96	**≈600**	**≈600**
α Sco	M1.5Iab	***249*± *6*‡**	**≈249**		
β Gru	M5III(W)	1187	**58**	833	
δ^1 Aps	M4III	***940 ± 10***	**48,≈65**	940	
δ^2 Gru	M3III	3000†	**24**		
ϵ Car	K3:III+B2:V	***860 ± 20***		833	
ϵ Col	K1II/III	***1430 ± 30***			
ϵ Mus	M5III		**63(+∼30)**,88	625	625
η^2 Dor	M2III	660 ± 20	**≈95**	667	667
η Scl	M2/M3III		**48**		
γ Cru	M4III	584 ± 8	**13, 16**	556	556
γ Phe	K4/K5 III	***194.2±0.3***			
γ Ret	M4III	930 ± 50		**909** or 345	**909**, 345
GZ Vel	K3II	***3000†***			270
HR 4177	K4/K5III:	***870 ± 20***		435	
HR 6166	K5III	510 ± 10		476	
κ Pyx	K4/K5III	531 ± 7		526	
L^2 Pup	M5e		**140**	**≈440**	
λ Vel	K4III	***1410 ± 90***		**≈1100**	
N Vel	K4/K5III	660 ± 10		625	
NS Pup	K4III	***1250 ± 40***		**≈1350**	
o^1 CMa^1	K3Iab	5000†	**179**	769 or **<1700**	if **≳2000**
ω Cap	K4III	***472 ± 2***		1250	
π Pup	K3Ib	***1300 ±100***	47,**37**	1250	
ψ Phe	M4III	580 ± 20		588 or 189	588
σ CMa	K4III	***1300 ±100***		**≥1250**	
σ Lib	M3/M4III	***590 ± 20***	**≈100**	556	
τ^4 Eri	M3/M4III	590 ± 10	**≈29**	588	588

Table 5.1: **Causes of radial-velocity variations.** This table summarizes the results of Sections 4.7, 4.9 and 4.10 by placing the revised radial-velocity timescales (see §4.8) in columns corresponding to their possible causes (with the exception of the binary orbit column, for which the best period for a binary orbit is tabulated unless the orbital fit is so poor that it could not possibly correspond to presence in a binary system). The spectral types given here are those from Table 1.1.

Timescales in **bold** are characteristic[2] and can not be due to a r-mode non-radial pulsation or a wide binary orbit. Binary orbits designated with a (‡) have a fit which requires the secondary star's mass to be larger than the primary star's mass and those with a (†) had the binary period arbitrarily fixed to the tabulated period. Binary orbits in ***bold-oblique*** are believed to have amplitudes significantly greater than the scatter about the fit and appear to be a good fit to the data, although if the timescales are characteristic these can not be binaries.

giants, one variable M supergiant and the eight stars which can not be considered to be varying. The stars not considered to be significantly varying consist of seven K giants and one K/M giant, which is consistent with K giants being by far the least variable of the stars in this region.

For the K giants and bright giants which are significantly varying and have reliable timescales, the possible causes of the observed radial-velocity variation timescales are almost exclusively (see Table 5.1) binary motion and rotational modulation (with the exception of GZ Vel, for which the secondary timescale must be due to ascent and descent of large convective cells). This is because the timescales of the radial-velocity variations for K giants are generally at least a hundred days, so are not consistent with acoustic pulsations. While predictions for fundamental pulsation for these stars range from 1–80 days, for seven of these stars the predicted fundamental and even first overtone period for radial pulsation is sufficiently long that if present and of a sufficiently large amplitude it should have been observed. This leads to the conclusion that radial pulsations of amplitudes larger than 200 m/s (as the precision of these radial-velocity measurements is about 50 m/s) in K giants are not pervasive and the long-term radial-velocity variations are mostly of binary or rotational modulation origin (although some form of non-acoustic non-radial pulsation can not be ruled out). Which is the most frequent cause of radial-velocity variation in K giants is not clear — there are four K giants which are certainly present in binaries (at least 30% (see §2.1) of the 22 or 23 K giants observed are expected to be in binaries which equates to 6–7 stars) and three or four which certainly have timescales due to rotational modulation. For the remaining K giants it is difficult to differentiate between rotational modulation and a binary orbit. This is a general problem for long-term relatively smooth radial-velocity variations — even concurrent photometry can not fully differentiate the two, as while the same variation in photometry will rule out a wide binary orbit, no variation in photometry does not rule out a starpatch! In addition, an erratic long-term radial-velocity variation may not be able to be caused by a wide binary orbit alone, but an erratic radial-velocity variation may be due to the superposition of a binary orbit and another intrinsic variation of similar amplitude.

For M giants the situation is very different. Of the 16 stars with statistically significant variations, 10 or 11 have timescales due to acoustic pulsation. Of the remaining five, two were discontinued after one year of observation, were not found to have any reliable timescales and have such short predicted timescales that intensive observations would be needed to see them. In addition to any short-term radial-velocity variations, most M giants (all but η Scl) have a long-term radial-velocity variation, hence binary and rotational modulation are still important for these stars. One or two stars have timescales that correspond to rotational modulation and one has a timescale that definitely corresponds to a binary orbit. The inability to distinguish between long-term radial-velocity variations due to a binary orbit and rotational modulation has already been discussed, but for the M giants this is made worse because the primitive convective cell estimations are often also comparable[3] in length.

Like M giants, the three supergiants with reliable radial-velocity timescales have both short and long-term timescales present in their radial velocities. For all three of these stars there is a timescale which can only correspond to acoustic pulsation and there is difficulty distinguishing between timescales due to binary orbits and surface features.

[3] As it happens, many of the large-amplitude radial-velocity variables are K giants and this results in the estimated cell numbers being low and timescales being significantly longer than those observed. More typically, however, K giants generally have smaller-amplitude radial-velocity variations, which implies more and smaller cells which in turn implies shorter convective cell timescales. However, short (i.e. less than a few hundred days) timescales are not generally observed.

5.1.1 Individual stars

The following conclusions can be drawn about the mechanism of radial-velocity variation of specific stars (see Table 5.1), where it is assumed that: these stars are not rotating far faster than is normal for their type, the primitive convective-cell estimations can be trusted within a factor of two and timescales will probably not represent a binary orbit unless they are found to be the "best binary fit"[4].

- The characteristic timescales of α Sco, η^2 Dor, η Scl, σ Lib and τ^4 Eri can only be due to acoustic pulsation.
- ϵ Col, γ Phe and ω Cap owe their observed radial-velocity period to their presence in a binary orbit.
- λ Vel, NS Pup and σ CMa's observed radial-velocity timescale can only be due to rotational modulation or non-radial g-mode pulsation. In σ CMa's case, the phase relationship between visual photometry and radial velocity is compatible with the presence of a starspot, and in NS Pup's case with a starpatch (although caution must be exercised when interpreting these phase relationships, as the observables are not concurrent).
- 62 Sgr's short-term timescales of 184 and 96-days are probably due to an acoustic pulsation, which would mean it was undergoing a multi-periodic pulsation. The cause of the star's characteristic timescale can not be determined and may result from either rotational modulation or the motion of large convective cells.
- β Gru and δ^1 Aps' short-term radial-velocity variations are due to some form of acoustic pulsation; however, the cause of the longer-term radial-velocity variations present can not definitely be determined and may result from either a binary orbit or rotational modulation. In addition, in δ^1 Aps' case there are two acoustic pulsations meaning the pulsation is multi-periodic.
- δ^2 Gru's $\geq$ 1429-day radial-velocity timescale is due to its presence in a binary orbit and its 24-day variation is due to radial pulsation, probably in its first overtone.
- ϵ Mus' 63-day characteristic timescale must be due to either fundamental radial pulsation, in which case the star seems to have less mass than that expected for its colour and visual magnitude, or non-radial g-mode pulsation. The apparent change in characteristic timescale from 63 days to $\sim$ 30 days is consistent with a switch from a fundamental radial pulsation to some higher order mode. However, if the 63-day timescale is from a radial pulsation then the star's 88-day timescale, if not an artifact of mode-switching, is probably due to non-acoustic non-radial pulsation. The 625-day timescale must be due to some kind of surface feature.
- γ Cru's 13 and 16-day characteristic timescales are due to multi-periodic acoustic pulsation. The cause of the longer-term variation is, however, completely open.
- GZ Vel's $\geq$ 2000-day radial-velocity timescale is due to its presence in a binary orbit and its short-term variation must be due either to the ascent and descent of large convective cells, or non-acoustic non-radial pulsation.
- L^2 Pup's 140-day characteristic timescale can only be due to radial pulsation. However, this indicates the star has much less mass than is expected for its colour and visual magnitude. It also has a long-term characteristic timescale of $\approx$440 days. This would have to be due to either rotational modulation or non-radial g-mode pulsation.

[4]With the exception of HR 4177's 435-day timescale which was found by **orbsol** to be 870 days, due to a large gap in the observations (see §4.7)

- o^1 CMa's longest variation in radial velocity seems likely to be related to a similar long-term trend in Hipparcos photometry, in which case it must be caused by some kind of surface feature. If this is the case, however, then either the 769-day timescale is related to the data's spectra window and the said long radial-velocity timescale, or is a non-acoustic non-radial pulsation.

  In addition, this star's dominant and characteristic timescale can only be due to radial pulsation; however, as the predicted fundamental period for this star is significantly smaller than 177 days, o^1 CMa must be at the high end of extra mass loss for supergiants or undergoing period doubling bifurcations. The alternating depth of light minima from the Mt John visual photometry and the long-term trend in Hipparcos visual photometry, strongly suggest that this star is an RVb-type RV Tauri star.

- ψ Phe's 189-day radial-velocity timescale is probably due to rotational modulation, in which case the longer-term variation may be due to either binary motion or the ascent and descent of large convective cells.

- The characteristic timescale of π Pup can only be due to acoustic pulsation and the slightly longer 47-day timescale is also probably due to acoustic pulsation. The long-term radial-velocity variation could be due to either one of rotational modulation or binary motion.

5.2 Further research

5.2.1 Stellar modelling

As has been mentioned there is considerable difficulty distinguishing between effects caused by rotational modulation, binary orbits and the motion of large convective cells, not to mention non-acoustic non-radial pulsation. Some of this stems from a lack of stellar models for these late-type evolved stars. While modelling of such stars is complex and difficult, at times to the point of impossibility, the following constitutes a "wish list" of modelling which would enable considerably more interpretation and clarification of the radial-velocity variations obtained for the 44 stars surveyed for this thesis.

While plausibility studies of large convective cell motion in red giants have been undertaken (see §2.2.1) along with a low mass red-giant model, to this author's knowledge there does not exist reliable convective cell models for a wide range of late-type stars. Predictions of expected timescales and amplitudes of the variations in both in light and radial velocity, would better enable the evaluation of whether or not the observed variations are due to the motion of large convective cells than the primitive estimations of §4.10.

Similarly, non-radial g-mode pulsations have also been investigated for red giants, but to this author's knowledge the stability of low spherical-harmonic order pulsations has not been investigated and (as is discussed in §2.3.5) only low spherical-harmonic order non-radial pulsations are likely to be visible given a radial-velocity precision of 50 m/s. In addition to the question of stability of low spherical-harmonic order non-radial pulsations, the expected amplitude of any such variations in these stars would certainly help clarify their influence on the radial velocities of the observed stars. Even worse, the potential excitation of non-radial r-mode pulsations has not to this author's knowledge been investigated for late-type evolved stars at all.

In addition, doubts about the mass of the stars and questions on the applicability of simple linear pulsation models to what is clearly often non-linear phenomena (see §4.9 and §2.3.3), mean that the theory does not well predict the radial-velocity and photometric variations and any comparison

of observed timescales with pulsations are relegated to an order of magnitude question. Non-linear pulsation models for these stars would be difficult, time-dependent convection would have to be handled carefully amongst other things, but the rewards would include improved expected periods and the expected radial-velocity and visual-photometry amplitudes of the variations. This latter is especially important, as it would help clarify whether or not the lack of detection of acoustic pulsations in the seven K giants for which the pulsations were sufficiently well sampled, indicates acoustic pulsations in K giants are only infrequently present. In the interim even improved linear pulsation models could help clarify matters, as lack of time-dependent convection, poor opacities and lack of non-equilibrium diffusion[5] mean the length of pulsations predicted by Ostlie & Cox [128] can be out by a factor of two (see footnote 29 in Chapter 2).

5.2.2 Observations and analysis

Future observations and analysis can also be looked at to clarify some issues. The most obvious question to be answered concerns the existence of acoustic pulsations in the K giants. Given the lack of any observation of these in this survey and the observations by other researchers (for examples see §1.1), it seems certain that better precision and more frequent observations are necessary to ensure the observation of any such variations in K giants. Hence the question remains open as to how common these pulsations really are in these stars.

In addition, some of the long-term radial-velocity variations have a similar variation in Hipparcos photometry (e.g. λ Vel, NS Pup and σ CMa). As the photometry and radial velocities are not concurrent it is difficult to determine precisely what is causing the variations, but rotational modulation seems a good candidate. Concurrent observations could confirm the variations as being more than coincidental and distinguish between a starpatch and starspot mechanism.

Obtaining more precise radial velocities is not simple, but a number of improvements can easily be made to the technique used for this thesis. For example: the avoidance of line blending, if it is desired to fit the cross-correlation with a gaussian to determine the location of its peak; a CCD more suited to spectroscopy i.e less square or larger, so that shifts in radial velocity do not cause such a large fraction of each order to be lost (cross-correlation with a synthetic spectrum can avoid this particular problem), as dissimilar spectra must be discarded or the cross-correlation function will be asymmetric; better pixel resolution, as this gives better fits to the cross-correlation function (see §3.5.4 for details). A less easily fixed problem has also come to light in the last few months. It is believed that there may be a systematic change in radial velocity (the same from order-to-order) with the signal-to-noise of the spectrum, even for signal-to-noise of over 100:1 (Skuljan et al. [152]). It is unknown what is causing this systematic effect, which can result in errors up to several hundred metres a second, but as these are not random effects differentiating between these and real changes in radial velocity is difficult. Careful consideration and monitoring of this problem will be necessary for any further observations using this CCD chip.

As is common, obtaining observations of a star at daily intervals yet over durations of the order of two weeks has been impossible for this thesis, given both poor weather and telescope time constraints. Yet to cover the expected duration of radial pulsations for K giants this would be almost essential. As the number of smaller telescopes decreases world wide, while such data runs would be illuminating (in conjunction with better precision), such scheduling of observations becomes increasingly difficult. This is especially true when the concurrent photometric observation

[5] Assuming equilibrium diffusion means to assume the real energy density in the star is that of local thermodynamic equilibrium. The balance of absorption and emission in local thermodynamic equilibrium is called Kirchhoff's law, see Clayton [36] page 176, and it means that the true emission is determined entirely by the temperature of the matter. However, in non-equilibrium conditions the specific intensity of the radiation becomes important for induced (caused by the radiation field) emission.

of these stars is needed. Nonetheless, such observations would be necessary to observe the short-term radial-velocity variations observed by other researchers and hence valuable in understanding K giants and well worthwhile. It is not just K giants for which such frequent observations would be beneficial either. While the observations obtained for this thesis indicate the situation in broad outline the details of the variations are not clear, especially with respect to short-term variations. For example, ϵ Mus' photometric variations seem to vary from a period of 60 days to 30 days over a timescale of about 200 days (see Figure 4.20). Unfortunately, frequent enough radial-velocity observations are not available to indicate if they also exhibit the same behaviour and this makes it difficult to fully interpret what is happening. It is difficult to say if this is a case of the star switching modes or perhaps starting to undergo pulsations similar to o^1 CMa, where the photometric variations have double the number of minima of the radial-velocity variations.

Also beneficial in determining the reality of pulsations in all types of stars would be higher accuracy and more frequent V and $(R-I)$ photometric observations (in conjunction with radial velocities), as these enable the the angular-diameter variations of the star to be compared (via the Barnes-Evans technique) with the radial-velocity variations (see §4.6.2, unfortunately during the period of most intensive concurrent observations the use of two different telescopes led to it being necessary to discard a sizable fraction of the photometric observations). The reality of possible rotational-modulation timescales could also be refined if the exact values of $v_{\rm equ}\sin(i)$ were known. This could potentially be measured at any time and the results used to refine the conclusions made in §4.10.

As far as the analysis is concerned, it is clear that the simple **T6** method of effectively doing a least-squares sine fit to the data then subtracting off the sine iteratively is not sufficient to give more than an indication of the timescales present. Application of methods like CLEAN (see §4.1) which do not pre-whiten the data, but instead attempt to take account of the data spacing when determining the reality of the peaks in the Fourier transform, would be an improvement if the data spacing was small enough. Fitting multiple periods using a nonlinear least-squares fit in a similar manner to that discussed in Irwin et al. [99], could also lead to a better determination of the underlying timescales. However over all, there is no substitution for well-sampled good-quality data, which can be used to model the expected variations. If rotational modulation is as important as the results for this thesis suggest, this may well be a way forward as starspot and starpatch modelling procedures have been undertaken by other researchers (see, for example, Dorren & Guinan [46] and Toner & Gray [166]).

Appendix A

Radial-velocity data plots for the 44 surveyed stars

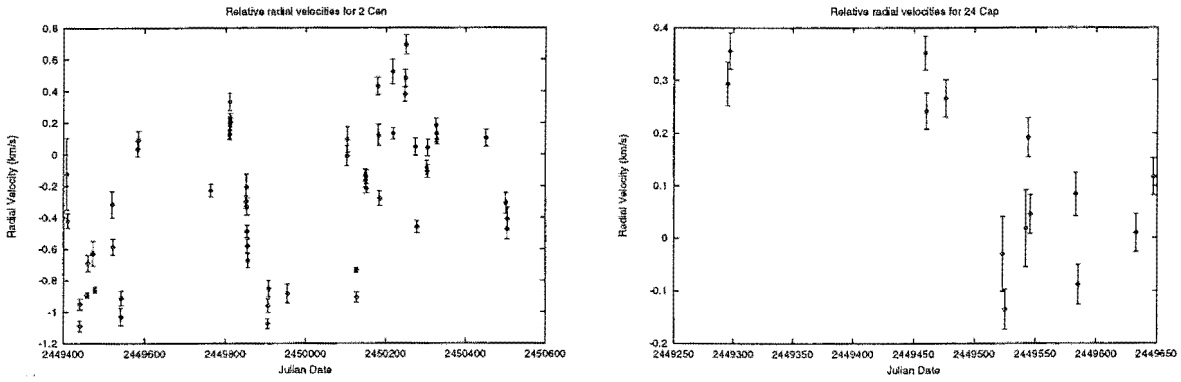

Figure A.1: The relative radial-velocity data for 2 Cen and 24 Cap. See Figures B.1 for the Lomb-Scargle Periodograms of these data.

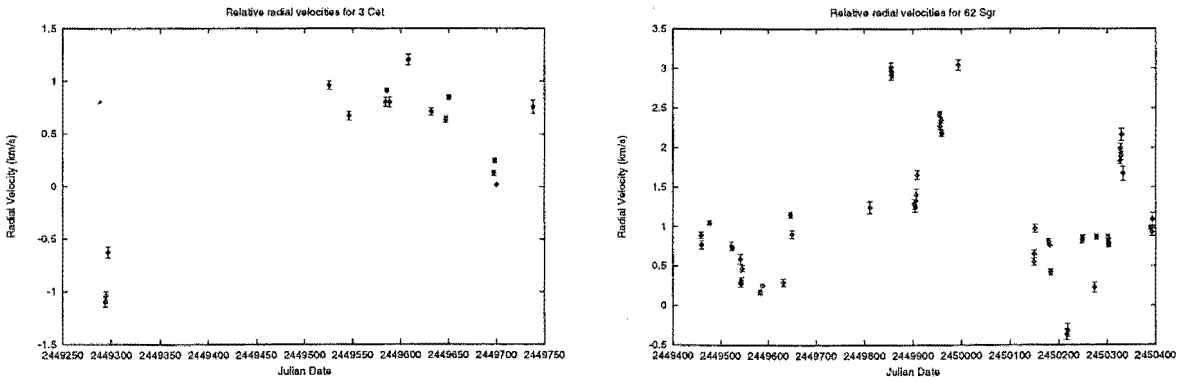

Figure A.2: The relative radial-velocity data for 3 Cet and 62 Sgr. See Figures B.2 for the Lomb-Scargle Periodograms of these data.

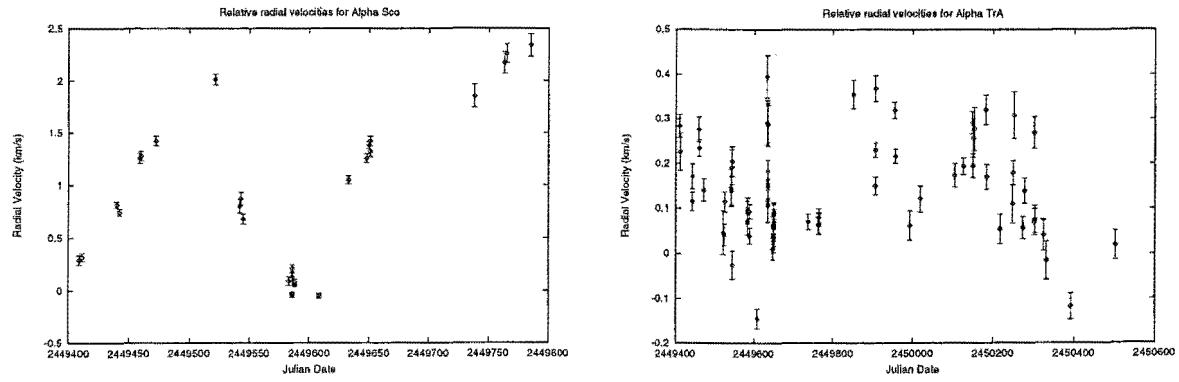

Figure A.3: The relative radial-velocity data for α Sco and α TrA. See Figures B.3 for the Lomb-Scargle Periodograms of these data.

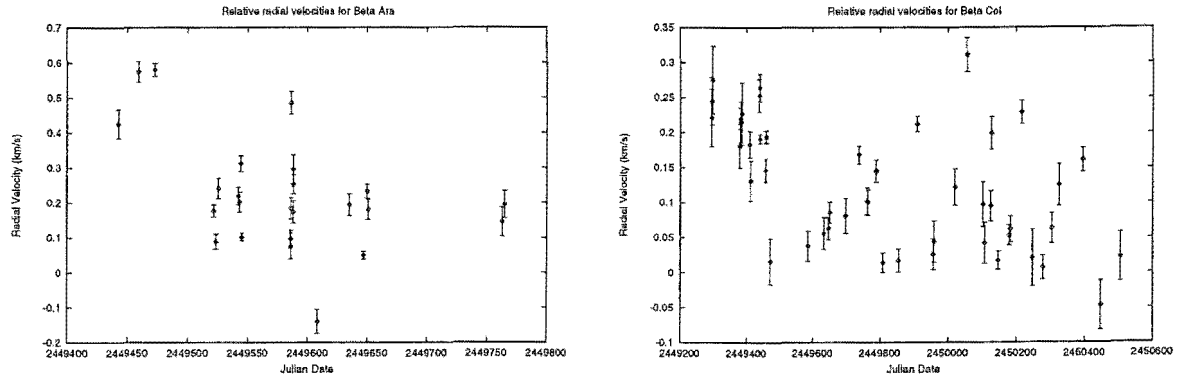

Figure A.4: The relative radial-velocity data for β Ara and β Col. See Figures B.4 for the Lomb-Scargle Periodograms of these data.

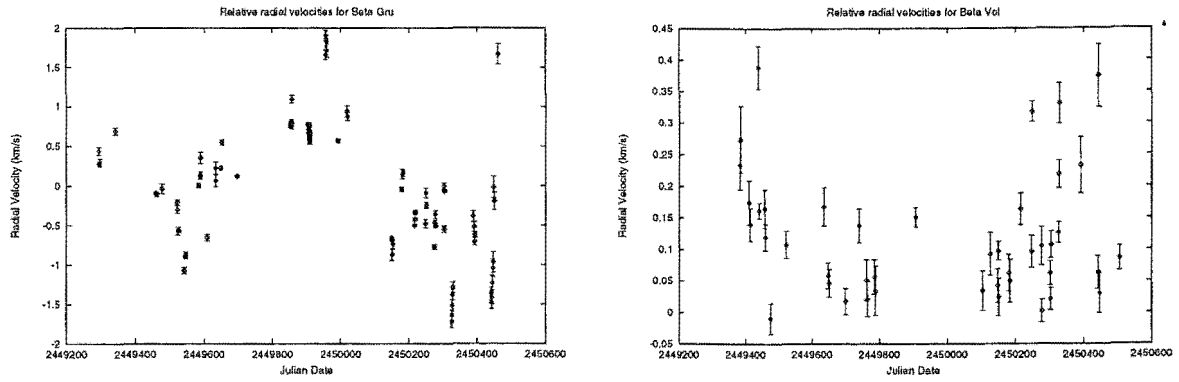

Figure A.5: The relative radial-velocity data for β Gru and β Vol. See Figures B.5 for the Lomb-Scargle Periodograms of these data.

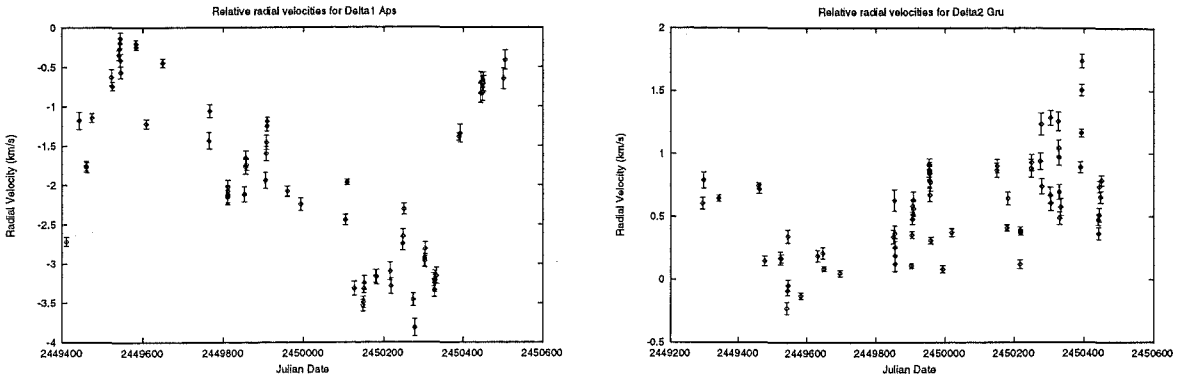

Figure A.6: The relative radial-velocity data for δ^1 Aps and δ^2 Gru. See Figures B.6 for the Lomb-Scargle Periodograms of these data.

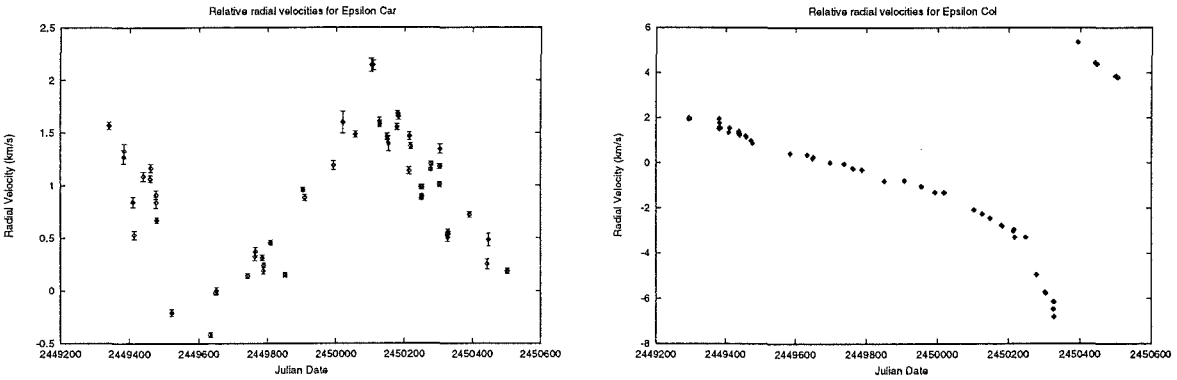

Figure A.7: The relative radial-velocity data for ϵ Car and ϵ Col. See Figures B.7 for the Lomb-Scargle Periodograms of these data.

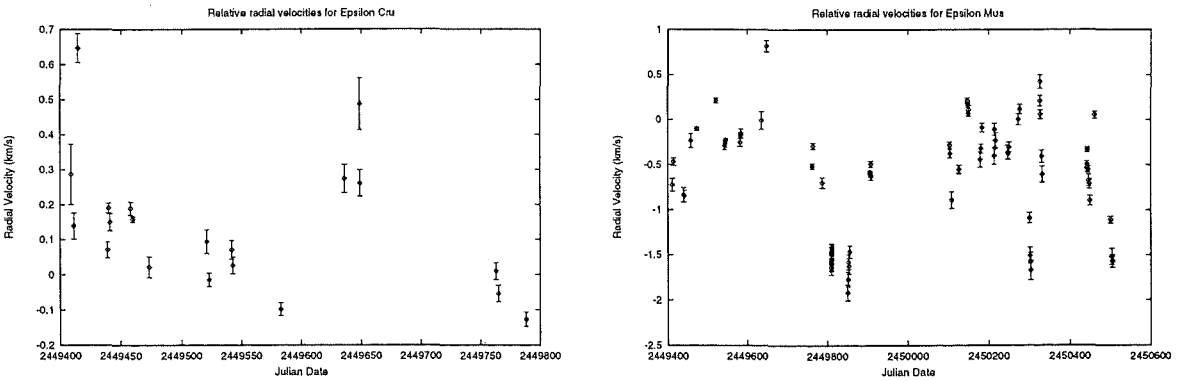

Figure A.8: The relative radial-velocity data for ϵ Cru and ϵ Mus. See Figures B.8 for the Lomb-Scargle Periodograms of these data.

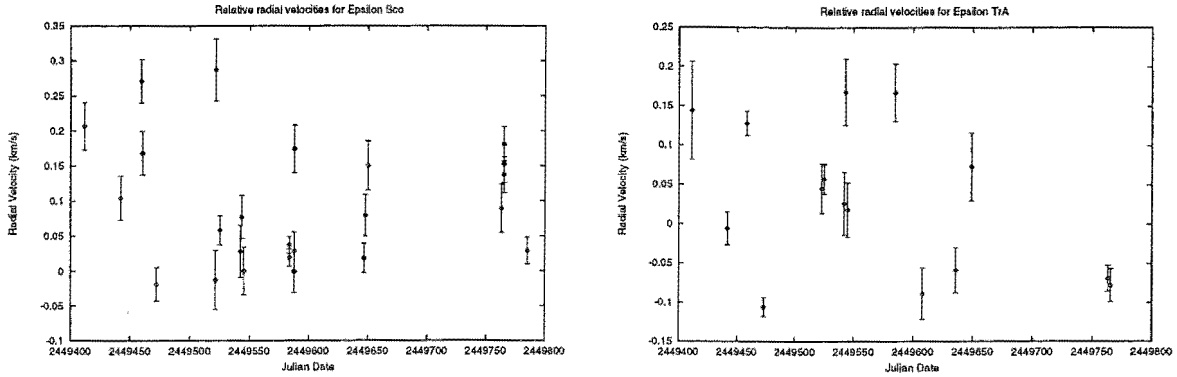

Figure A.9: The relative radial-velocity data for ϵ Sco and ϵ TrA. See Figures B.9 for the Lomb-Scargle Periodograms of these data.

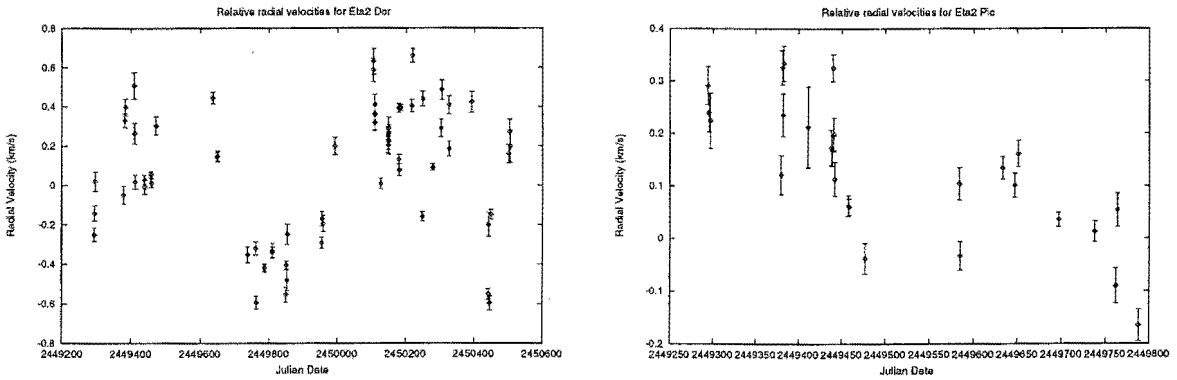

Figure A.10: The relative radial-velocity data for η^2 Dor and η^2 Pic. See Figures B.10 for the Lomb-Scargle Periodograms of these data.

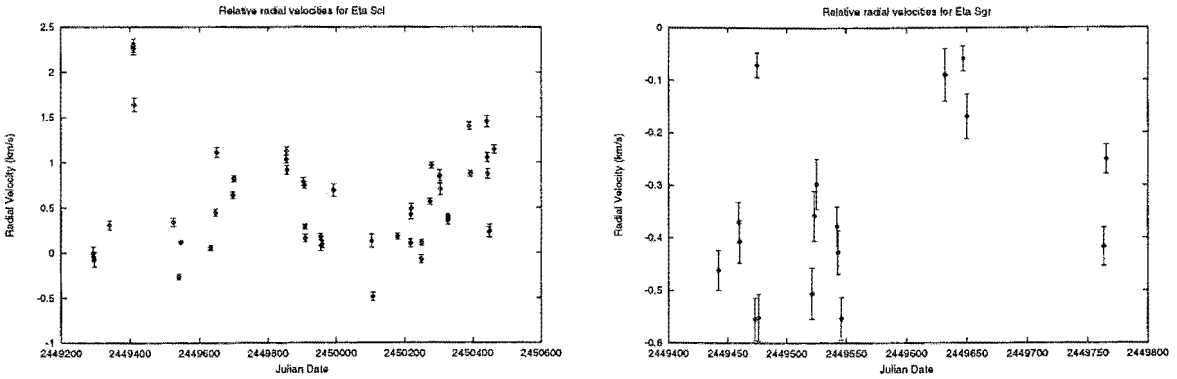

Figure A.11: The relative radial-velocity data for η Scl and η Sgr. See Figures B.11 for the Lomb-Scargle Periodograms of these data.

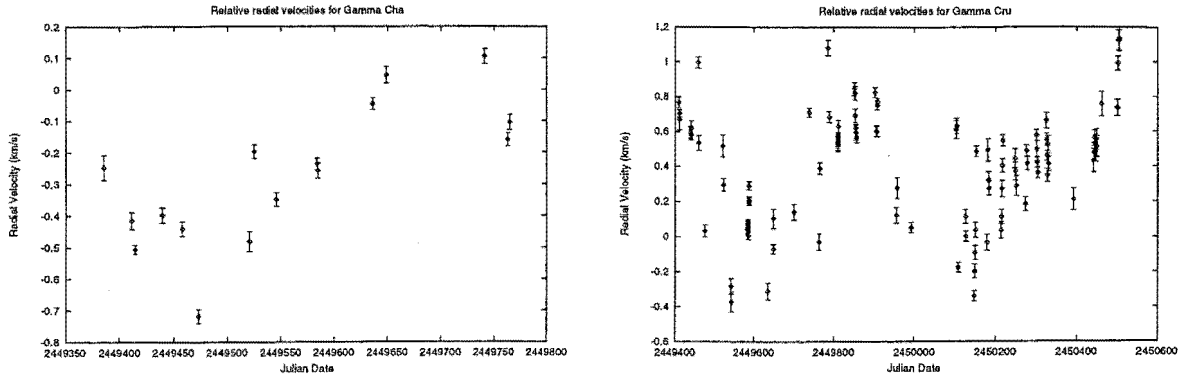

Figure A.12: The relative radial-velocity data for γ Cha and γ Cru. See Figures B.12 for the Lomb-Scargle Periodograms of these data.

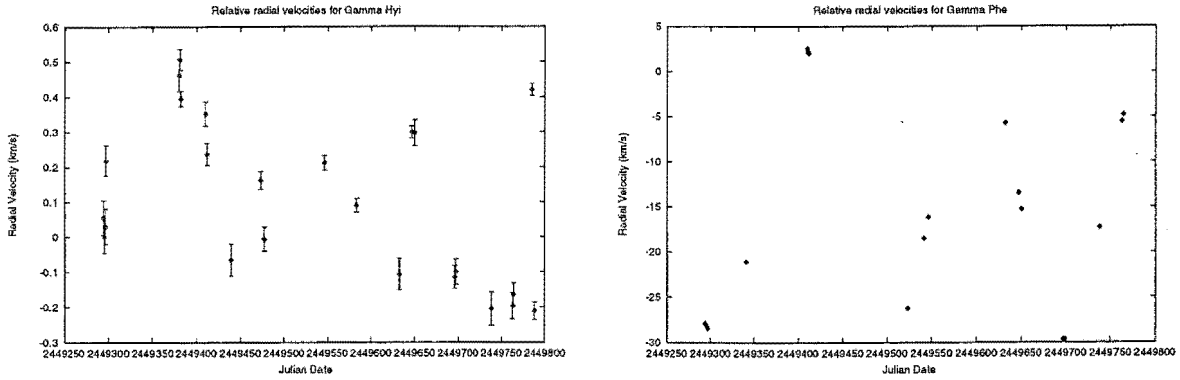

Figure A.13: The relative radial-velocity data for γ Hyi and γ Phe. See Figures B.13 for the Lomb-Scargle Periodograms of these data.

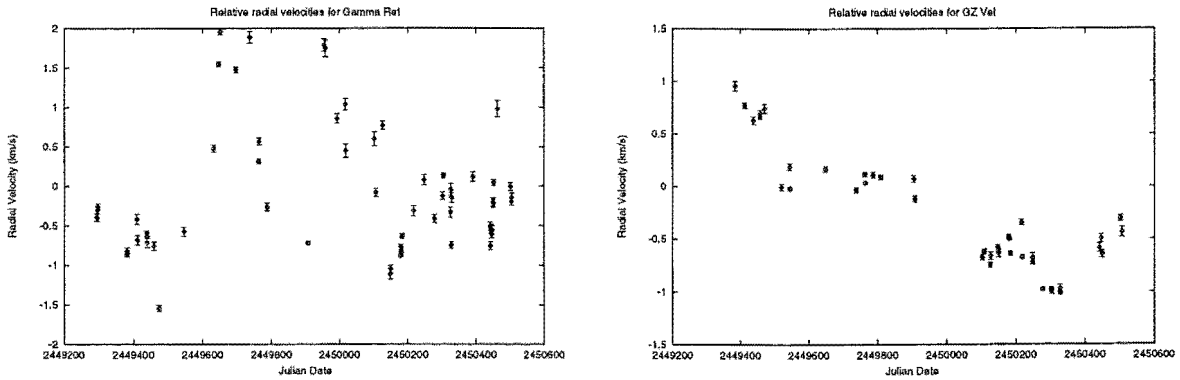

Figure A.14: The relative radial-velocity data for γ Ret and GZ Vel. See Figures B.14 for the Lomb-Scargle Periodograms of these data.

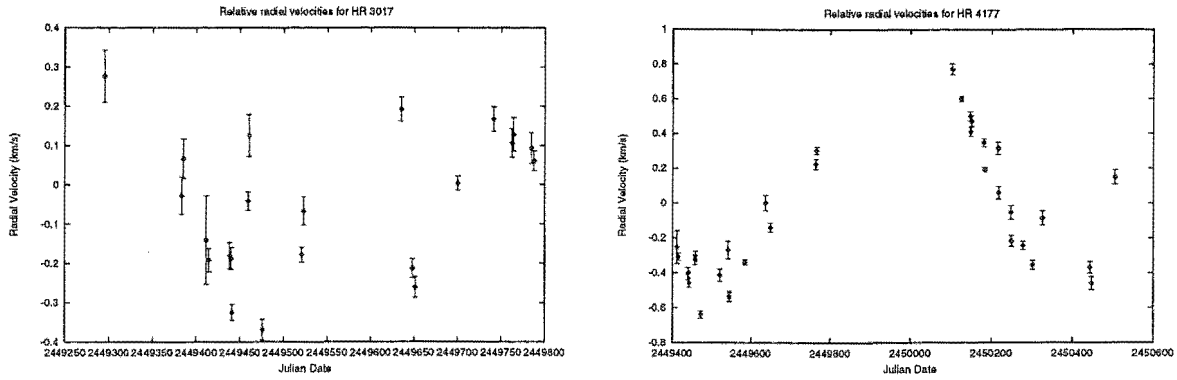

Figure A.15: The relative radial-velocity data for HR 3017 and HR 4177. See Figures B.15 for the Lomb-Scargle Periodograms of these data.

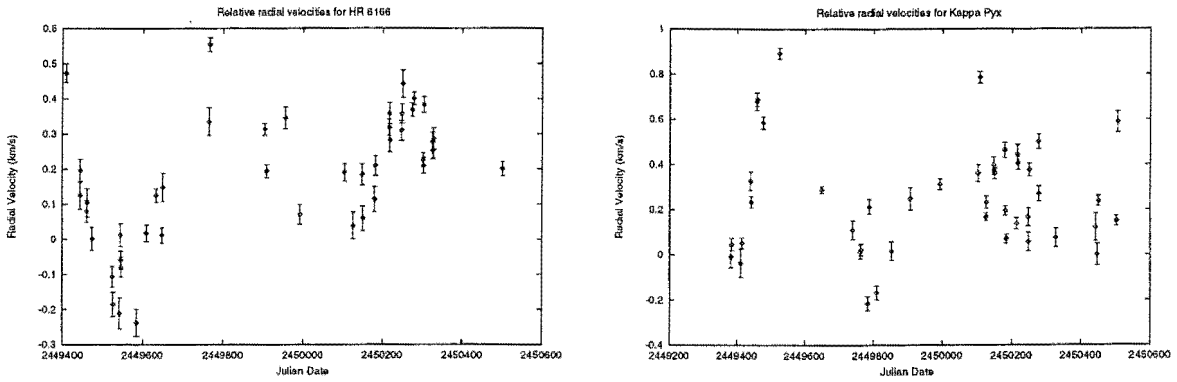

Figure A.16: The relative radial-velocity data for HR 6166 and κ Pyx. See Figures ?? for the Lomb-Scargle Periodograms of these data.

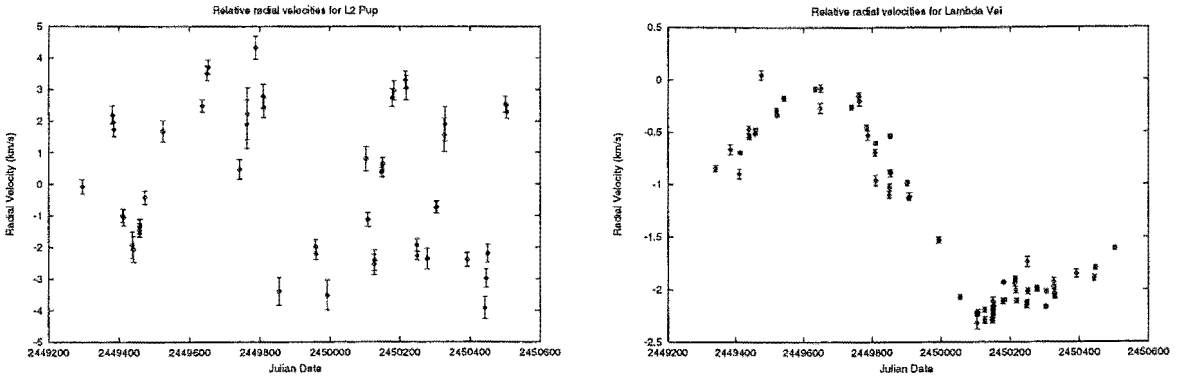

Figure A.17: The relative radial-velocity data for L^2 Pup and λ Vel. See Figures B.17 for the Lomb-Scargle Periodograms of these data.

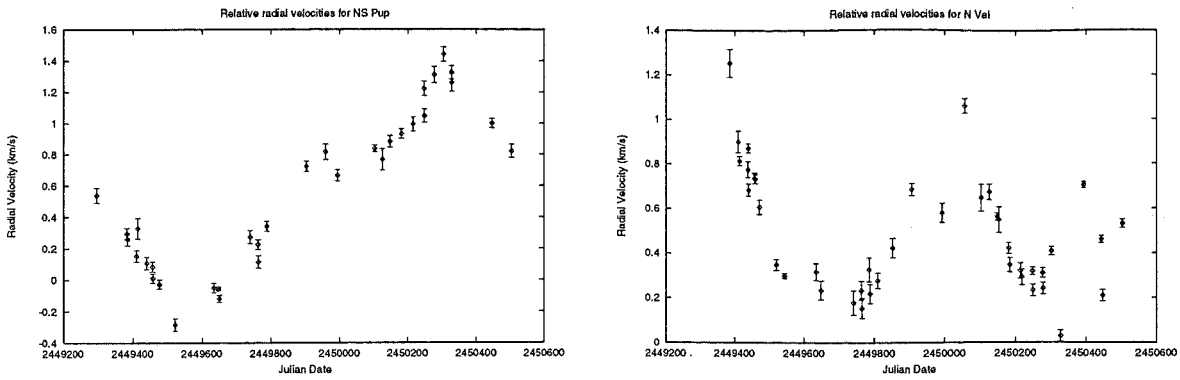

Figure A.18: The relative radial-velocity data for NS Pup and N Vel. See Figures B.18 for the Lomb-Scargle Periodograms of these data.

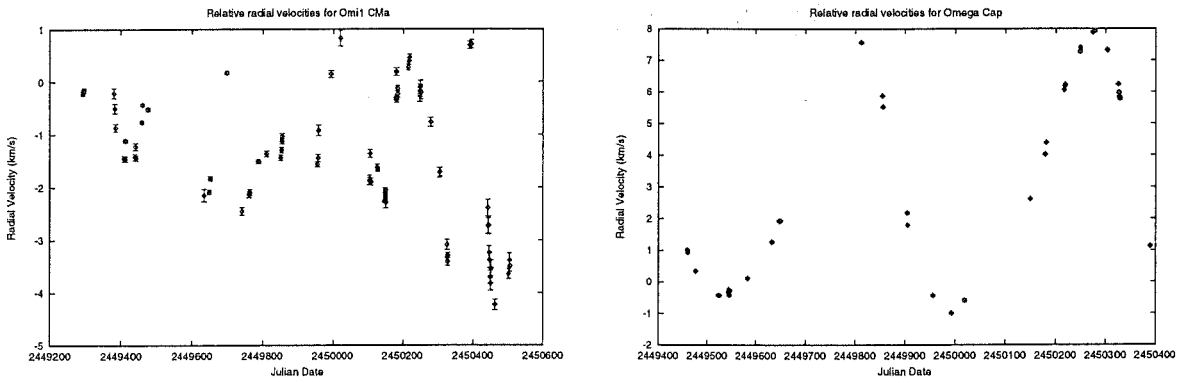

Figure A.19: The relative radial-velocity data for o^1 CMa and ω Cap. See Figures B.19 for the Lomb-Scargle Periodograms of these data.

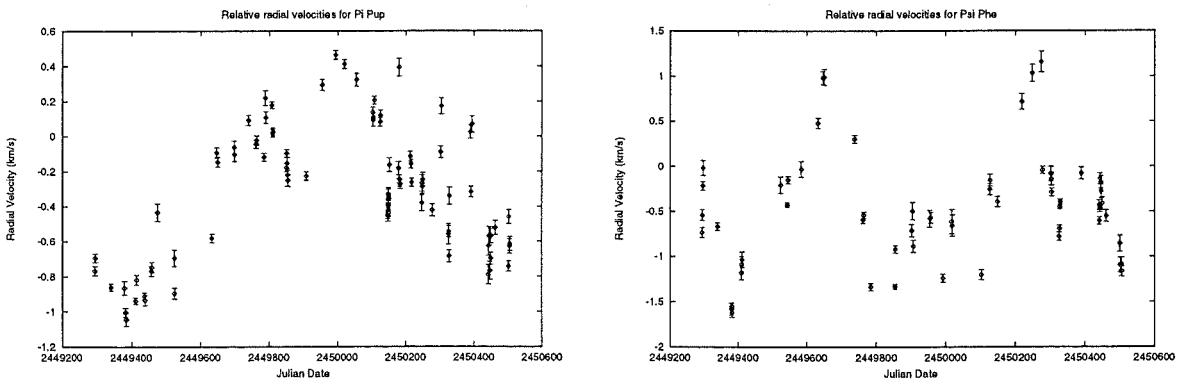

Figure A.20: The relative radial-velocity data for π Pup and ψ Phe. See Figures B.20 for the Lomb-Scargle Periodograms of these data.

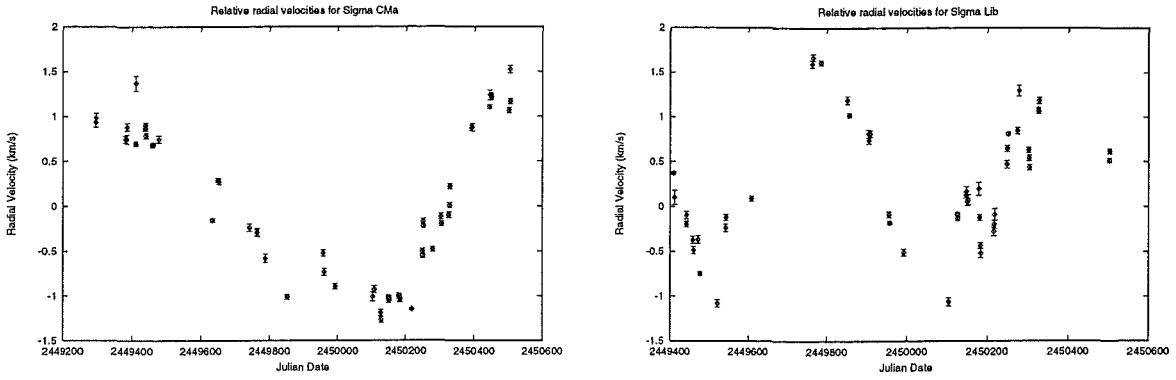

Figure A.21: The relative radial-velocity data for σ CMa and σ Lib. See Figures B.21 for the Lomb-Scargle Periodograms of these data.

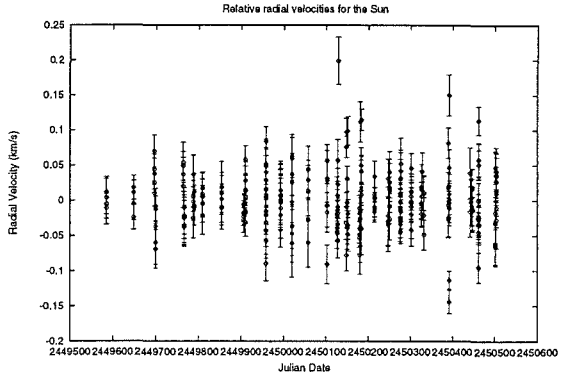

Figure A.22: The relative radial-velocity data for the Sun (after run corrections have been applied). See Figure B.22 for the Lomb-Scargle Periodogram of these data.

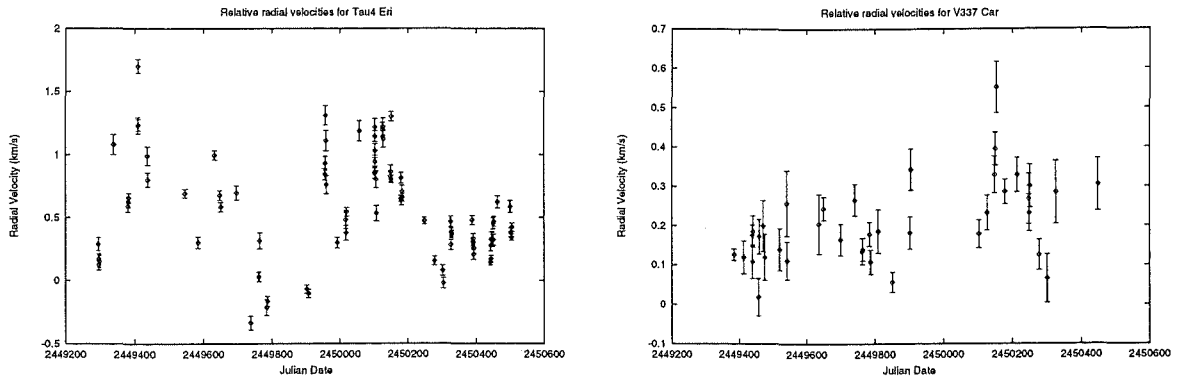

Figure A.23: The relative radial-velocity data for τ^4 Eri and V337 Car. See Figures B.23 for the Lomb-Scargle Periodograms of these data.

Appendix B

Lomb-Scargle Periodograms for the 44 surveyed stars' radial-velocities

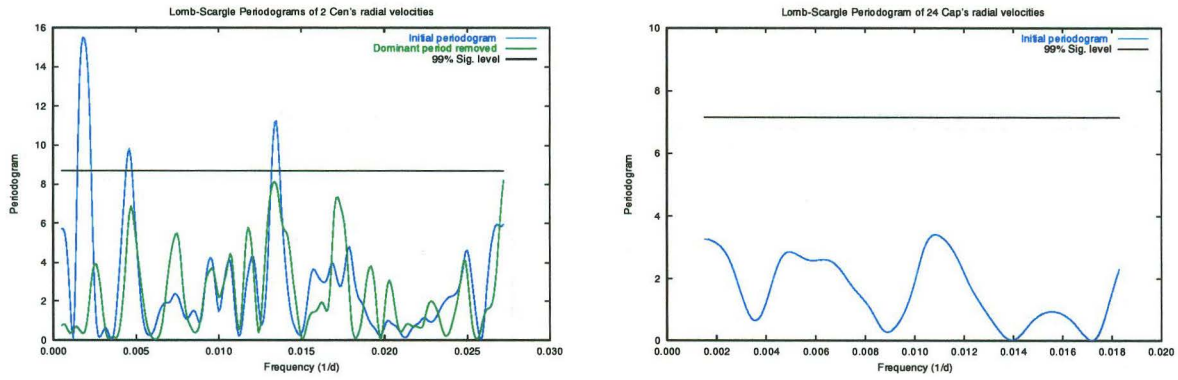

Figure B.1: The Lomb-Scargle Periodograms for the radial velocities of 2 Cen and 24 Cap.

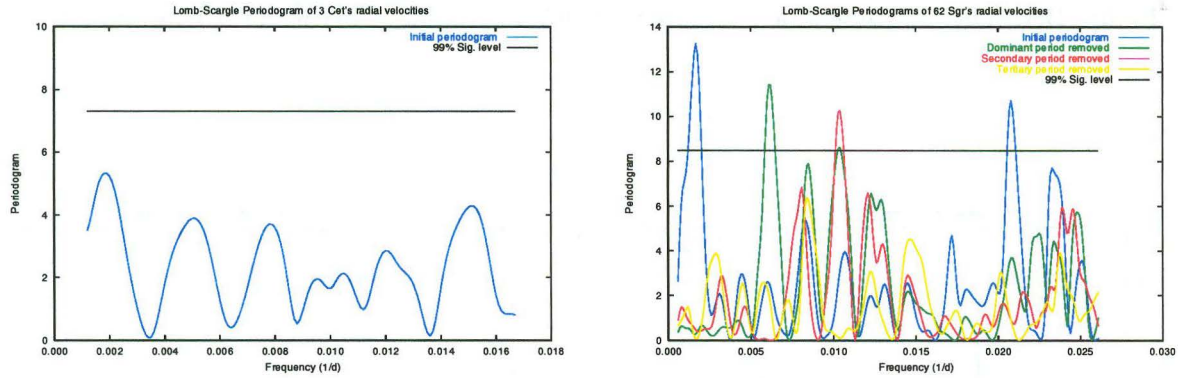

Figure B.2: The Lomb-Scargle Periodograms for the radial velocities of 3 Cet and 62 Sgr.

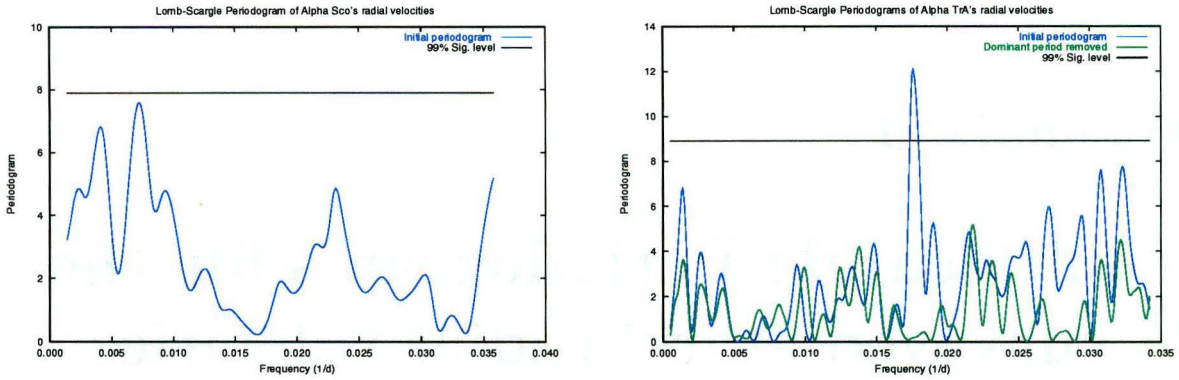

Figure B.3: The Lomb-Scargle Periodograms for the radial velocities of α Sco and α TrA.

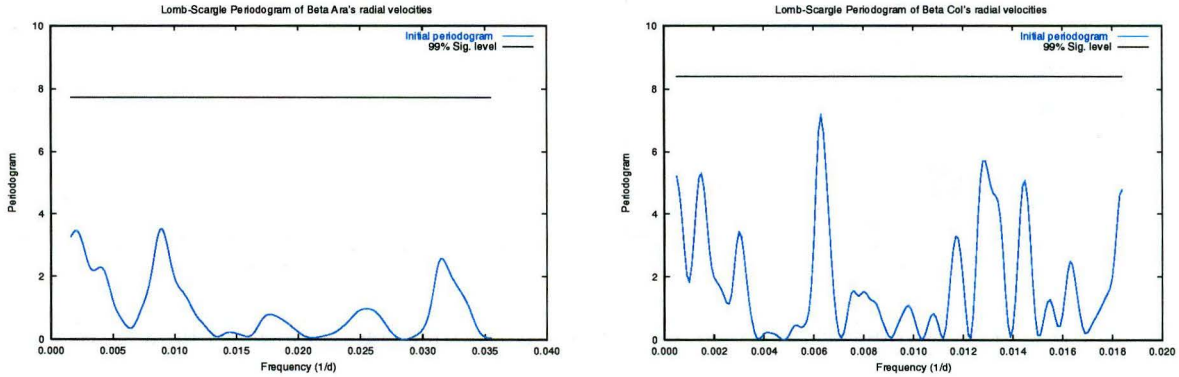

Figure B.4: The Lomb-Scargle Periodograms for the radial velocities of β Ara and β Col.

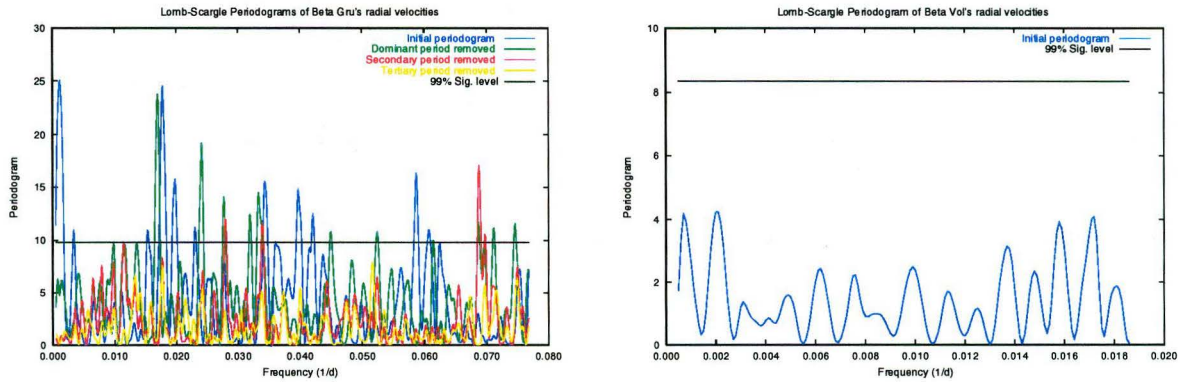

Figure B.5: The Lomb-Scargle Periodograms for the radial velocities of β Gru and β Vol.

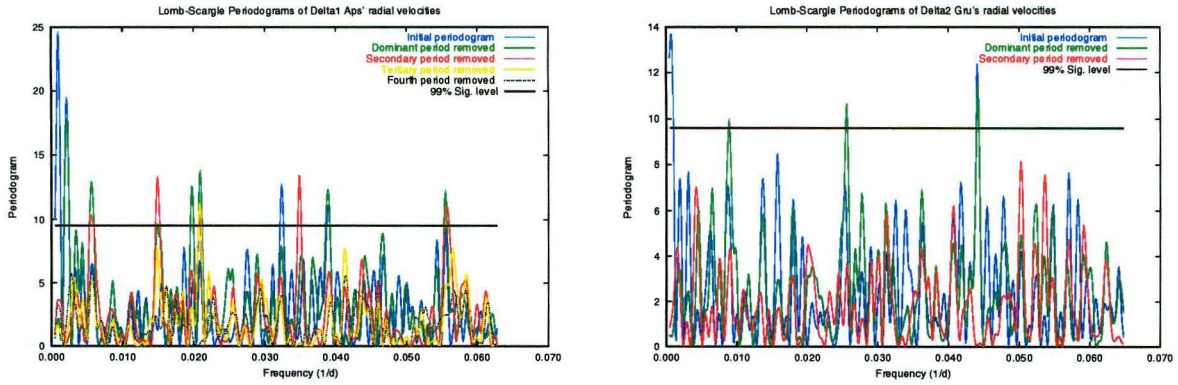

Figure B.6: The Lomb-Scargle Periodograms for the radial velocities of δ^1 Aps and δ^2 Gru.

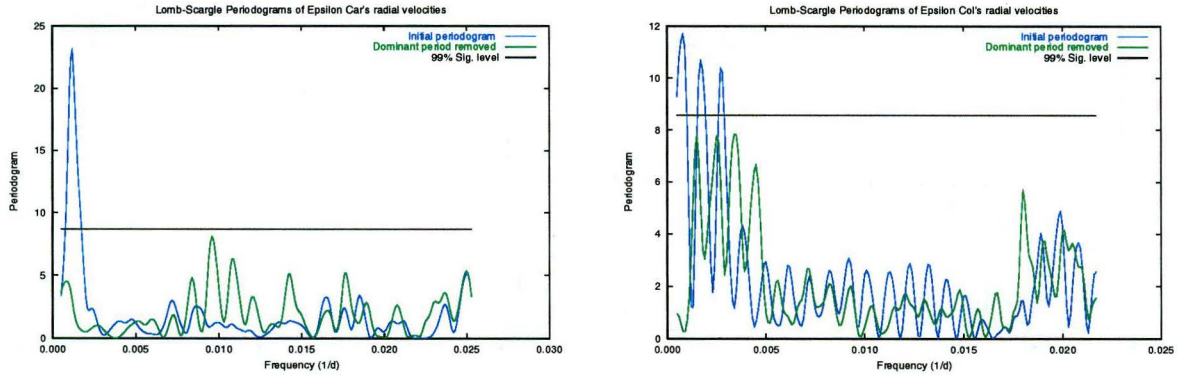

Figure B.7: The Lomb-Scargle Periodograms for the radial velocities of ϵ Car and ϵ Col.

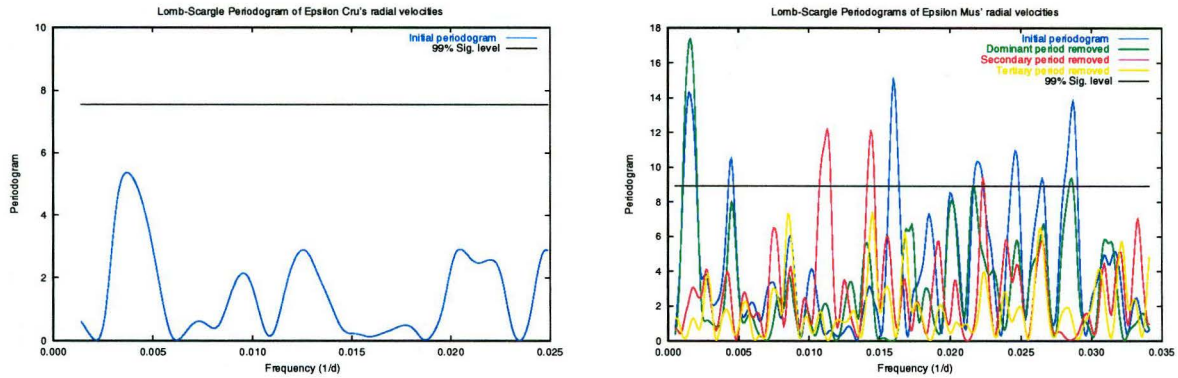

Figure B.8: The Lomb-Scargle Periodograms for the radial velocities of ϵ Cru and ϵ Mus.

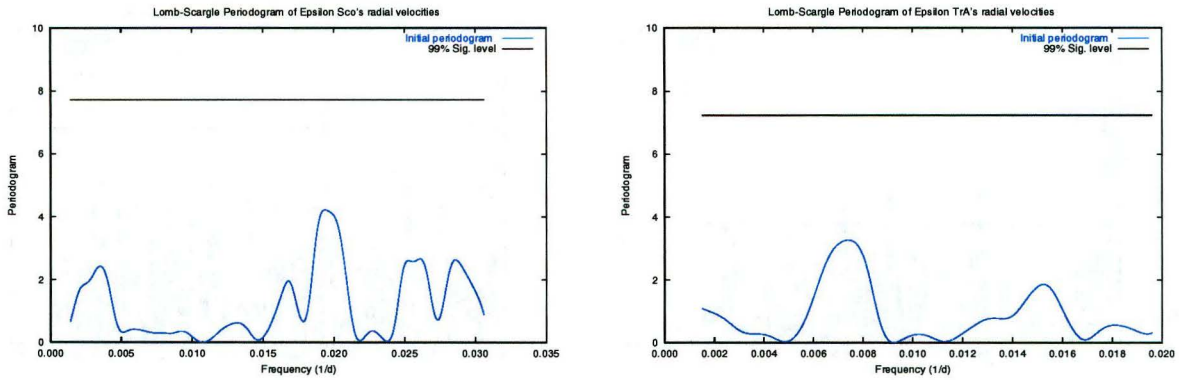

Figure B.9: The Lomb-Scargle Periodograms for the radial velocities of ϵ Sco and ϵ TrA.

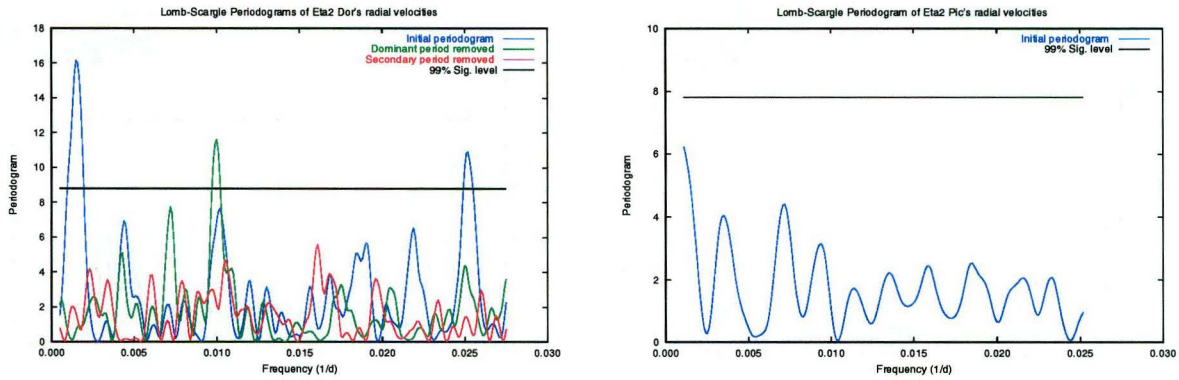

Figure B.10: The Lomb-Scargle Periodograms for the radial velocities of η^2 Dor and η^2 Pic.

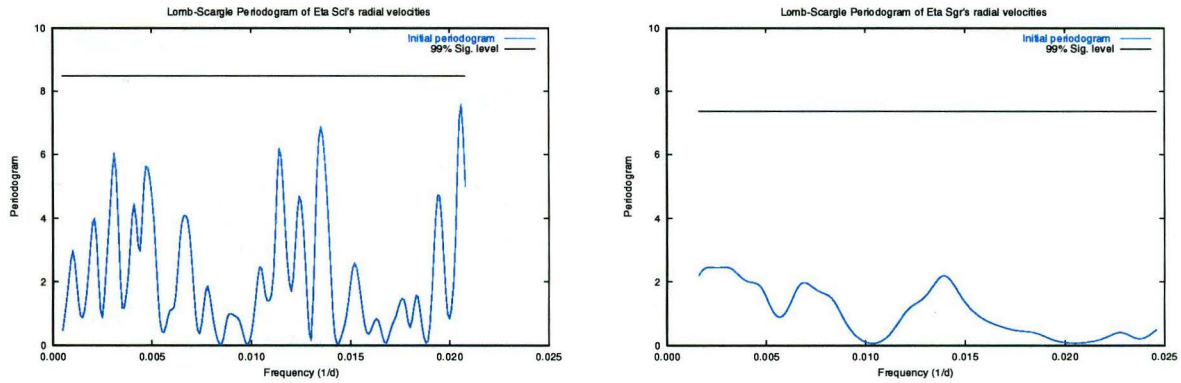

Figure B.11: The Lomb-Scargle Periodograms for the radial velocities of η Scl and η Sgr.

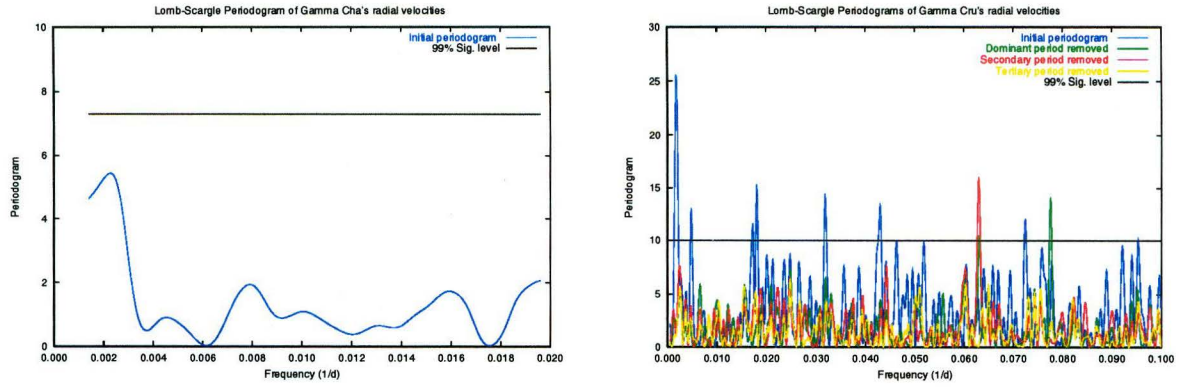

Figure B.12: The Lomb-Scargle Periodograms for the radial velocities of γ Cha and γ Cru.

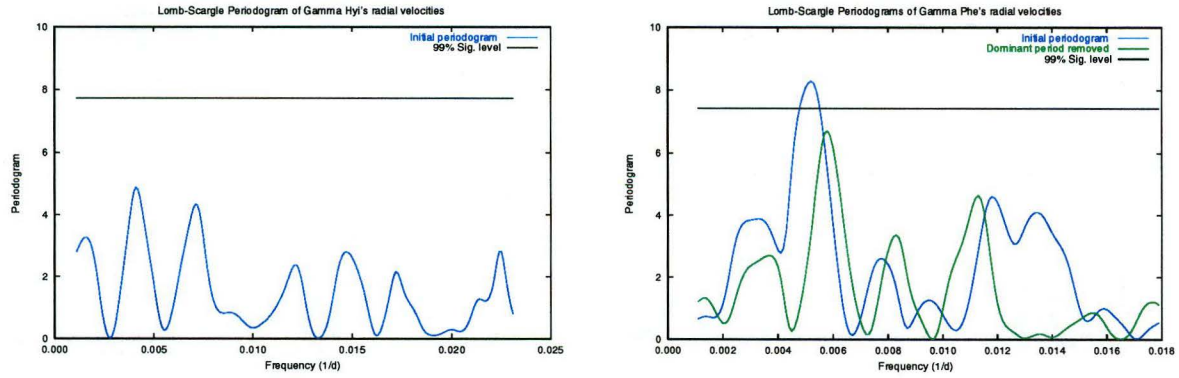

Figure B.13: The Lomb-Scargle Periodograms for the radial velocities of γ Hyi and γ Phe.

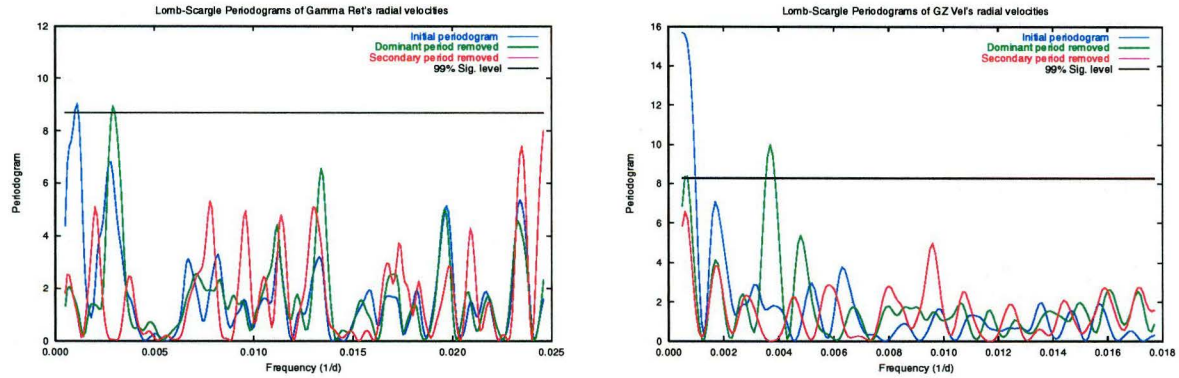

Figure B.14: The Lomb-Scargle Periodograms for the radial velocities of γ Ret and GZ Vel.

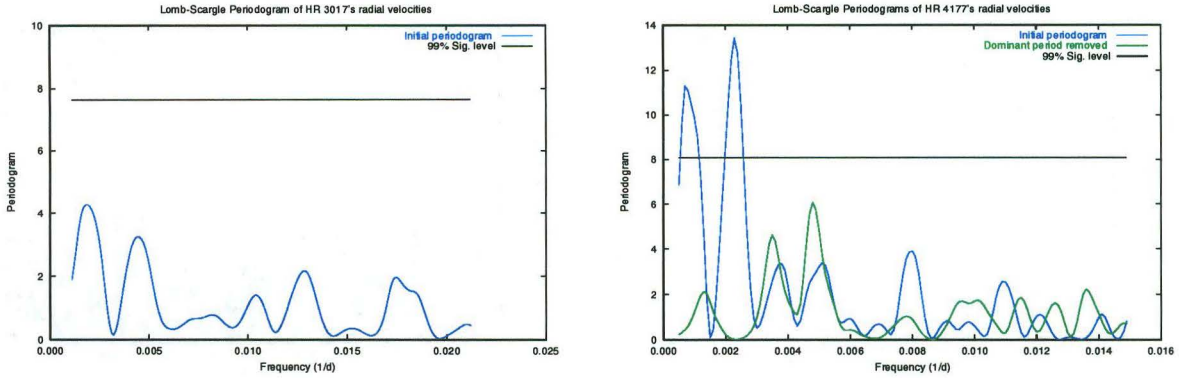

Figure B.15: The Lomb-Scargle Periodograms for the radial velocities of HR 3017 and HR 4177.

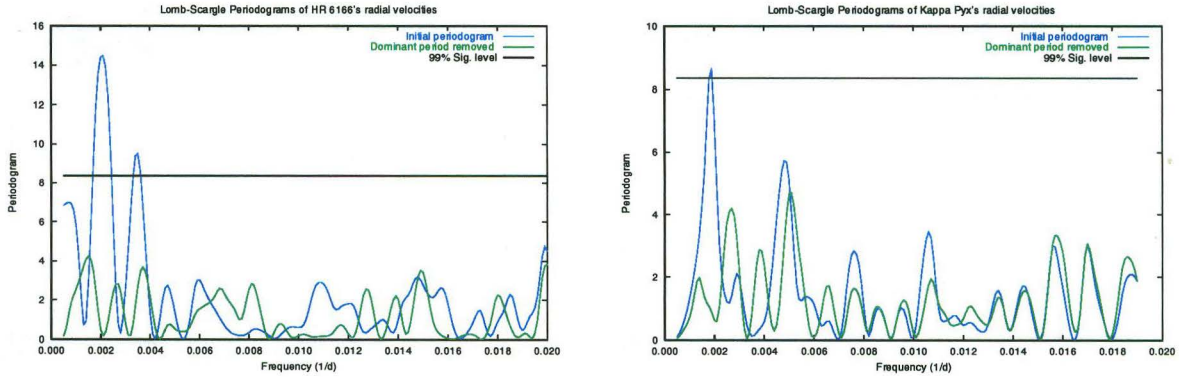

Figure B.16: The Lomb-Scargle Periodograms for the radial velocities of HR 6166 and κ Pyx.

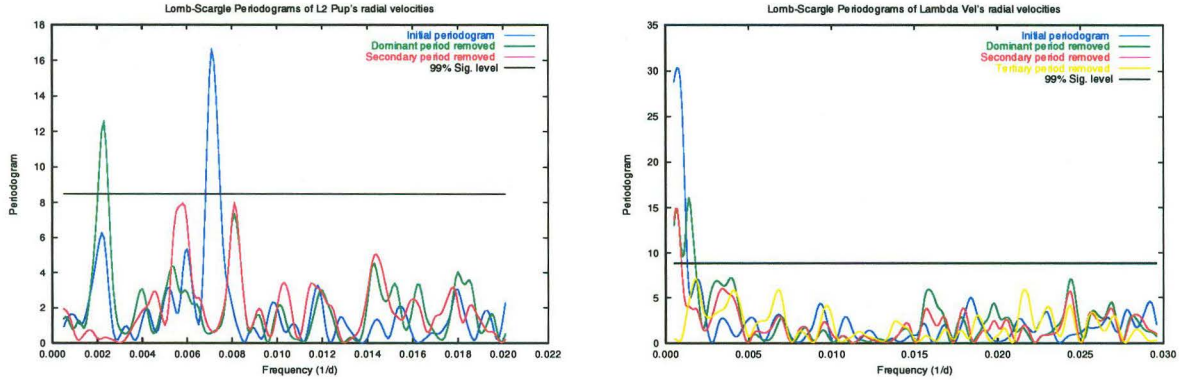

Figure B.17: The Lomb-Scargle Periodograms for the radial velocities of L^2 Pup and λ Vel.

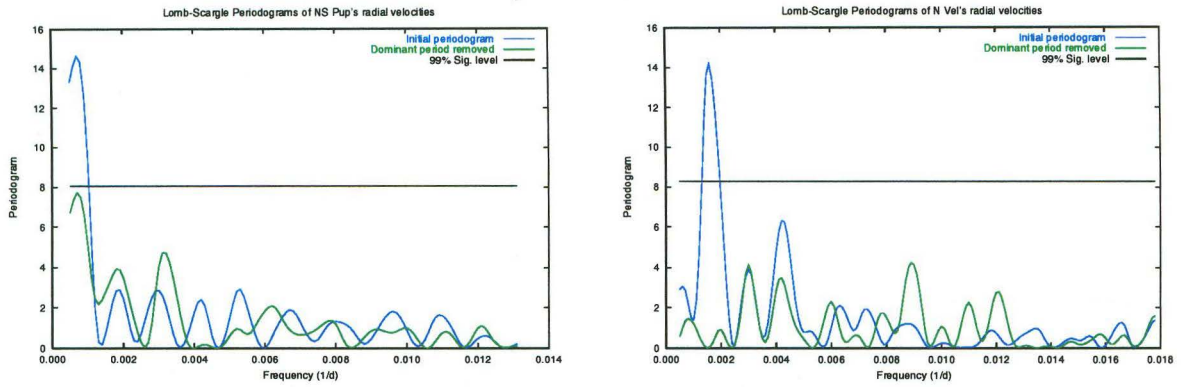

Figure B.18: The Lomb-Scargle Periodograms for the radial velocities of NS Pup and N Vel.

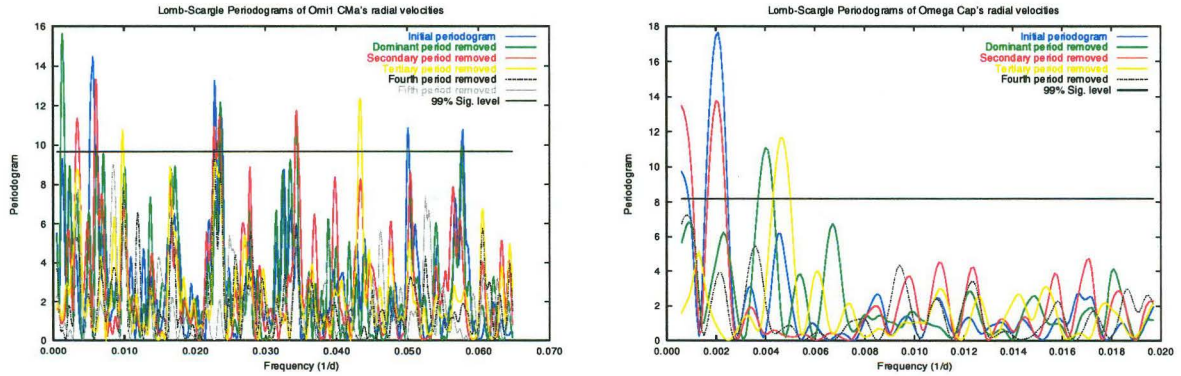

Figure B.19: The Lomb-Scargle Periodograms for the radial velocities of o^1 CMa and ω Cap.

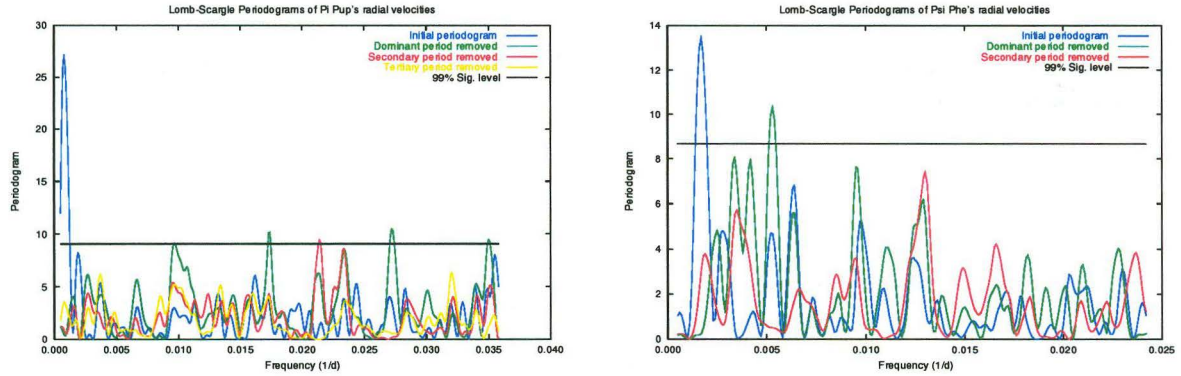

Figure B.20: The Lomb-Scargle Periodograms for the radial velocities of π Pup and ψ Phe.

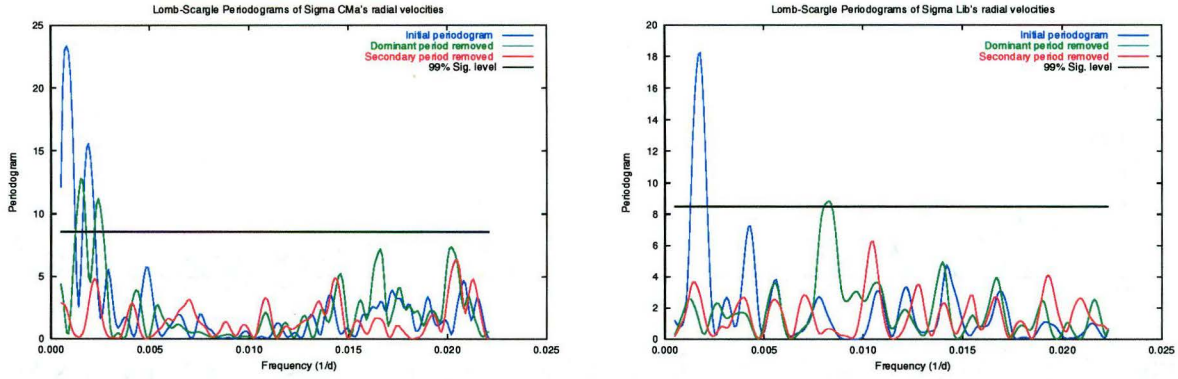

Figure B.21: The Lomb-Scargle Periodograms for the radial velocities of σ CMa and σ Lib.

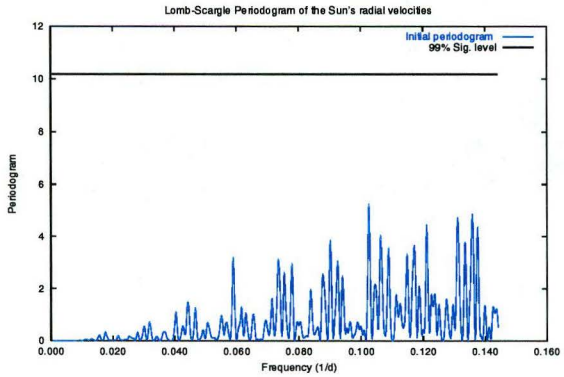

Figure B.22: The Lomb-Scargle Periodograms for the radial velocities of the Sun (after run corrections have been applied).

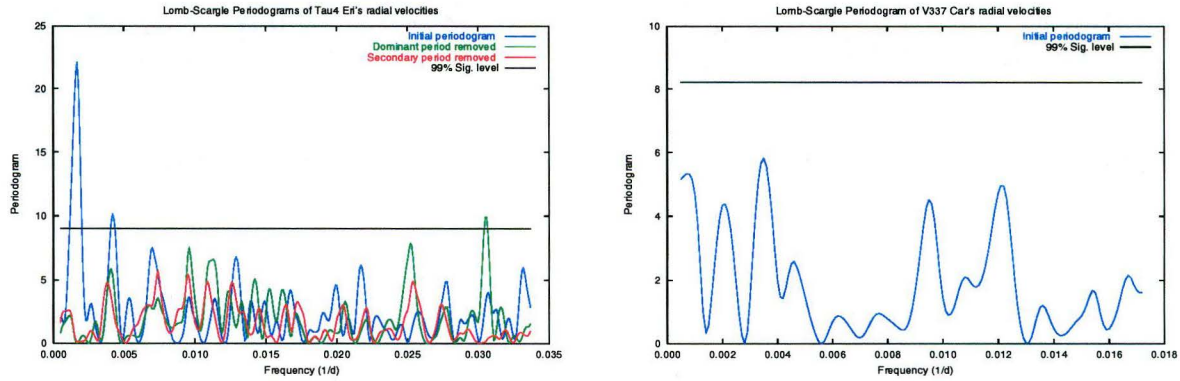

Figure B.23: The Lomb-Scargle Periodograms for the radial velocities of τ^4 Eri and V337 Car.

Appendix C

Phased relative radial velocities

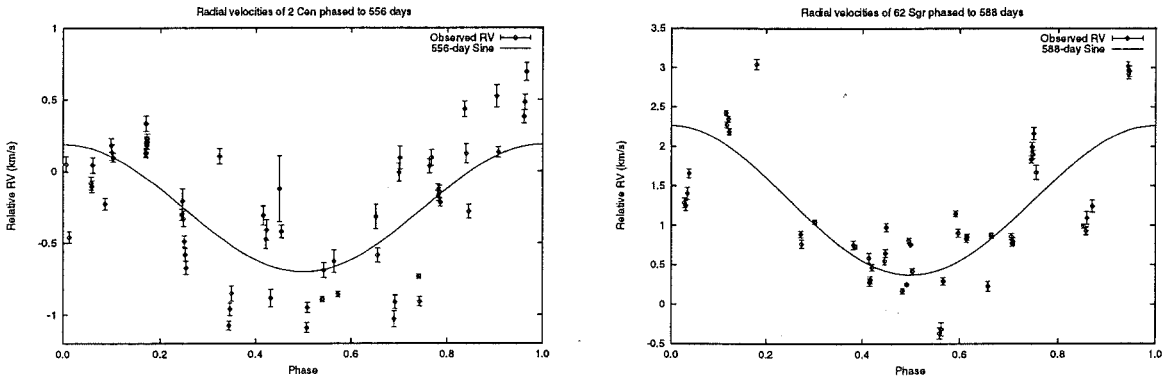

Figure C.1: Plots of radial velocities phased to the dominate timescale for 2 Cen and 62 Sgr. The plotted sine is that used for prewhitening by **T6**, with the addition of an arbitary constant.

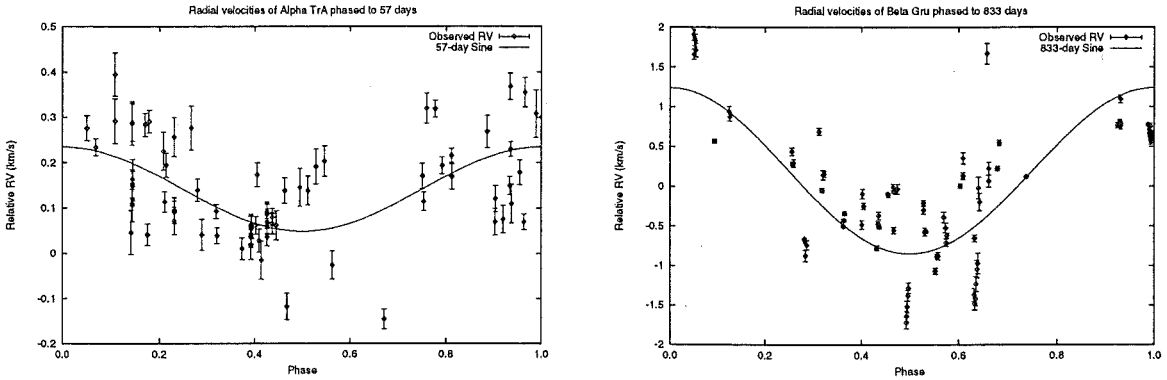

Figure C.2: Plots of radial velocities phased to the dominate timescale for α TrA and β Gru. The plotted sine is that used for prewhitening by **T6**, with the addition of an arbitary constant.

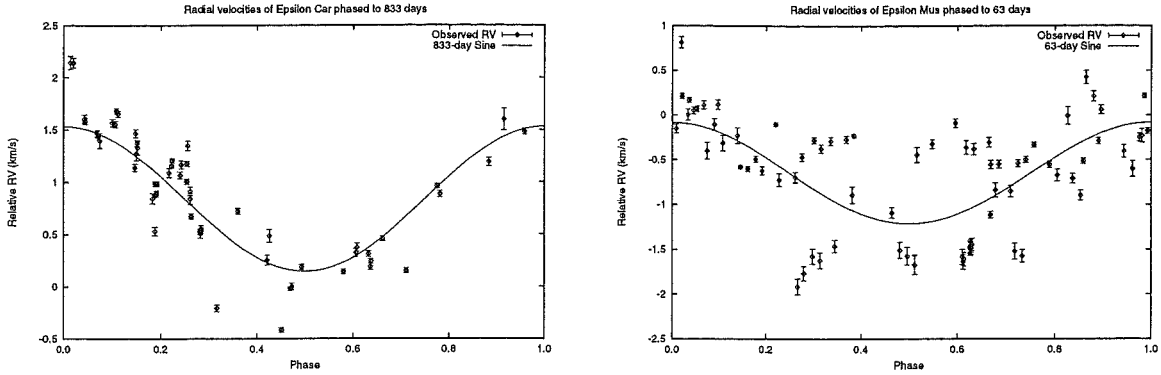

Figure C.3: Plots of radial velocities phased to the dominate timescale for ϵ Car and ϵ Mus. The plotted sine is that used for prewhitening by **T6**, with the addition of an arbitary constant.

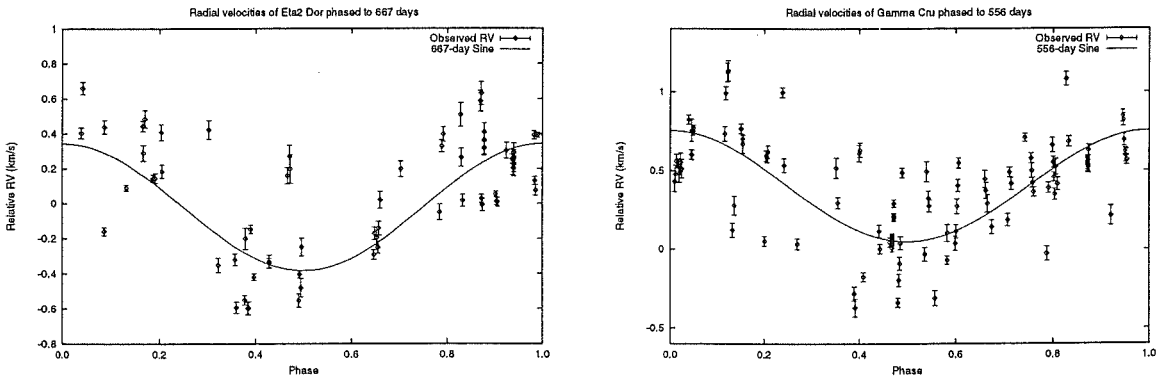

Figure C.4: Plots of radial velocities phased to the dominate timescale for η^2 Dor and γ Cru. The plotted sine is that used for prewhitening by **T6**, with the addition of an arbitary constant.

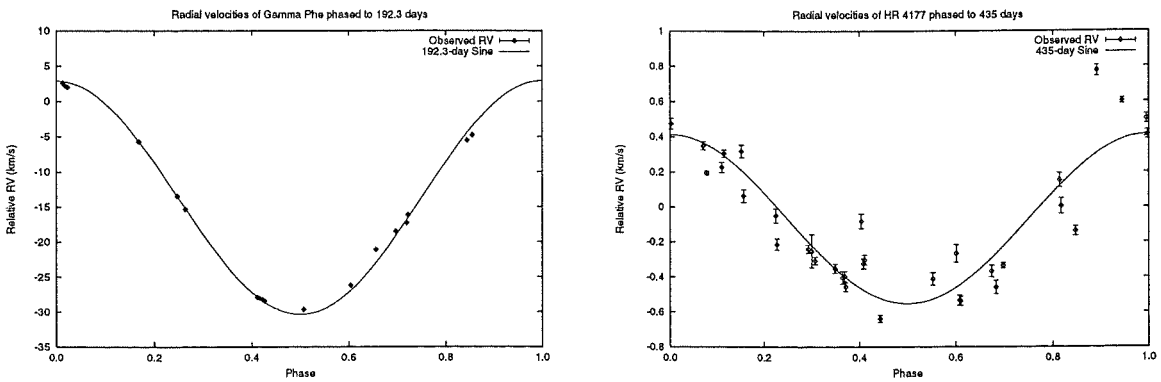

Figure C.5: Plots of radial velocities phased to the dominate timescale for γ Phe and HR 4177. The plotted sine is that used for prewhitening by **T6**, with the addition of an arbitary constant.

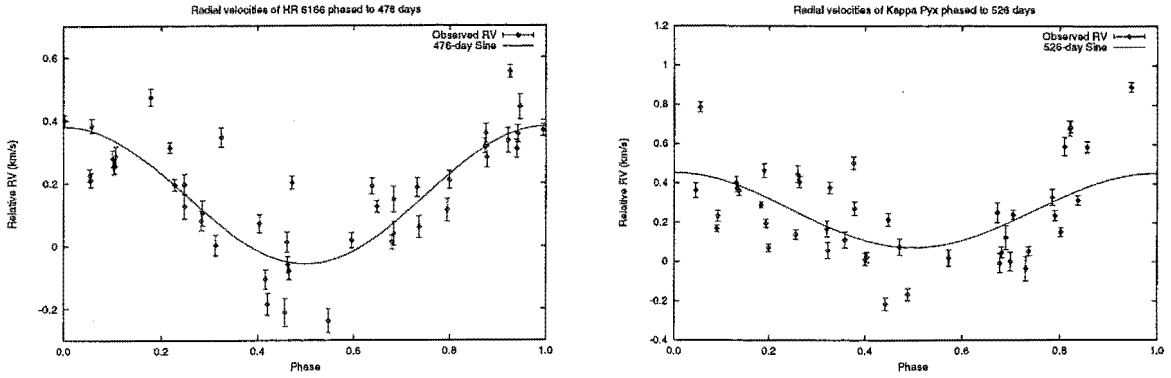

Figure C.6: Plots of radial velocities phased to the dominate timescale for HR 6166 and κ Pyx. The plotted sine is that used for prewhitening by **T6**, with the addition of an arbitary constant.

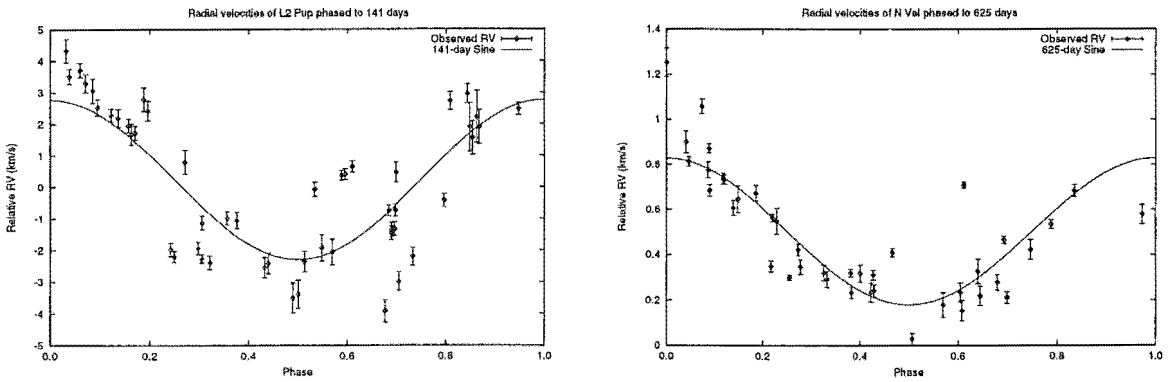

Figure C.7: Plots of radial velocities phased to the dominate timescale for L^2 Pup and N Vel. The plotted sine is that used for prewhitening by **T6**, with the addition of an arbitary constant.

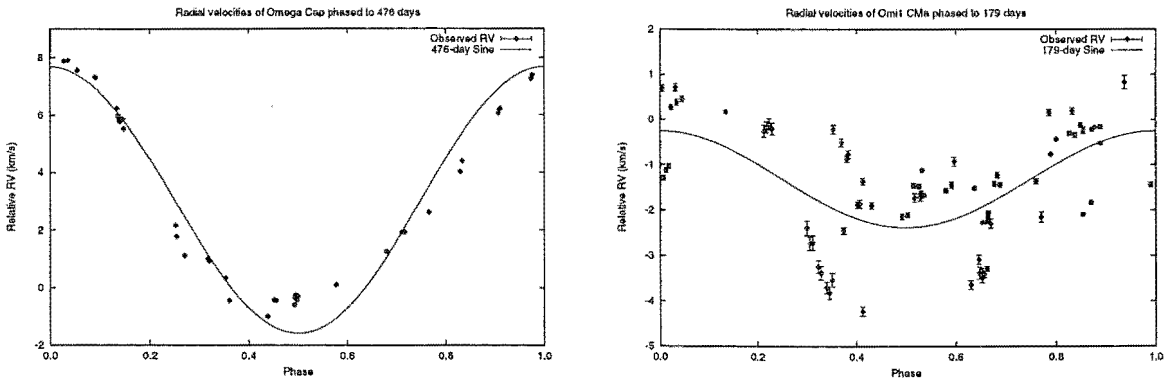

Figure C.8: Plots of radial velocities phased to the dominate timescale for ω Cap and o^1 CMa. The plotted sine is that used for prewhitening by **T6**, with the addition of an arbitary constant.

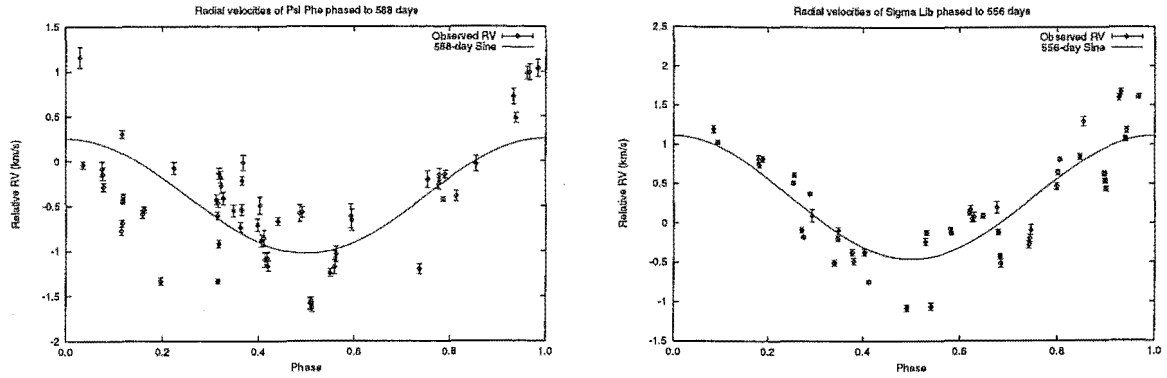

Figure C.9: Plots of radial velocities phased to the dominate timescale for ψ Phe and σ Lib. The plotted sine is that used for prewhitening by **T6**, with the addition of an arbitary constant.

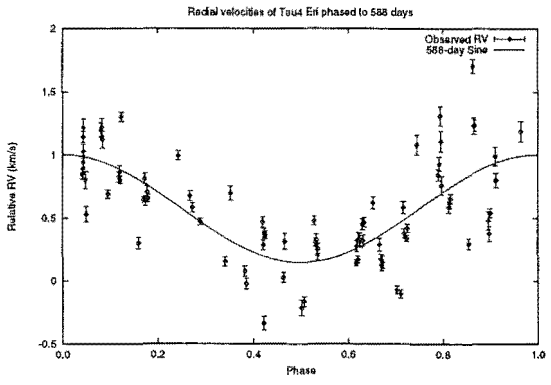

Figure C.10: The radial velocities of τ^4 Eri phased to their dominate timescale. The plotted sine is that used for prewhitening by **T6**, with the addition of an arbitary constant.

Appendix D

Mt John broad-band photometry data plots

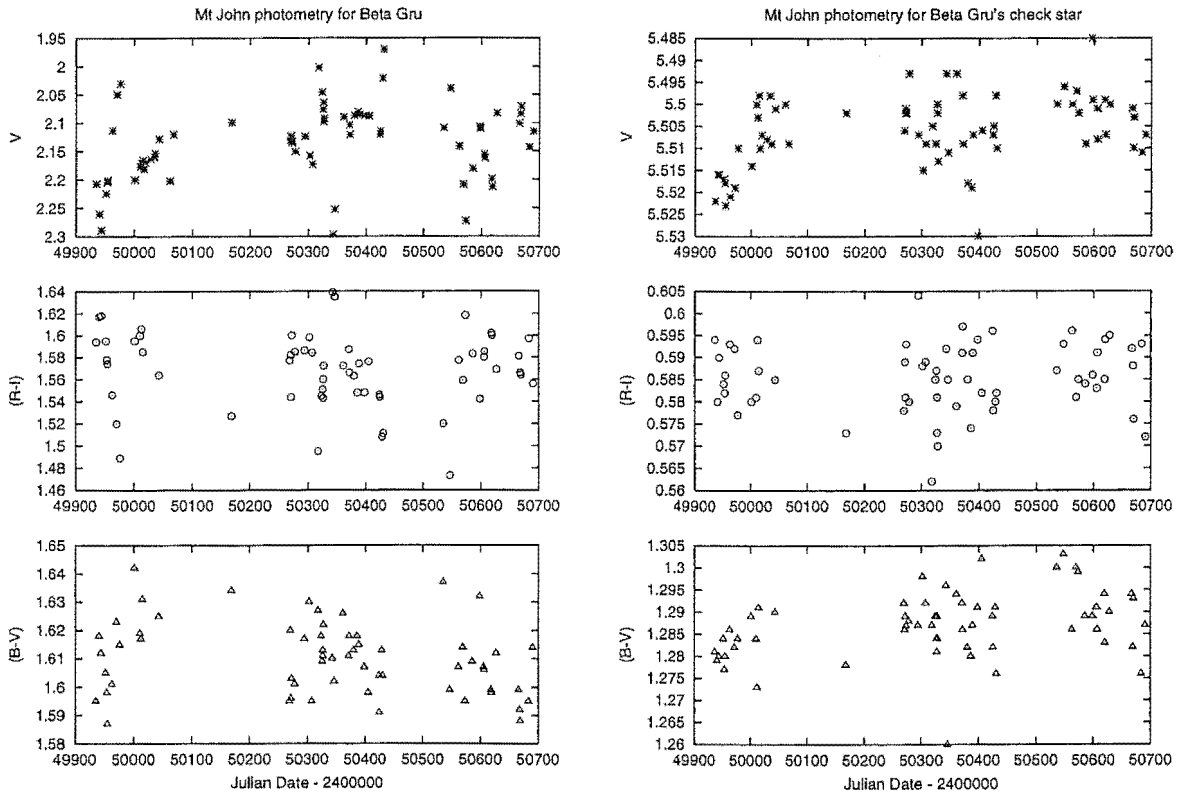

Figure D.1: $V_{\rm J}$, $(R-I)_{\rm C}$ and $(B-V)_{\rm C}$ photometry for β Gru and its check star.

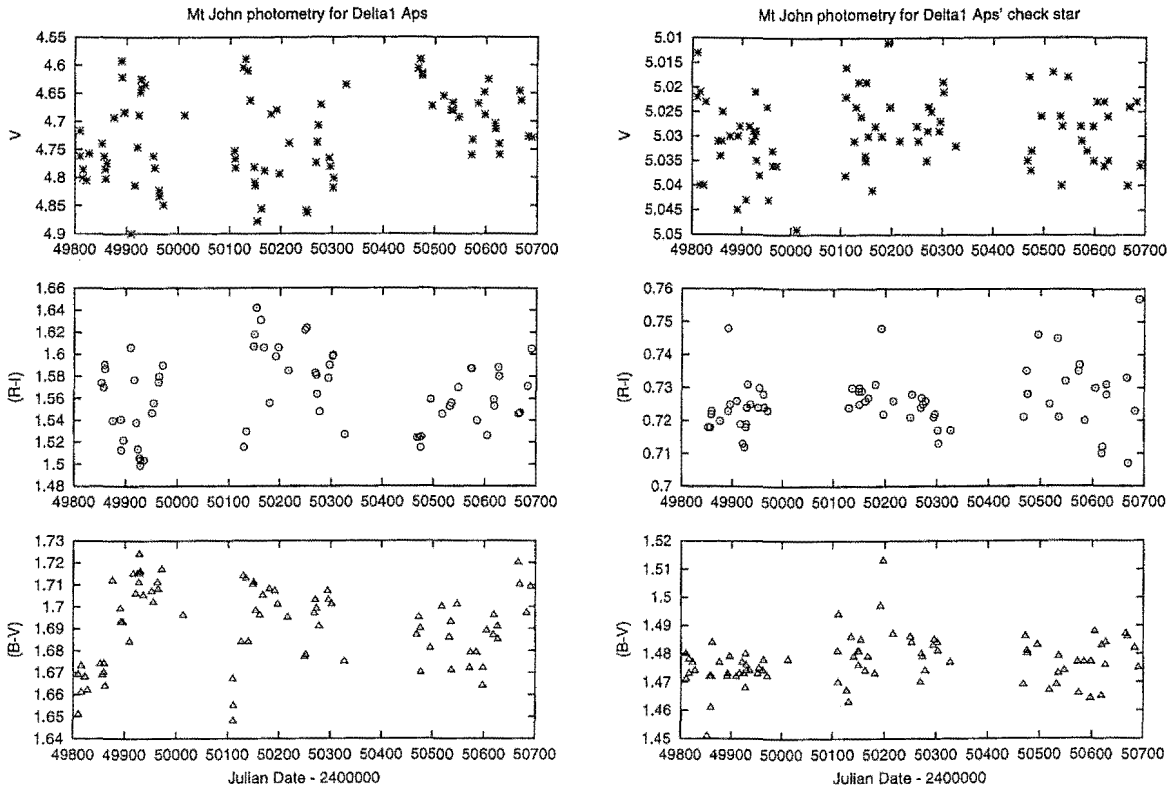

Figure D.2: $V_{\rm J}$, $(R-I)_{\rm C}$ and $(B-V)_{\rm C}$ photometry for δ^1 Aps and its check star.

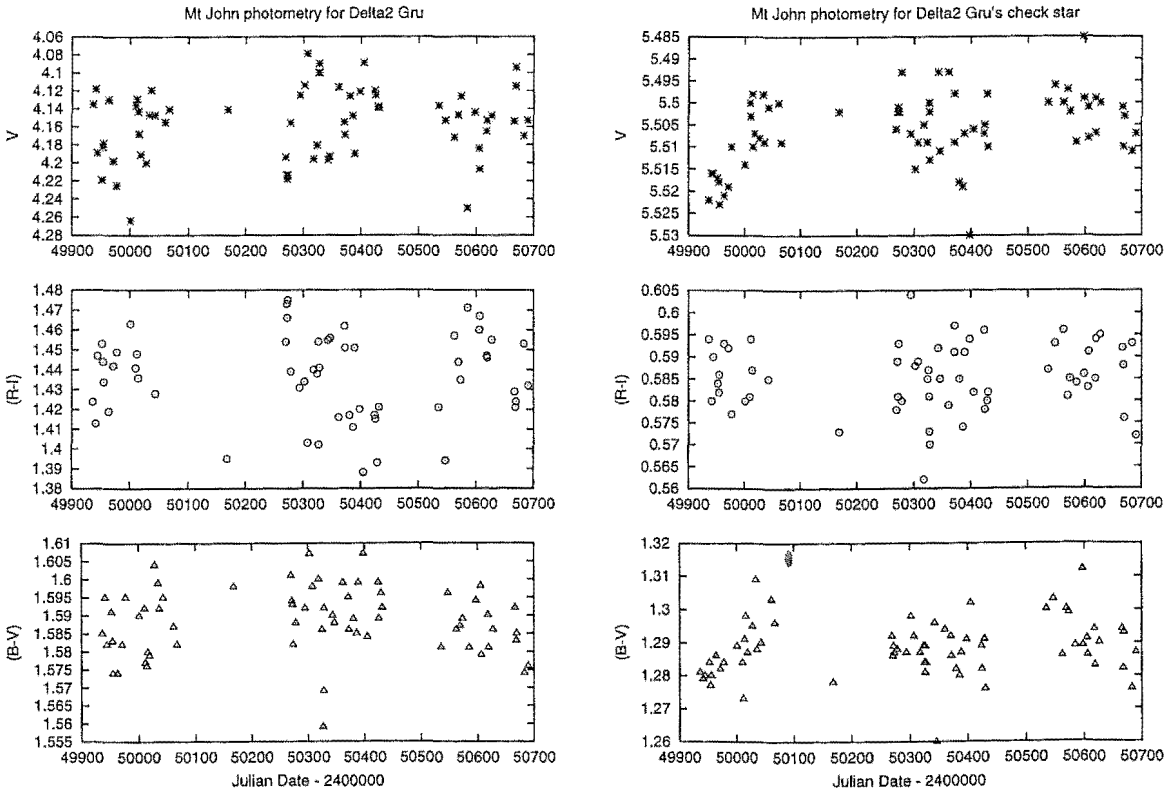

Figure D.3: $V_{\rm J}$, $(R-I)_{\rm C}$ and $(B-V)_{\rm C}$ photometry for δ^2 Gru and its check star.

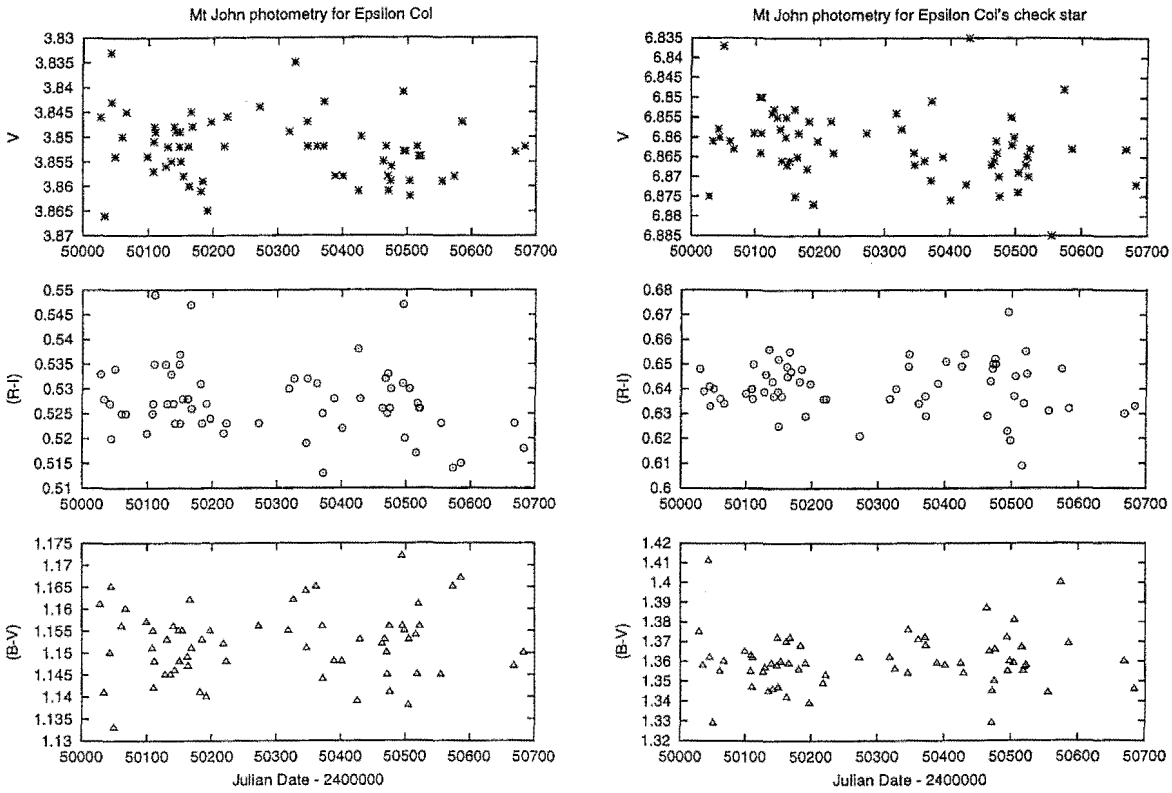

Figure D.4: V_J, $(R-I)_C$ and $(B-V)_C$ photometry for ϵ Col and its check star.

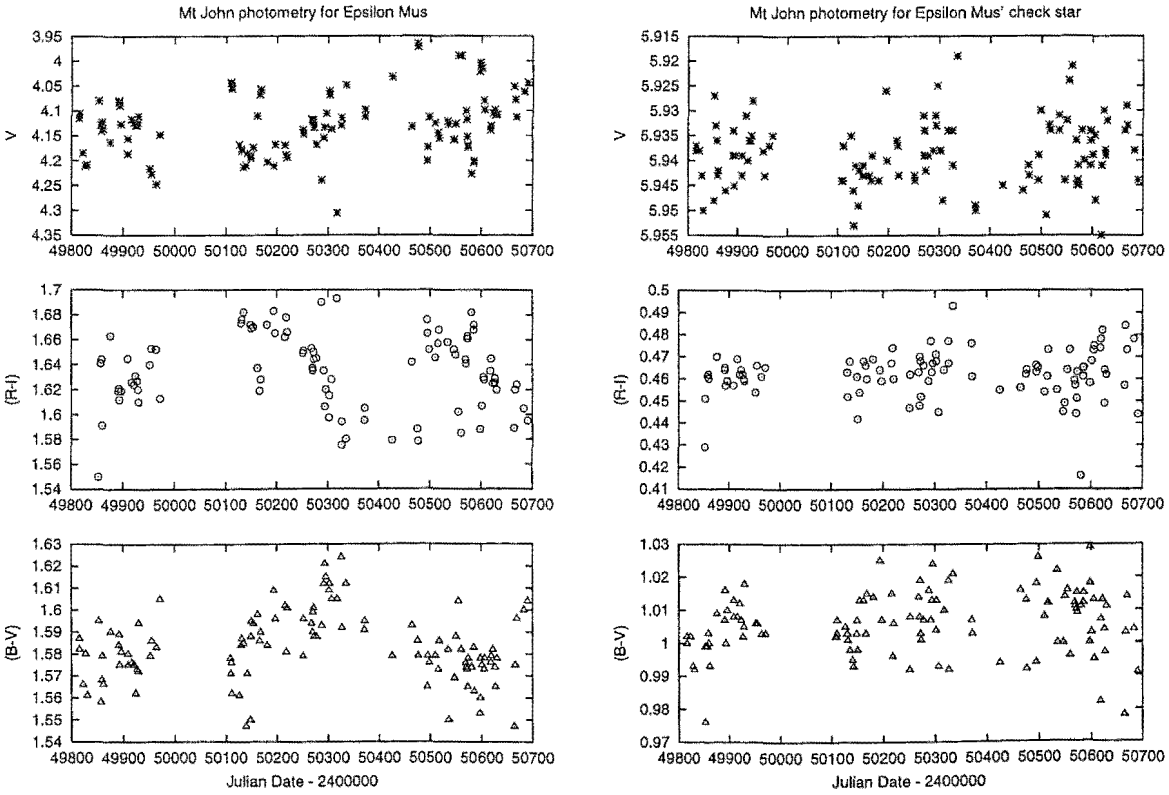

Figure D.5: V_J, $(R-I)_C$ and $(B-V)_C$ photometry for ϵ Mus and its check star.

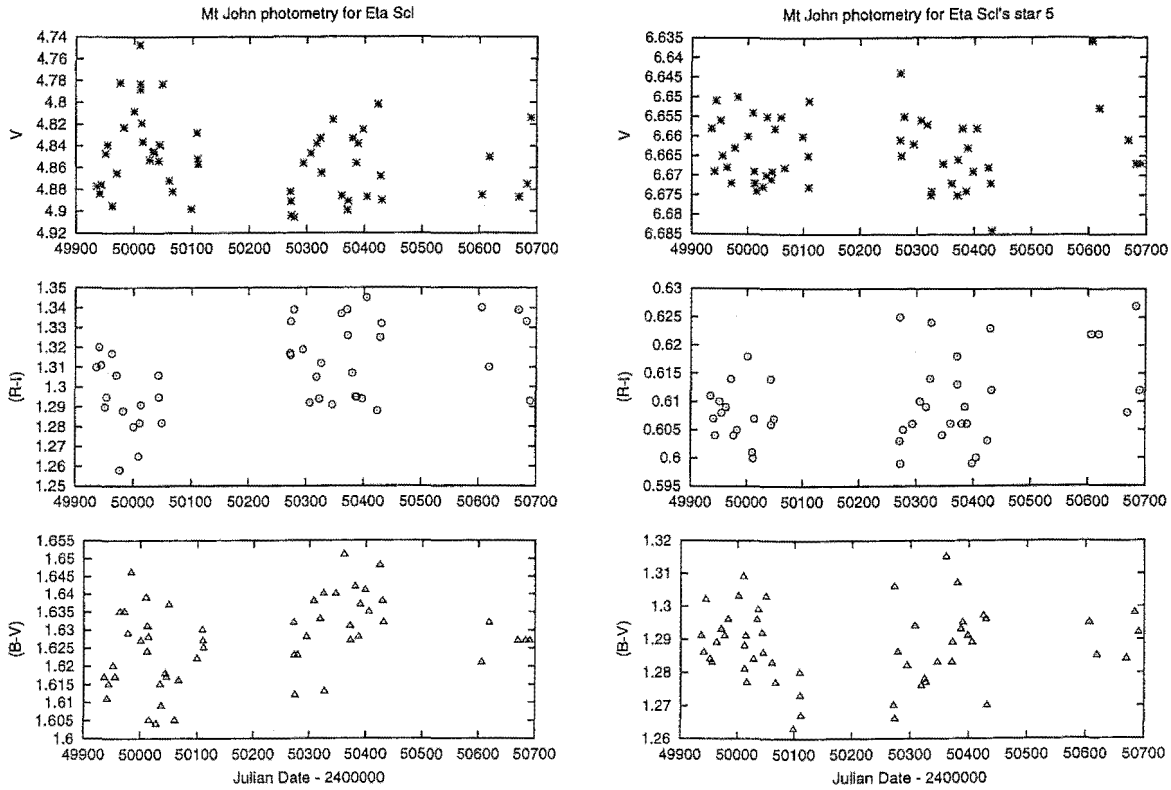

Figure D.6: $V_{\rm J}$, $(R-I)_{\rm C}$ and $(B-V)_{\rm C}$ photometry for η Scl and its "star 5".

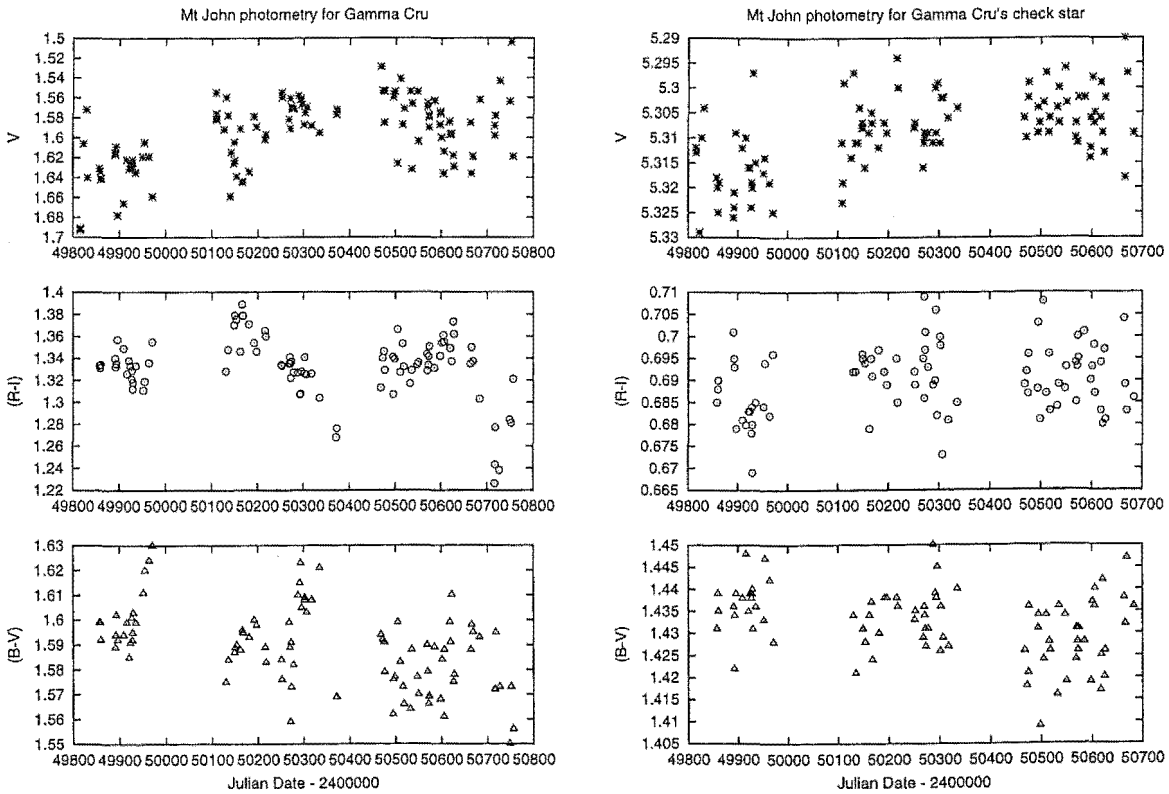

Figure D.7: $V_{\rm J}$, $(R-I)_{\rm C}$ and $(B-V)_{\rm C}$ photometry for γ Cru and its check star.

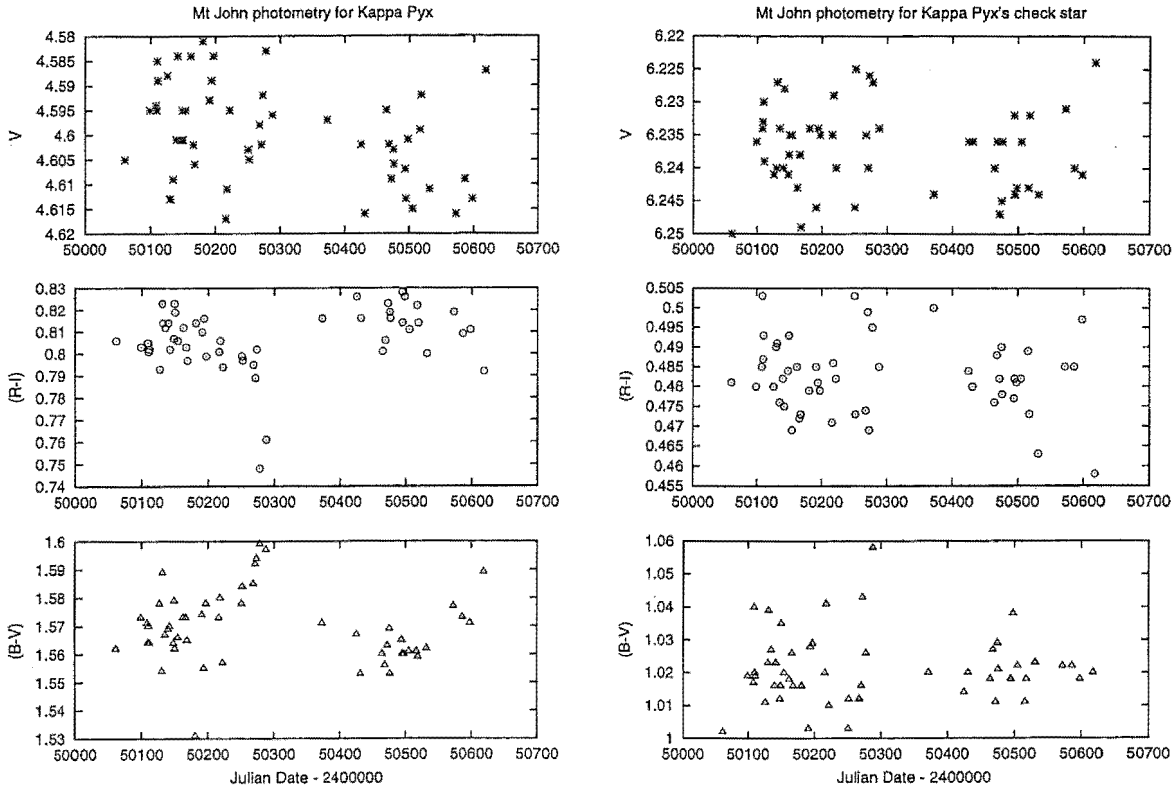

Figure D.8: V_J, $(R-I)_C$ and $(B-V)_C$ photometry for κ Pyx and its check star.

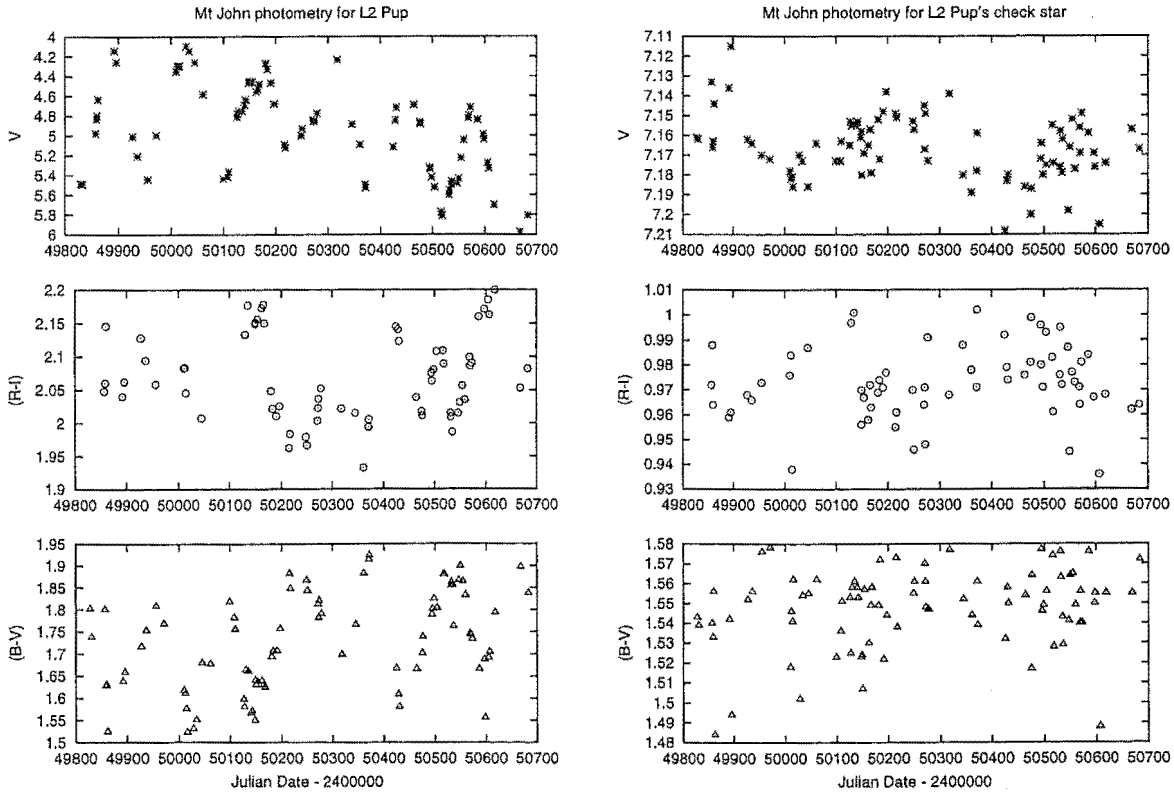

Figure D.9: V_J, $(R-I)_C$ and $(B-V)_C$ photometry for L^2 Pup and its check star.

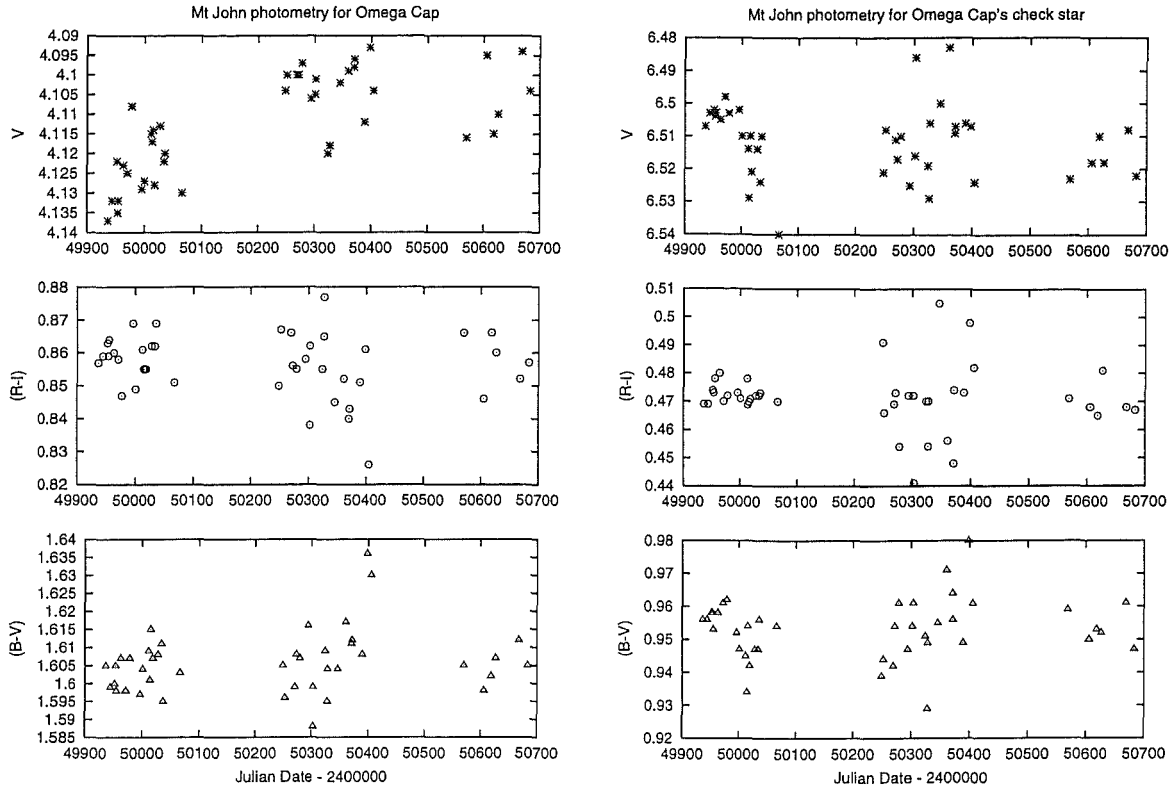

Figure D.10: $V_{\rm J}$, $(R-I)_{\rm C}$ and $(B-V)_{\rm C}$ photometry for ω Cap and its check star.

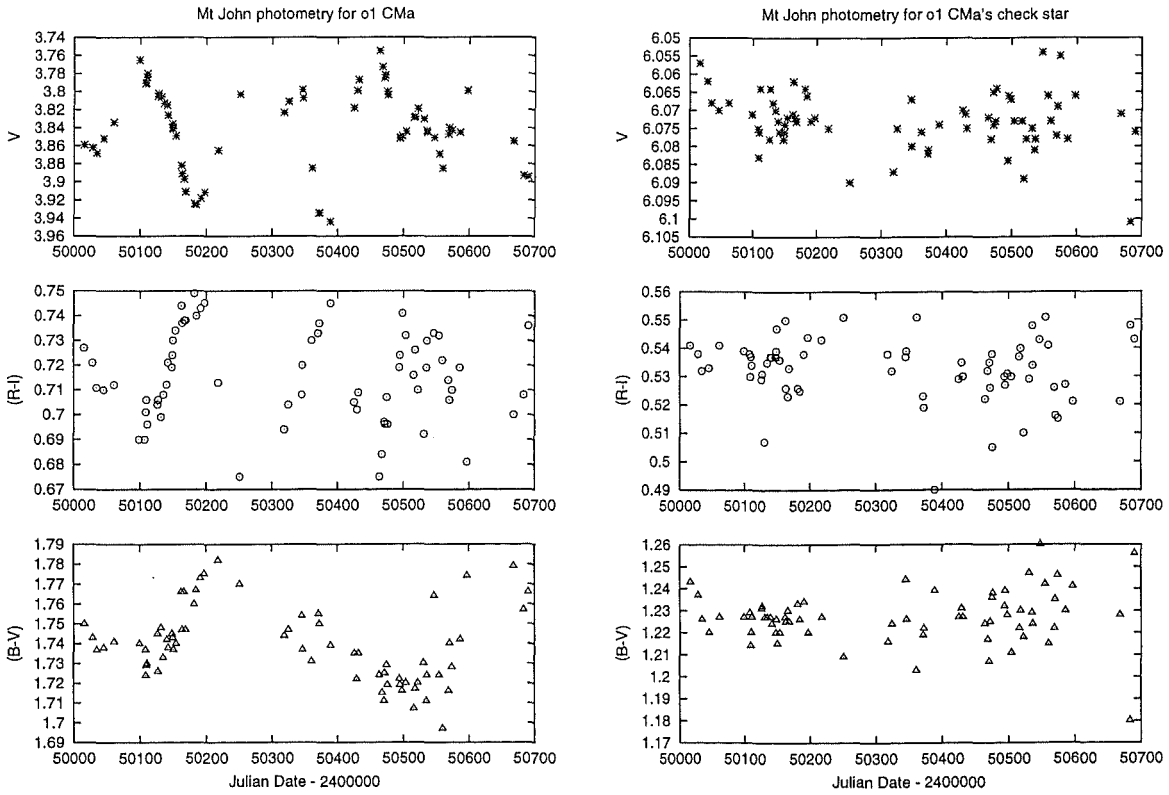

Figure D.11: $V_{\rm J}$, $(R-I)_{\rm C}$ and $(B-V)_{\rm C}$ photometry for o^1 CMa and its check star.

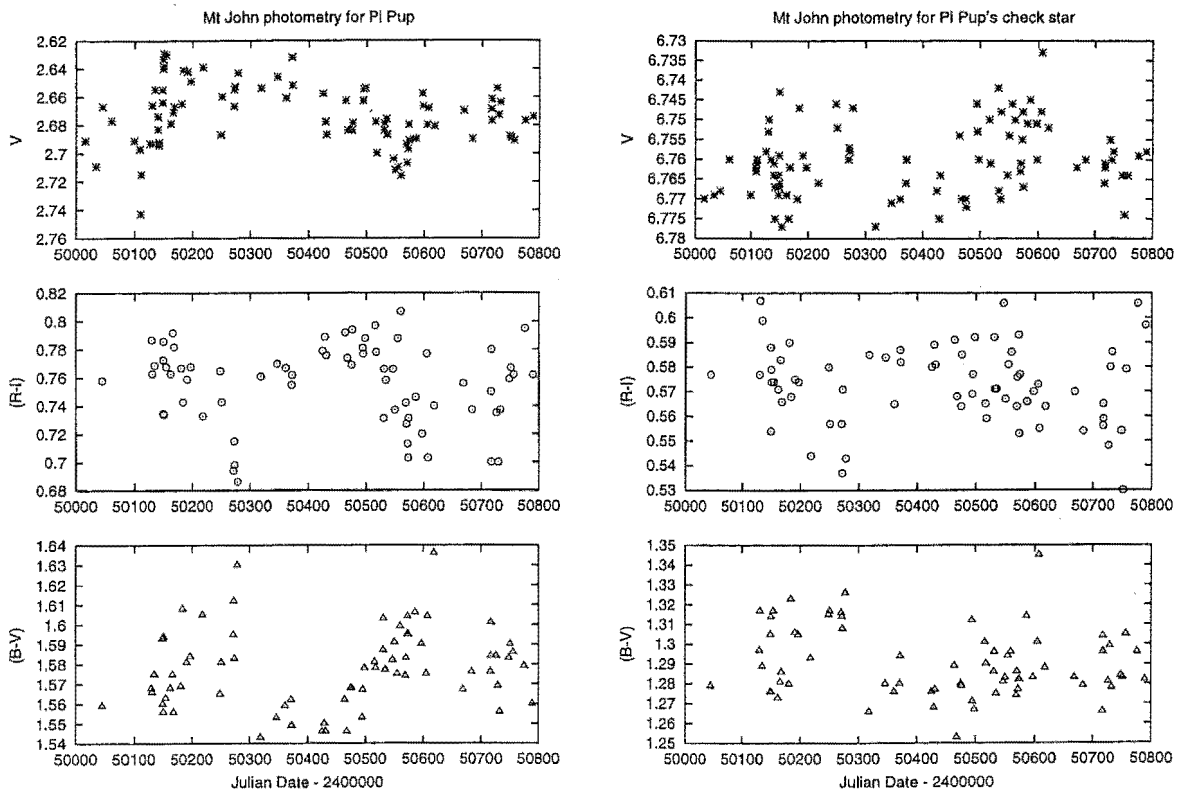

Figure D.12: V_J, $(R-I)_C$ and $(B-V)_C$ photometry for π Pup and its check star.

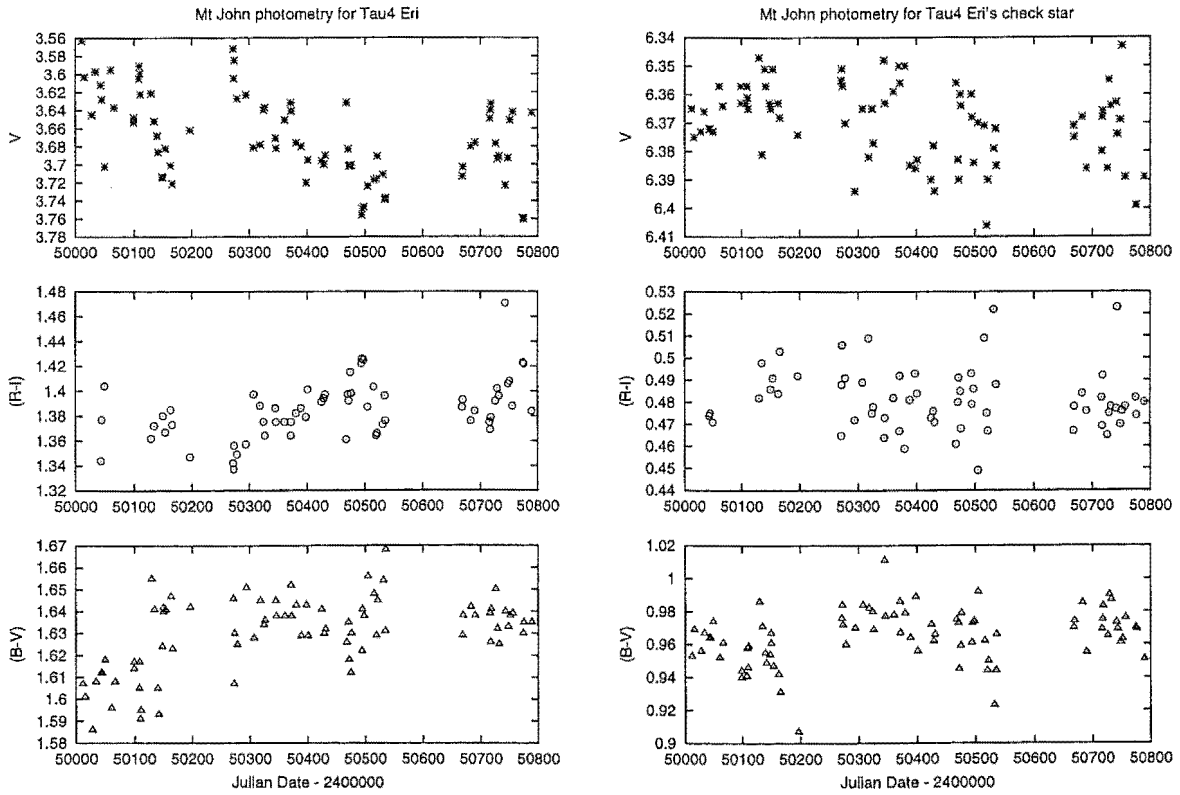

Figure D.13: V_J, $(R-I)_C$ and $(B-V)_C$ photometry for τ^4 Eri and its check star.

Appendix E

Hipparcos visual-photometry data plots for the 44 surveyed stars

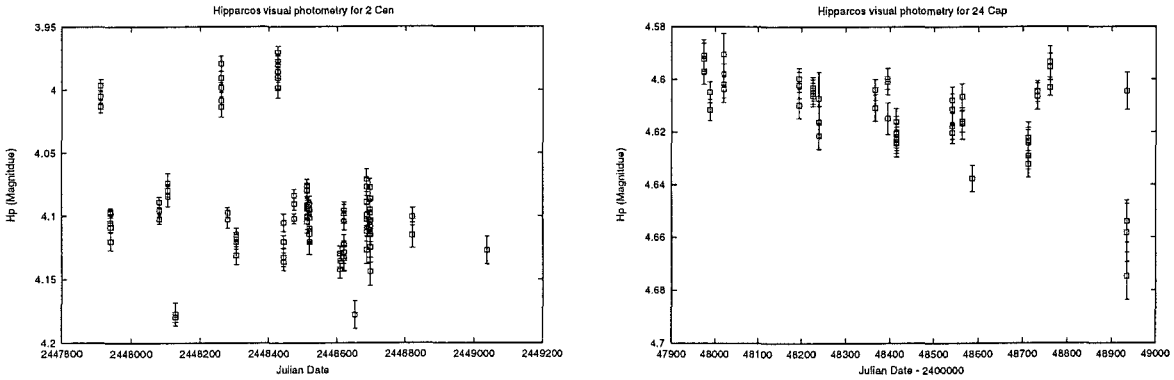

Figure E.1: The Hipparcos visual-photometry data for 2 Cen and 24 Cap.

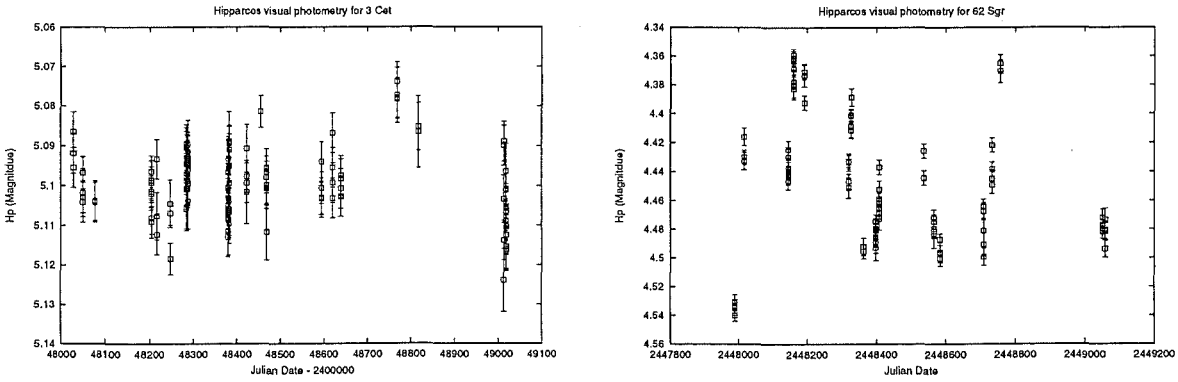

Figure E.2: The Hipparcos visual-photometry data for 3 Cet and 62 Sgr.

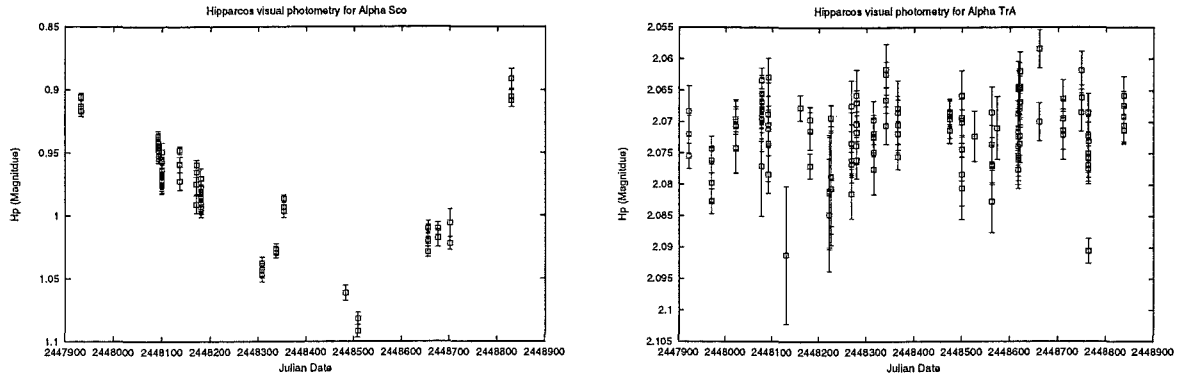

Figure E.3: The Hipparcos visual-photometry data for α Sco and α TrA.

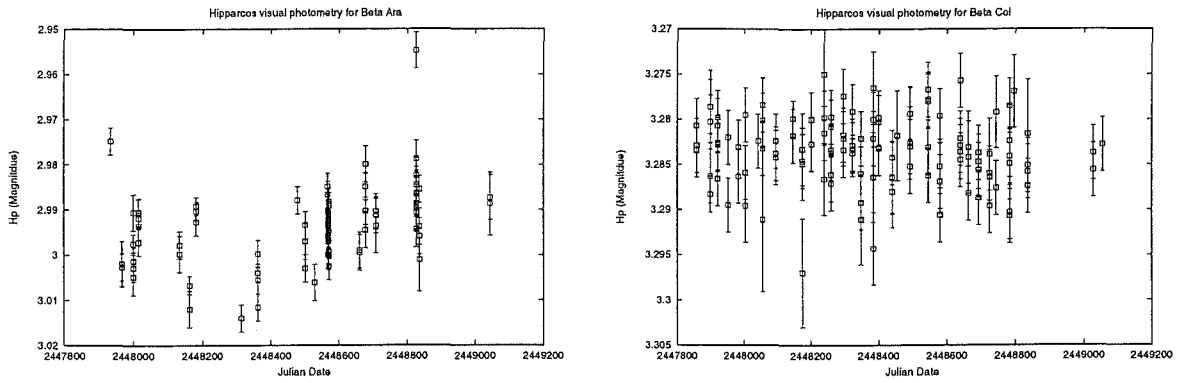

Figure E.4: The Hipparcos visual-photometry data for β Ara and β Col.

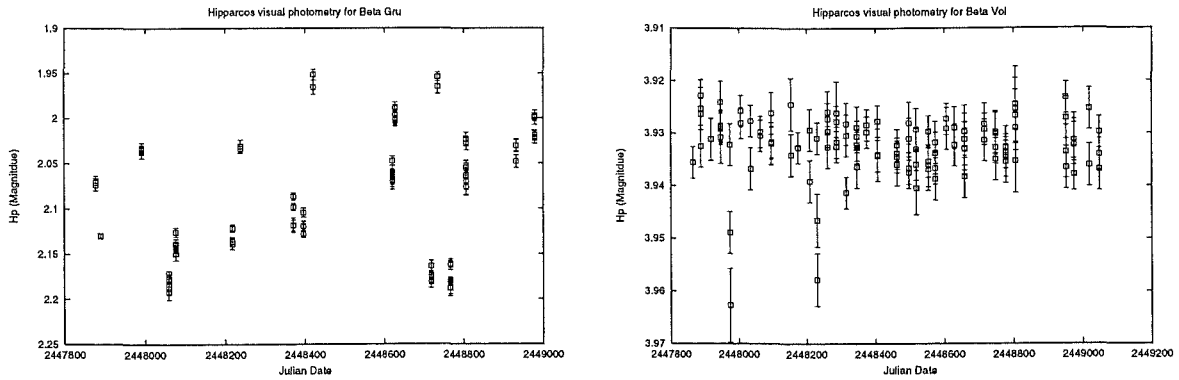

Figure E.5: The Hipparcos visual-photometry data for β Gru and β Vol.

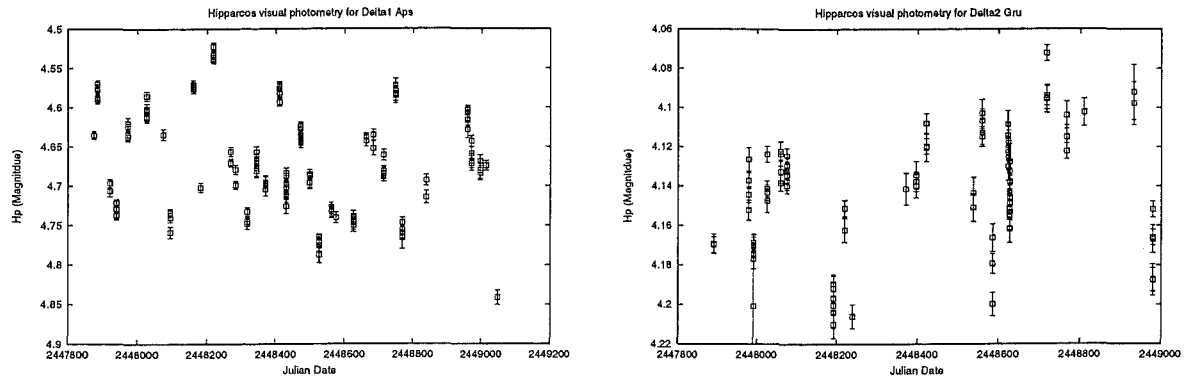

Figure E.6: The Hipparcos visual-photometry data for δ^1 Aps and δ^2 Gru.

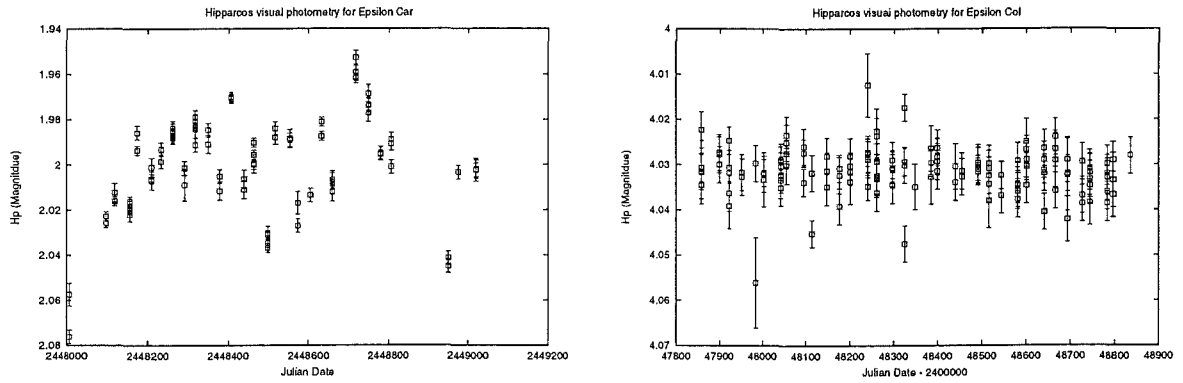

Figure E.7: The Hipparcos visual-photometry data for ϵ Car and ϵ Col.

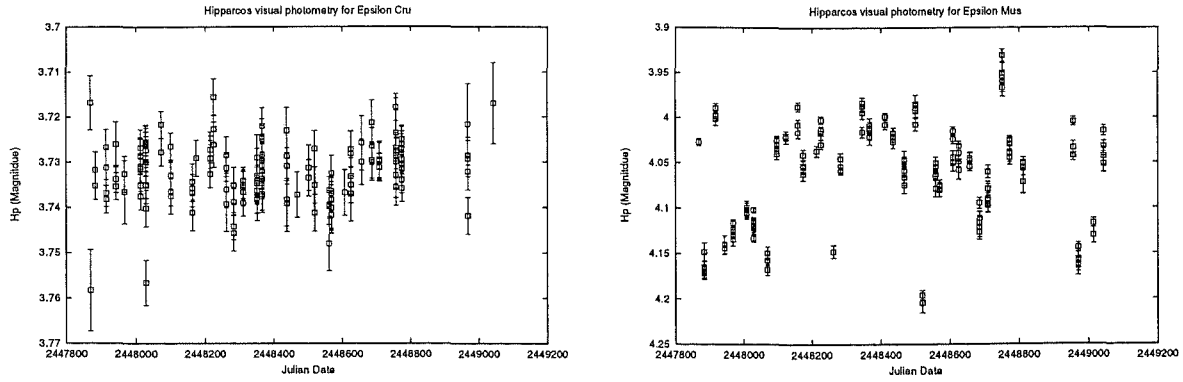

Figure E.8: The Hipparcos visual-photometry data for ϵ Cru and ϵ Mus.

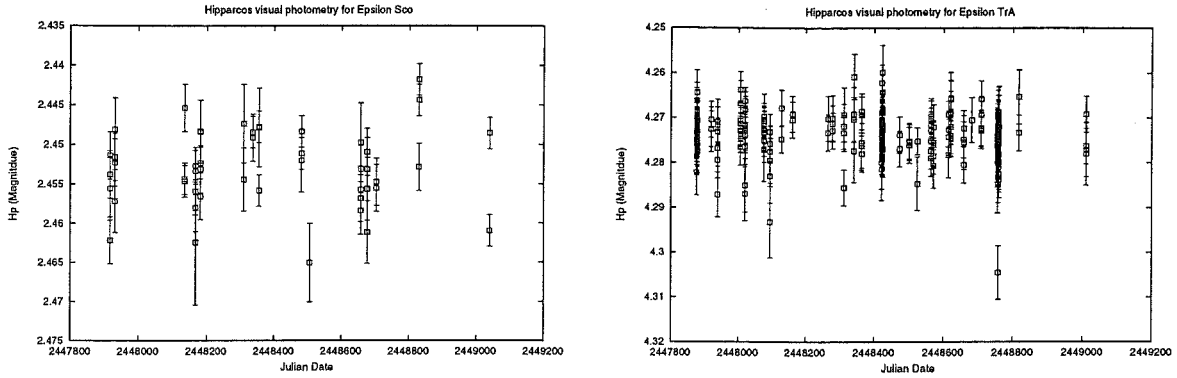

Figure E.9: The Hipparcos visual-photometry data for ϵ Sco and ϵ TrA.

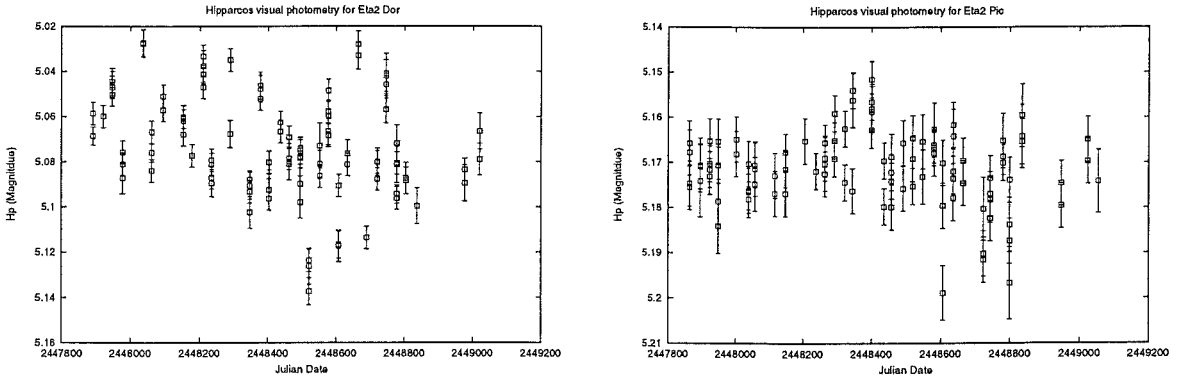

Figure E.10: The Hipparcos visual-photometry data for η^2 Dor and η^2 Pic.

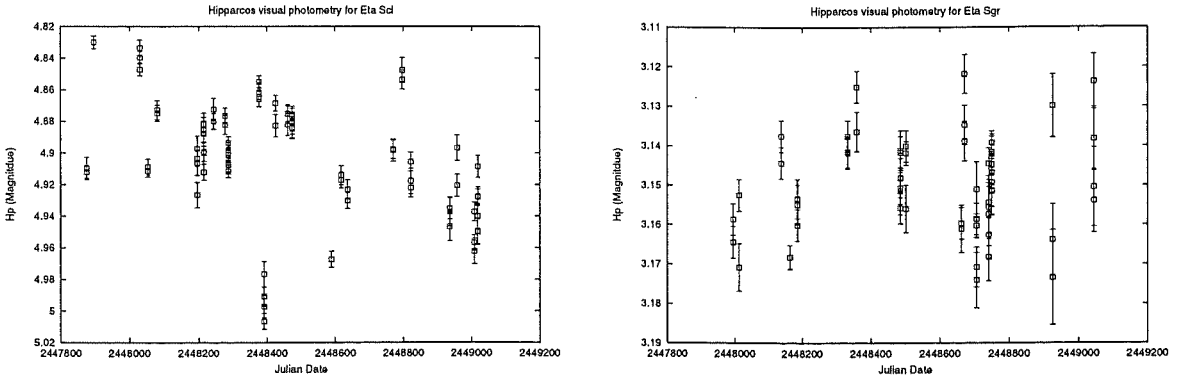

Figure E.11: The Hipparcos visual-photometry data for η Scl and η Sgr.

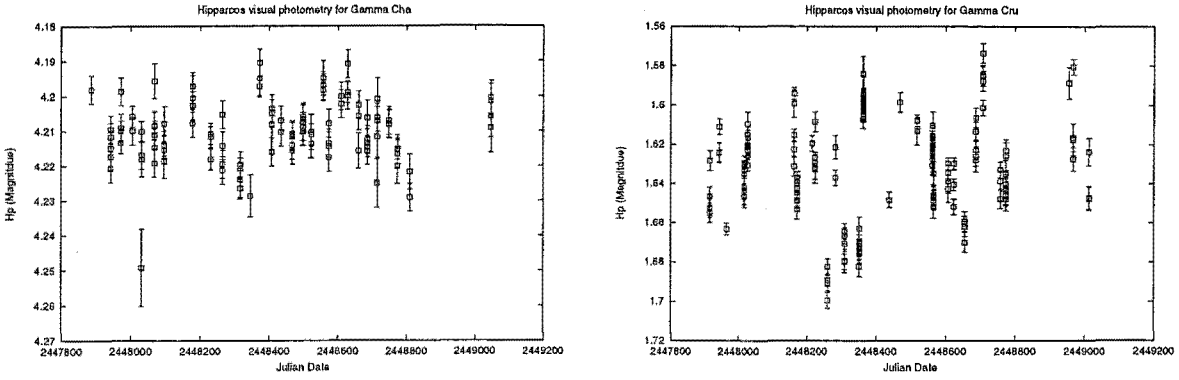

Figure E.12: The Hipparcos visual-photometry data for γ Cha and γ Cru.

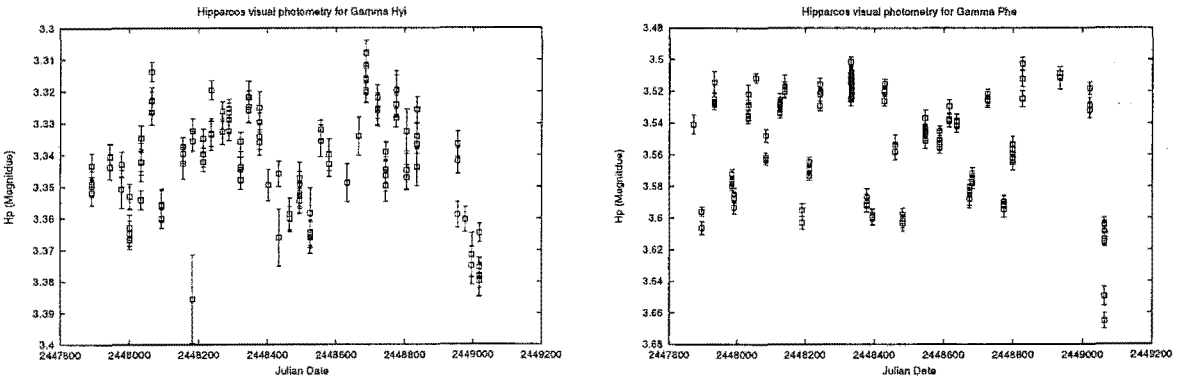

Figure E.13: The Hipparcos visual-photometry data for γ Hyi and γ Phe.

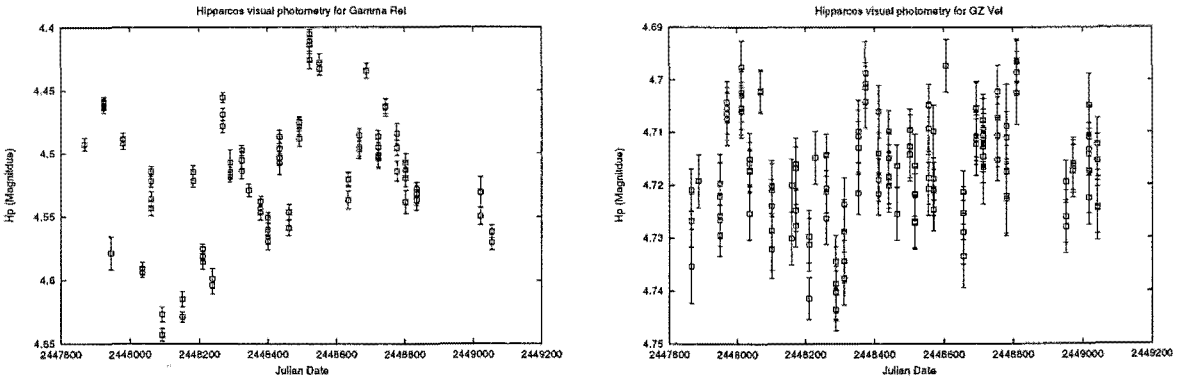

Figure E.14: The Hipparcos visual-photometry data for γ Ret and GZ Vel.

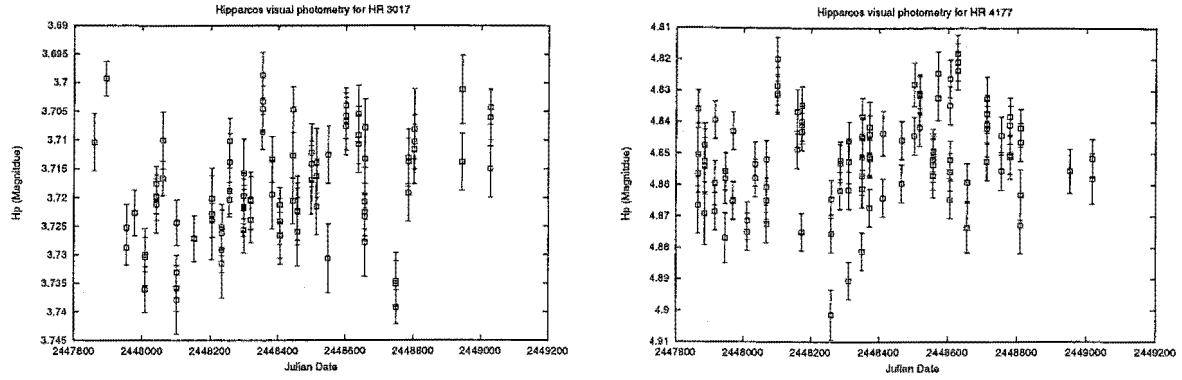

Figure E.15: The Hipparcos visual-photometry data for HR 3017 and HR 4177.

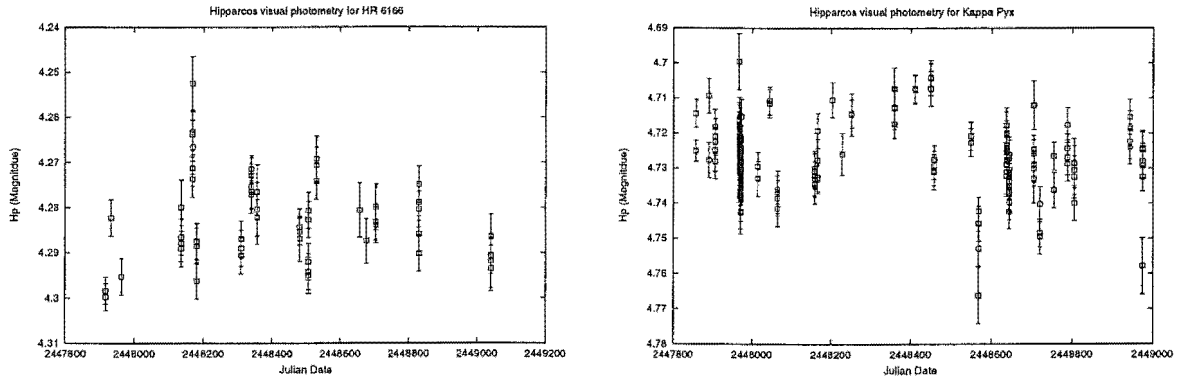

Figure E.16: The Hipparcos visual-photometry data for HR 6166 and κ Pyx.

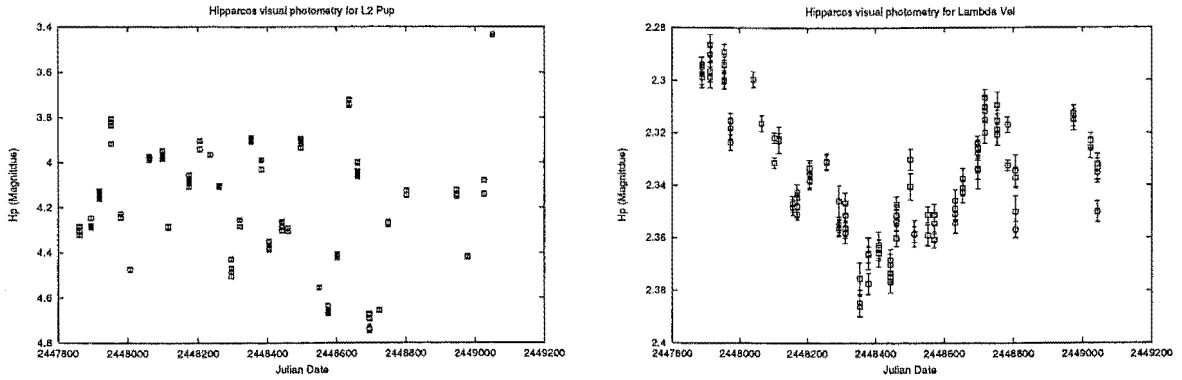

Figure E.17: The Hipparcos visual-photometry data for L^2 Pup and λ Vel.

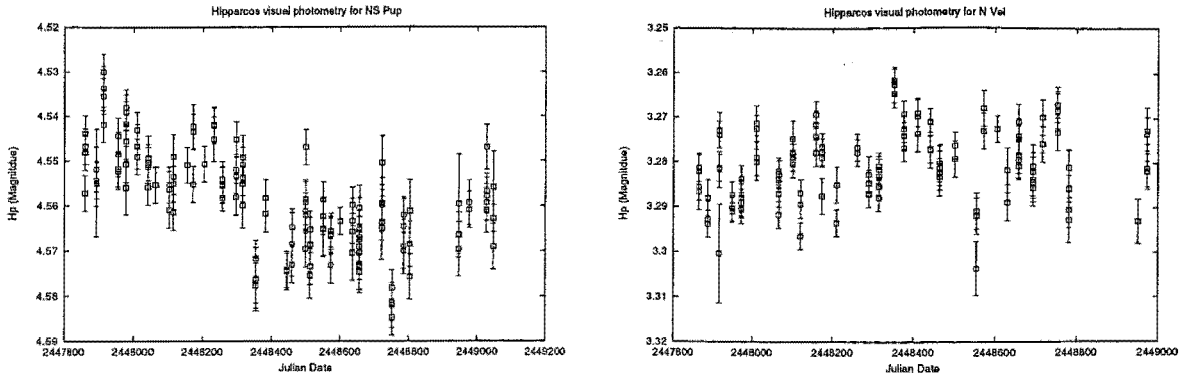

Figure E.18: The Hipparcos visual-photometry data for NS Pup and N Vel.

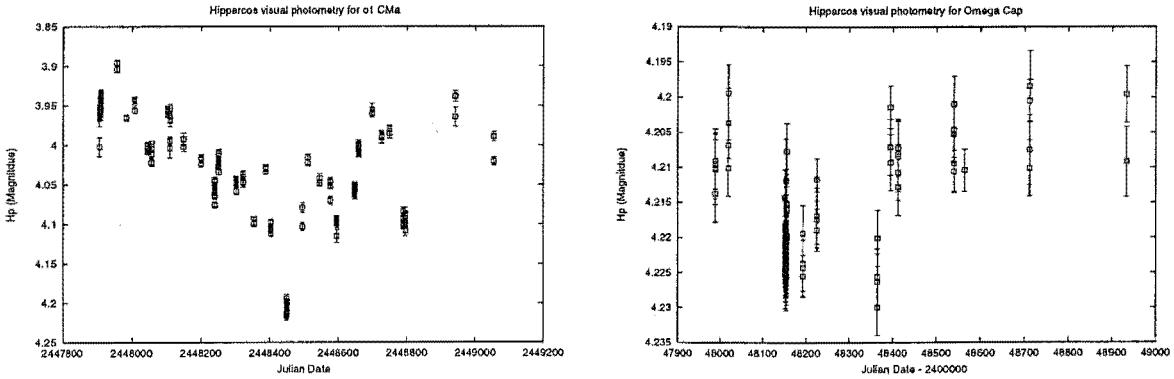

Figure E.19: The Hipparcos visual-photometry data for o^1 CMa and ω Cap.

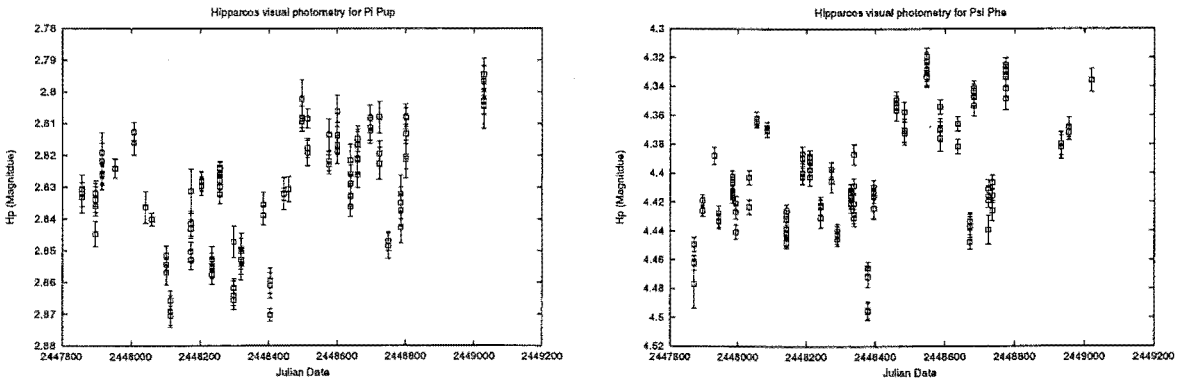

Figure E.20: The Hipparcos visual-photometry data for π Pup and ψ Phe.

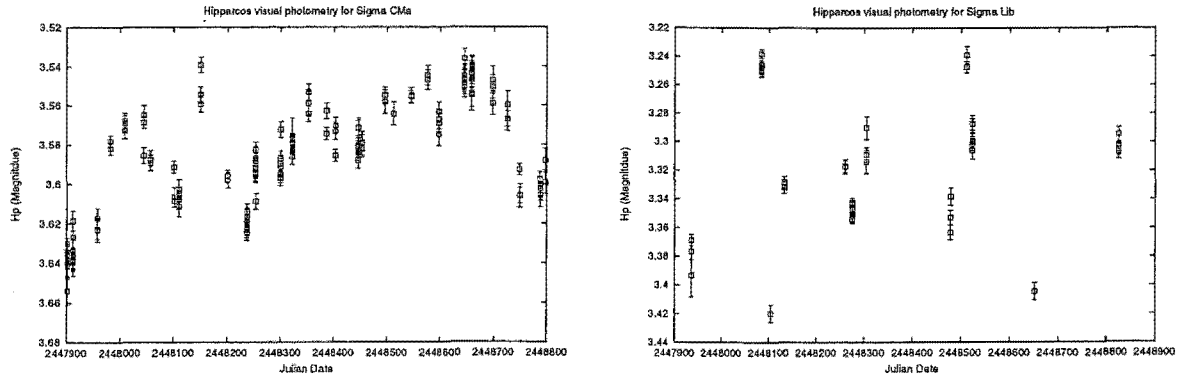

Figure E.21: The Hipparcos visual-photometry data for σ CMa and σ Lib.

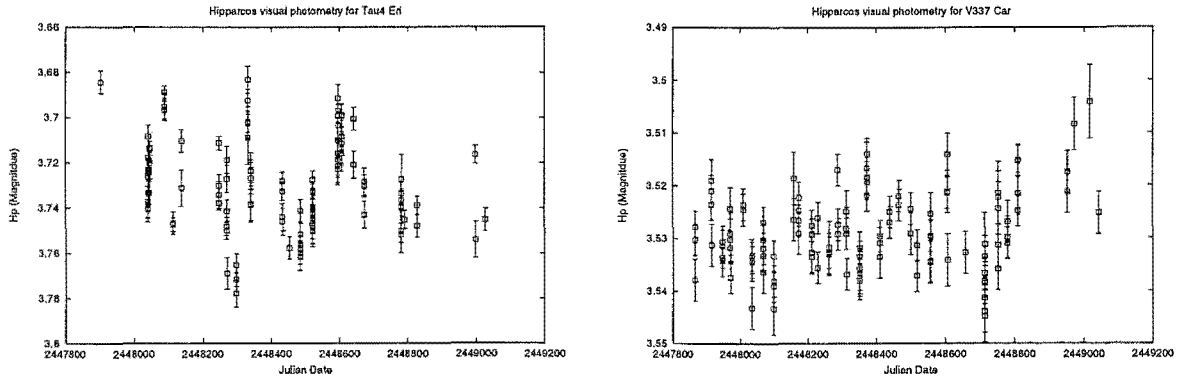

Figure E.22: The Hipparcos visual-photometry data for τ^4 Eri and V337 Car.

Appendix F

A step-by-step guide to data reduction

The CCD images are obtained at the Mt John University Observatory, where they are written to magnetic tape. They are then taken back to the University of Canterbury. There the data are read off the magnetic tapes onto the DEC VMS computer system[1], and then ftp'ed to the Unix-system computer, Cantua. Once there, the magnetic-tape files are changed from FITS format to a format compatible with the software package **Figaro**. By taking a directory listing and using the Unix language **awk**, it is possible to reformat an entire directory full of such files at once. Other than stellar spectra the images consist of the following:

A dark spectrum (the flash-ring illuminating the CCD only), which is the median of the three dark exposures taken at the beginning of each night of observations.

A flat-field image, one is taken every night and has the dark frame subtracted after its exposure.

Two thorium spectra per stellar exposure. The two thoriums, one taken before and one taken after each star's exposure, are the comparison spectra and two are taken to minimize the velocity error due to any thermal shift during the exposure. These have also been dark subtracted.

F.1 Rotation and cosmic-ray cleaning

Having converted the CCD images from the magnetic tape FITS format to one readable by **Figaro**, it is necessary to rotate the images by 90° so that the orders are running roughly parallel to the x-axis (horizontal, see Figure F.2 for the the orientation of the CCD image, after rotation, with respect to the x and y axis). This is necessary as **Figaro**'s order straightening command assumes the orders are in this orientation. Then the orders must be straightened, so they can be collapsed. For convenience the spectra are actually rotated three times, so that the wavelength increases with the x-axis and the order number decreases with the y-axis. When the rotation is complete the **Figaro** command

bclean *image=FILE-IN auto=n output=FILE-OUT crsig=3 crfact=0.3 crminv=20*

is used to remove cosmic rays from the image. The parameters relevant to choosing what is a cosmic ray are *crsig, crfact and crminv.* For a pixel to be considered to contain a cosmic ray it must have:

1. $(F_{\text{pixel}} - \overline{N}) > crsig \times \sqrt{\overline{N}}$, where $\overline{N}$ is the average value in the nearest neighbours to the pixel being considered and F_{pixel} is its flux. This reflects the standard deviation of the neighbouring pixels (which pixels are considered to be the neighbouring pixels is illustrated in Figure F.1).

[1]Initially a VAX 6430, but now an Alpha 4000

2. $(F_{\rm pixel} - \overline{N}) > crfact \times \overline{N}$. This is equivalent to expecting the cosmic rays to be a certain percent larger than their nearest neighbours.

3. $(F_{\rm pixel} - \overline{N}) > crminv$. That is all cosmic rays are expected to exceed a minimum intensity.

If $\overline{N} > 1$ (as will be true in the orders) and if $crsig > crfact$ the first two conditions are independent and both need to be considered[2]. By default, areas where cosmic rays are found have their original

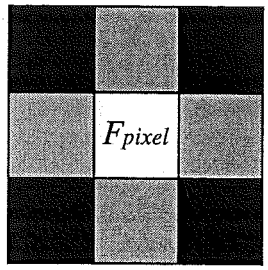

Figure F.1: The pixel in question is shown in white, its nearest neighbours in grey.

value interpolated by fitting local polynomials of degree three to the data. This value is used as a replacement for the "bad" pixel data areas. To check whether values of parameters are appropriate the **bclean** parameter *nofix* can be specified, in which case the bad datum is replaced by a datum whose value is 1000 ADUs less than the previous minimum in the image.

F.2 Order straightening

To straighten the CCD image orders a series of **Figaro** commands must be used. The following describes how a stellar spectrum, its two thorium exposures and the nightly flat-field exposure are straightened with respect to the s-distortion determined from the stellar spectrum. First the thorium and flat-field exposures associated with each stellar exposure (in addition to which exposures are stars) need to be determined. This is done using the csh-shell script **list.fig**.

F.2.1 List.fig

In order to determine which exposures are stars, which are thoriums and so on, files containing all the header information on the exposure are created for each of the files with *.dst* extension in the current directory, using the **Figaro** command **exam**. Then a list of the header file names, the object name and the time the exposure was taken is created using another csh-shell script **rename –time** (which simply searches through the header files for the relevant items). Using the system command **sort** at this point puts the file list into chronological order (the resulting file is called *HEADER.sorted*). Then the system language **awk** is used to search through *HEADER.sorted*. Any file which is not the object *TH_ARC* or *SMOOTH_FIELD* (hence dark exposures should be removed before this point) is designated as a stellar exposure. For every stellar exposure, the thorium nearest in time before the stellar exposure is the designated first thorium and that nearest in time after the stellar exposure is the last thorium. The appropriate flat-field is that nearest to the stellar exposure before it. These details are written to a file called *ls.next* in the form:

stellar-file 1st-thorium 2nd-thorium flat-field.

In the case where a thorium or flat-field is going to be used by more than one stellar exposure (the latter is extremely common) the image is copied to a file with a similar name to its stellar

[2]If $crsig < crfact$ (and $\overline{N} > 1$) then $crsig \times \sqrt{\overline{N}} < crfit \times \overline{N}$ and therefore if condition two is satisfied then condition one must be also!

exposure and *ls.next* is written accordingly. For example, the flat-field for the stellar exposure *TTTT-XX*[3] would be *TTTT-XXff*. Details of these file manipulations are written to a file called *dir.log*.

F.2.2 Choosing the order's centre then straightening it

Once *ls.next* has been generated the following steps are taken iteratively for each line on the list.

Initially a picture of the stellar spectrum must be displayed using

image *image=FILE-IN ystart=1 yend=384 xstart=1 xend=576 low=0 high=5000* \\,

where *low* and *high* determine the limits for the image flux to be displayed (values below or above this are set to these limits) and the other parameters give the CCD extent. All other parameters are taken as the default by the use of "\\". The approximate centre of each order is needed by **Figaro** for straightening and the command **icur** is used for this. This command enables a click of the mouse to indicate a point on the displayed spectrum (*F*2 gives a magnified view of the image and *F*4 unzooms it) and saves the positions thereby indicated to a file called *vars.dst* in the user's home directory.

After this interaction the rest of the program requires no assistance and, as the orders' positions do not change within an observing run, by copying the *vars.dst* file for later use it is possible to only interactively choose the orders' centres once per run — then just copy the relevant *vars.dst* file back to the home directory for all subsequent spectra[4]. A polynomial is fitted to the orders' centres by

sdist *image=FILE-IN col=8 tr=g wi=4 max=3 di=y so=y*.

It does so by taking the initial order centres (those returned via **icur**) and using them to determine the actual order centres at set intervals along the orders. The technique for each order is as follows: at each interval *col* pixels are averaged along the x-axis; then, a gaussian (*tr=g*) is fitted to the y-axis using the initial order centres as a starting point and assuming the gaussian has a half-width of *wi* (see Figure F.2). Having thus determined the order's centre at numerous points along the order, a polynomial of maximum degree *max* must be fitted to the centres as a function of the x-axis to find the s-distortion. The results are written to a file called *sdist.dat*. Having *so=y* indicates that the points determined to be the order centres and the fitted polynomial to the distortion, are to be plotted.

The **Figaro** command

cdist *image=FILE-IN ys=1 ye=384 out=FILE-OUT max=5*,

is then used to create a straightened spectrum of the stellar, flat-field and thorium spectra by the use of the distortion file *sdist.dat*. It determines where a straightened order should lie by taking the average position of the central third of the polynomial given by *sdist.dat*. Each column has a polynomial of degree *max=5* fitted to the difference between the actual order position (as determined by the **sdist** polynomials) and the position where the order should lie (as a function of the y-axis). **cdist** then shifts each pixel in a column according to this polynomial[5].

[3]Where *TTTT* stands for the magnetic tape name on which the image was recored and *XX* represents the sequential number of the image on the tape

[4]This doesn't always work, for some unknown reason, so details of the fits for the orders of each spectrum (as returned by **sdist**) are saved to a file and later searched to see if the fitting to any orders failed and therefore the step needs to be repeated by hand

[5]It is unknown whether flux is conserved during this or pixels are only moved by whole numbers — the source comments do not mention this point

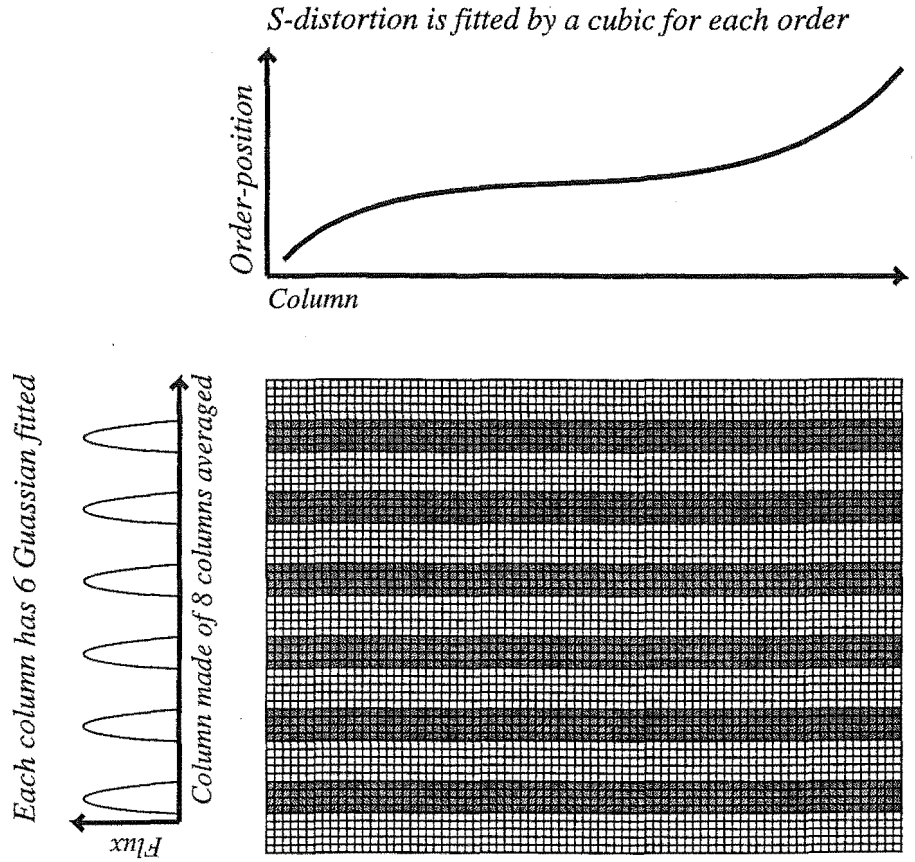

Figure F.2: Determining the order's centre from an initially specified point. The column number increases with x and the order position increases with y.

The reduction requires actually creating a file of the straightened spectrum rather than just knowing the orders' positions and taking this into consideration during order collapsing, as each order's extent along the y-axis needs to be determined. This is done by adding up all the columns of the CCD image (once straightened) and then choosing the orders' edges from this sum, displayed as a function of the row number. An important thing to note is that *sdist.dat* contains the position that the straightened spectrum's order centres are to be located at. By keeping this file for each straightened spectrum, it is therefore possible to remove most of the interaction out of collapsing the spectral orders (see Appendix F.3).

F.3 Collapsing the orders and flat-fielding

The straightened orders of the stellar spectrum are collapsed by using the **Figaro** command

echselect *image=FILE-IN pre=n wh=n xs=10 xe=576 ms=46 md=-1 objout=FILE-OUT skyout=SKY-FILE.*

This adds up columns in the CCD (hence the orders must be straightened first) and displays the result (see Figure F.3). Interaction is required at this stage in the form of using the mouse to identify the two order edges, so all the pixels along the column which are within the edges can be collapsed to give the desired one-dimensional order. It is necessary to do this order-by-order, moving onto the next order by the use of (<) or (>). Using (>) will increase the order number by *md* from an initial value of *ms*. *Wh=n* indicates that not all the columns in the CCD are to be used in the display, where *xs* and *xe* specify the initial and final columns to be used respectively. This is done

as the CCD edges can be flawed (as is the case in a few pixels for the Mt John CCD used to obtain data for this thesis). The result of the order selection is written to a file called *echselect.lis*, which is simply in the form of a list of the pixels to be used for each order. The thorium and flat-field spectra are both collapsed using the same pixels as the stellar spectrum, by using **echselect** with "*pre=y*" — meaning the file *echselect.lis* is to be found and the spectrum is to be displayed with the file's specifications already selected as a default. When light incident onto the slit comes out of a fibre which is kept exclusively on the star, selection of "sky" for subtraction off the object can be ignored.

If *sdist.dat* has been kept for each stellar spectrum the reduction can be simplified from this. The *echselect.lis* file relevant for the spectrum can be generated from *sdist.dat*, as the order width is a constant value (it is related to the optical fibre size, see footnote 10 Chapter 3) and therefore the number of pixels that it is desirable to collapse around the order centre is constant also. The stellar spectrum can then also be collapsed using "*pre=y*", which speeds up the reduction time dramatically. The other advantage of this approach is the number or pixels used to create the collapsed spectrum is then a known constant. This is important as the Turbo Pascal procedure **linenoise** (used for fitting a dispersion curve to the thorium spectra) needs to know what number of pixels were collapsed to create the one-dimensional spectrum seen. Orders 36 pixels wide are assumed.

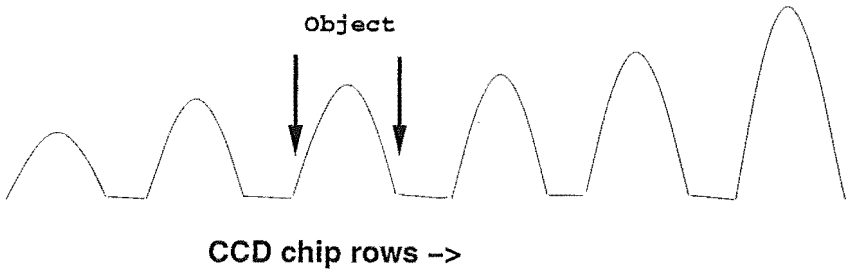

Figure F.3: The cross-section of the orders is displayed so each order's edge can be interactively chosen for collapsing.

The stellar spectrum can now be divided through by the flat-field (why this is the appropriate time for doing this is discussed in §3.4). The **Figaro** command

idiv *image=STAR image1=FLAT-FIELD out=NEW-NAME*

does this. Images can also be normalized using the command

icdiv *image=STAR fac=α out=NEW-NAME,*

which has the effect of dividing all the data through by some constant, α. In order that the Turbo Pascal procedure **linenoise** can calculate the noise in each pixel of a thorium line (see §3.5.3 on calculating the noise in a collapsed thorium line), it is necessary that the flat-field spectrum is subsetted into its six orders using the **Figaro** command **isubset** and then each of its orders is divided through by its mean value before the flat-fielding takes place[6].

F.4 From Figaro to Turbo Pascal

Having used **icol** on the orders to collapse them into a one-dimensional format, the csh-shell script **reduce.new** divides each spectrum (thorium, stellar and flat-field) into their six orders using **isubset**. The flat-field is then normalized by dividing it through by the mean for that particular order (using **icdiv**). Having done this each thorium and stellar exposure is divided by

[6]Therefore the star and thorium spectra must be subsetted also, so they can be divided by the relevant normalized flat-field order

its appropriate flat-field (as determined from *ls.next*). Then **ilist.new** is used to take each order from **Figaro** format into an ASCII data file (with the order number at the top of the file). The shell uses file name extensions to determine the appropriate files in the current directory and does them all. It also gets the relevant header details for the barycentric correction and puts them in an appropriately formatted file with a *.hdr* extension. In addition, the program renames the files so the stars have an *.spc* extension and the thoriums an *a.lmp* or *b.lmp* extension, depending on whether the thorium was taken before or after the stellar exposure. This program (but not the ones it calls) assumes the files with *.dst* extensions, returned from **reduce.new**, have names in the format *TTTT-XXffed.dst*.

F.4.1 Details of ilist.new

First the program gets a list of all the files with an *ffed.dst* extension present and puts them in a temporary file. The **Figaro** command **ilist** is now used on every filename in that list. The call to **ilist** outputs an ASCII file with 5×2 columns (one for the pixel number and one for the flux value) and a title on every page. A sub-shell **ilist.reduce** is called by **ilist.new** to turn these five sets into a single column of data only. It is after this that the order number is added in at the top of the file. Initially this was an artifact of the way **ilist** outputted things, but now the Turbo Pascal programs expect it to be this way. These ASCII data are then renamed, with the star files becoming *TTTXXX□.spc*[7] and the two thoriums belonging to the star files becoming *TTTXXX□a.lmp* and *TTTXXX□b.lmp*. The thoriums for each star file are again determined from the file *ls.next* and are given a name containing *a* or *b*, for the initial and final thorium spectra respectively.

With this done, the header data of all the stellar spectra are created using **Figaro**'s command **exam**. From these, files with the extension *.hdr* are created, with the day, month, year, hour, minute, second and the object name on consecutive lines. The Turbo Pascal procedure **BarycentricCorrection** has been adjusted so the file with extension *.hdr* it looks for is not dependent on order; therefore, only one header file is produced for the six stellar orders. Its name is the same as the main body of its stellar image's name, but without the last number (which is an order identifier), i.e. *s15203.hdr* is the header file for the six *s15203□.spc* files. It should be noted that the Unix system language **awk** was used to achieve most of the above file manipulations.

F.5 The dispersion solution

When the CCD data have been processed into one-dimensional form by **Figaro**, the results are either ftp'ed to a Personal Computer or left in a directory mounted on a P.C.[8]. Then the thorium spectra for each star are used to find the dispersion solution for the stellar spectrum using the Turbo Pascal program **ccddisp** (for most of the remaining reductions all orders are treated independently). This program calculates a quadratic least-squares fit of the from of

$$n = a_1 + a_2 \times (\lambda - \lambda_C) + a_3 \times (\lambda - \lambda_C)^2$$

to all the files with *.lmp* extensions in a given directory. It then averages the dispersion solutions arising from the two thorium spectra to get the mean dispersion solution

$$n = \frac{1}{2}(a_1 + b_1) + \frac{1}{2}(a_2 + b_2) \times (\lambda - \lambda_C) + \frac{1}{2}(a_3 + b_3) \times (\lambda - \lambda_C)^2.$$

The program begins by a call to the sub-procedure **Initialise**, which sets up all the relevant parameters' initial values. Then it calls **Editpars** (from the unit **ccdepar**) which displays the directories

[7] Where □ is a number from one to six representing orders 41 to 46

[8] As long the the file specifying the stellar cross-correlation pairs is in DOS format everything is fine — the *.spc*, *.hdr* and *.lmp* files can have either form of line end

in which the thorium files are to be found, where dispersion files and line deviation files are to be written and whether the fit of each thorium line should be plotted graphically. Then **ccddisp** repeatedly calls the procedures **ReadDPar, linepostionsinc, DispLSQ** and **Writedispersionfile** until every *.lmp* file in the stated directory has been analysed.

F.5.1 ReadDPar

On the first call to this procedure it opens up a file called *dpar.dat*[9] and assigns variables corresponding to:

1. the *.lmp* directory
2. the directory where unaveraged dispersion files are to be written
3. the maximum acceptable shift in the position of each thorium line's gaussian fit from its estimated position (this is typically 0.3 pixels)
4. whether or not the thorium line fits are to be plotted for the user's inspection
5. whether rejected lines should halt the program so a different rejection criterion can be tried, or if the program should just ignore the line and write its rejection to a file called *line.log*.

It should be noted that at this stage the program checks to make sure a directory was entered for the location of the *.lmp* files and if not prompts for it. The procedure then makes a listing of all the *.lmp* files in the nominated directory and sets a variable called *specfile* to the first on the list. At each successive call to **ReadDPar** *specfile* is set to the next name on the list, until there are no more names. At this last call, **ReadDPar** calls a procedure called **Makemeans**, which creates a file in the *.lmp* directory containing the averaged dispersion solutions (and their errors) for each lamp. **ReadDPar** then halts **ccddisp** and the program is finished.

F.5.2 Linepositionsinc (from the unit ccdplot)

Linepositionsinc is the procedure responsible for fitting a gaussian to the lines in the lamp spectra and thereby finding each line's central position. The first thing it does is to open up the file associated with *specfile* and assign variables to the ASCII data inside using the procedure **read_data** (from the unit **ccd**). From this the order being dealt with is determined, as is the flux in each pixel of the collapsed thorium spectra.

By calling the two **ccdplot** procedures **Linelist** and **Boundary**, the appropriate lines and their approximate positions along the CCD for the order in question are found (along with the average value of the flat-field for that order, which is used in **linenoise** — see below). Each order also has a particularly strong line in it, line number *lcrt*, which is taken as the starting point for line fitting along the order (the details of this line are also returned by the two procedures). Fitting the lines along the order is broken into three parts. In the first a call to the sub-procedure **Linefits** finds the position of the correction line, number *lcrt*, and from this the difference between the actual line positions and the tabulated line positions is found. This correction to the tabulated values (from line number *lcrt*) is then used by **linefits** to help find the line position for all the lines in the order before *lcrt* and then to help find the line position for all the lines in the order after *lcrt*. Having done this the centre of all the fitted lines (which have an acceptable shift in fit), their tabulated wavelength and their shift in fit are written to a file called *disp.dat*.

[9] It looks for this file in the working directory — all these Turbo Pascal programs assume this is where any files with *.dat* extensions are located

Sub-procedure Linefits

The first thing **Linefits** does is to consider the number of the line to which it is fitting. If it is the correction line, number *lcrt*, it considers a window 15 pixels either side of the tabulated line position and searches for the pixel with the largest flux value in that window, by a call to the **ccdplot** procedure **FindDimension**. It then assumes that the position of the maximum flux is the location of the line number *lcrt*[10] and sets a fitting window around this of ±3 pixels. If, as is true for most calls **Linepositionsinc** makes to **Linefits**, the line being fitted is not number *lcrt*, then the sub-procedure simply assumes the desired line is located at about the tabulated plus the correction value and sets a fitting window around this of ±3 pixels. To allow for the correction values changing slightly along the order, the correction value (which is initially found from line number *lcrt*) is used for the line nearest it then a new correction value is determined from the fitted position of the current line. The correction value is hence calculated at each step down (or up) the order[11].

The sub-procedure **Linefits** starts at a particular line number, either *lcrt*, *lcrt-1* or *lcrt+1*, then repeats its analysis on the next line until it runs out of lines. For each line, the window to be fitted is set and **FindDimension** is used to determine the greatest pixel value in the window. This value is used in the **ccdplot** procedure **Fitgaussian** as the initial value of the gaussian height. The midpoint of the fitting window is used as the initial gaussian central position and three as the gaussian half-width. The error in each pixel in the fitting window is determined by the **ccdplot** procedure **linenoise** (see §3.5.3 on working out the noise in a thorium line), which assumes that the thoriums have been flat-fielded[12] (the flat-field in question should have had each order normalized before the flat-fielding takes place, by division by its mean). Using these estimates **Linefits** calls **Fitgaussian**, which uses the Levenberg-Marquardt method of least squares (see Press et al. [134]) to fit a gaussian in the determined window. If the thorium lines are to be viewed, it is after this fitting that the thorium fitting window, data and gaussian are plotted on the monitor (see Figure F.4). If the line fit was unacceptable **Linefits** either asks for new window limits to be set for

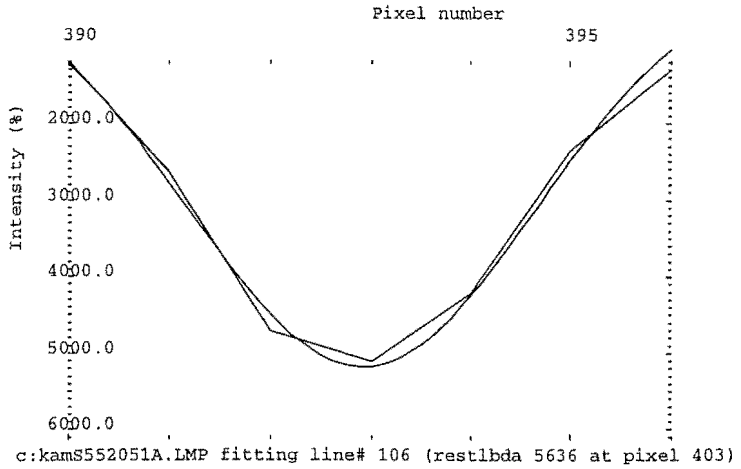

Figure F.4: Thorium lines, their fitting window and the fitted gaussian can be plotted on the monitor.

the fit or writes the news of the line rejection to a file called *line.log* (in the directory where the non-averaged dispersion solutions are written) depending on the parameter read from *dpar.dat*. In

[10]Hence line number *lcrt* must be the largest line within about 20 pixels

[11]A new correction value is only calculated if the gaussian fit to the current thorium line is considered acceptable

[12]That they have been flat-fielded is specified when the procedure is called

the former case, a gaussian fit is again attempted until either the user decides to give up or an acceptable fit is achieved. **Linefits** then repeats the procedure with the next line in the order, where the next line is numbered $(k-1)$ in the case of lines at smaller pixel values then line number *lcrt* and $(k+1)$ in the case of lines after line number *lcrt*, if (k) is the number of the current line.

F.5.3 DispLSQ: finding the dispersion solution from the thorium lines

This procedure is in **ccddisp** and it uses the information on the positions of lines in the thorium spectrum that was written to *disp.dat* (by **Linepostionsinc**). It does a least-squares fit (using the procedure **lfit** from the unit **fit**) of a second-order polynomial to the line positions found and their tabulated wavelengths (see Figure F.5). The coefficients of the fit and the errors, including

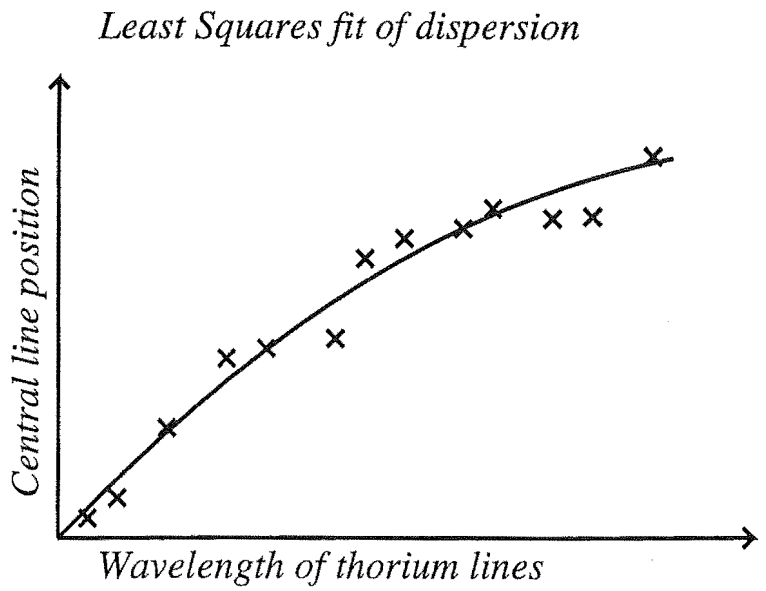

Figure F.5: A polynomial of second order is fitted to the line-positions found by **Linepostionsinc**.

the total deviation in fit, are written to a file (with the same name as the current thorium lamp, but with a *.dis* extension) by the procedure **Writedispersionfile**. The procedure **DisLSQ** also creates a file with a *.dev* extension (in the dispersion directory), and for every acceptably fitted line writes into it the difference between fitted line position (from *disp.dat*) and where the dispersion solution indicates it should be. This is useful for discovering widentified lines.

F.6 Getting the velocity shift using a cross-correlation

Once the dispersion solutions for the relevant thorium spectra have been obtained, the program **ccdXrun** is used to get the velocity shift between two spectra. This program takes two stellar spectra and uses their dispersion solutions to rebin them into logarithmic wavelength bins. This means for a given velocity shift, the shift in number of bins is the same at all wavelengths, that is

$$v = c \times \frac{1-E^2}{1+E^2},$$

where[13]

$$E = \exp(-\Delta \ln \lambda),$$

[13]The relationship between the velocity, v, and the number of bins shifted is not linear as $\Delta \ln \lambda = s \times \delta \ln \lambda$, where s is the bin shift and $\delta \ln \lambda$ (the change in logarithmic wavelength from bin to bin) is constant. However for small s and $v/c \ll 1$, $v/c \approx 1 - \exp(-\Delta \ln \lambda) \approx s \times \delta \ln \lambda$ is obtained.

as[14]

$$\frac{v}{c} = \frac{1-(\lambda_0/\lambda)^2}{1+(\lambda_0/\lambda)^2}$$

and $\Delta \ln \lambda$ is the shift in logarithmic wavelength, $(\ln(\lambda) - \ln(\lambda_0))$. How much one stellar spectrum has shifted in velocity compared to another is then determined by cross-correlating the two spectra together. Ignoring any noise in the spectra, the resulting function is a symmetric function with a peak at the shift[15]. This shift is in bins, which due to the rebinning can easily be changed to a corresponding shift in velocity. After the application of the barycentric correction to remove the effect of the Earth's movement between exposures, the shift in radial velocity of the star from one exposure to another relative to the solar system barycentre is found.

The program **ccdXrun** begins by asking if the cross-correlation of two spectra is desired, or that of a spectrum and a delta array (the latter case is the subject of Appendix G — the program also has the option to cross-correlate two thorium spectra, but this will not be discussed). In the former case, it then calls the procedure **EditPars** (from the unit **ccdepar**), which displays the name and path of the file containing the pairs of spectra to be cross-correlated. This should be in the same directory as the *.spc* files themselves, where *.spc* is the extension of the star files. It also displays the number of points of the cross-correlation function to be fitted, the directory containing the files where the velocity shift will be written (these files have a *.vel* extension), the directory path of reference spectra[16] and the type of fit required, where 3 is for a single-gaussian fitting function and 5 for a three-gaussian fitting function. **ccdXrun** then calls the procedure **Starrun** (in unit **ccdccf**) which does most of the work.

Starrun uses the **ccdccf** procedure **ReadParfile** to open up the file *par.dat* (which was displayed by **EditPars**) and assigns variables from it. **Starrun** then opens the file which gives the names of the pair of spectra to be cross-correlated and repeatedly reads in the names of the two stellar spectra to be analysed, adds on the correct extension (*.spc*), assigns the corresponding name of the dispersion file (same name, but with a *.dis* extension) and performs procedures **BarycentricCorrection, GetVel** and **WriteVelfile** until all the pairs on the list have been cross-correlated.

F.6.1 BarycentricCorrection

This procedure starts by opening up the file *coord.dat* and reading out of it the epoch of star coordinates and also the position of Mt John University Observatory. It then opens up the header file of the first *.spc* file (these are expected to have the same name as the *.spc* files, but with a *.hdr* extension and without the last character in the stellar file name, as this just indicates which order is being dealt with) and reads from it the mid time the observations took place and the star's name. If the star is the sky the procedure **radial_velocity** (from the unit **BarCor**) is called and it works out the radial-velocity correction due to the heliocentric motion of the telescope. This entails it finding the Sun's position in the sky from the *.hdr* data. However, if the object is not the sky then before **radial_velocity** is called **BarycentricCorrection** searches for the star name in the *coord.dat* file and assigns variables to the star's position. This is used by **radial_velocity** to find the velocity for the star in order to correct for barycentric motion of the telescope. In both cases **radial_velocity** is called twice, once for each exposure. The difference in correction returned is to be subtracted off the radial velocity found by the cross-correlation function fit.

[14]The relativistic formula is necessary, as with the motion of the Earth around the Sun being considered two exposures can be up to 60 km/s shifted!

[15]This is strictly only true for continuous cross-correlation (for more details see §3.5)

[16]The reference spectra are the first column in the spectra pair list. Each stellar exposure is compared with the star's reference to find the shift in velocity.

F.6.2 GetVel

This procedure carries out the bulk of the reduction including the re-binning of the spectra and the cross-correlation. It prepares the data for cross-correlation by using the sub-procedure **Setup**. Then it uses **samespectra** in an attempt to ensure the two spectra will only contain the spectra of the same rest-wavelength (or asymmetries will arise) and calculates the noise of the cross-correlation (to help in the calculation of fitting errors). A call to **Correl** (from unit **ccdprepare**) cross-correlates the prepared spectra (**GetVel** can then write the cross-correlation function to a file of the same name as the star, but with a *.ccf* extension if this is so desired). Its final action is to call **Fitvelocity**, which uses **Xfit** (from **ccdplot**) to fit a gaussian to the cross-correlation function and determine the position of its peak.

Setup

This procedure reads in the data of a stellar file using **read_data** (from unit **ccd**) and obtains the first and last thorium lines used to find the dispersion solution from procedures **Linelist** and **Boundary** (from unit **ccdplot**). This is important because the dispersion solution outside the wavelengths corresponding to these lines will be extrapolated, not interpolated, and hence is not as reliable. Therefore to increase precision, only the part of the spectrum inside these points should be cross-correlated. To this end, **Setup** assigns the number of bins to be the number of pixels between the first and last thorium lines[17], d, and calls **rebin** from **ccdprepare** to do the logarithmic re-binning. **Rebin** takes the d pixels between the thorium line extremes and rebins them into d bins while conserving flux. The change in logarithmic wavelength from pixel-to-pixel is[18]

$$\delta \ln \lambda = \ln(\lambda_f/\lambda_i) \times 1/d,$$

where λ_f and λ_i are the wavelengths of the first and last thorium lines. The resulting d bins start at bin number one and go to bin number d. The extra bins outside this are set to zero[19] (there must be 2^n bins for Fast Fourier transforms to be used in cross-correlations). It should be noted that **rebin** assumes that the flux that fell on each pixel was constant along the pixel extent (which is not generally valid), although this is not believed to have a large effect on the resulting radial velocities (see §3.5.4).

Samespectra

This procedure (internal to **getvel**) takes the rebinned stellar and reference spectra and determines the shift in bins caused by their different time of exposure in the Earth's orbit. In order to do this, the details which come out of **BarycentricCorrection** are considered. The spectra which are determined to be different between the two are then set to zero[20].

Once this is done, the mean value of the flux in the first non-zero bins is subtracted using **ccdprep**'s **subtractmean**; then, the procedure **ccfnoise** (internal to **getvel**) is called. This determines the cross-correlation function's noise, assuming that the arrays passed to it have first been mean subtracted (this is similar to **linenoise**). Finally a cosine-bell is applied to the outer 10% of the non-zero bins using **cosinebell** (from the unit **ccdprepare**). Doing the cosine-bell and mean

[17] As no resolution is gained by using more bins

[18] As λ_i defines the start of the first bin and λ_f the end of the last bin get d, not $(d-1)$, bins

[19] This also decreases overlapping in the space domain after cross-correlation, due to assuming the function is periodic (see §3.5.2 for further details)

[20] While this is far from perfect, due to the intrinsic variation of the star, the orbital velocities give by far the biggest radial-velocity shift for the small-amplitude variables which were observed for this thesis. In fact, for most of the observed stars the intrinsic variation is much less than a bin in size.

subtraction are both necessary to enable the determination of a filter for the cross-correlation function (see §3.5.2). Mean subtraction also removes complications for cross-correlation fitting, as is discussed in §3.5.

Correl

This procedure is located in the unit **ccdprep**. It takes two real spectra and transforms them both (at the same time) to the frequency domain. It then finds the Fast Fourier Transform of their cross-correlation and applies an optimum filter (discussed in §3.5.2) to the product. It then normalizes the transform by dividing it through by the "total power"[21] of each of the two contributing spectra. Finally the result is inversely transformed back to the measurement domain. It is basically **correl** from Press et al. [134] §12.5, with the filter described in §12.6 added in.

FitVelocity and Xfit

Fitvelocity begins by transforming the cross-correlation function, resulting from **correl**, into a form with its extrema at the shift in radial velocity (see Figure F.6). Once this is achieved the

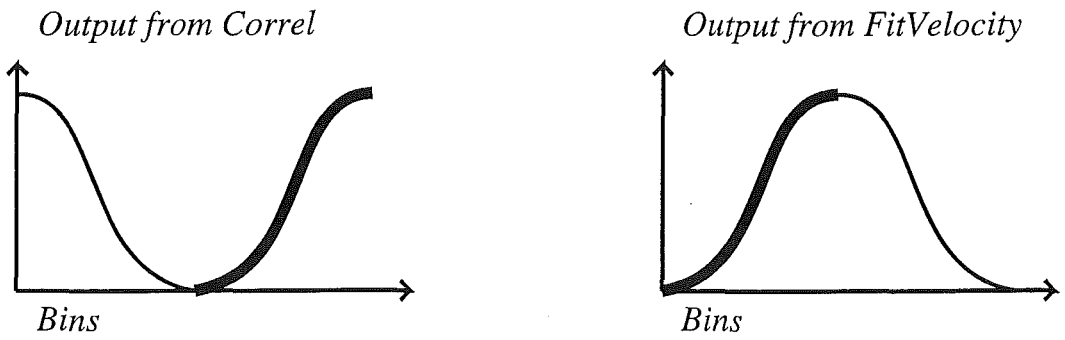

Figure F.6: The array resulting from **correl** is transformed into a form whose peak is more easily determined by **Xfit**.

ccdplot procedure **Xfit** is called. **Xfit** calls another **ccdplot** procedure **FindDimension**, which finds the peak in the data array passed to **Xfit**. A window from $(P - \text{round}(N_f/2) - 1)$ to $(P + \text{round}(N_f/2) + 1)$ is initially defined for the gaussian fit, where P is the position of the cross-correlation function's maximum and N_f is the number of points to be fitted to. This is then reduced until the window size is N_f. So a set N_f is used for all exposures — this means the same region of the cross-correlation function it fitted every time. This is desirable as the cross-correlation function turns out not to be entirely gaussian or symmetric (see the §3.5 on cross-correlation function fitting)! Because of this the following things are done:

- The same number of points are fitted from exposure to exposure
- An odd number of points is fitted
- Instead of a gaussian fit a three-gaussian fit (**threefit**) is usually used. This generally gives a better fit than a single gaussian, as is discussed in §3.5. This needs only five parameters to be fitted, these being half-width, height of the side and main peaks and the position of the side and main peaks. If this method fails a single gaussian fit (**fitgauss**) is used.

Both types of gaussian fit use the Levenberg-Marquardt method (Press et al. [134] §14.4) to fit the cross-correlation. For the main peak the initial position is taken to be the bin with the maximum flux (from **FindDimension**), initial height the maximum flux value and the initial half-width as

[21] For discrete function f this is $\sum_{i=1}^{N} |f_i|^2$

half the fitting region. **Fitgaussian** is then called to refine these initial values. The minor peaks are initially assumed to be one-fifth of the main peak size and to be near the edges of the fitting window. The resulting fit and cross-correlation function can be plotted on the monitor and the three gaussian parameters relevant to the main peak are written to the screen, along with the number of points used to find the fit and the error in velocity due to the fit.

F.6.3 WriteVelFile

This is a sub-procedure of **StarRun** which simply converts the cross-correlation function's fitted position in bins to a shift in radial velocity (in km/s). It also writes the two barycentric corrections, the Julian Date, the resulting corrected velocity, the errors in the two dispersion solutions (in km/s) along with the the error in the gaussian fit to the cross-correlation function (in km/s) to a file with the same name as the star, but with a *.vel* extension instead of *.spc*[22]. In addition, it writes the fitting parameter, N_f, the gaussian width in km/s, the half-width of the fitted gaussian(s) and a letter[23] representing the type of fit used to obtain the radial-velocity shift.

It should be noted that the convention of recessional velocity being positive (with respect to the reference spectrum's velocity) is used.

F.7 Finding the shift in radial velocity from six orders

The Turbo Pascal program **ccdskyrc** finds the exposure's shift in radial velocity from the six orders. It obtains the unweighted mean radial velocity of the six orders and then applies a run correction (where available) to this mean. Run corrections were found to be necessary from consideration of the radial velocities for sky exposures. These showed a radial-velocity variation from run-to-run, even though the Sun is known to be constant in velocity at this precision (see §3.5.3). Hence the Sun's apparent radial-velocity variation is used as the run correction. Weighted means could not be used as the theoretical errors for the radial velocities do not fully explain the deviations observed in the sky data, even when run corrections are applied. Instead (although undoubtedly untrue) it is assumed that all orders have the same error and an unweighted mean is found from the six orders. This is taken to be the radial velocity for that exposure and, when run corrected, is written to a file with the same name as the original *.vel* file, but with the extension *.rc*. Individual run corrections are not applied to each order, as the deviations from order-to-order are at least partially spectrum dependent and the sky spectra are quite different from the stars (see §3.5.4).

F.7.1 ccdskyrc

After forming a simple unweighted mean of six orders for an exposure, the program begins the run correction by opening a file called *config.sky* to find which run correction is relevant to that exposure (if any). Once this is known, the appropriate valude of the run correction is found from the file *sky.rc*. If the desired run correction is not found in the file *sky.rc*, it is calculated by opening the file *sky.vel* and averaging all the exposures relevant to the run. This average is a simple unweighted mean of all the radial velocities for the sky taken in that run and has the form of

$$\overline{s} = \frac{\sum_{o=41}^{46} \sum_{i=1}^{n} s[o,i]}{6n},$$

[22]It should be noted that in this case the stellar name that is relevant is the second in the pair, in other words the non-reference spectrum

[23]3 for a single-gaussian fit, 5 for a five parameter (three gaussian) fit and d for a five parameter fit for which some of the *covar* values are negative

where $s[o,i]$ is the sky's radial velocity for order o, from exposure i. The radial velocity written to the *.rc* file is hence

$$\frac{\sum_{o=41}^{46} v[o,i]}{6} - \overline{s} = \overline{v}[i] - \overline{s},$$

when a run correction is available (that is, sky exposures were taken during that run). Also written to the file is the Julian date and the error in the run-corrected mean[24]

$$\left(\frac{\sum_{o=41}^{46} (v[o,i] - \overline{v}[i])^2}{30} + \frac{\sum_{o=41}^{46} \sum_{i}^{n} (s[o,i] - \overline{s})^2}{6n(6n-1)} \right)^{\frac{1}{2}}.$$

If no run correction can be done the word *FALSE* is also written to the *.rc* file, otherwise the word *TRUE* is written.

[24] See §3.5.5

Appendix G

Using a delta-function array to form the cross-correlation

It was pointed out by Furenlid & Furenlid [53] that cross-correlating a stellar spectrum with a synthetic spectrum consisting of "delta" functions has a number of interesting astrophysical applications. Because such an array of delta functions allows the selection of specific lines to form the cross-correlation function, lines at different depths within the stellar atmosphere can be chosen and therefore an indication of the behaviour of radial velocity as a function of depth in the atmosphere can be determined. Such a cross-correlation is equivalent to adding up all the lines selected by the delta functions — the average is the cross-correlation function. Another interesting application is to use this to determine a mean line profile (for weak lines) and thereby study line asymmetries, for example using the mean line bisector.

Determining the radial-velocity variation at different depths of the atmosphere could be most illuminating. In a pulsating star shock waves and so on can cause different regions of the stellar atmosphere to behave dramatically differently. For a star in a wide binary orbit; however, the radial-velocity variation would be expected to be unchanged with line formation depth. So this method was regarded as an interesting way to gain further information on the cause of the radial-velocity variations observed for the 44 stars surveyed and it was decided to add another procedure to the Turbo Pascal program **ccdXrun** (see Appendix F.6 for a description of this program's main units and procedures) to enable such a cross-correlation to be undertaken. This procedure was called **deltarun** and it, along with the results of the cross-correlations, will be discussed in the following sections.

G.1 Method

The routine to do the cross-correlation of a delta array with the stellar spectra is part of **ccdXrun** and, like **Starrun**, requires that **ccdDisp** has already been used to find the dispersion solution appropriate for the stellar exposure. When a delta-array cross-correlation is chosen **ccdXrun** calls the procedure **deltarun** in the unit **ccdccf**. Then **deltarun** reads in the following parameters from a file called *delta.dat*:

- The full path of the file containing the list of the stellar exposures to be analysed (unlike **Starrun** the orders will not be treated independently, so the names in the list of stellar exposures should not include the order identifier).
- The directory containing the six stellar-line files for the delta array. Each file contains a line list with the rest-wavelength, line-depth and excitation-potential types[1] for lines of a specific

[1]Because different excitation potentials are assumed to indicate different line formation depths

order. Appendix G.1.1 describes how the wavelengths and lines appropriate for late-type stars were found.

- The directory to write the resulting velocity shift to.
- The maximum absolute velocity shift (aside from the barycentric correction and the known recessional velocity) expected for the lines.
- Whether the procedure is to find the radial velocity shift or do line-profile analysis. The procedures for the latter have not been written, as it was decided that the severe line blending and poor velocity resolution[2] did not lend themselves to such an analysis. However before this was determined, to facilitate the addition of the appropriate procedures, **deltarun** was written with the option of being able to obtain the mean-line profile by "adding the lines together" after division by their line depth.
- Whether or not each cross-correlation function and gaussian fit is to be plotted.
- The type of curve to fit to the cross-correlation function, where 5 is a three-gaussian fit and 3 is a single-gaussian fit (the fit used was typically a single-gaussian, as with the extra points "odd-even" affects should not be a problem).
- The excitation potential line type to be used to create the delta arrays.

Then the following is done for each stellar exposure in the list of stellar exposures. The barycentric correction is found from the information in a file with the same name as the stellar exposure, but with a *.hdr* extension. This, along with the maximum velocity shift and the expected recessional velocity (this is also found by **BarycentricCorrection** and is the recessional velocity tabulated in Hoffleit [92]), are passed to a procedure called **deltaconstants**, contained in the unit **delta**. The variables passed out of this procedure will remain the same for all six orders of the exposure. It passes back to **deltarun** the value of *dlnl* that is the ultimate size of the bins in logarithmic wavelength to be used by all orders and the maximum and minimum lags (in units of *dlnl*) the cross-correlation function peak could be at[3].

It is necessary for all orders to have the same bin size in logarithmic wavelengths, because the spectra's lines are so very blended that there is typically at most one line in a given order (of a given excitation potential type) which is suitable for use in the cross-correlation and hence it is necessary to form the cross-correlation function using lines from different orders. This is basically done by fixing *dlnl* and adjusting the starting wavelength for each order to give the desired bin size in logarithmic wavelength (see Appendix F.6 for details on how rebinning is normally undertaken). The ultimate bin size, *dlnl*, is about 2.4 m/s. A stellar spectrum with these size bins is generated by first rebinning the spectrum as usual (except with the starting wavelength chosen to give the desired final shift in logarithmic wavelength bins), then using cubic-spline interpolation on the rebinned spectrum to get a factor of about 1000 more points! This does not improve the stellar spectrum's real resolution, but it does enable the delta array to have a finer resolution than the stellar spectra, which has pixels at intervals of about 2.4 km/s. This results in a cross-correlation function which has a better velocity resolution than would be obtained by cross-correlation with a delta array with bins at 2.4 km/s intervals, because there is effectively only half the "smearing" effect.

[2]Adding together individual lines, in the way prescribed below, will improve the number of data points available, but not the pixel resolution because the pixels average all the data across the lines (rather than just discretely sampling it)

[3]This can not be bigger than 1024 or the arrays will be too small

After **deltaconstants**, **deltaruns** calls the procedure **subdeltaccf** for each of the six exposure's orders. This procedure begins by reading the data for the order from the *.spc* file and then reads in the appropriate dispersion coefficients from a file with the same name, but a *.dis* extension. The order number is passed (along with *dlnl*) to a **delta** procedure called **deltaorder** (these variables vary from order-to-order). This procedure finds the appropriate initial and final wavelengths the order is to have, the "central" wavelength appropriate to the order (which will have been used for the dispersion solution, see Appendix F.5) and the number of points per bin that splines are going to interpolate, m. The final wavelength is just the tabulated final wavelength of the order and the central wavelength is similarly taken from a table. The magnification, m, is determined by truncating to a whole number $\delta \ln \lambda / dlnl$, where $\delta \ln \lambda$ is the size the bins would be if rebinned as normal (i.e. without interpolation and with the default initial wavelength) and $dlnl$ is the ultimate size. Using this value of m, the initial wavelength is found by making the relation[4]

$$\lambda_i = \frac{\lambda_f}{\exp(dlnl \times (md))}$$

true, where d is the number of pixels between the first and last wavelength. All these values are then passed into **ccdprep**'s **rebin** which rebins the order accordingly.

The **delta** unit's procedure **deltalines** is then called. This opens up the stellar-line file appropriate to the current order and for those lines of the correct type uses the known initial wavelength of the order and *dlnl* to determine the bins into which the stellar lines' rest-wavelengths fall. It also determines, for each stellar line, the line depth and these are all passed back to **subdeltaccf**. The line weights for each stellar line are then determined. In the case of radial velocities being the aim, the weight has been chosen to be the same for all lines (see Appendix G.1.2). At this point the contribution to the error in the radial velocity due to the dispersion solution is calculated (this is larger than for a normal cross-correlation, as it has a contribution from the dispersion error of every order which had lines were added to the cross-correlation).

subdeltaccf now evaluates the cross-correlation of the rebinned and interpolated spectra and the delta array, over the lags corresponding to the expected peak position. This is equivalent to calculating

$$c(k) = \sum_{n=1}^{L} \omega_n g(l_n - k)$$

between the maximum and minimum lags, where $c(k)$ is the cross-correlation function at lag k, ω_n is the line weight, l_n is the bin number of the nth stellar line's rest-wavelength, L is the total number of stellar lines in this order and g is the rebinned (and interpolated) order. As the cross-correlation function is only being evaluated between the maximum and minimum lags, g need only be interpolated over the required lags about l_n. For each line, these lags cover the expected position of the line in the stellar spectrum. So **subdeltaccf** calls **dspline** for each of the L lines in the order, and **dspline** determines a spline across the expected position of the stellar line and finds the appropriate interpolated points. These are used by **subdeltaccf** to determine the part of the cross-correlation function[5] to come from the current order.

When all six orders have had **subdeltaccf** called, their cross-correlation functions are added up to make the total cross-correlation function. To this a gaussian is then fitted by **ccdplot**'s **Xfit**.

[4] See Appendix F footnote 18 for why the division involves d not $(d-1)$

[5] The approximate noise in the cross-correlation function is also determined here

G.1.1 The stellar-line list

Lines over the wavelengths observed were first identified in the solar spectrum using Beckers et al. [16]. Then as many lines as possible in the observed wavelength range of the solar spectrum had their wavelengths found, mainly with reference to Moore [122] with any additional lines identified using Reader et al. [137], Meggers et al. [121] and Moore [123].

From these the lines appropriate for a late-type giant were determined by the use of Hecker [68], who gives lines for Arcturus, and Griffin's [66] photometric atlas of Arcturus. For these lines the line depths (appropriate for a K-type giant), were found from Griffin [66] and the excitation potential for the lines from Moore [123]. The observed stellar spectra is not of as high resolution as the Griffin atlas, so the observed stellar spectrum of a typical K and a typical M-type star then had the distinguishable Arcturus lines found in them.

Of these distinguishable lines, those for which the apparent contamination of equivalent width by blends was no greater than 30% in the K-type star π Pup, were chosen to be suitable for the formation of the delta array. This is still badly blended and hence it was doubted that any meaningful results would be found, unless the change in radial-velocity variation with line formation depth was startling. Unfortunately, in order to have a variety of different excitation potentials with several lines available to form the cross-correlation function, inclusion of such badly blended lines was necessary (see Table G.1 for the list of lines). Perhaps a better place for such an analysis would be in the infrared, where line blending is less.

G.1.2 The weighting factors

Furenlid & Furenlid [53] sets the weights for all his delta functions equal to one. Yet weighing delta functions proportional to their corresponding line depth seems more appropriate for a synthetic spectrum — this is what happens when two spectra are cross-correlated, after all. Which method is better for radial velocities? To answer this question, the signal-to-noise in the cross-correlation function and the effect on the cross-correlation function's side lobes for the two cases will now be considered. If L_{T} is the total number of lines from all orders to be used for the cross-correlation then

$$c(k) = \sum_{n=1}^{L_{\mathrm{T}}} \omega_n g(l_n - k).$$

So if $\mathcal{g}_n(k) = g(l_n - k)$, then

$$\sigma_c^2 = \sum_{n=1}^{L_{\mathrm{T}}} \sigma_{\mathcal{g}_n}^2 \omega_n^2.$$

For ease of calculation that $\mathcal{g}_n$ is flat-fielded will be ignored, only photon noise will be considered and the lines will be regarded as emission spectra in a continuum of zero flux. Then the noise in the centre of the cross-correlation function will be

$$\sigma_c^2 = \sum_n S_n \omega_n^2,$$

where S_n is the signal in the centre of the nth line. However, it is the signal-to-noise,

$$(\frac{S}{N})^2 = \frac{(\sum_n S_n \omega_n)^2}{\sum_m S_m \omega_m^2},$$

[6] Clearly only one of these two lines will be visible in the observed spectra. However, it is unknown which the observed line equates to. It maybe that the two lines are both equally present, in which case both entries should be removed. Otherwise the smaller should. If this method of analysis was to be continued, this degeneracy should be fixed.

Order	λ	D	Type
46	5019.18[6]	4.5	2
46	5019.19	4.5	3
46	5024.842	9.15	1
46	5013.30	8.3	2
46	5017.591	7.55	2
45	5132.351	3.7	0
45	5134.528	5.65	0
45	5135.58	2.1	0
45	5135.707	2.1	0
45	5140.160	4.2	0
44	5238.560	8	1
44	5239.823	7.15	2
44	5240.878	3.9	2
44	5241.458	2.7	2
44	5242.495	7.8	2
43	5364.874	7.8	3
43	5365.403	7.35	2
43	5366.651	6.2	1
43	5367.470	8.0	3
43	5371.493	10.15	1
43	5373.704	6.1	3
43	5377.628	5.25	2
43	5379.580	6.65	2
42	5501.469	9.85	1
41	5622.9	2.65	0
41	5627.628	7.55	1
41	5632.469	3.0	1
41	5633.970	5.3	3
41	5638.266	6.65	3

Table G.1: **Table of lines used to create delta array for cross-correlation.** λ is the rest wavelength of the line, D is the depth of the lines in a K-type giant and "Type" indicates the excitation potential range the line is in, assumed to indicate the line formation depth. These types correspond to:
(0) Molecular lines of any excitation potential
(1) 0 to 1.10 eV
(2) 1.11 to 4.10 eV
(3) 4.11 eV and upwards.

that is really of interest, so:

1. if $\omega_n = 1$ for all n, then the signal-to-noise squared is simply $\sum_n S_n$.
2. if $\omega_n = S_n$ for all n, then the signal-to-noise squared is $\frac{(\sum_n S_n^2)^2}{\sum_m S_m^3}$.

From this it is not immediately obvious which gives the better signal-to-noise, but if both are multiplied by $\sum_m S_m^3$ and a single term is considered, it can be seen that the question is which of $(S_i S_j^3 + S_j S_i^3)$ and $(S_i^2 S_j^2 + S_j^2 S_i^2)$ is bigger (when $i \neq j$). Inserting in $S_i = (S_j + \alpha_{i,j})$ and $S_j = (S_i - \alpha_{i,j})$ and assuming $\alpha_{i,j} > 0$, it is possible to show that case one gives the better signal-to-noise.

So equal weighting to the delta functions give a better signal-to-noise — but what about the unwanted side lobes in the cross-correlation function? An illustrative example is a spectrum made up of two lines, of strength a and b respectively (see Figure G.1). The ratio of the the main-peak

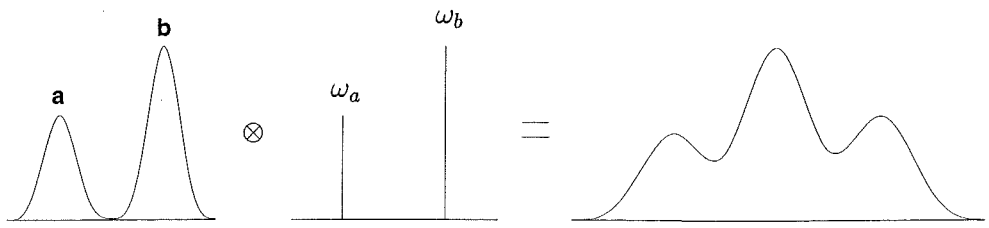

Figure G.1: The left-hand side represents the spectra and the weighted delta-function array. The right-hand side is the resulting cross-correlation function, with its distinctive lobes.

maximum to the side-lobe size is what is important and for the two cases:

1. if $\omega_a = a$ and $\omega_b = b$, then the ratio is $\frac{a^2+b^2}{ab}$
2. if $\omega_a = \omega_b = 1$, then the ratio is either $1 + \frac{a}{b}$ or $1 + \frac{b}{a}$.

Hence the latter case will have one lobe smaller that the weighted case and one lobe bigger, so not weighting the delta-functions will produce an asymmetry in the cross-correlation function unless the lines are well separated. Symmetry is highly desirable for the cross-correlation function; however, if two nearby lines are of different excitation potentials they should not be included together anyway. Alternatively, if two nearby lines were of the same excitation potential, then the asymmetry added to the cross-correlation function should remain the same over time and the relative radial velocity would be unaffected. Hence it was decided to weight lines evenly, for the certain gain of better signal-to-noise in the cross-correlation function.

G.2 Results

Cross-correlating delta arrays with stellar spectra was undertaken for all 44 stars for which radial velocities had been obtain for this thesis, using data up to and including the time at which 13 stars had their spectroscopic observations discontinued. It was not felt that the radial velocities obtained gave any useful information, so at this stage work on this analysis creased. In addition, poor pixel resolution and, most importantly, severe line blending were likely to make the obtained radial-velocity variations of dubious value.

Figure G.2 shows typical radial velocities obtained for the stars. As these figures illustrate, the radial-velocity variation of lines with different excitation potentials generally mimics the radial-velocity variations obtained by the cross-correlation of two stellar spectra. The scatter in the data points was generally larger and the radial velocities due to molecular lines were about 3 km/s greater than those obtained from other types, presumably due to asymmetry caused by nearby lines in the stellar spectrum.

The only star not to follow this general pattern was L^2 Pup, for which the resulting cross-correlation function was often unfittable (see Figure G.3). Due to this difficulty in forming fittable delta-array cross-correlation functions, it is unclear what is causing the apparently different radial velocities for lines of different excitation potentials. Instead of a symptom of different lines with different

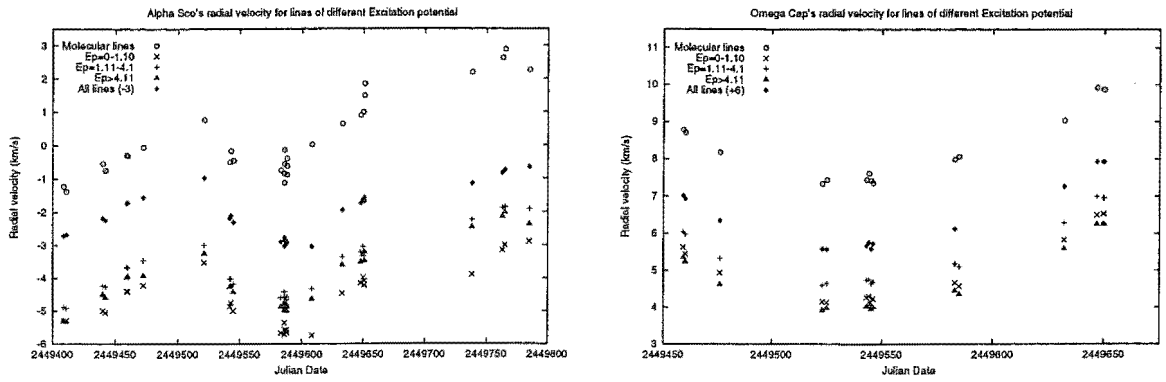

Figure G.2: This figure shows the radial-velocity variation for lines of different excitation potentials, for two typical large amplitude variables. The star to the left is α Sco, an M-type supergiant which is believed to be undergoing fundamental pulsation and to the right is ω Cap, a K-type giant which is believed to be a spectroscopic binary (see §5.1.1).

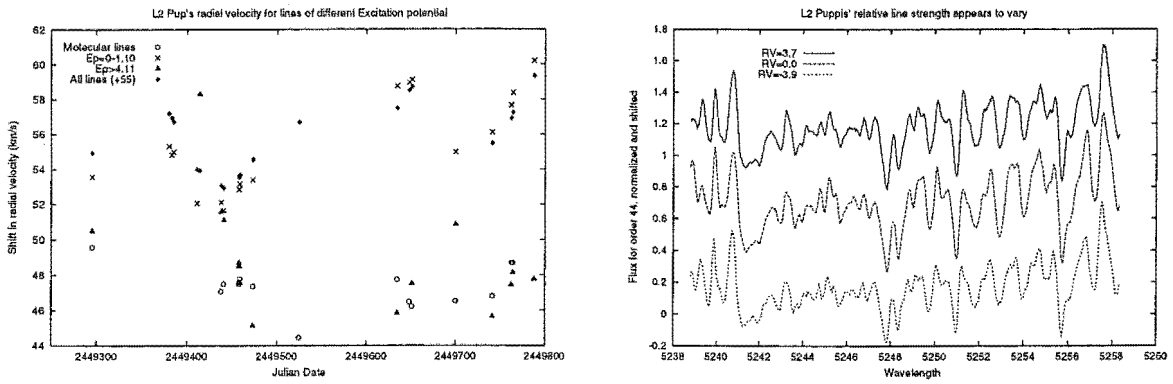

Figure G.3: The left-hand figure shows the resulting radial velocities from cross-correlating the spectra of L^2 Pup with a delta array. Some points are missing, because the resulting cross-correlation function was unfittable. It is unknown why the cross-correlations from this star were so erratic, but one possibility might be that the spectrum of the star was varying. Certainly no huge changes were present, but it is possible that the relative line strength were varying from exposure-to-exposure. This is illustrated in the right-hand figure for order 44 (see about 5251–5254 Å) However, it is not clearly related to the radial-velocity variations.

radial velocities, this could be the symptom of something else like the spectrum of the star varying, or be connected to the fact that this star is so cool that some of the chosen lines are no longer distinguishable. For stars such as L^2 Pup, this analysis using equipment with higher wavelength and pixel resolution, in a region of little line blending, would be interesting.

Acknowledgements

I would like to thank my supervisor, Prof. John Hearnshaw for his help, guidance and rescuing me from a career in mathematics.

I would also like to thank all the people who have been kind enough to obtain observations for me, or let me have theirs: Mike Clark, Jovan Skuljan, Stan Walker and H. Williams. A very special thanks must go to Pam Kilmartin and Alan Gilmore who were responsible for doing all the photometric service observations which have been so useful.

My understanding of the complex field of stellar pulsations has been much enhanced by discussions with: Stephenson Yang, David Gray, Arthur Cox, Paul Bradley and especially Joyce Guzik who helped me get up to speed with exactly what it is pulsational theorists do on those big computers in Los Alamos. Discussions with Alan Gilmore and Jovan Skuljan have also been fortuitous.

During the course of this work I have received financial support in the form of the following scholarships and awards: University of Canterbury Doctoral Scholarship, Sadie-Balkind Scholarship and Award, William & Ina Cartwright Scholarship, Roper Scholarship in Science and a Charles Cook, Warwick House, Memorial Scholarship. Without this support the course of my Ph.D. would have been much the rockier and I would like to thank the University of Canterbury Scholarship staff for their help, especially Jacky Creelman and Jane Bolton.

I would also like to acknowledge the funding provided by the Frank Bradshaw & Elizabeth Pepper Wood Fund, Royal Society of New Zealand's Young Scientist's Fund, my department's overseas conference allowance and the Los Alamos National Lab Conference Travel Grant, which allowed me to attend conferences in Los Alamos, New Mexico and Victoria, Canada.

My acknowledgements can not possibly be complete without thanking my fellow astronomy students Lyndon, Jovan, Ljiljana and Orlon for providing light relief, Ed and my other friends for not disowning me when I forgot to return their calls and emails, and my parents for supporting me even if they are not entirely certain exactly what it is I have been doing all these years.

This research has made use of the Simbad database, operated at CDS, Strasbourg, France and NASA's Astrophysics Data System Bibliographic Services.

References

[1] ABT, H. Wesselink's method and shock waves in RR Lyrae. *Ap. J. 130* (1959), 824–833.

[2] AIKAWA, T. The cause of the type I intermittency for hydrodynamic pulsation models. *Ap. & Space Sci. 149* (1988), 149–161.

[3] AIKAWA, T. Hydrodynamic pulsation models of yellow supergiant stars in the post-asymptotic giant branch. *Ap. J. 374* (1991), 700–706.

[4] ALLEN, C. *Astrophysical Quantities*, 3 ed. The Athlone Press, 1976.

[5] ANDO, H. Overstability of acoustic modes in late-type stars and its observational implication. *Publ. Astron. Soc. Japan 28* (1976), 517–531.

[6] ANTIA, H., ET AL. Convection in the envelopes of red giants. *Ap. J. 282* (1984), 574–583.

[7] BALMFORTH, N., ET AL. Pulsations of Arcturus. In *Challenges to theories of the structure of moderate-mass stars* (University of California, Santa Barbara, CA, USA, 1991), D. Gough and J. Toomre, Eds., vol. 388 of *Lecture Notes in Physics*, Springer-Verlag, pp. 381–386.

[8] BARANNE, A., ET AL. ELODIE: A spectrograph for accurate radial-velocity measurements. *Astron. & Astrophys. Suppl. Ser. 119* (1996), 373–390.

[9] BARNES, T. An independent distance scale for variable stars. In *Changing trends in variable star research* (Hamilton, NZ, 1979), F. Bateson et al., Eds., IAU Coll.46, University of Waikato, pp. 409–416.

[10] BARNES, T., ET AL. The distances of Cepheid variables. *Mon. Not. R. astr. Soc. 178* (1977), 661–674.

[11] BARNES, T., AND EVANS, D. Stellar angular diameters and visual surface brightness - I. late spectral types. *Mon. Not. R. astr. Soc. 174* (1976), 489–502.

[12] BARNES, T., AND EVANS, D. Stellar angular diameters and visual surface brightness - II. early and intermediate spectral types. *Mon. Not. R. astr. Soc. 174* (1976), 503–512.

[13] BARNES, T., AND EVANS, D. Stellar angular diameters and visual surface brightness - III. an improved definition of the relationship. *Mon. Not. R. astr. Soc. 183* (1978), 285–304.

[14] BATTEN, A. *Binary and multiple systems of stars*, vol. 50 of *Natural Philosophy*. Pergamon Press, 1973.

[15] BATTEN, A., ET AL. *Eighth Catalogue of the Orbital Elements of Spectroscopic Binary Systems*, vol. 17 of *Publications of the Dominion Astrophysical Observatory*. Dominion Astrophysical Observatory, 1989. Electronic version from "Selected Astronomical Catalogs" (ADC) used.

[16] BECKERS, J., ET AL. A high resolution spectral atlas of the solar irradiance from 380 to 700 Nanometers VII: graphical form. Tech. rep., Air Force Geophysics Laboratory, June 1976. Sacramento Peak Observatory Project 7649.

[17] BELMONTE, J., ET AL. Acoustic oscillations in the KIII star Arcturus. *Ap. & Space Sci. 169* (1990), 77–84.

[18] BESSELL, M. *UBVRI* photometry II: The Cousins *VRI* system, its temperature and absolute flux calibration, and relevance for two-dimensional photometry. *Publ. A.S.P. 91* (1979), 589–607.

[19] BESSELL, M., ET AL. Colors and stratification of extended static model photospheres of M stars located on the FGB, AGB and supergiant branch. *Astron. & Astrophys. Suppl. Ser. 89* (1991), 335–366.

[20] BESSELL, M., AND WOOD, P. A note on bolometric corrections for late-type stars and long-period variables. *Publ. A.S.P. 96* (1984), 247–249.

[21] BEVINGTON, P., AND ROBINSON, D. *Data reduction and error analysis for the physical sciences.* McGraw-Hill, 1992.

[22] BOHLENDER, D., ET AL. Precise $\Delta T_{\rm eff}$ and $\Delta(R-I)$ for solar-type stars. *Publ. A.S.P. 104* (1992), 1152–1159.

[23] BOPP, B., AND STENCEL, R. The FK Comae stars. *Ap. J. 247* (1981), L131–L134.

[24] BOWEN, G. Dynamical modelling of long-period variable star atmospheres. *Ap. J. 329* (1988), 299–317.

[25] BOWEN, G. Dynamical phenomena in pulsating star atmospheres. In *The numerical modelling of nonlinear stellar pulsation: problems and prospects* (Les Arcs, France, 1990), J. Buchler, Ed., vol. 302 of *Series C*, Kluwer Academic Publishers, pp. 155–171. Proceedings of a NATO advanced research workshop.

[26] BRACEWELL, R. *The Fourier transform and its application.* McGraw-Hill, 1965.

[27] BRAULT, J., AND WHITE, O. The analysis and restoration of astronomical data via the Fast Fourier Transform. *Astron. & Astrophys. 13* (1971), 169–189.

[28] BRIGHAM, E. *The Fast Fourier Transform.* Prentice-Hall, 1974.

[29] BUCHLER, J., AND KOVÁCS, G. Period doubling bifurcations and chaos in W Virginis models. *Ap. J. 320* (1987), L57–L62.

[30] BURKI, G., AND MEYLAN, G. RR Lyrae, Delta Scuti, SX Phoenicis stars and Baade-Wesselink method II. physical parameters and distance of RR Cet. *Astron. & Astrophys. 156* (1986), 131–136.

[31] BUTLER, R., ET AL. Attaining Doppler precision of 3 m/s. *Publ. A.S.P. 108* (1996), 500–509.

[32] CAMPBELL, B., ET AL. Evidence for periodic radial velocity variation in Arctrus. Presentation at 160th AAS meeting, Troy, NY, 1982.

[33] CAMPBELL, B., ET AL. A search for substellar companions to solar-type stars. *Ap. J. 331* (1988), 902–921.

[34] CASTOR, J. A simplified picture of the Cepheid phase lag. *Ap. J. 154* (1968), 793–798.

[35] CASTOR, J. On the calculation of linear, nonadiabatic pulsations of stellar models. *Ap. J. 166* (1971), 109–129.

[36] CLAYTON, D. *Principles of stellar evolution and nucleosynthesis.* The University of Chicago Press, 1983.

[37] COCHRAN, W. Confirmation of radial velocity variability in Arcturus. *Ap. J. 334* (1988), 349–356.

[38] COX, A., ET AL. *Astrophysical processes in upper main sequence stars.* No. 13 in Advanced course of the Swiss society of astronomy and astrophysics. Geneva Observatory, 1983.

[39] COX, J. Pulsating stars. *Rep. Prog. Phys. 37* (1974), 563–698.

[40] COX, J. *Theory of Stellar Pulsation.* Princeton University Press, 1980.

[41] COX, J., AND GIULI, R. *Principles of stellar structure*, vol. 2. Gordon and Breach, science publishers, 1968.

[42] COX, J., AND GIULI, R. *Principles of stellar structure*, vol. 1. Gordon and Breach, science publishers, 1968.

[43] CUMMINGS, I., HEARNSHAW, J., CLARK, M., WALKER, W., AND WILLIAMS, H. High precision radial-velocity measurements of late-type giant stars. *Southern Stars 36* (1996), 201–210.

[44] CUMMINGS, I., HEARNSHAW, J., GILMORE, A., AND KILMARTIN, P. High precision observations of small amplitude radial-velocity variations in red giants. In *A Half Century of Stellar Pulsation Interpretations: A Tribute to Arthur N. Cox* (Los Alamos, New Mexico, USA, 1998), P. Bradley and J. Guzik, Eds., vol. 135 of *ASP Conference Series*, pp. 213–218.

[45] DAVID, M., AND VERSCHUEREN, W. Model-mismatch errors in least-squares 1-D centering. *Astron. & Astrophys. Suppl. Ser. 111* (1995), 183–193.

[46] DORREN, J., AND GUINAN, E. Evidence for starspots on single solar-like stars. *Astron. J. 87* (1982), 1546–1557.

[47] DRAVINS, D., AND NORDLUND, A. Stellar granulation V. Synthetic spectral lines in disk-integrated starlight. *Astron. & Astrophys. 228* (1990), 203–217.

[48] DUPUY, D., AND HOFFMAN, G. A Jurkevisch period search program. *IAPP*, 20 (June 1985), 1–17.

[49] DYSON, J., AND WILLIAMS, D. *The physics of the interstellar medium.* Manchester University Press, 1980.

[50] ESA. The Hipparcos and Tycho catalogues, 1997. SP-SP1200.

[51] FOKIN, A. Nonlinear pulsations of the RV Tauri stars. *Astron. & Astrophys. 292* (1994), 133–151.

[52] FUKUDA, I. A statistical study of rotational velocities of the stars. *Publ. A.S.P. 94* (1982), 271–284.

[53] FURENLID, I., AND FURENLID, L. A variation of the cross-correlation technique. *Publ. A.S.P. 102* (1990), 592–597.

[54] GAPOSCHKIN, S. On γ Velorum, ϵ Carinae and a Carinae as eclipsing variables. *Astron. J. 64* (1959), 127.

[55] GILMOUR, A. Standards reduction procedure, 1987. Unpublished, Memorandum.

[56] GRAY, D. *The observation and analysis of stellar photospheres.* John Wiley and Sons, 1976.

[57] GRAY, D. Rotation and turbulence in G giants. *Ap. J. 251* (1981), 155–161.

[58] GRAY, D. The temperature dependence of rotation and turbulence in giant stars. *Ap. J. 262* (1982), 682–699.

[59] GRAY, D. *Lectures on spectral-line analysis: F, G and K stars.* The Publisher, 1988.

[60] GRAY, D. Nonthermal phenomena in the photospheres of cool stars. In *FGK stars and T Tauri stars* (1989), L. Cram et al., Eds., SP-502, NASA.

[61] GRAY, D. *The observation and analysis of stellar photospheres*, 2 ed., vol. 20 of *Cambridge Astrophysics Series.* Cambridge University Press, 1992.

[62] GRAY, D., AND NAGAR, P. The rotational discontinuity shown by luminosity class IV stars. *Ap. J. 298* (1985), 756–760.

[63] GRAY, D., AND TONER, C. Rotation and macroturbulence in bright giants. *Ap. J. 310* (1986), 277–283.

[64] GRAY, D., AND TONER, C. An analysis of the photospheric line profiles in F, G and K supergiants. *Ap. J. 322* (1987), 360–367.

[65] GRIFFIN, R. A photoelectric radial-velocity spectrometer. *Ap. J. 148* (1967), 465–476.

[66] GRIFFIN, R. *A photometric atlas of the spectrum of Arcturus : 3600-8825 Å.* Cambridge Philosophical Society, 1968.

[67] GRIFFIN, R., AND GRIFFIN, R. On the possibility of determining stellar radial velocities to 0.01 km/s. *Mon. Not. R. astr. Soc. 162* (1973), 243–253.

[68] HACKER, S. *The spectrum of Arcturus.* No. 16. Contrib. Princeton Uni. Observ., 1935.

[69] HANSEN, C., AND KAWALER, S. *Stellar Interiors: Physical principles, structure, and evolution.* Astronomy and Astrophysics Library. Springer-Verlag, 1994.

[70] HARDIE, R. *Astronomical Techniques.* In Hiltner [86], 1962, ch. Photoelectric Reductions, pp. 178–208.

[71] HARMANEC, P. A reliable transformation of Hipparcos H_P magnitudes into Johnson V and B magnitdues. *Astron. & Astrophys. 335* (1998), 173–178.

[72] HATZES, A. Simulations of stellar radial-velocity and spectral line bisector variations I. Nonradial pulsations. *Publ. A.S.P. 108* (1996), 839–843.

[73] HATZES, A., AND COCHRAN, W. Long-period radial velocity variations in three K giants. *Ap. J. 413* (1993), 339–348.

[74] HATZES, A., AND COCHRAN, W. The radial velocity variability of the K giant β Oph: I. the detection of low-amplitude, short-period pulsations. *Ap. J. 432* (1994), 763–769.

[75] HATZES, A., AND COCHRAN, W. Short-period radial velocity variations of α Bòòtis: evidence for radial pulsations. *Ap. J. 422* (1994), 366–373.

[76] HATZES, A., AND COCHRAN, W. The radial velocity variability of the K giant β Ophiuchi: II. the long-period variations. *Ap. J. 468* (1996), 391–397.

[77] HAWLEY, S., AND BARNES, T. A surface brightness analysis of eight RR Lyrae stars. In *Stellar Pulsation* (Los Alamos, New Mexico, USA, 1987), A. Cox et al., Eds., vol. 274 of *Lecture Notes in Physics*, Memorial to John P. Cox, Springer-Verlag, pp. 235–238.

[78] HEARNSHAW, J. The Cassegrain Echelle spectrograph at Mt John Observatory. *Astronomical Society of Australia 3*, 2 (1977), 102–103. Proceedings.

[79] HEARNSHAW, J. *The analysis of starlight: One hundred and fifty years of astronomical spectroscopy.* Cambridge University Press, 1986.

[80] HEARNSHAW, J. The analysis of starlight: some comments on the development of stellar spectroscopy, 1815-1965. *Vistas in Astron. 30* (1987), 319–375.

[81] HEARNSHAW, J. Doppler and Vogel - two notable anniversaries in stellar astronomy. *Vistas in Astron. 35* (1992), 157–177.

[82] HEARNSHAW, J. The measurement of stellar radial velocities: Part I: a century of progress. In *Current topics in astrofundamental physics*, N. Sanchez and C. Aichichi, Eds., Science and culture - Astrophysics. World Scientific Publishing, Erice, Italy, 1992, pp. 739–745. International School of Astrophysics "D Chalonge".

[83] HILDEBRAND, F. *Advanced calculus for applications*, second ed. Prentice-Hall, 1976.

[84] HILL, G. The reduction of spectra-IV VCROSS, and interactive cross-correlation velocity program. *Publications of the Dominion Astrophysical Observatory XVI*, 5 (1982), 59–66. NRC NO.20445.

[85] HILL, S., AND WILLSON, L. Theoretical velocity structure of long-period variable star photospheres. *Ap. J. 229* (1979), 1029–1045.

[86] HILTNER, W., Ed. *Astronomical Techniques.* Stars and Stellar Systems, Compendium of Astronomy. The University of Chicago Press, 1962.

[87] HINKLE, K. Infrared spectroscopy of Mira variables. I. R Leonis: the CO and OH vibration-rotation overtone bands. *Ap. J. 220* (1978), 210–228.

[88] HINKLE, K., AND BARNES, T. Infrared spectroscopy of Mira variables. II. R Leonis: The H_2O vibration-rotation bands. *Ap. J. 227* (1979), 923–934.

[89] HINKLE, K., AND BARNES, T. Infrared spectroscopy of Mira variables. III. R Leonis: The atomic lines. *Ap. J. 234* (1979), 548–555.

[90] HINKLE, K., ET AL. Time series infrared spectroscopy of the Mira variable χ Cygni. *Ap. J. 252* (1982), 697–714.

[91] HIRSHFELD, A., AND SINNOTT, R., Eds. *Sky Catalogue 2000.0: Double Stars, Variable Stars and Nonstellar Objects*, vol. 2. Cambridge University Press, 1985.

[92] HOFFLEIT, D. *The Bright Star Catalogue*, 4 ed. Yale University Observatory, 1982.

[93] HOFFMEISTER, C., ET AL. *Variable Stars.* Springer-Verlag, 1985. Translation of the second German edition of Veränderliche Sterne.

[94] HOUK, N. Michigan catalogue of two-dimensional spectral types for the HD stars. Ann Arbor, Dept. of Astronomy, Univ. Michigan, 1978. Volume 2.

[132] PILACHOWSKI, C., ET AL. Velocity structure in long period variable star atmospheres. In *Current Problems in Stellar Pulsation Instabilities* (Goddard Space Flight Centre, Greenbelt, Maryland, 1980), D. Fischel et al., Eds., TM-80625, NASA, pp. 577–609.

[133] POLLARD, K. *The nature of the low mass supergiants: RV Tauri and R Coronae Borealis variables.* PhD thesis, University of Canterbury, 1994.

[134] PRESS, W., ET AL. *Numerical Recipes, The Art of Scientific Computing.* Cambridge University Press, 1989.

[135] PRESS, W., AND TEUKOLSKY, S. Search algorithm for weak periodic signals in unevenly spaced data. *Computers in Physics* (Nov/Dec 1988), 77–82.

[136] QUERCI, M. Spectroscopy and nonthermal processes. In *The M-type stars* (1986), H. Johnson and F. Querci, Eds., SP-492, NASA, pp. 113–208.

[137] READER, J., ET AL. *Wavelength and transition probabilities for Atoms and Atomic Ions*, vol. NSRDS-NBS 68 of *National Standard Reference Data System.* United States Department of Commerce, 1980.

[138] ROBERTS, D., ET AL. Time series analysis with CLEAN. I. Derivation of a spectrum. *Astron. J. 93* (1987), 968–989.

[139] ROSSELAND, S. *The Pulsation Theory of Variable Stars.* The International Series of Monographs on Physics. Oxford University Press, 1949.

[140] SAHADE, J., AND WOOD, F. *Interacting Binary Stars*, vol. 95 of *Natural Philosophy.* Pergamon Press, 1978.

[141] SASSELOV, D. Normal supergiants and their imitations I. Sodium as a mass indicator? *Publ. A.S.P. 98* (1986), 561–571.

[142] SCARGLE, J. Studies in astronomical timeseries analysis. II. Statistical aspects of spectral analysis of unevenly spaced data. *Ap. J. 263* (1982), 835–853.

[143] SCHAIFERS, K., AND VOIGT, H., Eds. *Landolt-Börnstein: Numerical Data and Function Relationships in Science and Technology*, vol. 2b of *Group VI: Astronomy, Astrophysics and Space Research.* Springer-Verlag, 1982. Stars and Star Clusters.

[144] SCHALLER, G. Pulsation of supergiant stars. In *Confrontations between stellar pulsation and evolution* (Bologna, 1990), C. Cacciari and G. Clementini, Eds., vol. 11 of *ASP Conference Series*, pp. 300–303.

[145] SCHALLER, G., ET AL. New grids of stellar models from 0.8 to 120 $M_\odot$ at $Z = 0.020$ and $Z = 0.001$. *Astron. & Astrophys. Suppl. Ser. 96* (1992), 269–331.

[146] SCHATZMAN, ET AL. *The Stars.* Springer-Verlag, 1993.

[147] SCHMIDT, E. A photometric study of four classical Cepheids. *Ap. J. 165* (1971), 335–363.

[148] SCHRIJERS, C., ET AL. Line-profile variations due to adiabatic non-radial pulsations in rotating stars I. Observable charactersitcs of spheroidal modes. *Astron. & Astrophys. Suppl. Ser. 121* (1997), 343–368.

[149] SCHWARZSCHILD, M. On the scale of photospheric convection in red giants and supergiants. *Ap. J. 195* (1975), 137–144.

[150] SHIBAHASHI, H., AND OSAKI, Y. Vibrational stability of gravity modes in massive stars during the shell-hydrogen-burning stage. *Publ. Astron. Soc. Japan 28* (1976), 533–542.

[151] SIMKIN, S. Measurements of velocity dispersions and Doppler shifts from digitized optical spectra. *Astron. & Astrophys. 31* (1974), 129–136.

[152] SKULJAN, J., ET AL. Absolute radial velocities by cross-correlation with synthetic spectra. In *Precise stellar radial velocities* (1999?), J. Hearnshaw and C. Scarfe, Eds., ASP Conference Series, IAU Coll. 170. In Press.

[153] SLETTEBAK, A. Stellar axial rotation and equatorial breakup. *Ap. J. 145* (1966), 126–129.

[154] SMITH, M. Precise radial velocities. I - A preliminary search for oscillations in Arcturus. *Ap. J. 253* (1982), 727–734.

[155] SMITH, M. Precise radial velocities II. A possible detection of oscillation or running waves in Adebaran and Arcturus. *Ap. J. 265* (1983), 325–330.

[156] SMITH, M., ET AL. Radial velocity variations in α Ori, α Sco and α Her. *Astron. J. 98* (1989), 2233–2248.

[157] SMITH, P., ET AL. Evidence for periodic radial velocity variation in Arctrus. *Ap. J. 317* (1987), L79–L84.

[158] SOBOUTI, Y. A definition of the g- and p-modes of self-gravitating fluids. *Astron. & Astrophys. 55* (1977), 327–337.

[159] STERKEN, C., AND JASCHEK, C., Eds. *Light curves of variable stars: A Pictorial Atlas.* Cambridge University Press, 1996.

[160] STROHMEIER, W. *Variable Stars.* Pergamon Press, 1972.

[161] SWINGLER, D. A relationship between the Jurkevich periodogram and the Fourier transform spectral estimator. *Astron. J. 90* (1985), 675–679.

[162] TAKEUTI, M. Regular and irregular pulsations. In *The numerical modelling of nonlinear stellar pulsation: problems and prospects* (Les Arcs, France, 1990), J. Buchler, Ed., vol. 302 of *Series C*, Kluwer Academic Publishers, pp. 121–141. Proceedings of a NATO advanced research workshop.

[163] TASSOUL, J. *Theory of rotating stars.* Princeton Series in Astrophysics. Princeton University Press, 1978.

[164] TAYLOR, B. Transformation equations and other aids for *VRI* photometry. *Ap. J. Suppl. 60* (1986), 577–599.

[165] TOBIN, W. Astronomical photometry, 1993. Unpublished, Lectures at the University of Canterbury.

[166] TONER, C., AND GRAY, D. The starpatch on the G8 dwarf ξ Bóòtis A. *Ap. J. 334* (1988), 1008–1020.

[167] UNNO, W., ET AL. *Nonradial oscillations of stars.* University of Tokyo Press, 1979.

[168] VOGT, S., ET AL. Doppler images of rotating stars using maximum entropy image reconstruction. *Ap. J. 321* (1987), 496–515.

[169] VOGT, S., AND PENROD, G. Doppler imaging of spotted stars - application to the RS Canum Venaticorum star HR 1099. *Publ. A.S.P. 95* (1983), 565–576.

[170] WALKER, G., ET AL. Yellow giants: A new class of radial velocity variable? *Ap. J. 343* (1989), L21–L24.

[171] WALKER, G., ET AL. γ Cephei: Rotation or planetary companion? *Ap. J. 396* (1992), L91–L94.

[172] WALKER, M. A second photoelectric study of 16 Lacertae. *Ap. J. 120* (1954), 58–65.

[173] WALKER, M. Three-color photoelectric photometry of HD 199140. *Ap. J. 119* (1954), 631–639.

[174] WALKER, W. Cool giants and supergiants. Presented at the 75th annual RASNZ conference. This may be published at a later date in Southern Stars, July 1998.

[175] WALKER, W., ET AL. L^2 Puppis — a multiple-period pulsator? *Southern Stars 34* (1992), 381–391.

[176] WESSELINK, A. Surface brightnesses in the U, B, V system with application of M_V and dimensions of stars. *Mon. Not. R. astr. Soc. 144* (1969), 297–311.

[177] WILLSON, L. The interpretation of radial velocity observation of long period variable stars. In *Changing trends in variable star research* (Hamilton, NZ, 1979), F. Bateson et al., Eds., IAU coll. 46, University of Waikato, pp. 199–211.

[178] WILLSON, L. IUE observations of pulsating stars: Atmospheric structure, shock waves and stellar winds. In *A decade of UV astronomy with the IUE satellite* (Goddard Space flight centre, Greenbelt Maryland, USA, 1988), E. Rolfe, Ed., vol. 1 of *SP-281*, ESA, NASA, pp. 29–40.

[179] WILLSON, L., ET AL. Atmospheric kinematics of high velocity long period variables. *Mon. Not. R. astr. Soc. 198* (1982), 483–516.

[180] WOOD, P. Models of asymptotic-giant-branch stars. *Ap. J. 190* (1974), 609–630.

[181] WOOD, P. Pulsation and evolution of Mira variables. In *From Miras to planetary nebulae: Which path for stellar evolution?* (Montpellier, France, 1990), M. Mennessier and A. Omont, Eds., Editions Frontieres, pp. 67–84.

[182] WORLEY, C., AND HEINTZ, W. 4th catalog of orbits of visual binaries. Publ. U.S. Naval Obs. (2) 24, part VII, 1983. Electronic version from "Selected Astronomical Catalogs" (ADC) used.

[183] YA'ARI, A., AND YUCHMAN, Y. Long-term nonlinear thermal effects in the pulsation of Mira variables. *Ap. J. 456* (1996), 350–355.